*Research sponsored by the Office of Fusion Energy, U.S. Department of Energy, under contract DE-AC05-84OR21400 with Martin Marietta Energy Systems, Incorporated.

Proceedings of

U.S.–Japan

Heliotron-Stellarator

Workshop

Volume III

held at

Oak Ridge National Laboratory
Oak Ridge, Tennessee, U.S.A.

November 9-13, 1987

CONF-871179--Vol.3

DE88 004788

AGENDA FOR US-JAPAN STELLARATOR/HELIOTRON WORKSHOP

FUSION ENGINEERING DESIGN CENTER, OAK RIDGE

NOVEMBER 9–13, 1987

Table of Contents

Monday, November 9

Tuesday, November 10

1:00 P.M. Confinement - O. Motojima, Chairman Volume II

Ripple Transport at Arbitrary Collision Frequency – W.N.G. Hitchon (U. Wisc.)

Transport Scaling in the Collisionless–Detrapping Regime – E. C. Crume (ORNL)

Transport Analysis for Heliotron E – T. Mutoh (Kyoto PPL)

Transport Analysis for ATF – H. C. Howe (ORNL)

Simulation Analysis of Heating and Transport – T. Amano (Nagoya IPP)

Analysis of W VII-A Data – H. Renner (IPP Garching)

7:00 P.M. Reception - Home of W. R. Wing

Wednesday, November 11

8:30 A.M. ECH and NBI - M. Murakami, Chairman

Numerical Study of Fast Ion Confinement – K. Hanatani (Kyoto, PPL)

Benchmarks of NBI Codes for Stellarators – R. H. Fowler (ORNL)

ECH Commissioning and Plans for ATF – T. L. White (ORNL)

ECH and ICH Startup Analysis – M. D. Carter (ORNL)

11:30 A.M. Lunch

1:00 P.M. Ion Cyclotron Heating - T. Amano, Chairman Volume III

Heliotron E ICRF Heating Experiment – T. Mutoh (Kyoto PPL)

CHS Heating Systems (NBI, ECH, ICH) – K. Nishimura (Nagoya IPP)

ICH Program for ATF – F. W. Baity (ORNL)

ICRF Wave Propagation – D. B. Batchelor (ORNL)

The HBQM Heliac Work – B. A. Nelson (U. Washington)

Volume III (continued)

Thursday, November 12

8:30 A.M. Configuration Studies - G. H. Neilson, Chairman

Configuration Studies – K. Nishimura (Nagoya IPP)

Compact Torsatron Studies – B. A. Carreras (ORNL)

Low Aspect Ratio Torsatron Design – J. Hanson (Auburn)

Optimized Small Stellarator Designs – D. T. Anderson (U. Wisc.)

Configuration Studies for ATF – J. H. Harris (ORNL)

11:30 A.M. Lunch

1:00 P.M. Configuration Studies - K. Matsuoka, Chairman

Currents in ATF – B. A. Carreras (ORNL)

Computations of 3-D Equilibria with Islands – A. Reiman (PPPL)

Magnetic Surface Mapping Studies – D. G. Swanson (Auburn)

Magnetic Field Alignment and Mapping on ATF – F.S.B. Anderson (U. Wisc.)

Divertor Experiments in IMS – D. T. Anderson (U. Wisc.)

Friday, November 13

8:30 A.M. General Experimental - H. Renner, Chairman

PMI Program and Wall Conditioning for ATF – P. K. Mioduszewski (ORNL)

Hard X-ray Suppression on ATF – D. A. Rasmussen (ORNL)

Plasma Rotation and Potential Measurement – O. Motojima, (Kyoto PPL)

Status of Heavy Ion Beam Probe for ATF – A. Carnevali (RPI)

11:30 A.M. Lunch

1:00 P.M. Private discussions, Fusion Energy Division

Visit to Large Coil Facility?

ICRF HEATING IN HELIOTRON E

T. MUTOH
HELIOTRON GROUP

ICRF SYSTEMS

FAST WAVE HEATING
- H & 3He MINORITY HEATING
- SECOND HARMONIC HEATING

HIGH ENERGY TAIL FORMATION &
HIGH ENERGY PARTICLE CONFINEMENT

ICRF HEATING OBJECTIVES

- TO STUDY THE PHYSICS OF ICRF HEATING IN HELICAL SYSTEM
- TO DEVELOP THE OPTIMUM PROGRAM TO OBTAIN HIGH ION TEMPERATURE PLASMA
- TO STUDY THE CONFINEMENT PROPERTIES OF ICRF HEATED PLASMA, ESPECIALLY IN RARE COLLIONAL REGIME
- TO STUDY THE CONFINEMENT OF HIGH ENERGY PARTICLES IN HELICAL SYSTEM

HELIOTRON E ICRF ANTENNA CHARACTERISTICS

- Four pairs of loop antennas (eight loops) with four feed through ports were used.

- 70 % part of the each antenna loop excited waves from hig field side, and the residual part excited from the low field side.

- The sizes of an antenna are followings.
  Length = 50 cm, Width = 10 cm,
  Hight = 4 ~ 7 cm

- The antennas were distributed in half area of the toroidal section.

- Antenna materials

central conducter:	Copper coated SUS 304	
Faraday shield:	outer	Titanium
	inner	SUS 304
Side protecter:	TiC coated SUS 304 (~'87, March)	
	Carbon ('87 April ~)	

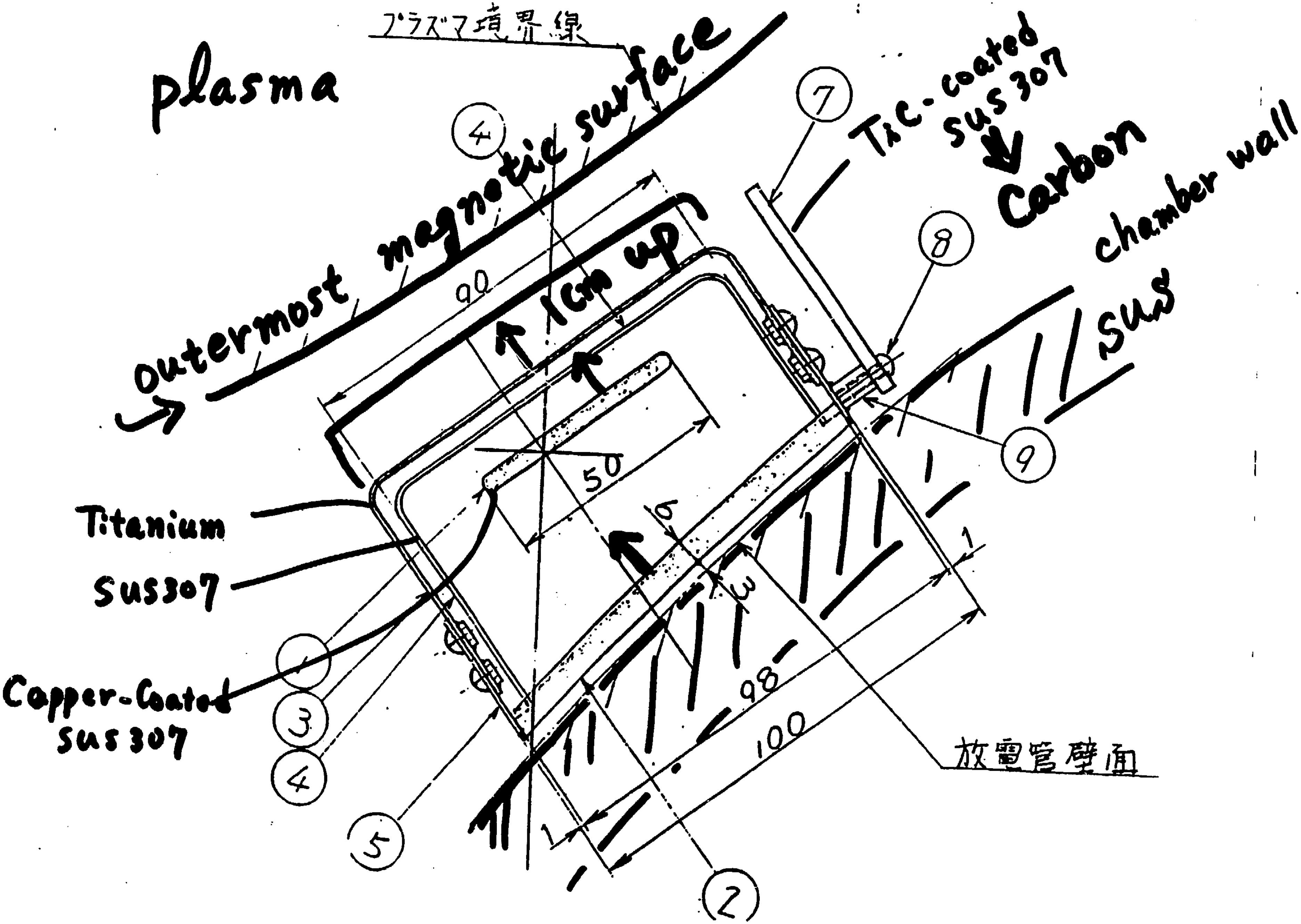

プラズマ境界線
plasma
outermost magnetic surface
1cm up
TiC-coated
SUS 307
Carbon
chamber wall
SUS
90
50
6
3
98
100
1
1
Titanium
SUS307
Copper-Coated
SUS 307
放電管壁面
1
2
3
4
4
5
7
8
9

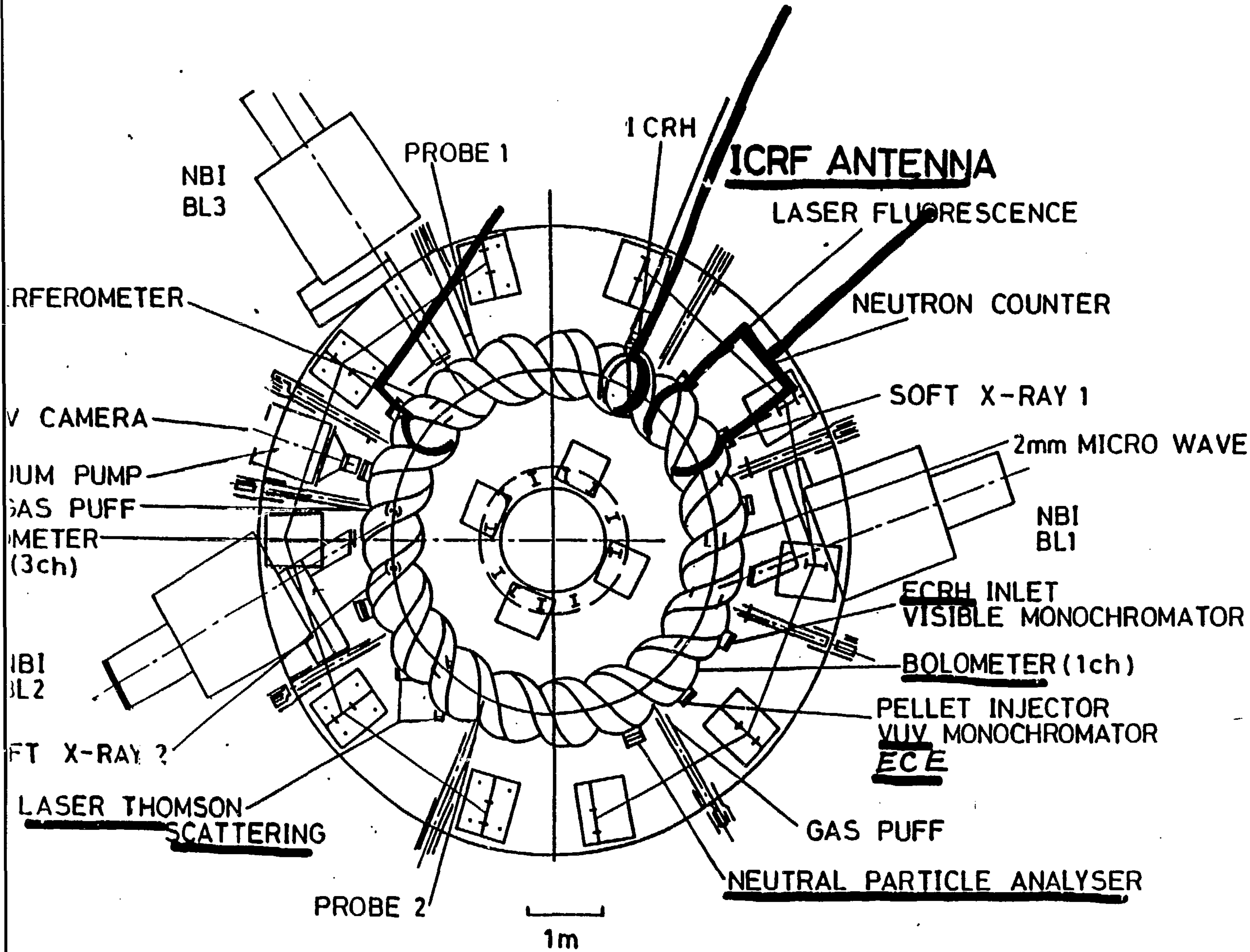

NBI
BL3
PROBE 1
1 CRH
ICRF ANTENNA
LASER FLUORESCENCE
RFEROMETER
NEUTRON COUNTER
SOFT X-RAY 1
V CAMERA
2mm MICRO WAVE
UUM PUMP
GAS PUFF
METER
(3ch)
NBI
BL1
ECRH INLET
VISIBLE MONOCHROMATOR
BOLOMETER (1ch)
PELLET INJECTOR
VUV MONOCHROMATOR
ECE
FT X-RAY 2
LASER THOMSON
SCATTERING
GAS PUFF
NEUTRAL PARTICLE ANALYSER
PROBE 2
1m

ICRF HARDWARE CHARACTERISTICS

Power source			
tube	TH518		
max. power	1.5MW x 2		
pulse length	200 msec		
Frequencies	26.7 MHz	1.75 T	H minority, D majority
&	28.22 MHz	1.85 T	H minority, D majority
Heating modes	17.8 MHz	1.75 T	^{3}He minority, D majority
	53.4 MHz	1.75	H 2nd Harmonic
	58.2 MHz	1.86	H 2nd Harmonic

ECH (53.2 GHz) frequency resonate with B = 1.9 T

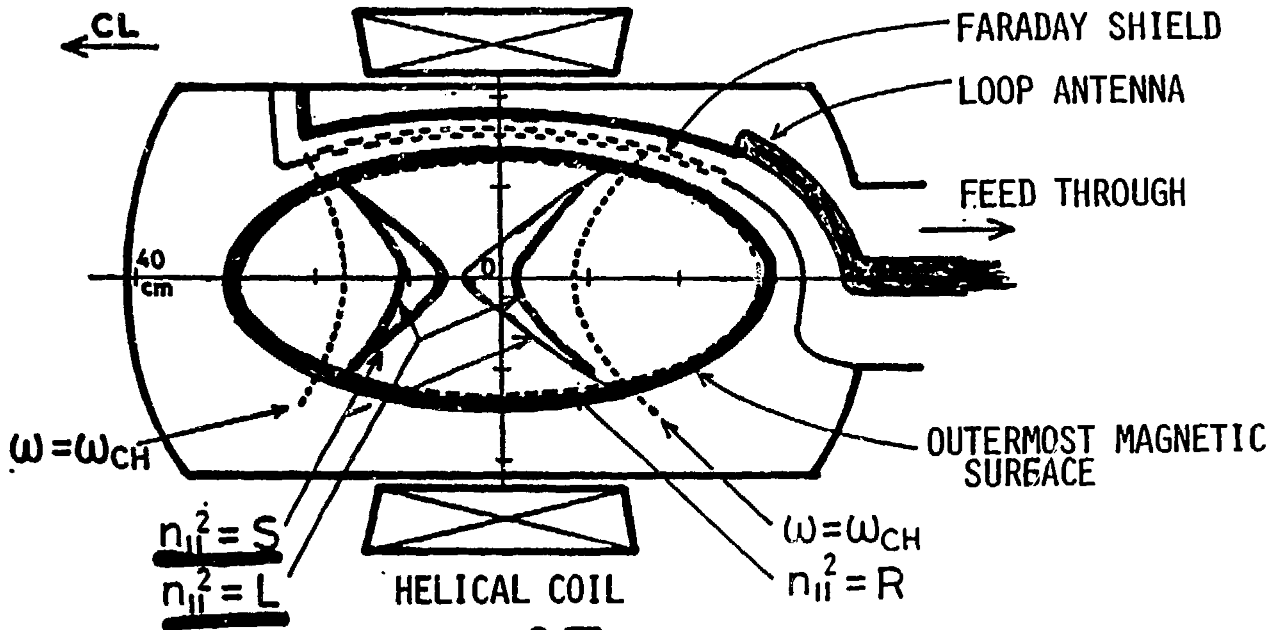

$B = 1.9$ T

$f_{\cdot} = 26.7$ MHz

$H/H+D = 0.15$

$k_{\parallel} = 8.6\ m^{-1}$

$n_e(0) = 4 \times 10^{19}\ m^{-3}$

```
RF   = 28.220   BB  =  1.860   RRC =  0.270   IJ  AJ  PHASE      R          X
RKZ  =  4.318   RA  =  0.140   H1  =  4.318    1  1.0   0.0   1.904E-01 -6.776E-01
NNOD=     907   NELM=   1700   P= 1.904E-01
```

IS	PA	PZ	PN	PNS	PZCL	PTPR	PTPP	PTS	PABS
1	5.446E-04	-1.	3.000E-01	1.000E-02	0.010	0.500	0.500	0.0	3.045E-02
2	2.000E+00	1.	2.970E-01	9.900E-03	0.010	0.500	0.500	0.0	3.076E-02
3	1.000E+00	1.	3.000E-03	1.000E-04	0.010	0.500	0.500	0.0	1.291E-01

by A. Fukuyama (Okayama Univ.) et al.

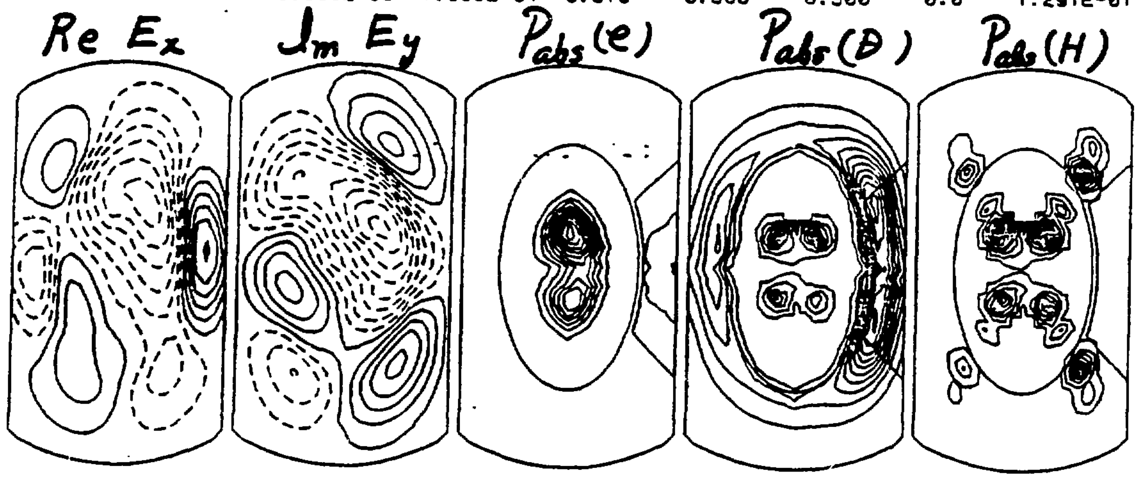

EX REAL	EY IMAG	PABS IS= 1	PABS IS= 2	PABS IS= 3
STP= 10	STP= 10	STP= 10	STP= 10	STP= 10
MAX= 2.29E+01	MAX= 1.42E+01	MAX= 2.09E+00	MAX= 6.31E-01	MAX= 8.75E+00
MIN=-2.44E+01	MIN=-2.34E+01	MIN= 9.62E-11	MIN=-7.64E-14	MIN=-1.05E-15
DLT= 4.07E+00	DLT= 2.99E+00	DLT= 2.09E-01	DLT= 6.31E-02	DLT= 8.75E-01

$B = 1.86\,T$ $\quad T_e(0) = 500\,eV$

$f = 28.22\,MHz$ $\quad T_i(0) = 500\,eV$

$n_e(0) = 3 \times 10^{19}\,m^{-3}$

$H/D = 0.01$

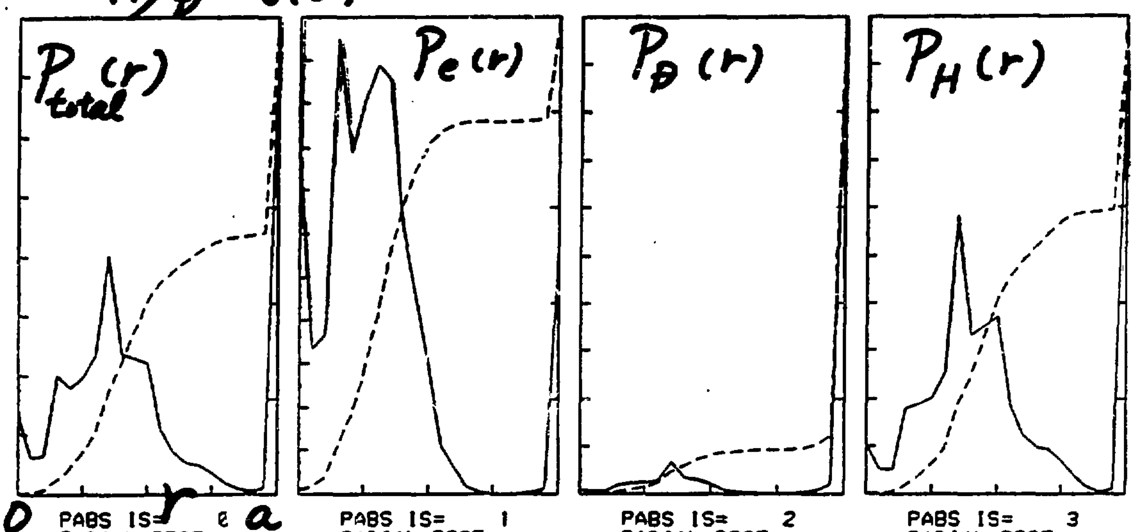

PABS IS= 0	PABS IS= 1	PABS IS= 2	PABS IS= 3
RADIAL PROF	RADIAL PROF	RADIAL PROF	RADIAL PROF
MAX= 7.47E-03	MAX= 1.05E-03	MAX= 2.35E-03	MAX= 4.56E-03
MIN= 4.16E-05	MIN= 1.50E-07	MIN= 1.86E-06	MIN= 1.60E-05
DLT= 1.00E-03	DLT= 1.00E-04	DLT= 2.50E-04	DLT= 5.00E-04

A. Fukuyama

RF = 26.700	BB = 1.900	RRC = 0.270	IJ	AJ	PHASE	R	X		
RKZ = 4.318	RA = 0.140	HI = 4.318	1	1.0	0.0	2.793E-01	-1.983E+00		
NNOD= 907	NELM= 1700	P= 2.793E-01							

IS	PA	PZ	PN	PNS	PZCL	PTPR	PTPP	PTS	PABS
1	5.446E-04	-1.	3.000E-01	1.000E-02	0.010	0.500	0.500	0.0	1.343E-02
2	2.000E+00	1.	2.550E-01	8.500E-03	0.010	0.500	0.500	0.0	1.984E-03
3	1.000E+00	1.	4.500E-02	1.500E-03	0.010	0.500	0.500	0.0	2.639E-01

EX REAL
STP= 10
MAX= 1.29E+01
MIN=-4.72E+00
DLT= 1.46E+00

EY IMAG
STP= 10
MAX= 1.35E+01
MIN=-5.27E-01
DLT= 1.55E+00

PABS IS= 1
STP= 10
MAX= 8.90E-01
MIN= 5.73E-10
DLT= 8.90E-02

PABS IS= 2
STP= 10
MAX= 9.49E-02
MIN=-2.40E-15
DLT= 9.49E-03

PABS IS= 3
STP= 10
MAX= 3.95E+01
MIN=-4.33E-15
DLT= 3.95E+00

$B = 1.9\,T$

$T_e(0) = T_i(0) = 500\ eV$

$f = 26.7\,MHz$

$n_e(0) = 3 \times 10^{19}\,m^{-3}$

$H/D = 0.15$

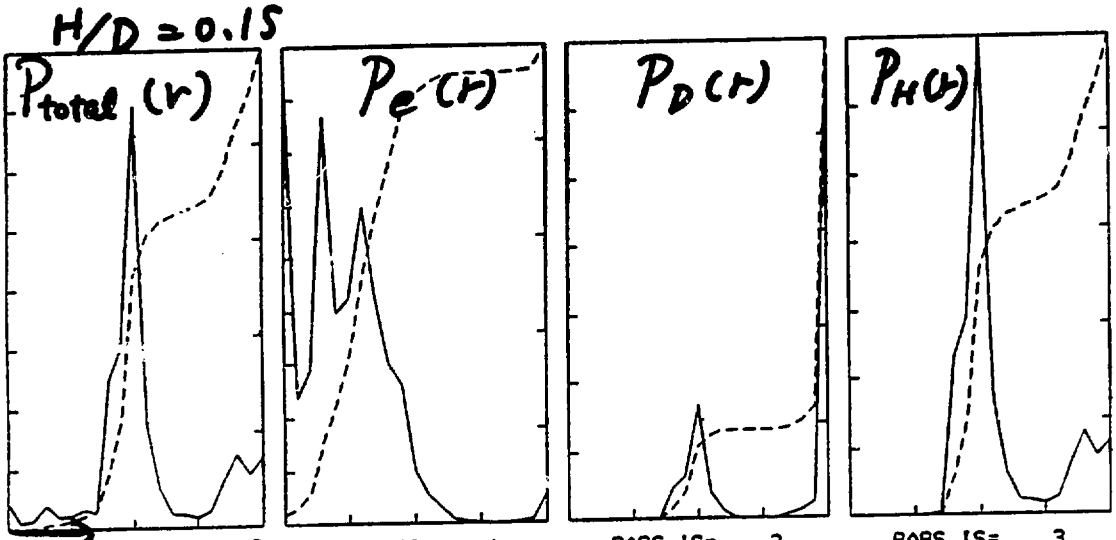

PABS IS= 0
RADIAL PROF
MAX= 1.41E-02
MIN= 2.36E-04
DLT= 2.00E-03

PABS IS= 1
RADIAL PROF
MAX= 8.80E-04
MIN= 1.18E-07
DLT= 1.00E-04

PABS IS= 2
RADIAL PROF
MAX= 1.33E-04
MIN=-6.06E-19
DLT= 2.00E-05

PABS IS= 3
RADIAL PROF
MAX= 1.40E-02
MIN=-8.11E-19
DLT= 2.00E-03

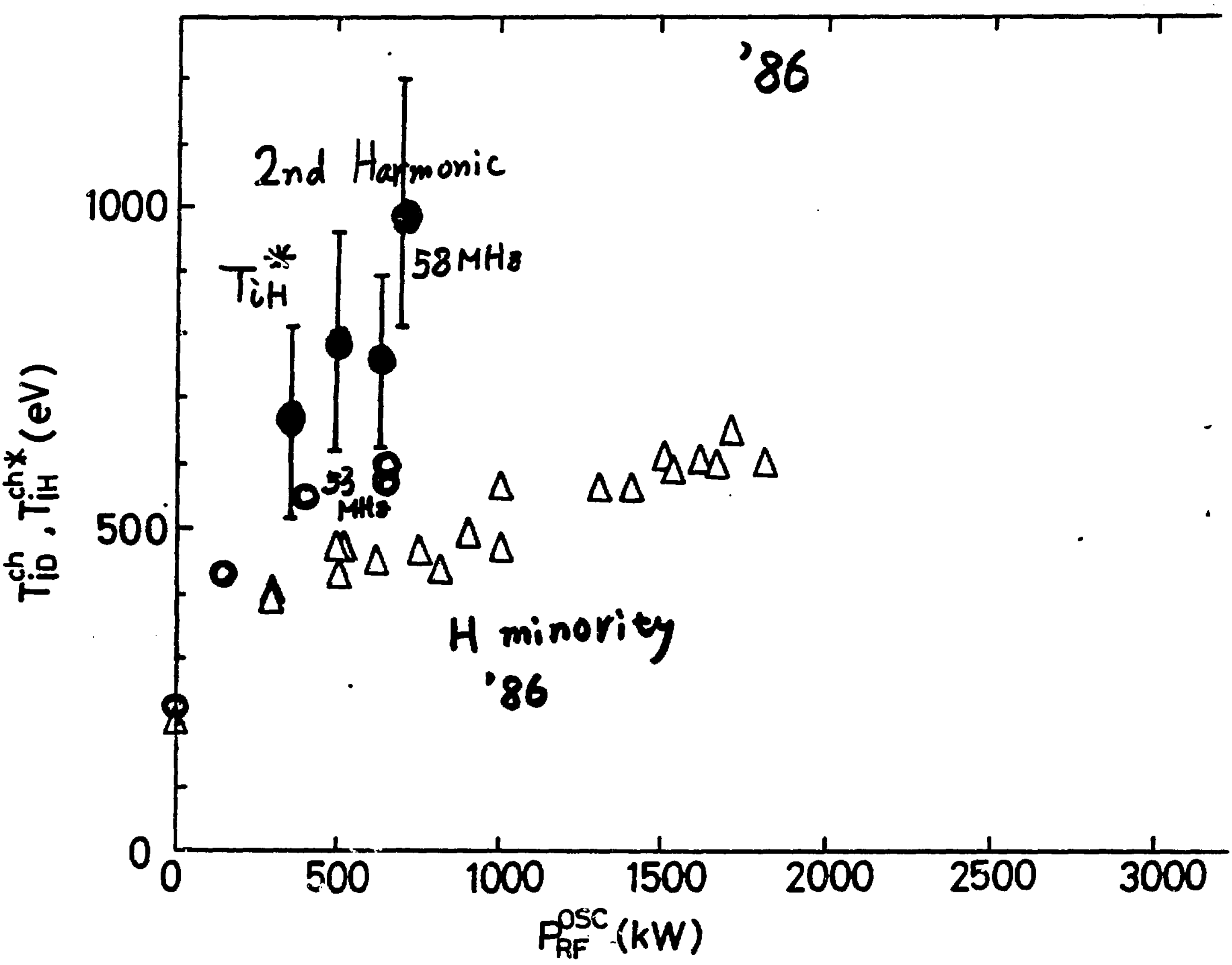
'86
2nd Harmonic
1000
500
0
T_{iH}^{*}
58 MHz
53 MHz
T_{iD}^{ch}, T_{iH}^{ch*} (eV)
H minority
'86
0
500
1000
1500
2000
2500
3000
P_{RF}^{OSC} (kW)

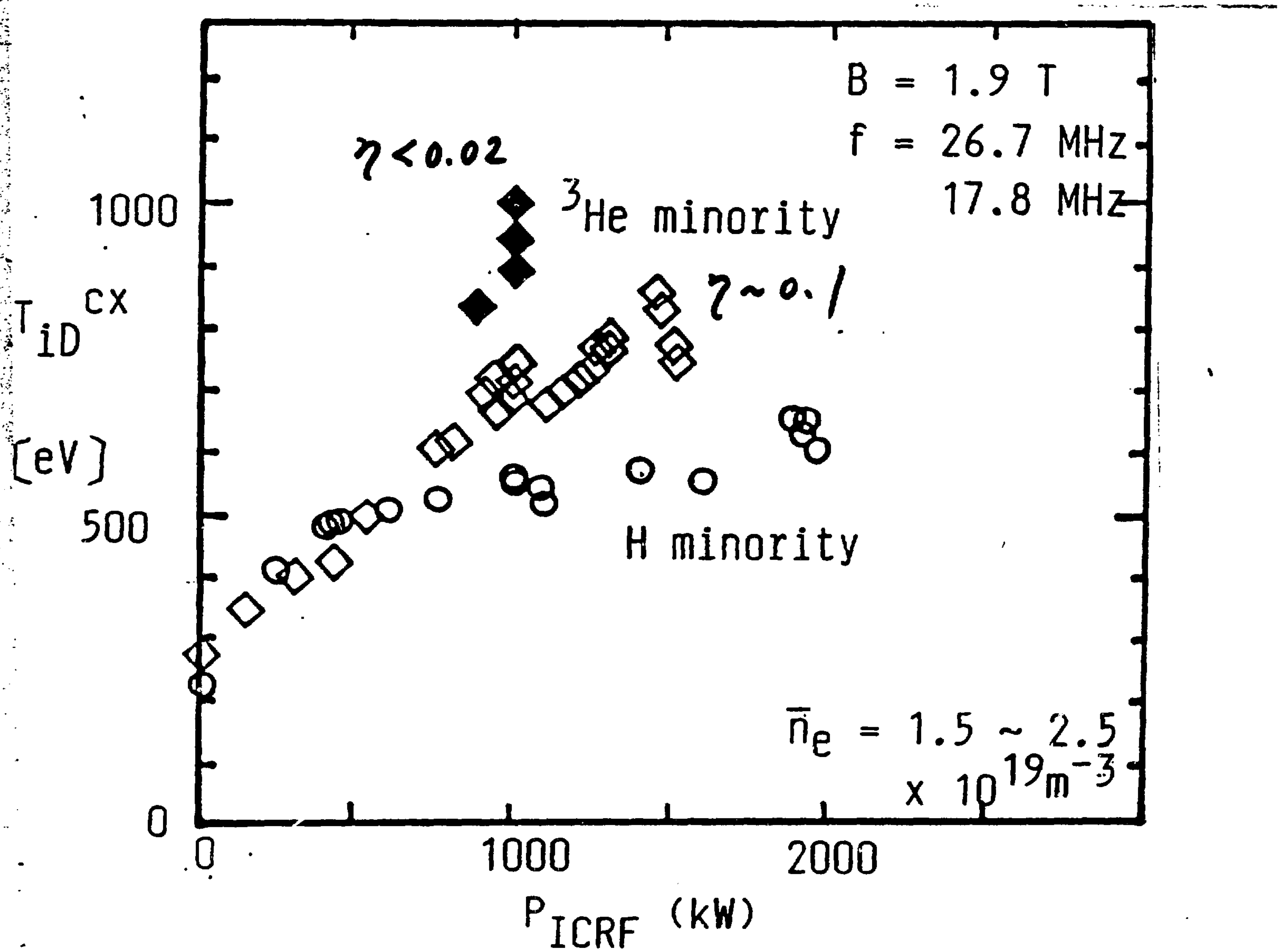

B = 1.9 T
f = 26.7 MHz
17.8 MHz
η<0.02
³He minority
η~0.1
H minority
$\bar{n}_e$ = 1.5 ~ 2.5
x 10¹⁹m⁻³
T_{iD}^{cx}
[eV]
1000
500
0
0
1000
2000
P_{ICRF} (kW)

H·minority heating

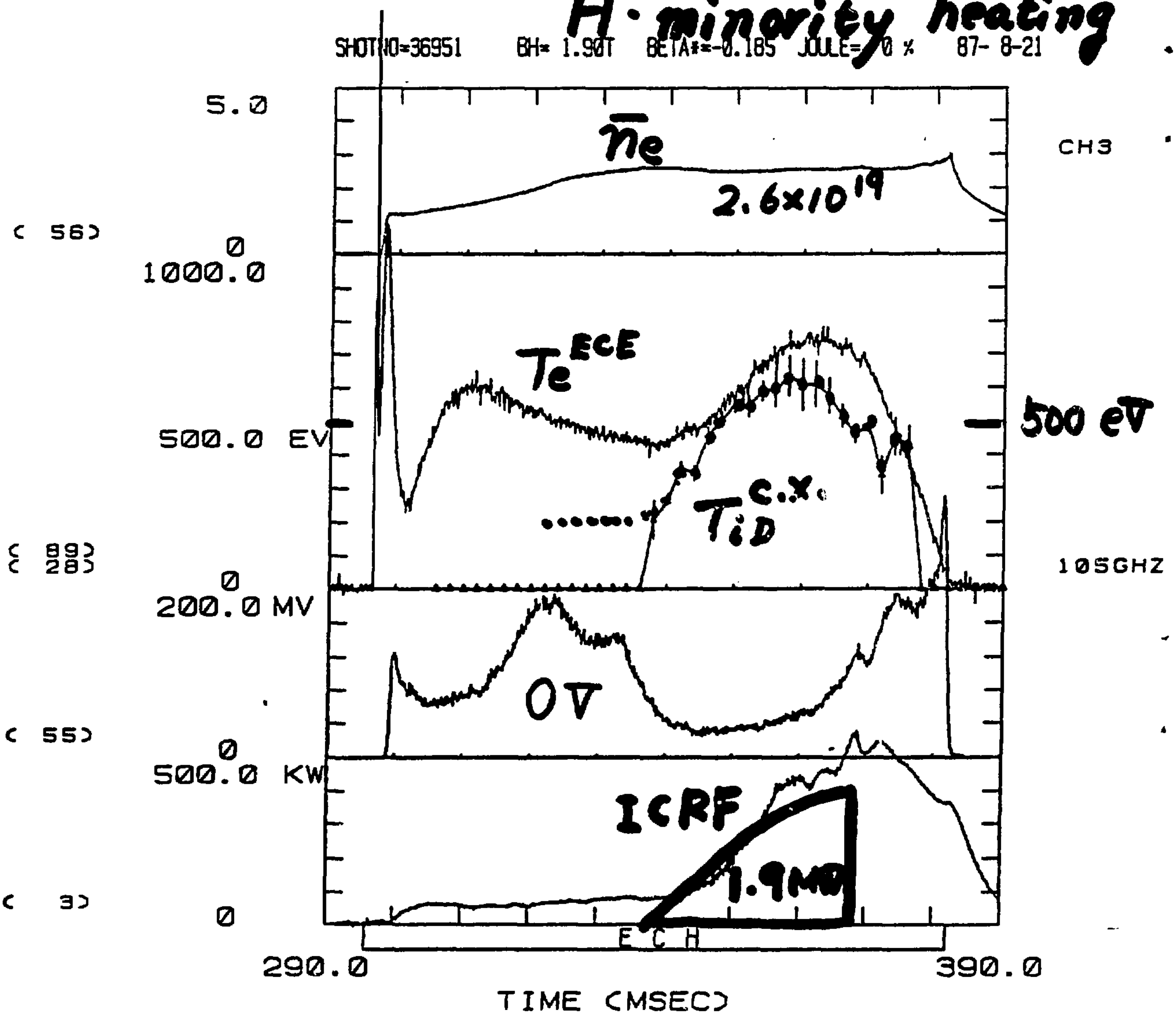

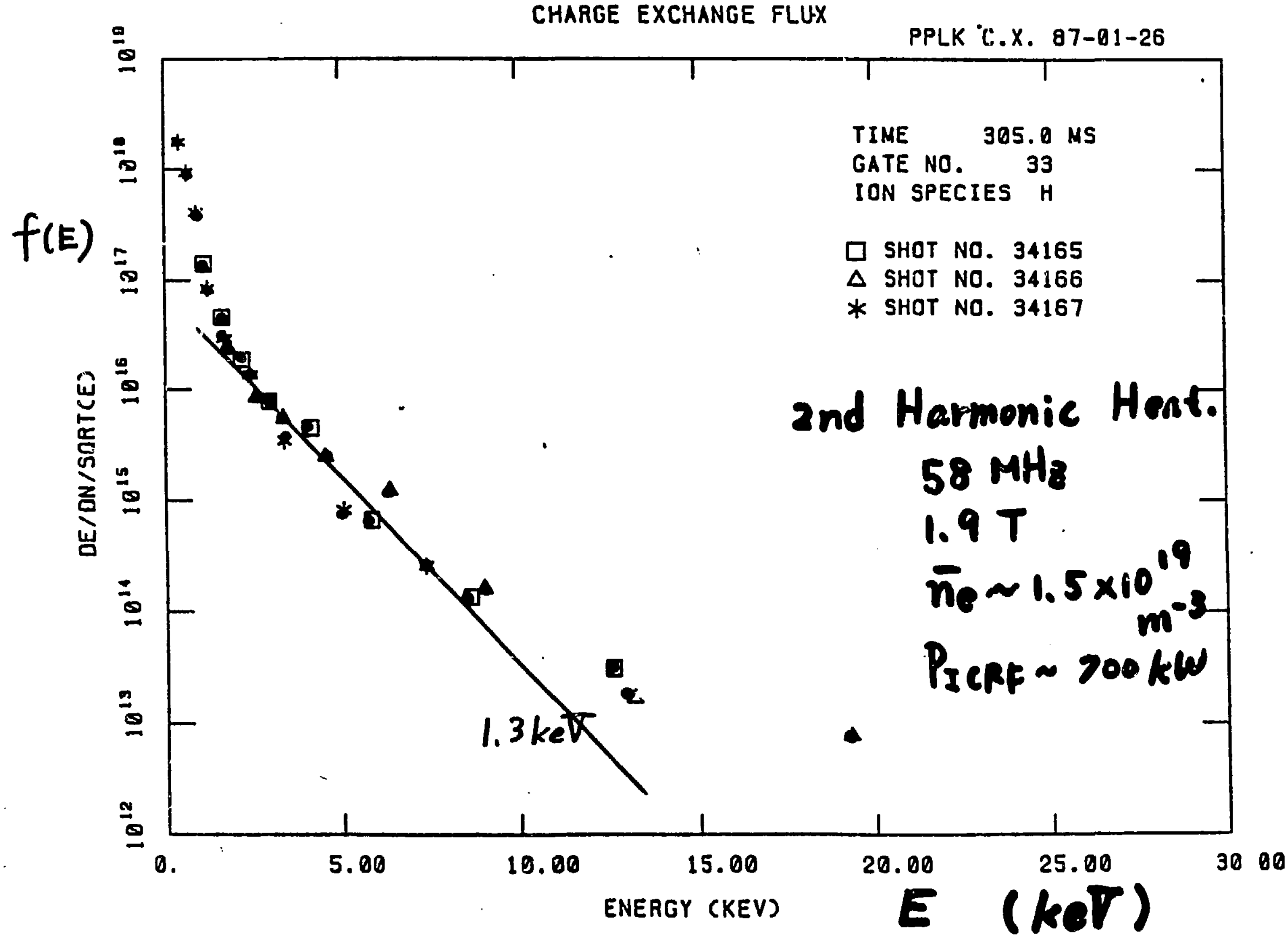
CHARGE EXCHANGE FLUX
PPLK C.X. 87-01-26
TIME 305.0 MS
GATE NO. 33
ION SPECIES H
□ SHOT NO. 34165
△ SHOT NO. 34166
* SHOT NO. 34167
f(E)
DE/DN/SQRT(E)
ENERGY (KEV)
E (keV)
1.3 keV
2nd Harmonic Heat.
58 MHz
1.9 T
n̄e ~ 1.5 x 10^19 m^-3
P_ICRF ~ 700 kW

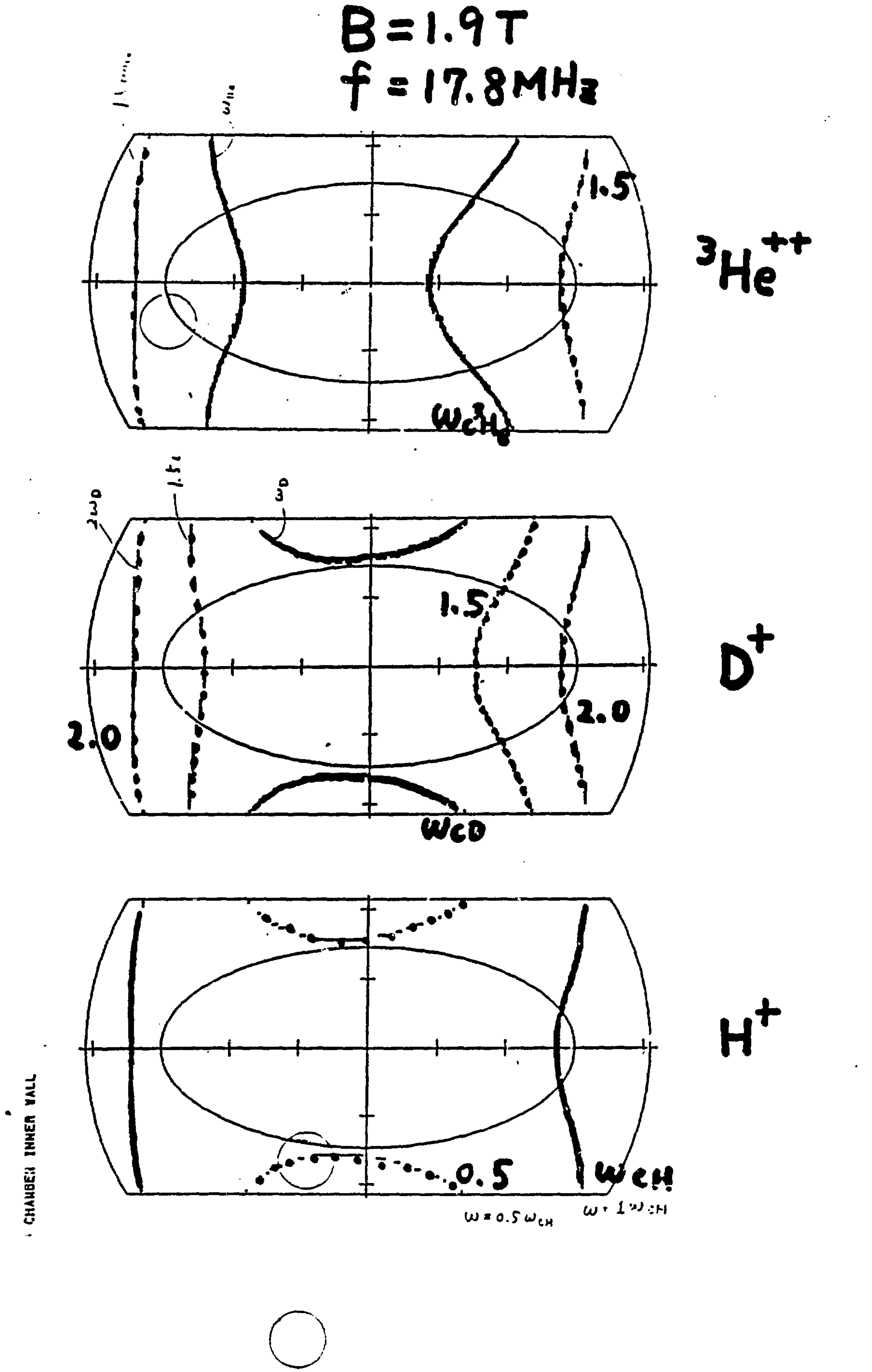

B=1.9T
f=17.8MHz
1.5
³He⁺⁺
ω_{c^3He}
$2\omega_D$
ω_D
1.5
2.0
2.0
D⁺
ω_{cD}
H⁺
0.5
ω_{cH}
$\omega = 0.5\,\omega_{cH}$
CHAMBER INNER WALL

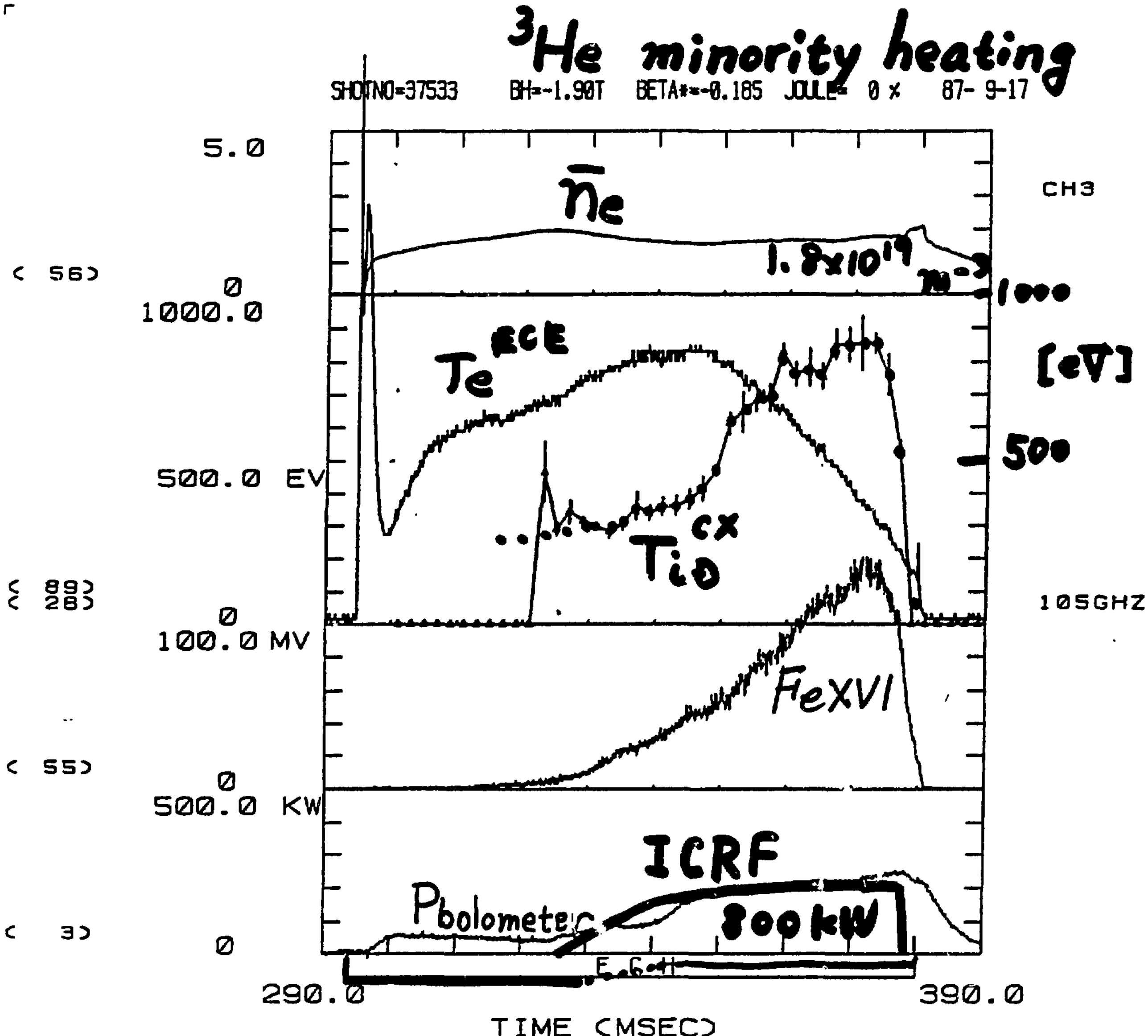

$^3He/D < 0.02$

$B = 1.9T$

$f = 19.8$ MHz

^3He minority heating

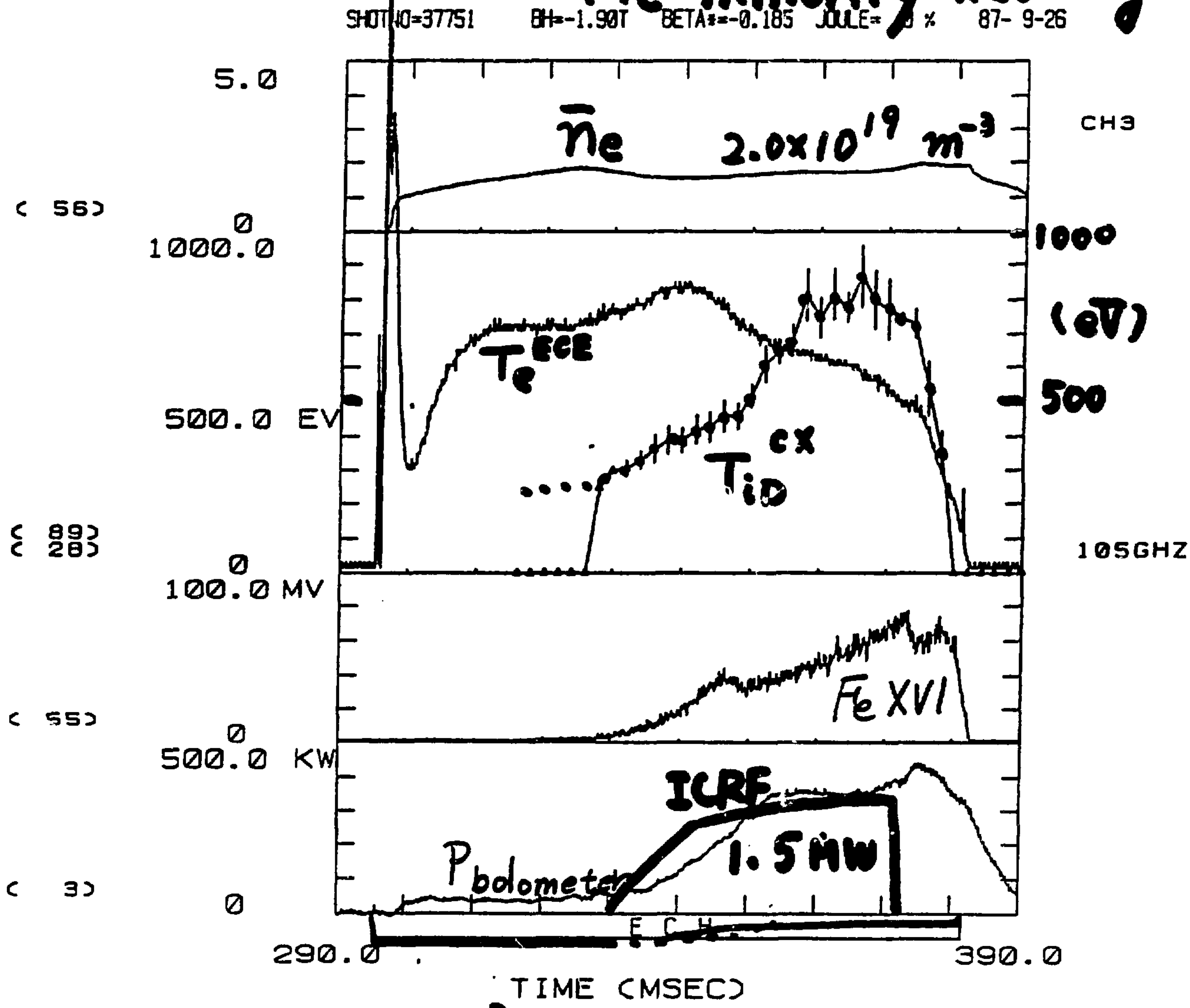

$^3He/D = 0.1 \sim 0.2$

$B = 1.9T$, $f = 17.8 MHz$

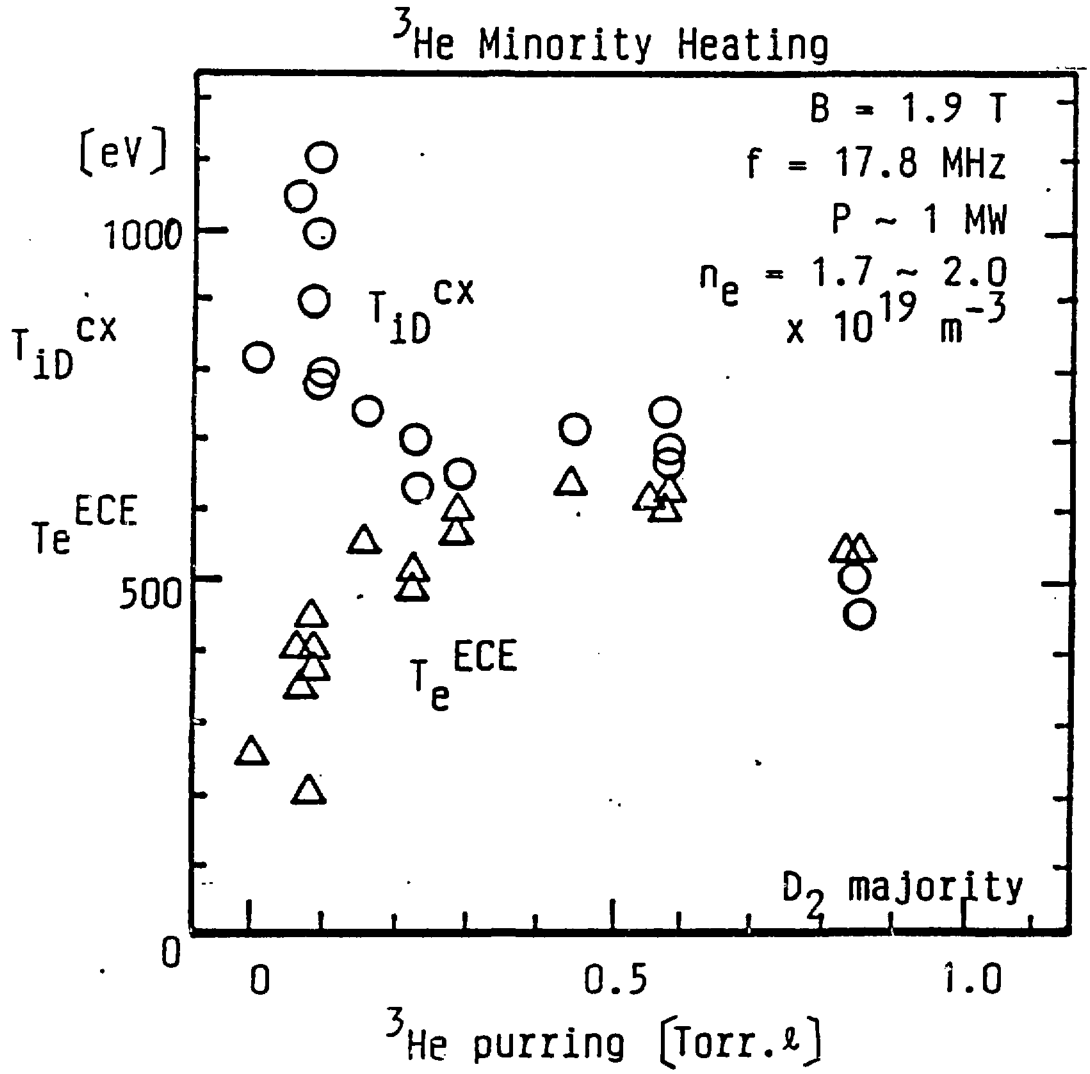

³He Minority Heating
[eV]
1000
500
0
T_{iD}^{cx}
Te^{ECE}
T_{iD}^{cx}
T_e^{ECE}
B = 1.9 T
f = 17.8 MHz
P ~ 1 MW
n_e = 1.7 ~ 2.0
x 10^{19} m^{-3}
D_2 majority
0
0.5
1.0
³He purring [Torr.ℓ]

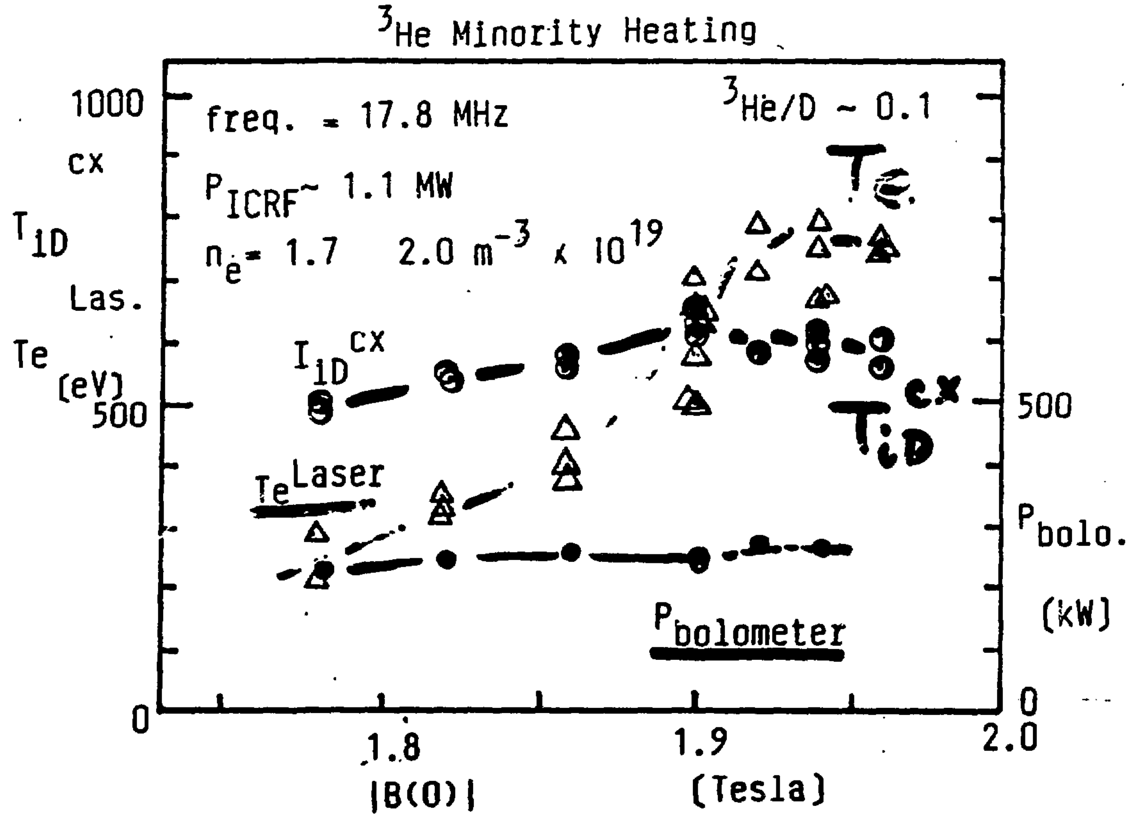

3He Minority Heating
freq. = 17.8 MHz
PICRF~ 1.1 MW
ne= 1.7 2.0 m-3 x 10^19
3He/D ~ 0.1
1000
cx
T1D
Las.
Te
(eV)
500
0
Te
TiD cx
I1D cx
TeLaser
Pbolometer
500
Pbolo.
(kW)
0
1.8
1.9
2.0
|B(0)|
(Tesla)

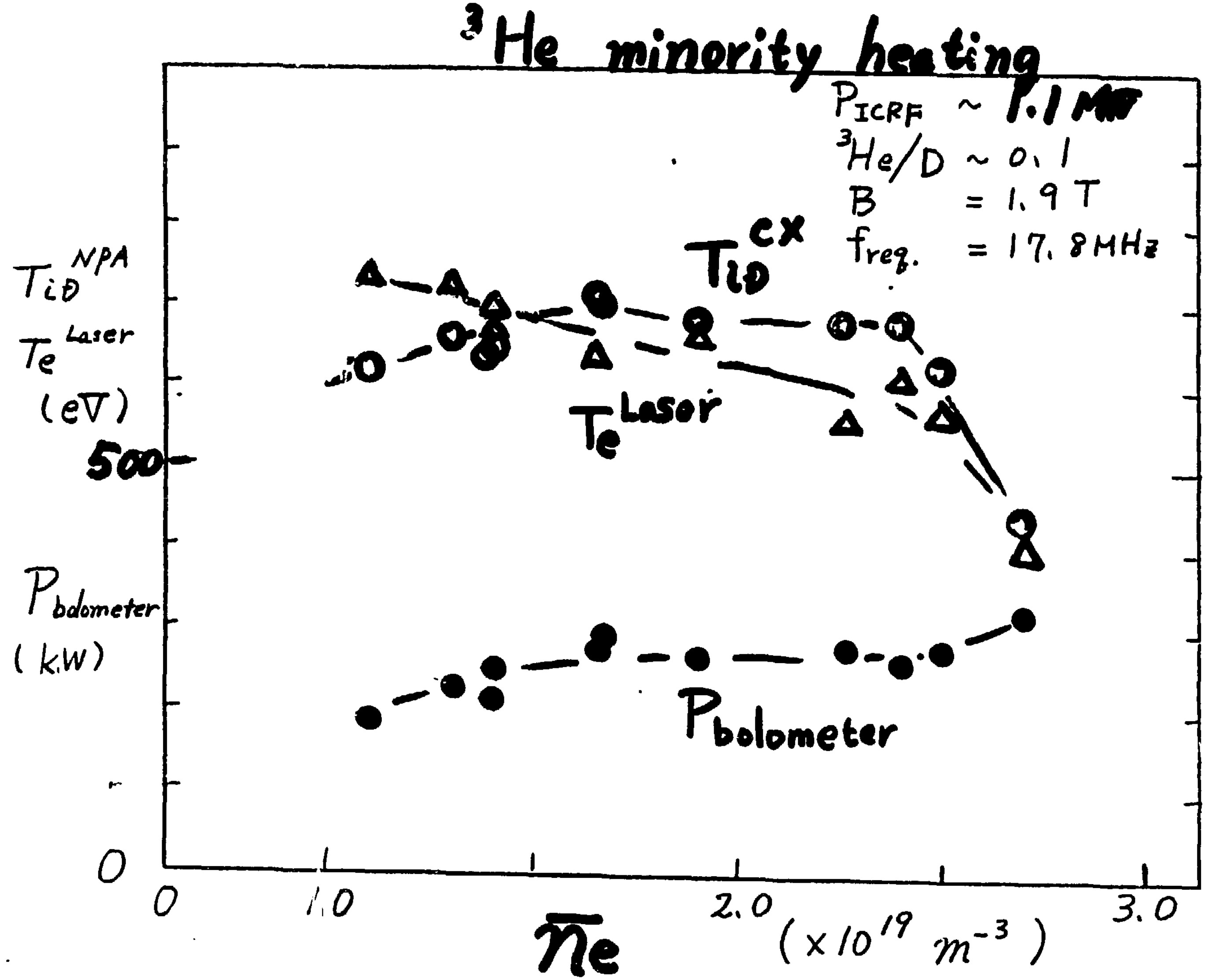

³He minority heating
P_ICRF ~ 1.1 MW
³He/D ~ 0.1
B = 1.9 T
freq. = 17.8 MHz
T_iD^NPA
T_e^Laser
(eV)
500
P_bolometer
(kW)
0
T_iD^CX
T_e^Laser
P_bolometer
0
1.0
2.0
3.0
n̄e
(×10^19 m^-3)

SUMMARY (HEATING)

- Antenna position was raised 1cm in the '87 experiment. Loading resistance was improved 20-50%. Heating efficiency was improved in the low power range(< 500kW), but not changed in the high power range.

- ^{3}He minority heating mode had higher heating efficiency than the H minority mode.
  Power dependence of ion temperature of ^{3}He minority mode was stronger than that of H minority mode.

- Some part of ICRF power may be divided to the direct IBW excitation.

- With simultaneous NBI heating, high energy tail enhancement was obserbed.

MEASUREMENT OF HIGH ENERGY SPECTRA OF MINORITY PROTON

H. ZUSHI
K. KONDO
T. MUTOH

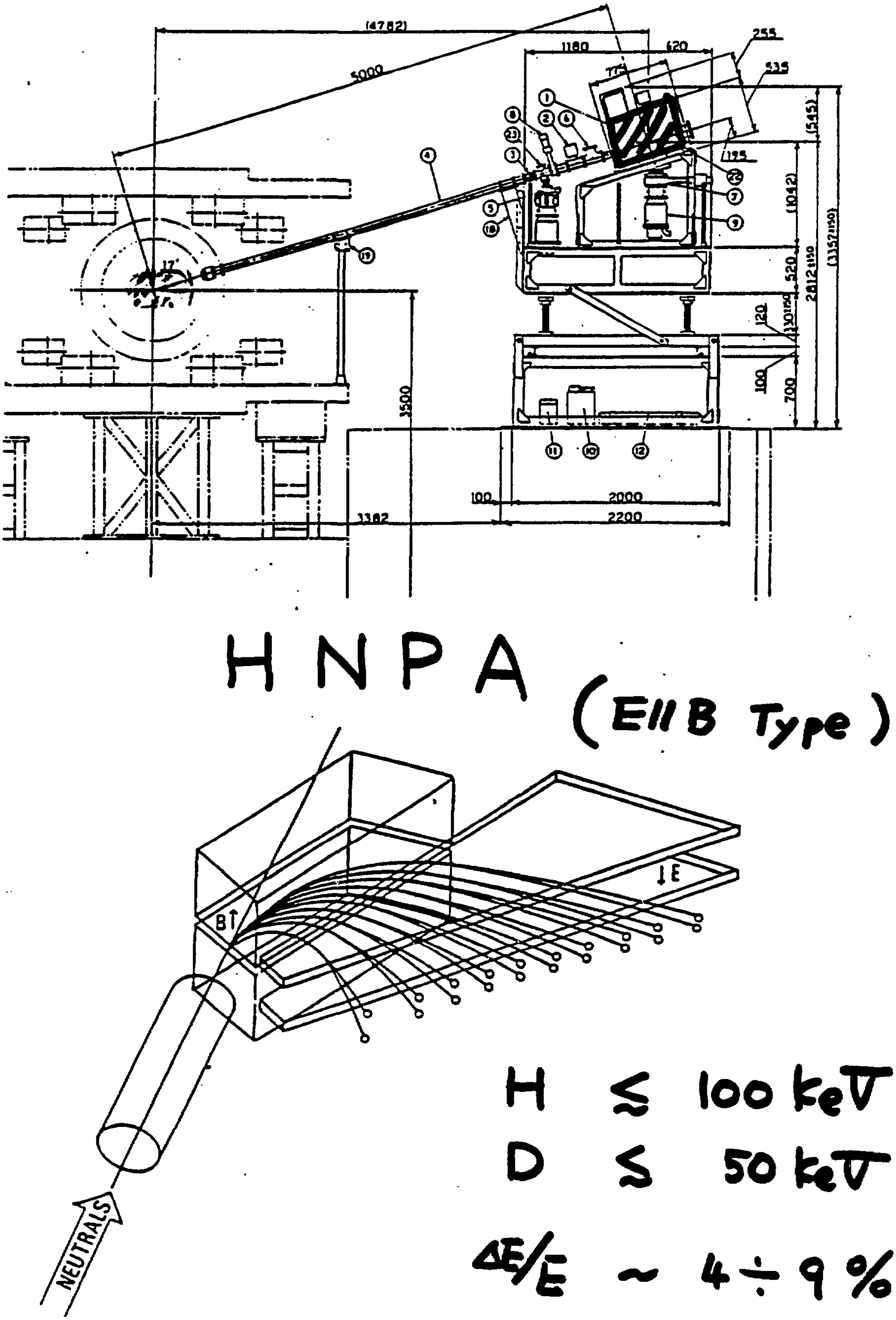

FIG. 1. Schematic of analyzer concept.

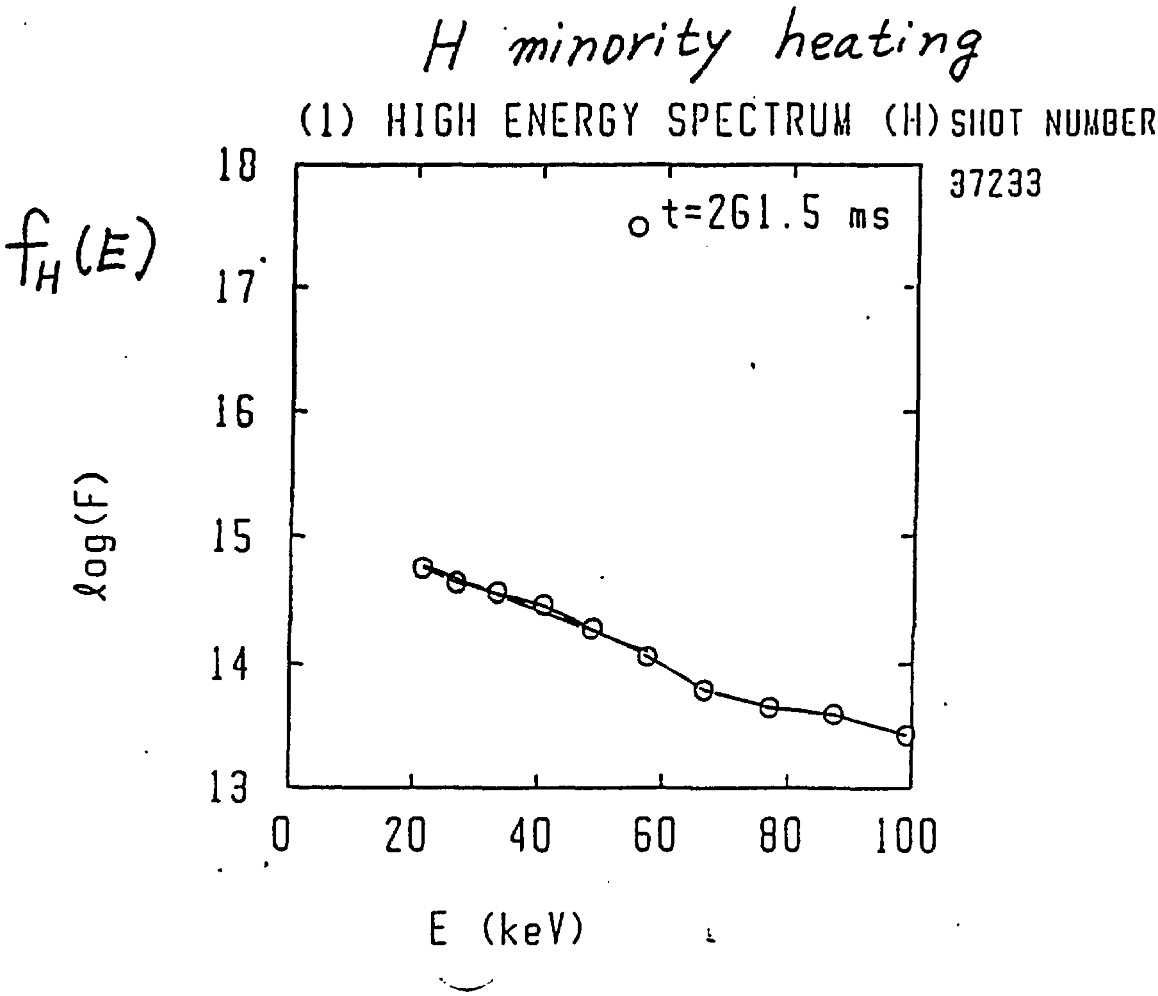
H minority heating
(1) HIGH ENERGY SPECTRUM (H) SHOT NUMBER
37233
o t=261.5 ms
$f_H(E)$
log(F)
18
17
16
15
14
13
0
20
40
60
80
100
E (keV)

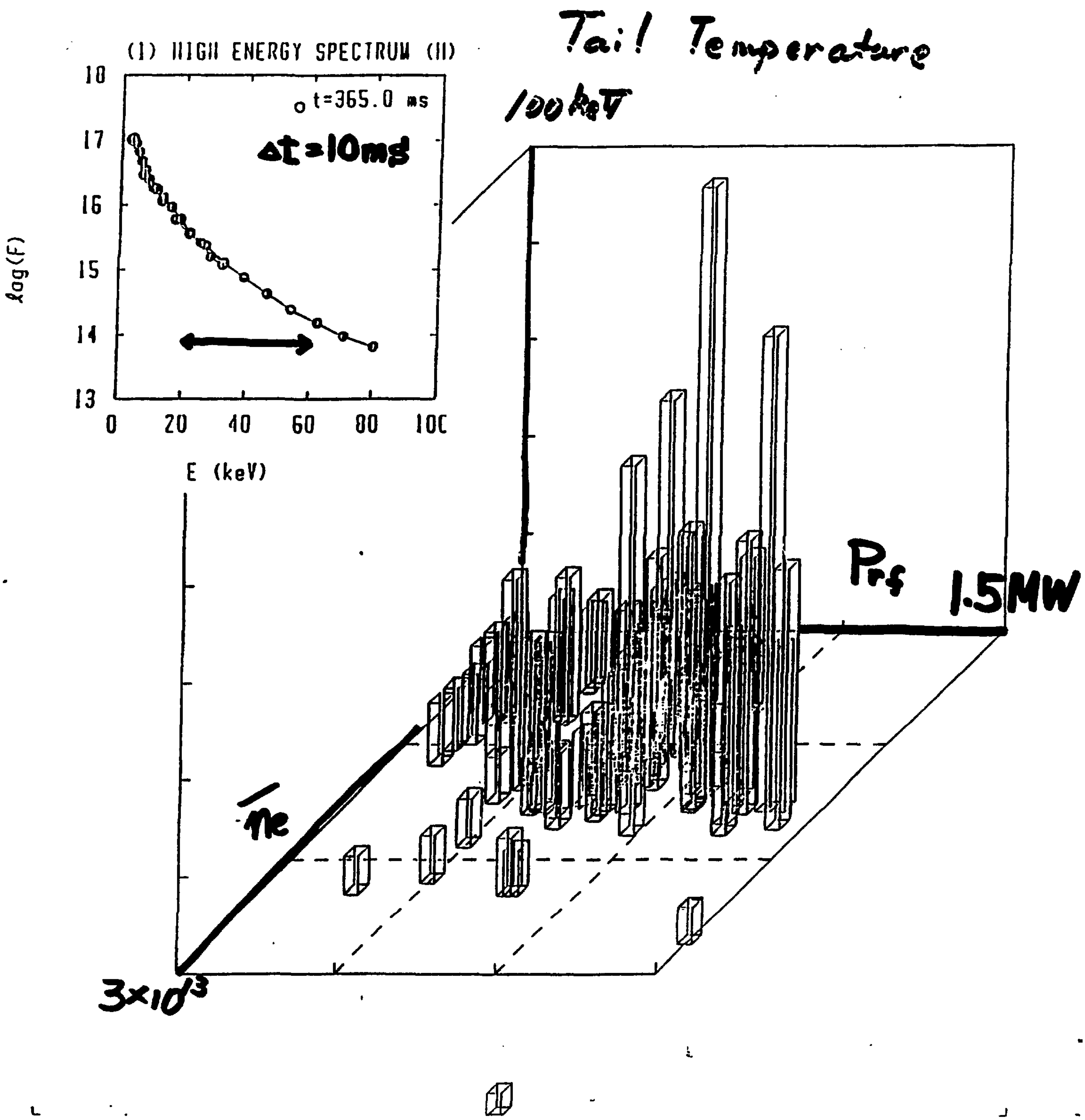
Tail Temperature
100keV
(I) HIGH ENERGY SPECTRUM (II)
t=365.0 ms
Δt=10ms
log(F)
E (keV)
Prf
1.5MW
ne
3×10³

磁場依存性

B-dependence

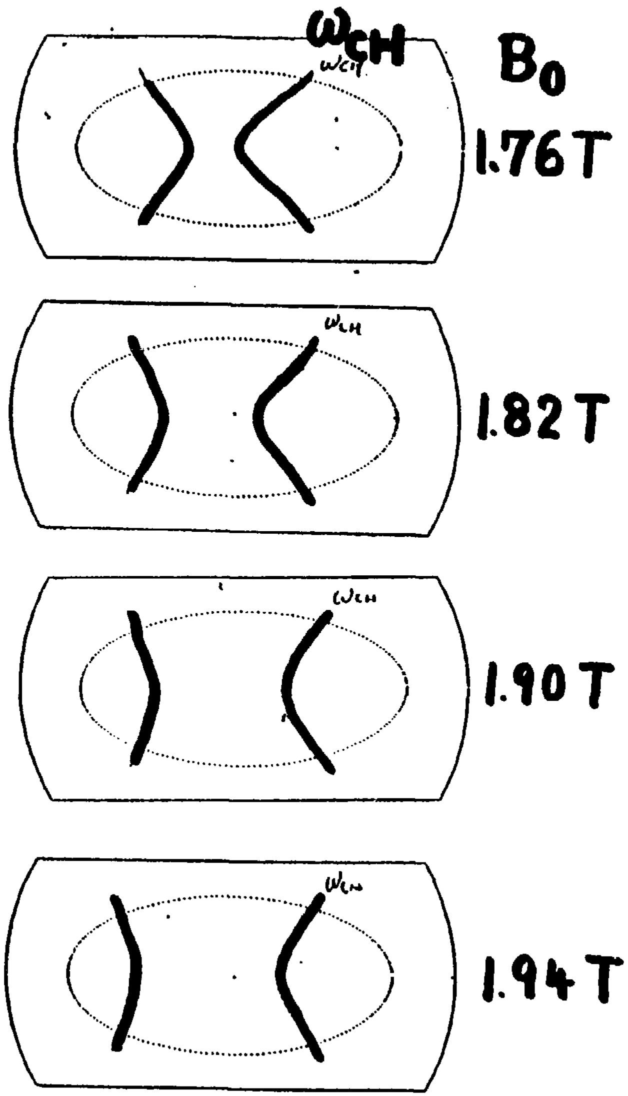

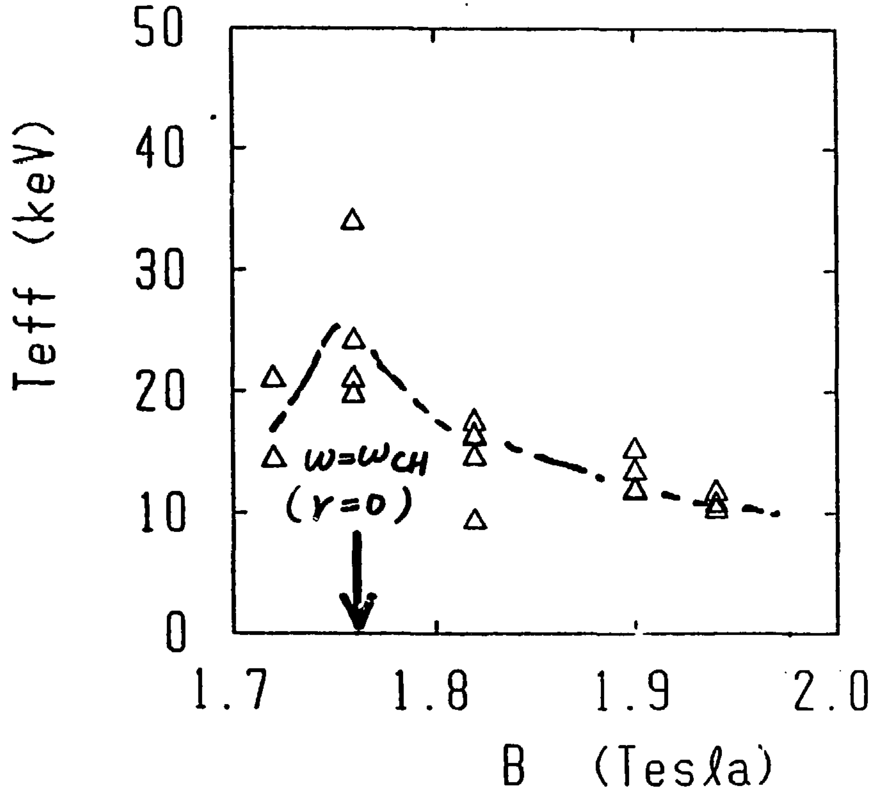

- ω_{CH} がプラズマ中心の時 T_{eff} が高い
- ただし bulk plasma も変化 (ECH)

パワー依存性

Power dependence

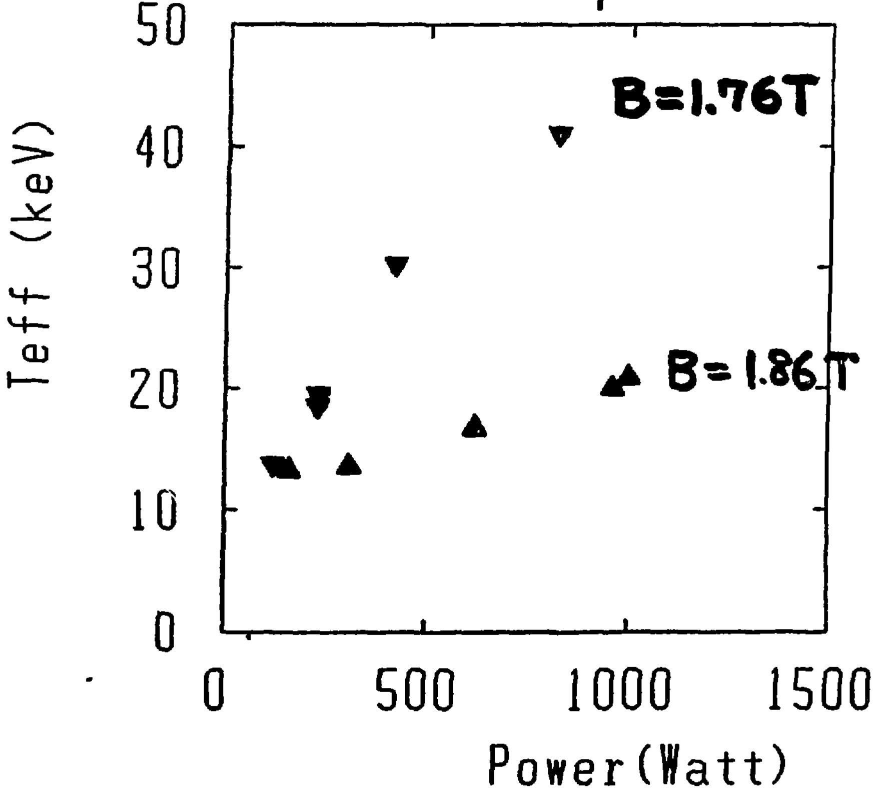

Teff is off-set linear

- パワーに対して offset-Linear に増大する

$$T_{eff} \sim \frac{3}{2}\xi T_e \sim \left(\frac{P}{n_H}\right)\tau_s$$

密度依存性

density dependence

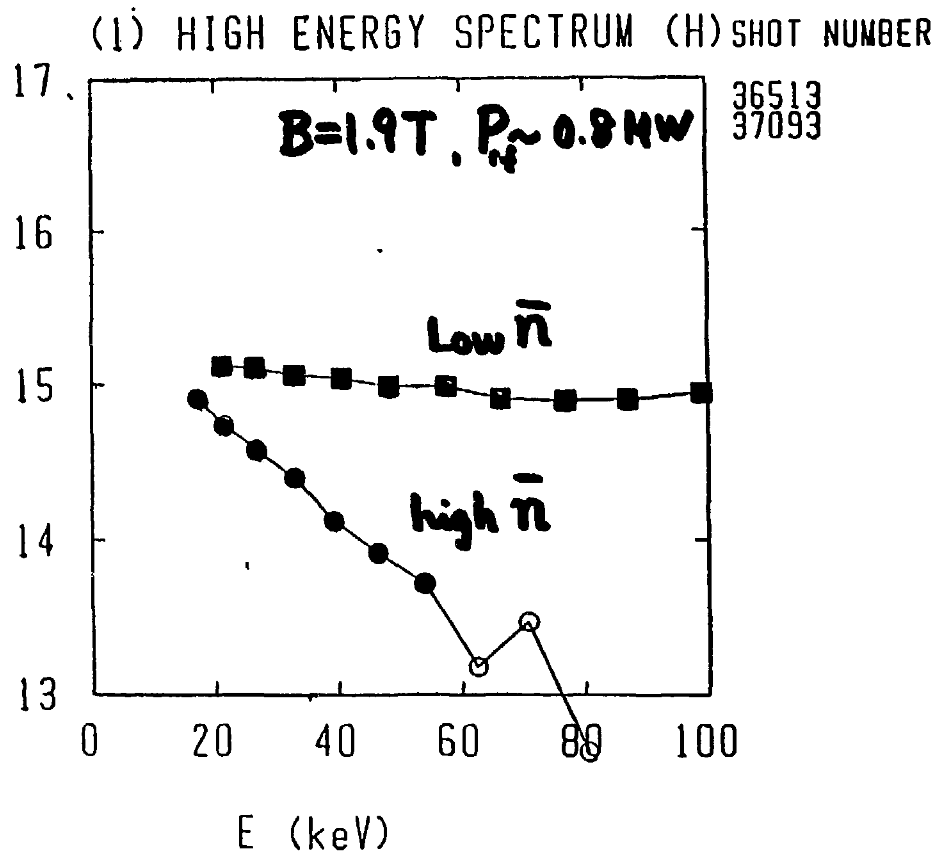

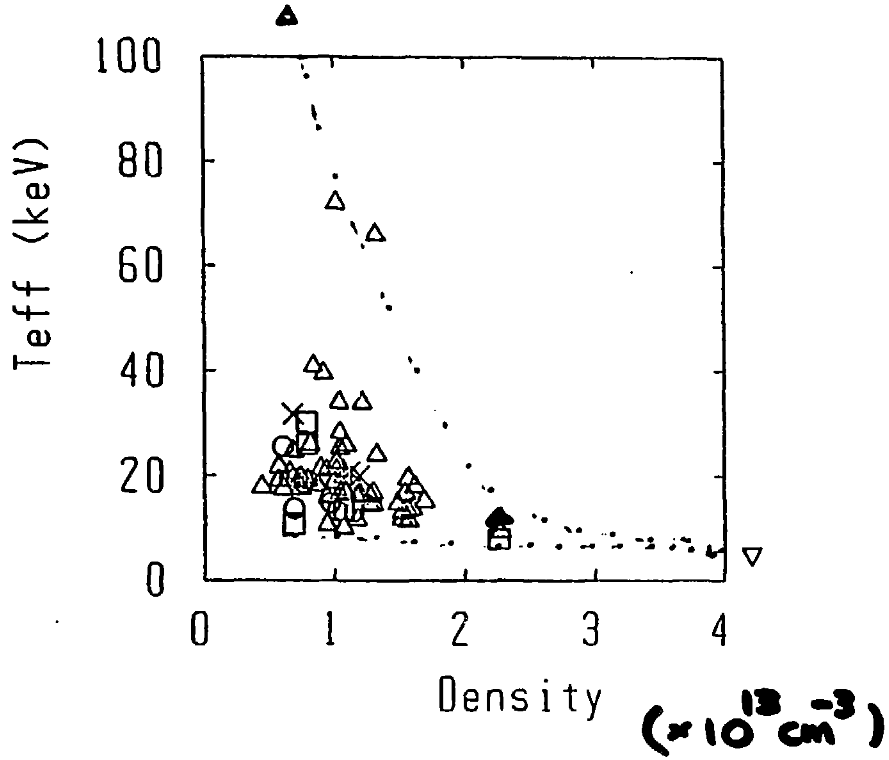

・密度が高いと Teff は低い

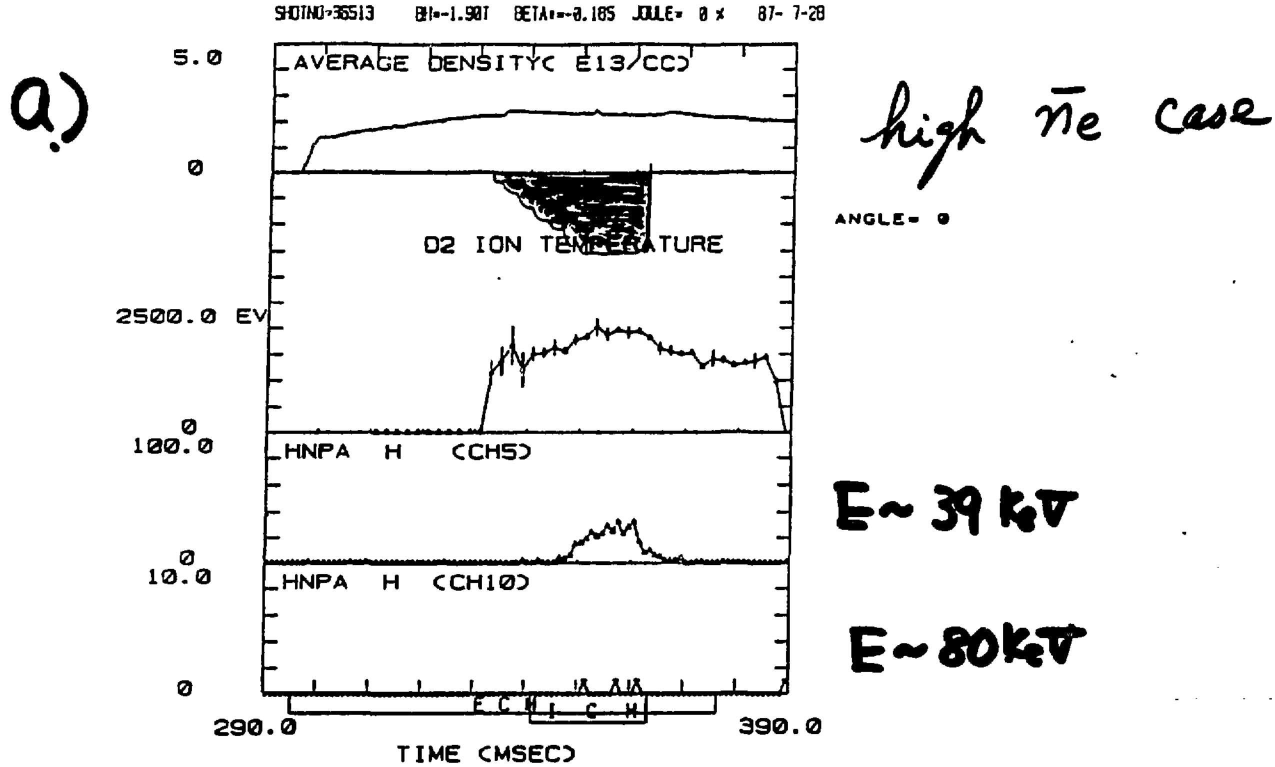

SHOTNO=36513 BH=-1.90T BETA*=-0.185 JOULE= 0 % 87-7-28
a)
high $\bar{n}_e$ case
AVERAGE DENSITY(E13/CC)
5.0
0
D2 ION TEMPERATURE
ANGLE= 0
2500.0 EV
0
HNPA H (CH5)
100.0
E~39 keV
0
HNPA H (CH10)
10.0
E~80keV
0
ECH
ICH
290.0
390.0
TIME (MSEC)

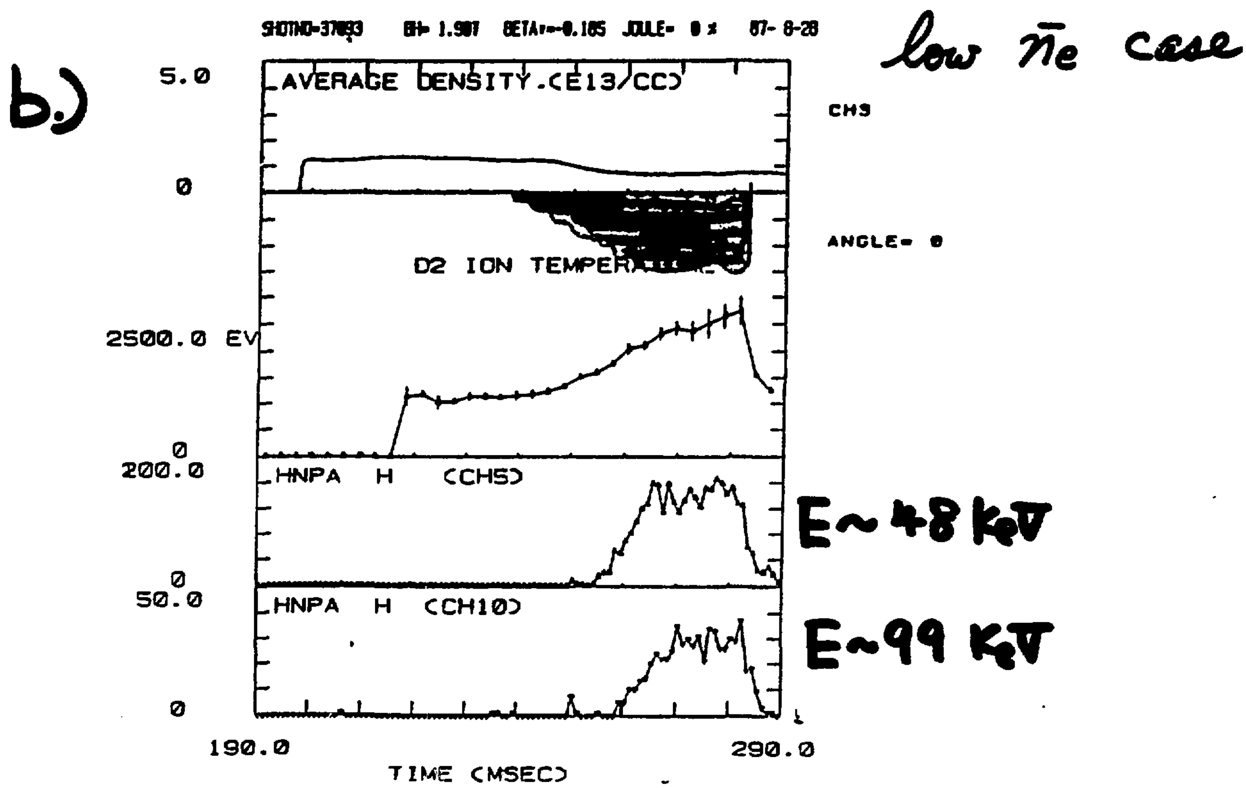

SHOTNO=37093 BH=1.90T BETA*=-0.185 JOULE= 0 % 87-8-28
b.)
low $\bar{n}_e$ case
AVERAGE DENSITY (E13/CC)
5.0
0
CH3
D2 ION TEMPERATURE
ANGLE= 0
2500.0 EV
0
HNPA H (CH5)
200.0
E~48 keV
0
HNPA H (CH10)
50.0
E~99 keV
0
190.0
290.0
TIME (MSEC)

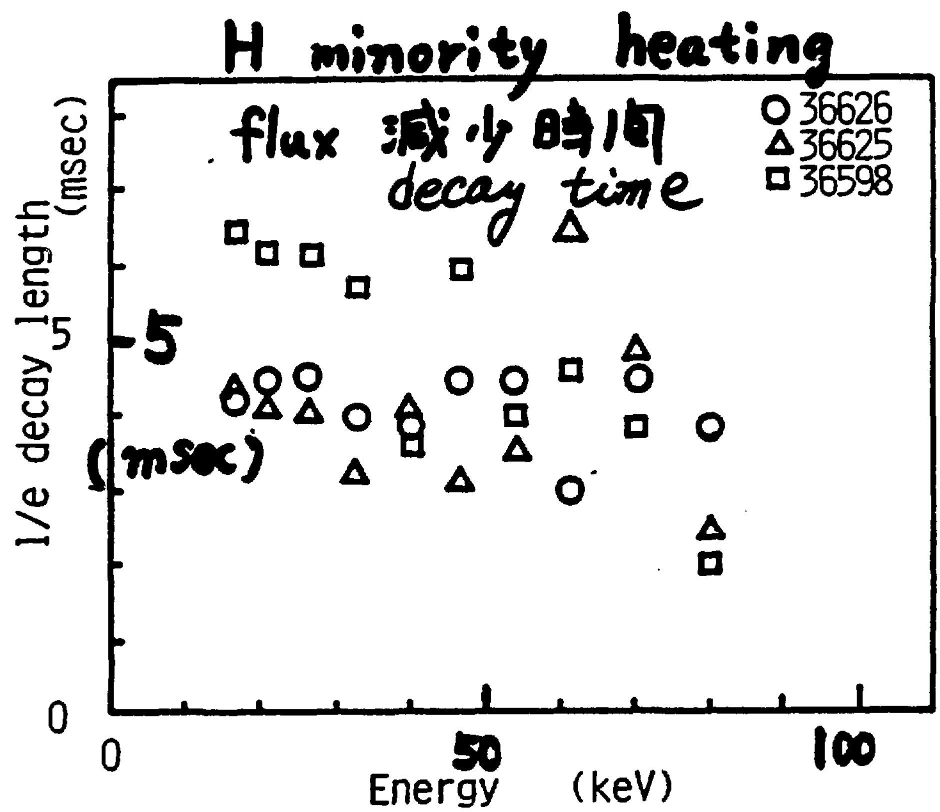
H minority heating
flux 減少時間
decay time
○ 36626
△ 36625
□ 36598
1/e decay length (msec)
5
(msec)
0
0
50
100
Energy (keV)

減衰時間と Stopping time の相関
decay time &

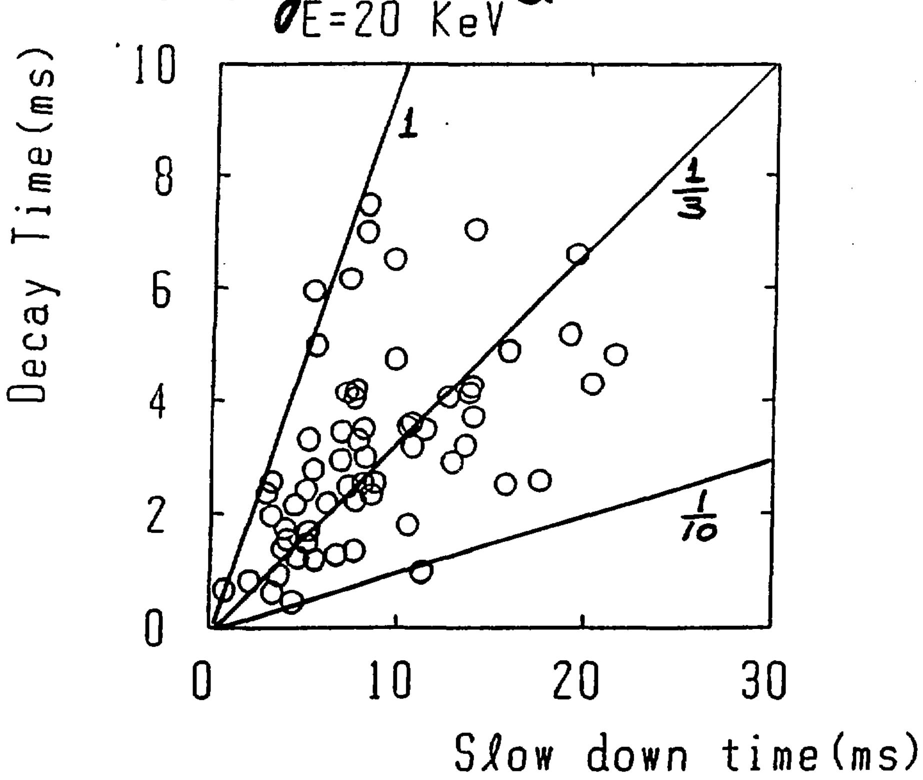

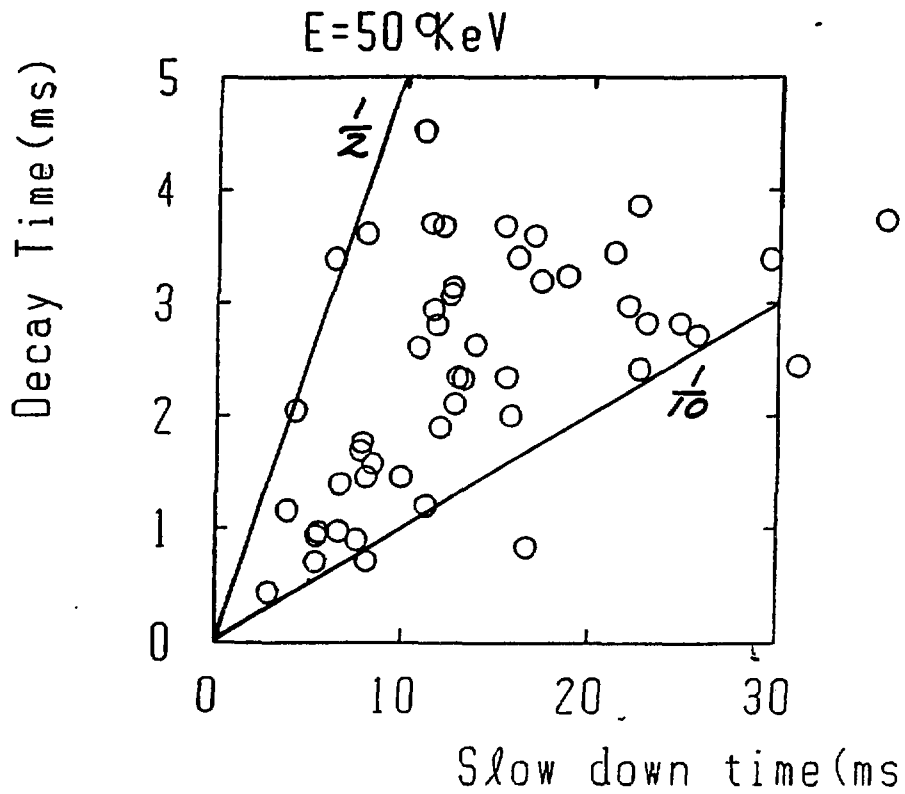

; T_e (r<0.3a)

$$\tau_{stop} = \frac{\tau_s}{3} \ln\left[1 + \left(\frac{E}{E_c}\right)^{3/2}\right]$$

; $Z_{eff}=2$

; $\bar{n}_e$

垂直磁場依存性

Bvertical scan

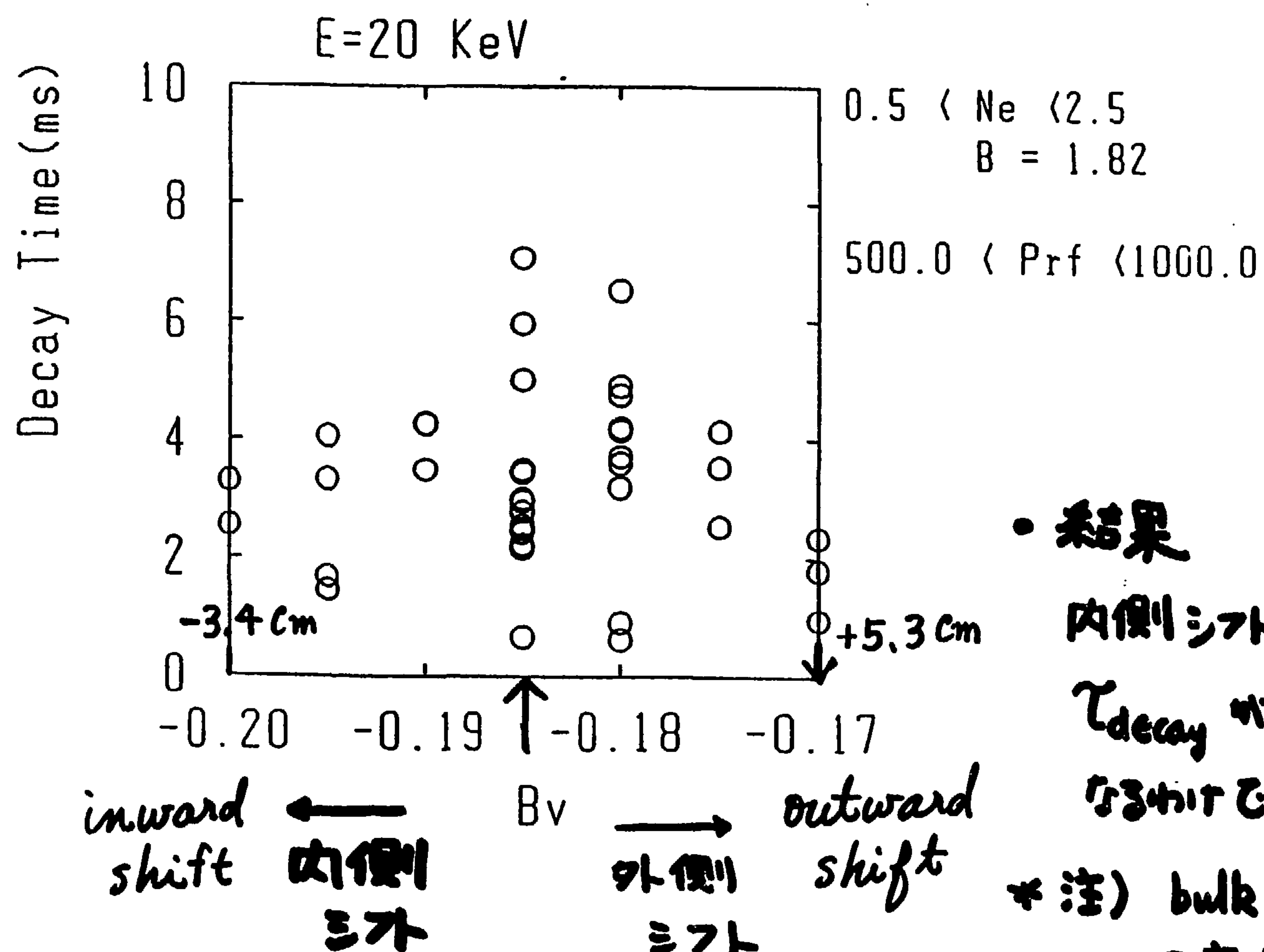

- 結果
内側シフトで τ_{decay} が長くなるわけではない

＊注）bulk plasma の変化

垂直磁場効果

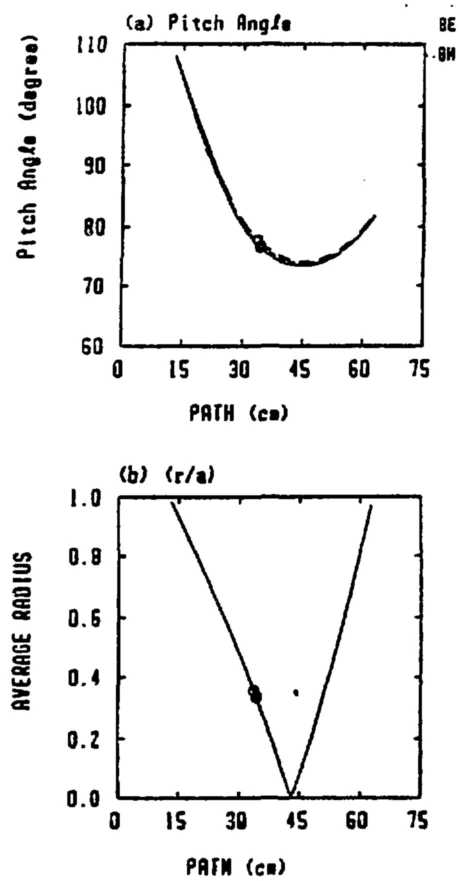

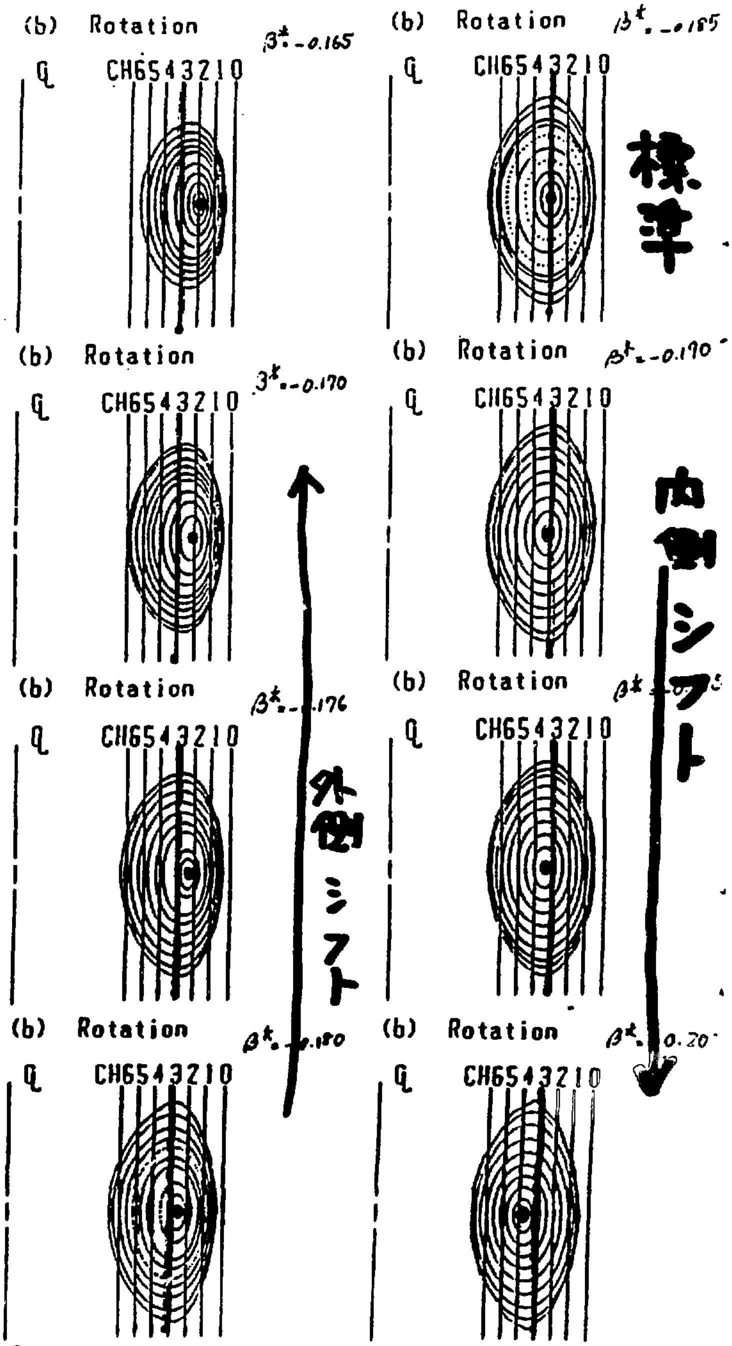

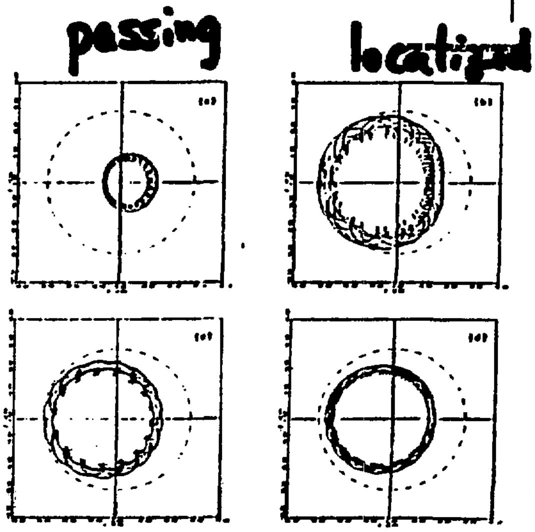

: 予想

内側シフトで better confinement

by Hanatani

SUMMARY (HIGH ENERGY PARTICLE MEASUREMENT)

- Up to 100keV proton particle was observed.

- No signs of loss cone and critical energy of confinement was recognized.

- Tail temperature was high when
  cyclotron resonance layer locates on center,
  high ICRF power,
  low plasma density.

- Flux decay time had correlation with the stopping time.

- Flux decay time and bulk ion heating efficiency were not improved by the inward shift of the magnetic axis due to the additional vertical field in the experiment range.

CALCULATIN OF HIGH ENERGY PARTICLE ORBIT

PRELIMINARY

H. OKADA

What kind of particles we observed?

Where those particles could be confined?

磁場変化とピッチ角

pitch angle between line of sight and $\vec{B}$

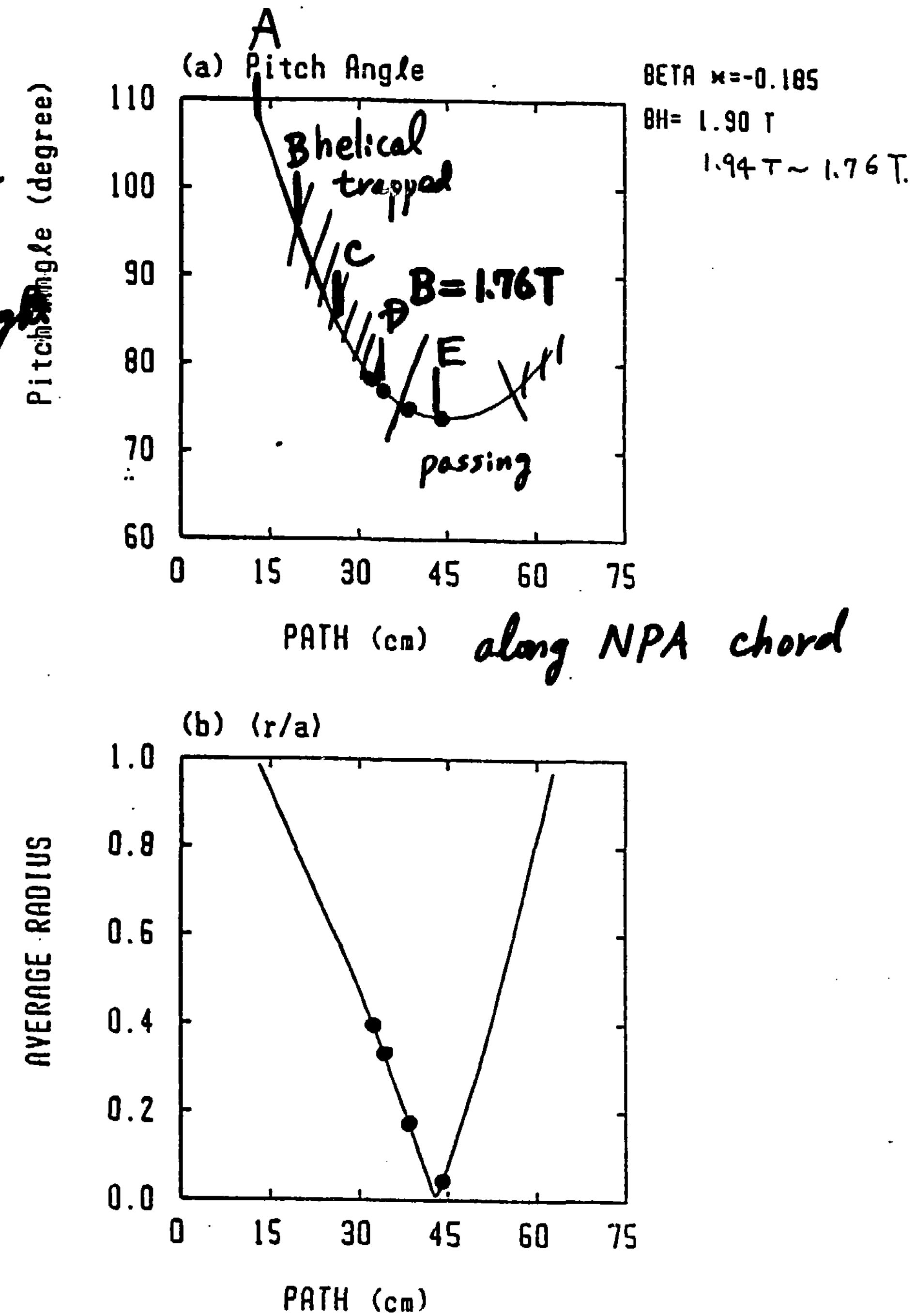

Preliminary

Particle trajectory

H^+ 100keV

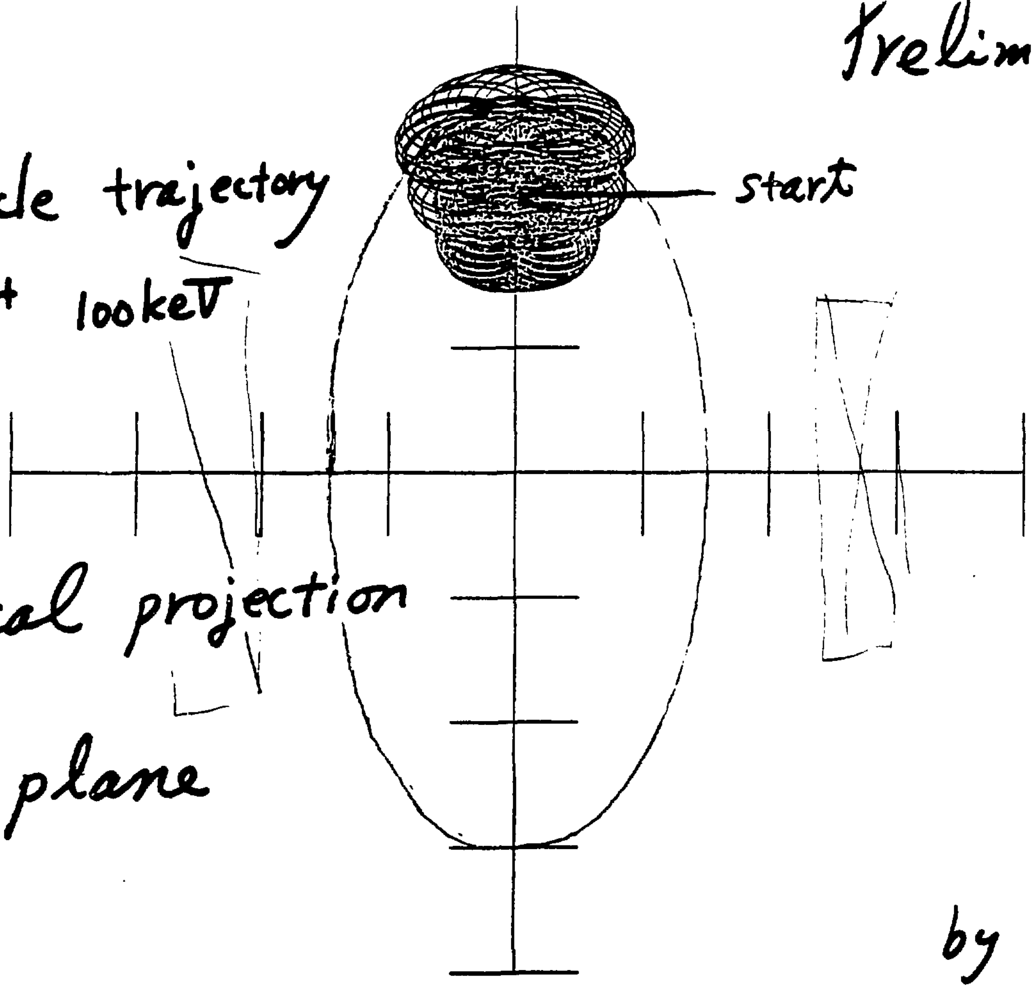

Helical projection on r-θ plane

(B)

by H. Okada

vertical projection on equatorial plane

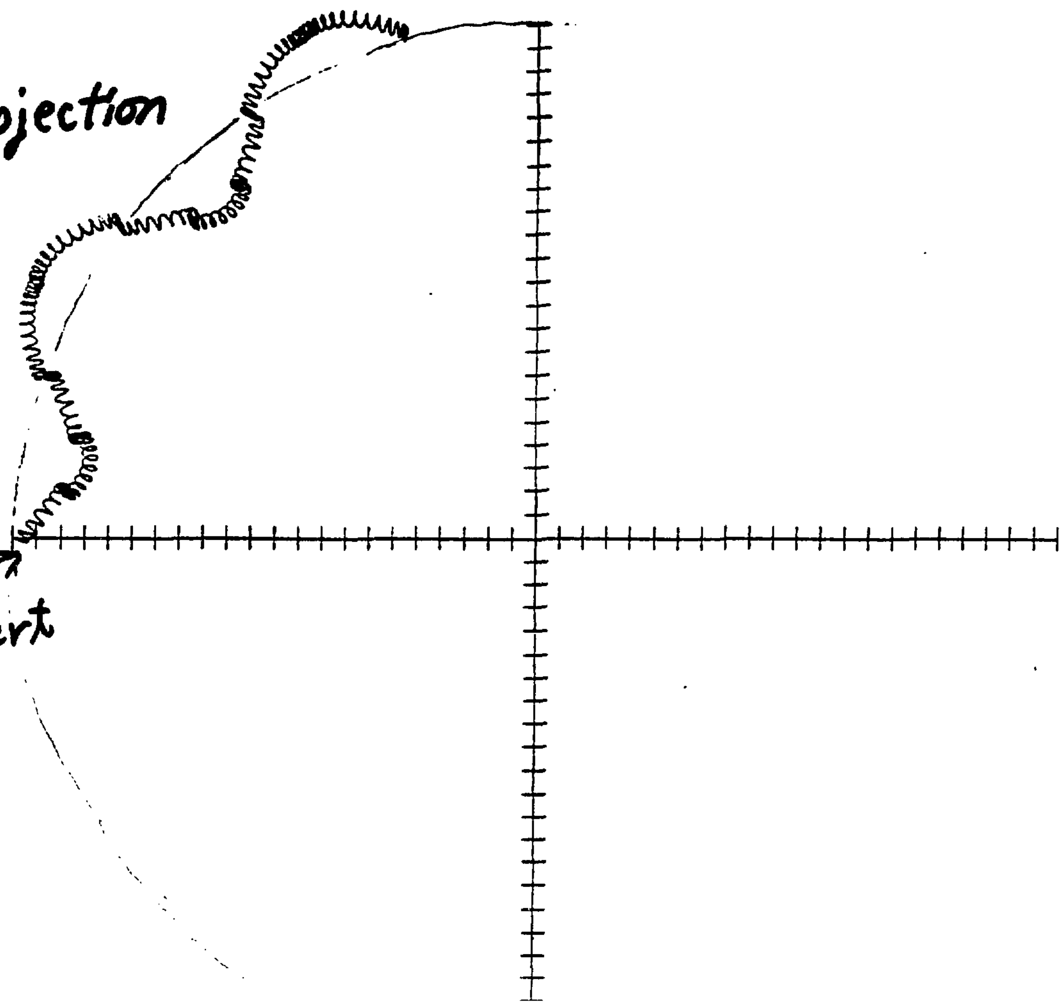

Start

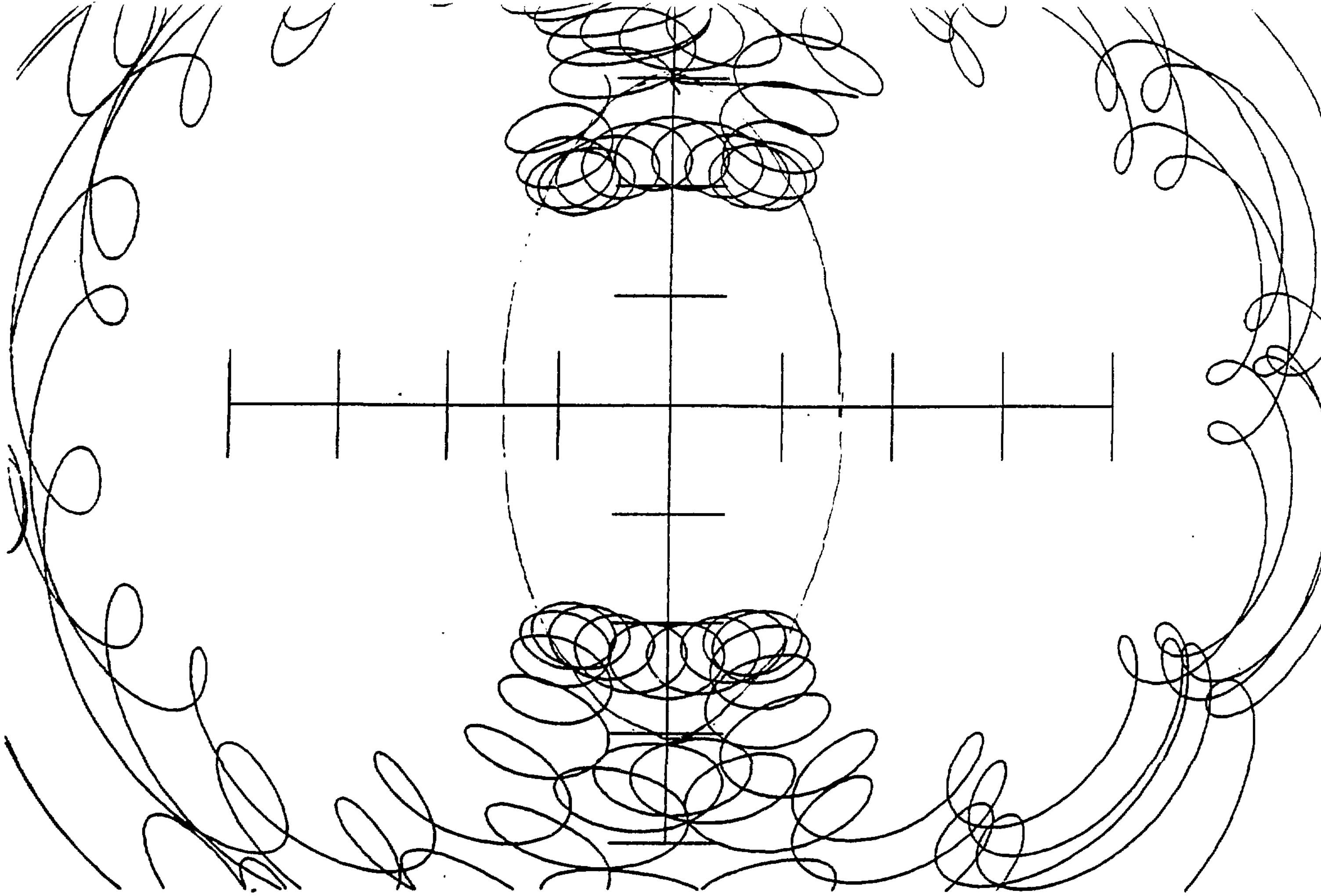

A

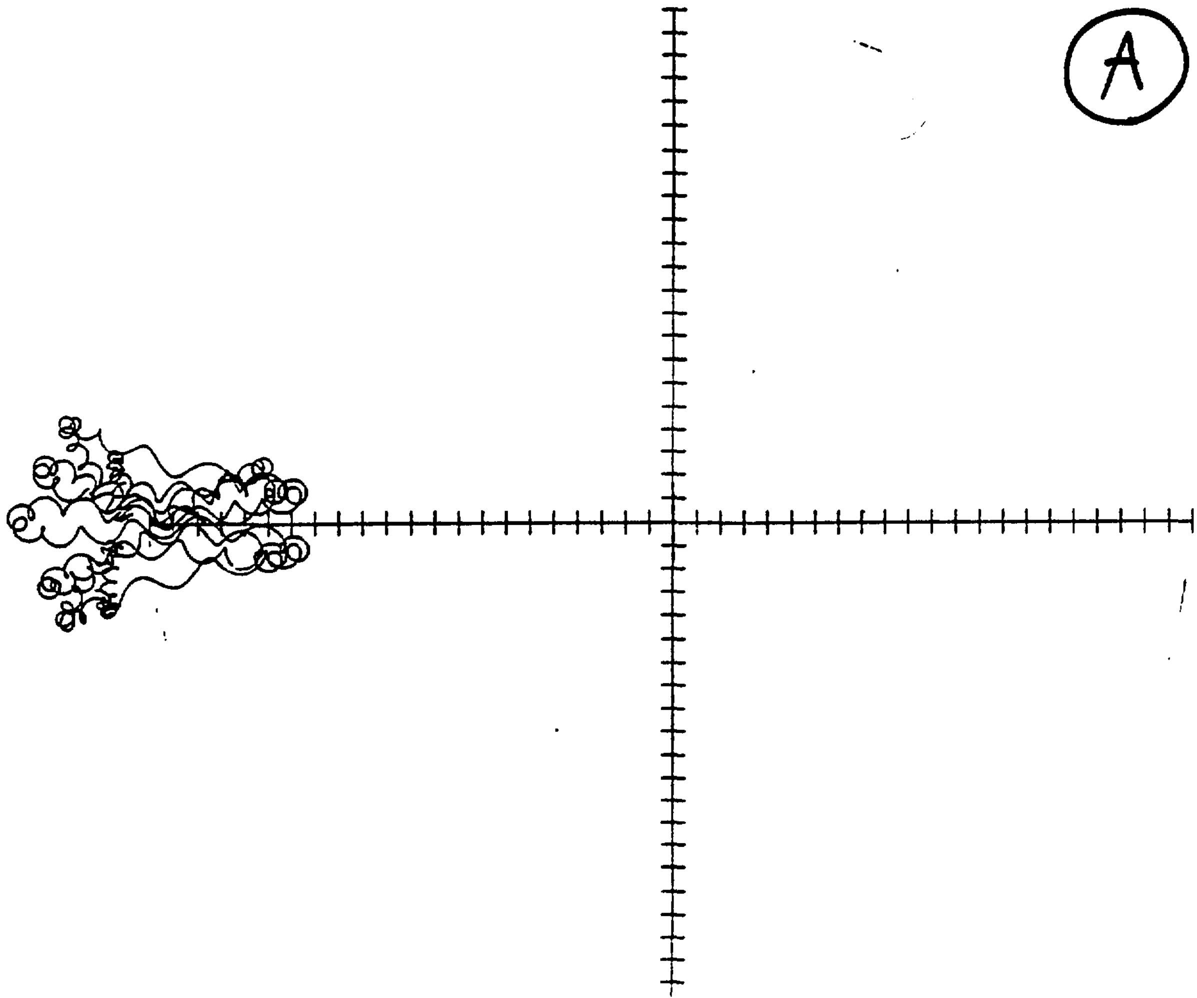

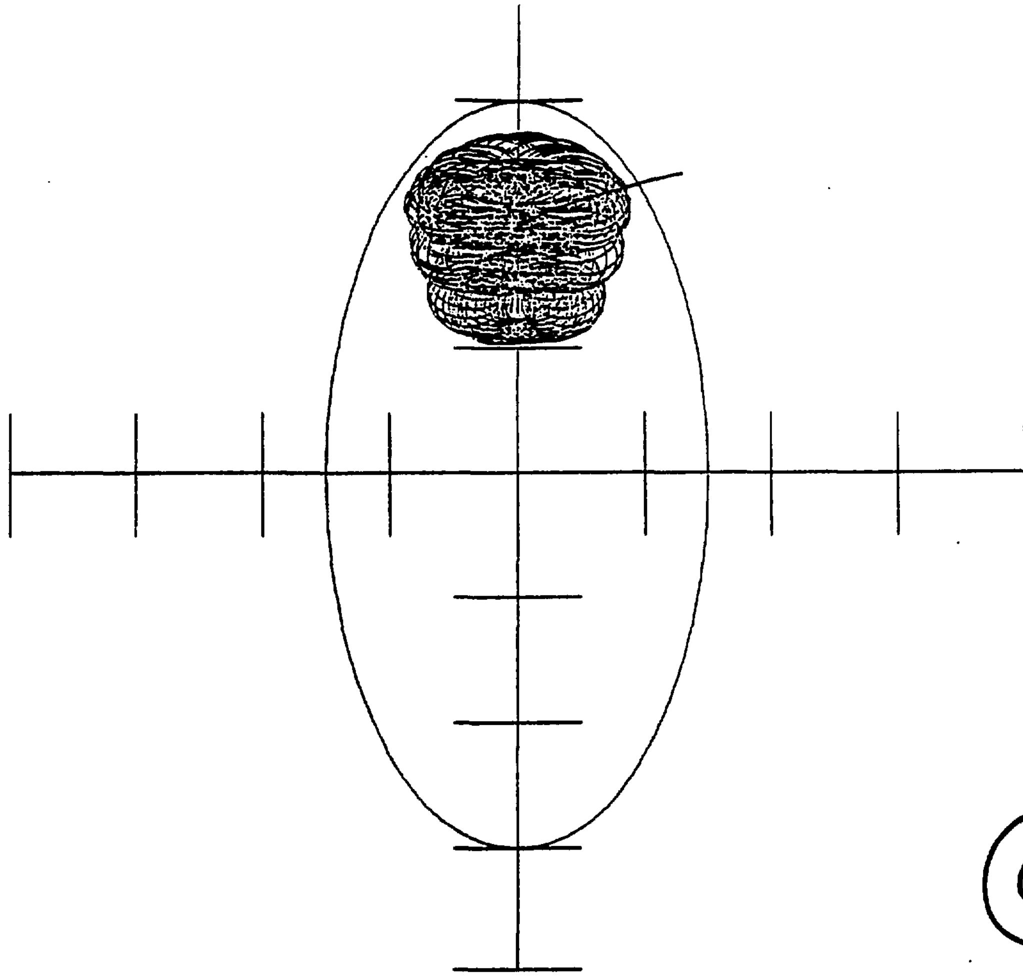

C

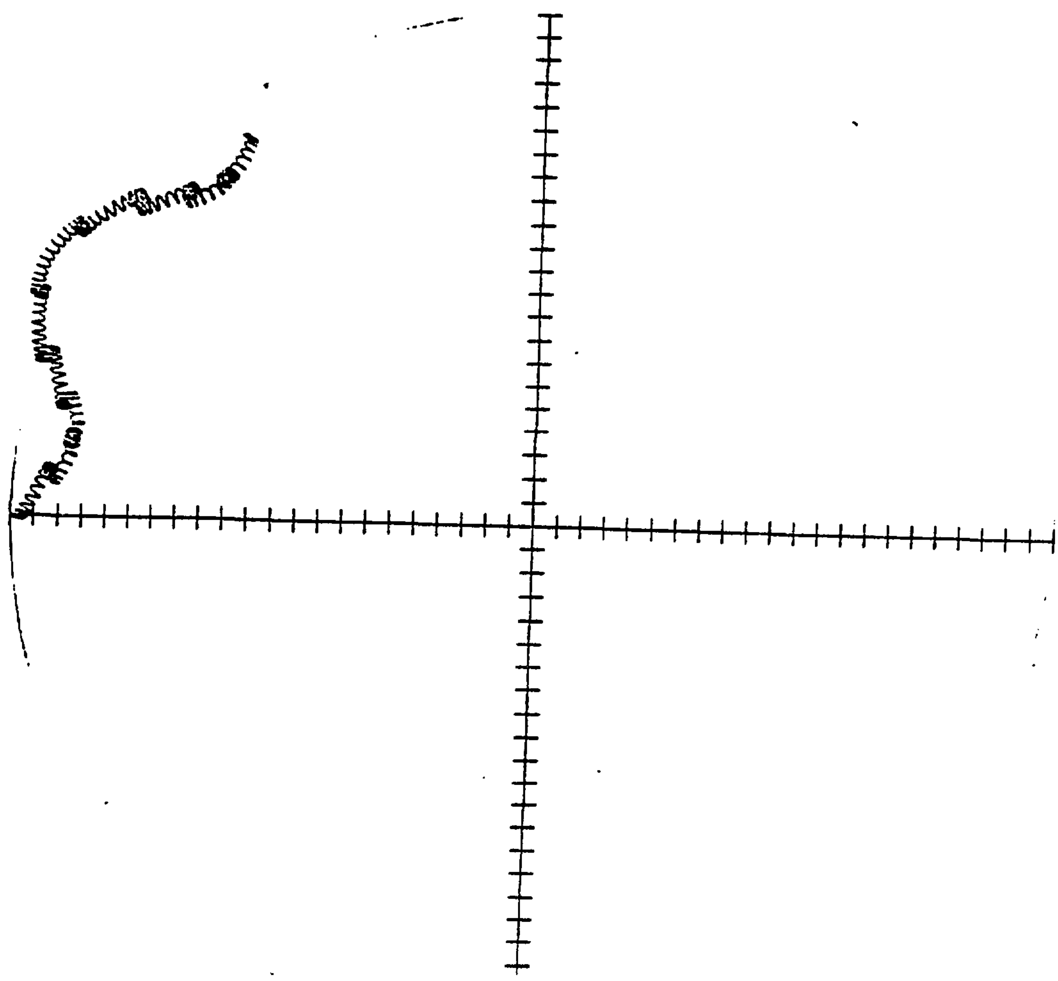

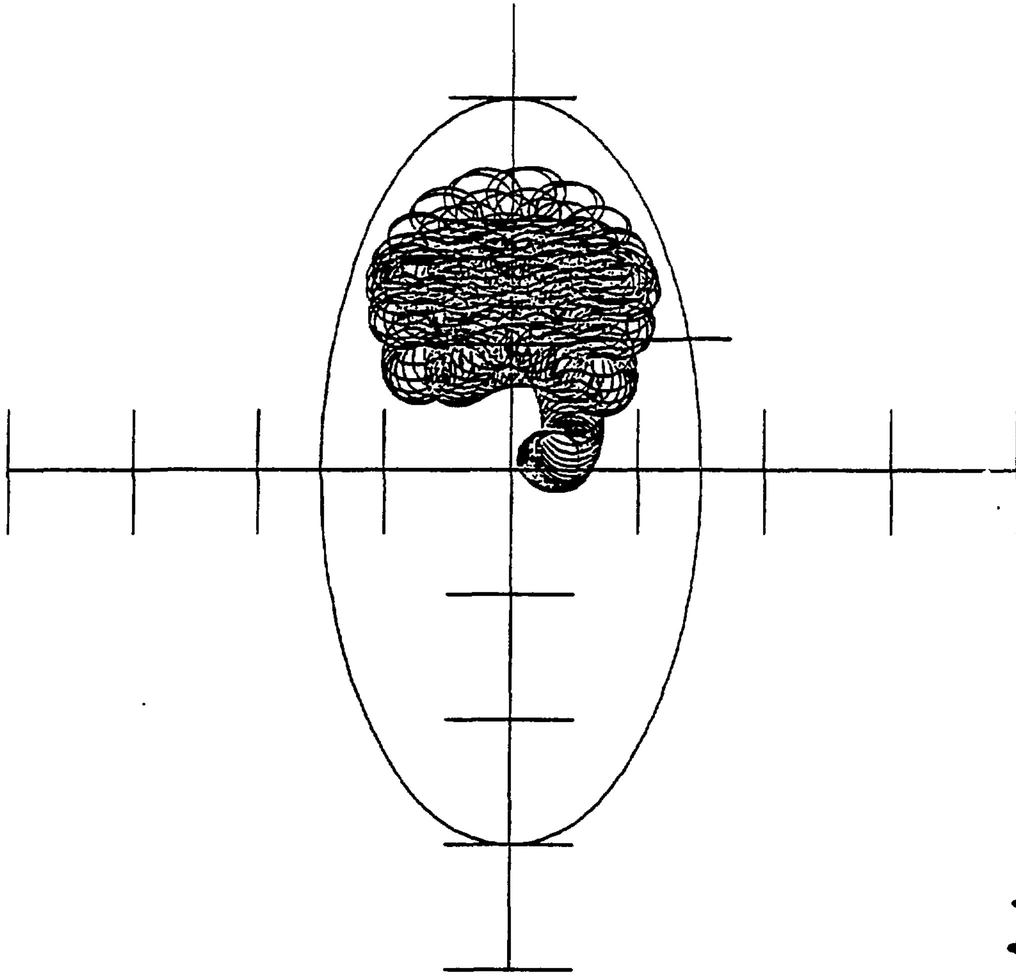

D

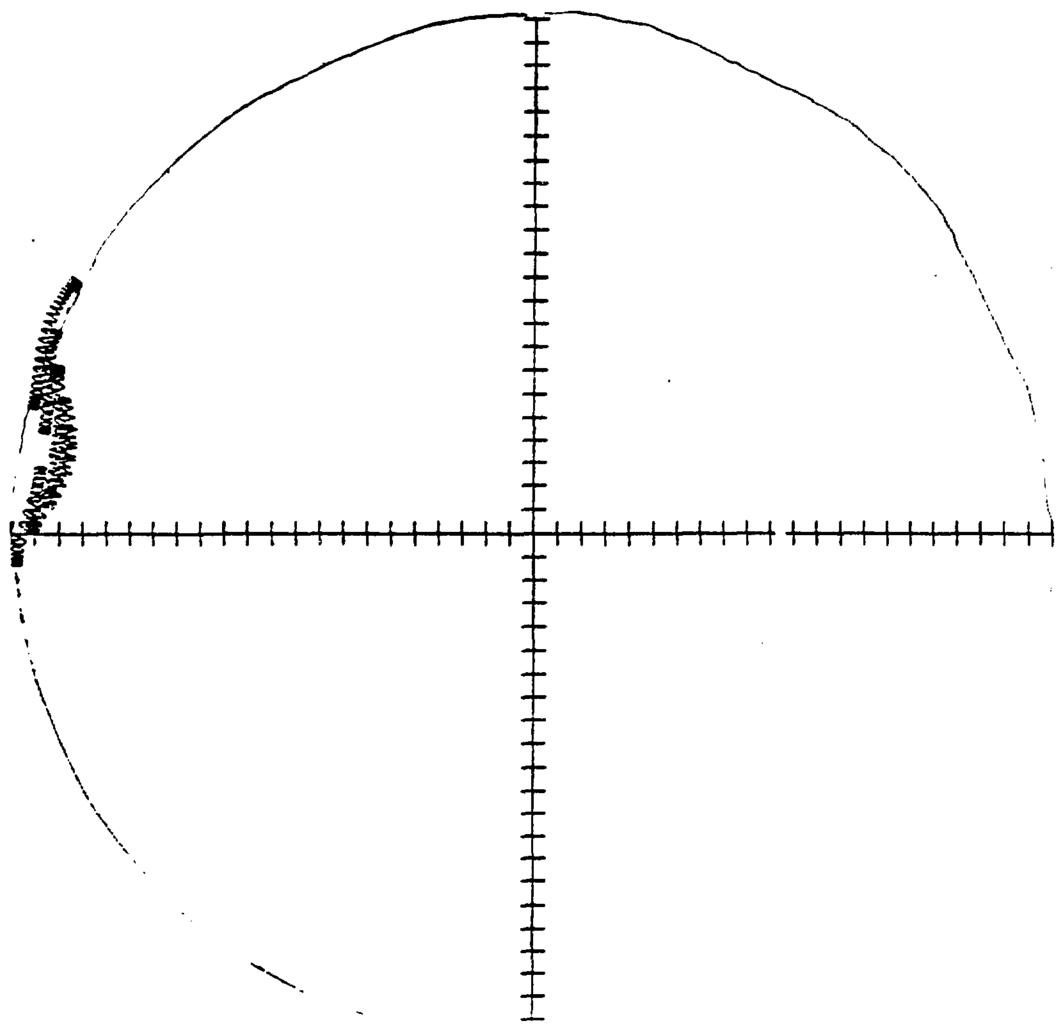

CHS Heating Systems
(NBI,ECH,ICH)

Institute of Plasma Physics, Nagoya Univ.

K. Nishimura, CHS group, RF Heating Group and Plasma Thech. group.

• ECH

* Plasma production and heating.
  28GHz/200kW/ 75msec.
  56GHz/200kW/100msec.
  112GHz/500kW/ - under consideration
* X-O mixed mode.
* $TE_{02} \rightarrow TE_{01}$ mode conversion.
* High field injection.

• NBI

* 3MW/40kV/1sec./2 beam lines.
* Variable injection angle.
* Counter injection/2 beam lines.

• ICH

* High density plasma production by Whistler Wave.
  f=40-200 MHz in B=0.5-2 T.
* Ion Bernstein Wave heating.
  Effective heating even in a high density plasma ($10^{14} cm^{-3}$).
  Installed at low field side and movable.

CHS Heating Systems
(NBI,ECH,ICH)

K. Nishimura, CHS group, RF Heating Group
and Plasma Thech. group.
Institute of Plasma Physics, Nagoya University, Nagoya 464, Japan

ECH is used for the plasma production and heating from the beginning of the experiment. The capacity of the gyrotron which we have now is as follows. Its frequency is 28 GHz, output power 200 kW and pulse length 75 msec. Its operation regime is around 1 Tesla and the expected plasma density is $\sim 1\times10^{13}cm^{-3}$. With the reinforcement of the power supply in 1988, we will buy a new gyrotron which frequency is 56 GHz, output power 200 kW and pulse length 100 msec. Usually, injection from a high field side is difficult for the helical coils in a helical system. However, we chose a specified injecting angle and we made it possible to inject from the equivalent high field side.

NBI is an effective heating method in any systems. To get a good deposition profile, a long beam line is desirable. From this point of view, we will install two tangential injecting NBIs. One has a variable injecting angle for the research of the loss cone effect. Another has a fixed injecting angle. Using two NBI, we can do the beam driven currentless experiments. Each NBI has [redacted] 1.5 MW injection power at the injecting port and its beam energy is 40 kV. Expected absorption rate is about 80 % in $\langle n_e\rangle=2\times10^{13}cm^{-3}$.

ICH is a useful method for a plasma production and heating because it has a wide operating range of a frequency and a magnetic field strength. We are planning the plasma production by the slow wave and m=0 whistler mode and the heating by the slow wave and the ion Bernstein wave. Now we are designing the movable antenna systems and their matching systems.

Schedule of Machine Construction

FY		1987	1988	1989	1990	1991
Experiment Phase			ECH Plasma Confinement Plasma Production with ICRF	Additional Heating with NBI,ICRF Phase I	Additional Heating with NBI,ICRF Phase II	High Beta Plasma Helical Axis
Magnetic Field Vacuum Vessel		Coils,Vessel and Power Supply for 1.5 Tesla Field	Modification of Power Supply for 2.0 Tesla Field	Carbon Tile Pump Limiter	Pellet Injector	Helical Axis Configuration
Heating Systems	ECH	28 GHz (200kV)	56 GHz (200kV)		112 GHz (500kV)	
	NBI		40keV (1.5MW) 1	40keV (1.5MW) 2		
	ICRF	Transmitter 1MW Antennas (Phase I)		Transmitter 3MW Antennas (Phase II)		
Diagnostics		Basic Diagnostics Thomson Scattering HCN Interferometer Fast Neutral Particles Visible Spectroscopy Magnetic Measurement Data Acquisition System	Additional Diagnostics ECE, SX High Energy Particles X ray Spectroscopy Edge Region Diagnostics	Electric Field Diagnostics Heavy Ion Beam Probe Doppler Shift	CX Recombination Spectroscopy	

Experimental Schedule

FY		1987	1988	1989	1990	1991
Machines	Bmax		Bmax=1.5 Tesla		Bmax=2.0 Tesla	
	ECH		28GHz	28GHz+56GHz		56GHz+112GHz
	NBI			40keV 1.5MW	40keV 3MW (2 Injectors)	
	ICRF		ICRF 1MW		ICRF 4MW	
Experimental Scenario		Installation Performance Check Vacuum Pumping	Discharge Cleaning Magnetic Surface Measurements 28GHz ECH Parameter Survey Poloidal Coil Control ICRF Plasma Production ICRF Wave Measurements	56GHz ECH NBI,ICRF Heating Impurity Control Injection Angle Control for NBI High Energy Particles Measurements	Strong Additional Heating Detailed Magnetic Measurements Particle Control NBI Balanced Injection Elec. Field Measurements	Parameter Survey for Te,Ti Electric Field Control High Beta Experiments Helical Axis Experiments
Related Subjects			Confinement Scaling I Configuration Studies Ergodic Layer Structure	High Te Plasma with ECH Xe Profile ICRF Heating Physics Pitch Angle and Confinement	Additional Heating Scaling MHD Stability High Energy Particle Confinement Toroidal Rotation Particle Balance Wall Loading	Confinement Scaling II Radial Electric Field High Beta Physics Helical Axis Physics

Initial Phase Schedule

FY	Vacuum Wall	ICRF Antenna	Plasma	Schedule
1988	Stainless Steel(Ti gettering)	Discharge Cleaning	ECH	Magnetic Surface Measurements Discharge Cleaning ICRF Plasma Production (preliminary) 28GHz ECH with 1 Tesla Field Plasma Position and Shaping Control Optimization of Poloidal Field Confinement Scaling Measurements of Plasma Boundary and Edge Structure by Instrumented Limiter and Langmuir Probes Final Determination of ICRF Antenna Design ICRF Plasma Production ICRF Wave Propagation Measurements 56GHz ECH with 2 Tesla Fiels
1989	Carbon Limiter Carbon Tile	Installation of Heating Antennas	ICRF ECH	Installation of Carbon Tiles Additional Heating by NBI and ICRF

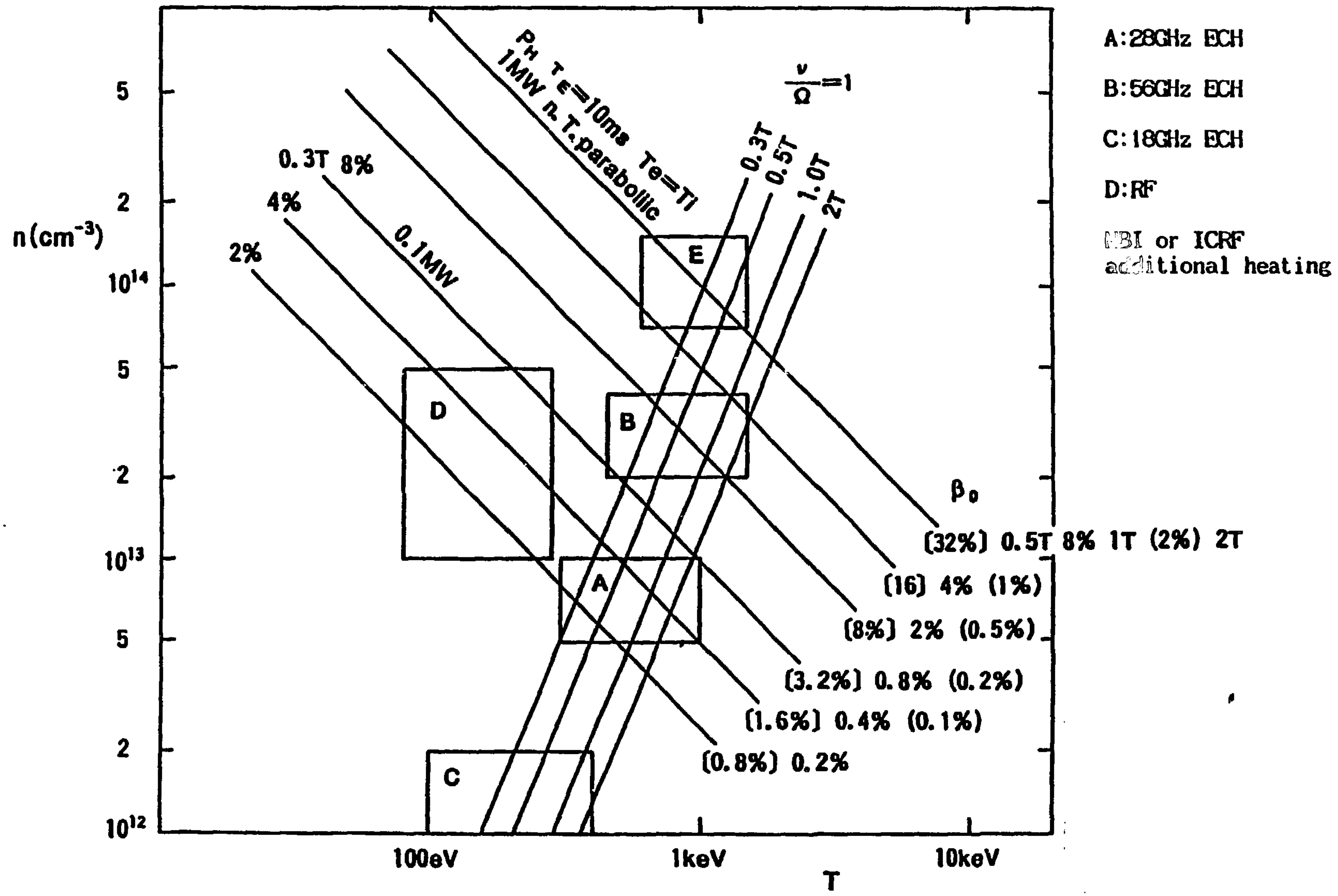

n(cm^-3)
5
2
10^14
5
2
10^13
5
2
10^12
100eV
1keV
10keV
T
P_H τ_E=10ms Te=Ti
1MW n,T,parabolic
0.1MW
0.3T 8%
4%
2%
ν/Ω=1
0.3T
0.5T
1.0T
2T
A
B
C
D
E
β_0
(32%) 0.5T 8% 1T (2%) 2T
(16) 4% (1%)
(8%) 2% (0.5%)
(3.2%) 0.8% (0.2%)
(1.6%) 0.4% (0.1%)
(0.8%) 0.2%
A:28GHz ECH
B:56GHz ECH
C:18GHz ECH
D:RF
NBI or ICRF
additional heating

Ray tracing

$$\frac{d\mathbf{r}}{d\tau} = \frac{\partial g}{\partial \mathbf{k}}$$

$$\frac{d\mathbf{k}}{d\tau} = -\frac{\partial g}{\partial \mathbf{r}}$$

Runge-Kutta

~ Adams method

$$g = \det \begin{bmatrix} \varepsilon_{11} - n_\parallel^2, & \varepsilon_{12}, & \varepsilon_{13} + n_\perp n_\parallel \\ \varepsilon_{21}, & \varepsilon_{22} - n^2, & \varepsilon_{23} \\ \varepsilon_{31} + n_\perp n_\parallel, & \varepsilon_{32}, & \varepsilon_{33} - n_\perp^2 \end{bmatrix}$$

Cold

$$\varepsilon_{11} = 1 - \frac{\omega_{pe}^2}{\omega^2} \cdot \frac{1}{1 - \frac{\Omega_e^2}{\omega^2}} - \sum_\sigma \frac{\omega_{p\sigma}^2}{\omega^2} \frac{1}{1 - \frac{\Omega_\sigma^2}{\omega^2}}$$
$$= \varepsilon_{22}$$

$$\varepsilon_{12} = -\varepsilon_{21} = -i \left(-\frac{\omega_{pe}^2}{\omega^2} \frac{\frac{\Omega_e}{\omega}}{1 - \frac{\Omega_e^2}{\omega^2}} + \sum_\sigma \frac{\omega_{p\sigma}^2}{\omega^2} \cdot \frac{\frac{\Omega_\sigma}{\omega}}{1 - \frac{\Omega_\sigma^2}{\omega^2}} \right)$$

$$\varepsilon_{13} = \varepsilon_{31} = 0$$

$$\varepsilon_{32} = \varepsilon_{23} = 0$$

$$\varepsilon_{33} = 1 - \frac{\omega_{pe}^2}{\omega^2} - \sum_\sigma \frac{\omega_{p\sigma}^2}{\omega^2}$$

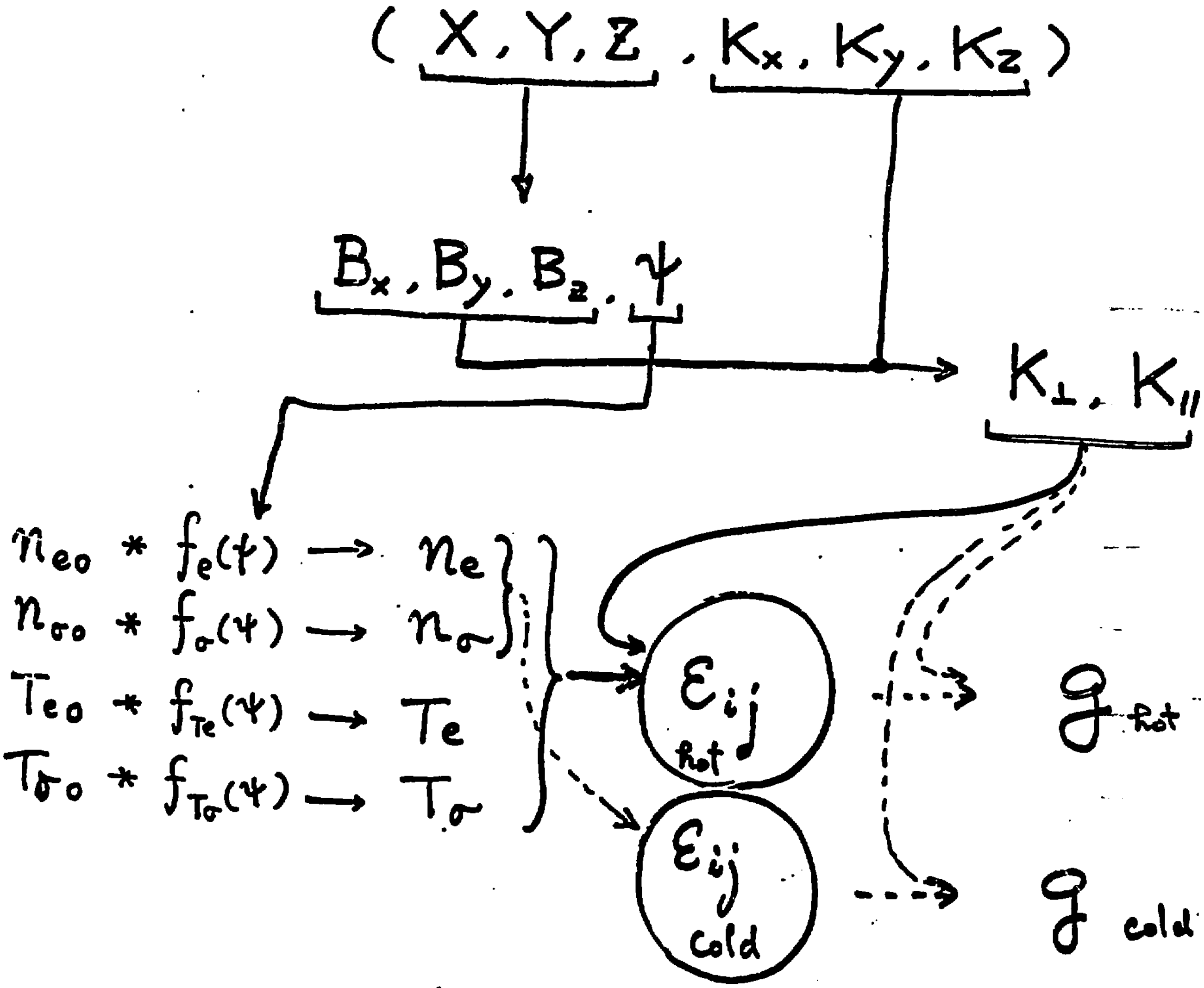

Ray

$$\begin{cases} \dfrac{d\mathbf{r}}{d\tau} = \dfrac{\partial \, \mathrm{Re}(g_{cold})}{\partial \mathbf{k}} \\[2ex] \dfrac{d\mathbf{k}}{d\tau} = -\dfrac{\partial \, \mathrm{Re}(g_{cold})}{\partial \mathbf{r}} \end{cases}$$

Absorption

$$1 - \exp\left[2\int \mathbf{k}_i \cdot ds\right] \sim 1 - \exp\int 2 \cdot \mathrm{Im}(g_{hot})\, d\tau$$

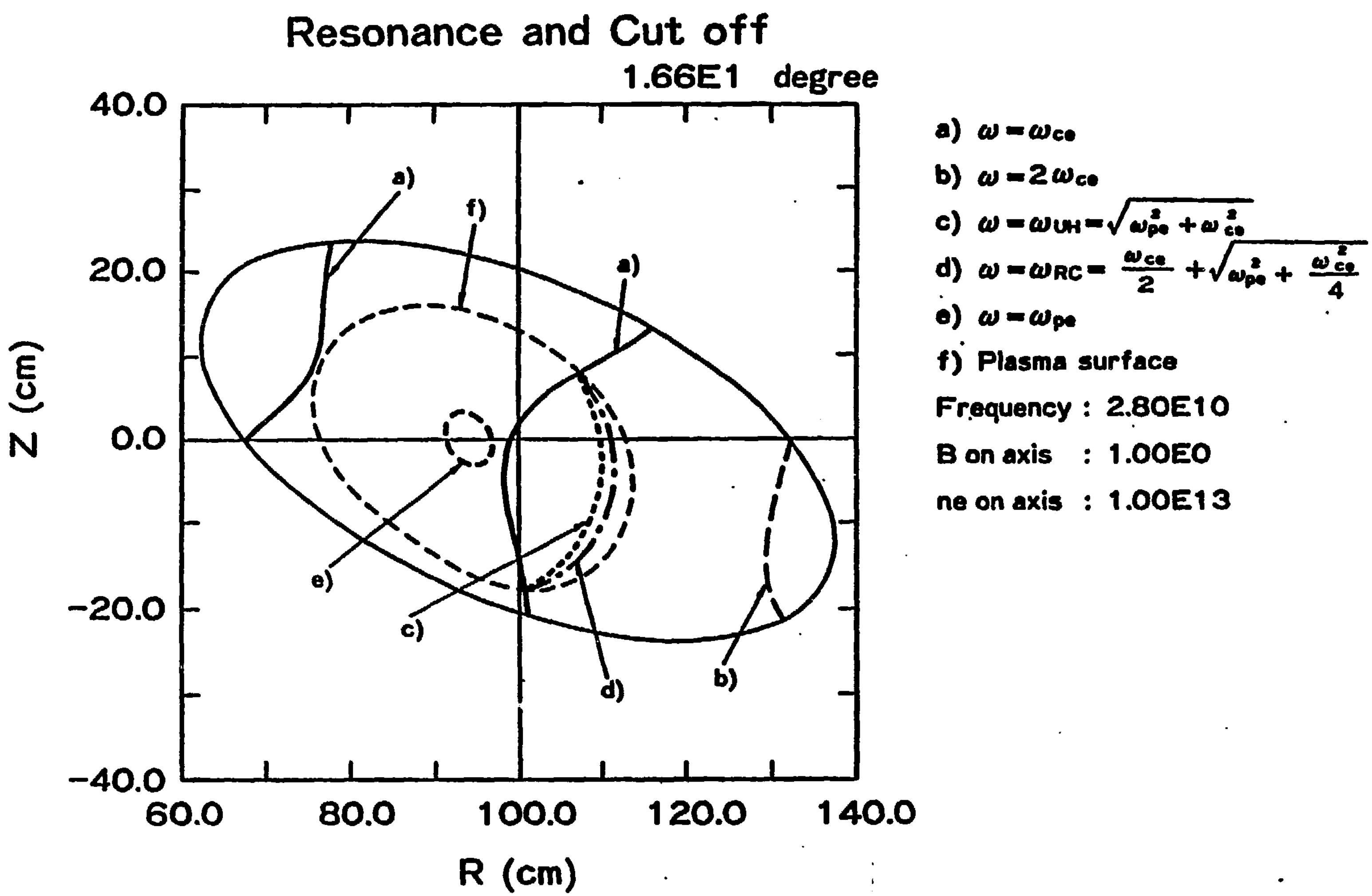
Resonance and Cut off
1.66E1 degree
40.0
20.0
0.0
-20.0
-40.0
Z (cm)
60.0
80.0
100.0
120.0
140.0
R (cm)
a)
f)
a)
e)
c)
d)
b)
a) $\omega = \omega_{ce}$
b) $\omega = 2\omega_{ce}$
c) $\omega = \omega_{UH} = \sqrt{\omega_{pe}^2 + \omega_{ce}^2}$
d) $\omega = \omega_{RC} = \frac{\omega_{ce}}{2} + \sqrt{\omega_{pe}^2 + \frac{\omega_{ce}^2}{4}}$
e) $\omega = \omega_{pe}$
f) Plasma surface
Frequency : 2.80E10
B on axis : 1.00E0
ne on axis : 1.00E13

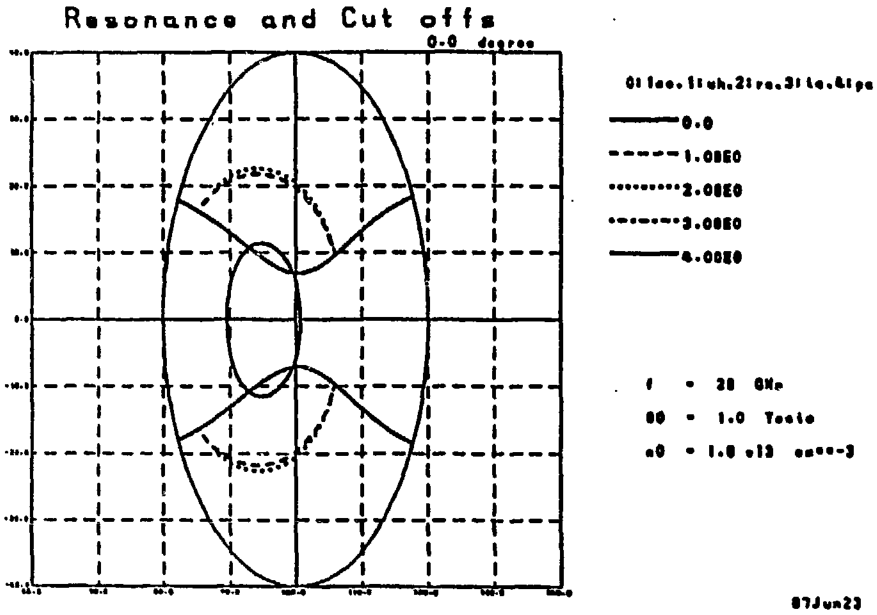
Resonance and Cut offs
0.0 degree
0:lec,1:uh,2:rc,3:lc,4:pc
0.0
1.00E0
2.00E0
3.00E0
4.00E0
f = 28 GHz
B0 = 1.0 Tesla
n0 = 1.0 e13 cm**-3
87Jun23

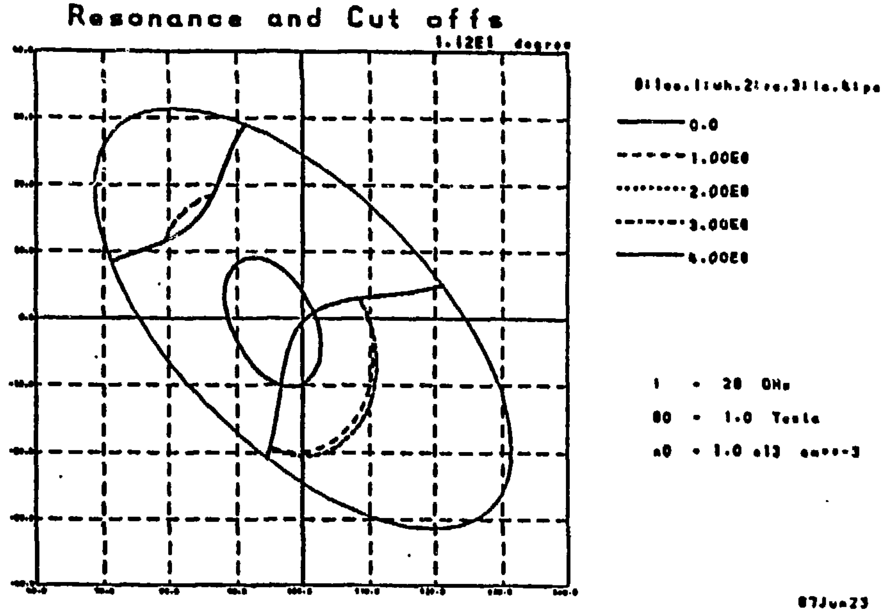
Resonance and Cut offs
1.12E1 degree
0:lec,1:uh,2:rc,3:lc,4:pc
0.0
1.00E0
2.00E0
3.00E0
4.00E0
f = 28 GHz
B0 = 1.0 Tesla
n0 = 1.0 e13 cm**-3
87Jun23

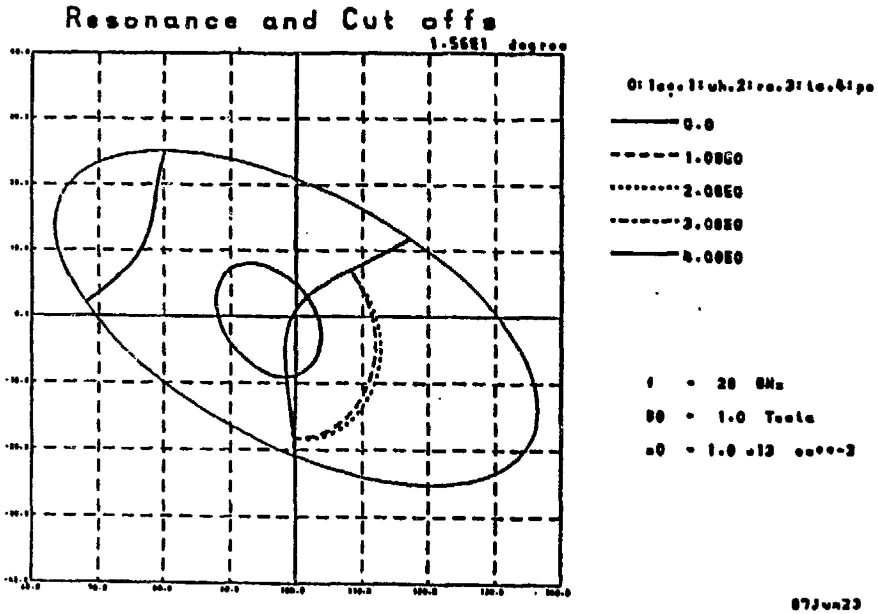
Resonance and Cut offs
1.56E1 degree
0:lec,1:uh,2:rc,3:lc,4:pc
0.0
1.00E0
2.00E0
3.00E0
4.00E0
f = 28 GHz
B0 = 1.0 Tesla
n0 = 1.0 e13 cm**-3
87Jun23

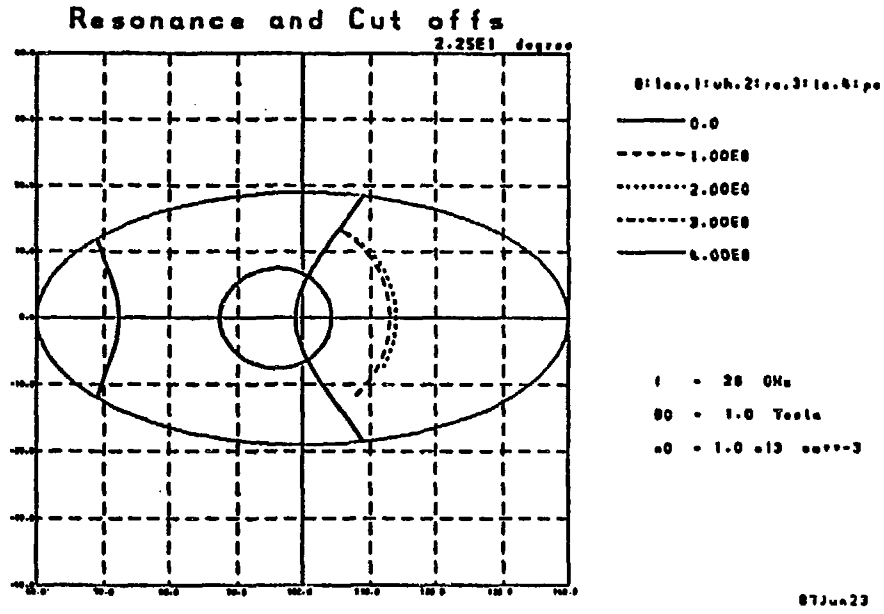
Resonance and Cut offs
2.25E1 degree
0:lec,1:uh,2:rc,3:lc,4:pc
0.0
1.00E0
2.00E0
3.00E0
4.00E0
f = 28 GHz
B0 = 1.0 Tesla
n0 = 1.0 e13 cm**-3
87Jun23

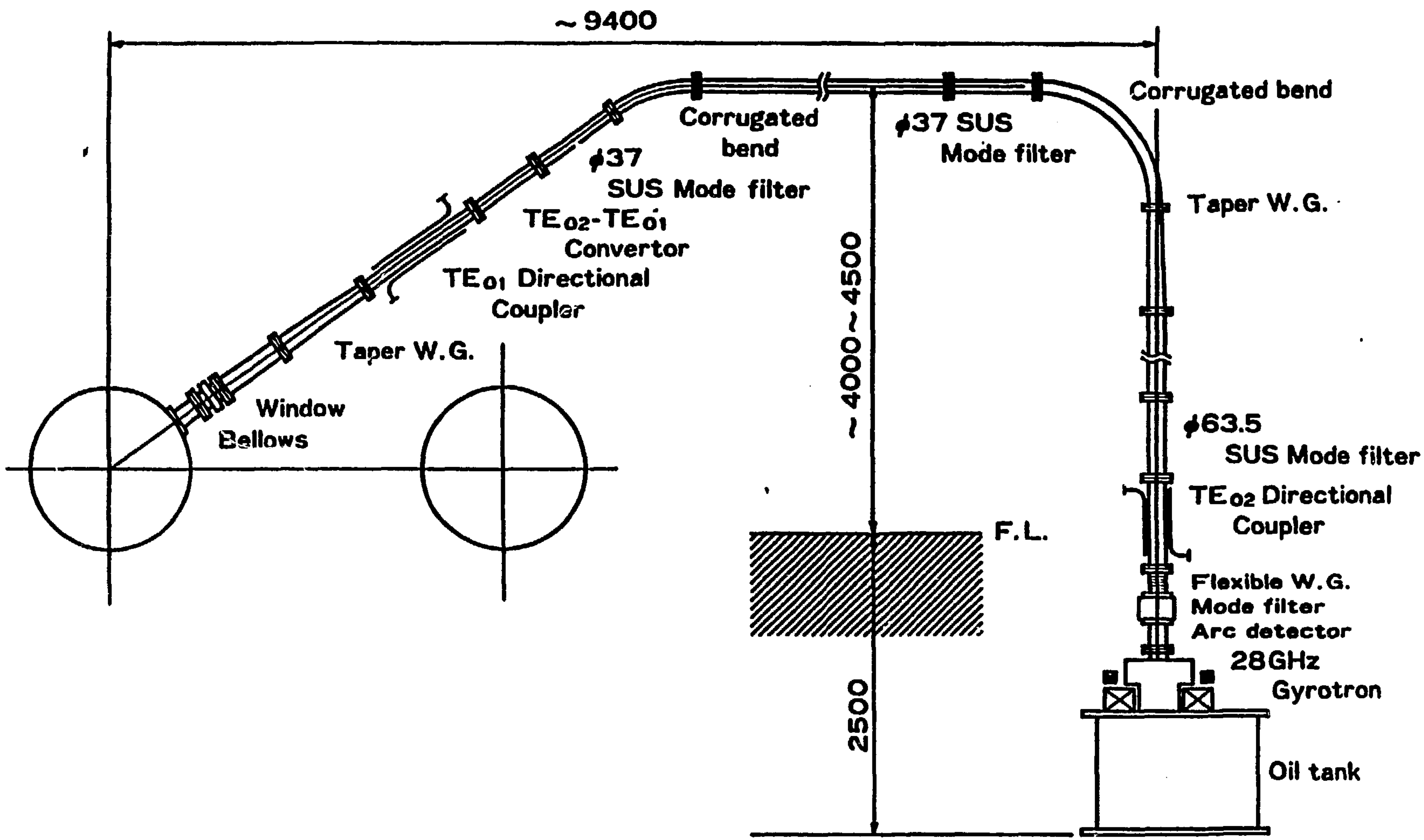

~ 9400
Corrugated bend
Corrugated bend
ϕ37 SUS Mode filter
ϕ37 SUS Mode filter
TE02-TE01 Convertor
TE01 Directional Coupler
Taper W.G.
Window
Bellows
~4000~4500
2500
F.L.
Taper W.G.
ϕ63.5 SUS Mode filter
TE02 Directional Coupler
Flexible W.G.
Mode filter
Arc detector
28GHz Gyrotron
Oil tank

P079.CHS.MOD.TOTAL.DATA

CHSAOH

Frequency = 2.80E10 (Hz) : X-mode

B0 = 1.00E0 (Tesla)

ne0 = 1.00E13 (cm**-3)

TE0 = 1.00E2 (eV)

n(O(1) = 1.00E13 (cm**-3)

Ti(O(1) = 1.00E2 (eV), A=1, Z=1

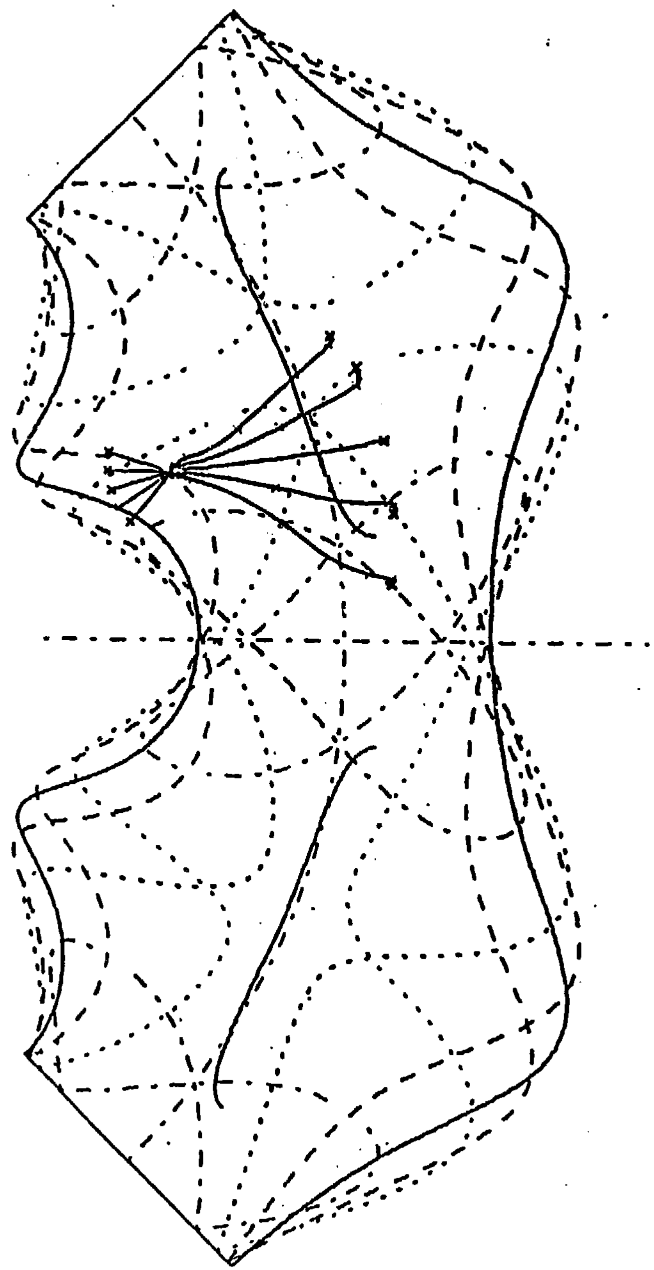

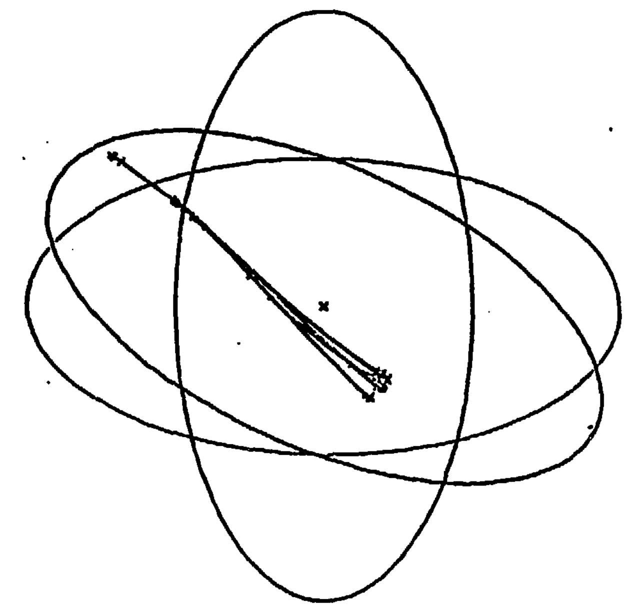

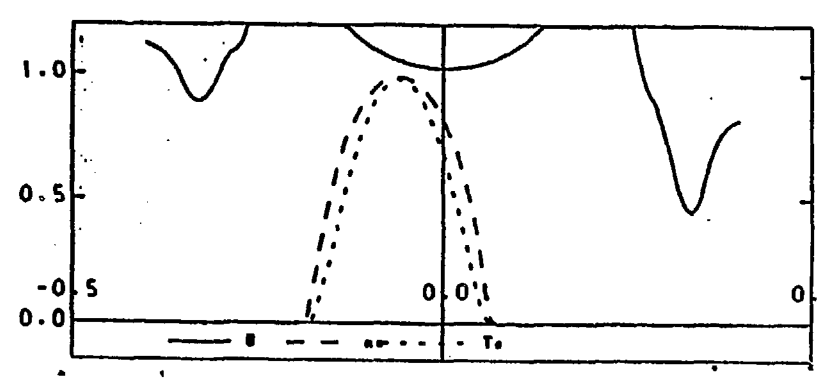

P079.CHS.MOD.TOTAL.DATA
CHSADM
Frequency = 2.80E10 (Hz) : O-mode
B0 = 1.00E0 (Tesla)
ne0 = 1.00E13 (cm**-3)
TE0 = 1.00E2 (eV)
ni0(1) = 1.00E13 (cm**-3)
Ti0(1) = 1.00E2 (eV), A=1, Z=1

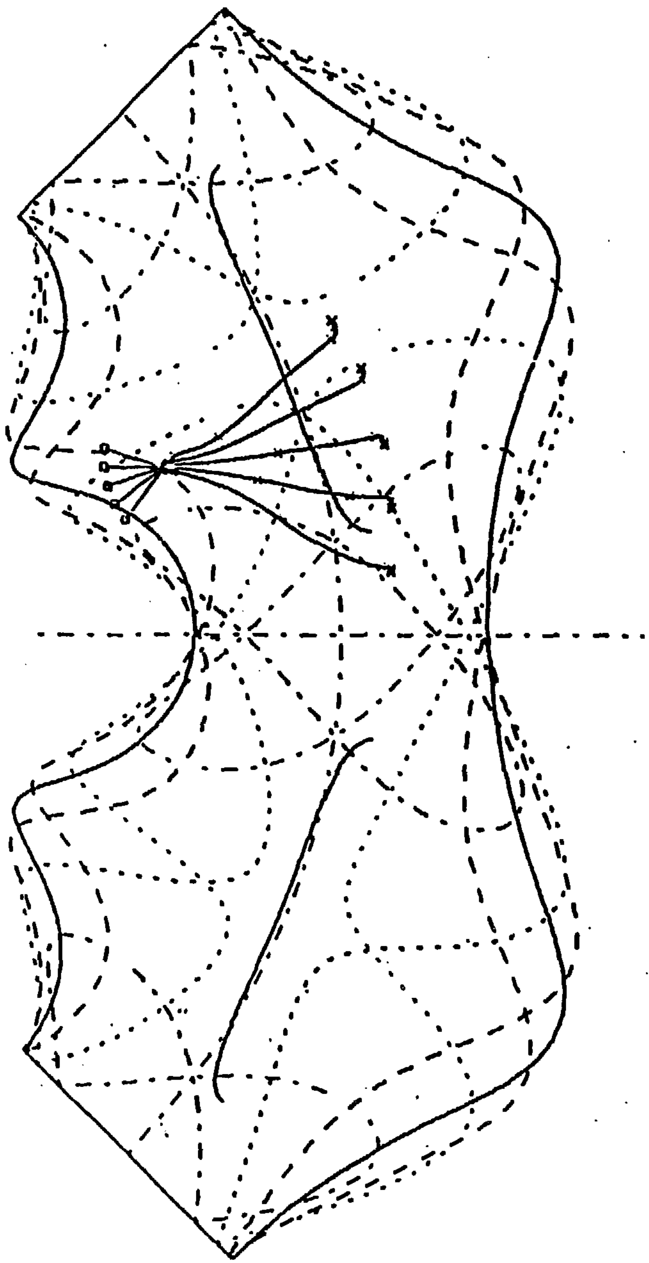

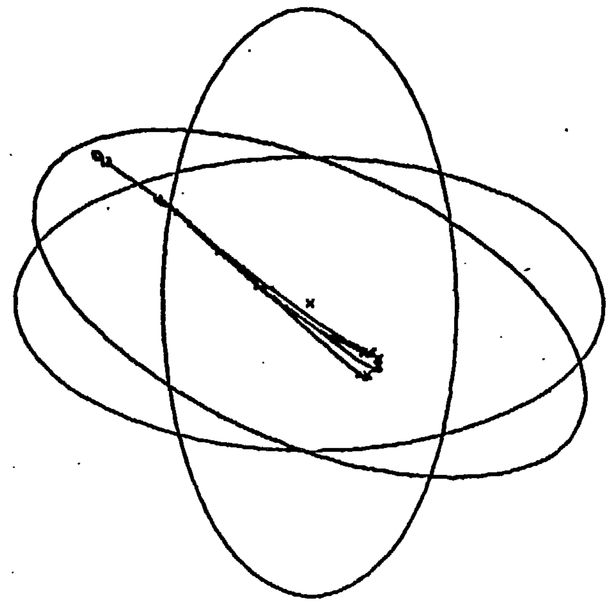

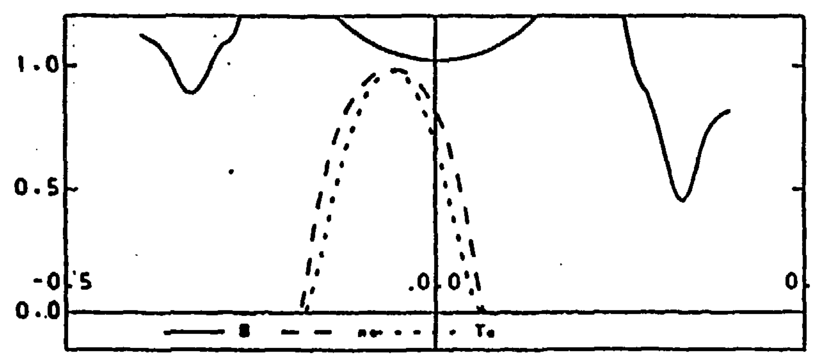

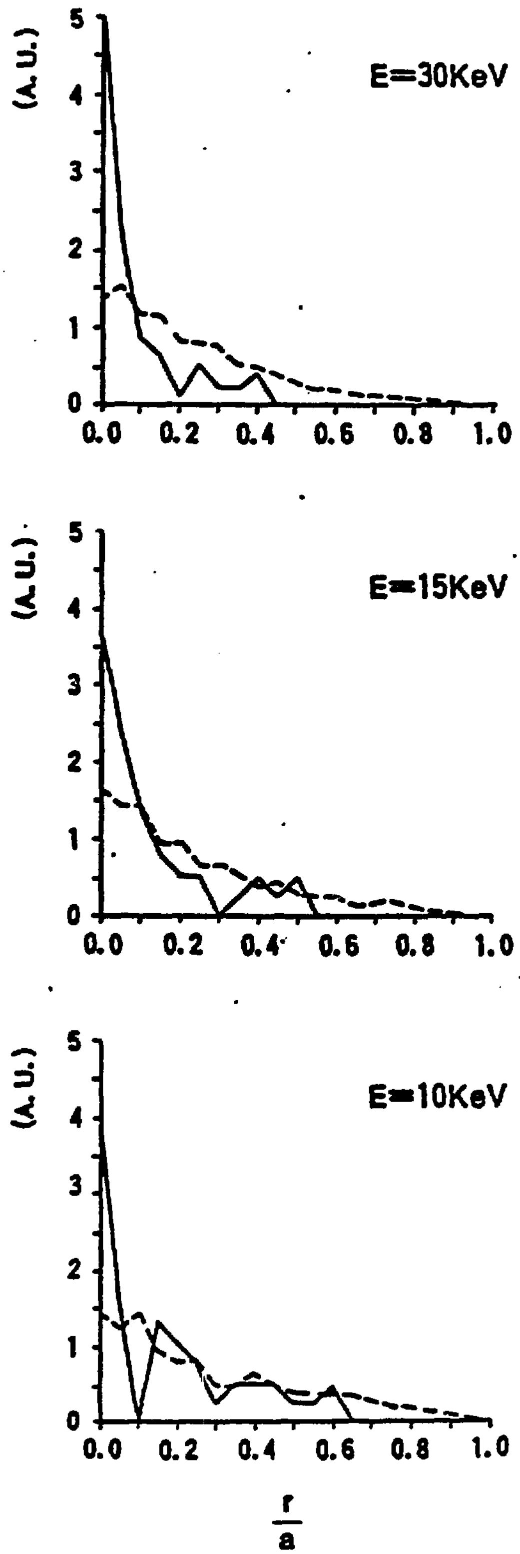
E=30KeV
E=15KeV
E=10KeV
(A.U.)
0.0 0.2 0.4 0.6 0.8 1.0
r/a

Cace		Ne (cm^{-3})	B	P_{NBI} P_{ECH}	global τ_E	electrons			ions			⟨β⟩ (beam ioms)
						τ_E	$T_e(o)$	⟨T_e⟩	τ_E	$T_i(o)$	⟨T_i⟩	
I	Reference	5×10^{13}	1.5 T	2 MW 0.2 MW	8.1 ms	24 ms	1.9 keV	0.8 keV	4.2 ms	1.9 keV	0.6 keV	3.0% (2.0%)
II	Lower density	3×10^{13}	1.5 T	2 MW 0.2 MW	7.3 ms	13 ms	2.0 keV	0.8 keV	4.0 ms	1.7 keV	0.5 keV	2.7% (2.2%)
III	Anomaly only No ripple	5×10^{13}	1.5 T	2 MW 0.2 MW	15 ms	23 ms	2.0 keV	1.1 keV	11 ms	1.9 keV	1.0 keV	3.4% (1.4%)
IV	Anomaly and Ripple	5×10^{13}	1.5 T	2 MW 0.2 MW	7.1 ms	13 ms	1.6 keV	0.7 keV	4.4 ms	1.6 keV	0.6 keV	2.9% (2.0%)

(1) Beam absorbed power is approximately 1MW

(2) Anomaly is set as a half of INTOR scaling : $D = 5\times10^{16} \cdot n_e^{-1}$ (cm^2/s), $\chi_e = 2.5\times10^{17} \cdot n_e^{-1}$ (cm^2/s)

(3) Ripple profile : $\epsilon_h = 0.2 \left(\frac{r}{a}\right)^2$

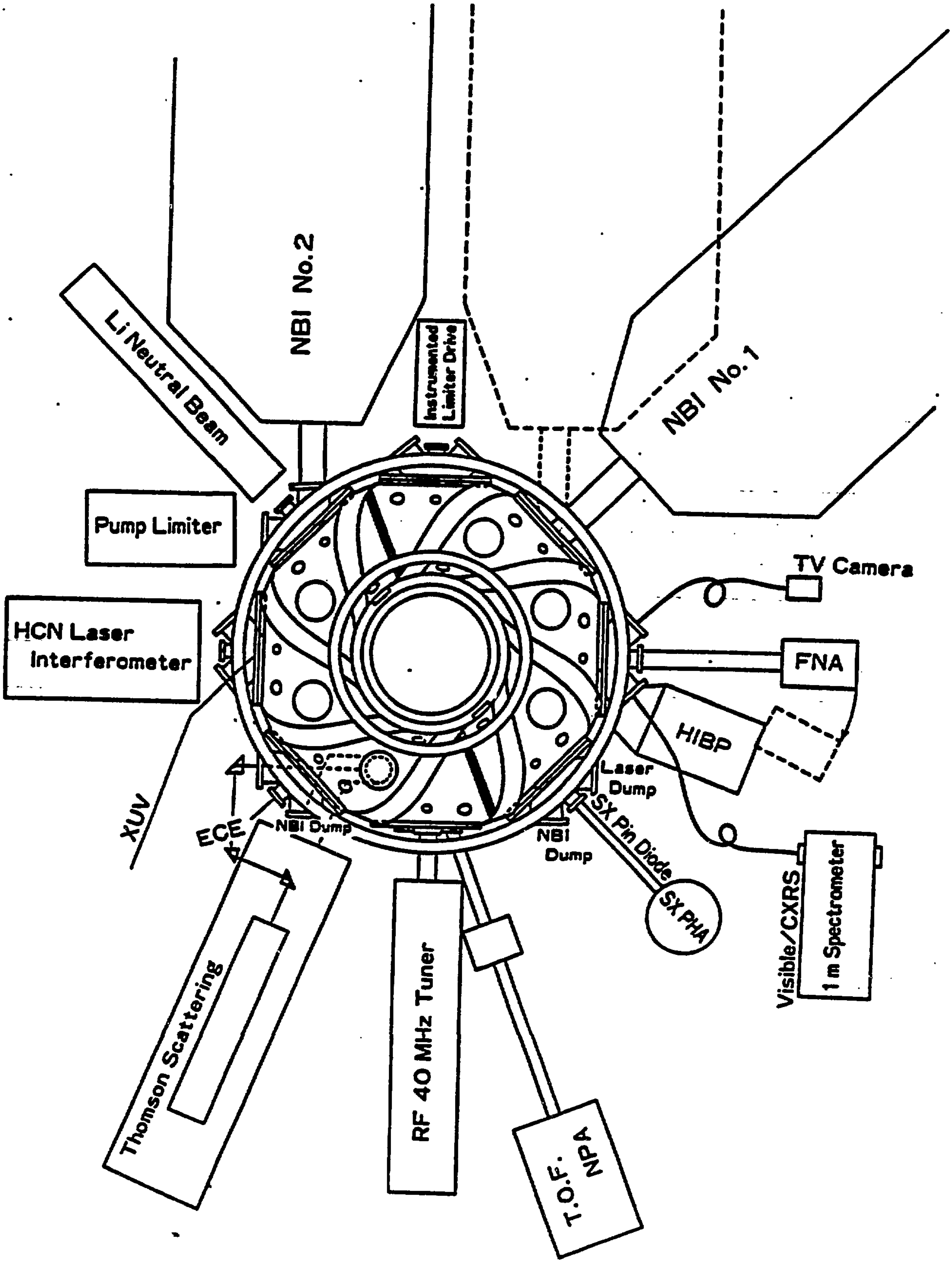
NBI No.2
Li Neutral Beam
Instrumented Limiter Drive
NBI No.1
Pump Limiter
HCN Laser Interferometer
TV Camera
FNA
HIBP
Laser Dump
XUV
ECE
NBI Dump
NBI Dump
SX Pin Diode
SX PHA
Visible/CXRS
1 m Spectrometer
Thomson Scattering
RF 40 MHz Tuner
T.O.F. NPA

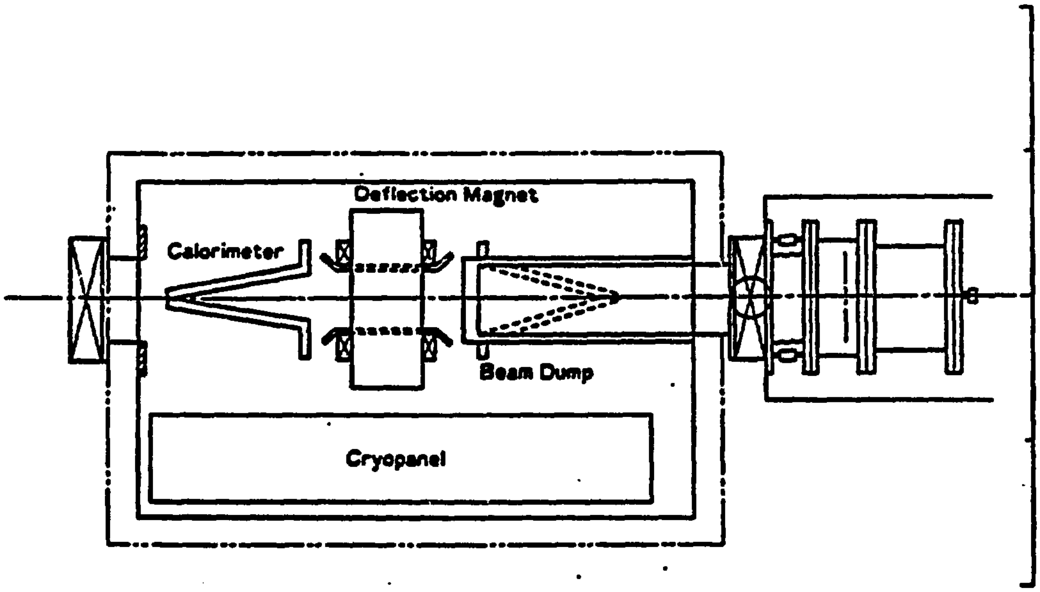

Deflection Magnet
Calorimeter
Beam Dump
Cryopanel

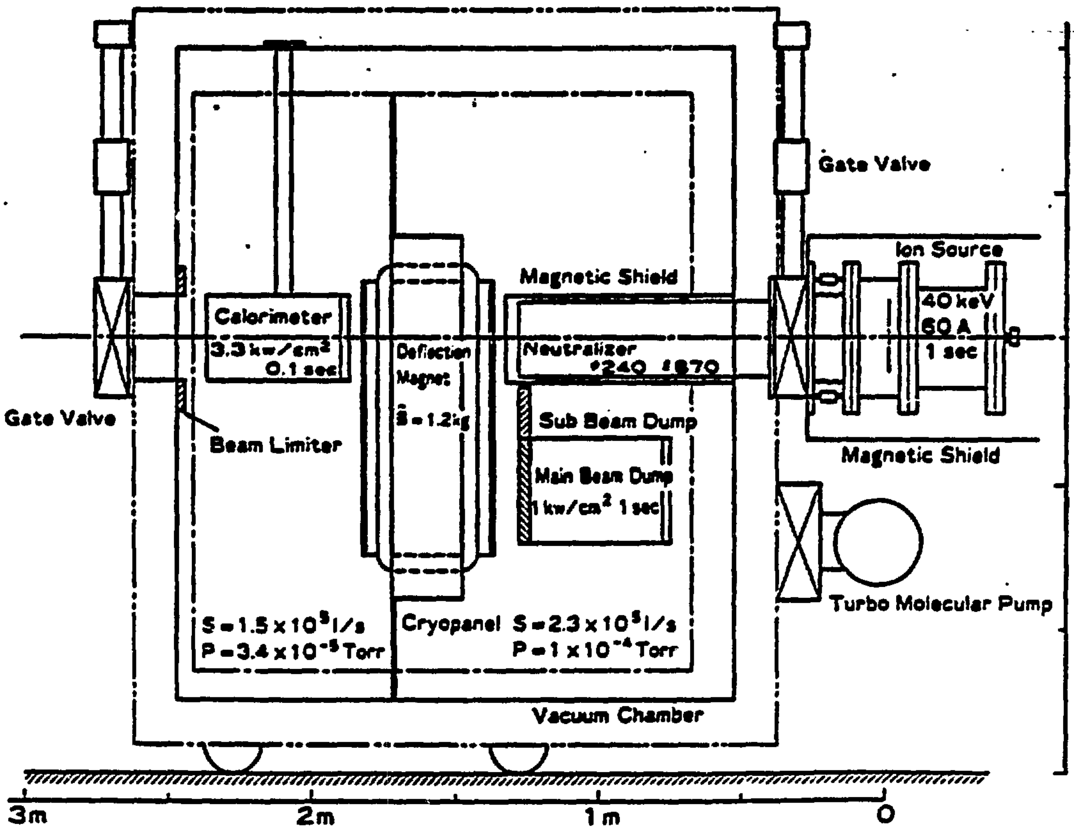

Gate Valve
Ion Source
Magnetic Shield
Calorimeter
3.3 kw/cm²
0.1 sec
Deflection Magnet
B = 1.2kg
Neutralizer
ϕ240 ϕ870
Sub Beam Dump
Main Beam Dump
1 kw/cm² 1 sec
40 keV
60 A
1 sec
Magnetic Shield
Gate Valve
Beam Limiter
Turbo Molecular Pump
S = 1.5 x 10⁵ l/s
P = 3.4 x 10⁻⁵ Torr
Cryopanel
S = 2.3 x 10⁵ l/s
P = 1 x 10⁻⁴ Torr
Vacuum Chamber
3m
2m
1 m
0

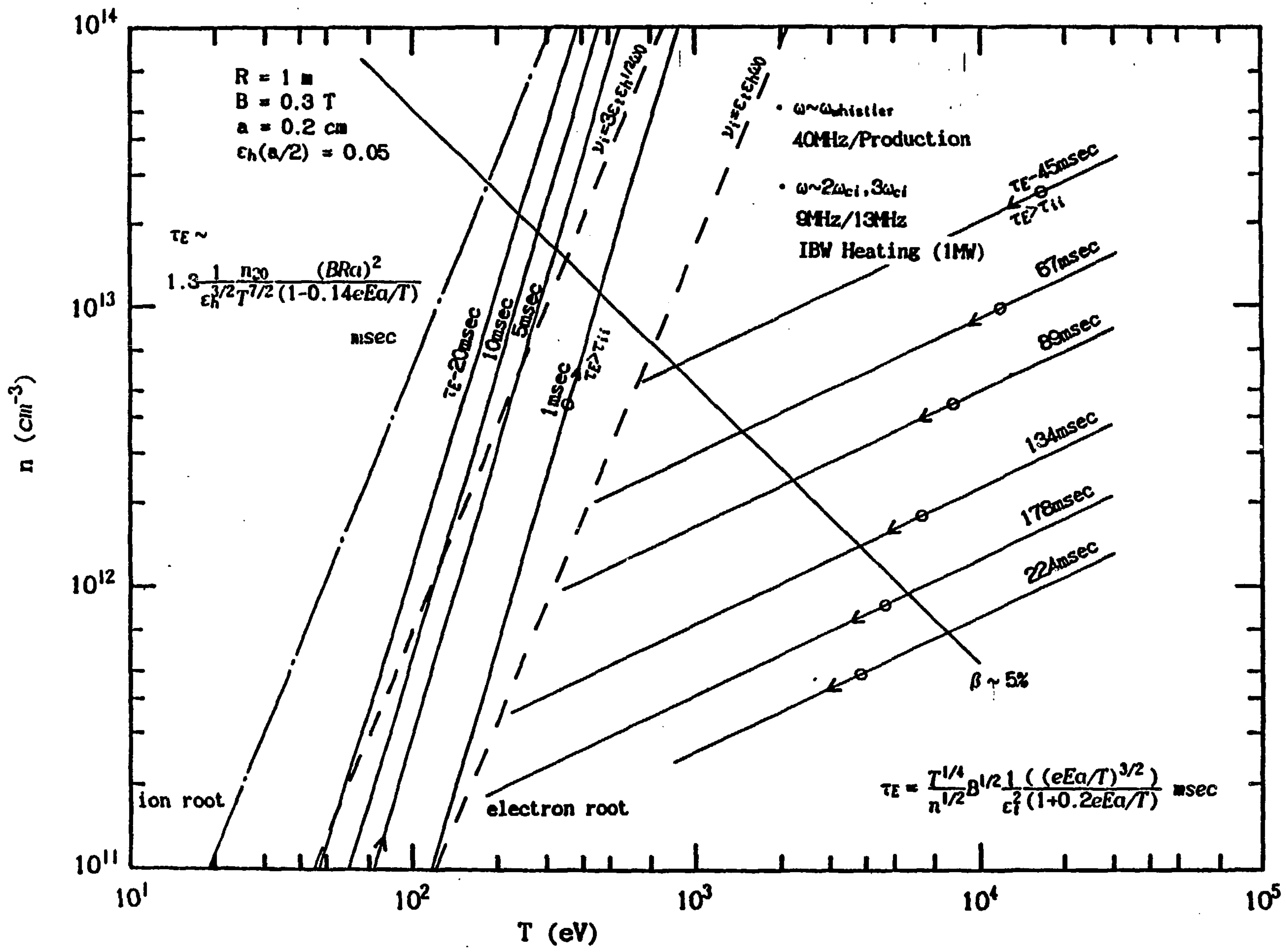
R = 1 m
B = 0.3 T
a = 0.2 cm
εh(a/2) = 0.05
τE ~ 1.3 (1/εh^3/2)(n20/T^7/2)((BRa)^2/(1-0.14eEa/T)) msec
τE~20msec
10msec
5msec
1msec
τE>τii
νi=3εtεh^1/2ω0
νi=εtεhω0
• ω~ωwhistler 40MHz/Production
• ω~2ωci,3ωci 9MHz/13MHz IBW Heating (1MW)
τE~45msec
τE>τii
67msec
89msec
134msec
178msec
224msec
β ~ 5%
ion root
electron root
τE = (T^1/4/n^1/2) B^1/2 (1/εt^2) ((eEa/T)^3/2/(1+0.2eEa/T)) msec
n (cm^-3)
T (eV)
10^14
10^13
10^12
10^11
10^1
10^2
10^3
10^4
10^5

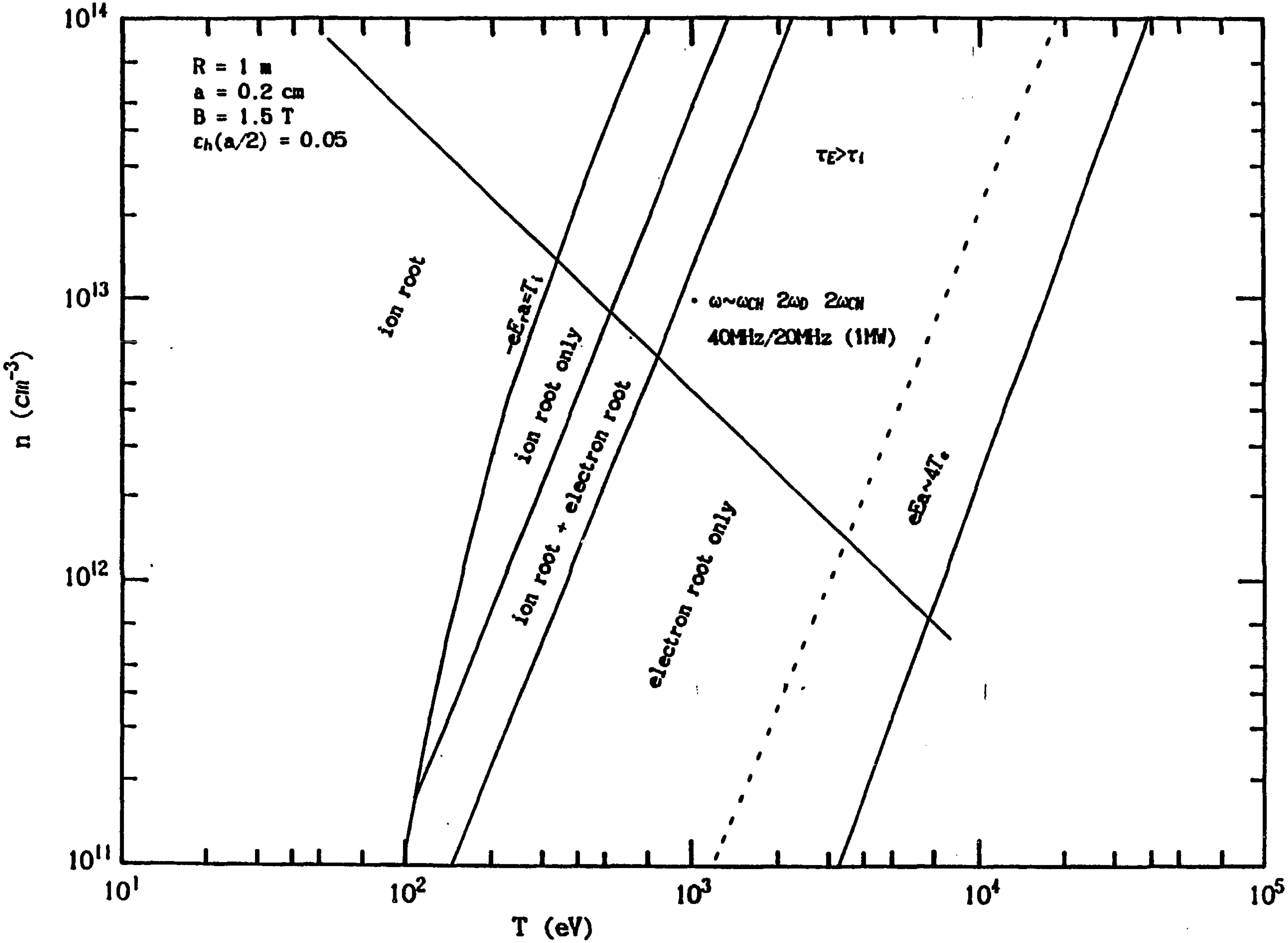

R = 1 m
a = 0.2 cm
B = 1.5 T
$\epsilon_h(a/2)$ = 0.05
ion root
$-eE_ra=T_i$
ion root only
ion root + electron root
electron root only
$\tau_E>\tau_i$
$\omega\sim\omega_{cH}$ $2\omega_D$ $2\omega_{cH}$
40MHz/20MHz (1MW)
$eE_a\sim 4T_e$
n (cm^{-3})
T (eV)

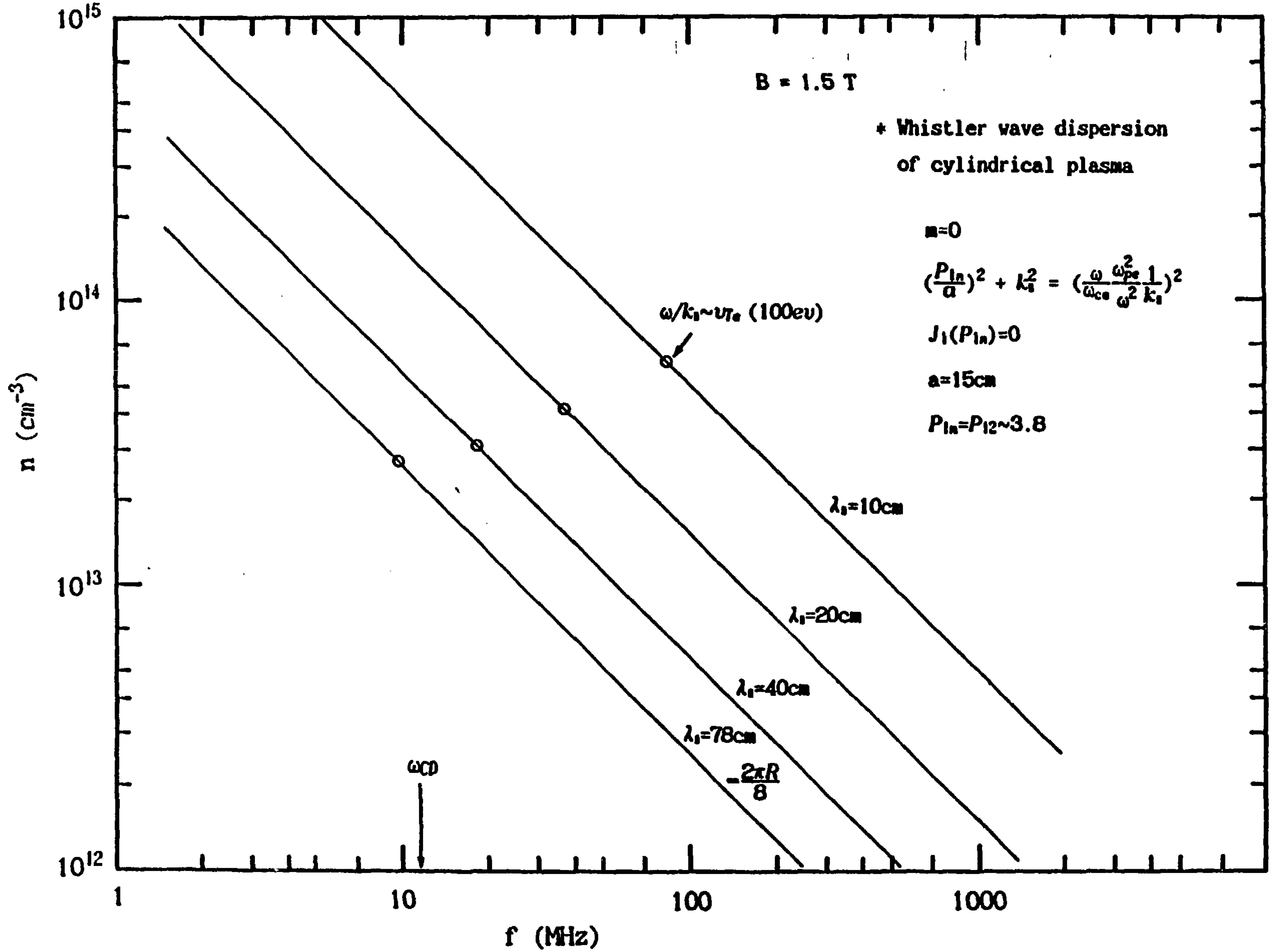

B = 1.5 T
* Whistler wave dispersion of cylindrical plasma
m=0
$(\frac{P_{1n}}{a})^2 + k_\parallel^2 = (\frac{\omega}{\omega_{ce}}\frac{\omega_{pe}^2}{\omega^2}\frac{1}{k_\parallel})^2$
$J_1(P_{1n})=0$
a=15cm
$P_{1n}=P_{12}\sim3.8$
$\omega/k_\parallel\sim v_{Te}$ (100ev)
$\lambda_\parallel$=10cm
$\lambda_\parallel$=20cm
$\lambda_\parallel$=40cm
$\lambda_\parallel$=78cm
$=\frac{2\pi R}{8}$
ω_{CD}
n (cm^{-3})
f (MHz)
10^{15}
10^{14}
10^{13}
10^{12}
1
10
100
1000

Heating

	Hydrogen			Deuterium		
B_0(T)	f_{CH}	$2f_{CH}$	$3f_{CH}$(MHz)	f_{CD}	$2f_{CD}$	$3f_{CD}$(MHz)
0.5	7.6	15.2	21.8	3.8	7.6	11.4
1.0	15.2	30.4	43.6	7.6	15.2	22.8
1.5	22.8	45.6	65.4	11.4	22.8	34.2

Production

Wave	Antenna	n_0(cm^{-3})	$\lambda_{\parallel}$ (cm)	f (MHz)
Slow	Half turn	3×10^{13}	7.9	11/$\omega\sim0.5\omega_{ci}$
Ion Bernstein	TYPE III	$\sim10^{13}$	15	46/$\omega\sim2\omega_{ci}$
Whitsler	m=0 (Loop)	4×10^{13}	20	40/$\omega_{ci}<\omega\ll\omega_{ce}$
Lower Hybrid	Half turn	$\sim10^{13}$	100	500/$\omega\sim\omega_{LH}$

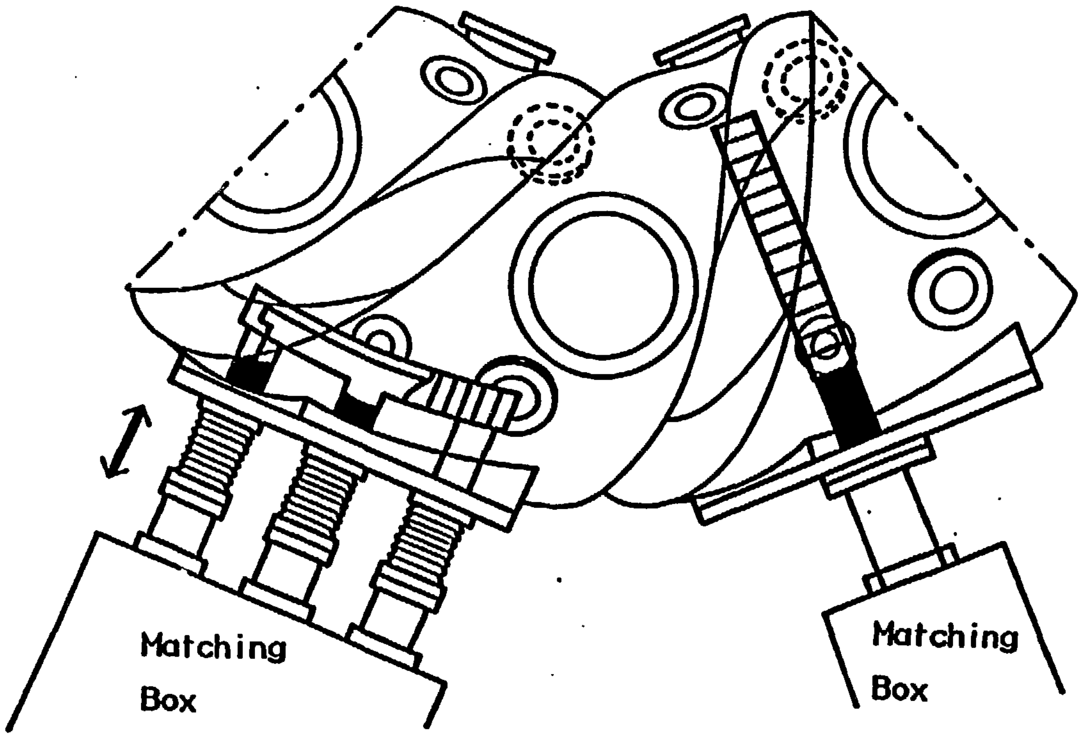

Ion Bernstein Wave Heating

Slow/Fast Wave Heating

Whistler Wave Plasma Production

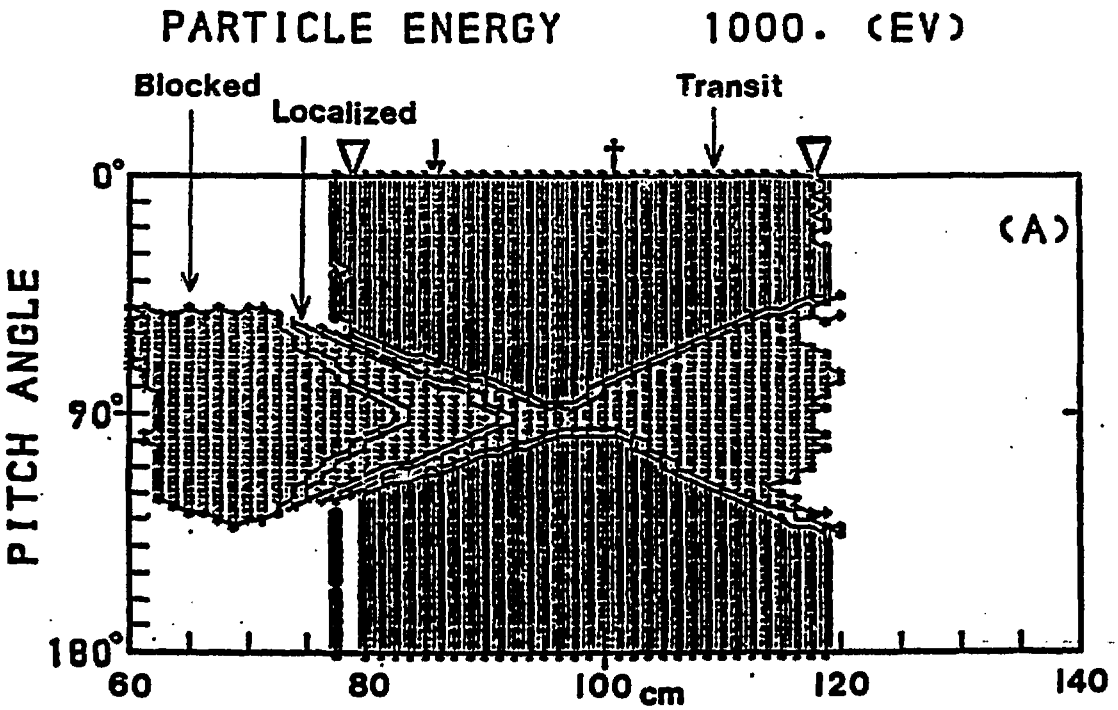

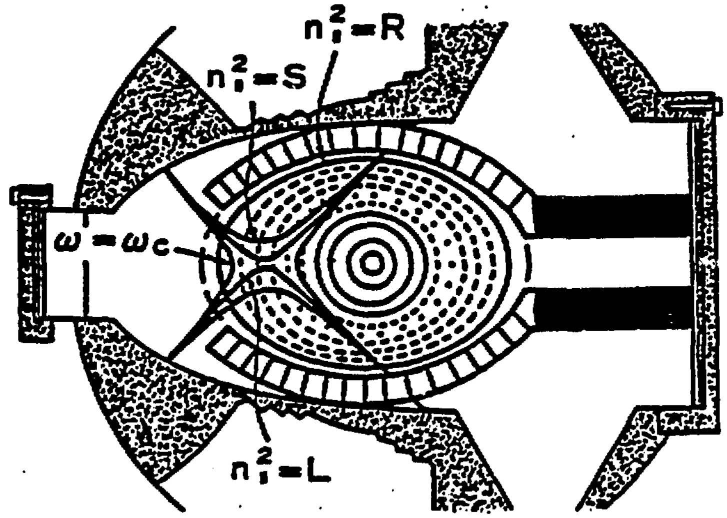

Fast Wave Heating (Slow)

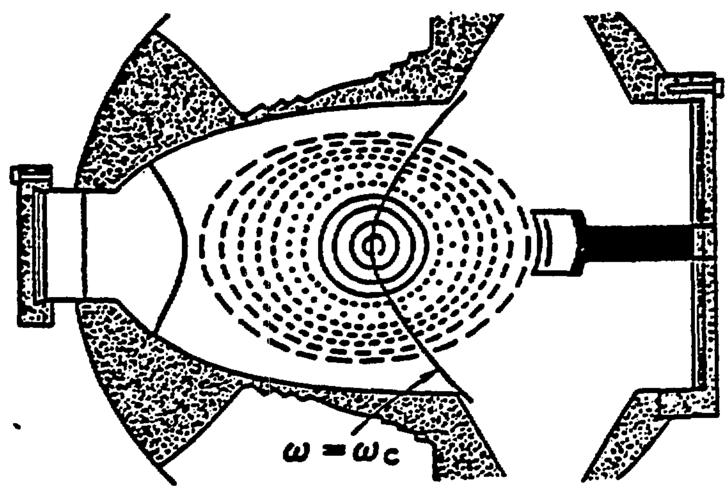

Ion Bernstein Wave Heating

Slow/Fast Wave Heating

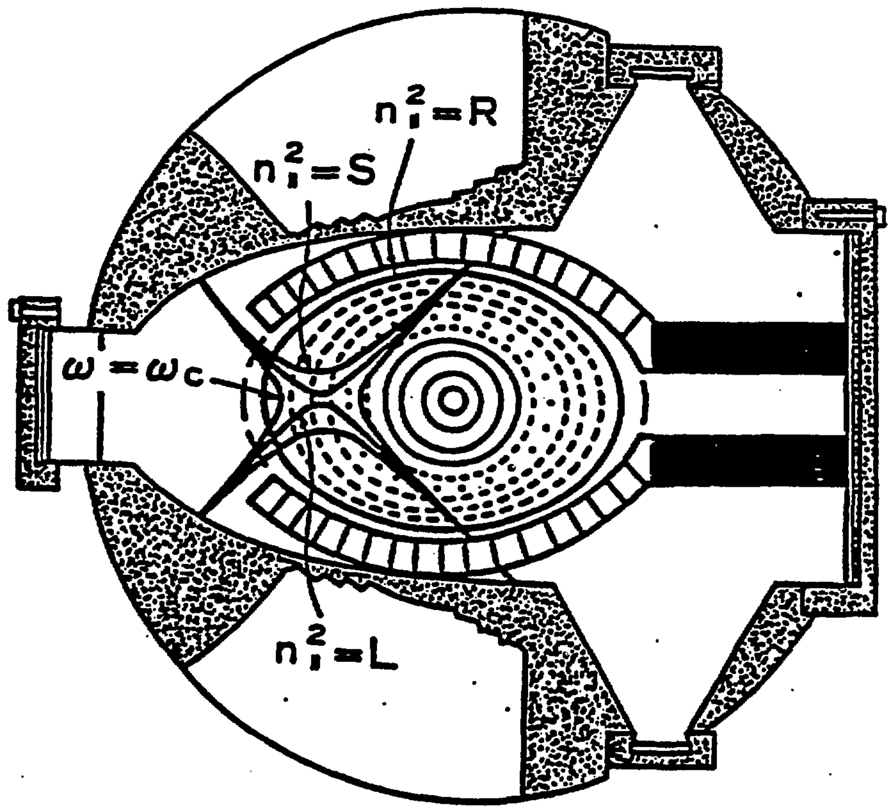

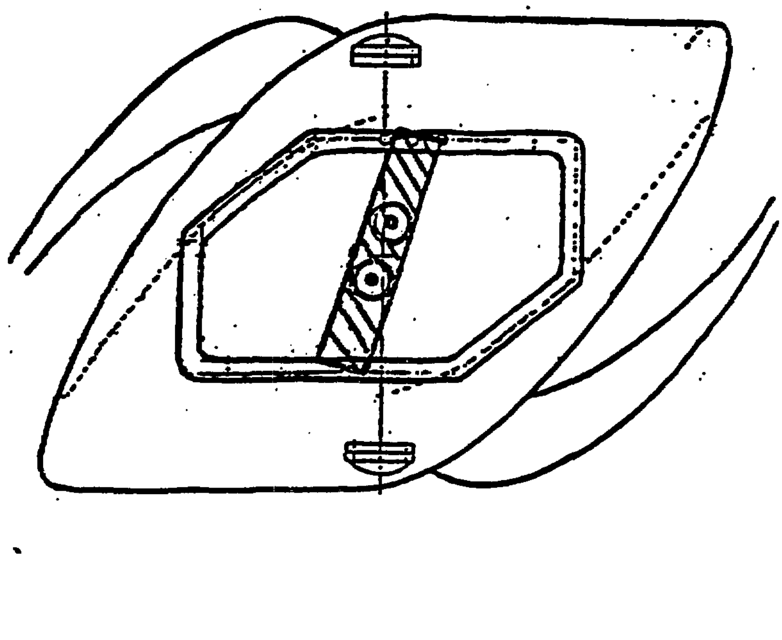

Ion Bernstein Wave Heating

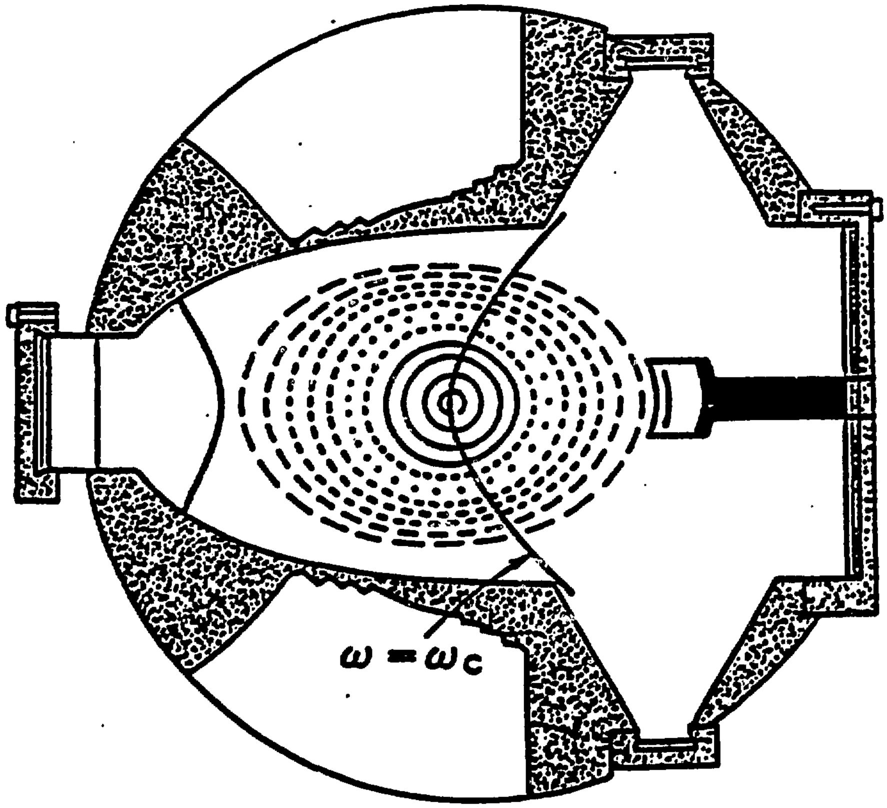

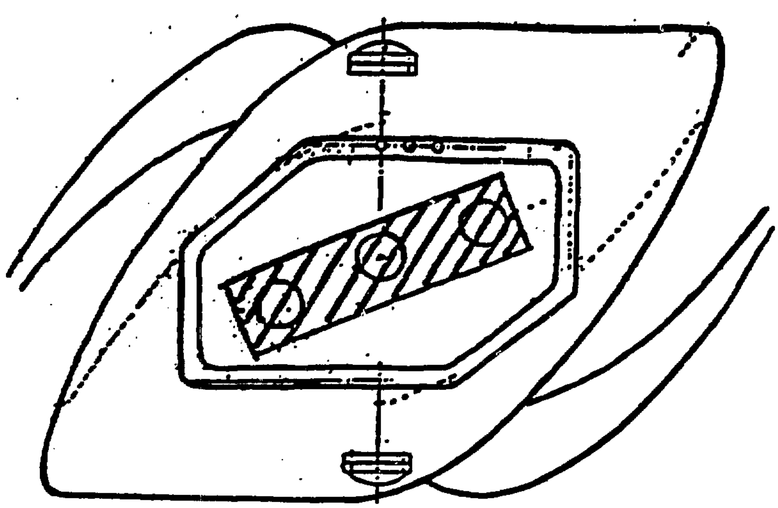

Ion Bernstein Wave Heating

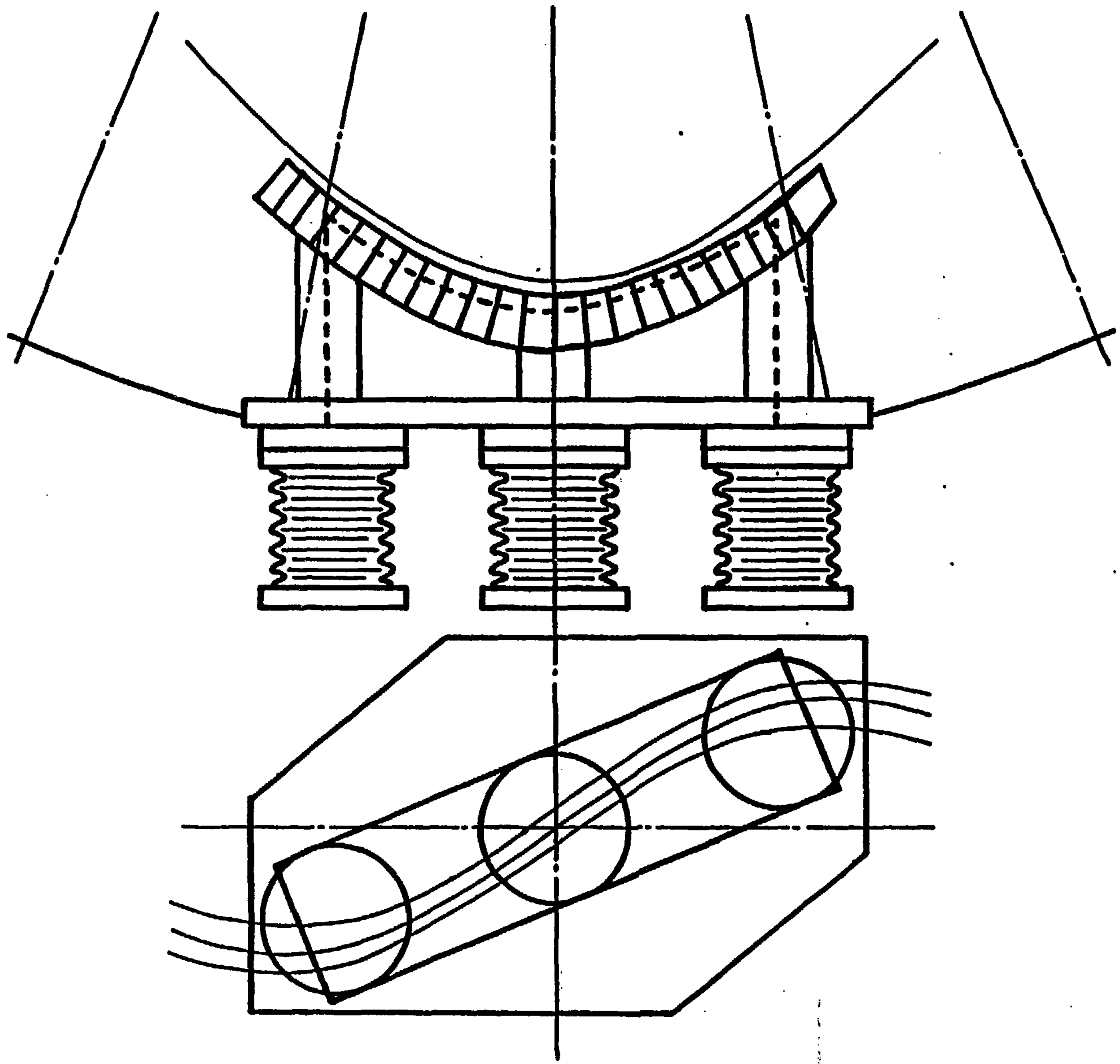

Ray tracing

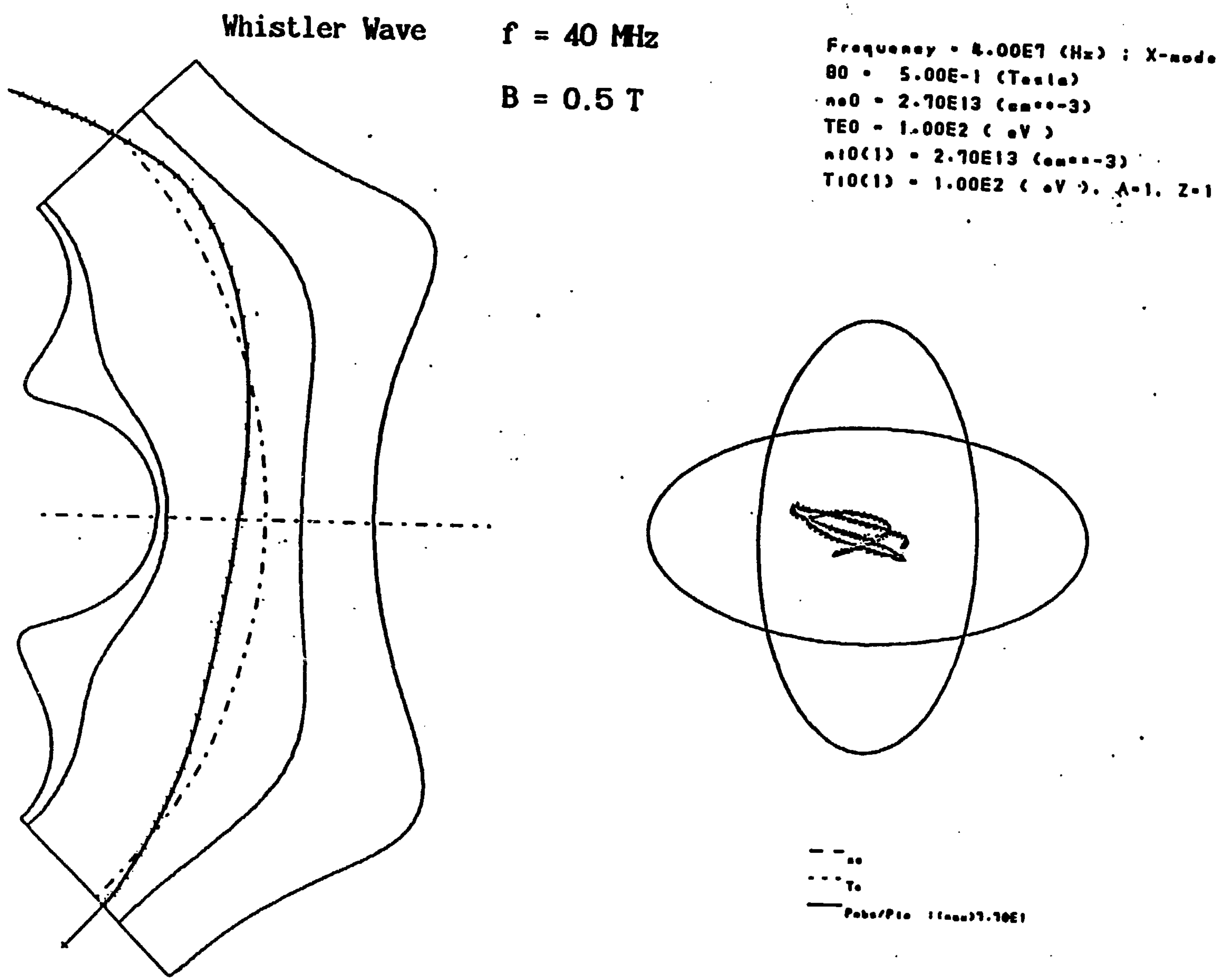
Whistler Wave
f = 40 MHz
B = 0.5 T
Frequency = 4.00E7 (Hz) : X-mode
B0 = 5.00E-1 (Tesla)
ne0 = 2.70E13 (cm**-3)
TE0 = 1.00E2 (eV)
ni0(1) = 2.70E13 (cm**-3)
Ti0(1) = 1.00E2 (eV), A=1, Z=1
ne
Te

Ray tracing

Whistler Wave : f = 40 MHz

B = 1 T

Frequency = 4.00E7 (Hz) : X-mode
B0 = 1.00E0 (Tesla)
ne0 = 2.70E13 (cm**-3)
TE0 = 1.00E2 (eV)
ni0(1) = 2.70E13 (cm**-3)
Ti0(1) = 1.00E2 (eV), A=1, Z=1

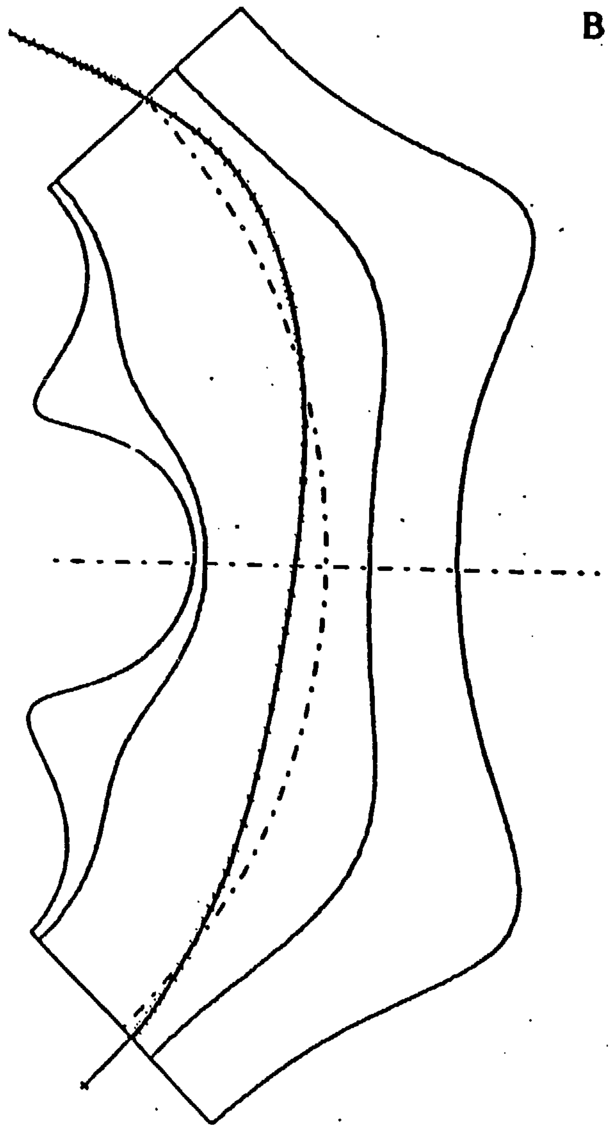

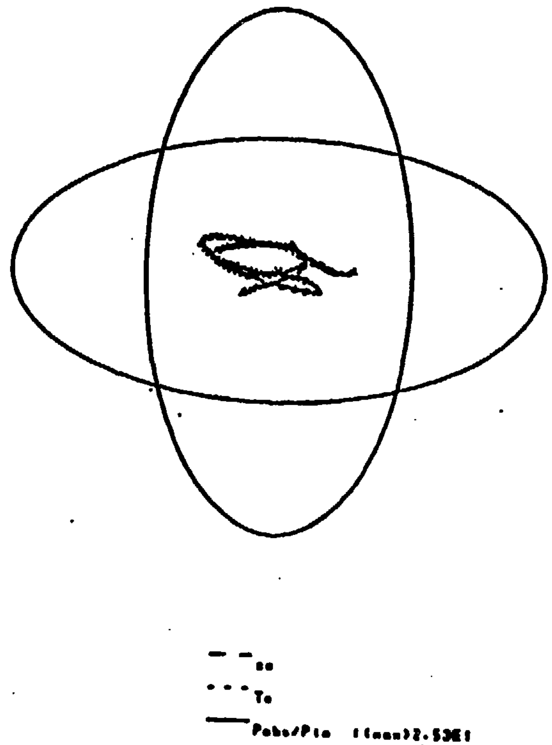

The ICRF Heating Program for ATF

F. W. Baity
November 11, 1987

ATF rf heating

Objectives of the ATF ICRF Program

Near-term

1. Evaluate the effectiveness of different heating modes (e.g., fast wave, ion Bernstein wave)
2. Evaluate the technological problems (e.g., impurity generation)
3. Provide substantial auxiliary heating power for ATF experiments

Long-term

1. Provide cost-effective high power heating for ATF
2. Provide long-pulse or steady-state heating capability

ATF rf heating

FWB Wed, Nov 11, 1987

ICRF Heating Program Plan Overview

Period	Task
Phase IB,II	Evaluate fast wave heating (moderate power)
Phase III (1989)	Evaluate ion Bernstein wave heating
Phase IV (1989)	Modify "best" antenna for high power operation (1-2 MW, 1 s)
Phase V (1990)	Install water-cooled long-pulse antennas
Phase VI (1991)	Install additonal rf power sources

ATF rf heating

FWB Wed, Nov 11, 1987

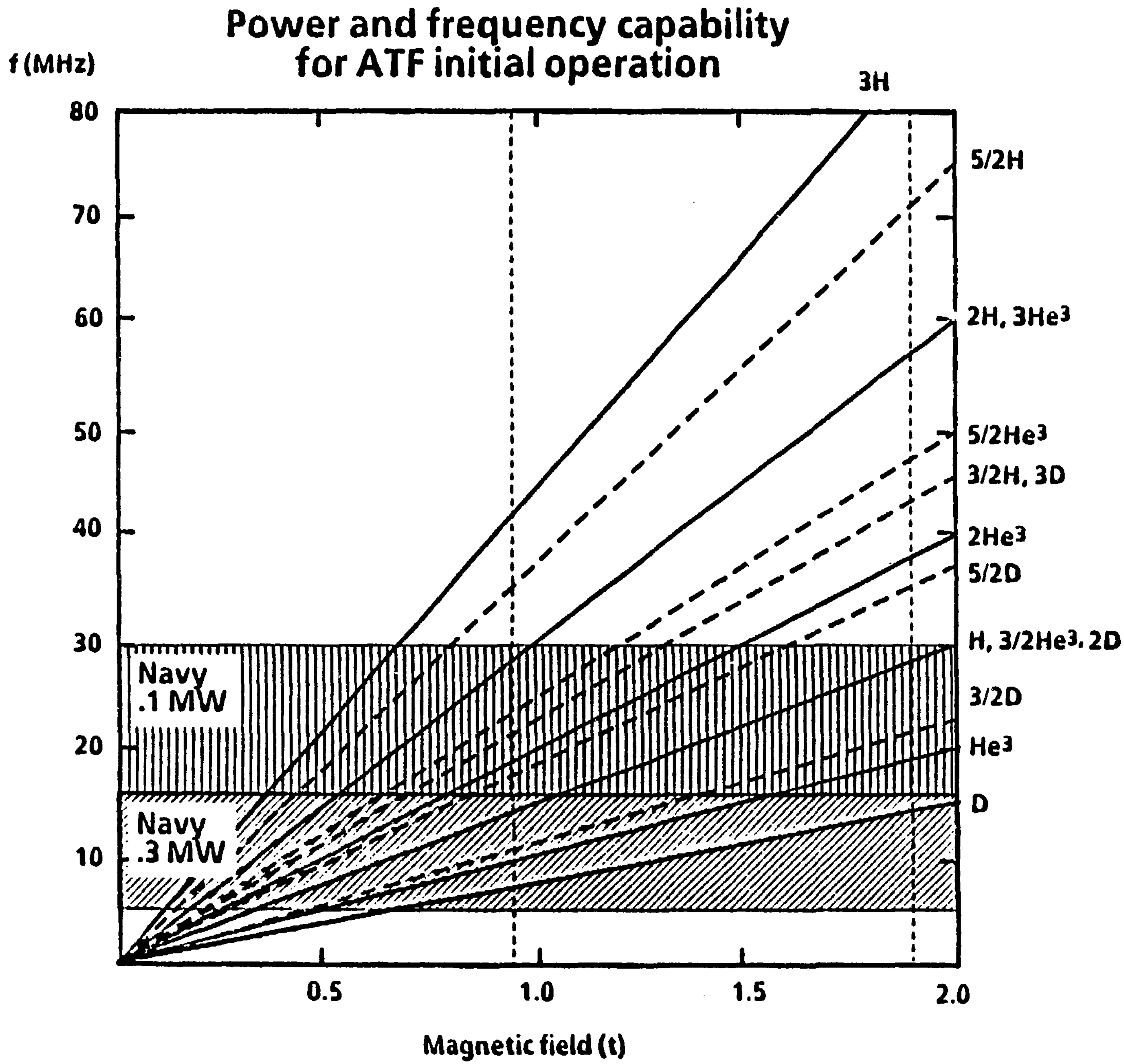
Power and frequency capability
for ATF initial operation
f (MHz)
80
70
60
50
40
30
20
10
0.5
1.0
1.5
2.0
Magnetic field (t)
3H
5/2H
2H, 3He3
5/2He3
3/2H, 3D
2He3
5/2D
H, 3/2He3, 2D
3/2D
He3
D
Navy .1 MW
Navy .3 MW

DW S 2/25/87

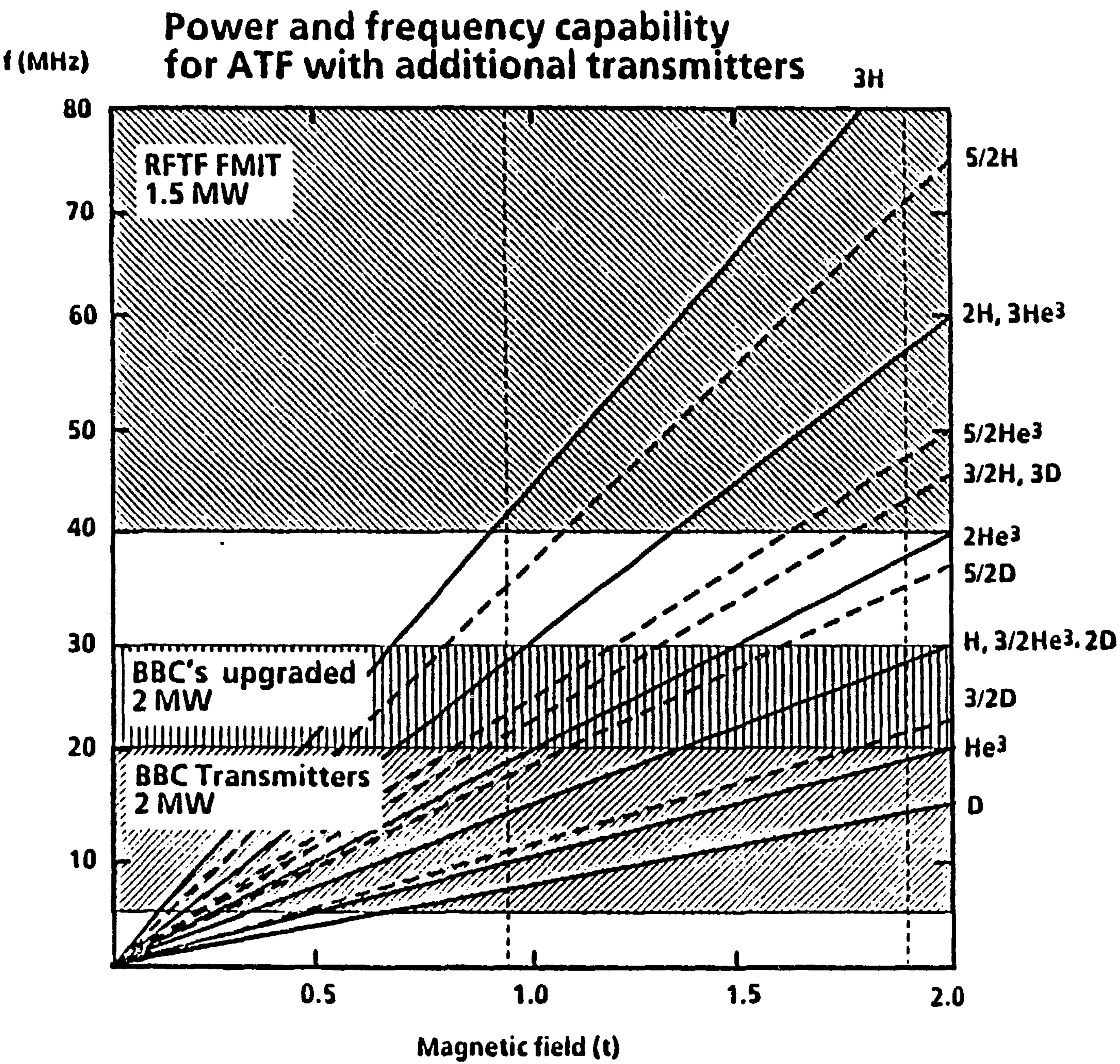
Power and frequency capability
for ATF with additional transmitters
f (MHz)
80
70
60
50
40
30
20
10
RFTF FMIT
1.5 MW
BBC's upgraded
2 MW
BBC Transmitters
2 MW
3H
5/2H
2H, 3He3
5/2He3
3/2H, 3D
2He3
5/2D
H, 3/2He3, 2D
3/2D
He3
D
0.5
1.0
1.5
2.0
Magnetic field (t)

DW S 2/25/87

The goal of the first phase of the ATF ICRF heating program is to determine the feasibility of low–field–side wave launch.

- A prototype resonant double loop antenna for fast wave launch is under construction.
- Low power ($\leq$ 300 kW), short pulse ($\leq$ 0.5 s) experiments will be conducted during Phase II of ATF operation.
- The prototype antenna will be converted to the ion Bernstein wave polarization during Phase III of ATF operation.

The prototype ICRF antenna draws from the TFTR and Tore Supra designs.

- RDL designed to cover 10 — 30 MHz (mockup tunes 9.3 — 32.6 MHz) .
- 2-tier graphite-coated Faraday shield.
- Graphite armor tiles on sides of housing.
- Movable radially over a 15-cm range.
- No water cooling required for short pulse operation.

ATF *rf heating*

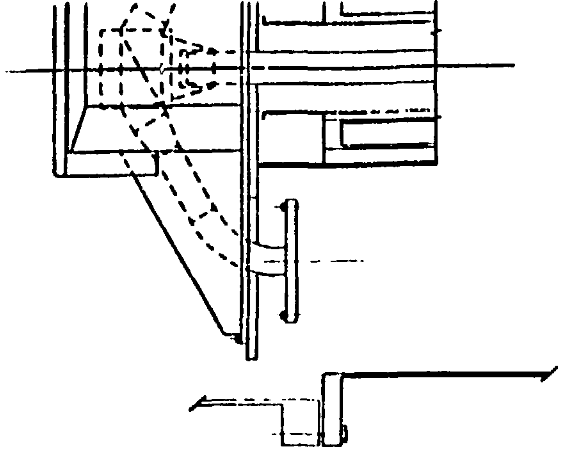

Mockup of Prototype ATF Antenna

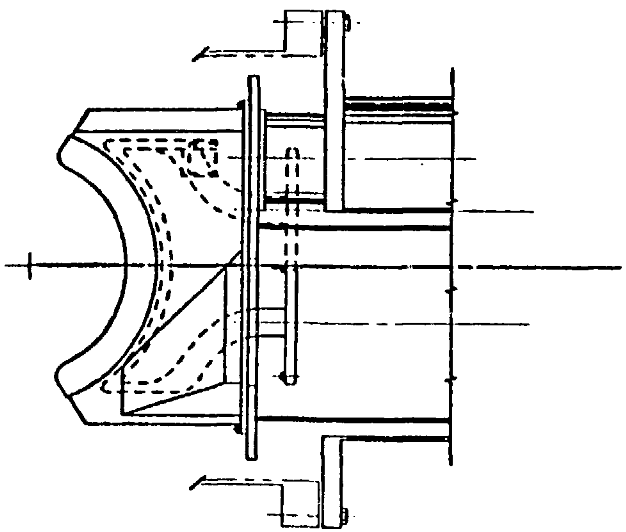

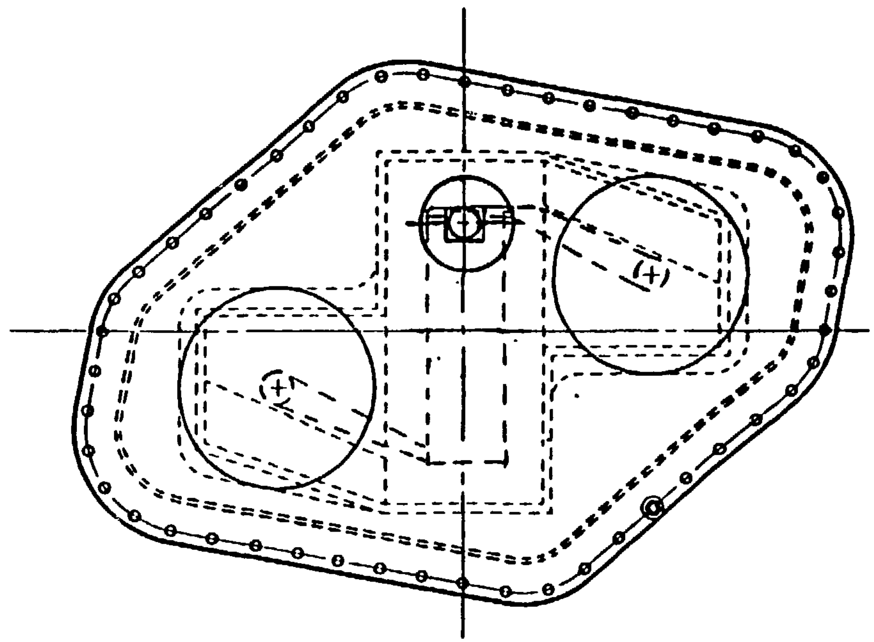

ATF rf heating

Measurements of antenna parameters were made on a full-scale mockup and compared to circuit models.

- Resonant double loop design developed at ORNL integrates tuning and matching elements in the antenna structure.
- Uses the same 100-1600 pf vacuum variable capacitors as the prototype ATF antenna.
- Faraday shield consists of 2 tiers of round tubes (as on DIII-D, TFTR, and Tore Supra).
- Total inductance of 384 nh produces a tuning range of 9.3 to 32.6 MHz.
- Internal loss resistance is 114 mΩ at 15 MHz ($\propto\sqrt{f}$).

ATF rf heating

FWB Wed, Nov 11, 1987

Tuning capacitance required for a 50Ω match as a function of frequency calculated using a lumped parameter model and compared with actual measurements

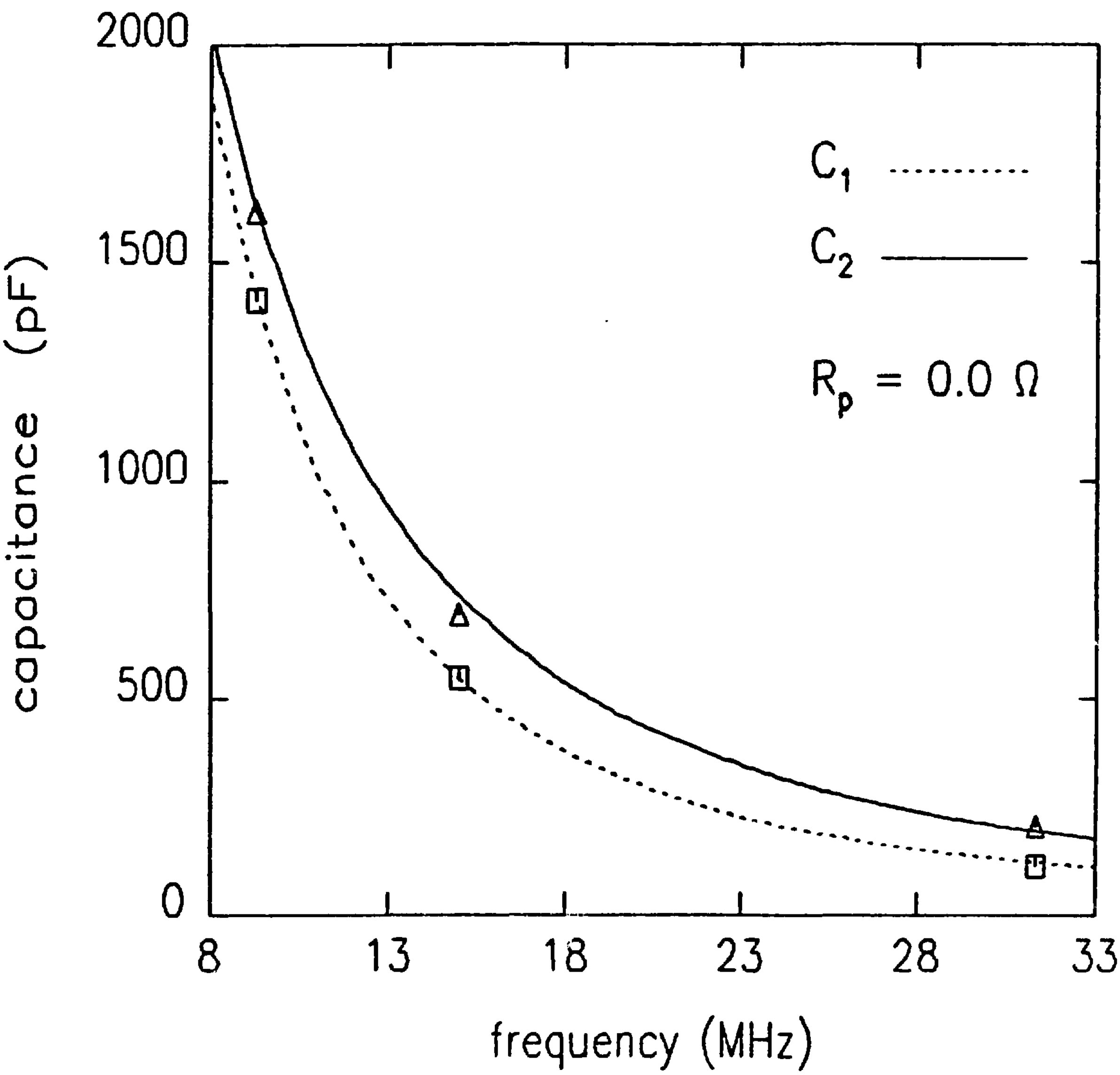

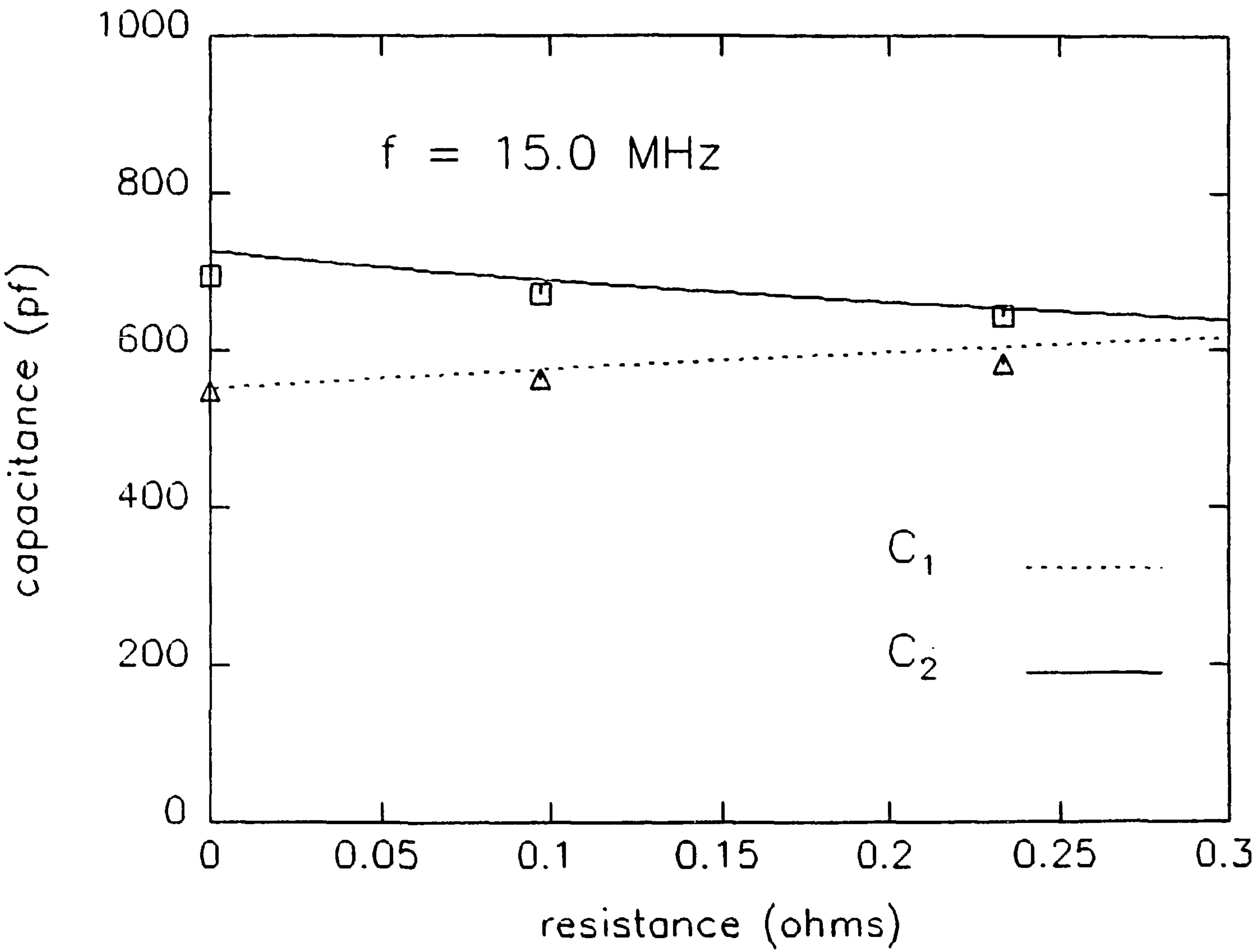

f = 15.0 MHz
capacitance (pf)
resistance (ohms)
1000
800
600
400
200
0
0
0.05
0.1
0.15
0.2
0.25
0.3
C_1
C_2

Maximum coupled power as a function of frequency and antenna loading

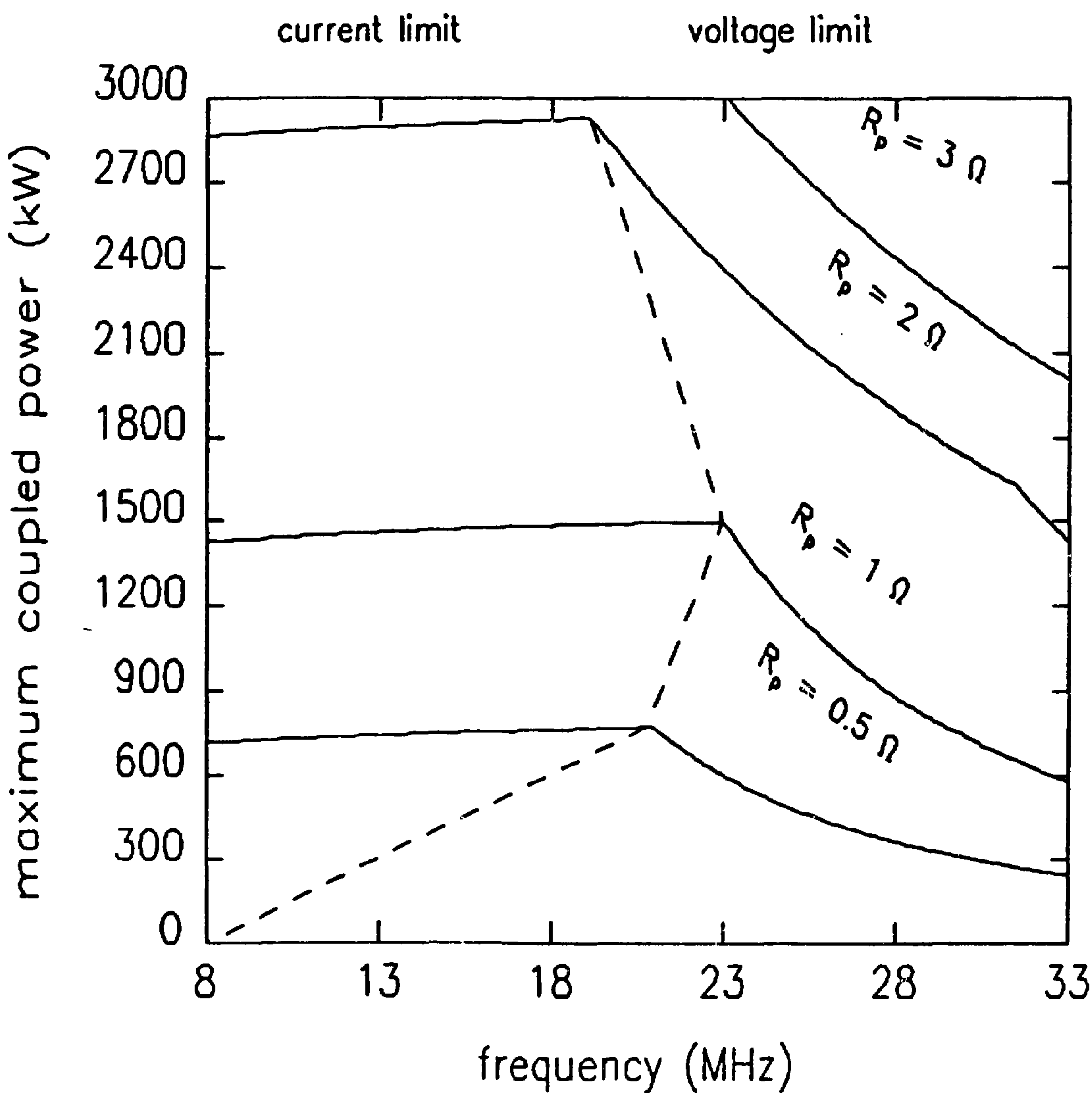

V_{max} (peak) = 35 kV I_{max} (RMS) = 1200 A

Current and voltage profiles along ATF mockup strap calculated using a lossy transmission line model with $f = 9.3 MHz$ and $R_p = 0.2\Omega$.

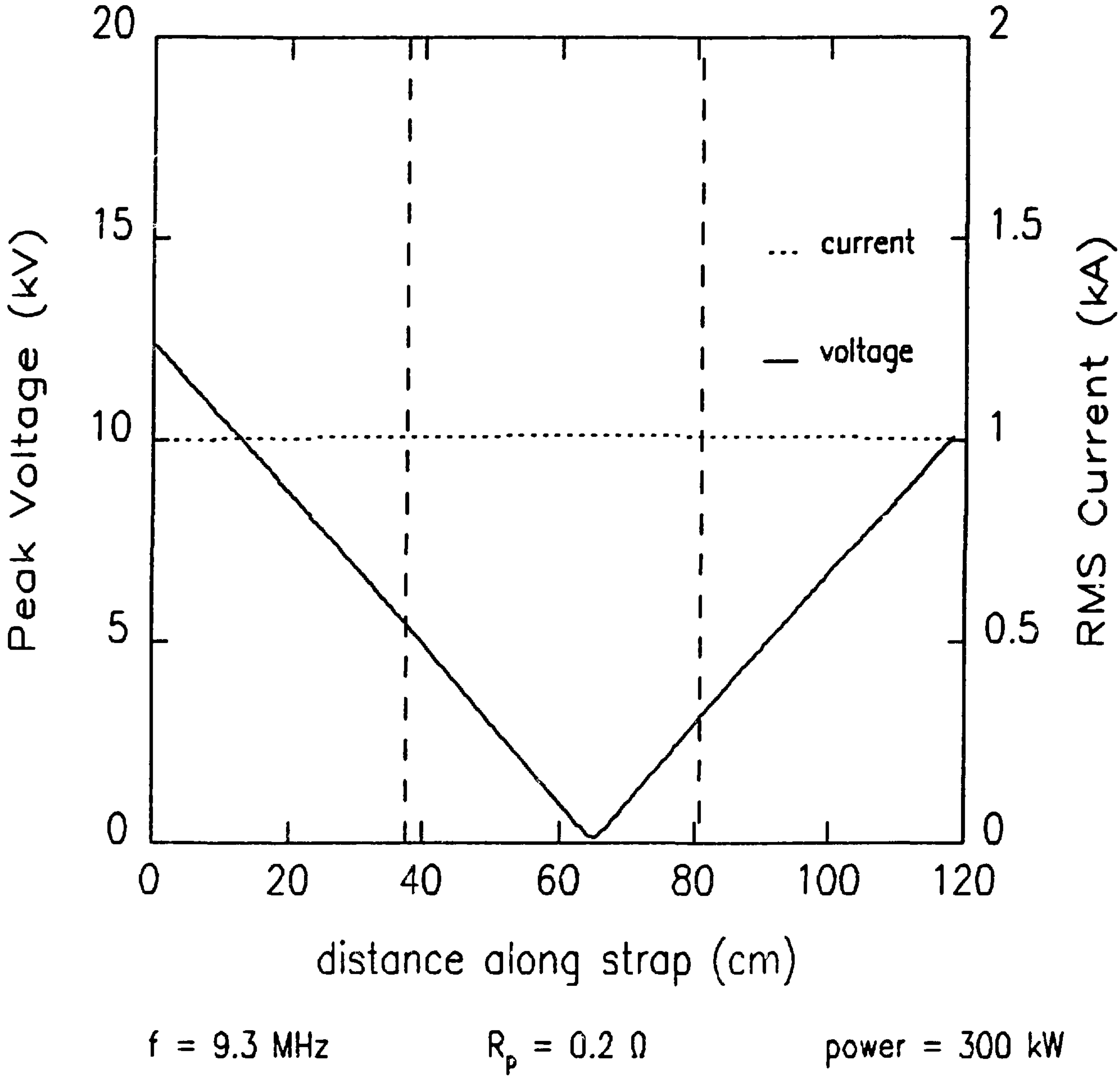

Current and voltage profiles along ATF mockup strap calculated using a lossy transmission line model with $f = 15MHz$ and $R_p = 1\Omega$.

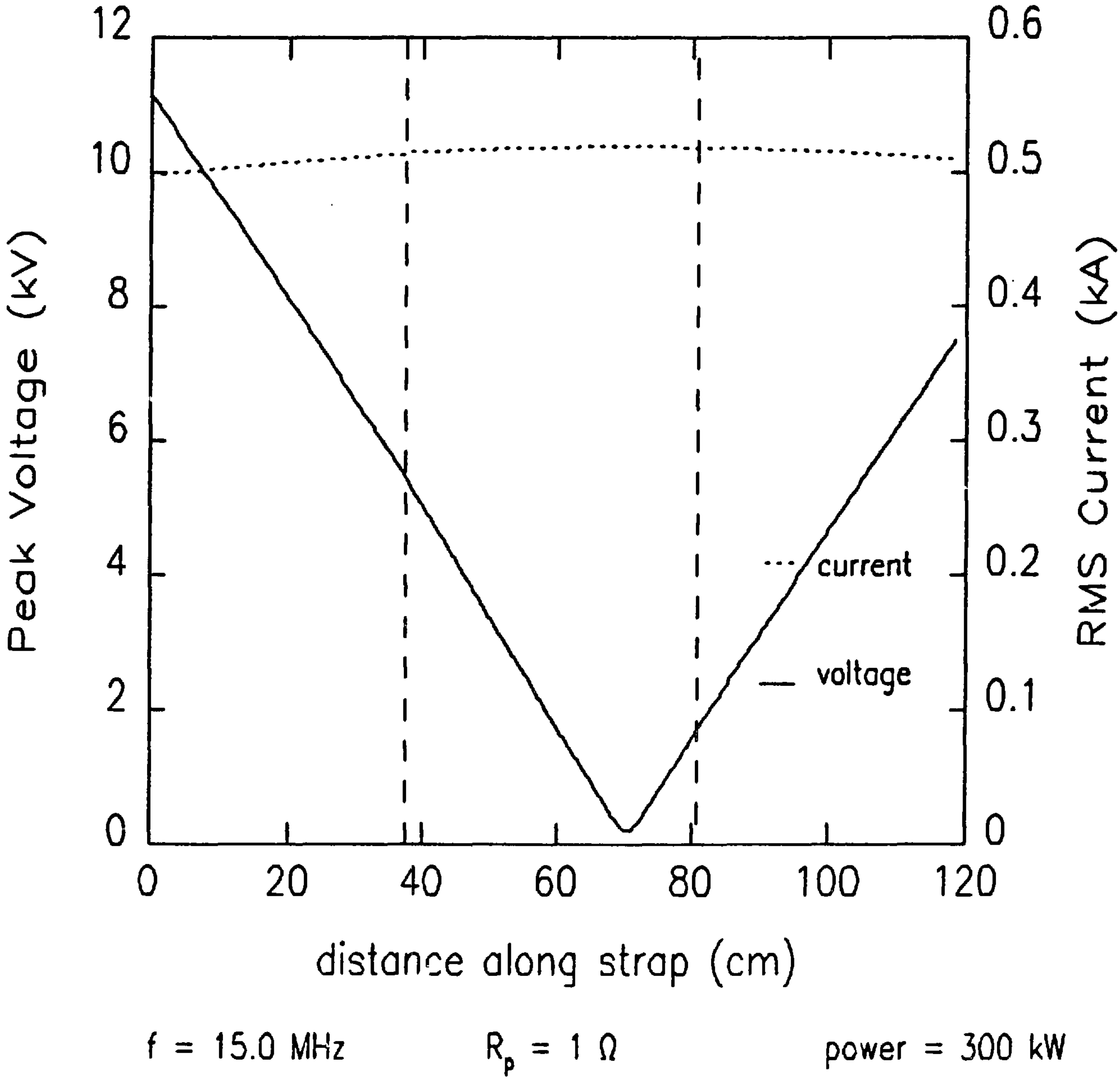

Current and voltage profiles along ATF mockup strap calculated using a lossy transmission line model with $f = 30MHz$ and $R_p = 1\Omega$.

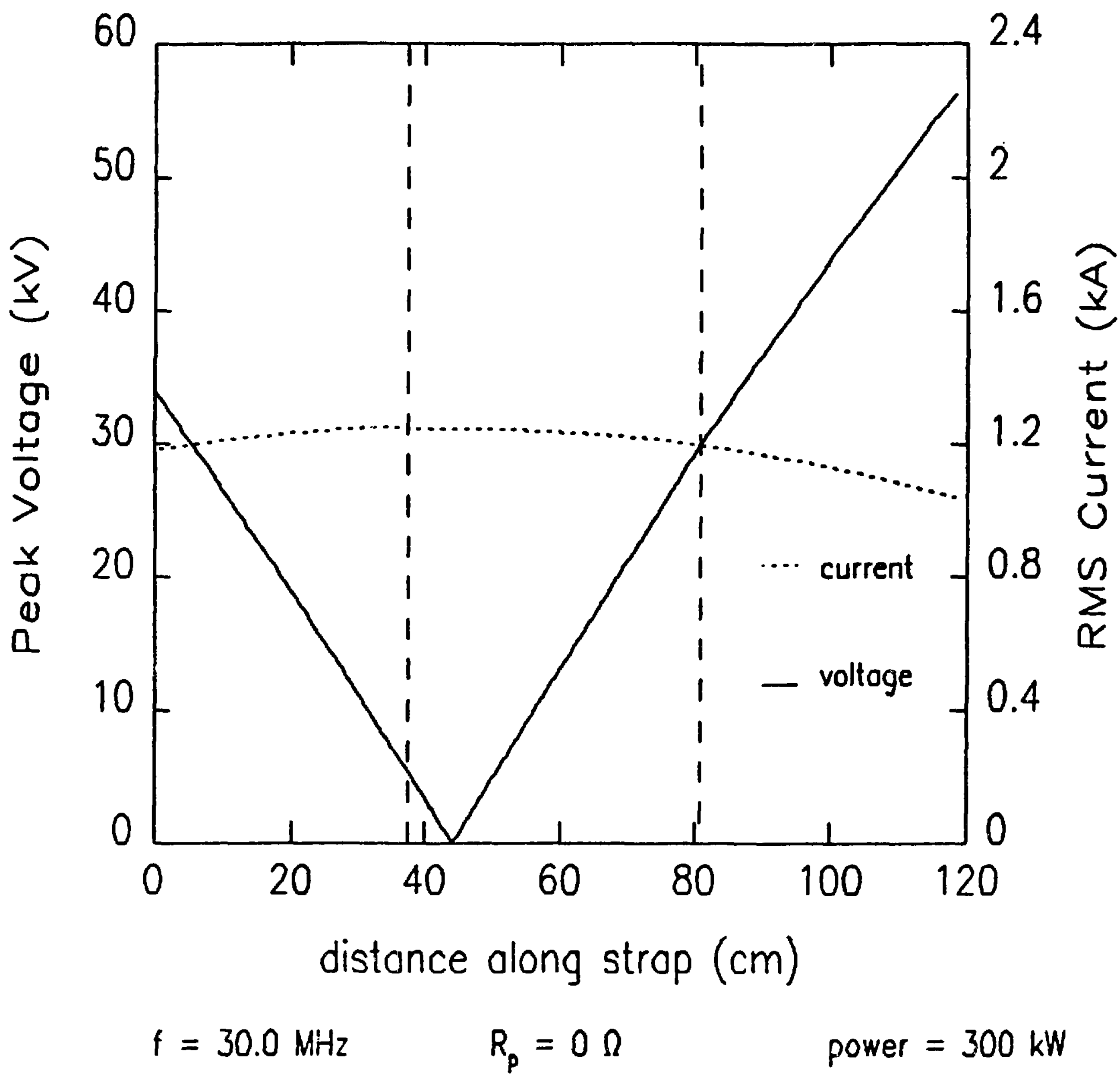

Modification of Prototype ATF Antenna for Ion Bernstein Wave Launch

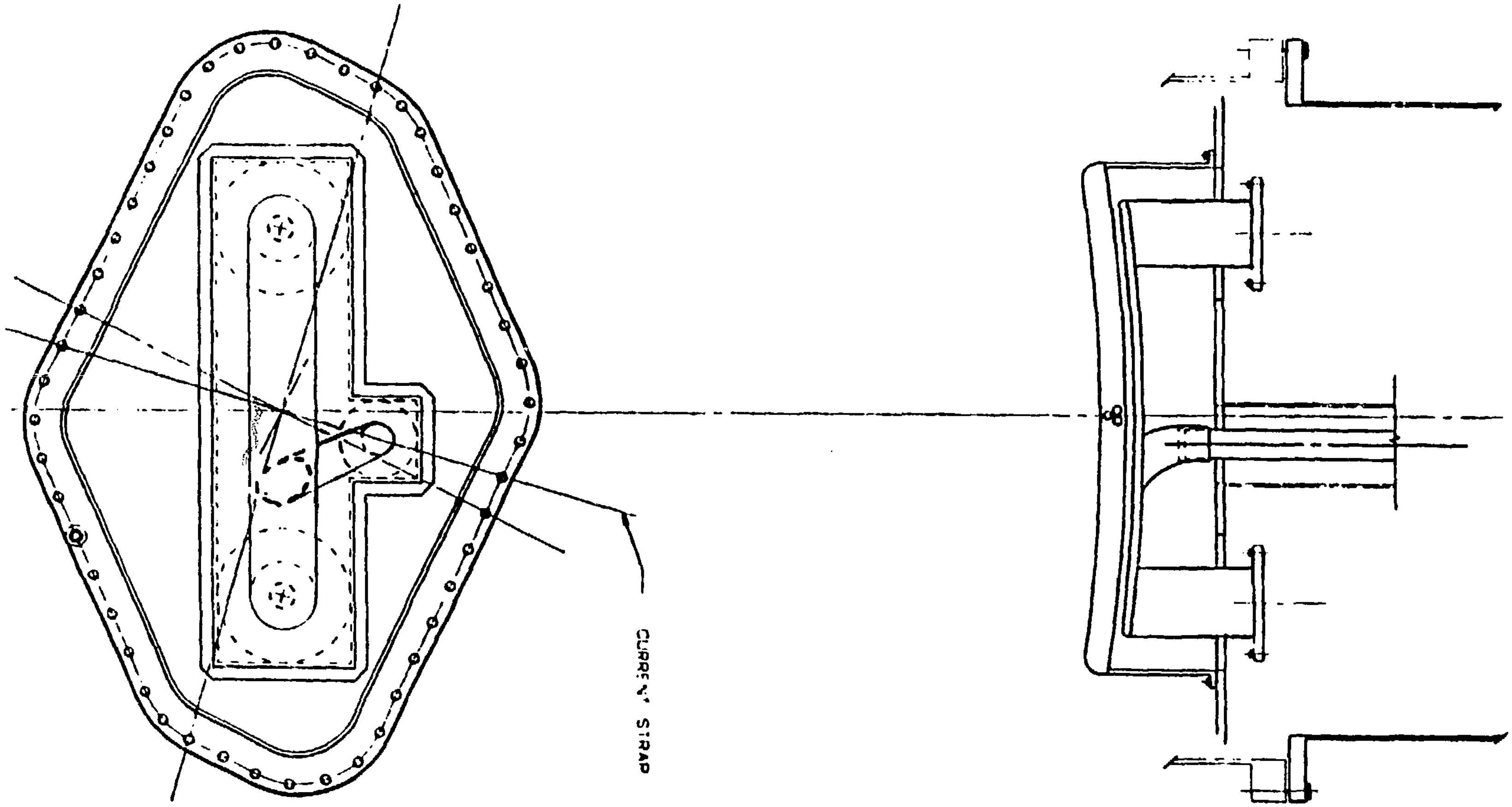

ATF rf heating

IBW Modification Faraday Shield

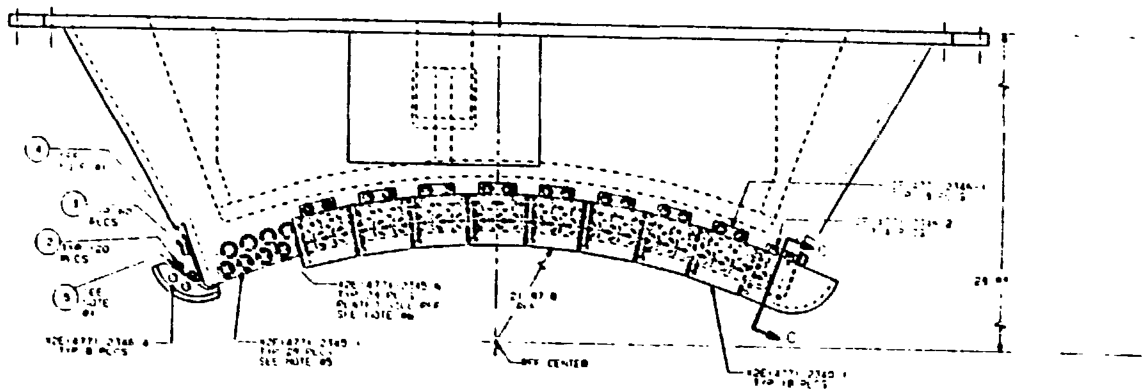

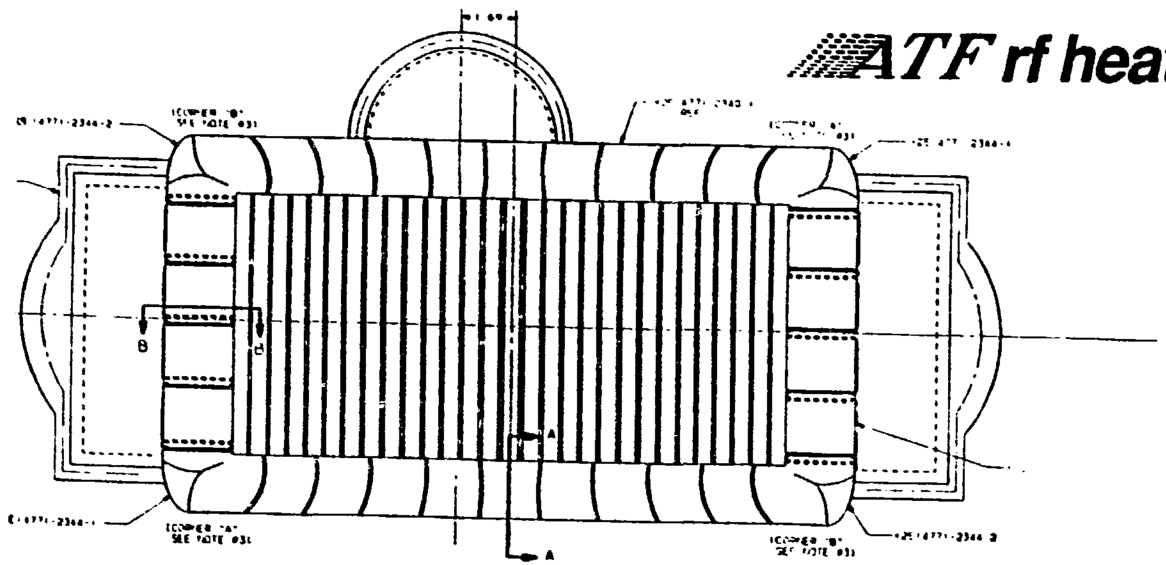

ATF rf heating

ICRF Heating Summary

- Measurements on the mockup have verified the wide-band antenna design for the prototype ATF launcher.
- The prototype fast wave antenna is now being fabricated.
- Initial ICRF heating experiments will begin in the spring of 1988.
- Ion Bernstein wave heating will be attempted in 1989.
- Two 1 MW transmitters will be installed in the spring of 1989.

ATF rf heating

ICRF WAVE PROPAGATION IN ATF

US-Japan Stellarator/Heliotron Workshop

Nov. 9-13, 1987

D.B Batchelor, M.D. Carter, R.C. Goldfinger, E.F. Jaeger (ORNL)

H. Weitzner, K. Imre (NYU)

- ICRF Heating Scenarios in ATF
- Theoretical ICRF Studies for ATF
- Ongoing Theoretical Work

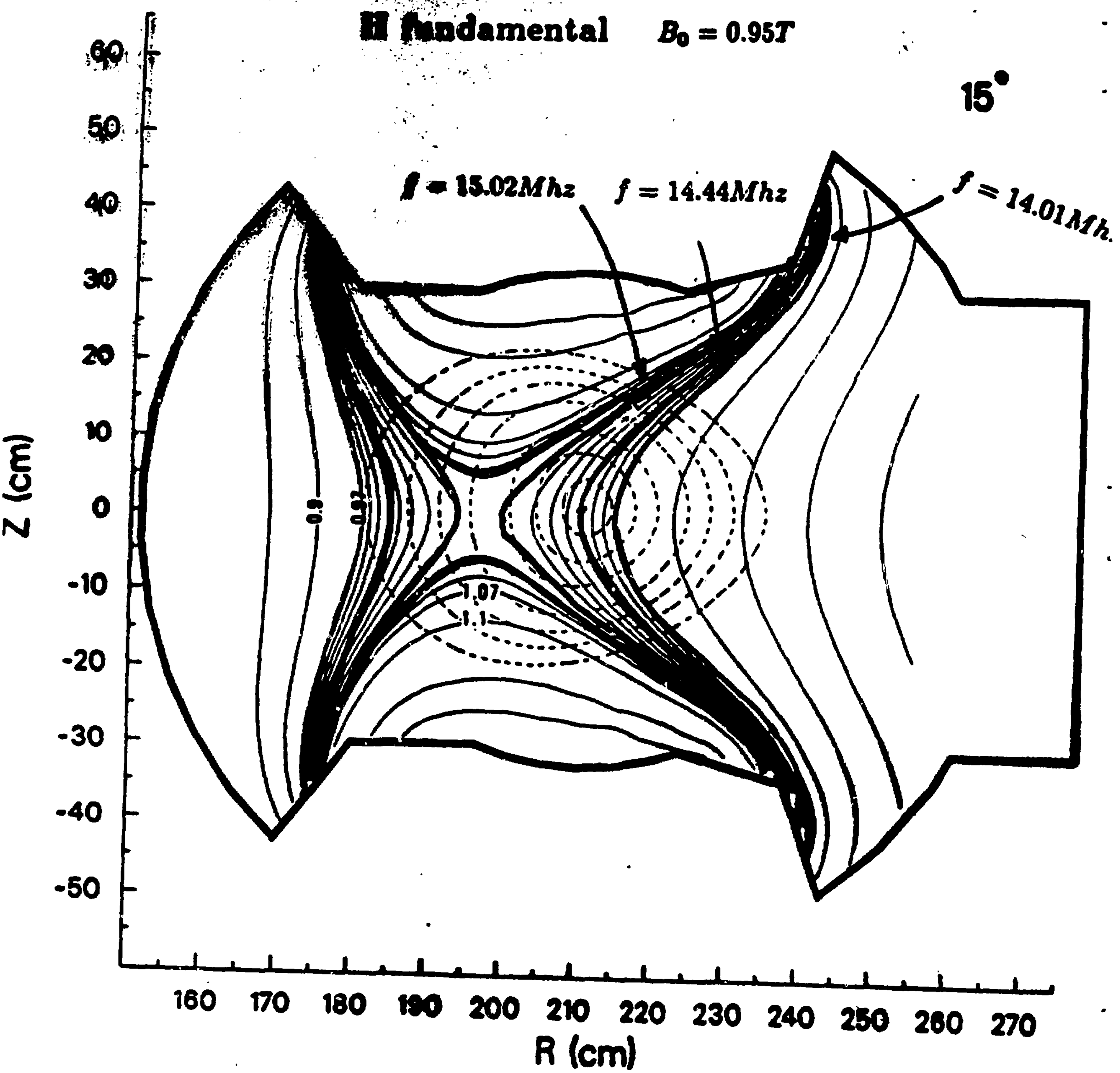
H fundamental $B_0 = 0.95T$
15°
f = 15.02Mhz
f = 14.44Mhz
f = 14.01Mh
0.9
0.97
1.07
1.1
Z (cm)
R (cm)
60
50
40
30
20
10
0
-10
-20
-30
-40
-50
160 170 180 190 200 210 220 230 240 250 260 270

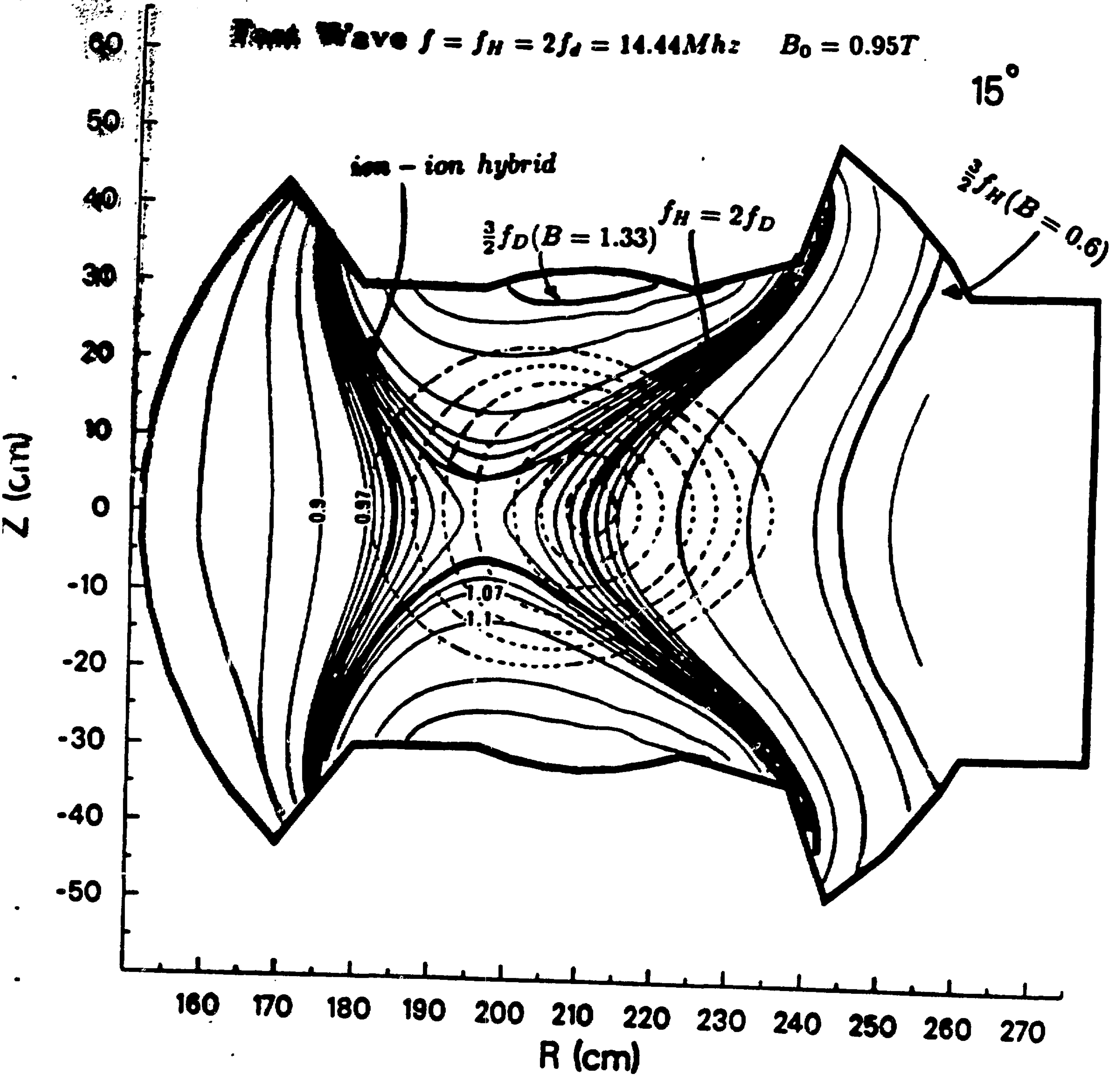

Fast Wave $f = f_H = 2f_d = 14.44 Mhz$ $B_0 = 0.95T$
15°
ion – ion hybrid
$\frac{3}{2}f_D(B = 1.33)$
$f_H = 2f_D$
$\frac{3}{2}f_H(B = 0.6)$
0.9
0.97
1.07
1.1
Z (cm)
R (cm)
60
50
40
30
20
10
0
-10
-20
-30
-40
-50
160
170
180
190
200
210
220
230
240
250
260
270

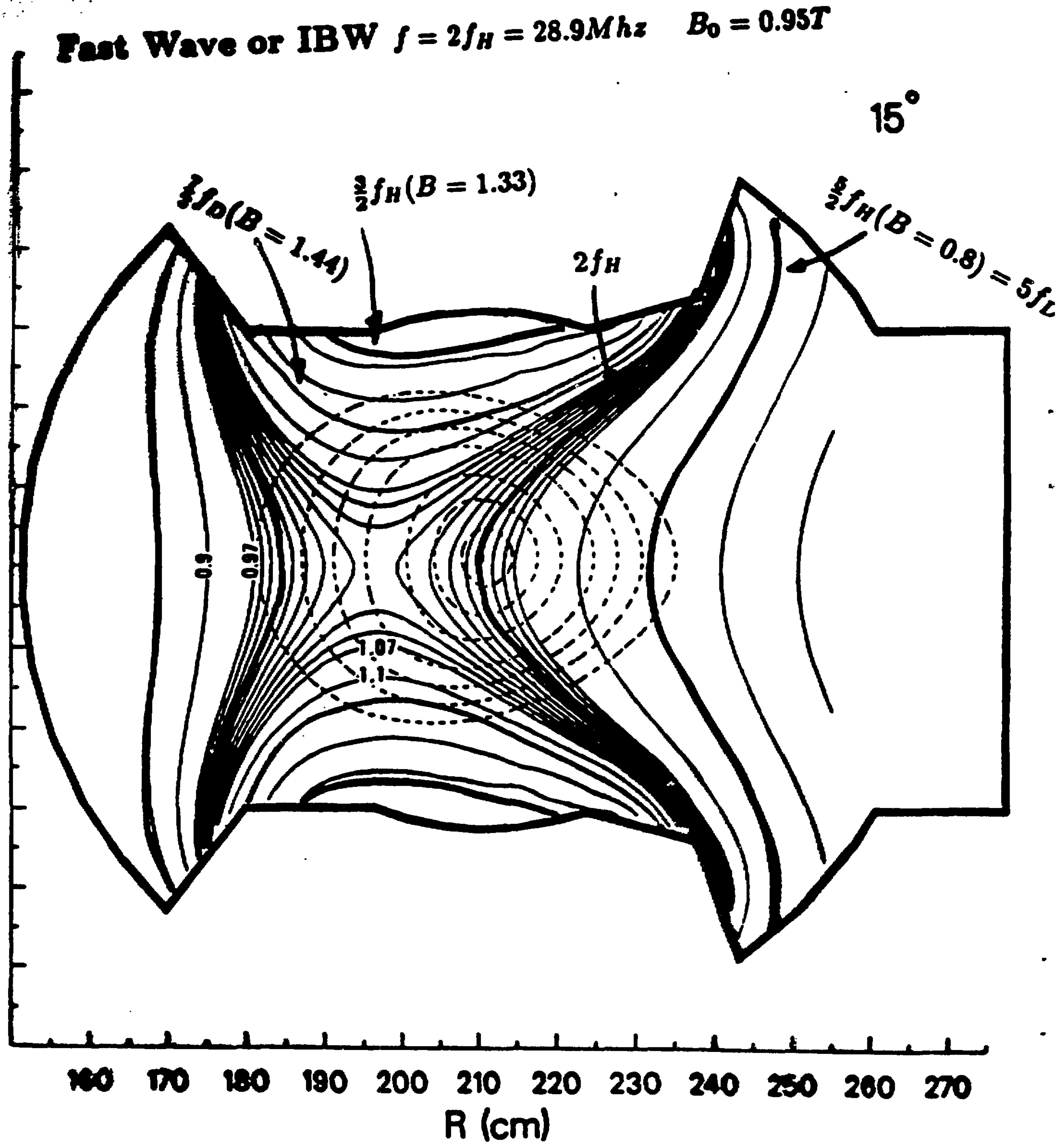

Fast Wave or IBW $f = 2f_H = 28.9Mhz$ $B_0 = 0.95T$
15°
$\frac{7}{2}f_D(B = 1.44)$
$\frac{3}{2}f_H(B = 1.33)$
$2f_H$
$\frac{5}{2}f_H(B = 0.8) = 5f_D$
0.9
0.97
1.07
1.1
Z (cm)
R (cm)
60
50
40
30
20
10
0
-10
-20
-30
-40
-50
160
170
180
190
200
210
220
230
240
250
260
270

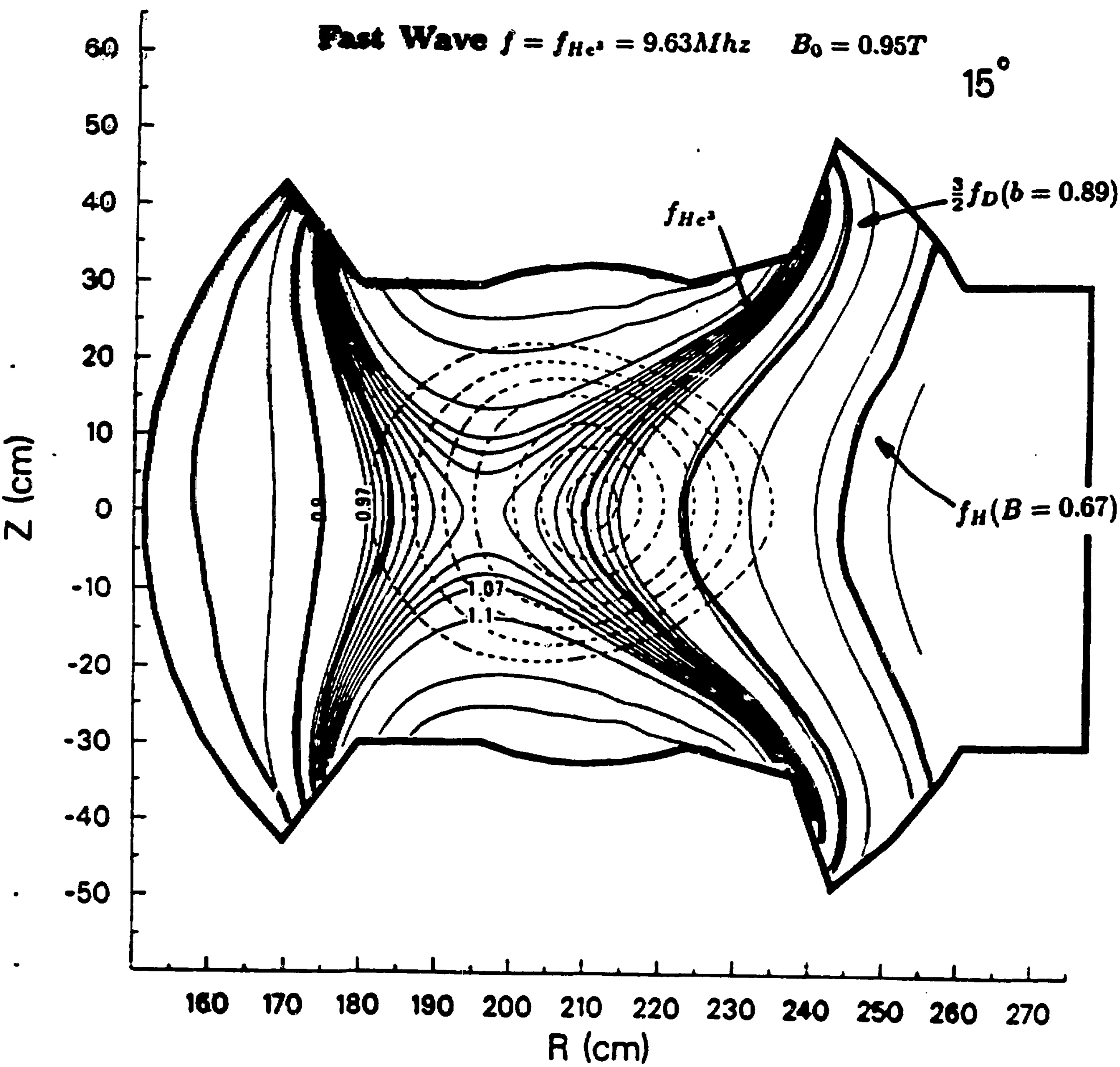

Fast Wave $f = f_{He^3} = 9.63 Mhz$ $B_0 = 0.95T$
15°
f_{He^3}
$\frac{3}{2} f_D (b = 0.89)$
$f_H (B = 0.67)$
0.97
1.07
1.1
Z (cm)
R (cm)
60
50
40
30
20
10
0
-10
-20
-30
-40
-50
160
170
180
190
200
210
220
230
240
250
260
270

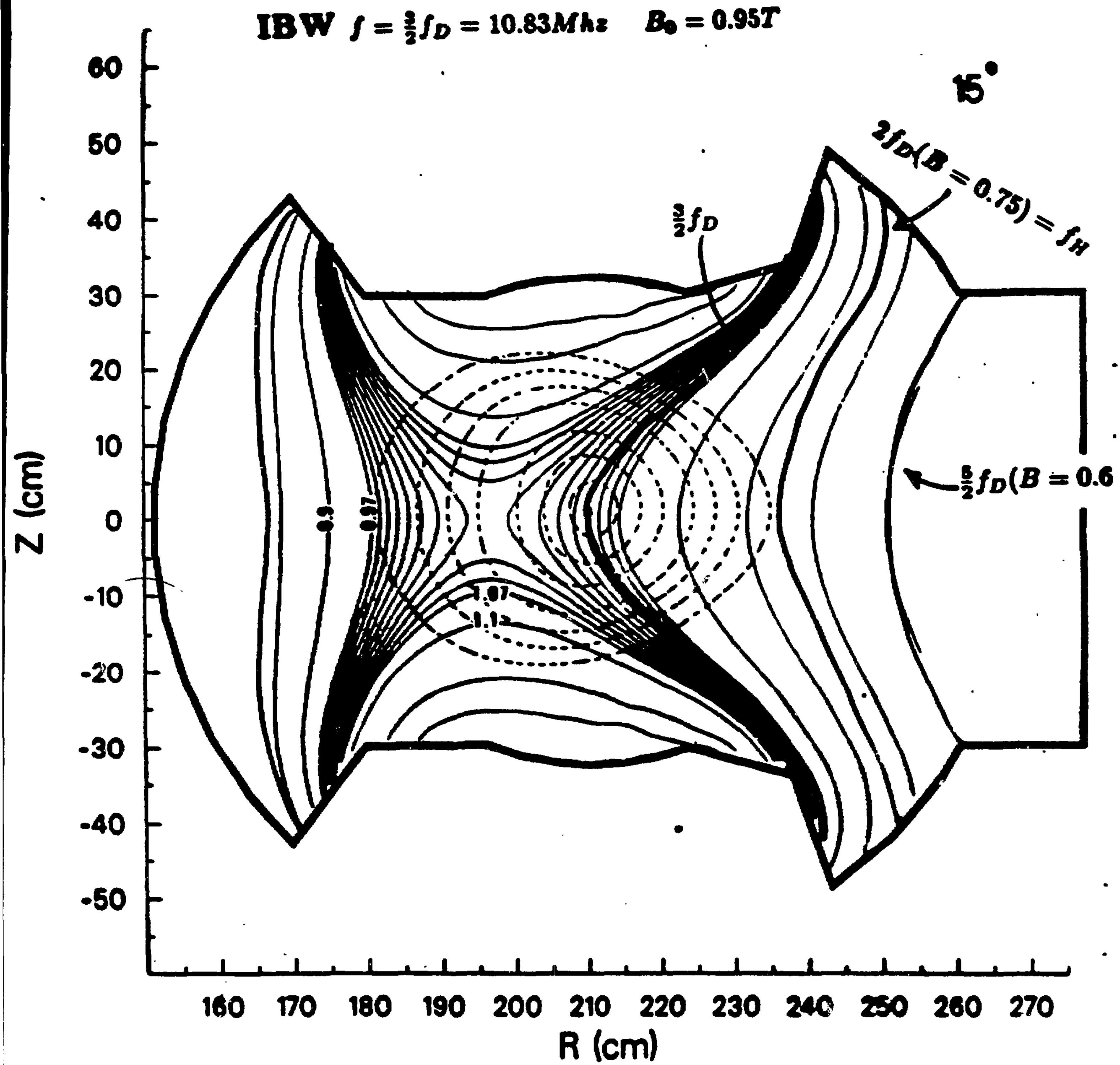

IBW $f = \frac{3}{2} f_D = 10.83 Mhz$ $B_0 = 0.95T$
15°
$2f_D(B = 0.75) = f_H$
$\frac{3}{2} f_D$
$\frac{5}{2} f_D(B = 0.6$
0.9
0.97
1.07
1.1
Z (cm)
R (cm)
60
50
40
30
20
10
0
-10
-20
-30
-40
-50
160
170
180
190
200
210
220
230
240
250
260
270

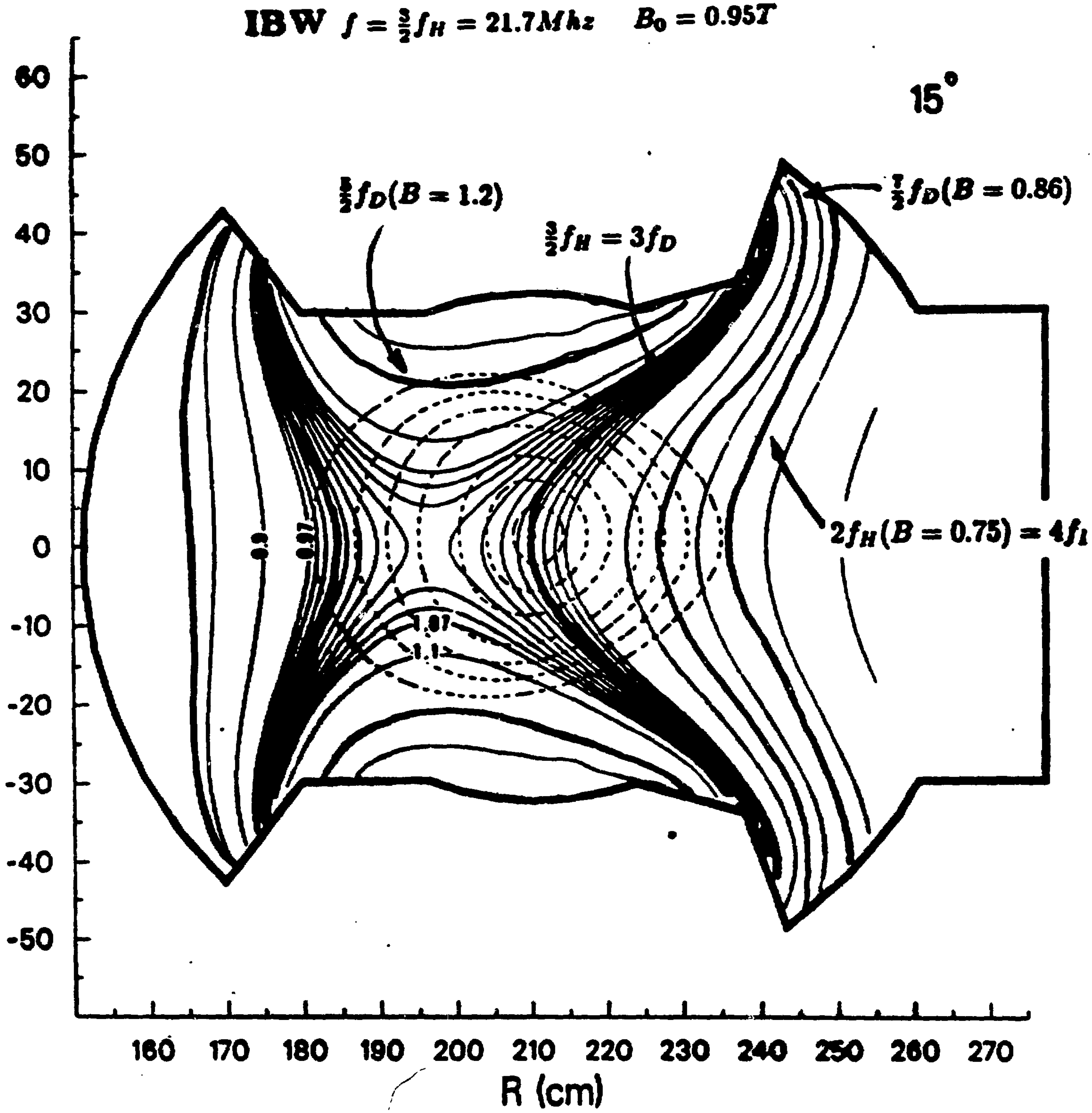

IBW $f = \frac{3}{2} f_H = 21.7 Mhz$ $B_0 = 0.95T$
15°
$\frac{5}{2} f_D (B = 1.2)$
$\frac{3}{2} f_H = 3 f_D$
$\frac{7}{2} f_D (B = 0.86)$
$2 f_H (B = 0.75) = 4 f_l$
Z (cm)
R (cm)

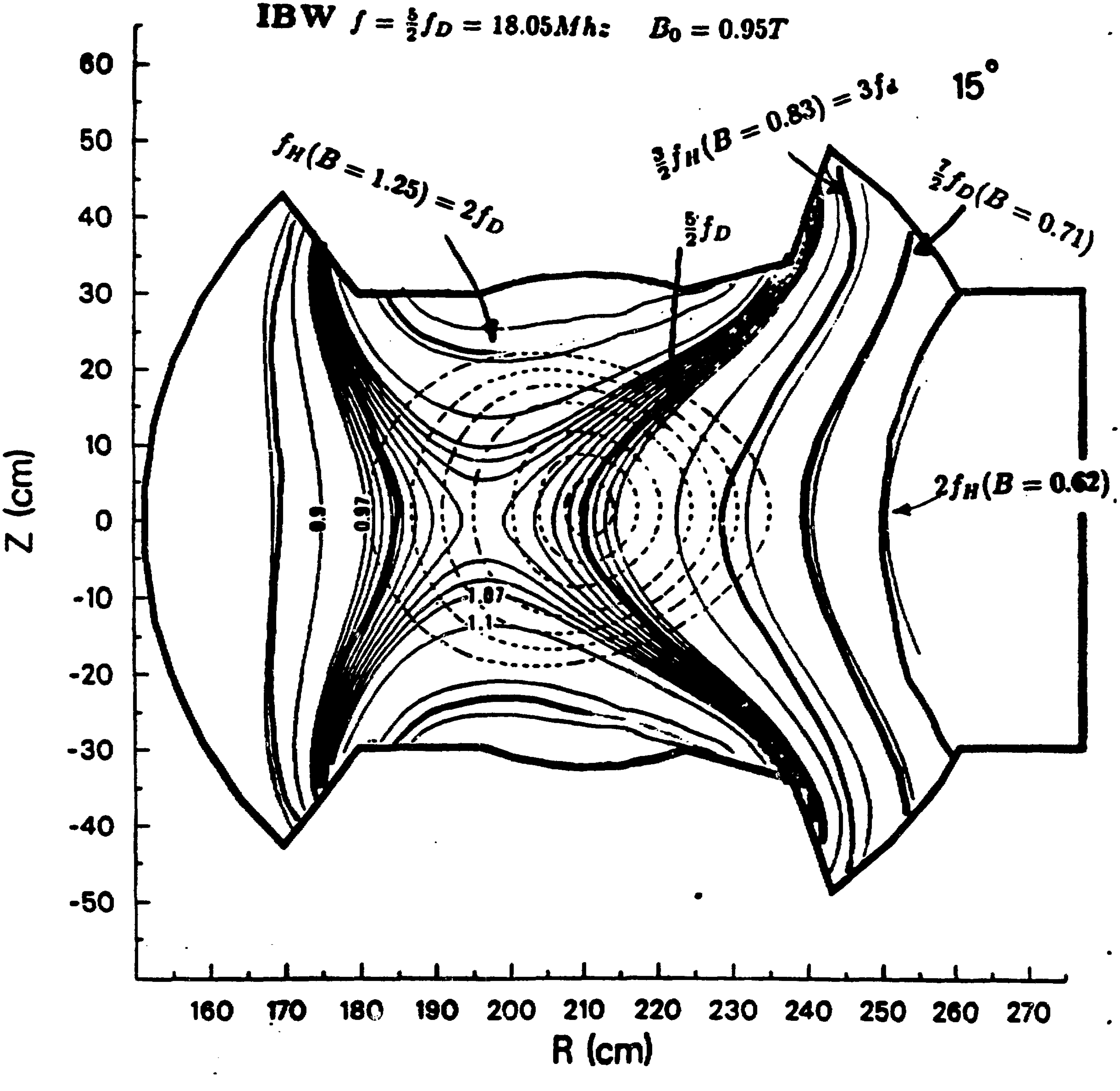

IBW $f = \frac{5}{2} f_D = 18.05 Mhz$ $B_0 = 0.95T$
15°
$f_H(B = 1.25) = 2f_D$
$\frac{3}{2} f_H(B = 0.83) = 3f_d$
$\frac{5}{2} f_D$
$\frac{7}{2} f_D(B = 0.71)$
$2f_H(B = 0.62)$
0.9
0.97
1.07
1.1
Z (cm)
R (cm)
60
50
40
30
20
10
0
-10
-20
-30
-40
-50
160
170
180
190
200
210
220
230
240
250
260
270

IBW $f = \frac{3}{2} f_H = 21.7 Mhz \quad B_0 = 0.95T$

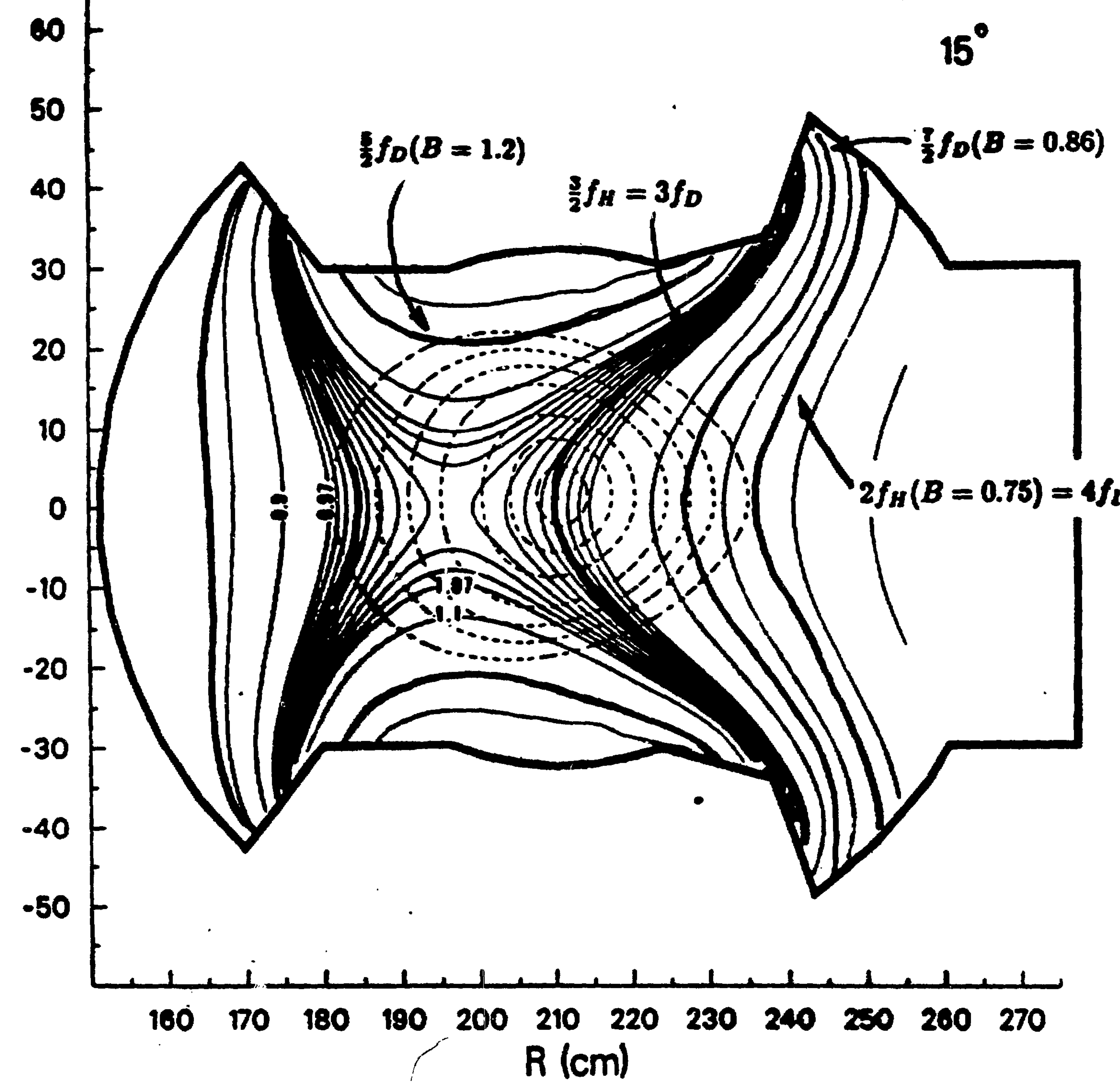

Mode	Advantages	Disadvantages
Fast Wave $f = f_H(0) = 14.4$ mhz D(H) minority	works in tokamaks at high power no competing linear resonances calculations for ATF show good heating	produces large $T_\perp$ minority tail
Fast Wave $f = 2f_H(0) = 28.9$ mhz	works in tokamaks at high power can use "ATF" FMIT no competing linear resonances	produces large $T_\perp$ bulk tail
Fast Wave $f = f_{^3He}(0) = 9.63$ mhz	works in tokamaks at high power $^3He^{++}$ more collisional, faster tail equilibration	produces large $T_\perp$ minority tail H^+ (impurity) resonance at B= .67
IBW $f = \frac{3}{2} f_D(0) = 10.83$ mhz	most IBW experience on tokamaks Heats bulk, no tail	H^+ fundamental at B= .75
IBW $f = \frac{5}{2} f_D(0) = 18.06$ mhz	some experience on tokamaks Heats bulk, no tail	several linear [$2f_H$, $3f_D$, $2f_D$, f_4] and non-linear [$\frac{7}{2} f_D$, $\frac{3}{2} f_H$] resonance at plasma edge
IBW $f = \frac{3}{2} f_H(0) = 21.7$ mhz	some experience on tokamaks Heats bulk, no tail	linear H resonance ($2f_H$) near antenna several non-linear D impurity resonances at plasma edge [$\frac{5}{2} f_D$, $\frac{7}{2} f_D$]
IBW $f = 2f_D(0) = 14.4$ mhz	No competing linear resonances fundamental H resonance gives additional damping	No experience on tokamaks fundamental H impurity resonance may tend to produce tail

CONCLUSIONS

- There are many possible heating modes, any of which could be sucessful on ATF.

- None of the methods is without possible problems. The major issues are:
  (1) Can energetic tails be confined in ATF? If so then minority hydrogen or hydrogen 2nd harmonic should work well.
  (2) Can hydrogen concentrations be kept sufficiently low in deuterium discharges to avoid parasitic resonances? If so then IBW at $\frac{3}{2}$D and fast wave He^3 minority should work well.

- The presence of a saddle point in *mod*(B), characteristic of torsatrons, makes heating much different than in tokamaks.
  (1) Resonant surfaces are bifurcated and can change topology depending on density and frequency.
  (2) The large magnetic field scale-length near the saddle point is favorable to cyclotron damping.
  (3) The rapid fall of *mod*(B) on the outside makes high harmonic heating more difficult by introducing additional resonances.

Theoretical Calculations of ICRF in Stellarator Geometry

- **2D Full Wave Calculations**

  Helically symmetric straight stellarator or tokamak geometry

  Non-circular cross section boundary

  Improved model for flux surfaces

  Cyclotron resonance broadened by ad hoc collisions

  Or

  Use of approximate warm plasma conductivity for fast waves. i.e.

  cyclotron resonance broadened by $Z(\frac{\omega-\Omega_i}{k_\parallel v_i})$ rather than collisions

  $k_\perp$ which appears in σ is determined from fast wave root of warm plasma dispersion relation

  assume $k_\parallel = k_{toroidal} = const$

  effect of Bernstein wave on fast wave is included although Bernstein wave does not appear in model

- **1D Full Wave Kinetic Model**

  Vlasov equation expanded to 2nd order in gyroradius, includes diamagnetic drift and Bernstein mode

  $E_\parallel$ retained to include Landau damping

  all x dependence retained in plasma pressure and B field

- **Fokker Planck Modelling of RF Heated Distribution Functions**

  2D in velocity space

  0D model for radial diffusion and dirft orbit losses

- **Ray Tracing Studies**

  full 3D toroidal equilibria

2-D Global Waves using Finite Differences

Assumptions and Limits of Validity

- Wavelength and width of absorption layer must be large compared to the mesh size (prohibits ion Bernstein waves in 2-D for example)

- Equilibrium must have at least one ignorable coordinate to allow Fourier decomposition of fields (e.g. the axisymmetric tokamak or the helically symmetric stellarator)

- $m_e/m_i = 0$ implies $\mathbf{E}_\parallel = 0$ (limits validity to low frequencies; reasonable for $\omega \sim \Omega_i$ and $n \geq 10^{11}\ cm^{-3}$)

- Absorption occurs by:
  (a) Cold plasma - ad hoc collisions (Fukuyama)
  (b) Warm plasma - approximate mode conversion (Colestock) (limits validity to $k_\perp \rho_i \ll 1$ and $k_\parallel = k_z$)

(a) Cold Plasma Absorption - Ad hoc Collisions

- **Solve the vector wave equation in 2 dimensions**

$$-\nabla \times \nabla \times \mathbf{E} + \frac{\omega^2}{c^2}\mathbf{E} + i\omega\mu_0\sigma \cdot \mathbf{E} = -i\omega\mu_0\mathbf{J}_{ext}$$

- **Calculate plasma current using cold plasma theory**

$$\mathbf{K} = \mathbf{I} + \frac{i}{\omega\epsilon_0}\sigma = \begin{pmatrix} K_\perp & -iK_x & 0 \\ iK_x & K_\perp & 0 \\ 0 & 0 & K_\parallel \end{pmatrix}$$

where

$$K_\perp = 1 - \sum_j \frac{\omega_{pj}^2}{\omega^2 - \Omega_j^2}; \quad K_x = \sum_j \frac{\Omega_j}{\omega}\frac{\omega_{pj}^2}{\omega^2 - \Omega_j^2}$$

$$K_\parallel = 1 - \sum_j \frac{\omega_{pj}^2}{\omega^2}$$

- **Resolve singularity in K at $\omega = \Omega_j$ by introducing a collision term in the Lorentz force equation**

$$m_j \rightarrow m_j^* = m_j(1 + i\nu/\omega)$$

(b) Warm plasma Absorption - Mode Conversion Model

(Colestock, Kay, Cairns, Lashmore-Davies, Francis, and Bers)

- **Solve the vector wave equation in 2 dimensions**

$$-\nabla \times \nabla \times \mathbf{E} + \frac{\omega^2}{c^2}\mathbf{E} + i\omega\mu_0 \sum_s \mathbf{J}_s = -i\omega\mu_0 \mathbf{J}_{ext}$$

- **Calculate plasma current from the linearized Vlasov equation expanded to 2^{nd} order in $k_\perp \rho_i$; for infinite uniform plasma with B constant and $k_\parallel = k_z$, this gives**

$$-\frac{c^2}{\omega^2}(\nabla \times \nabla \times \mathbf{E}) + \left(\epsilon^{(0)} + \epsilon^{(1)} \cdot \nabla_\perp + \epsilon^{(2)} \cdot \nabla_\perp^2\right)\mathbf{E} = -\frac{i}{\omega\epsilon_0}\mathbf{J}_{ext}$$

- **Local dispersion relation: ($\nabla_\perp \mathbf{E} \rightarrow ik_\perp \mathbf{E}$)**

$$Det\left[\mathbf{nn} - |\mathbf{n}|^2\mathbf{I} + \epsilon^{(0)} + ik_\perp\epsilon^{(1)} - k_\perp^2\epsilon^{(2)}\right] = 0$$

For $E_z = 0$ this is 4^{th} order (bi-quadradic) in $k_\perp$

- **Mode conversion model: solve for fast wave root only and take $\nabla_\perp \rightarrow ik_{\perp,fast}$ in the warm plasma terms of wave equation:**

$$-\frac{1}{k_0^2}(\nabla \times \nabla \times \mathbf{E}) + \underbrace{\left(\epsilon^{(0)} + ik_\perp\epsilon^{(1)} - k_\perp^2\epsilon^{(2)}\right)}_{\mathbf{K}} \cdot \mathbf{E} = -\frac{i}{\omega\epsilon_0}\mathbf{J}_{ext}$$

Magnetic Field Model

- **Transform from cylindrical coordinates (r, θ, z) to helical coordinates (r', ϕ, z')**

$$r' = r$$
$$\phi = \theta - hz \quad (h = \textit{helical pitch})$$
$$z' = z$$

- **Introduce flux functions $\psi(r,\phi)$ and $\chi(r,\phi)$ such that $\nabla \cdot \mathbf{B}^0 = 0$, $\nabla \cdot \mathbf{J} = 0$ and $\mathbf{B}^0$ is independent of z (helical symmetry); then**

$$\mathbf{B}^0(r,\phi) = \frac{\partial \psi}{\partial \phi}\frac{\hat{\mathbf{r}}}{r} - \frac{\partial \psi}{\partial r}\frac{\hat{\boldsymbol{\theta}} - hr\hat{\mathbf{z}}}{1 + h^2 r^2} + \chi \frac{\hat{\mathbf{z}} + hr\hat{\boldsymbol{\theta}}}{1 + h^2 r^2}$$

- **For an (l, m) helically symmetric stellarator, take $h = \frac{m}{lR_T}$, and**

$$\psi(r,\phi) = \frac{B_0}{2}hr^2 - r\sum_l \epsilon_l I_l'(lhr)\cos(l\phi)$$
$$\chi(r,\phi) = B_0 = constant$$

- **For an approximate Solov'ev equilibrium, we take $h = 0$, $\phi = \theta$ and**

$$\psi(r,\theta) = \frac{-\epsilon_0 B_0}{2R_T}\left[\frac{(1 + x/R_T)^2}{\kappa^2}y^2 + (1 + \frac{x}{2R_T})^2 x^2\right]$$
$$\chi(r,\theta) = \frac{B_0}{1 + x/R_T}$$

Helically Symmetric Equilibrium for Heliotron-E

Contours of constant $\psi(r,\phi)$

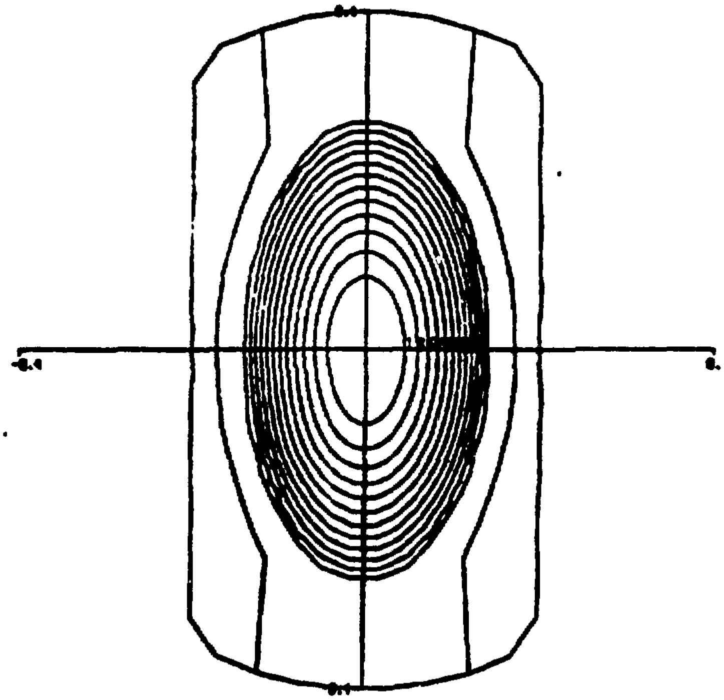

Contours of constant $|\mathbf{B}(r,\phi)|$

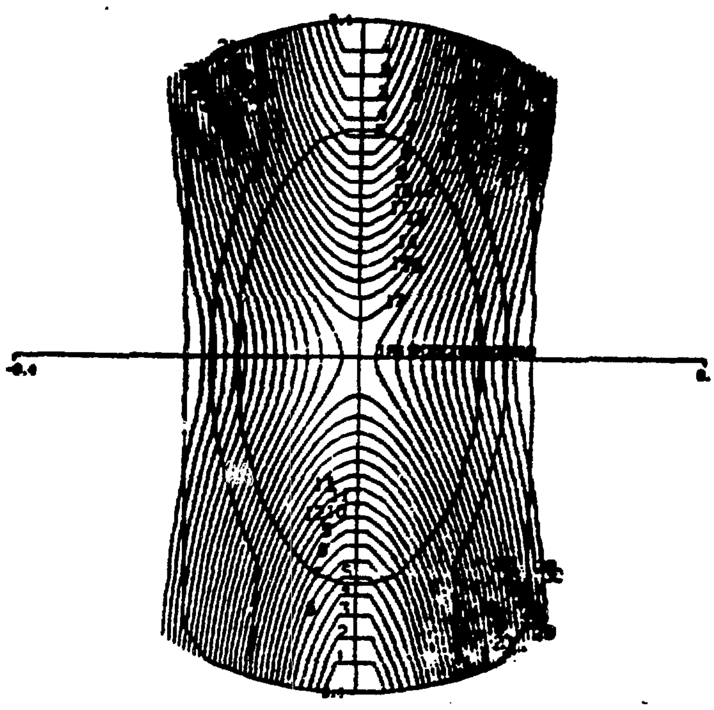

- Since z' is ignorable in these equilibria, Fourier decompose in z'

$$\mathbf{E}(r', \phi, z') = \sum_{k_z} \mathbf{E}_{k_z}(r', \phi)\, e^{ik_z z'}$$

- Construct unit vectors

$$\hat{\mathbf{e}}_1 = \nabla\psi / \mid \nabla\psi \mid$$
$$\hat{\mathbf{e}}_2 = \hat{\mathbf{b}} \times \hat{\mathbf{e}}_1$$
$$\hat{\mathbf{e}}_3 = \hat{\mathbf{b}} = \mathbf{B}^0 / \mid \mathbf{B}^0 \mid$$

- Obtain two equations for the r and ϕ components of $\mathbf{E}$ by dotting $\hat{\mathbf{e}}_1$ and $\hat{\mathbf{e}}_2$ with the wave equation

Quantities Calculated

- **Wave fields**

$$\mathbf{E}_1 = \mathbf{E}\cdot\hat{\mathbf{e}}_1 \quad and \quad \mathbf{E}_2 = \mathbf{E}\cdot\hat{\mathbf{e}}_2$$

or alternatively left and right hand polarizations

$$\mathbf{E}_\pm = \mathbf{E}_1 \pm i\mathbf{E}_2$$

- **Local energy deposition**

$$\begin{aligned}\dot{W}(\mathbf{x}) &= \frac{1}{2}Re\{\mathbf{E}^*\cdot\sigma\cdot\mathbf{E}\}\\ &= Re(\sigma_{xx}^{(0)} - k_\perp^2\sigma_{xx}^{(2)})\frac{|E_1|^2}{2} + Re(\sigma_{yy}^{(0)} - k_\perp^2\sigma_{yy}^{(2)})\frac{|E_2|^2}{2}\\ &\quad - Im(\sigma_{xy}^{(0)} - k_\perp^2\sigma_{xy}^{(2)})Im(E_1^*E_2)\end{aligned}$$

$$\begin{aligned}P_d(\mathbf{x}) &= \frac{1}{2}Re\{\mathbf{E}^*\cdot\sigma\cdot\mathbf{E}\} - \nabla\cdot\mathbf{Q}\\ &= Re(\sigma_{xx}^{(0)} - |k_\perp|^2\sigma_{xx}^{(2)})\frac{|E_1|^2}{2} + Re(\sigma_{yy}^{(0)} - |k_\perp|^2\sigma_{yy}^{(2)})\frac{|E_2|^2}{2}\\ &\quad - Im(\sigma_{xy}^{(0)} - |k_\perp|^2\sigma_{xy}^{(2)})Im(E_1^*E_2)\end{aligned}$$

- **Total power absorbed**

$$\mathbf{P}_{abs} = \int \dot{\mathbf{W}}(\mathbf{x})\ d^3\mathbf{x}$$

- **Complex antenna impedance**

$$\mathbf{Z}(\omega) = \frac{1}{\mathbf{I}^2}\int \mathbf{J}_{ext}^*\cdot\mathbf{E}\ d^3\mathbf{x}$$

Power Deposition: Lorentz Collision Model

power deposition contours $\dot{W}(r, \phi)$

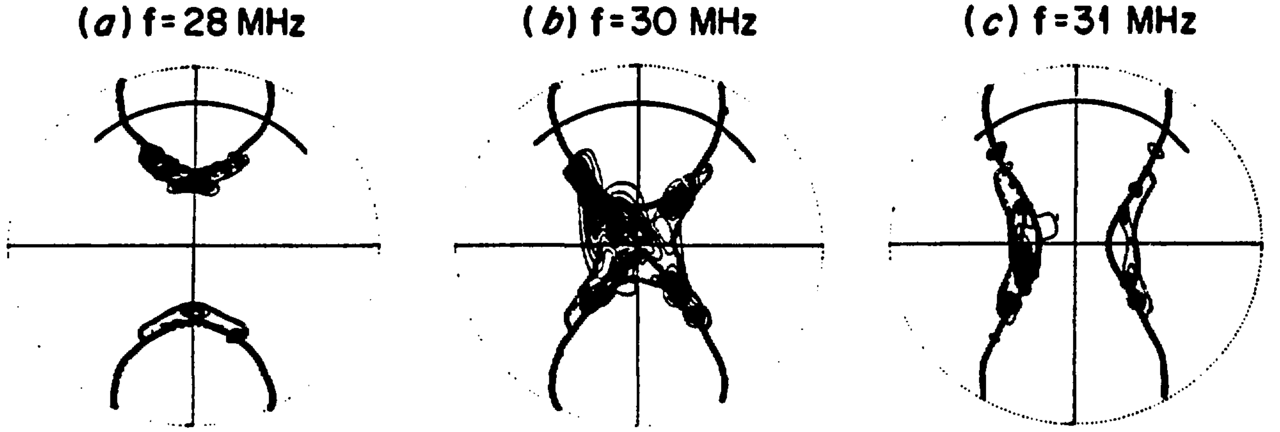

flux surface average of power absorbed

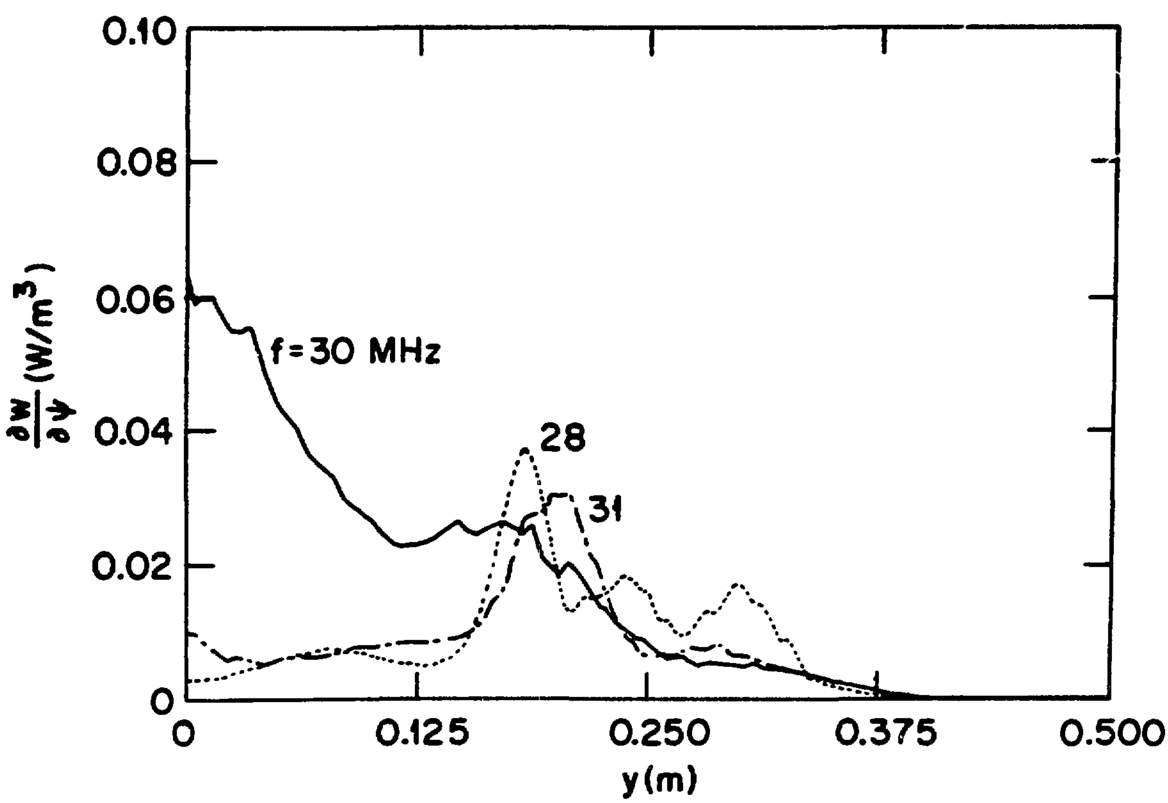

Power Deposition: Warm Plasma Conductivity

with $k_\perp \rho_i = 0$, and $k_\parallel \to k_z$

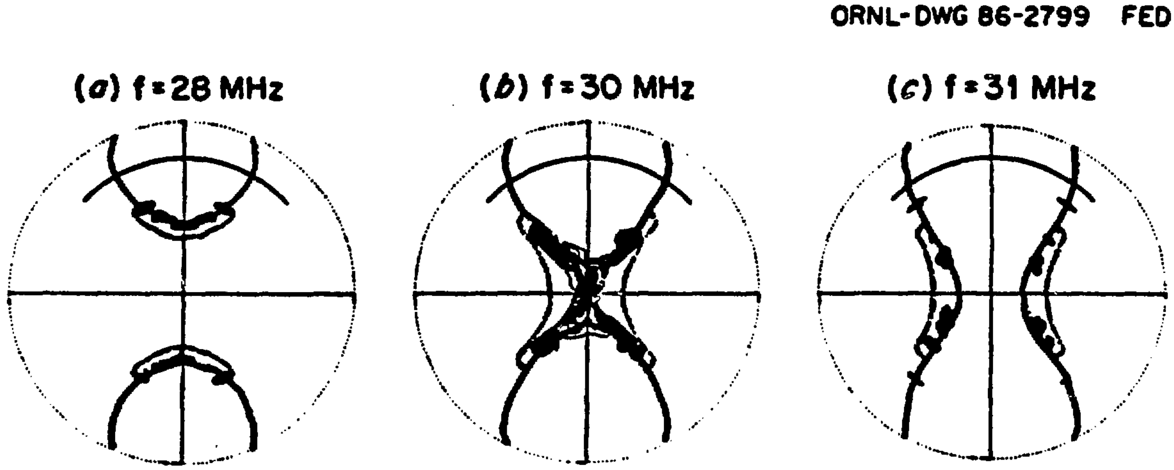

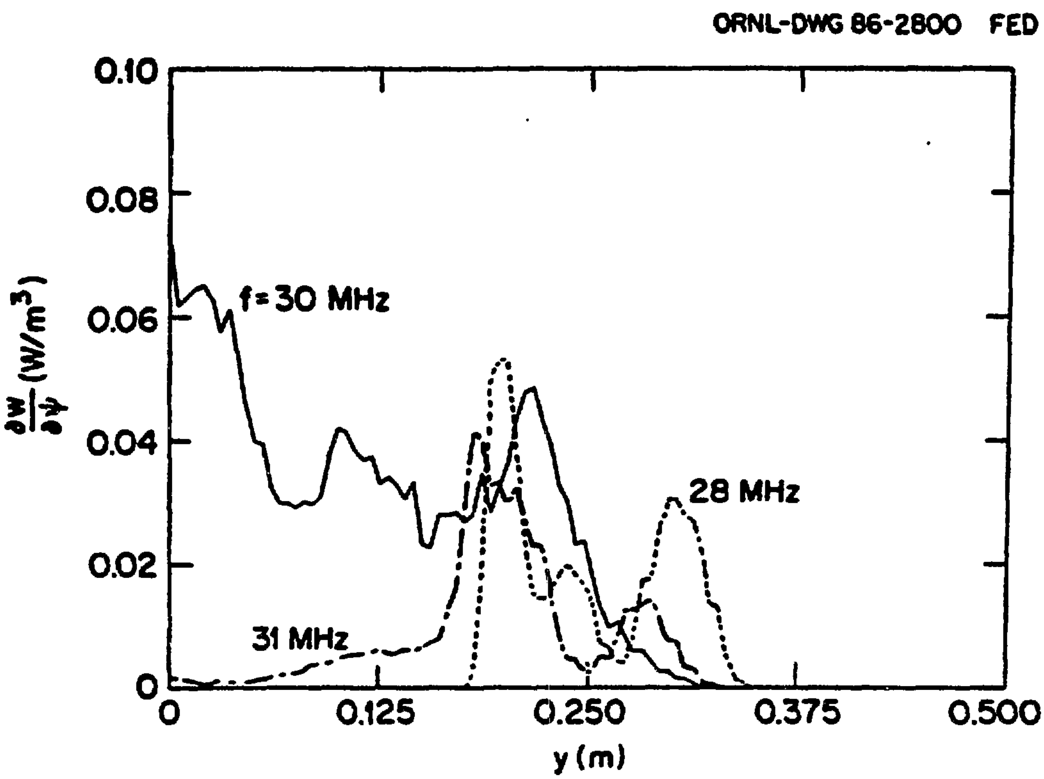

Second Harmonic Fast Wave Heating in ATF

Heating Contours

2nd harmonic resonance

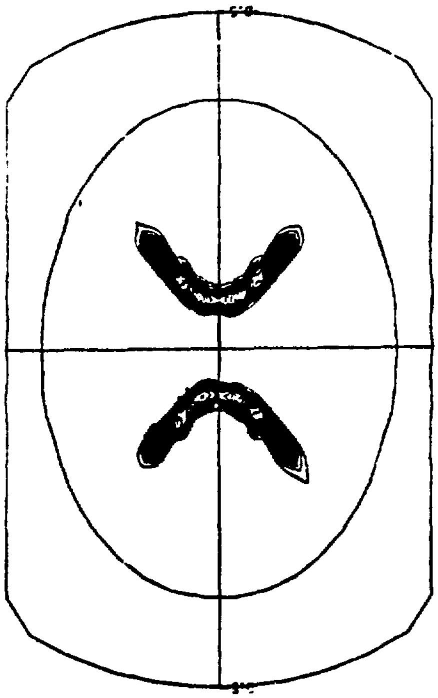

vacuum vessel

plasma boundary

Heating Profile

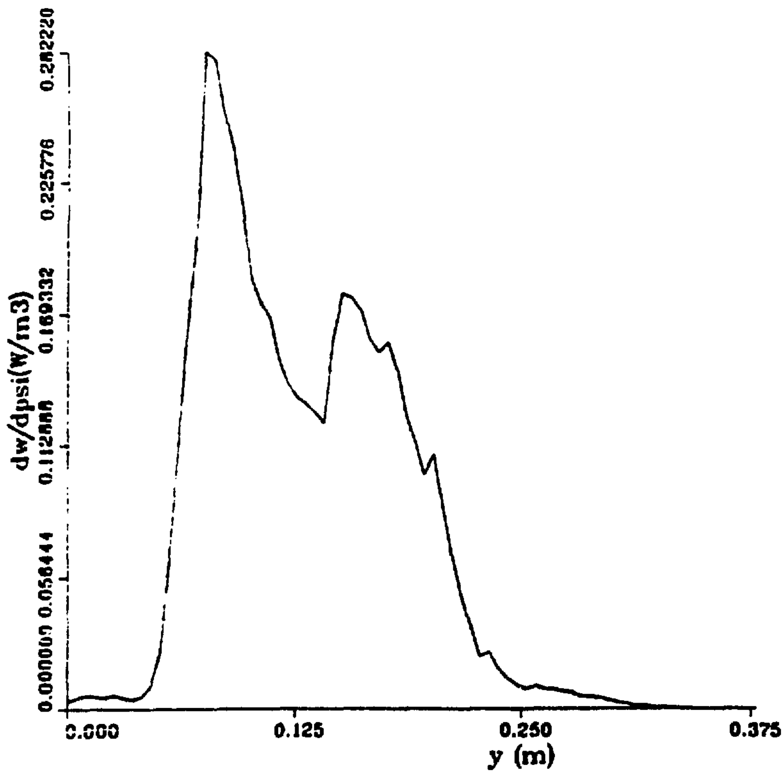

- Approximate warm plasma conductivity tensor allows for 2nd harmonic cyclotron absorption (not in cold plasma theory) and givès natural (thermal) resonance width
- For ATF at $T_i = 1kev$ we find antenna loading $\approx 1\Omega$. Comparable to value for minority heating.

Antenna Design for ATF

plasma loading versus antenna angle, $\alpha = tan^{-1}(j_z/j_\theta)$

ORNL-DWG 86-3045 FED

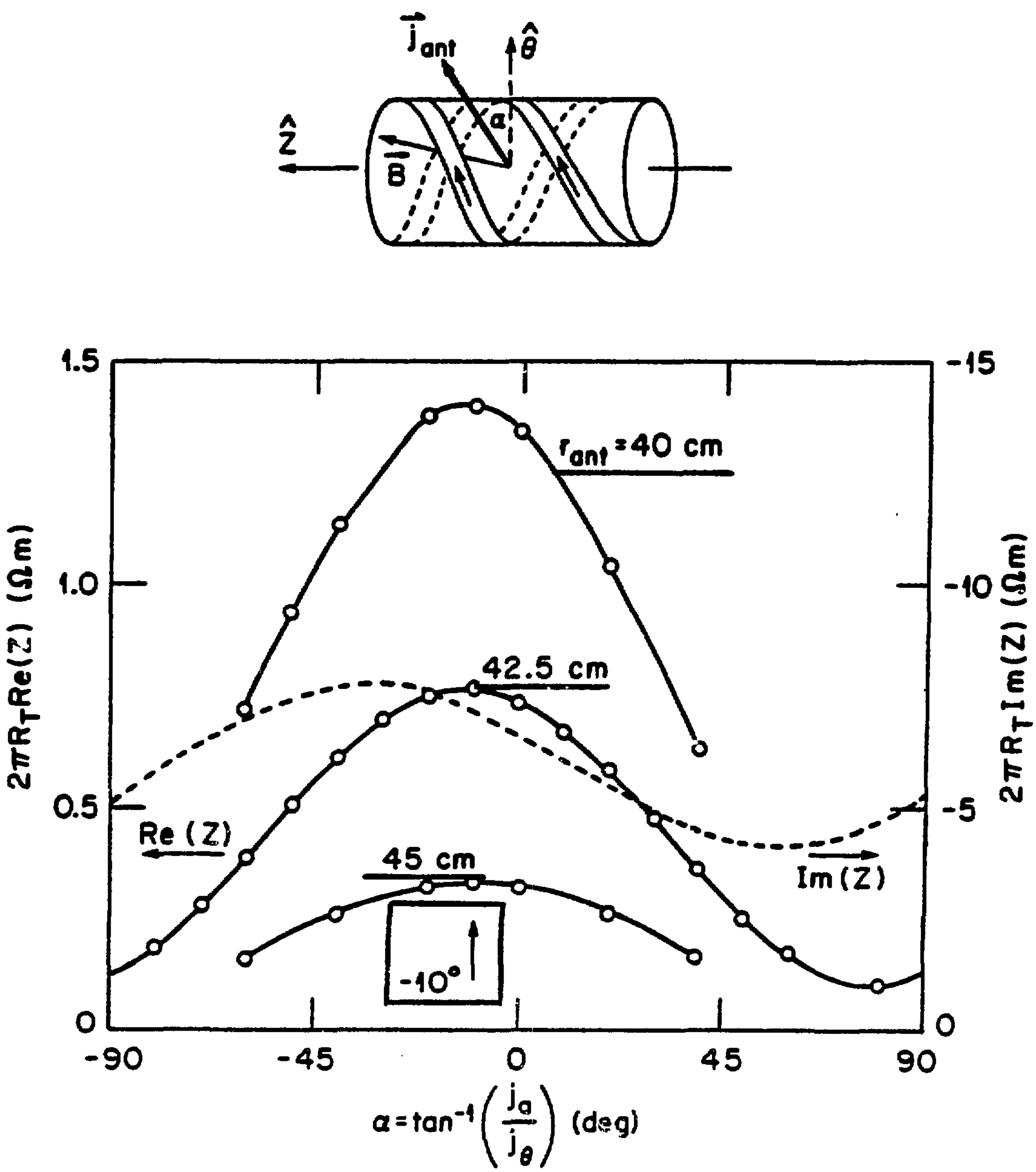

1-D Global Waves using Finite Differences

Assumptions and Limits of Validity

- Wavelength and width of absorption layer must be large compared to the mesh size (allows ion Bernstein waves in 1-D)
- Equilibrium must have at least two ignorable coordinates to allow Fourier decomposition of fields in y and z (e.g. the perpendicularly stratified plasma slab)
- $m_e/m_i \neq 0$ implies $E_z \neq 0$ (allows Landau damping of the ion Bernstein wave)
- Absorption occurs by cyclotron and Landau damping; plasma current is calculated from second order expansion of Vlasov equation in $k_\perp \rho_i$ assuming perpendicular stratification (limits validity to $k_\perp \rho_i \ll 1$ and $k_\parallel = k_z$)
- Assumes cold plasma at edge; warm plasma effects must be negligible at the warm - cold interface.

Perpendicularly Stratified 1-D Warm Plasma

- Solve the vector wave equation in 1 dimension

$$\boxed{-\nabla \times \nabla \times \mathbf{E} + \frac{\omega^2}{c^2}\mathbf{E} + i\omega\mu_0 \sum_s \mathbf{J}_s = -i\omega\mu_0 \mathbf{J}_{ext}}$$

- Calculate plasma current from the linearized Vlasov equation expanded to 2^{nd} order in $k_\perp \rho_i$

- Solve for the equilibrium distribution function to 2^{nd} order in ρ_i/L to ensure self-adjoint system (Romero; Vaclavik)

$$F(x, v_\perp, v_\parallel, \phi) = F^M(x, v_\perp, v_\parallel) + \frac{v_y}{\Omega}\frac{\partial F^M}{\partial x} + \frac{v_y^2}{2\Omega}\frac{\partial}{\partial x}\left[\frac{1}{\Omega}\frac{\partial F^M}{\partial x}\right]$$

- $\mathbf{E}_\parallel$ is retained to include Landau damping of the ion Bernstein wave (allows vacuum at edge)

- Slab geometry: y and z are ignorable, $\mathbf{B} = B(x)\hat{\mathbf{z}}$
  Fourier decompose in y and z:

$$\mathbf{E}(x, y, z) = \sum_{k_y, k_z} \mathbf{E}_{k_y, k_z}(x) e^{i(k_y y + k_z z)}$$

Finite Larmor Radius Expansion of Plasma Current

- Keeping all x dependence in $\mathbf{E}(x), F(v,x)$ and $(\omega - n\Omega_i(x) - k_\parallel v_\parallel)^{-1}$ gives (Martin and Vaclavik)

$$\mathbf{J}_s = (\sigma_s^{(0)} + \rho_s^{(1)} + \tau_s^{(2)}) \cdot \mathbf{E} + (\sigma_s^{(1)} + \rho_s^{(2)})_U \cdot \frac{\partial \mathbf{E}}{\partial x}$$
$$+ \frac{\partial}{\partial x}([\sigma_s^{(1)} + \rho_s^{(2)}]_L \cdot \mathbf{E}) + \frac{\partial}{\partial x}(\sigma_s^{(2)} \cdot \frac{\partial \mathbf{E}}{\partial x})$$

where

$$\sigma^{(0)} = \begin{pmatrix} \sigma_{xx}^{(0)} & \sigma_{xy}^{(0)} & 0 \\ \sigma_{yx}^{(0)} & \sigma_{yy}^{(0)} & 0 \\ 0 & 0 & \sigma_{zz}^{(0)} \end{pmatrix}, \qquad \rho^{(1)} = \begin{pmatrix} 0 & 0 & \rho_{xz}^{(1)} \\ 0 & 0 & \rho_{yz}^{(1)} \\ \rho_{zx}^{(1)} & \rho_{zy}^{(1)} & 0 \end{pmatrix}$$

$$\tau^{(2)} = \begin{pmatrix} \tau_{xx}^{(2)} & \tau_{xy}^{(2)} & 0 \\ \tau_{yx}^{(2)} & \tau_{yy}^{(2)} & 0 \\ 0 & 0 & \tau_{zz}^{(2)} \end{pmatrix}, \qquad [\sigma^{(1)} + \rho^{(2)}]_U = \begin{pmatrix} 0 & \rho_{xy}^{(2)} & \sigma_{xz}^{(1)} \\ 0 & 0 & \sigma_{yz}^{(1)} \\ 0 & 0 & 0 \end{pmatrix}$$

$$\sigma^{(2)} = \begin{pmatrix} \sigma_{xx}^{(2)} & \sigma_{xy}^{(2)} & 0 \\ \sigma_{yx}^{(2)} & \sigma_{yy}^{(2)} & 0 \\ 0 & 0 & \sigma_{zz}^{(2)} \end{pmatrix}, \qquad [\sigma^{(1)} + \rho^{(2)}]_L = \begin{pmatrix} 0 & 0 & 0 \\ \rho_{yx}^{(2)} & 0 & 0 \\ \sigma_{zx}^{(1)} & \sigma_{zy}^{(1)} & 0 \end{pmatrix}$$

Perpendicularly Stratified 1-D Geometry

2-point boundary value problem

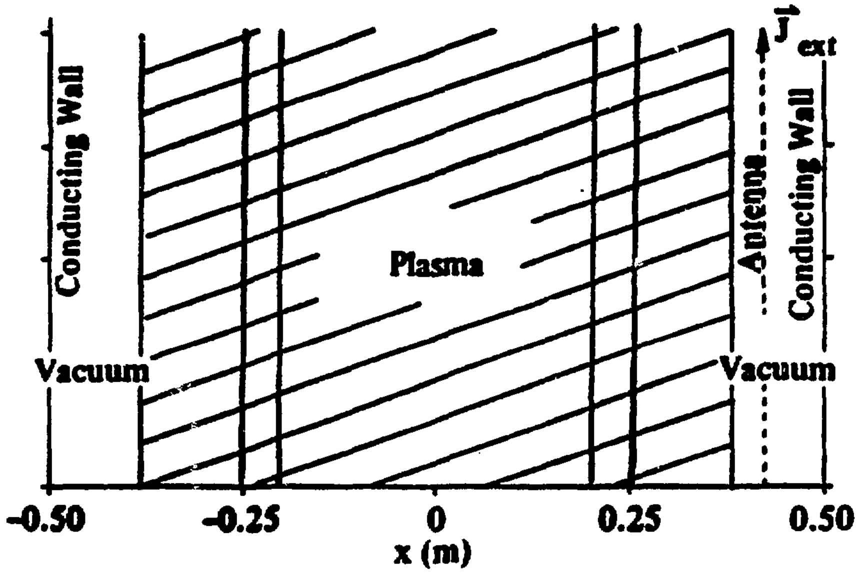

plasma profiles and magnetic field for ATF

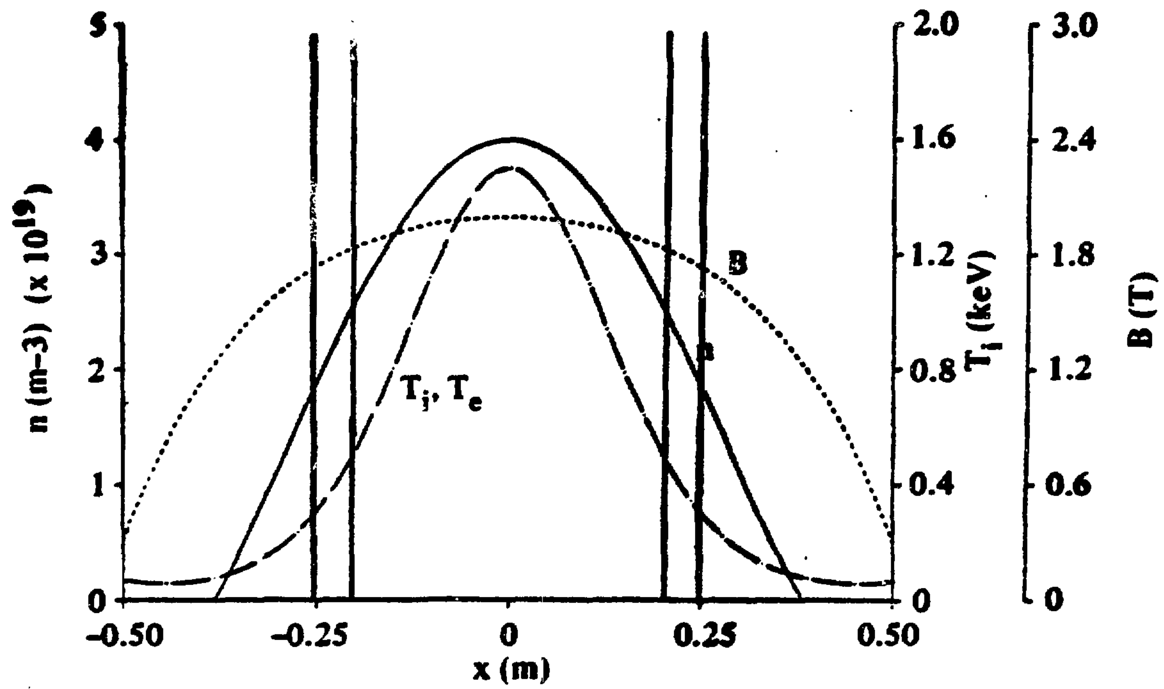

Wave Fields: Complete 6th Order Wave Equation

- strongly evanescent Bernstein waves in the low field regions do not grow exponentially as in shooting methods

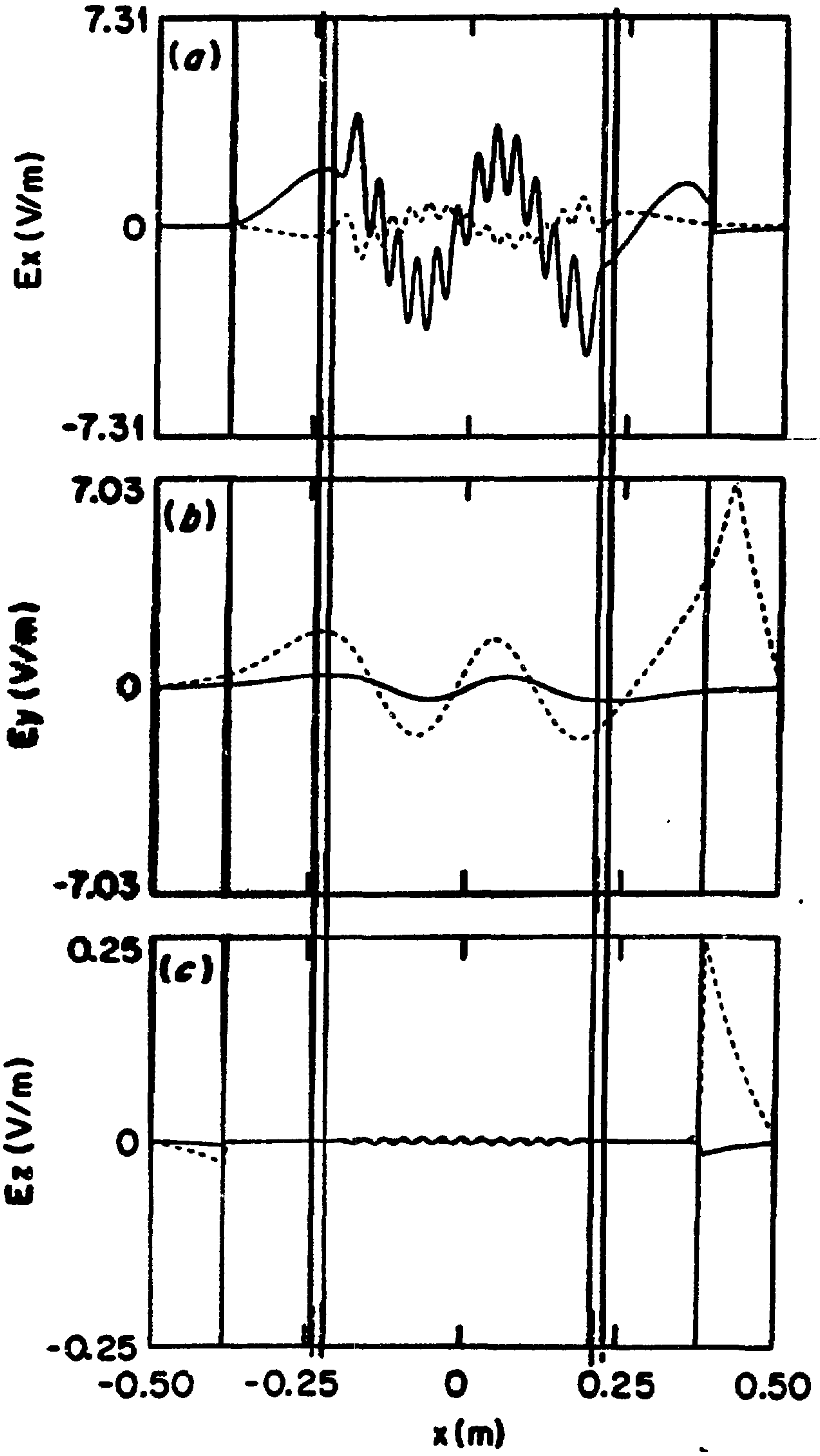

"TOROIDAL" HELIAC EXPERIMENTS ON A LINEAR DEVICE

B. A. Nelson, F. L. Ribe, D. C. Barnes*
University of Washington, Seattle WA

Previous experiments on the High Beta Q Machine (HBQM) have shown that a heliac plasma can be created at high beta ($\langle \beta \rangle \sim 0.2 - 0.3$) by applying fast-rising currents through $l = 1$ coils (1.2 MA, 350 ns) and an axial hard core (30 kA, 1μs) to a 20 % pre-ionized D_2 gas. Detailed structure of the magnetic fields and the flux function were measured with internal magnetic field probes.[1]

Analytical and numerical studies show that the vacuum magnetic field harmonic structure of a toroidal heliac with large toroidal aspect ratio is very similar to that of a linear heliac with a "shifted" (linearly translated) hardcore. Modifications are presently underway to allow the HBQM hardcore to be shifted with respect to the $l = 1$ stellarator axis, up to 2.5 cm. This approximates a toroidal heliac with a major radius of $R_0 =$ 148 cm ($R_0/a \sim 14$). The hardcore shifting apparatus is being designed to operate under vacuum, allowing "toroidal" effects to be alternately "turned on and off" during an experimental run period.

Numerical and analytical studies of the heliac vacuum fields show the equivalence of toroidal curvature and hardcore shift. These studies also show the formation of magnetic islands and their suppression by either an additional helical current about the shifted hardcore (simulation of a "flexible" heliac) or even by shifting the hardcore in a true toroidal heliac.

Future experiments on the HBQM are aimed at observing magnetic island formation and behaviour at high β, and their possible suppression by a helical hardcore.

---

* Science Applications International, Inc., Austin TX

[1] C. M. Greenfield, *et al.*, Bull. Am. Phys. Soc., 1987.

"TOROIDAL" HELIAC EXPERIMENTS ON A LINEAR DEVICE

UNIVERSITY OF WASHINGTON—SEATTLE

FACULTY

PROF. F. L. RIBE

DR. B. A. NELSON

SAIC, INC. AUSTIN, TX

DR. D. C. BARNES

STAFF

N. G. WARD, TECHNICIAN

M. CEKIĆ

G. SPANJERS

E. FOWLES

B. MILLER

DR. C. M. GREENFIELD, GA-TECH., LAJOLLA, CA

HIGH BETA Q MACHINE

$n = 10^{15}\ cm^{-3}$

$T_e + T_i = 60-80\ eV$

$B_z = 3.9\ kG$

3 m LONG $\ell = 1$ COMPRESSION COIL
(SEGMENTED)

$I_{MAX} = 1.2\ MA$

$r_c = 11\ cm$

$r_h = 2\ cm$

$h \equiv 2\pi / L = 0.154\ cm^{-1}$

FOR $L = 40.64\ cm$

HARDCORE:

$r_{HC} = 0.5\ cm$

$I_{HC} = 20-30\ kA$

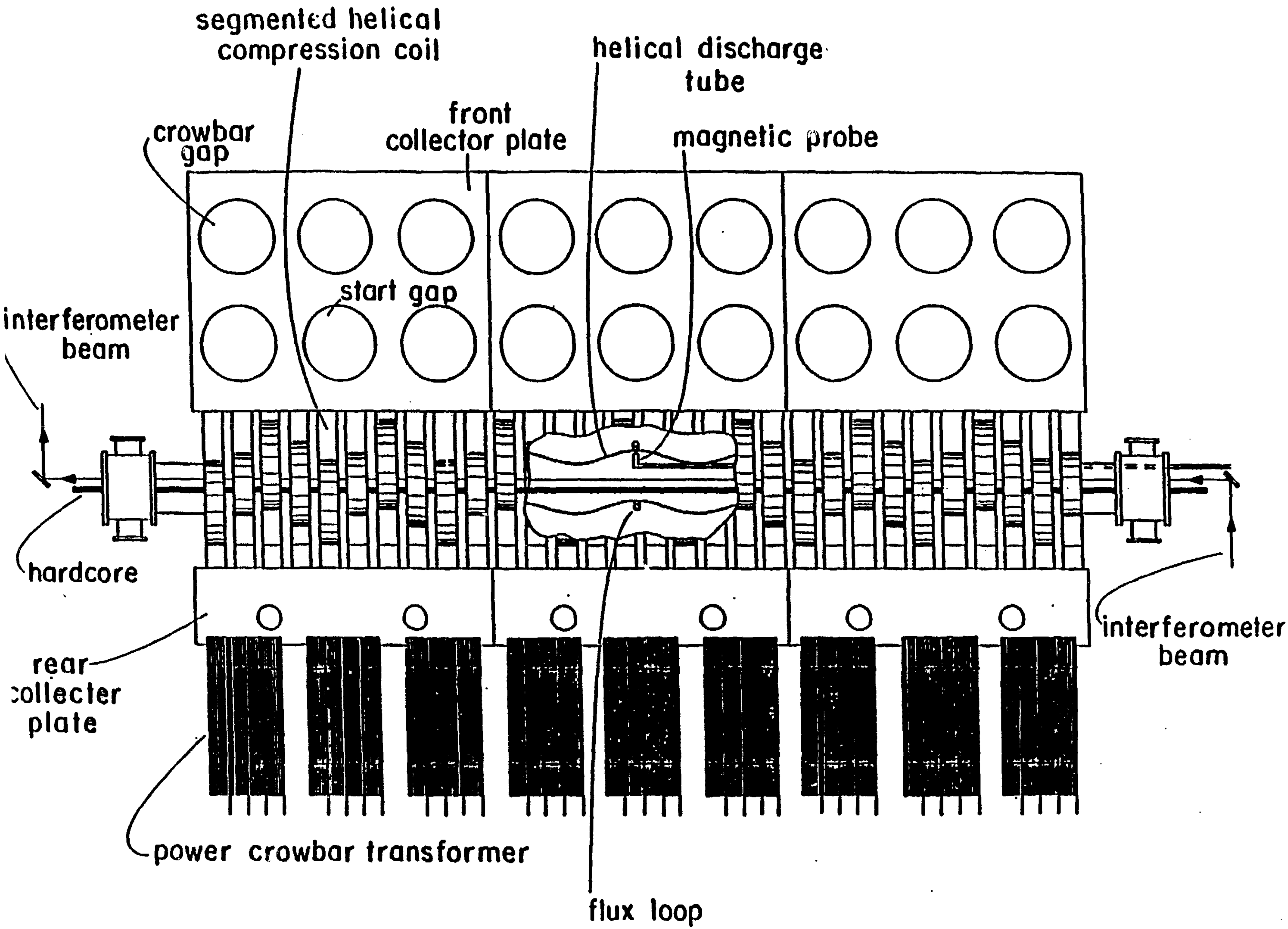
segmented helical compression coil
helical discharge tube
front collector plate
crowbar gap
magnetic probe
start gap
interferometer beam
hardcore
rear collecter plate
interferometer beam
power crowbar transformer
flux loop

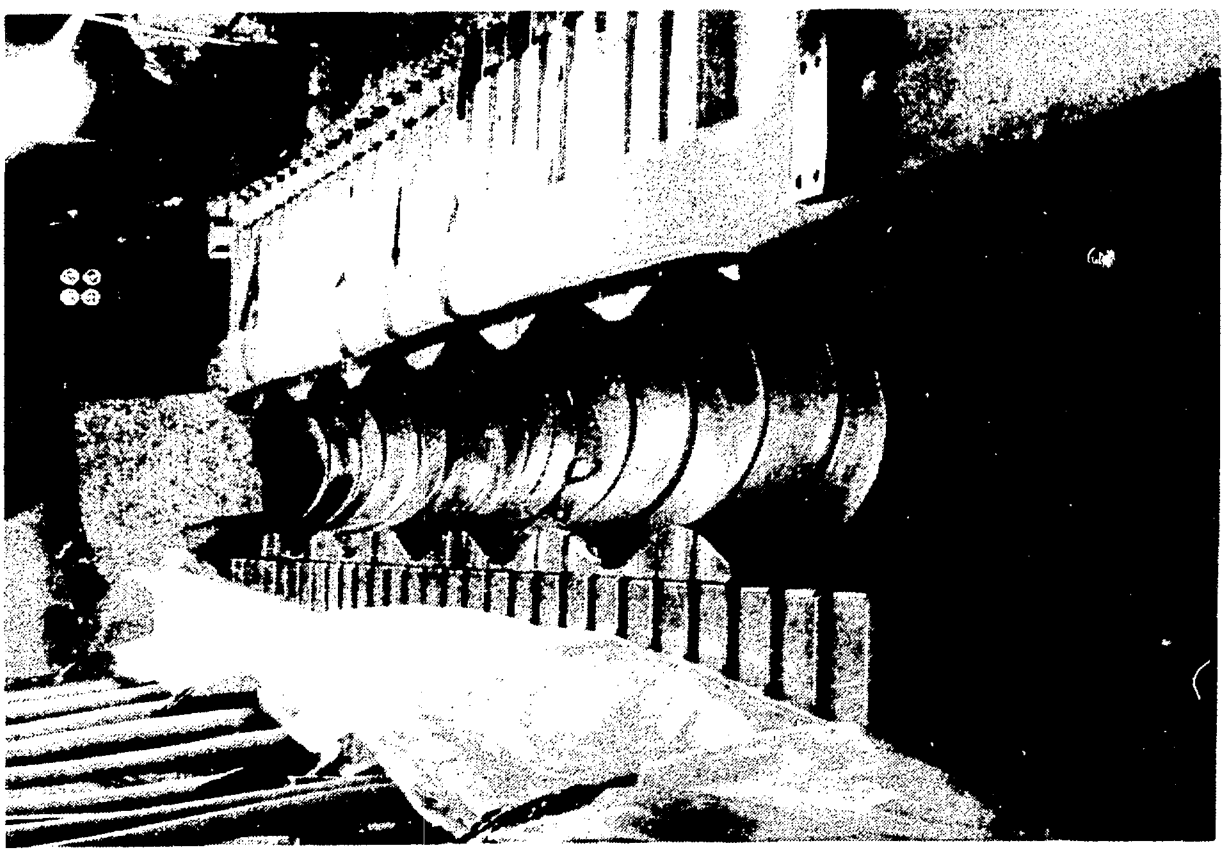

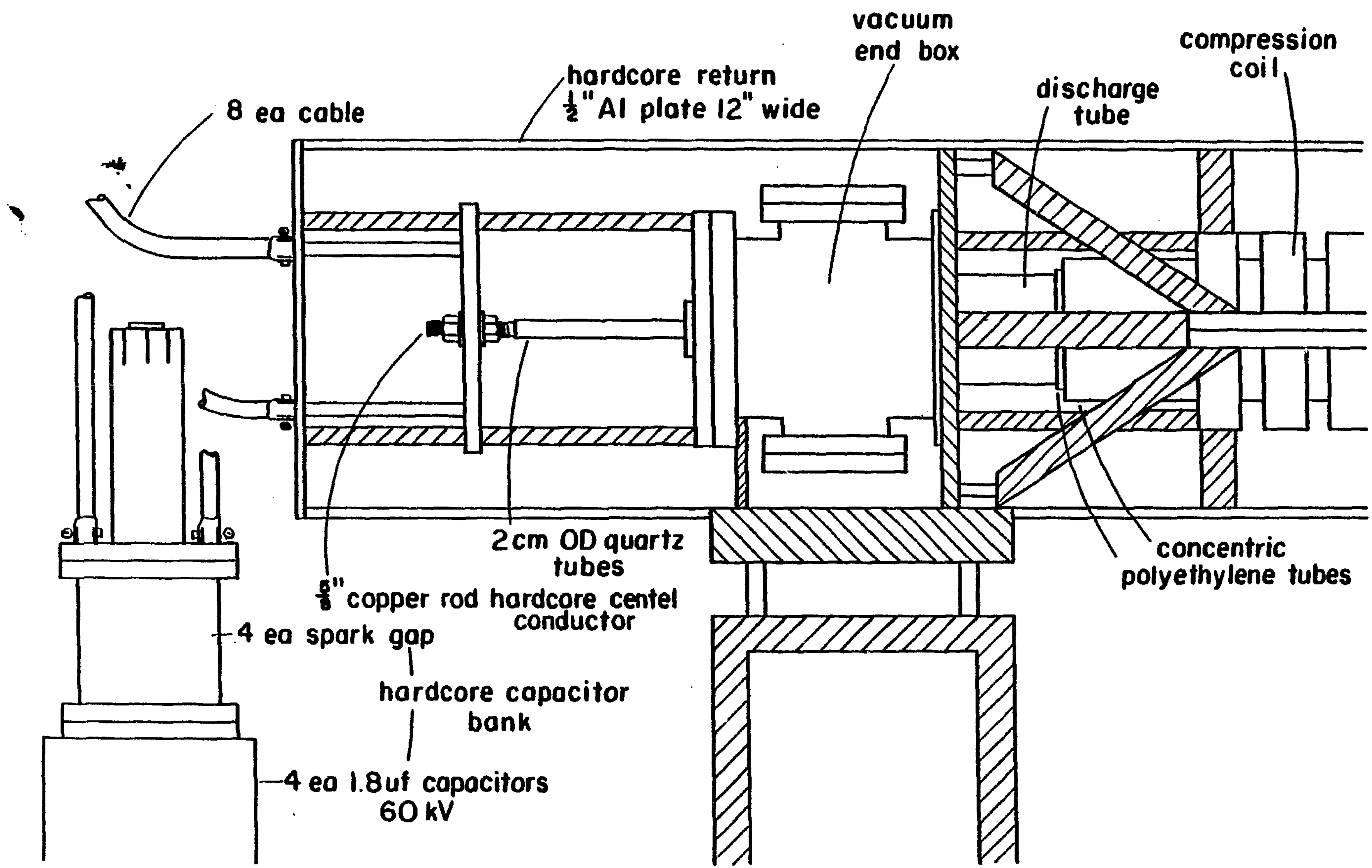
vacuum
end box
compression
coil
hardcore return
½" Al plate 12" wide
discharge
tube
8 ea cable
2cm OD quartz
tubes
concentric
polyethylene tubes
⅝" copper rod hardcore centel
conductor
4 ea spark gap
hardcore capacitor
bank
4 ea 1.8uf capacitors
60 kV

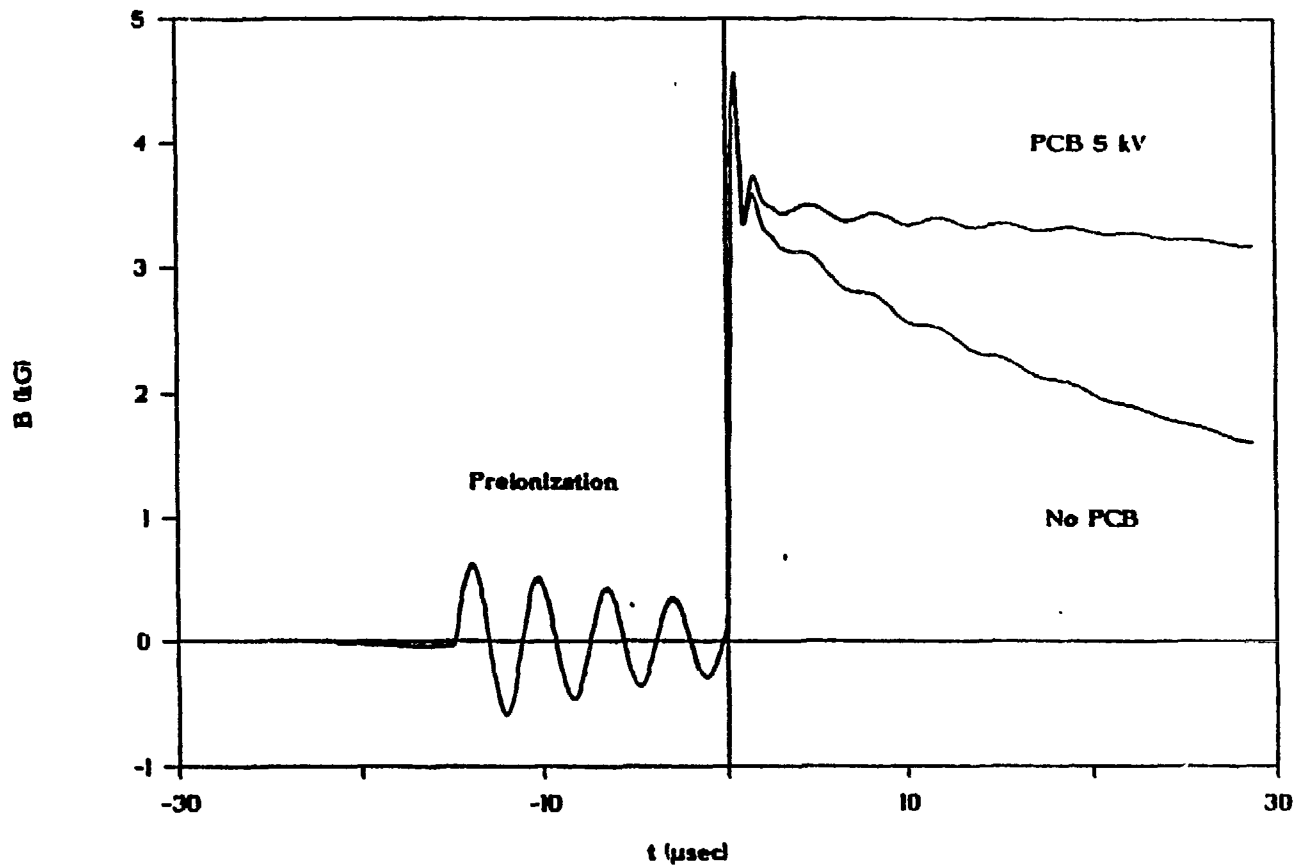

Figure 7. Waveforms of external B_z during a typical discharge showing the preionization and compression fields (with and without the power crowbar).

Axial Field and Hard Core Current

1/2/87 p0 - 0 mtorr

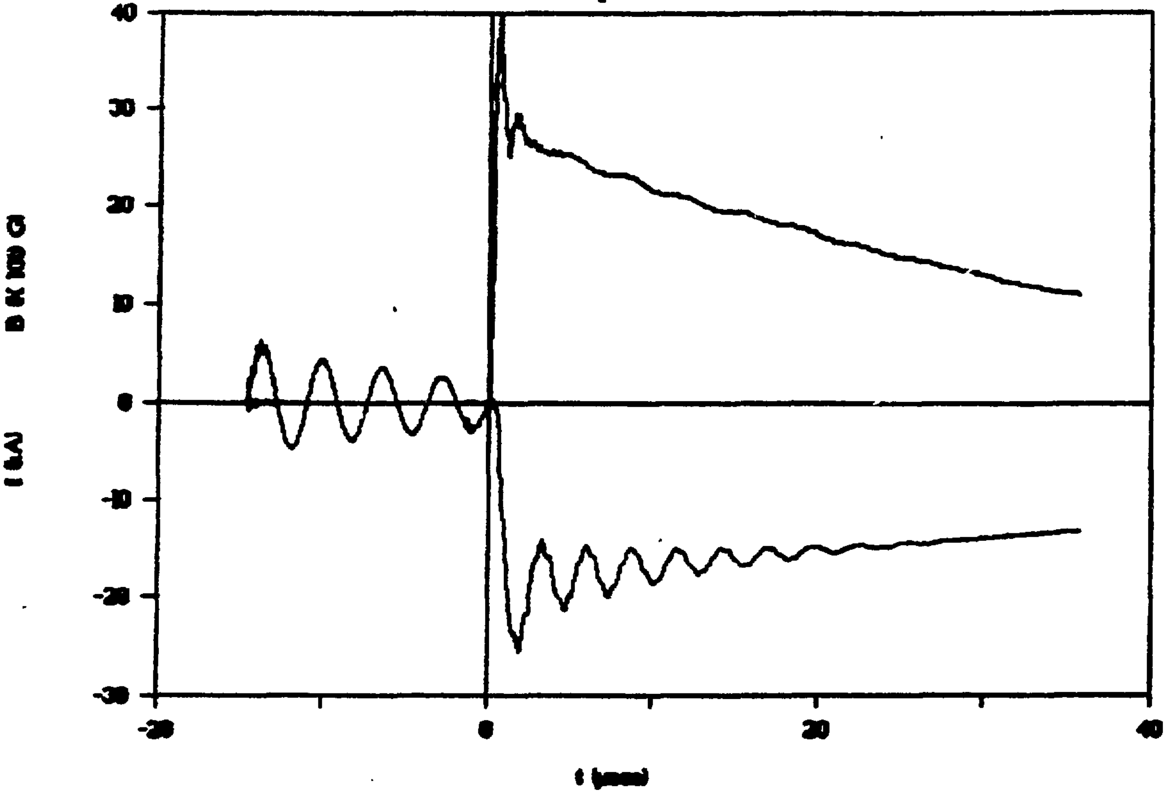

Axial Field and Hard Core Current

1/2/87 p0 - 7 mtorr

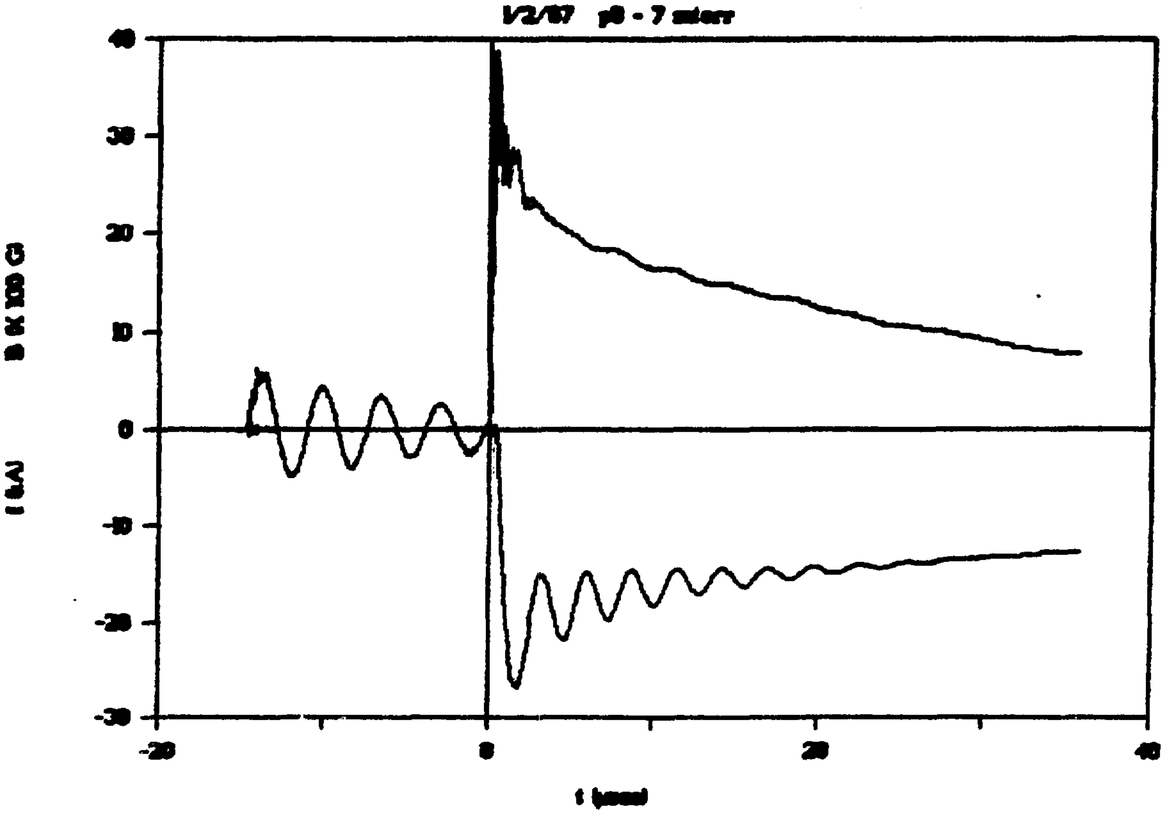

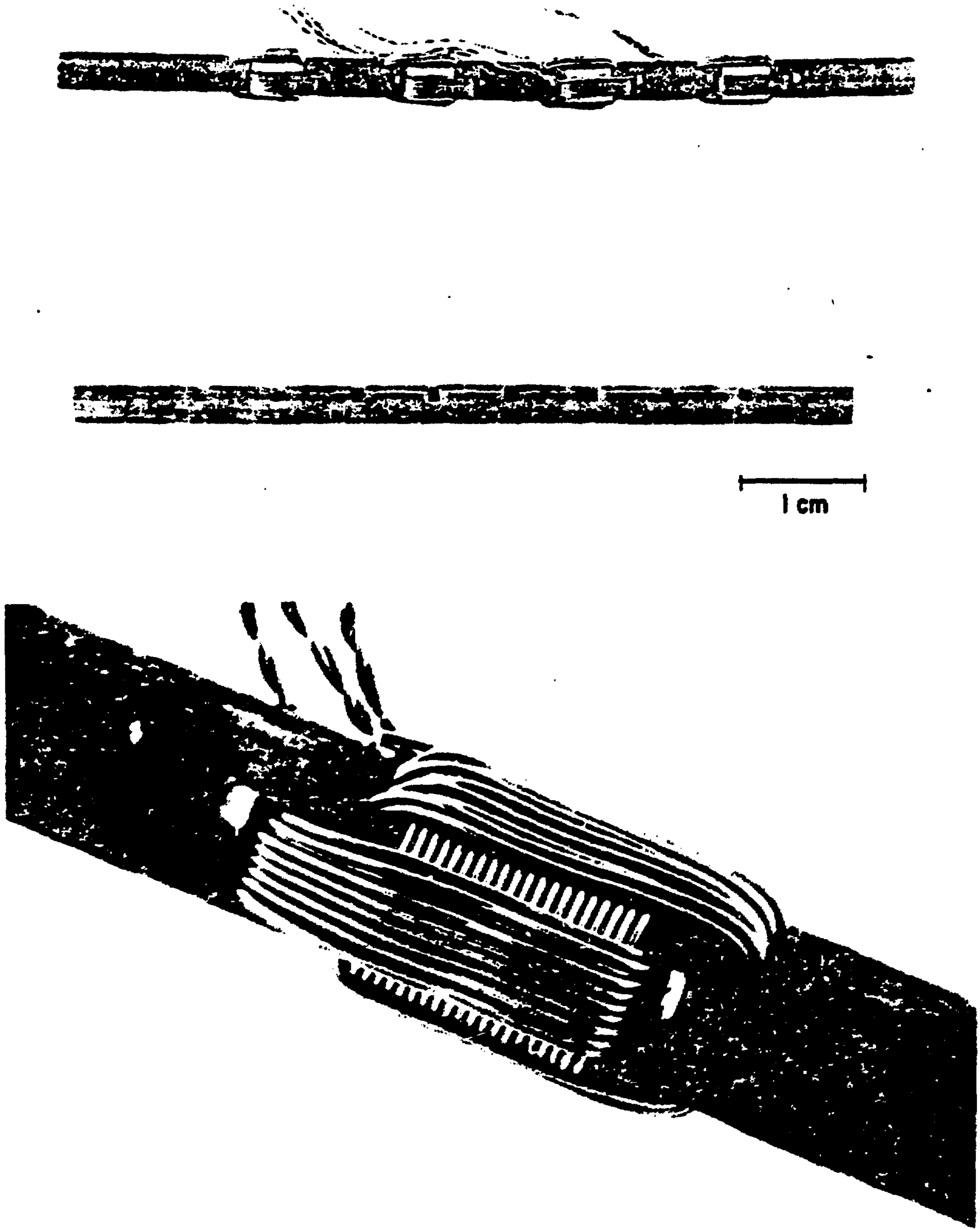

Internal magnetic field probe

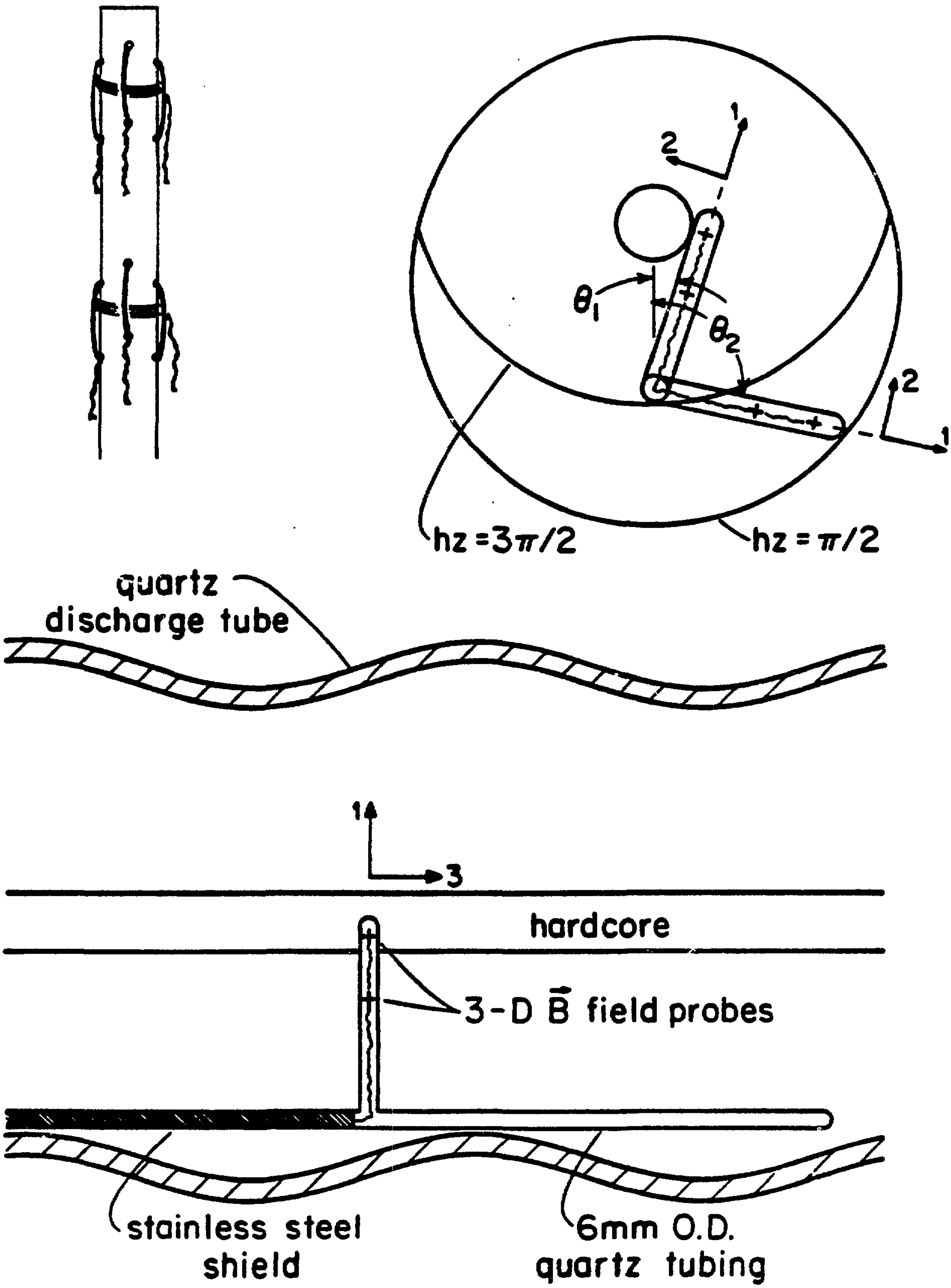
1
2
θ1
θ2
2
1
hz = 3π/2
hz = π/2
quartz
discharge tube
1
3
hardcore
3-D B field probes
stainless steel
shield
6mm O.D.
quartz tubing

HELICAL SYMMETRY

- ALL PARAMETERS FUNCTIONS OF r AND u

viz.,

$$f = f(r, u)$$

WHERE

$$u = l\theta + hz$$

$$l = 1$$

$$h = 2\pi / L = 0.154 \text{ cm}^{-1}$$

- SLIDE PROBE ALONG z WHILE POINTING TOWARD THE HARDCORE

  $\Rightarrow$ MAPPING OUT (r, u) PLANE

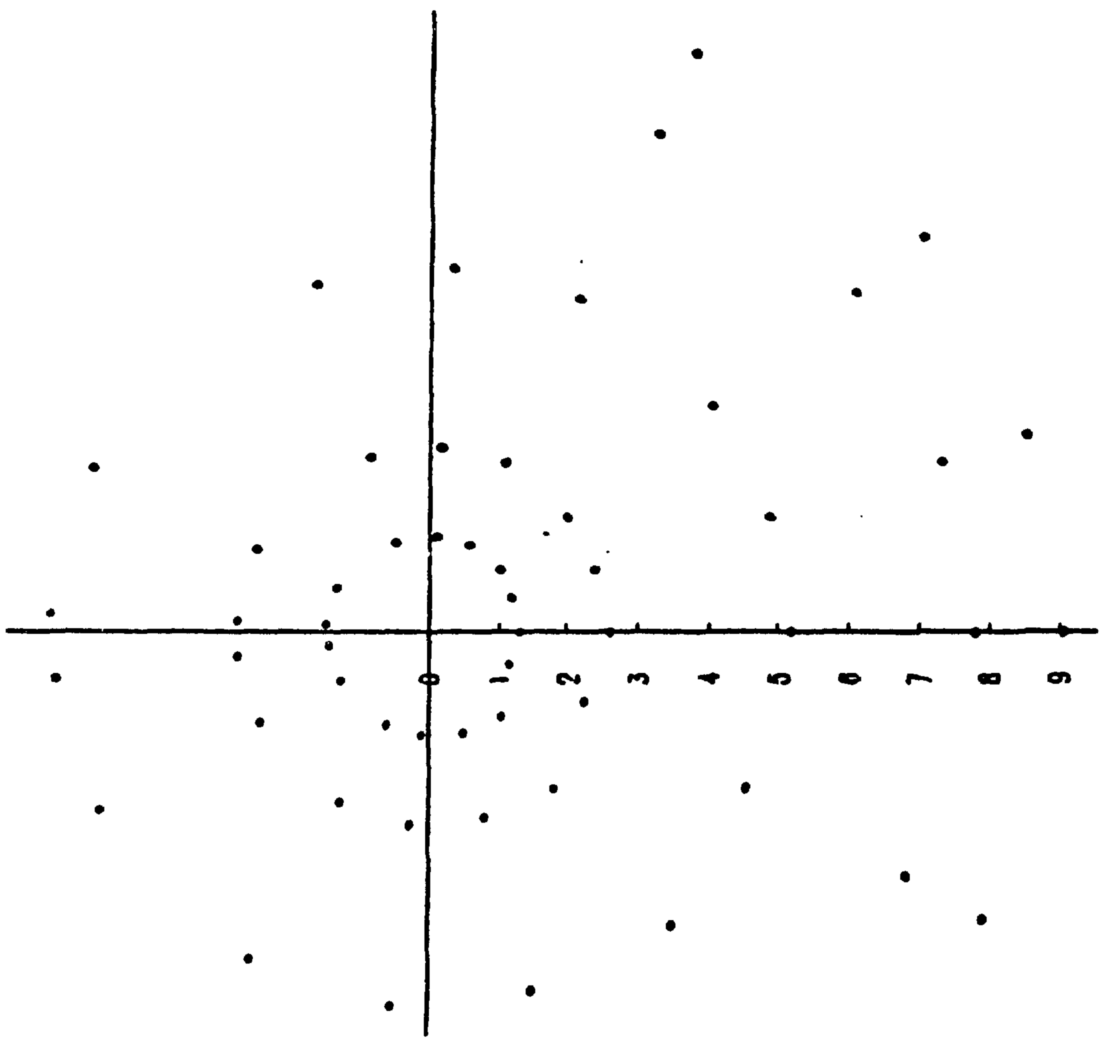

Figure 42. Internal probe data point locations. Hardcore risetime = 1.3 μsec, I_{HC} = 17 KA.

FLUX FUNCTIONS

$$\underline{B} \cdot \underline{\nabla} \psi = 0$$

$$\partial_r \psi = B_\theta + h r B_z$$

$$\partial_u \psi = -r B_r$$

WHERE

$$B_r = -b_1 I_1'(hr) \sin(u)$$

$$B_\theta = -\frac{b_1}{hr} I_1(hr) \cos(u) + \frac{\mu_0 I_{HC}}{2\pi r}$$

$$B_z = B_0 - b_1 I_1(hr) \cos(u)$$

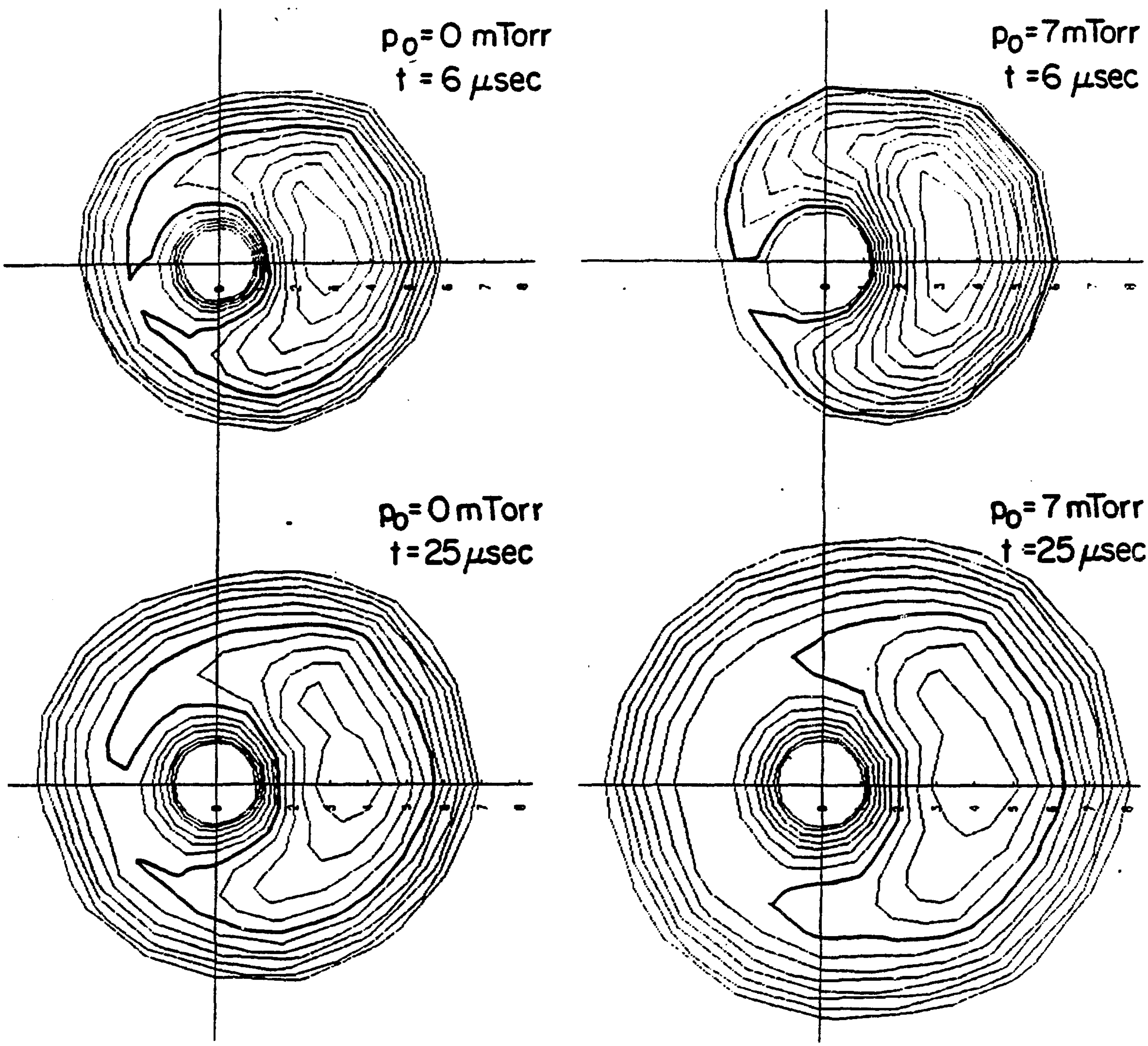

p_0= 0 mTorr
t = 6 μsec
p_0= 7 mTorr
t = 6 μsec
p_0= 0 mTorr
t = 25 μsec
p_0= 7 mTorr
t = 25 μsec

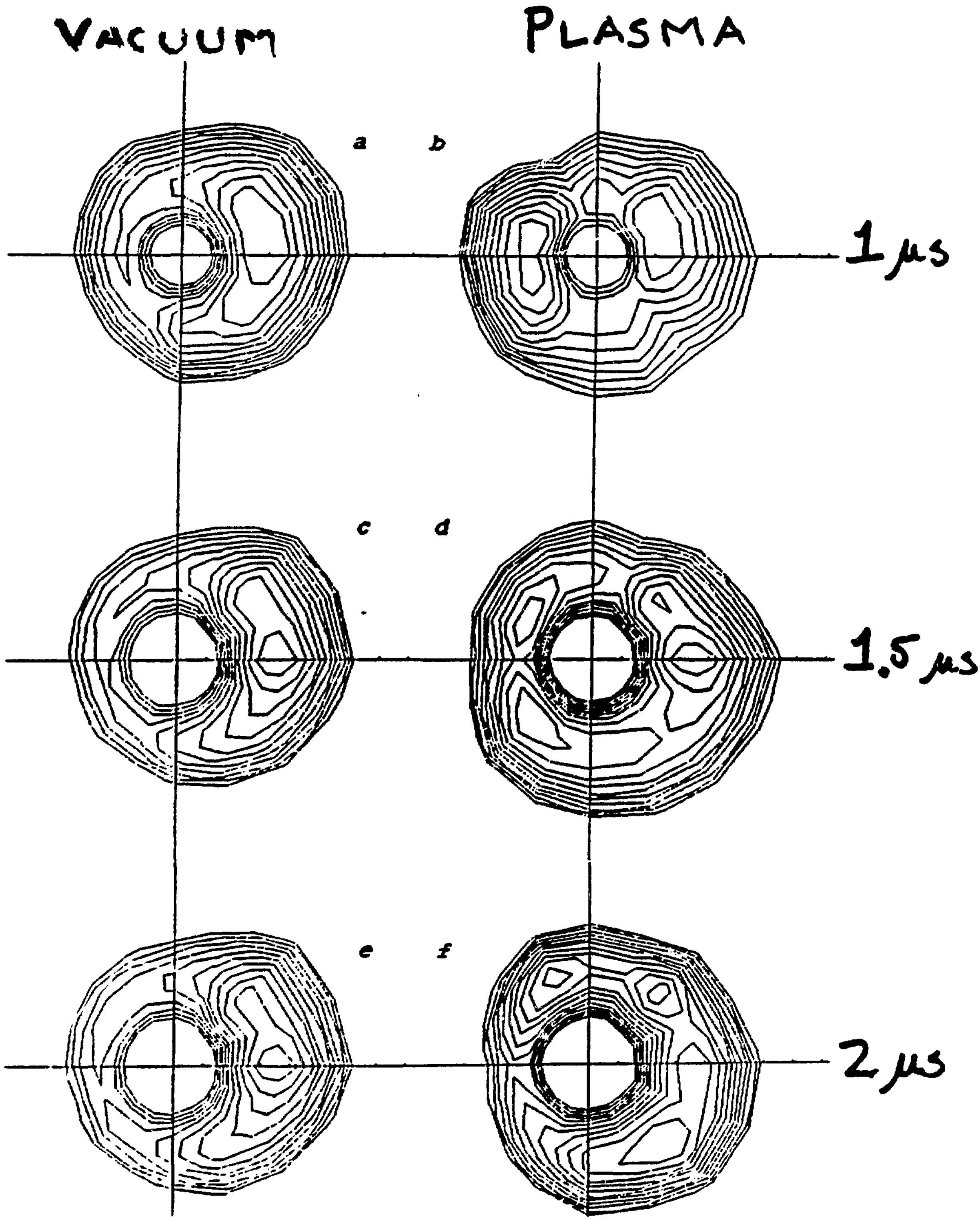

Figure 44. Flux contours. $\Delta\psi$ = 190 G-cm.
a. p_0=0 mtorr, 1.0 μsec; b. p_0=7 mtorr, 1.0 μsec;
c. p_0=0 mtorr, 1.5 μsec; d. p_0=7 mtorr, 1.5 μsec;
e. p_0=0 mtorr, 2.0 μsec; f. p_0=7 mtorr, 2.0 μsec.
Hardcore risetime = 1.3 μsec, I_{HC} = 17 KA.

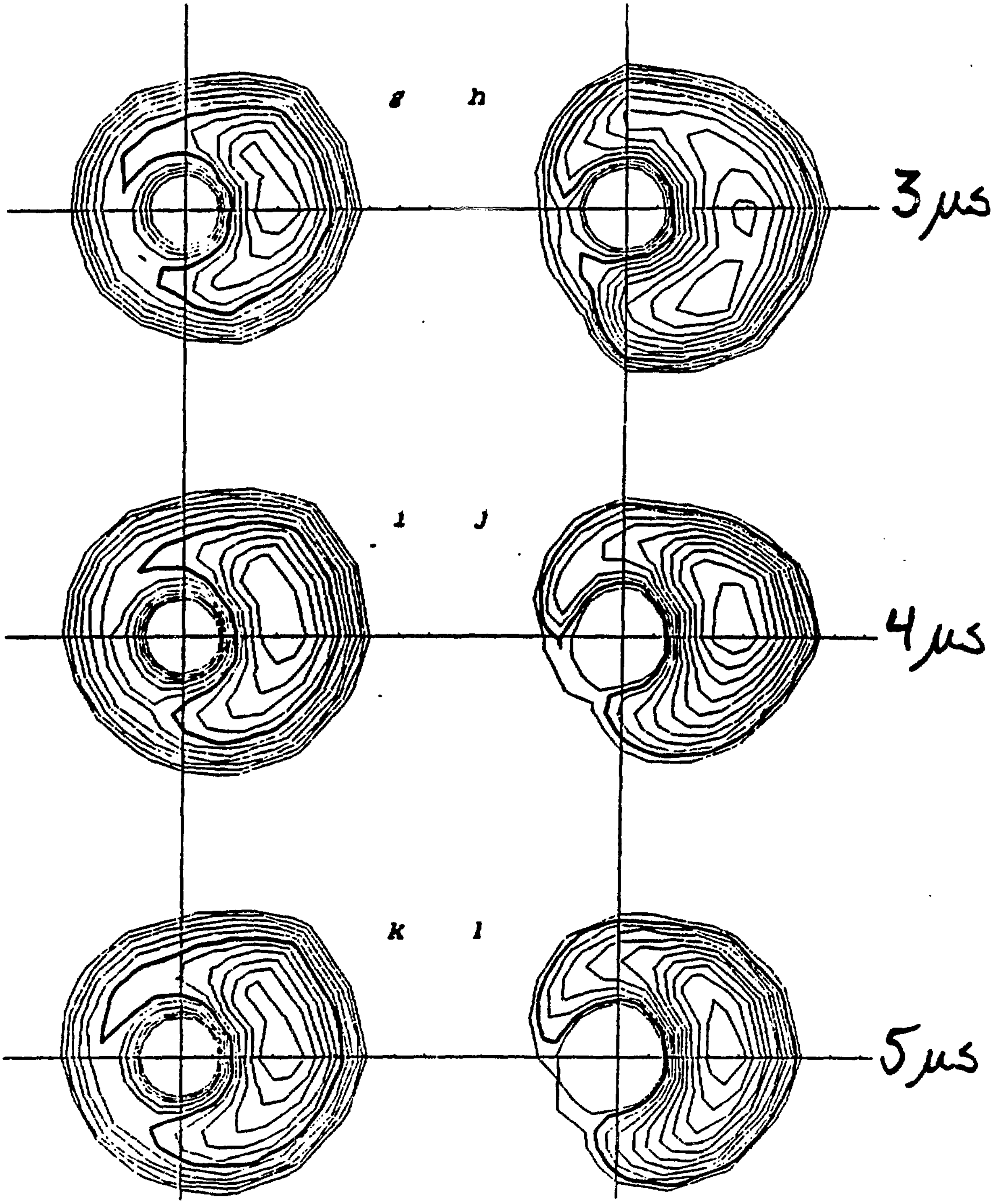

Figure 44. Flux contours. $\Delta\psi$ = 190 G-cm. g. p_0=0 mtorr, 3 μsec; h. p_0=7 mtorr, 3 μsec; i. p_0=0 mtorr, 4 μsec; j. p_0=7 mtorr, 4 μsec; k. p_0=0 mtorr, 5 μsec; l. p_0=7 mtorr, 5 μsec. Hardcore risetime = 1.3 μsec, I_{HC} = 17 KA.

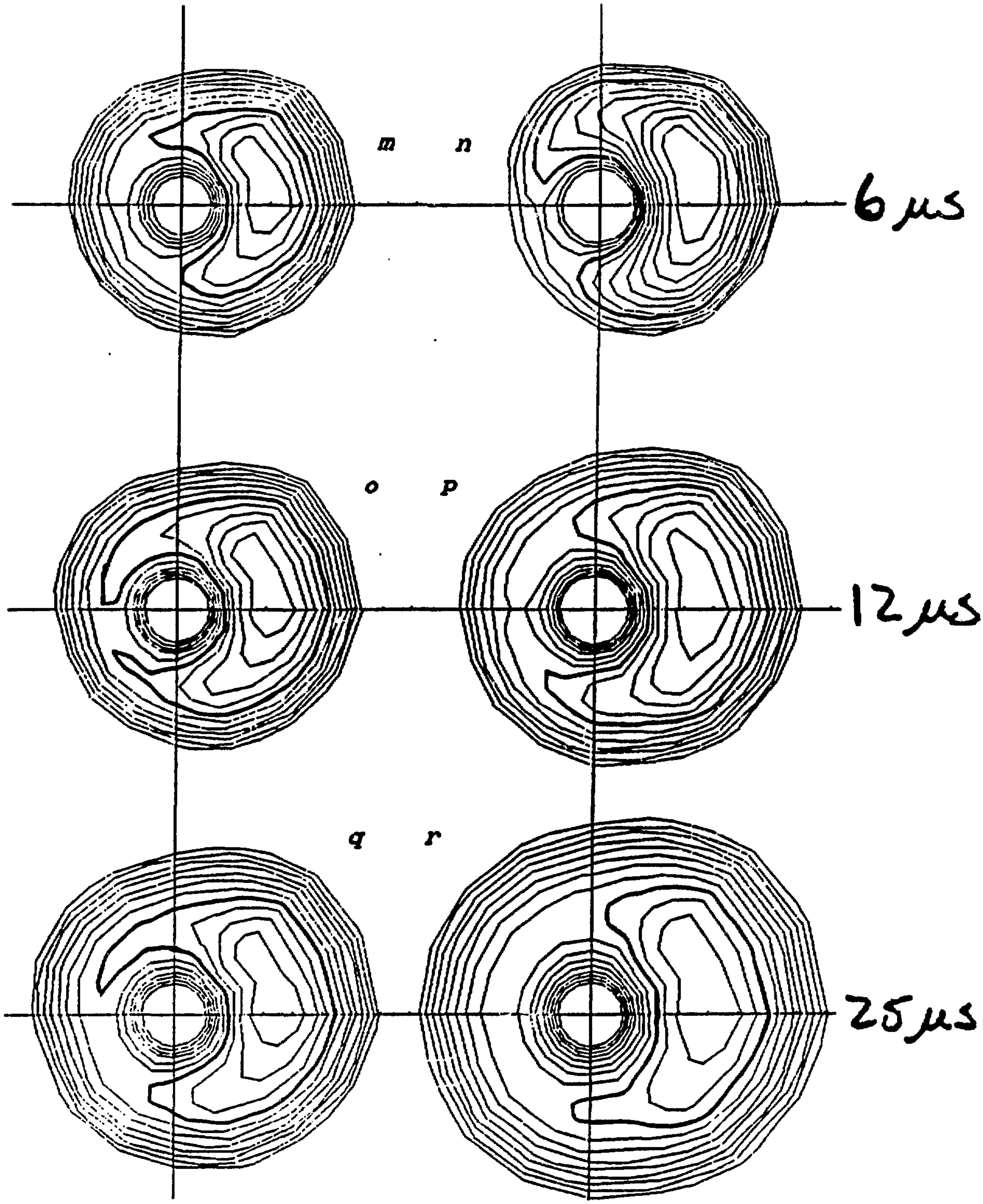

Figure 44. Flux contours. $\Delta\Psi$ = 190 G-cm.
m. p_0=0 mtorr, 6 μsec; n. p_0=7 mtorr, 6 μsec;
o. p_0=0 mtorr, 12 μsec; p. p_0=7 mtorr, 12 μsec;
q. p_0=0 mtorr, 25 μsec; r. p_0=7 mtorr, 25 μsec.
Hardcore risetime = 1.3 μsec, I_{HC} = 17 kA.

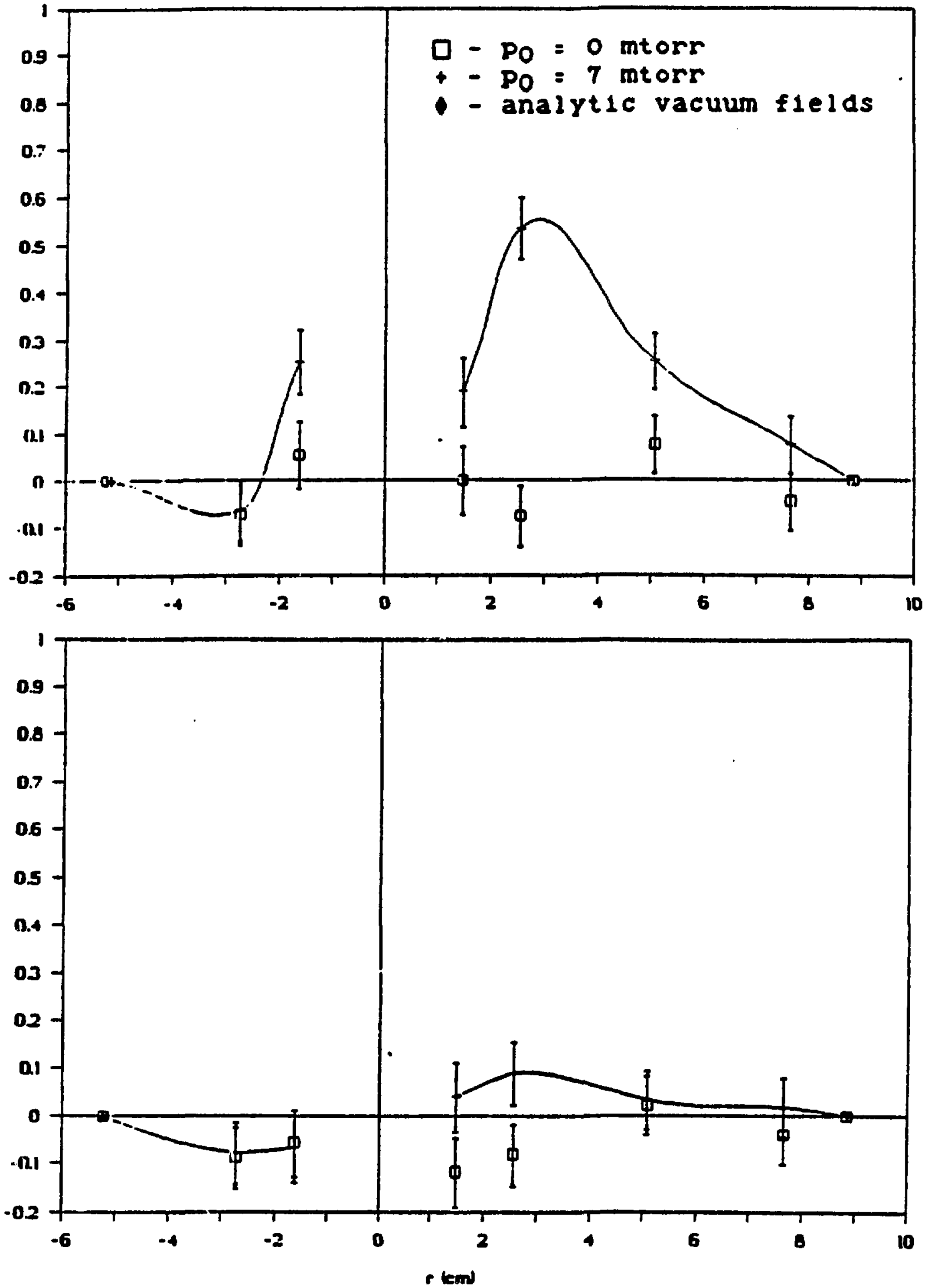
□ - p_0 = 0 mtorr
+ - p_0 = 7 mtorr
♦ - analytic vacuum fields
r (cm)

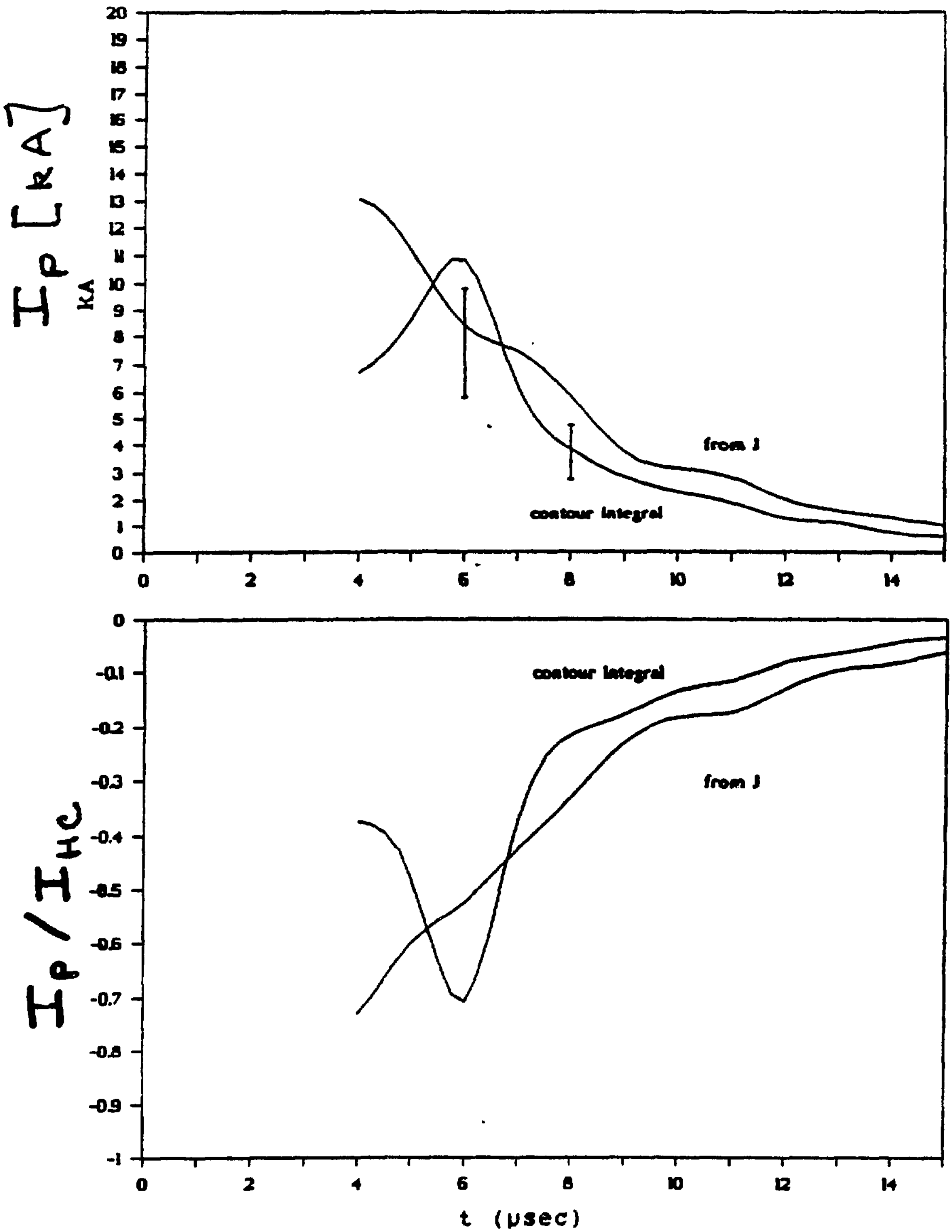

Figure 51. a. Total current flowing in heliac plasma vs. time; b. Total plasma current as a fraction of hardcore current. Hardcore risetime = 1.3 μsec, I_{HC} = 17 KA.

t (μs)

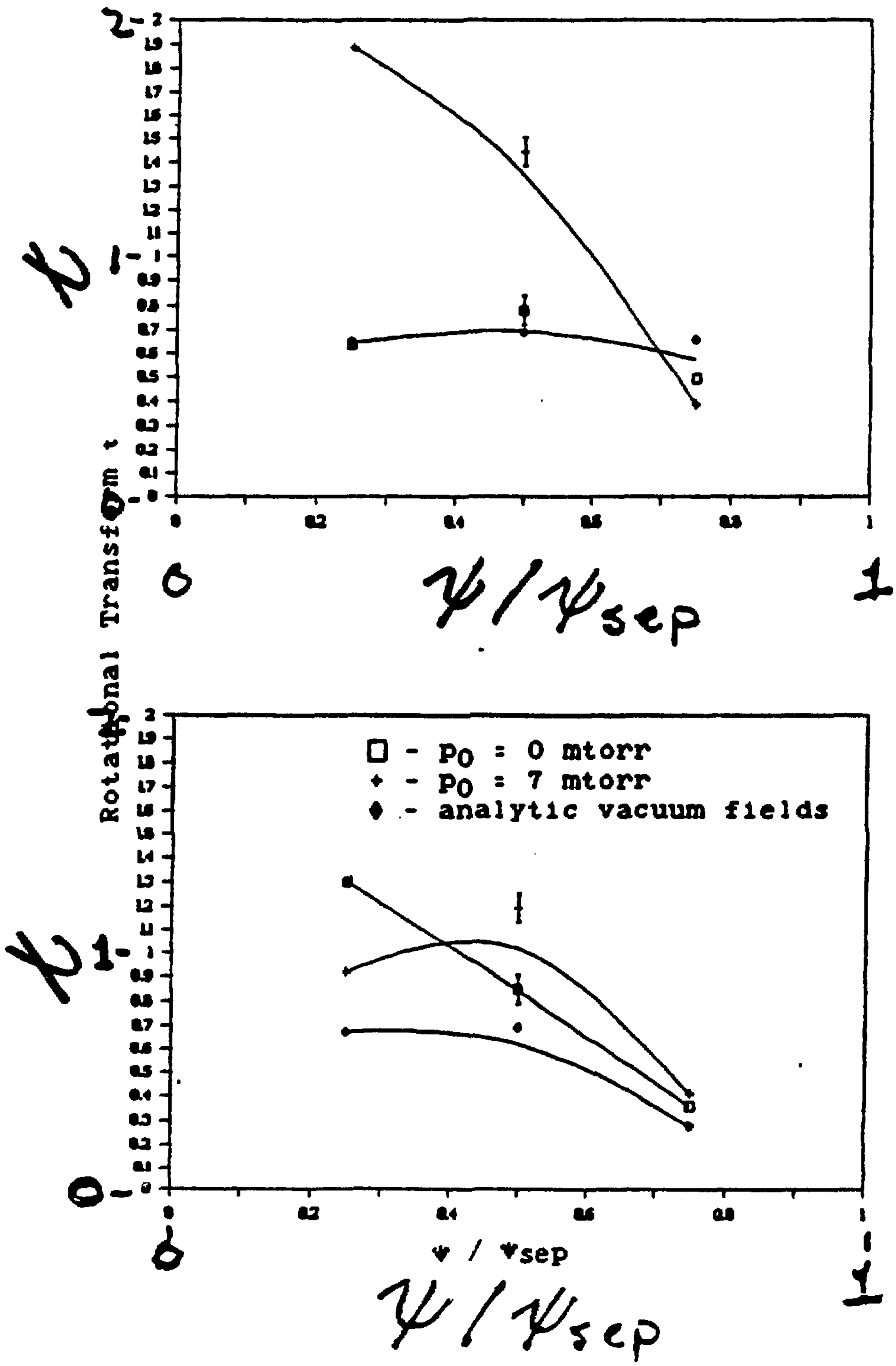

Figure 53. Rotational transform per period at a. 6 μsec and b. 12 μsec. Hardcore risetime = 1.3 μsec, I_{HC} = 17 KA.

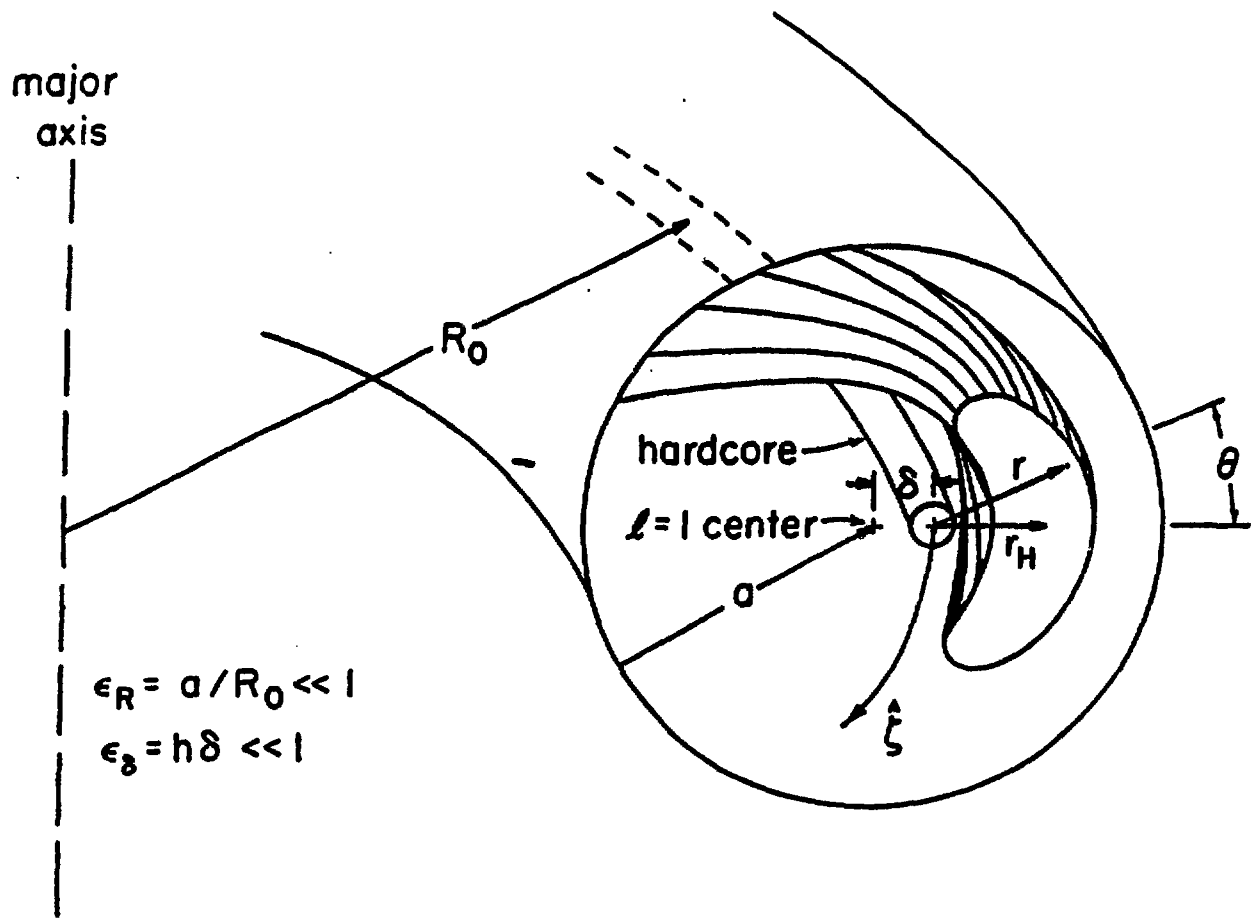

Fig. 7. Diagram of a shifted-hard-core, large-aspect-ratio heliac.

Scalar Magnetic Potential

$$\underline{B} = \nabla \Phi$$

$$\Phi_0 = B_0 z - \frac{1}{h} b_1 I_1(hr) \sin(u) + \frac{\mu_0 I_{HC} \theta}{2\pi}$$

$$\Phi = \Phi_0 + \varepsilon_T \Phi_T + \varepsilon_S \Phi_S$$

Toroidal Correction (Ra ≫ 1)

$$\Phi_T = \frac{b_1}{4} \left\{ \left[\left. \frac{I_1 + hr I_2}{I_0} \right|_{r=r_W} I_0 - \frac{r}{r_W} (I_1 + hr I_2) \right] \cos(hz) \right.$$

$$+ \left[\left. \frac{I_1 + hr I_0}{I_2} \right|_{r=r_W} I_2 - \frac{r}{r_W} (I_1 + hr I_0) \right] \cos(2\theta + hz)$$

$$+ \frac{I_z}{2} \left[r \log(r/r_{HC}) - r \right] \sin(\theta)$$

Shift Correction

$$\Phi_S = \frac{b_1}{2} \left[I_0 \cos(hz) + I_2 \cos(2\theta + hz) \right]$$

MAGNETIC FIELD SPECTRA

- BOOZER $1/B^2$ HARMONICS

$$a_{mn} \cos(m\theta - n\phi)$$ ← ¡NOTE NOTATION!

(1,1), (2,2) . . . STRAIGHT HELIAC

(1,0) TOROIDAL / δ SHIFT

(0,1) BUMPY

- EQUIVALENCE OF δ AND R

$$\delta R = 371 \text{ cm}^2$$

$$\delta = 2.5 \text{ cm} \Rightarrow R = 148 \text{ cm}$$

$$R/a \gtrsim 14$$

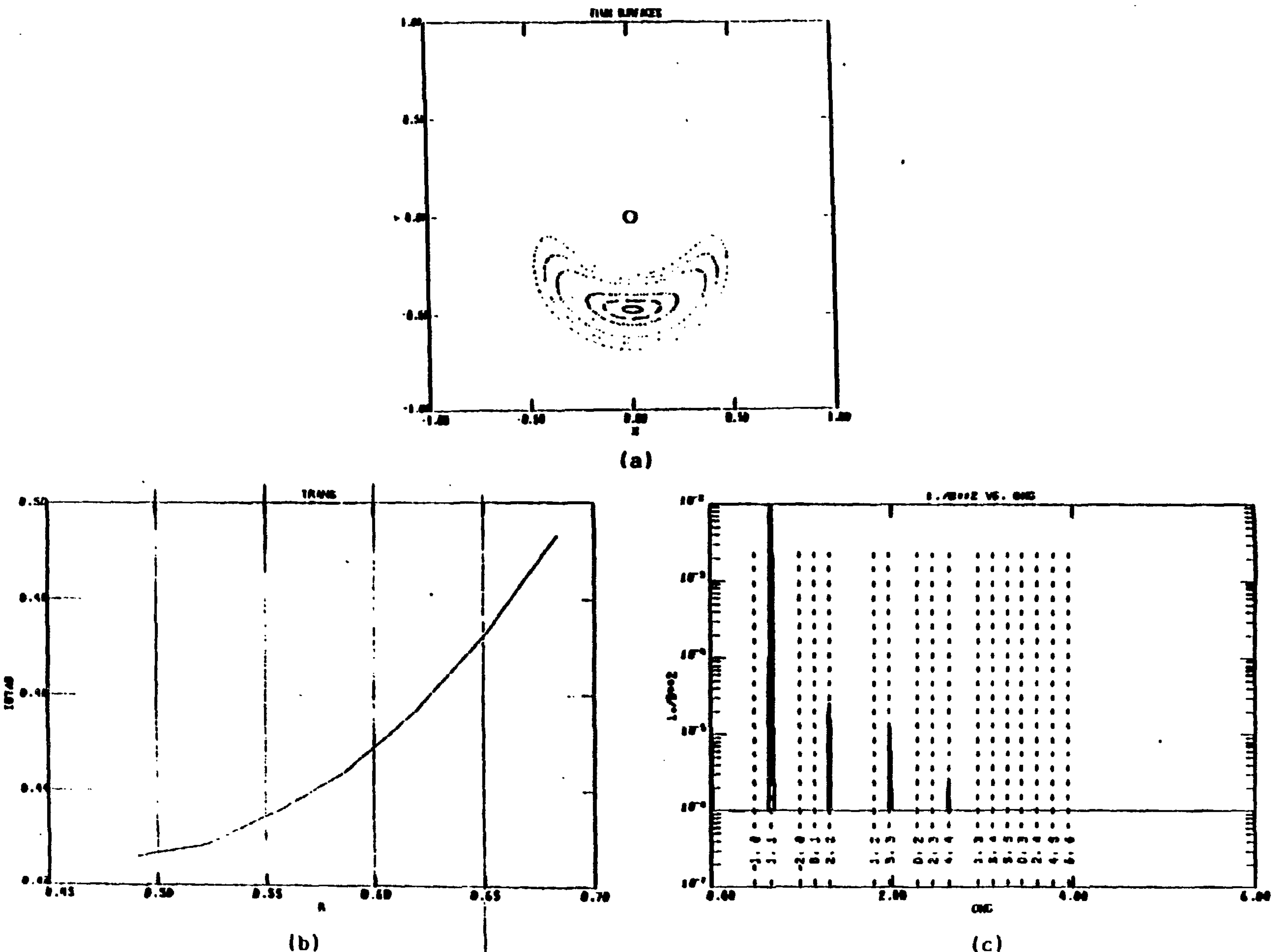

Figure 3. (a) Flux surfaces for the baseline HBQM; (b) Rotational transform versus radius for the baseline HBQM; (c) Spectrum of $1/B^2$ for the baseline HBQM.

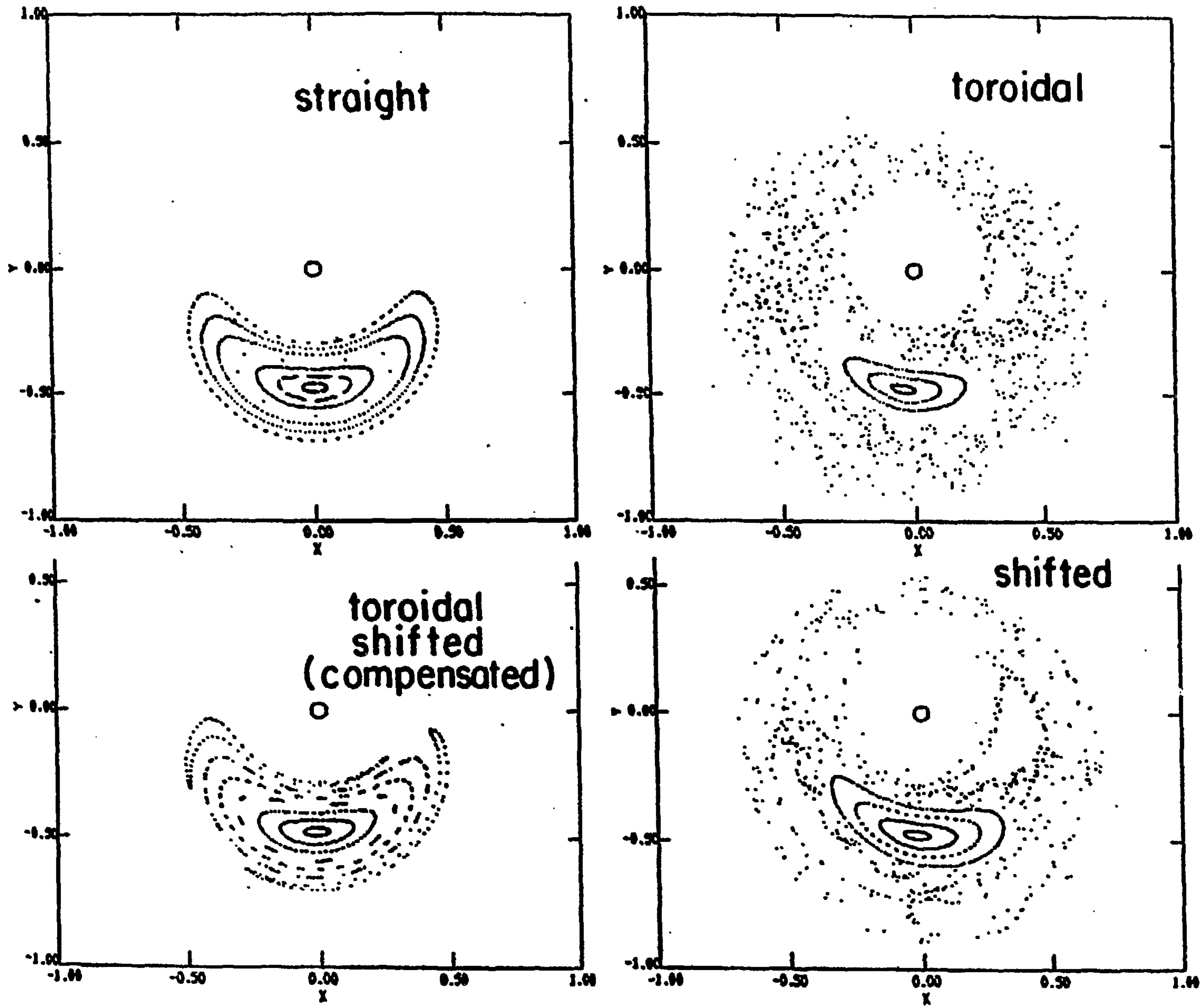
straight
toroidal
toroidal
shifted
(compensated)
shifted
X
-1.00
-0.50
0.00
0.50
1.00

Fig. 6

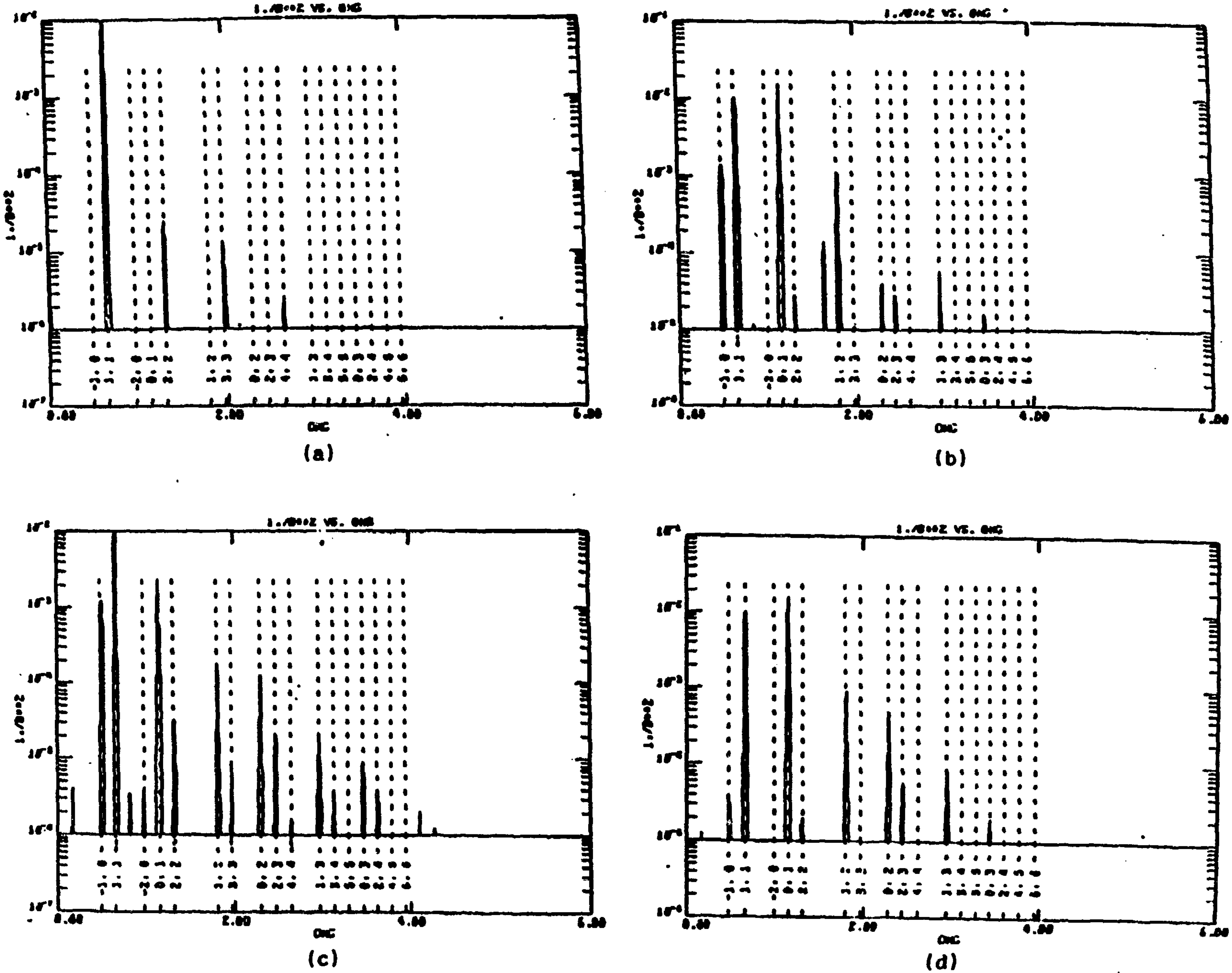

Fig. 9. Comparison of Reiman-Boozer spectra for (a) straight baseline heliac case, (b) shifted hardcore, (c) toroidal, and (d) compensated shift-toroidal cases of Fig. 8.

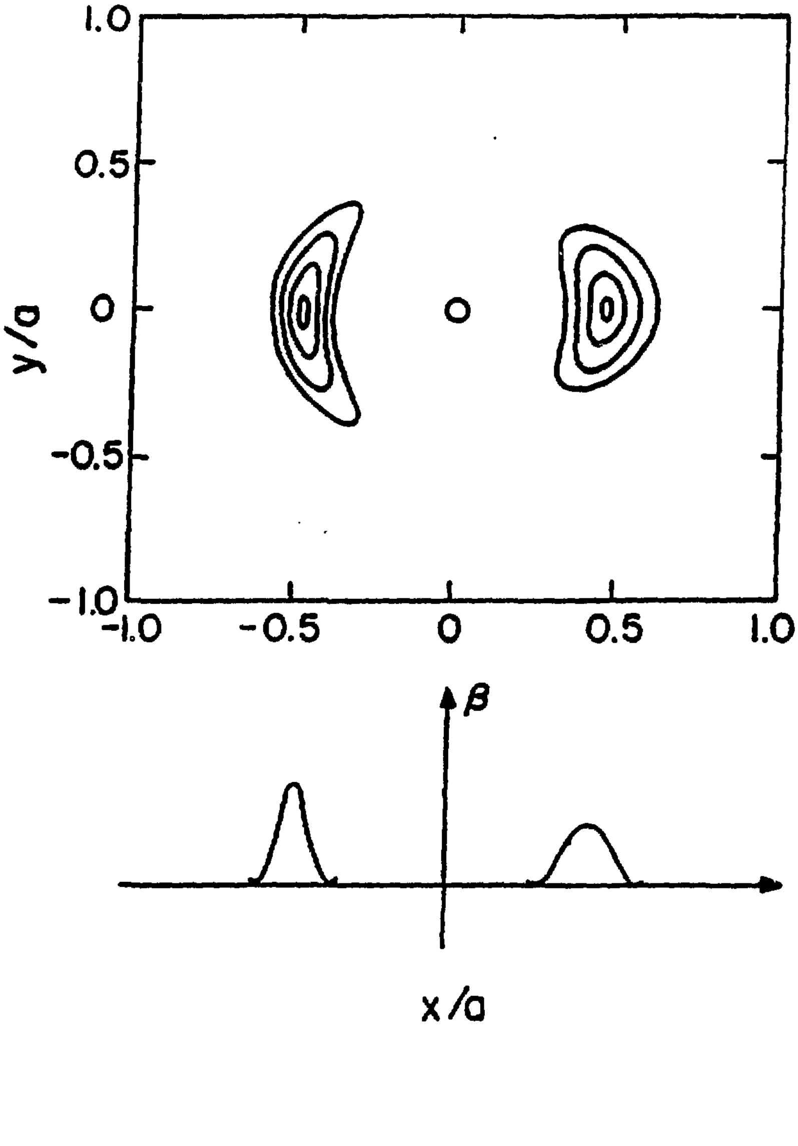

Fig. 13. Heliac shifted-hardcore flux-surfaces cross sections, one-half helical period apart with associated pressure profiles.

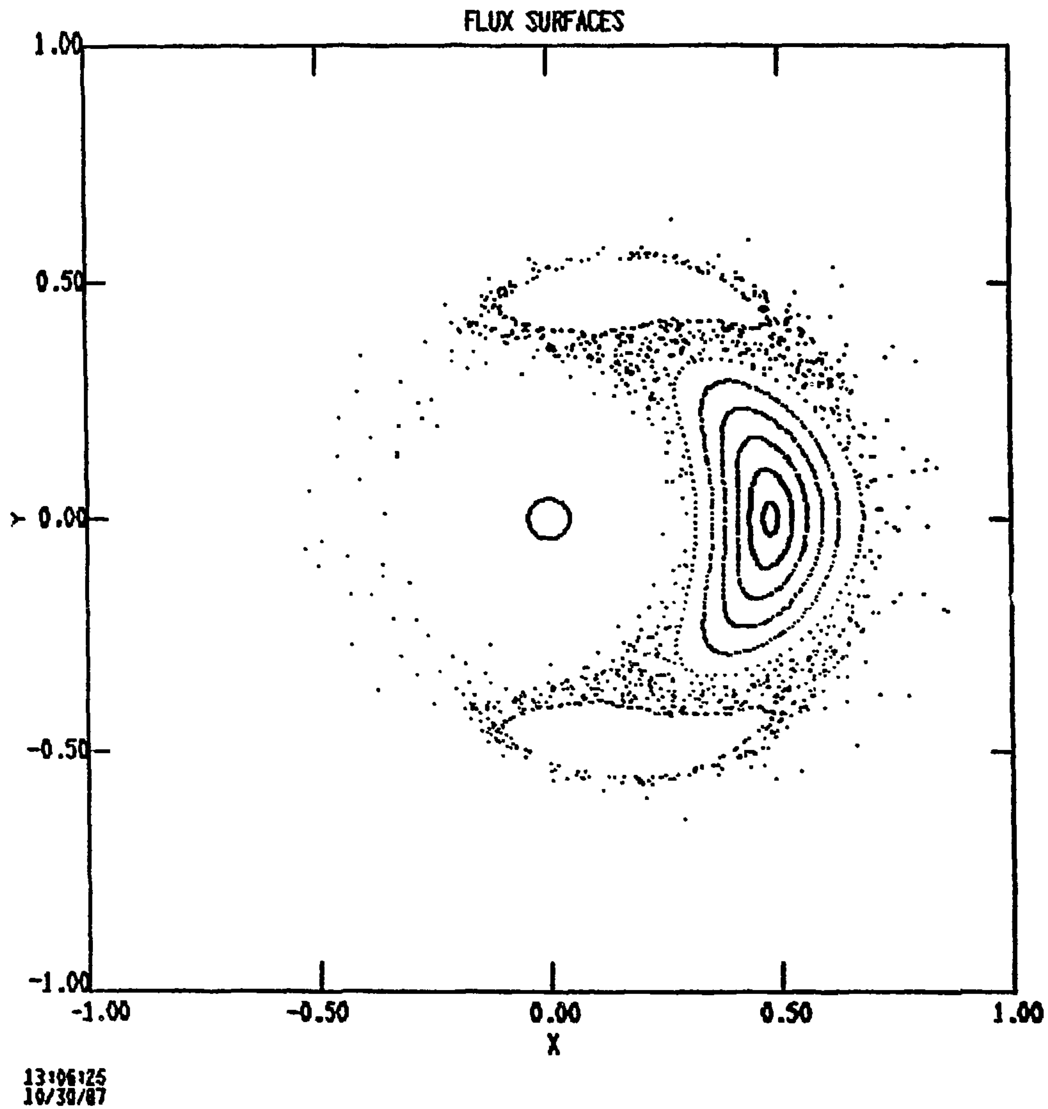
FLUX SURFACES
1.00
0.50
Y 0.00
-0.50
-1.00
-1.00
-0.50
0.00
0.50
1.00
X
13:06:25
10/30/87

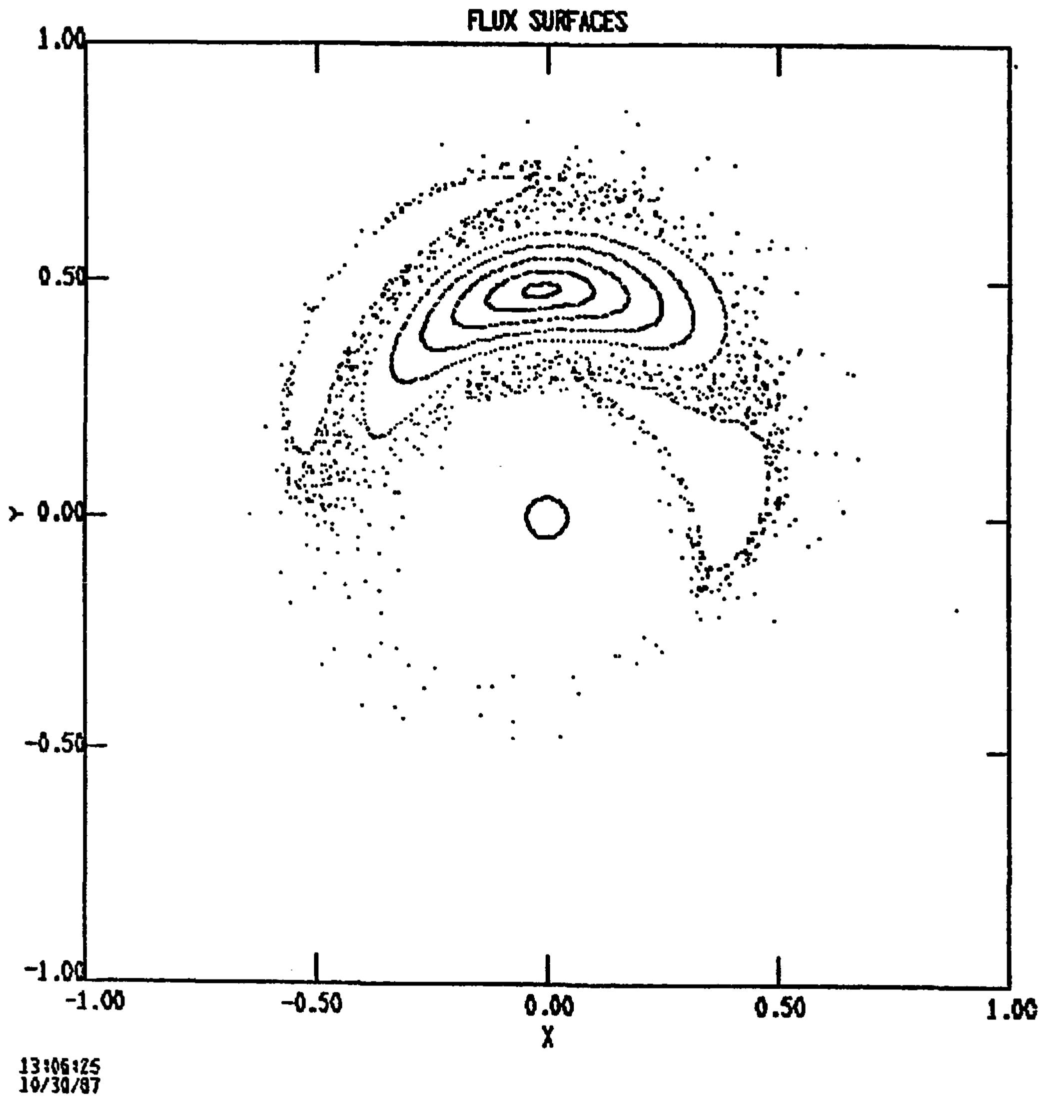
FLUX SURFACES
1.00
0.50
Y 0.00
-0.50
-1.00
-1.00
-0.50
0.00
0.50
1.00
X
13:06:25
10/30/87

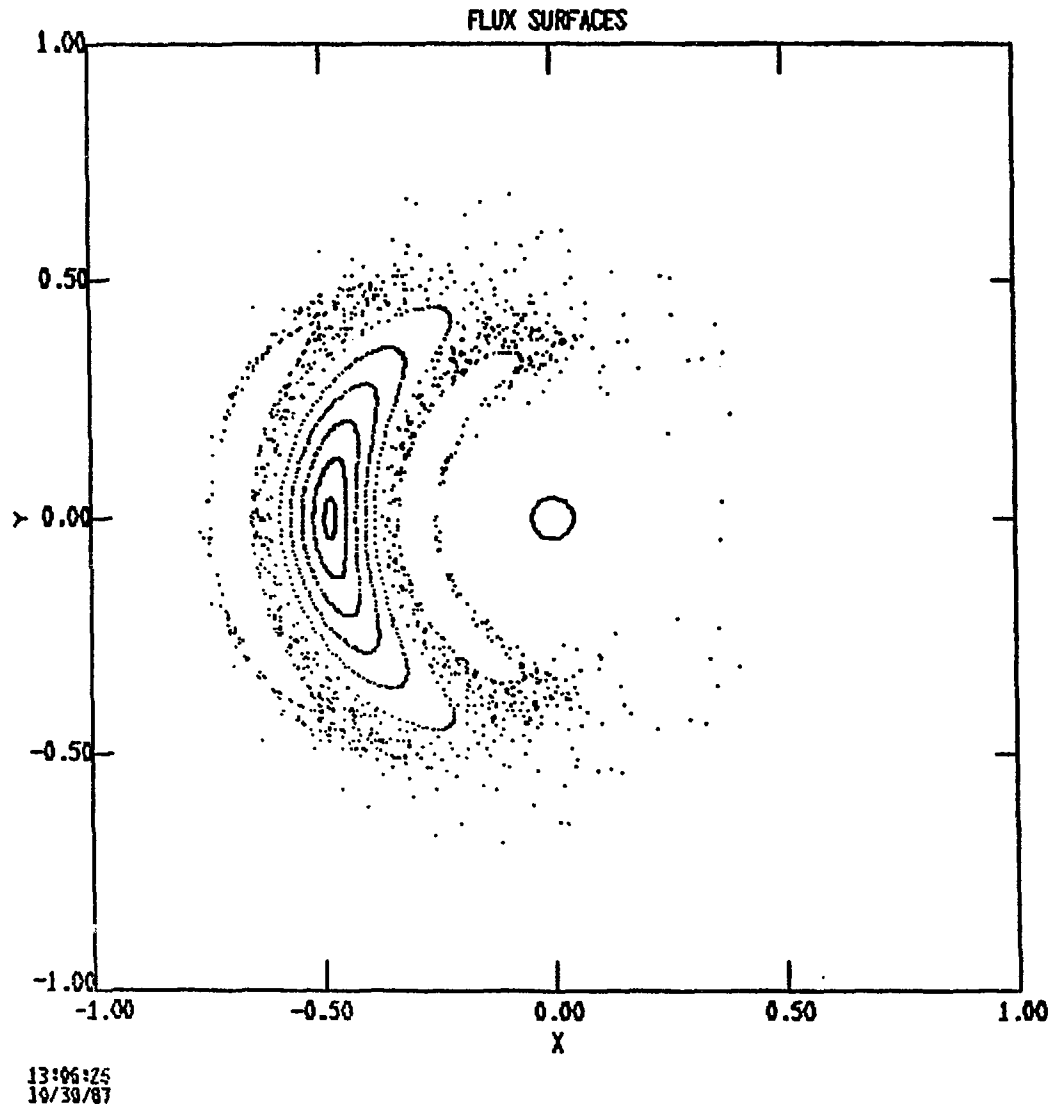
FLUX SURFACES
1.00
0.50
Y 0.00
-0.50
-1.00
-1.00
-0.50
0.00
0.50
1.00
X
13:06:25
10/30/87

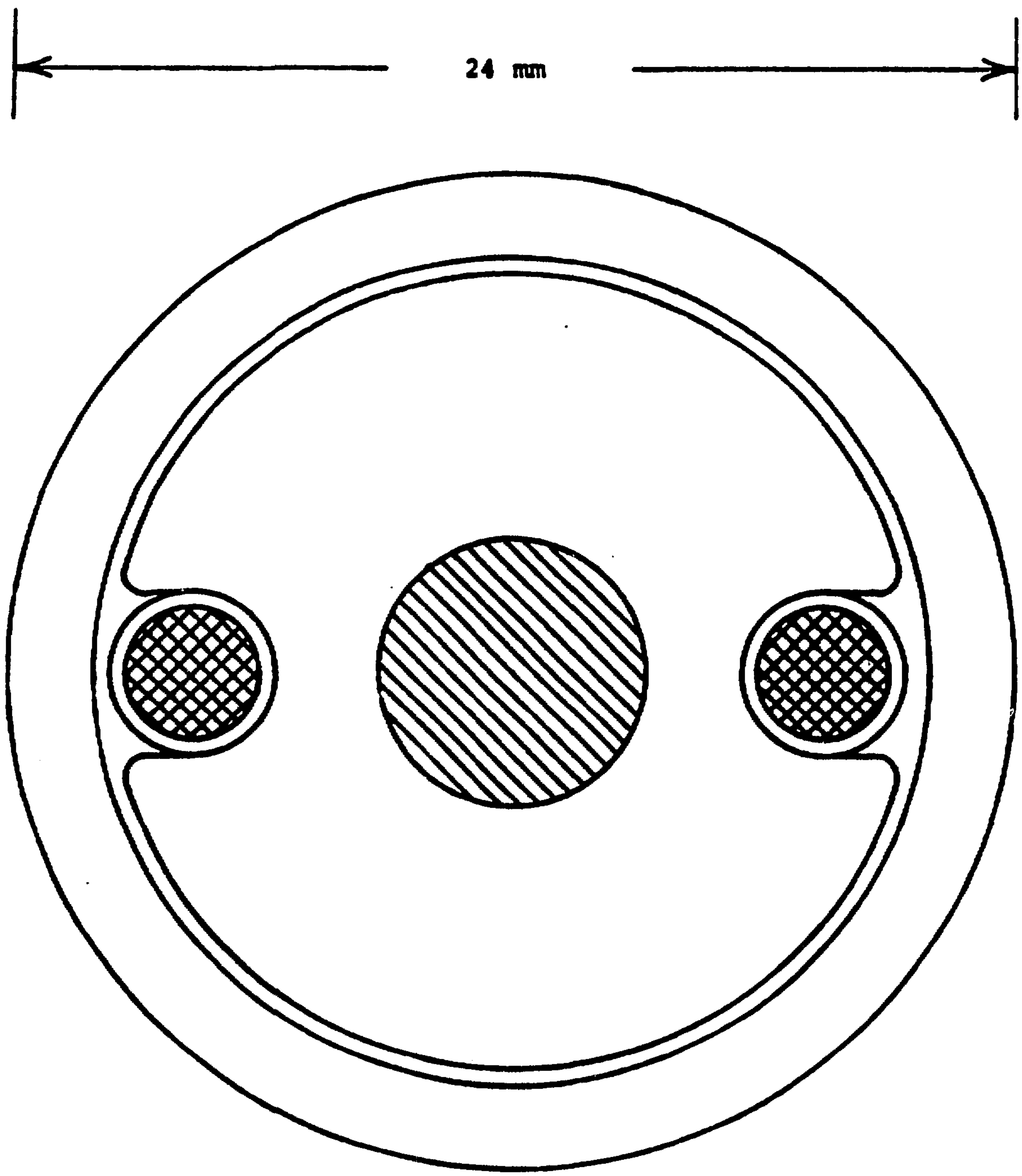
24 mm

40

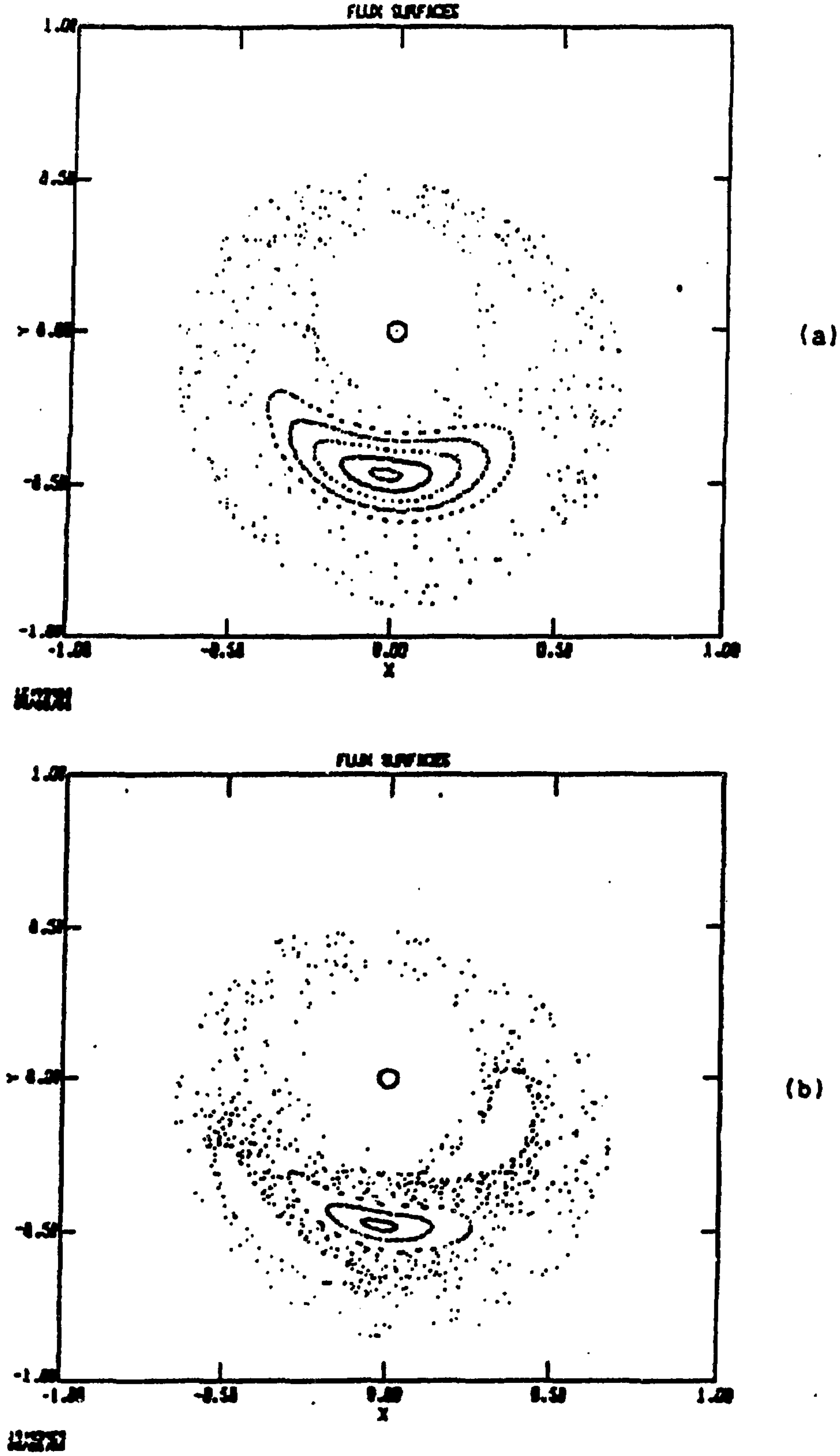

Fig. 11. Heliac flux surfaces for 1.25-cm hardcore shift combined with (a) HHC = -0.04 and (b) HHC = +0.04.

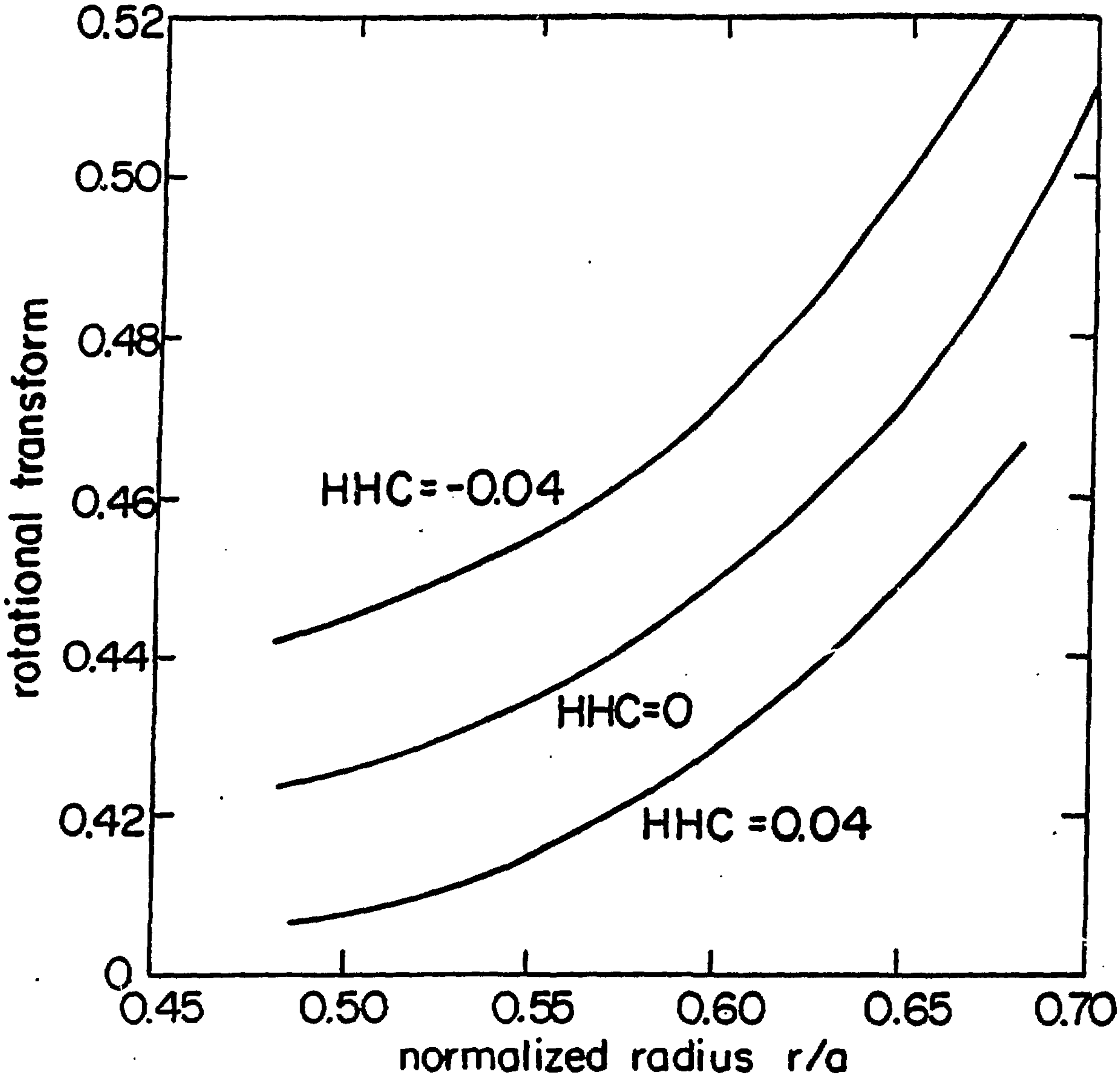

Fig. 10. Rotational transform versus radius for (a) HBQM straight heliac, (b) straight heliac with helical hardcore parameter HHC = -0.04, and (c) HHC = + 0.04.

Configuration Studies

K. Nishimura and M. Fujiwara
Institute of Plasma Physics, Nagoya University, Nagoya 464, Japan

There are many difficulties to design a helical system. Magnetic characteristics which are needed in each experimental item are different. In a low beta experiment, the configuration which can obtain a good particle and energy confinements is needed. In a high beta experiment, magnetic well configuration is needed to ensure the stability. In a divertor experiment, clean scrape-off layer and a long pulse system are needed for impurity control.

Large aspect ratio system is desirable for a good helical symmetry, particle confinement and a control of the neo-classical diffusion. But it has following defects. As the stability is depend on a magnetic shear, the average beta $\langle\beta\rangle$ is restricted to 1~2 %. And a device size becomes large and, as a result, its cost also becomes large. Low aspect ratio is desirable for the high beta and compactness of the device. But its defects are as follows. Particle confinement and transport become worse. Divertor layer ergodizes and an outermost surface approaches the wall of the vacuum chamber for the torus effect. Helical axis is desirable for the high beta plasma in theory. But it has few experimental data base.

To obtain a good confinement in a low aspect ratio system, we modulated a helical coil width. As a result, the current density in an inner region of the torus became large and the clearance between the outermost surface and the chamber's wall was improved and the symmetry of the magnetic surfaces was improved.

Configuration Studies

Institute of Plasma Physics, Nagoya Univ., Japan

K. Nishimura and M. Fujiwara

<< Problems >>

(1) Large aspect ratio is desirable for good helical symmetry, particle confinement and the control of the neo-classical diffusion. But it has following defects.

* As the stability is depend on the magnetic shear, the average beta $\langle\beta\rangle$ is restricted to 1-2 %.
* A device size becomes large and, as a result, its cost also becomes large.

(2) Low aspect ratio is desirable for the high beta, compactness of the device and good accessibility. But its defects are as follows.

* Particle confinement and transport become worse.
* Divertor layer ergodizes.
* Outer most surface approaches the wall of the vacuum chamber for the torus effect.

<< Coil width modulation >>

- standard coil width C_{w0} = 80 cm

  height C_{h0} = 45 cm

- modulation law

$$Ch = C_{h0}$$

$$Cw = C_{w0}(1 + \varepsilon_{wm} * \cos(m\psi))$$

ε_{wm} : width modulation rate

m : toroidal periodicity

ψ : toroidal angle

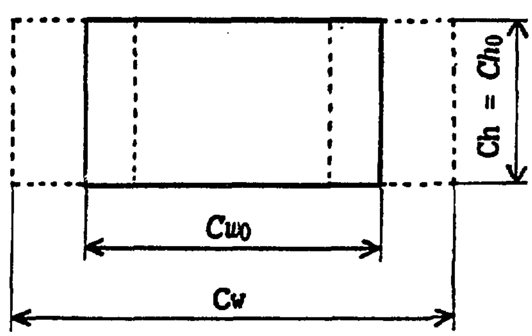

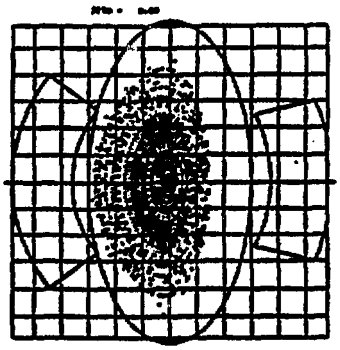

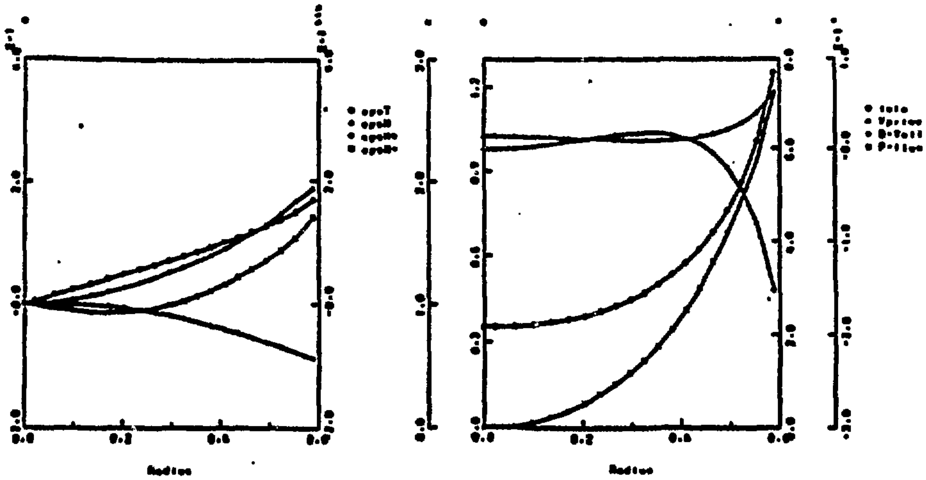

m=10, v.m.=0.0, A_p=7

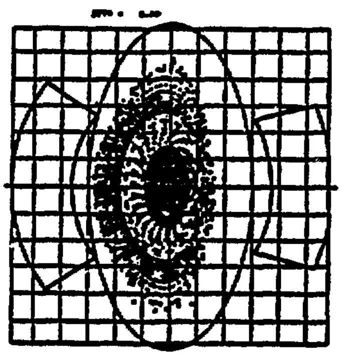

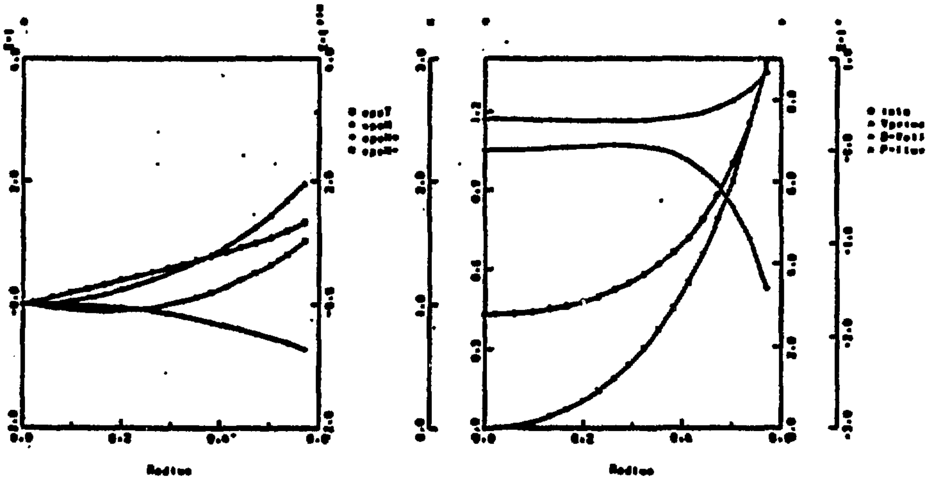

m=12, v.m.=0.0, A_p=8

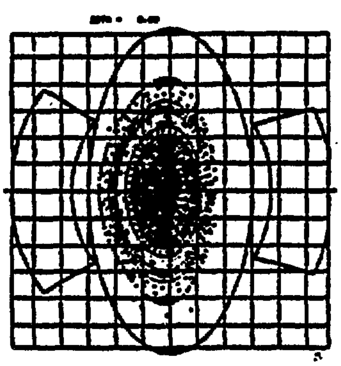

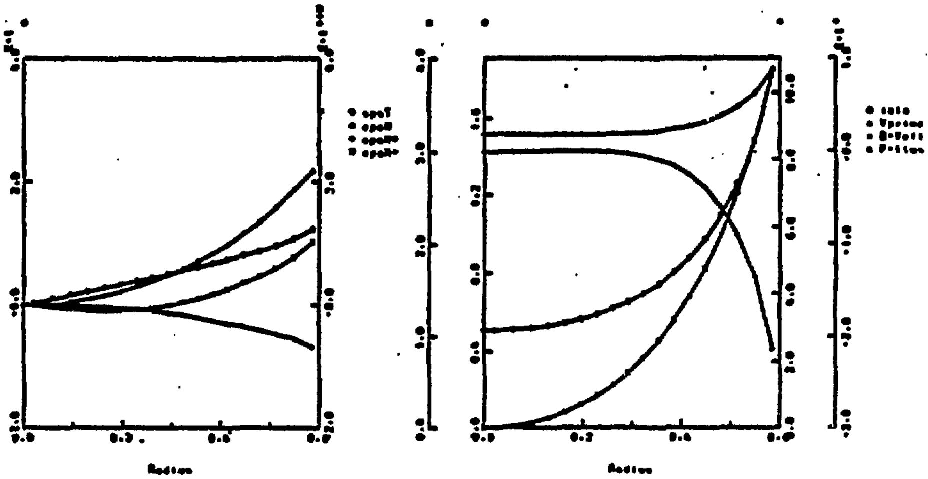

m=14, v.m.=0.0, A_p=9

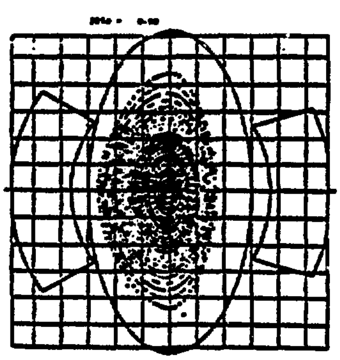

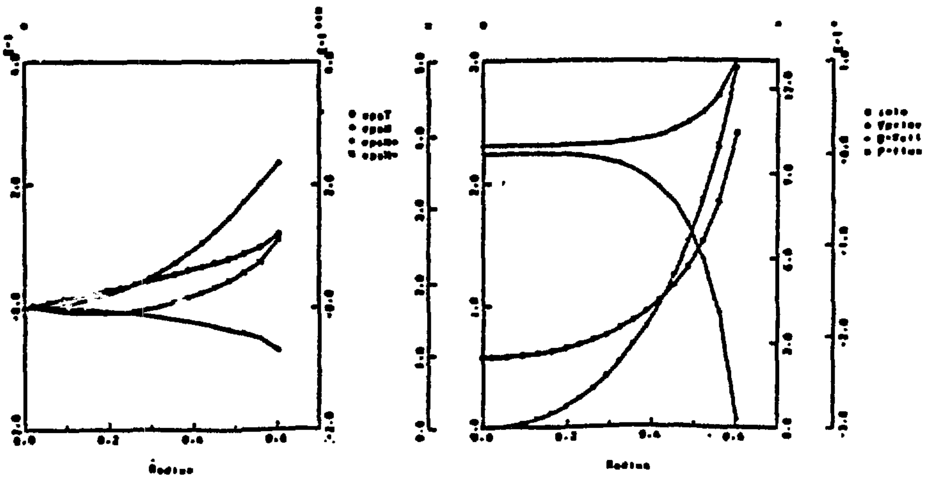

m=16, v.m.=0.0, A_p=11

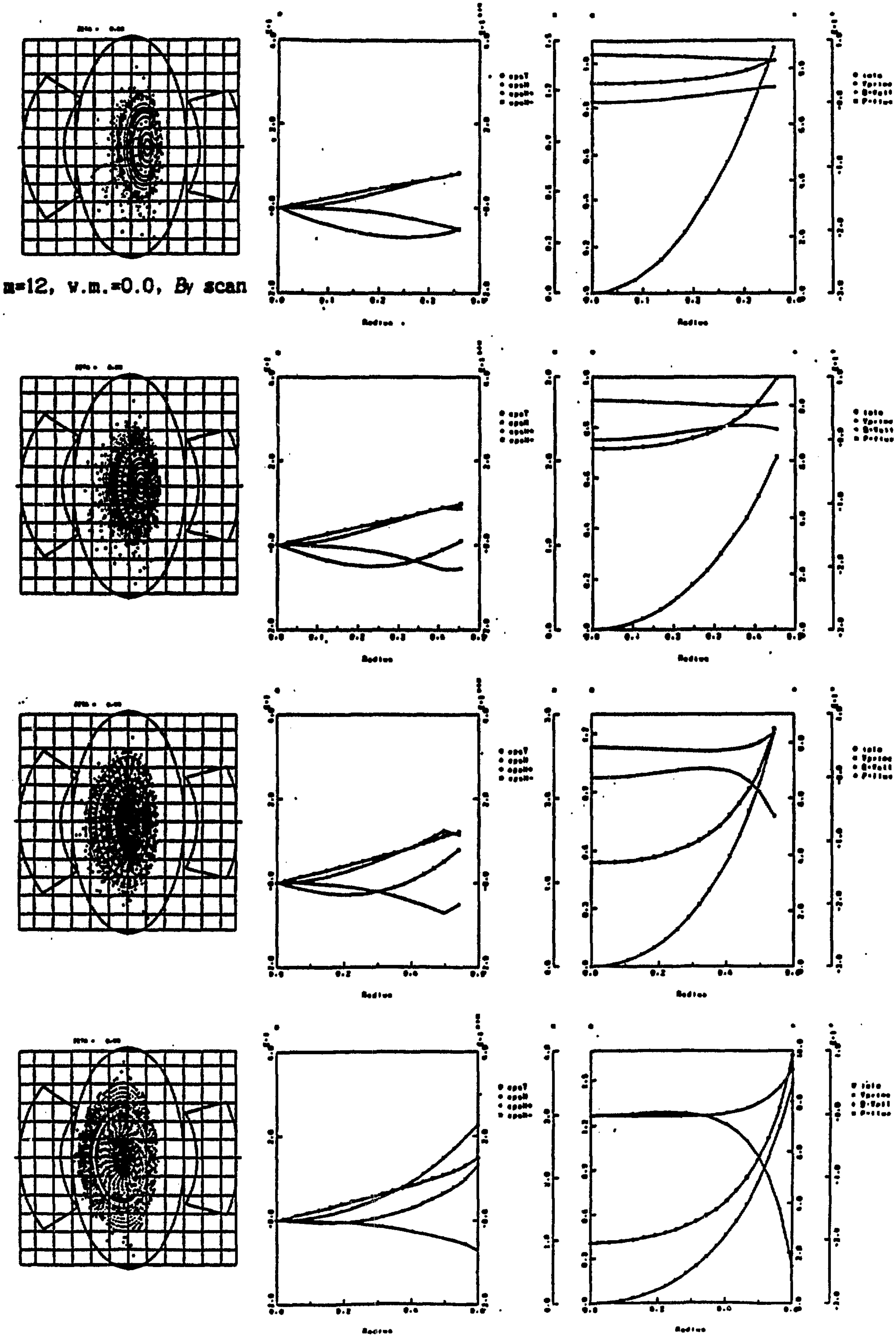
m=12, v.m.=0.0, By scan
Radius

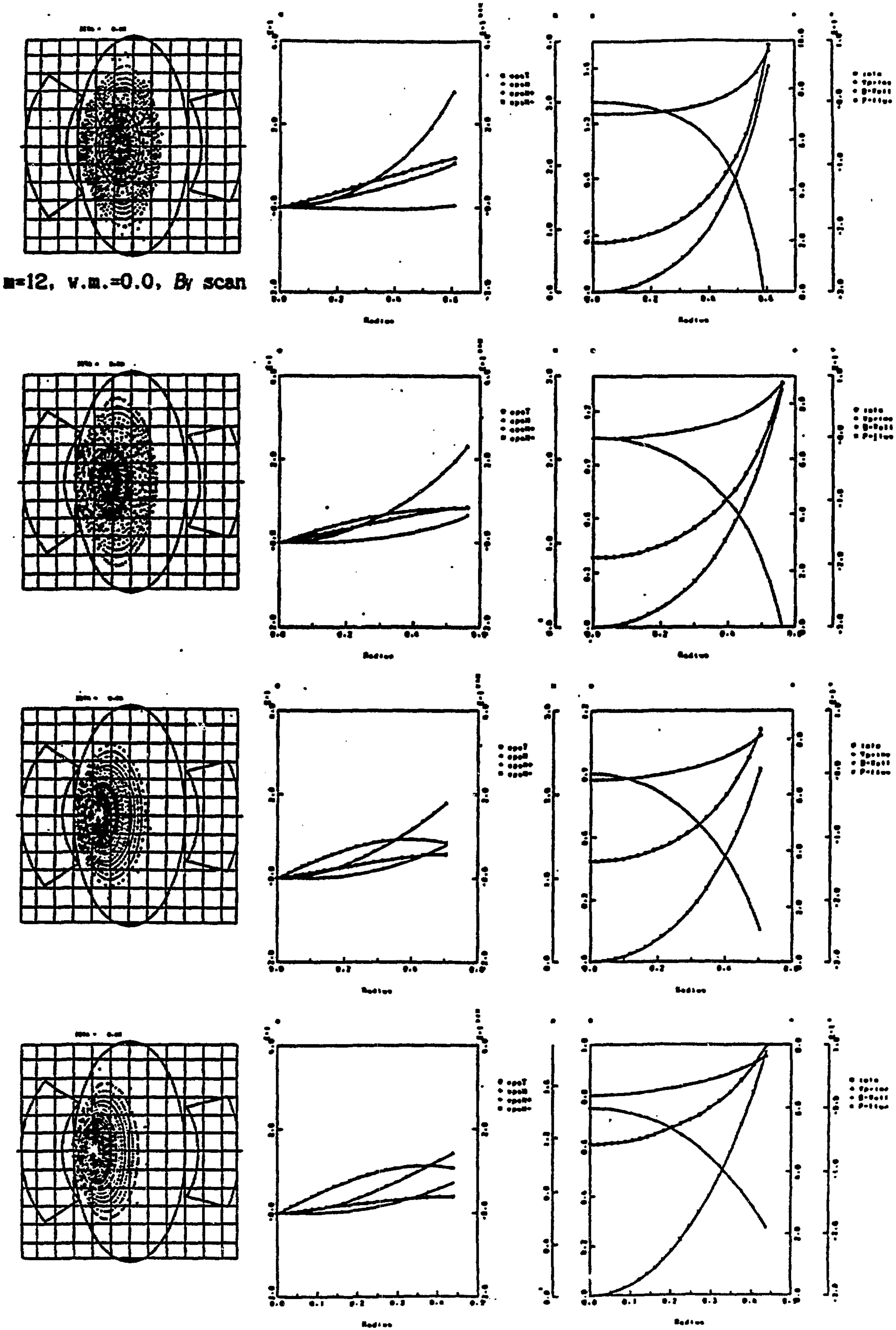

m=12, v.m.=0.0, B_l scan

m=10, R=4m, α_c=0.96m

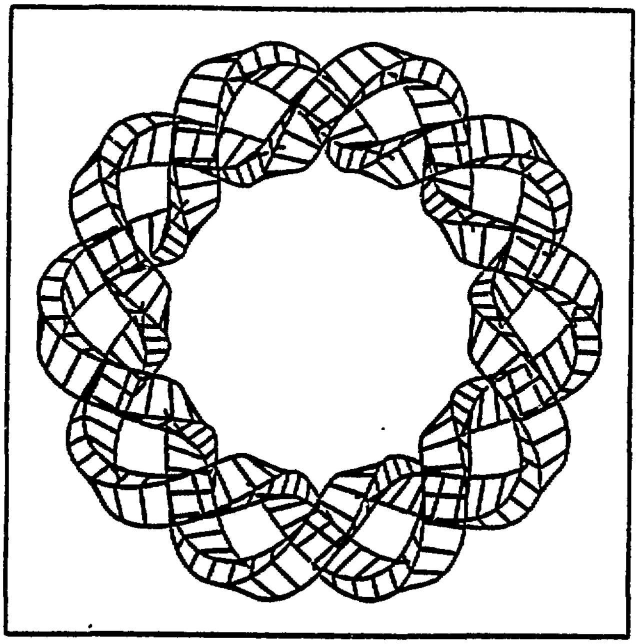

v.m.=0.0

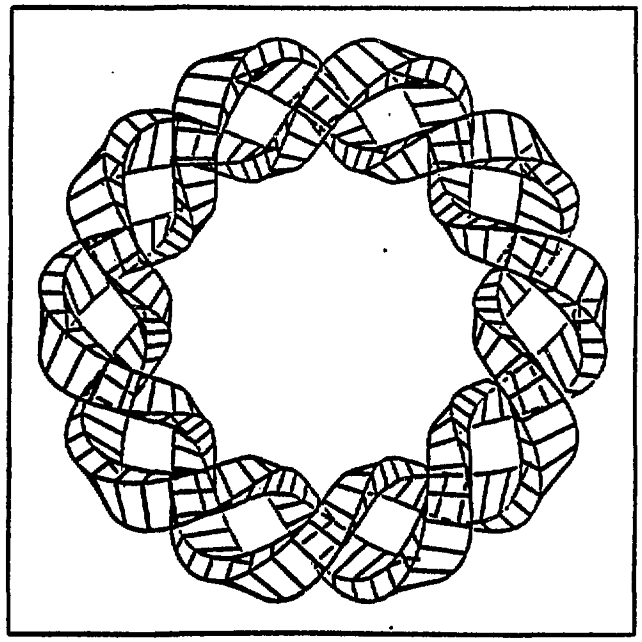

v.m.=0.3

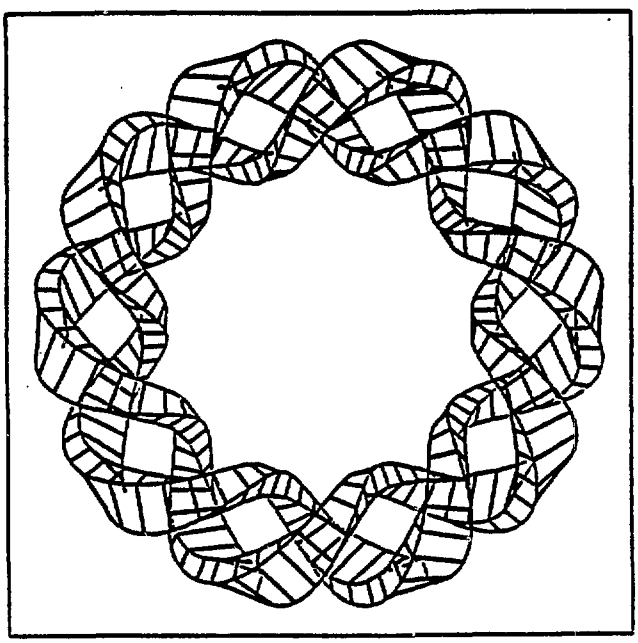

v.m.=0.5

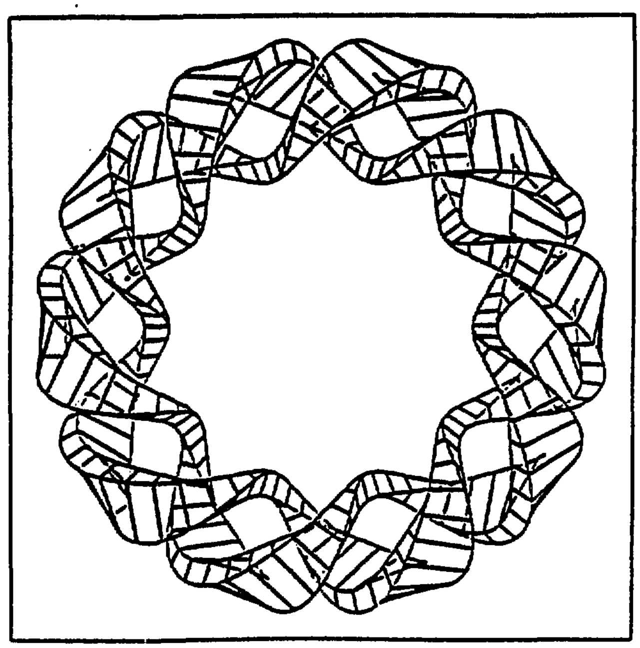

v.m.=0.9

EFFECT OF WIDTH MODURATION $\ell=2/m=10$

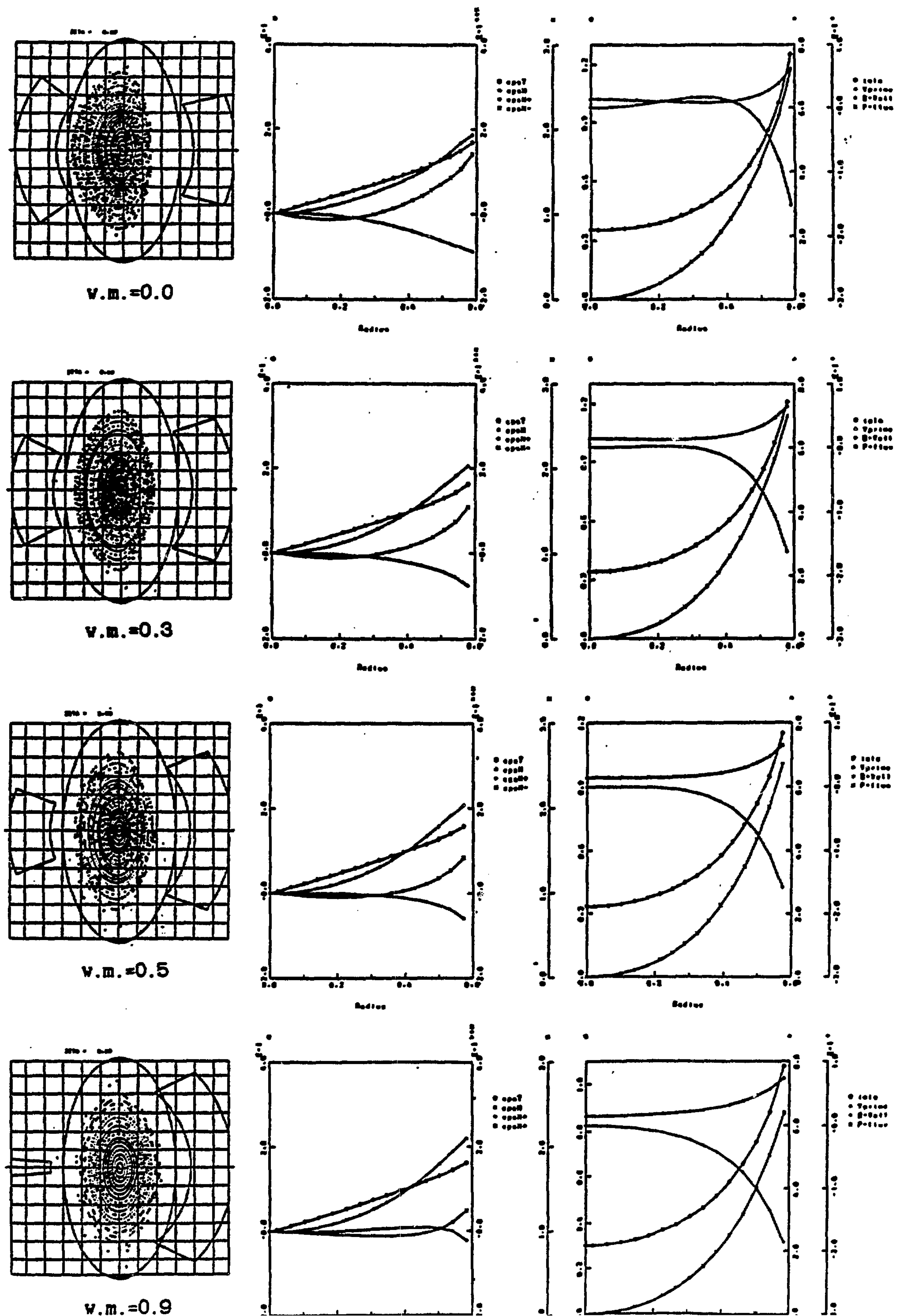

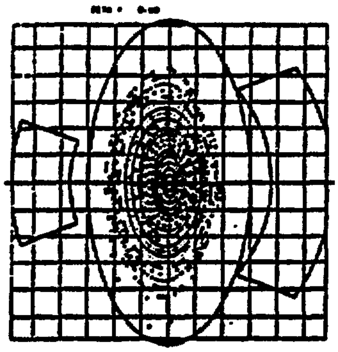

m=10, v.m.=0.5, A_p=7

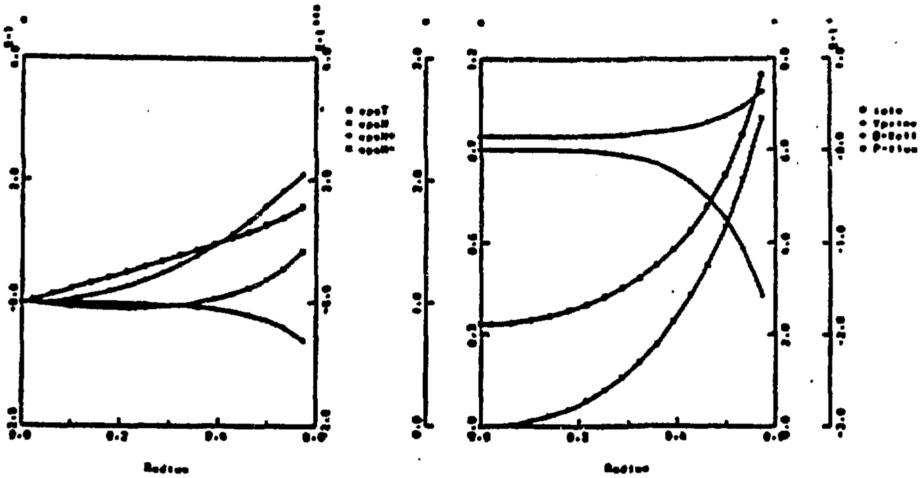

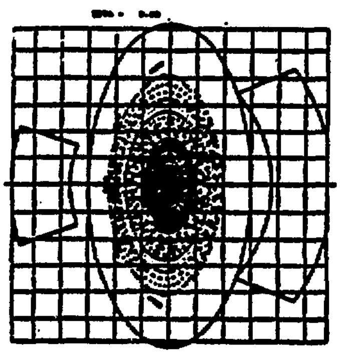

m=12, v.m.=0.5, A_p=8

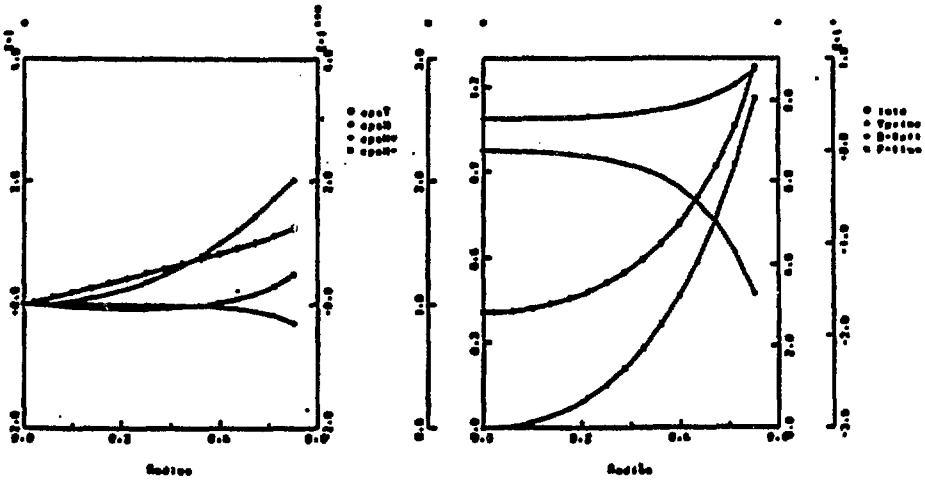

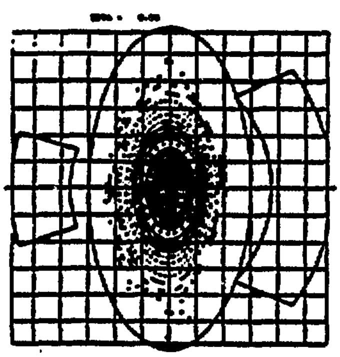

m=14, v.m.=0.5, A_p=9

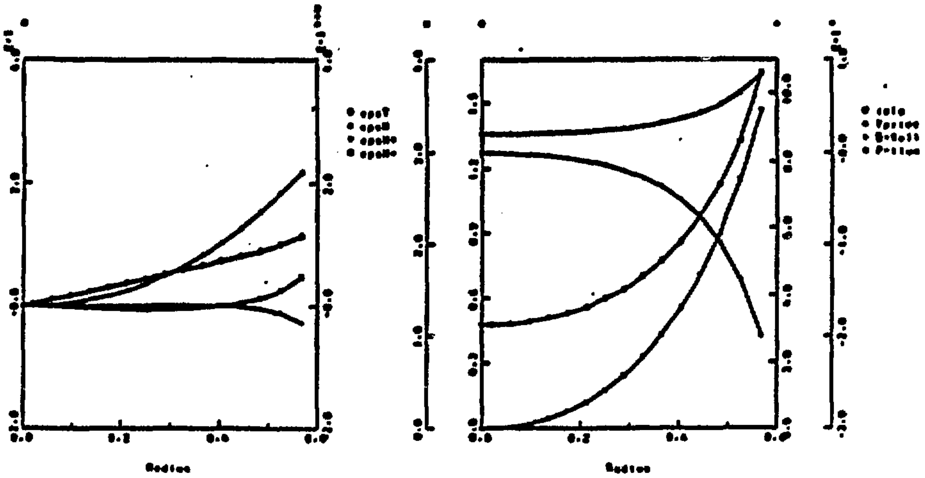

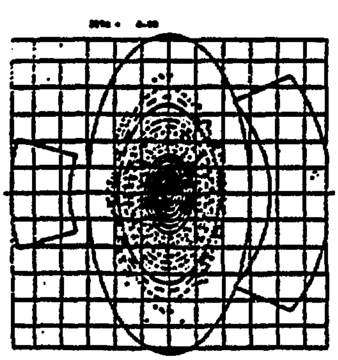

m=16, v.m.=0.5, A_p=11

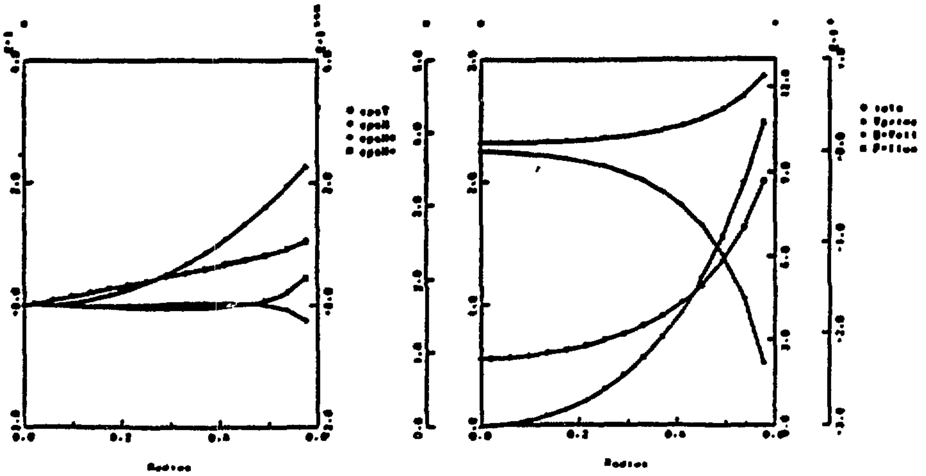

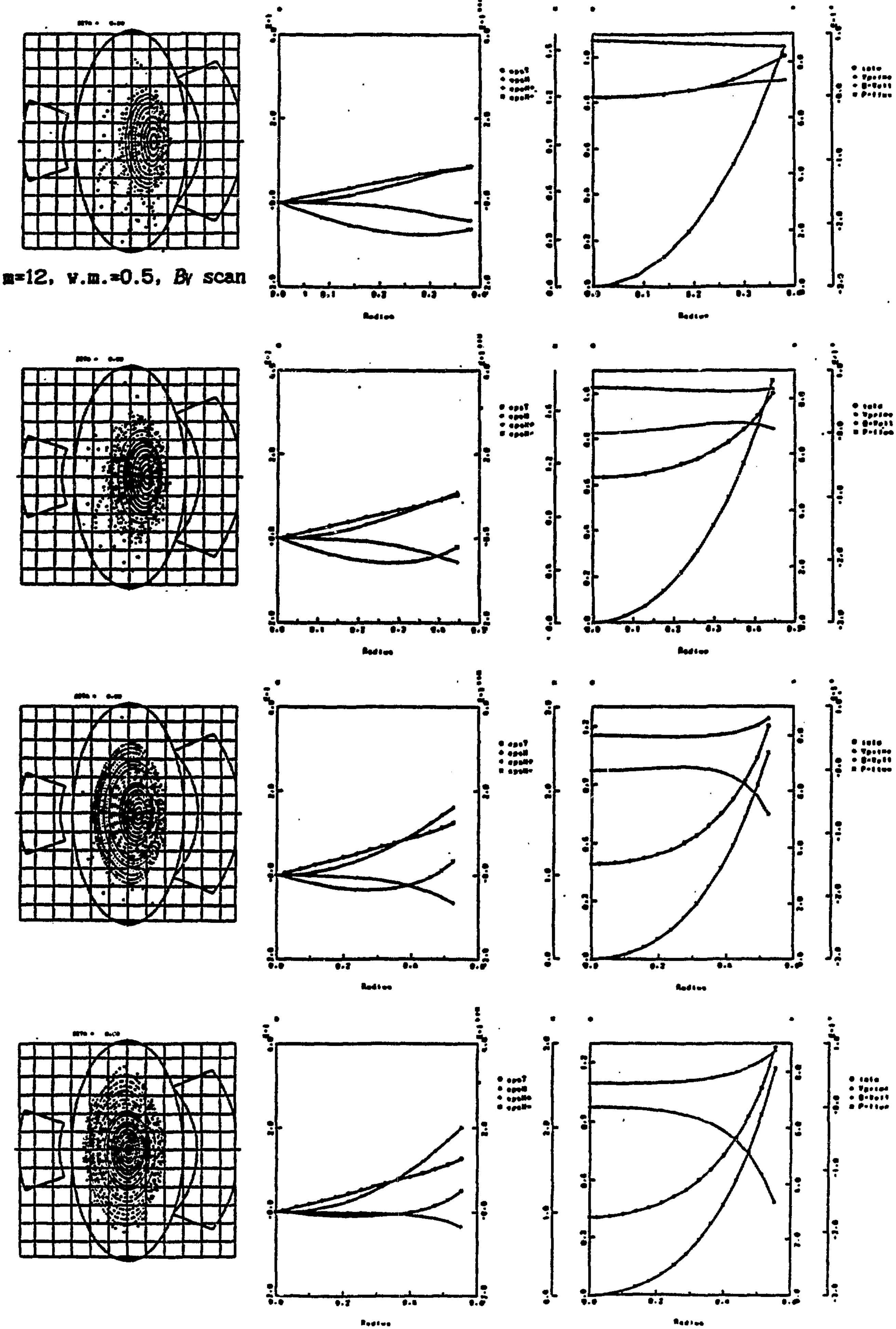

m=12, v.m.=0.5, B_V scan

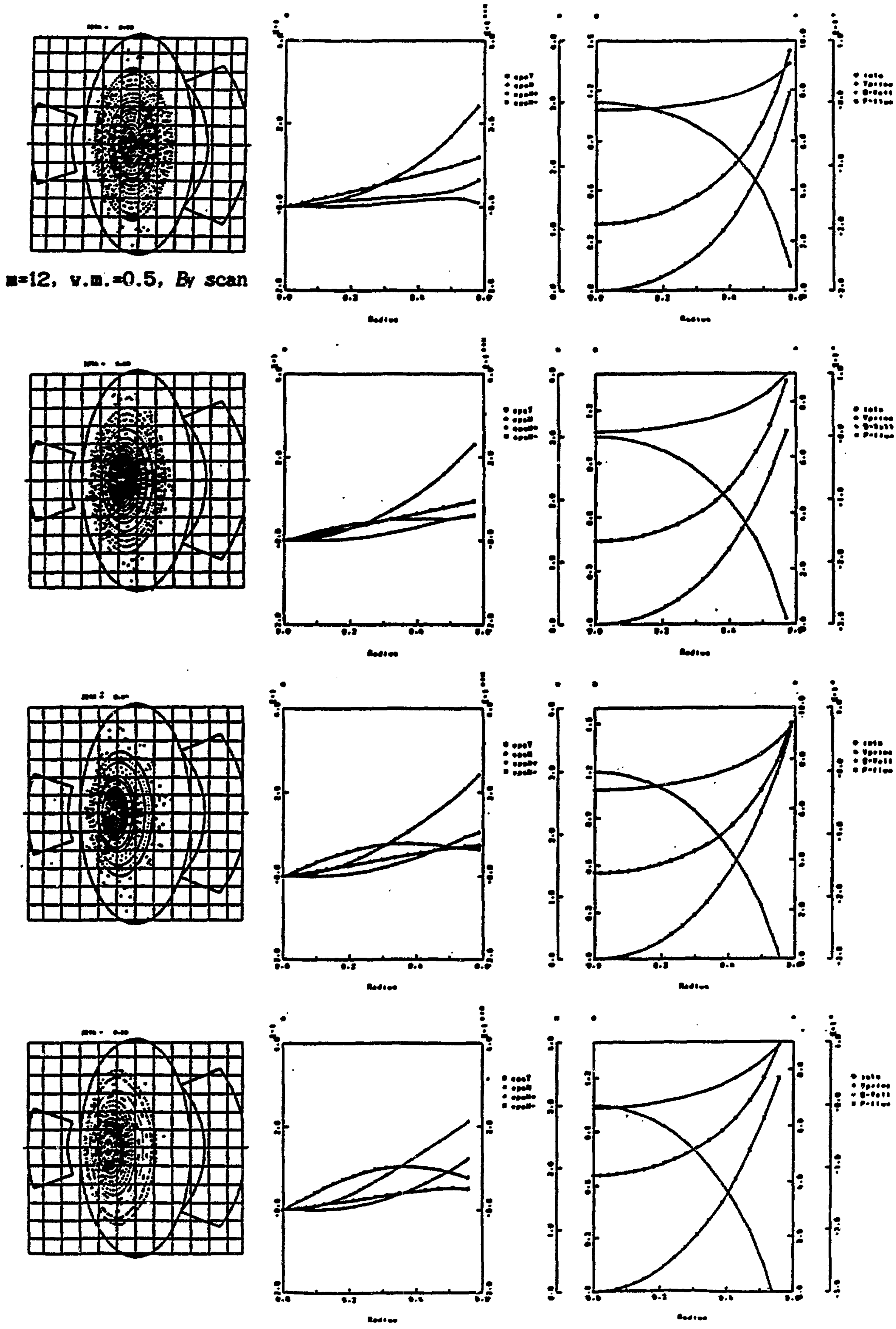
m=12, v.m.=0.5, By scan

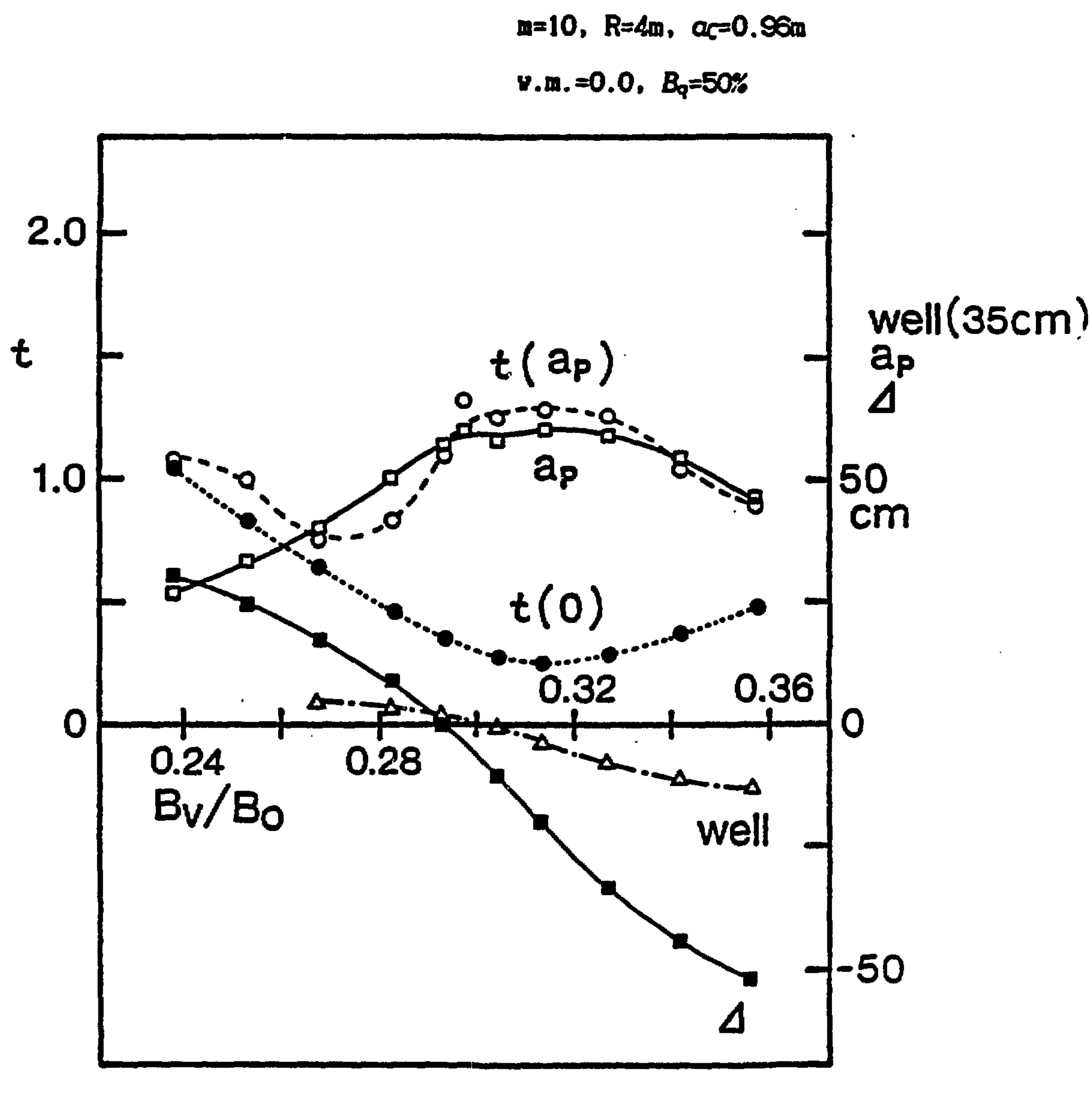

m=10, R=4m, a_C=0.96m
v.m.=0.0, B_q=50%
2.0
t
1.0
0
t (a_P)
a_P
t(0)
0.24
0.28
0.32
0.36
Bv/Bo
well
Δ
well(35cm)
a_P
Δ
50
cm
0
-50

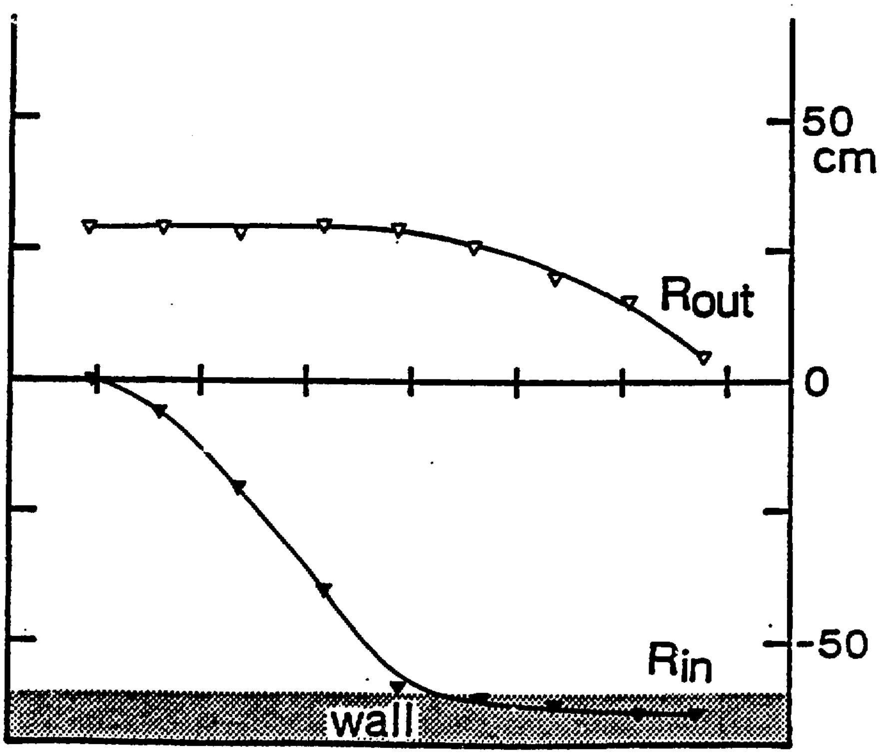

m=10, R=4m, a_c=0.96m

v.m.=0.0, B_q=50%

m=12, R=4.8m, a_c=0.96m

v.m.=0.0, B_q=50%

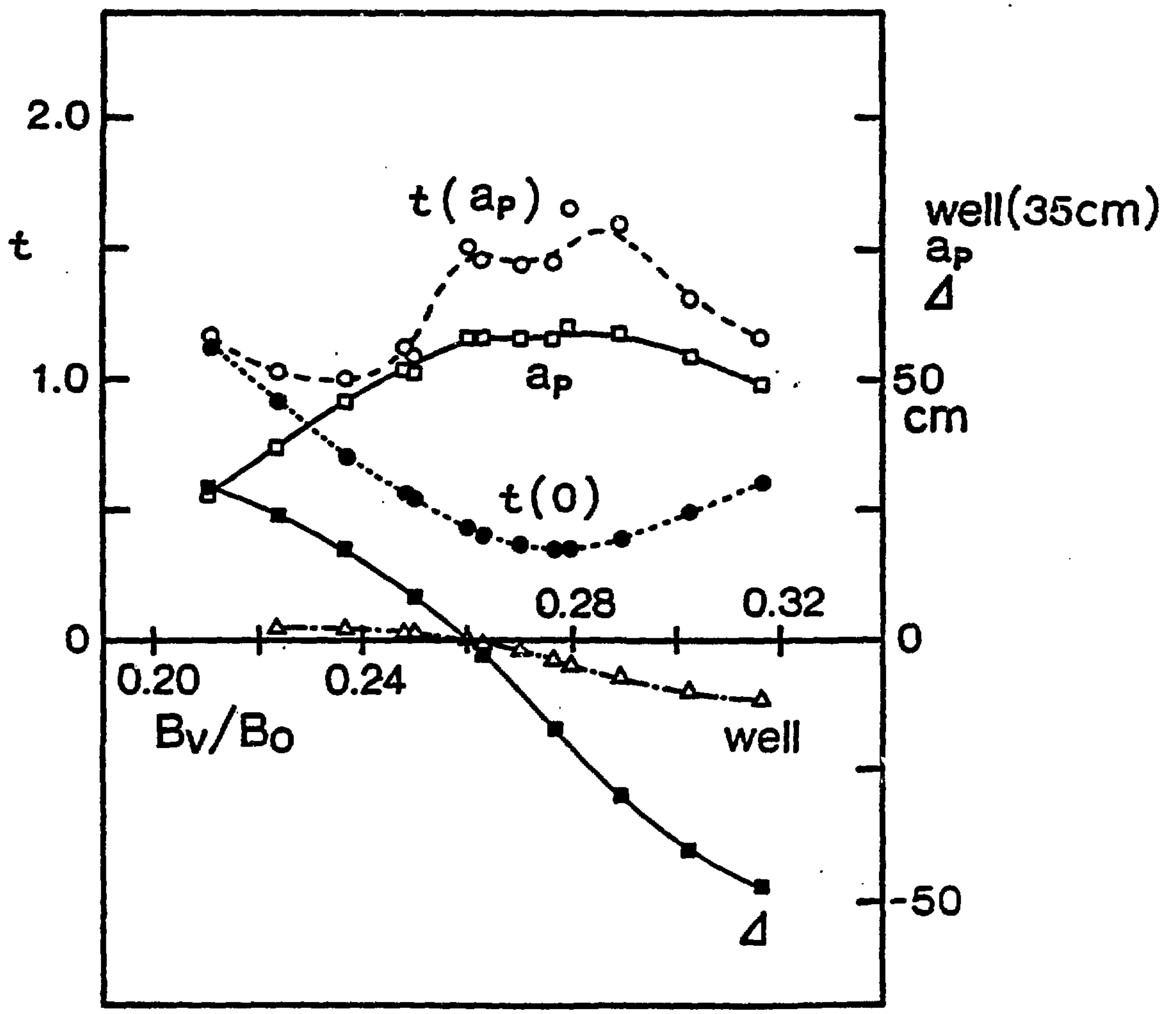

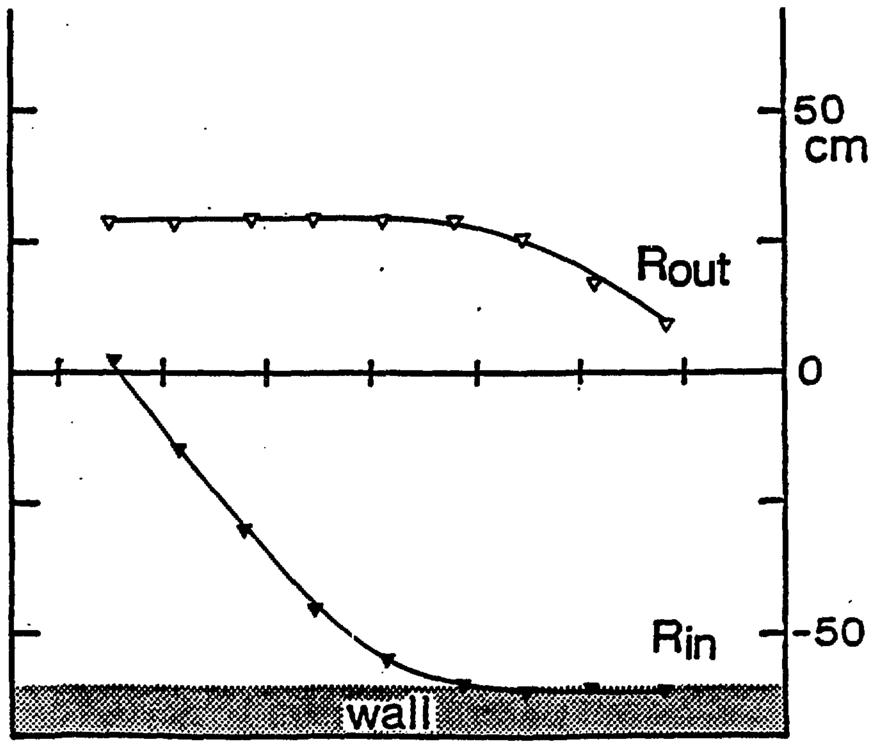

m=12, R=4.8m, a_C=0.96m

v.m.=0.0, B_q=50%

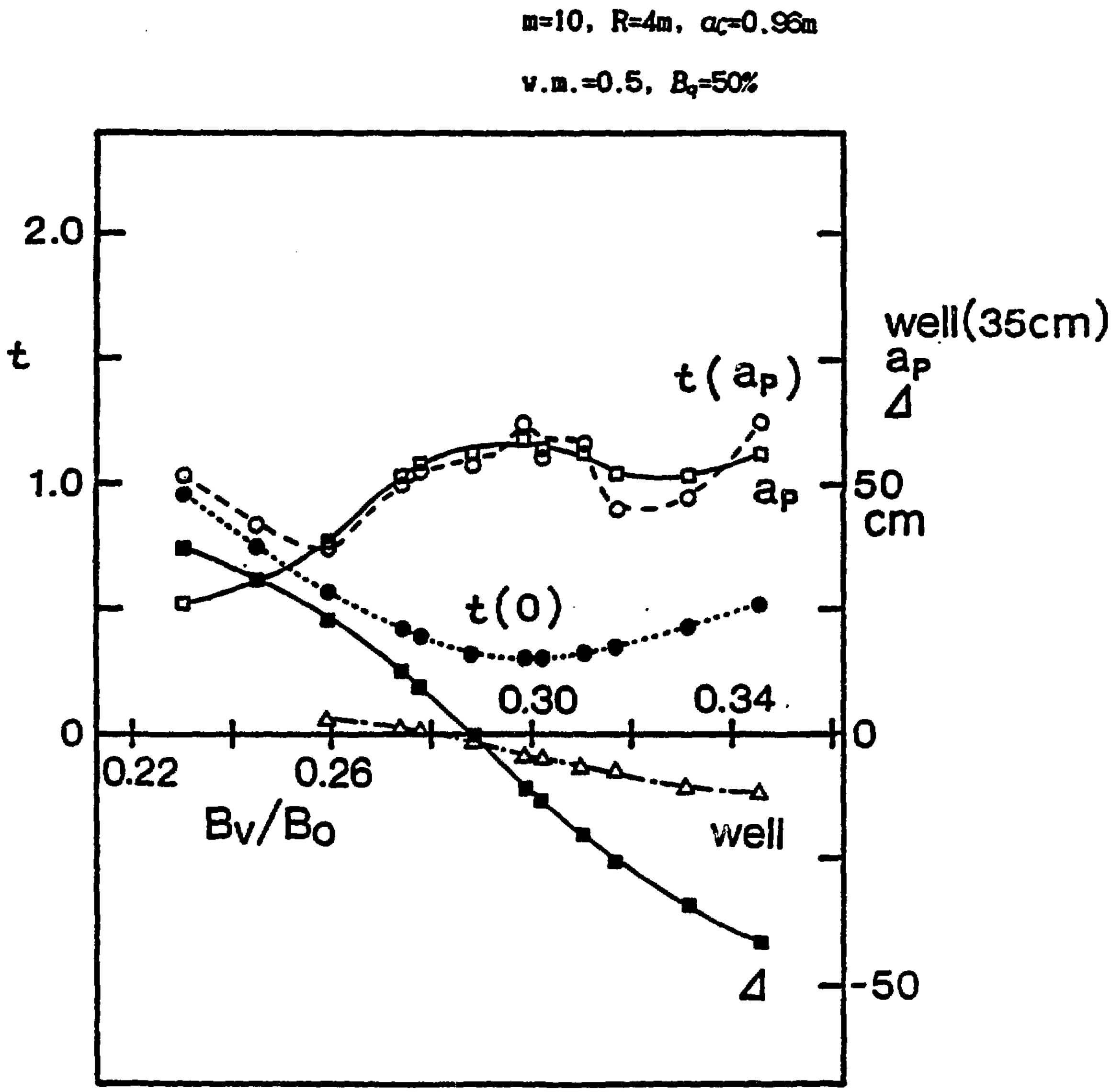
m=10, R=4m, a_C=0.96m
v.m.=0.5, B_q=50%
2.0
t
1.0
0
0.22
0.26
0.30
0.34
Bv/Bo
t (ap)
t(0)
ap
well
Δ
well(35cm)
ap
Δ
50
cm
0
-50

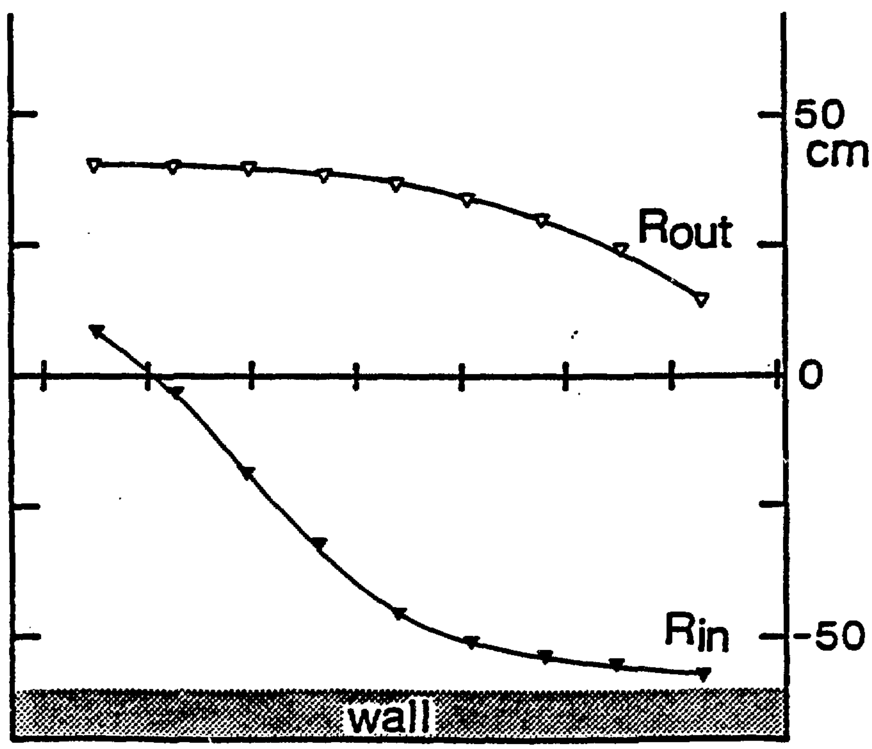

m=10, R=4m, a_C=0.96m

v.m.=0.5, B_q=50%

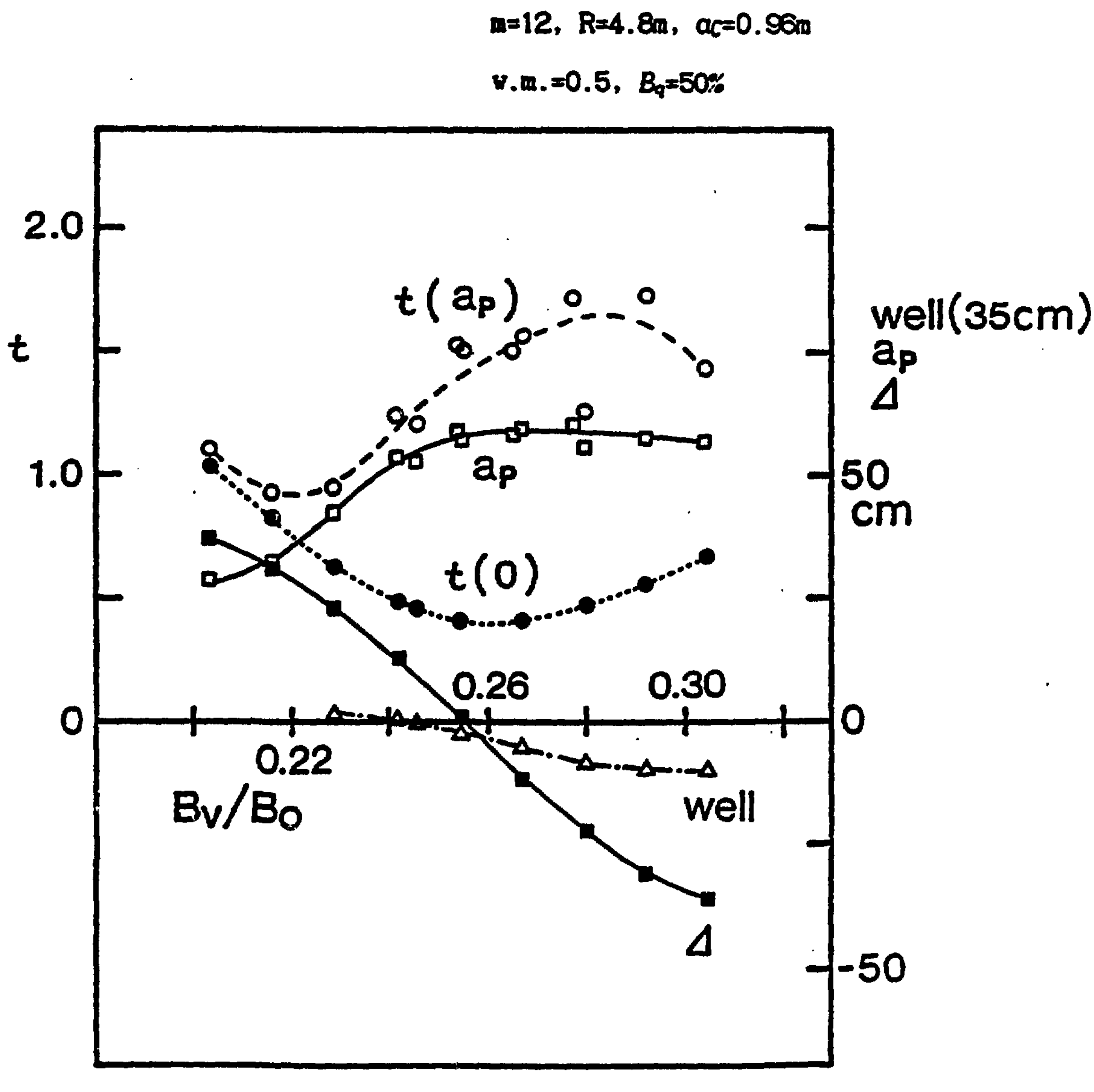

m=12, R=4.8m, a_c=0.96m
v.m.=0.5, B_q=50%
2.0
t
1.0
0
t(a_p)
a_p
t(0)
0.26
0.30
0.22
B_v/B_o
well
Δ
well(35cm)
a_p
Δ
50
cm
0
-50

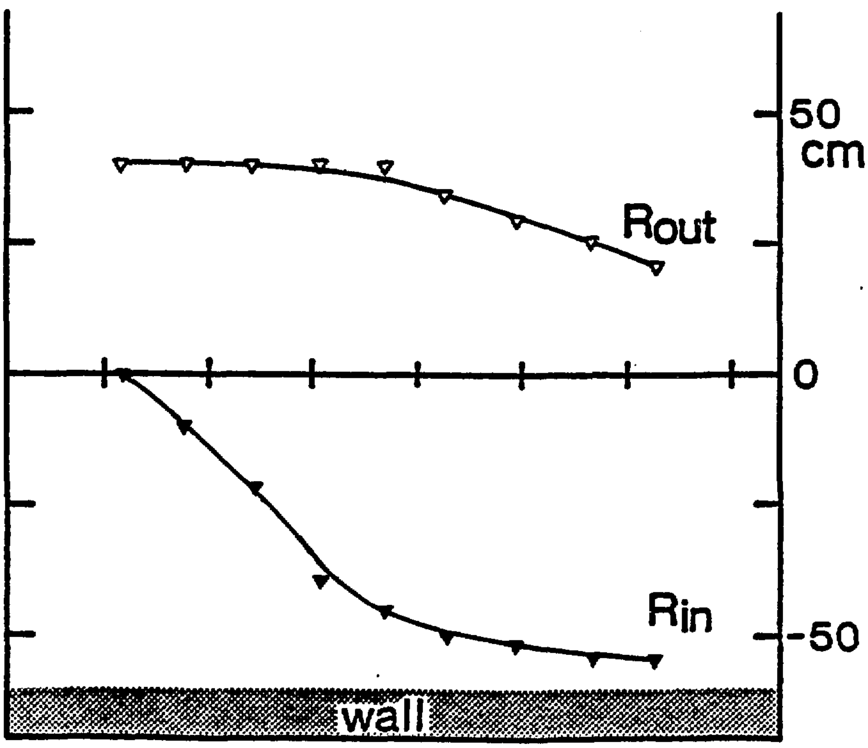

m=12, R=4.8m, a_C=0.96m

v.m.=0.5, B_q=50%

m=14, R=5.6m, a_C=0.96m

v.m.=0.5, B_q=50%

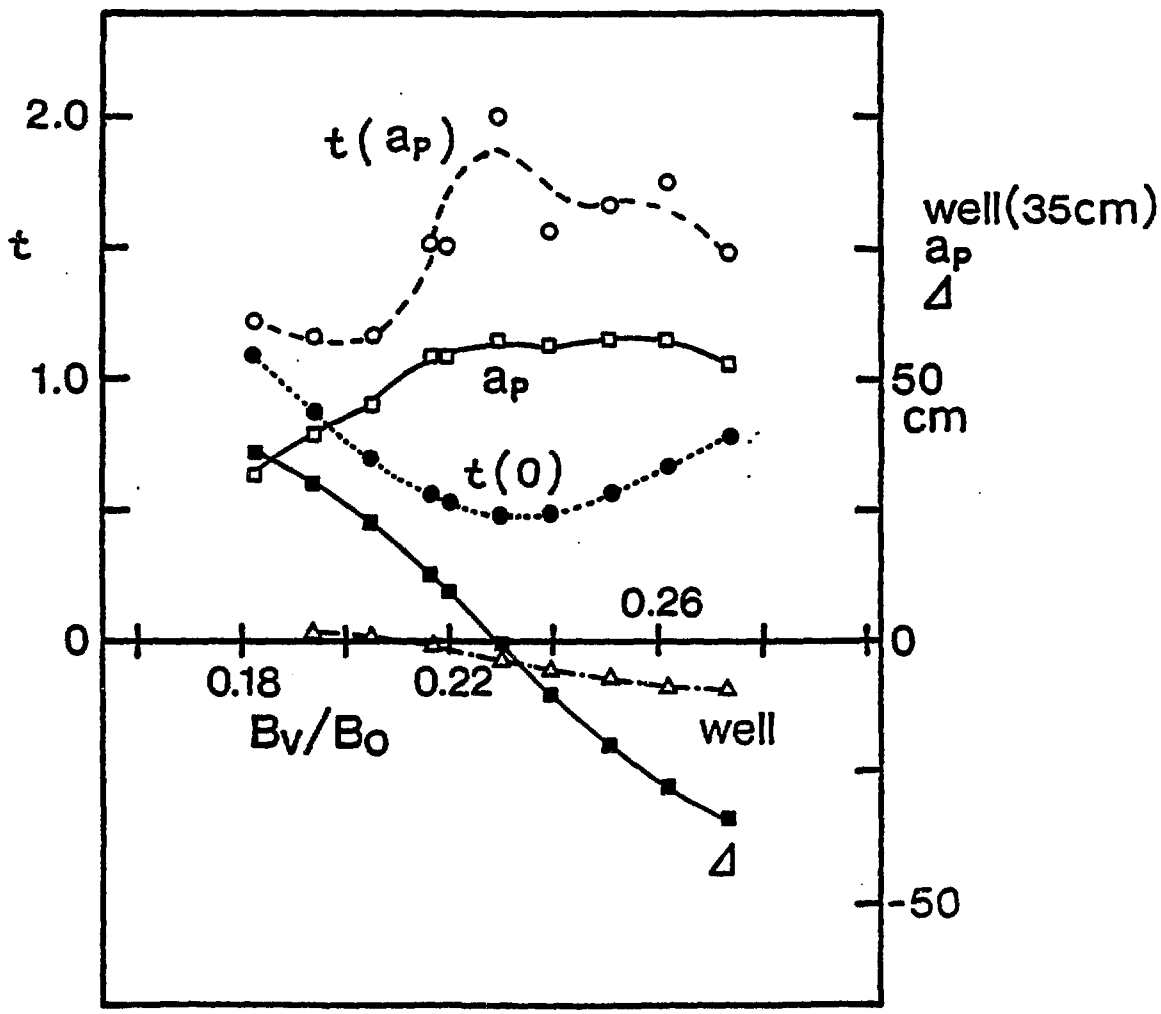

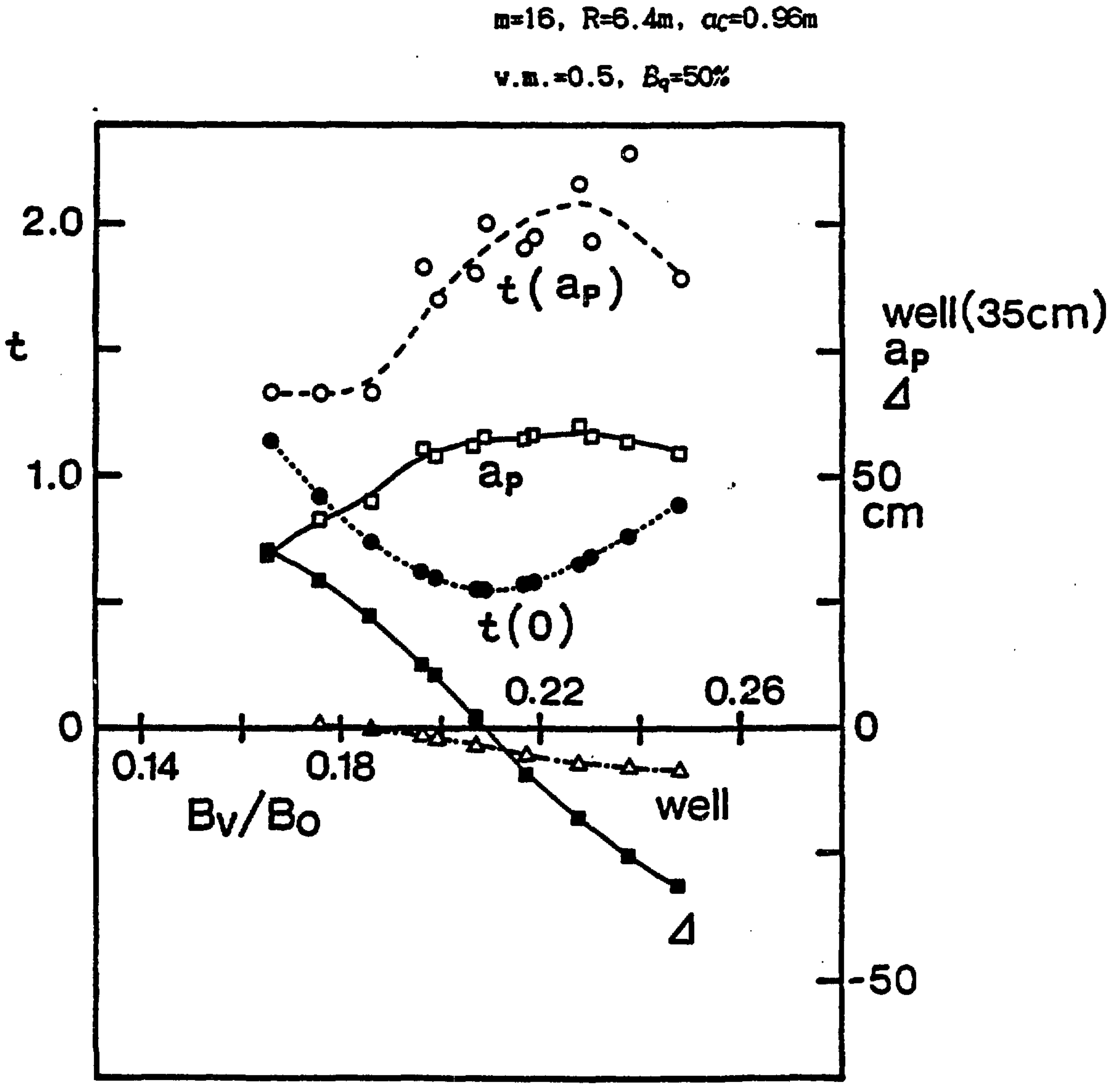
m=16, R=6.4m, a_c=0.96m
v.m.=0.5, B_q=50%
2.0
t
1.0
0
t (a_P)
a_P
t(0)
0.22
0.26
0.14
0.18
B_V/B_O
well
Δ
well(35cm)
a_P
Δ
50
cm
0
-50

OPERATION REGIME OF PLANE AXIS HELICAL SYSTEM

ℓ=2/m=12/R=4.8m/a_C=0.96m/γ_C=1.2/B=4T

coil width 80cm/thickness 45cm/width modulation rate 0.5

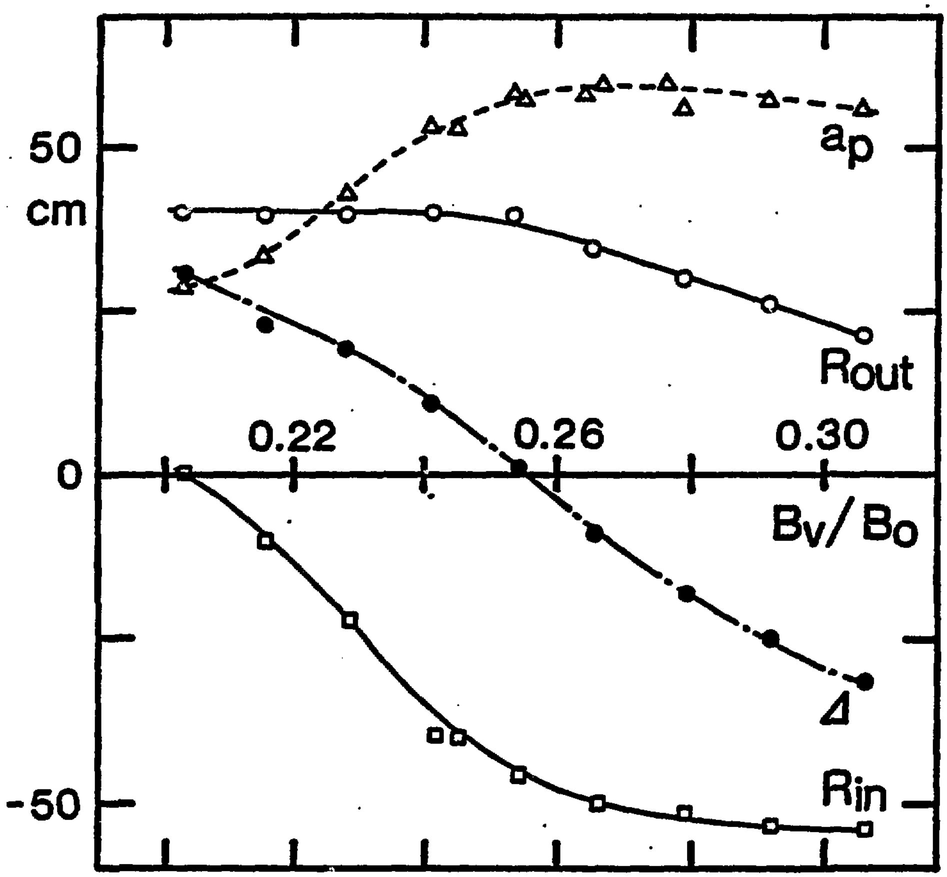

M.H.D.	well.	hill, shear stab.	
CONF.	$\varepsilon_h \approx \varepsilon_t$ ϕ, β effect		$\varepsilon_h \gg \varepsilon_t, \sigma$
DIVERTOR		clean divertor	

<< CONCLUSION >>

- In spite of the low aspect ratio, coil width modulation improved a helical symmetry and, as a result, harmonics components ($\varepsilon_1, \varepsilon_3$) decreased.
- Clearance between the outermost surface and the wall of the vacuum chamber was improved.
  (This is important for the divertor experiments.)

<< Problems >>

1) Increase of the current density.
2) Increase of the maximum field.
3) Worse accessibility of the measuring and injection port.

Configuration Studies for ATF

J. H. Harris
G. H. Neilson
D. K. Lee
S. P. Hirshman
H. C. Howe
R. N. Morris

Oak Ridge National Laboratory

Presented at the
US-Japan Stellarator/Heliotron Workshop
November 9-13, 1987

Introduction

- **ATF—efficient analysis and control of configuration important for:**
  - Operation—runaways, limiter spacing, etc.
  - Diagnostic interpretation—FIR interf., CXA, etc.
  - MHD equilibrium/stability: shift, effects of currents, ι and V'', self-stabilization

- **. . . but made difficult by stellarator magnetic structure**
  - 3-D character—problems to visualize
  - follow field lines (costly) to get flux surfaces, integral properties, etc.
  - time-varying configuration
  - efficient representation is the first step toward control.

- This talk:
  - representation of vacuum and finite-β configurations
  - characteristics of high-β equilibria

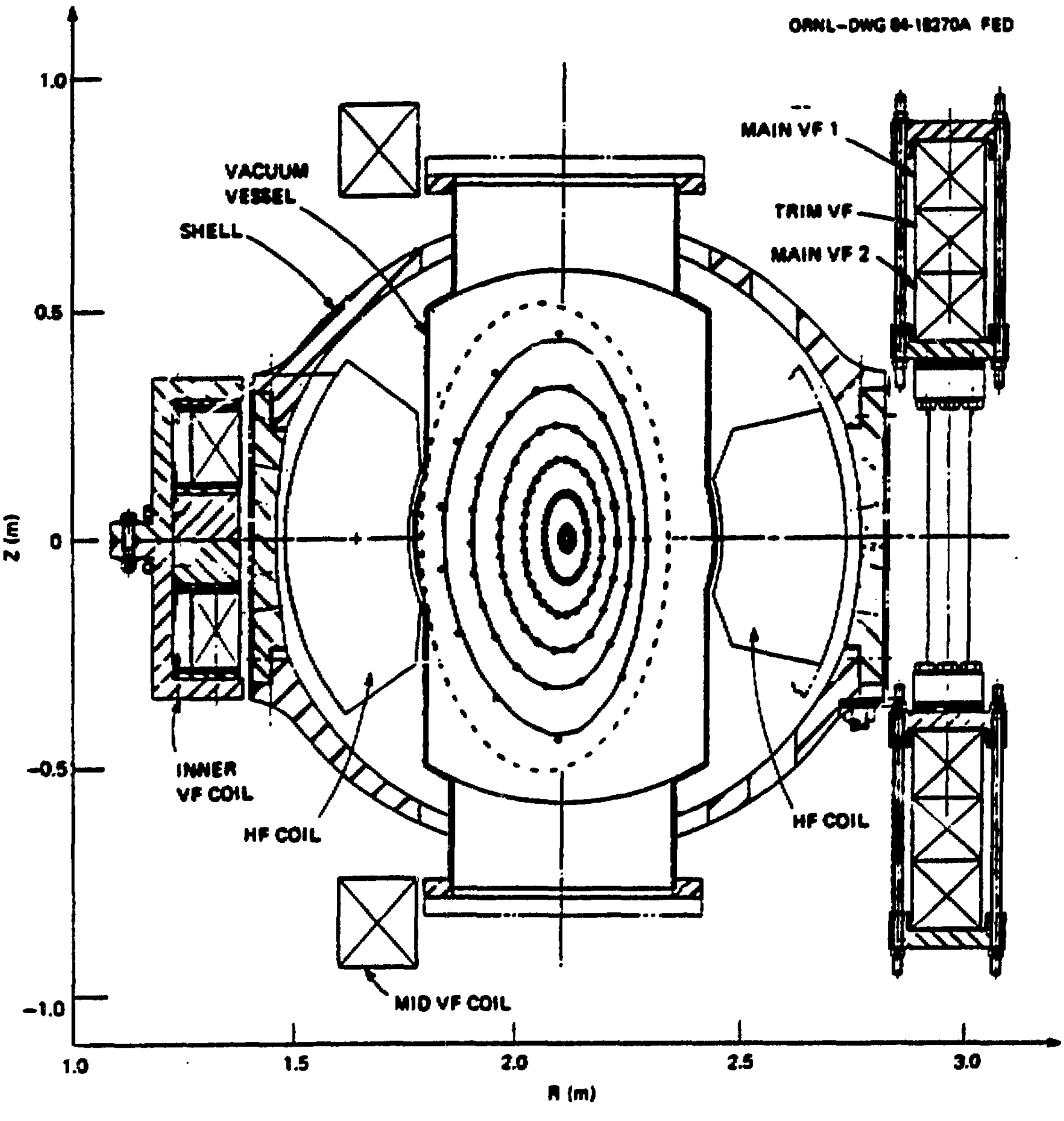
ORNL-DWG 84-18270A FED
MAIN VF 1
TRIM VF
MAIN VF 2
VACUUM VESSEL
SHELL
INNER VF COIL
HF COIL
HF COIL
MID VF COIL
1.0
0.5
0
-0.5
-1.0
Z (m)
1.0
1.5
2.0
2.5
3.0
R (m)

Vacuum Configurations

- Flexible VF coil system
- Fourier spectral representation of flux surfaces (already being used in ORNL Heliotron-E modelling)

$$R(\rho,\theta,\phi) = \sum R_{mn}(\rho) \cos(m\theta - n\phi)$$

$$Z(\rho,\theta,\phi) = \sum Z_{mn}(\rho) \sin(m\theta - n\phi)$$

→ θ chosen to minimize spectral width → "optimal" representation

- Use of 6-7 harmonic components adequate for experimental accuracy (error ≲ 1 cm); smooth radial dependence; potential for semi-analytic representation.

$\phi = 0$

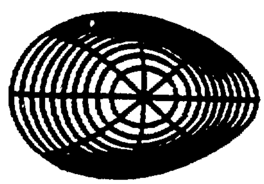

$\phi = 1/2$ period

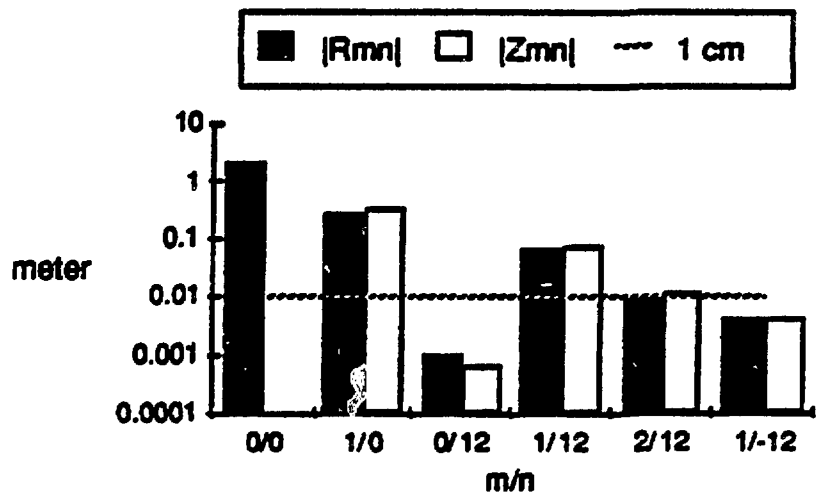

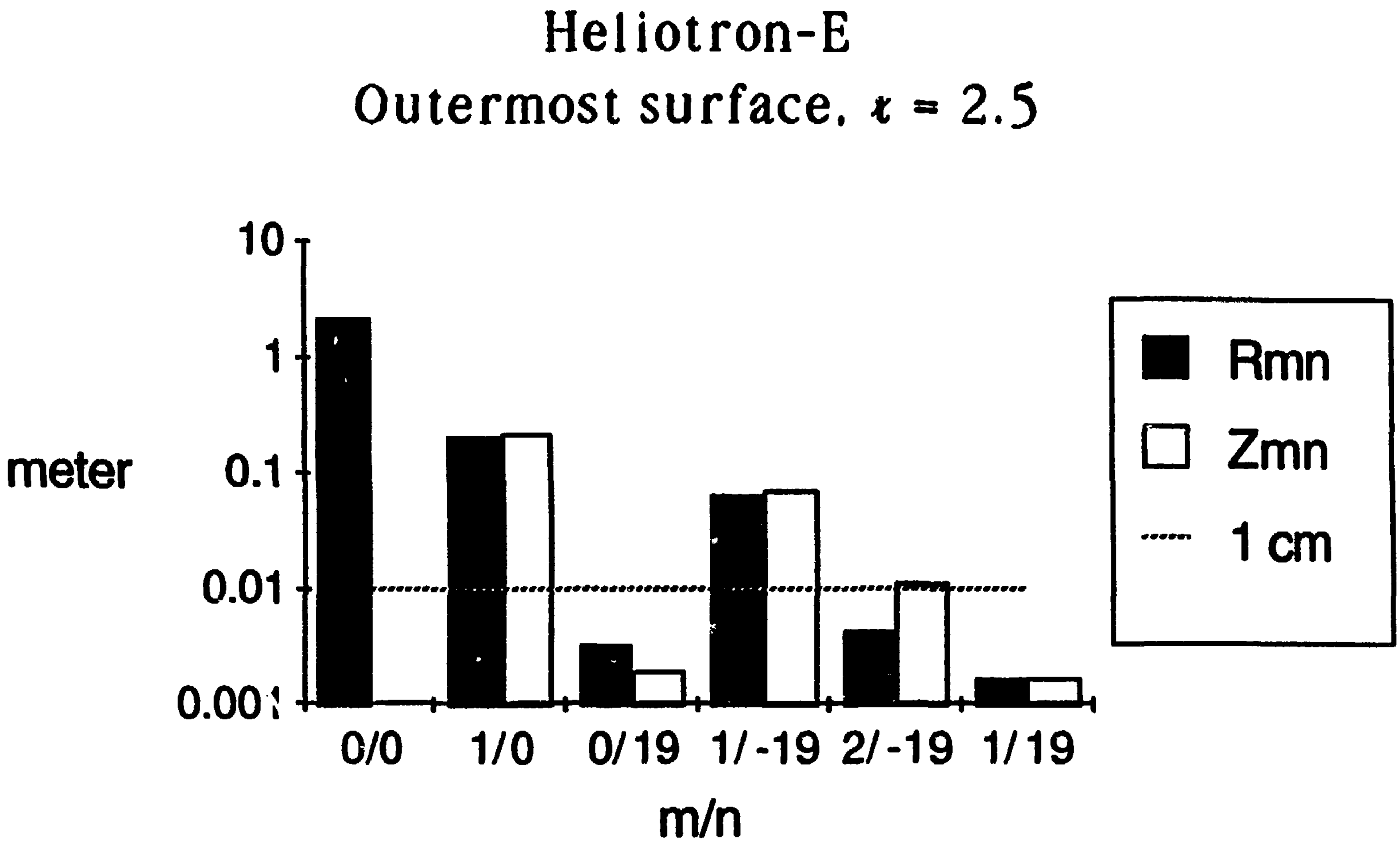

Heliotron-E
Outermost surface, ι = 2.5
10
1
0.1
0.01
0.001
meter
0/0
1/0
0/19
1/-19
2/-19
1/19
m/n
Rmn
Zmn
1 cm

Variation of Vacuum Configurations

- Decomposition of vertical field into axisymmetric dipole (Q_1) and quadrupole (Q_2) moments.
- Main effects: $\Delta Q_1 \rightarrow$ position, magnetic well/hill, $\Delta Q_2 \rightarrow$ elongation Both vary ι.
- Systematic variation of flux surface shapes and Fourier harmonic content with Q_1 and Q_2.

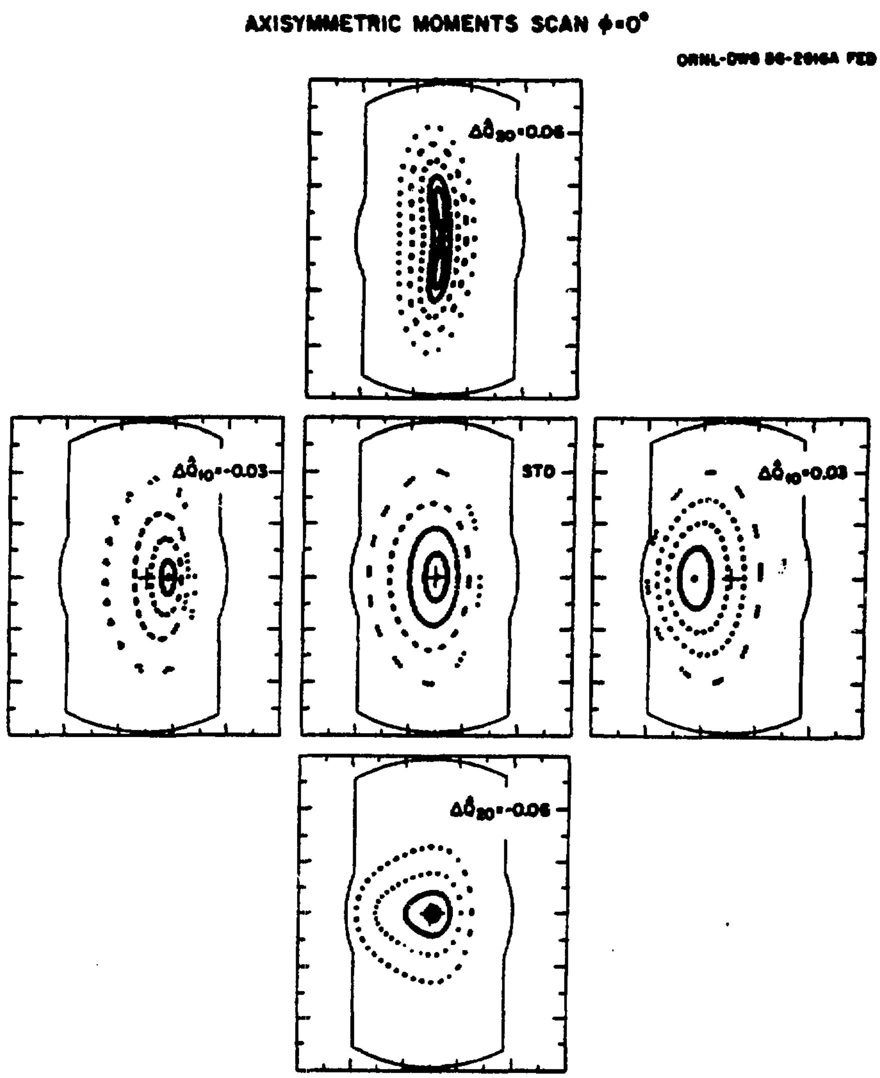

Dependence of Principal Harmonics on Dipole Moment Q1

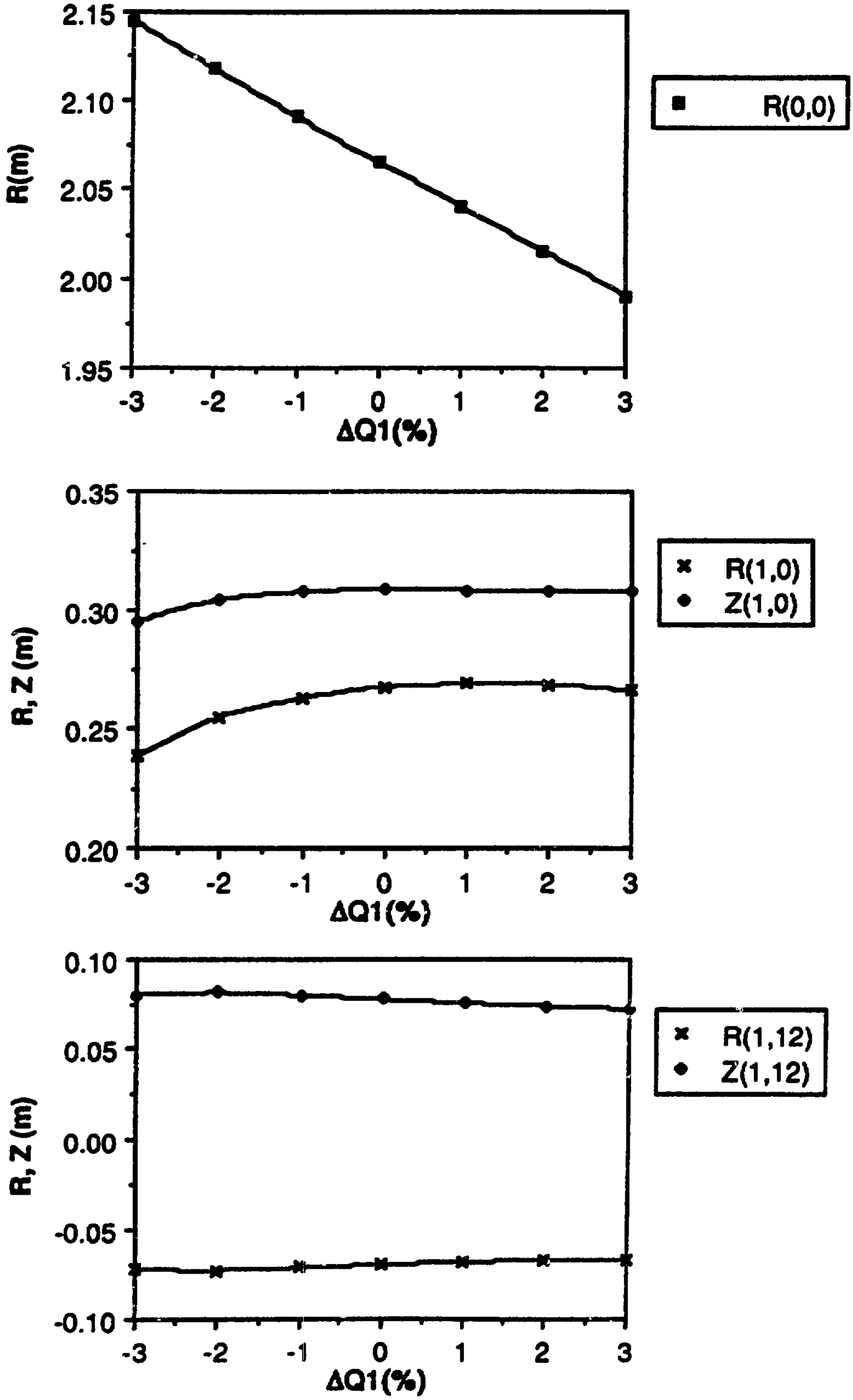

Dependence of Principal Harmonics on Dipole Moment Q1

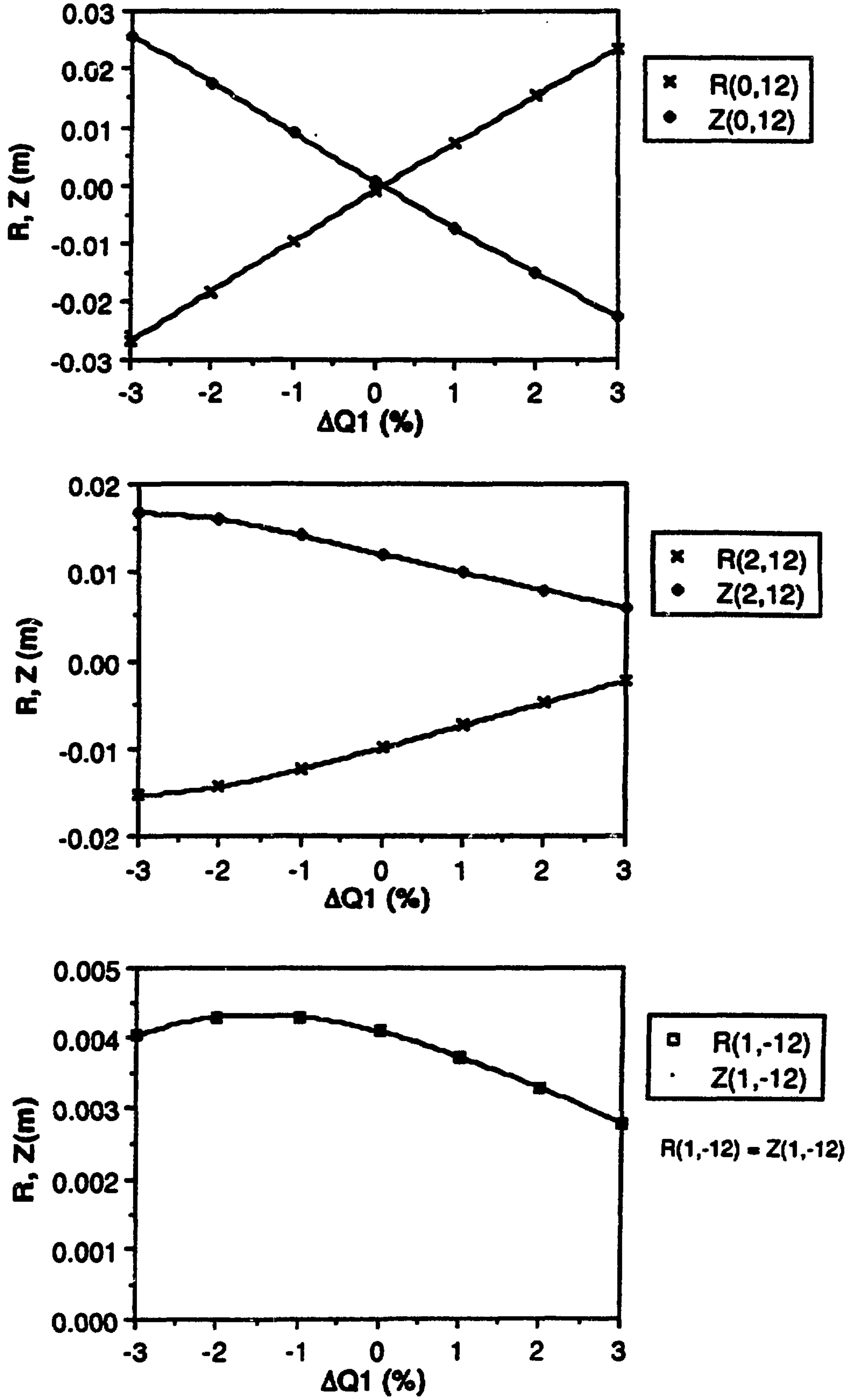

Dependence of Principal Harmonics on Dipole Moment Q2

Outermost surface

ι = 0.98

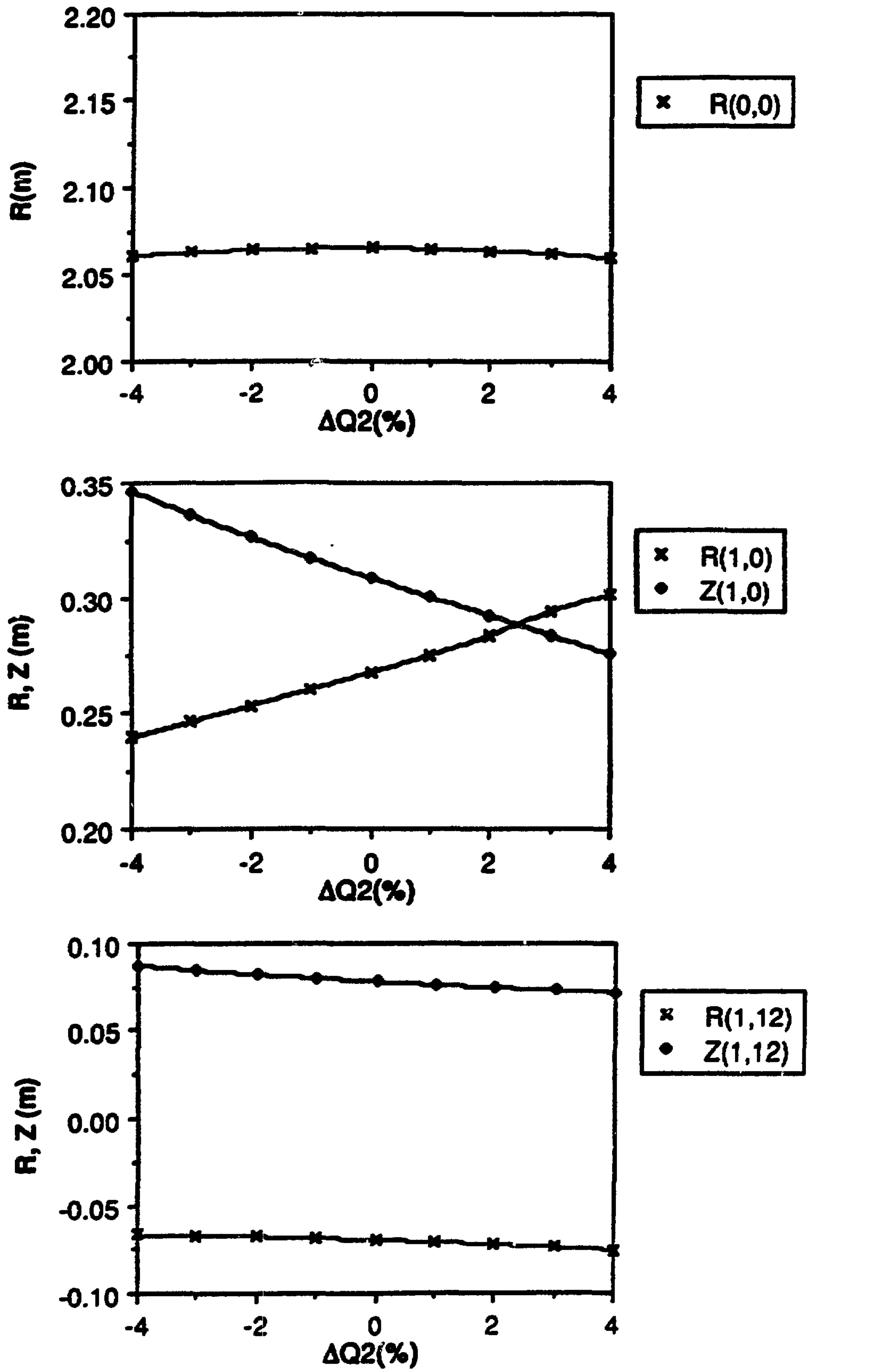

Dependence of Principal Harmonics on Dipole Moment Q2

Outermost surface

$\varepsilon = 0.98$

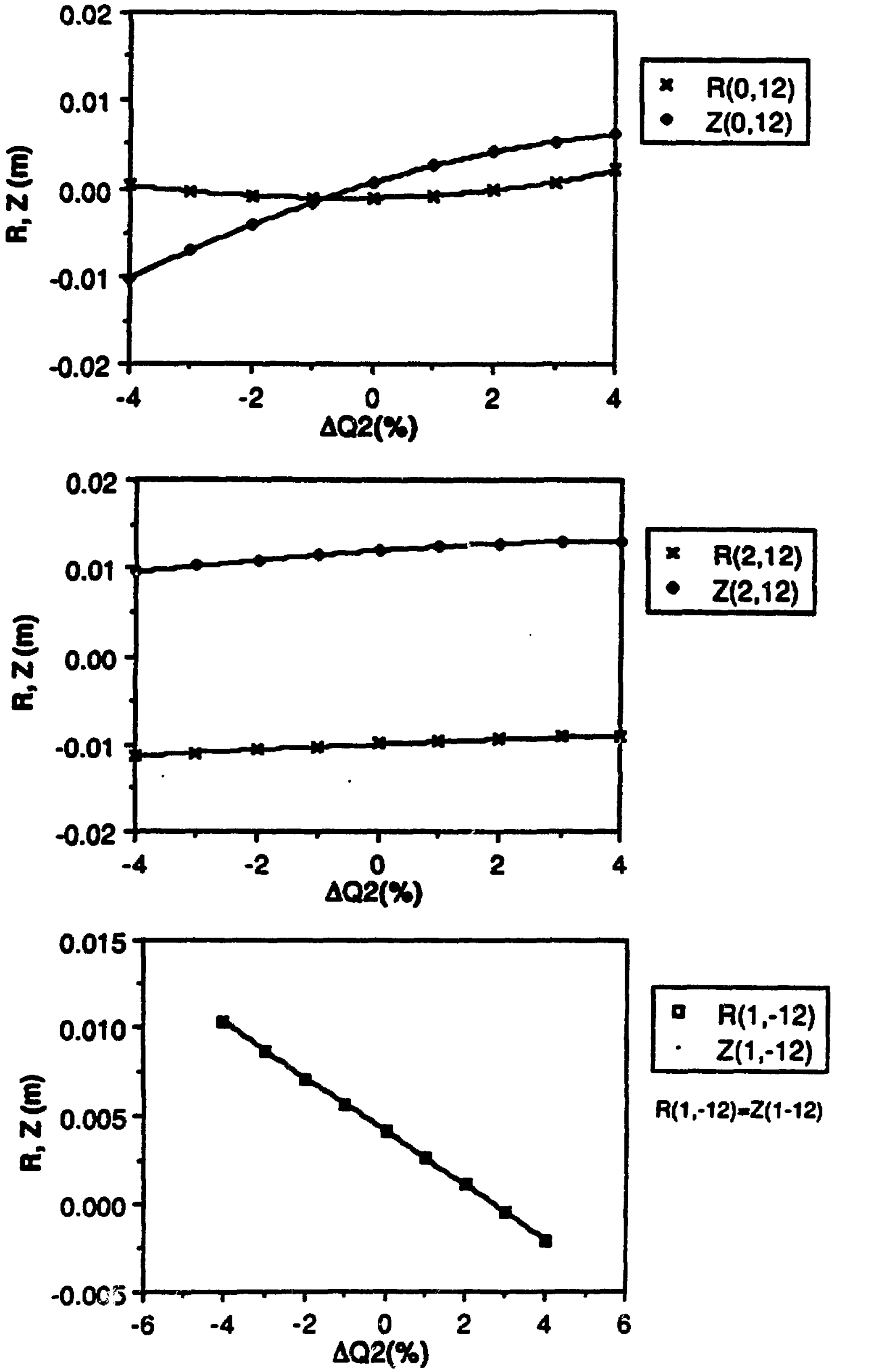

Finite-Beta Configurations

- Studied with 3-D VMEC code that determines the R_{mn} and Z_{mn}. For these studies, external configuration fixed.

- Basic effect: Pfirsch-Schlüter currents → dipole field → outward shift.
  - Axis shift > edge shift. Flux surface shape changes reflected in harmonic content.

- Check dependence of equilibria on
  - pressure profile
  - flux conserving or zero-current evolution

- Try to establish relationship of equilibrium parameters to diagnostic measurements.

  - $\langle\beta\rangle$: diamagnetic loops, segmented Rogowski coil to measure changes to dipole field due to P-S currents.

  - β_0: Thomson scattering, FIR interf., CX measurements, etc.

- Explore finite-β effects on geometry:simplification possible for experimental purposes ?

Pressure Profiles Used in Computations

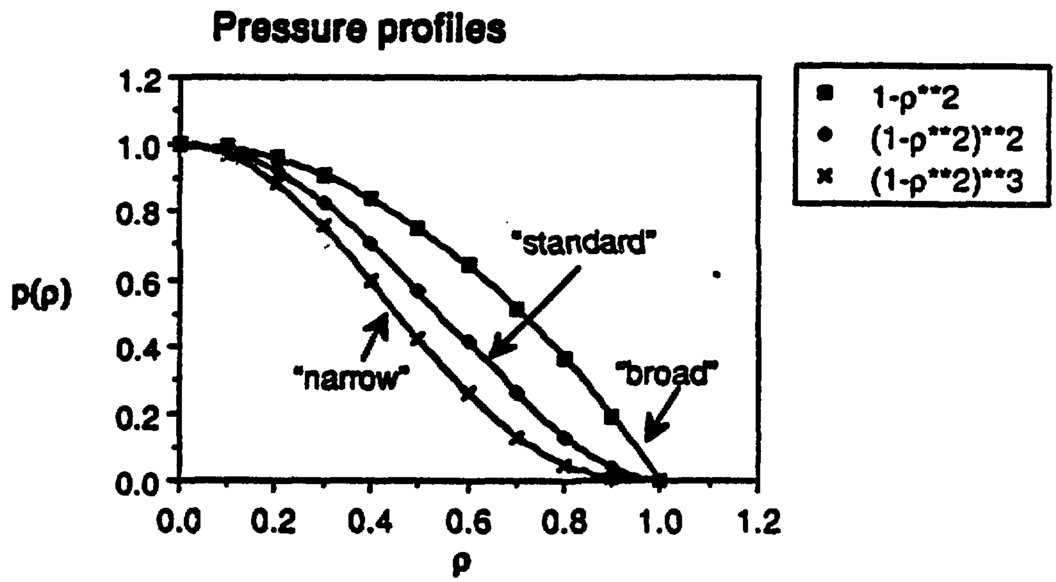

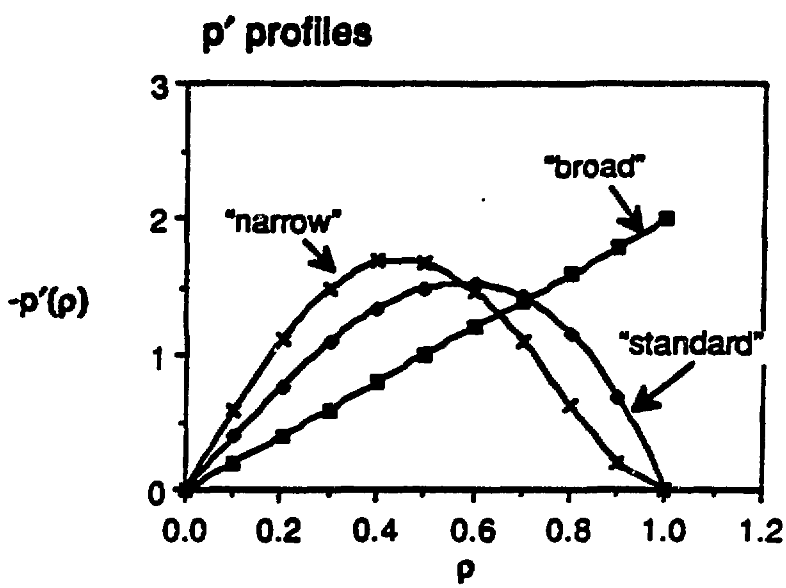

Rotational Transform Profiles

- Both flux-conserving ($\iota \equiv \iota_{vac}$) and zero-net-current equilibria calculated. For zero net current, $\Delta\iota$ is significant.

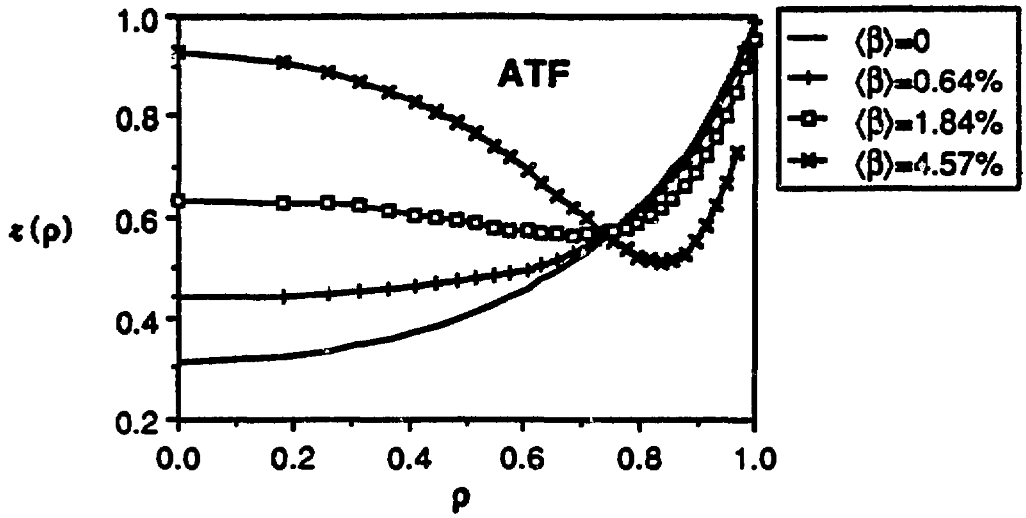

- Ultimate goal → use ATF VF coil system to control transform to maintain $\iota \approx \iota_{vac}$.

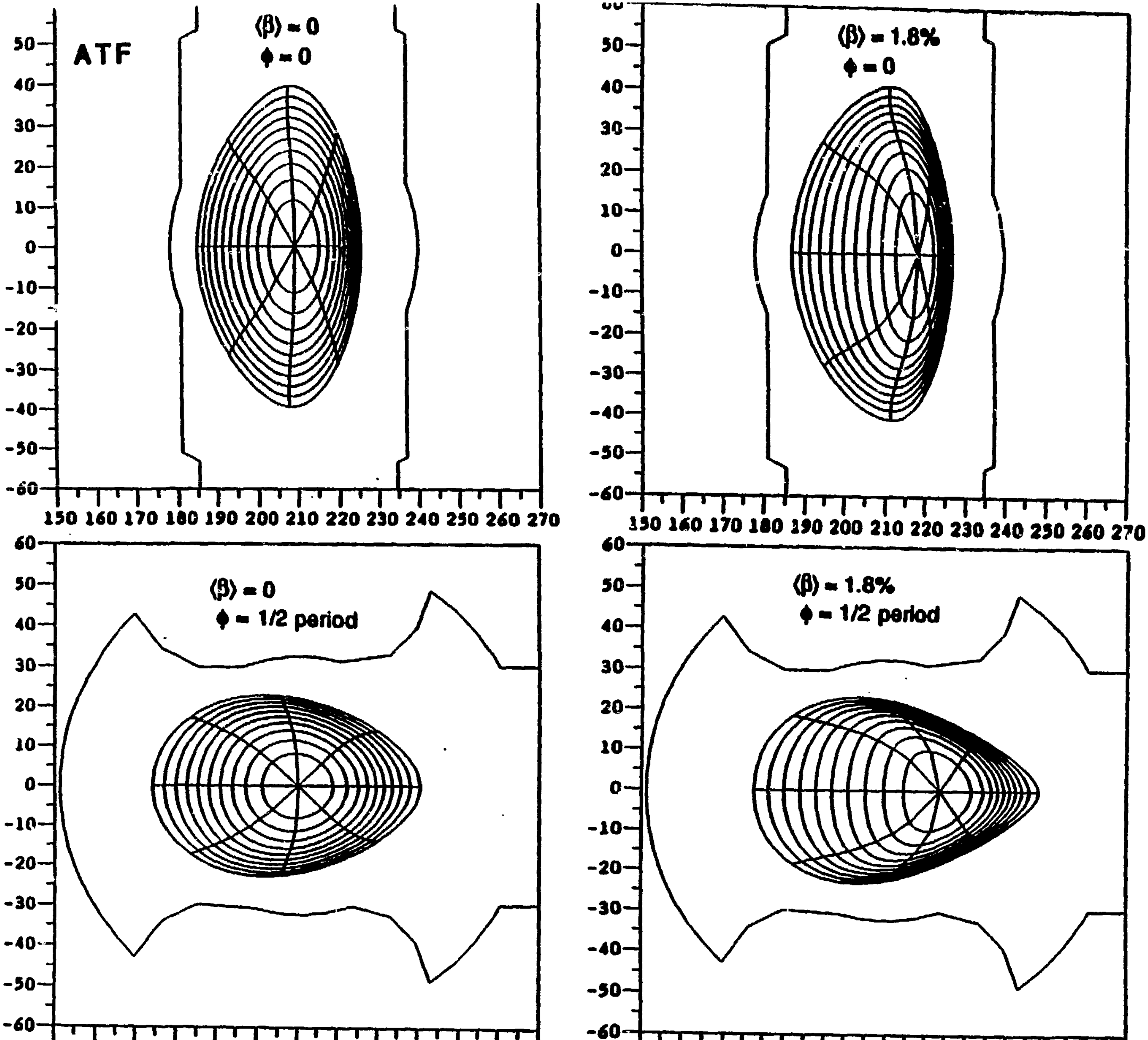

ATF
⟨β⟩ = 0
ϕ = 0
⟨β⟩ = 1.8%
ϕ = 0
⟨β⟩ = 0
ϕ = 1/2 period
⟨β⟩ = 1.8%
ϕ = 1/2 period

Finite-Beta Shift (1)

- Axisymmetric shift (ΔR_{00}):
  - Axis shift correlates well with β_0, essentially independently of pressure profile and equilibrium constraint.

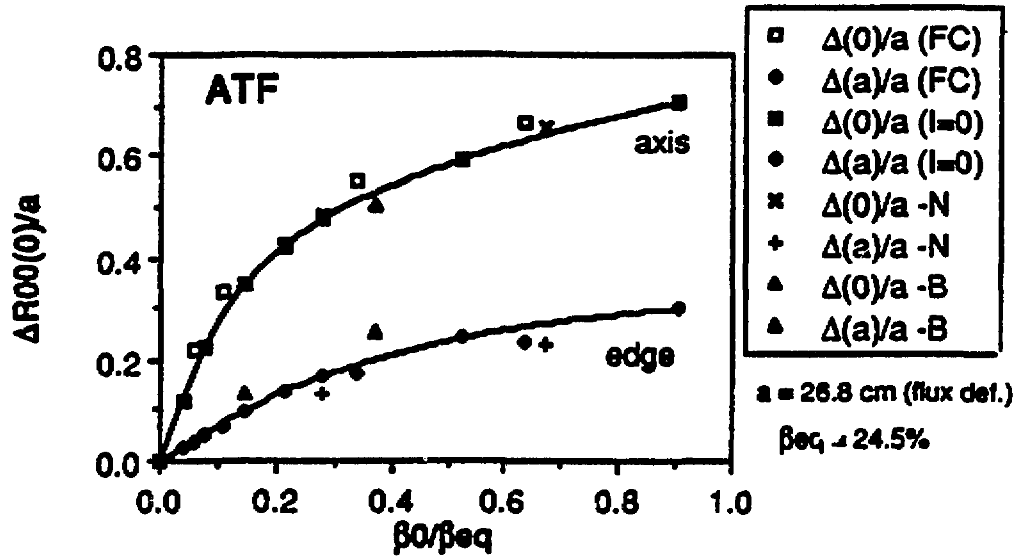

  - Edge shift correlates well with $\langle\beta\rangle$

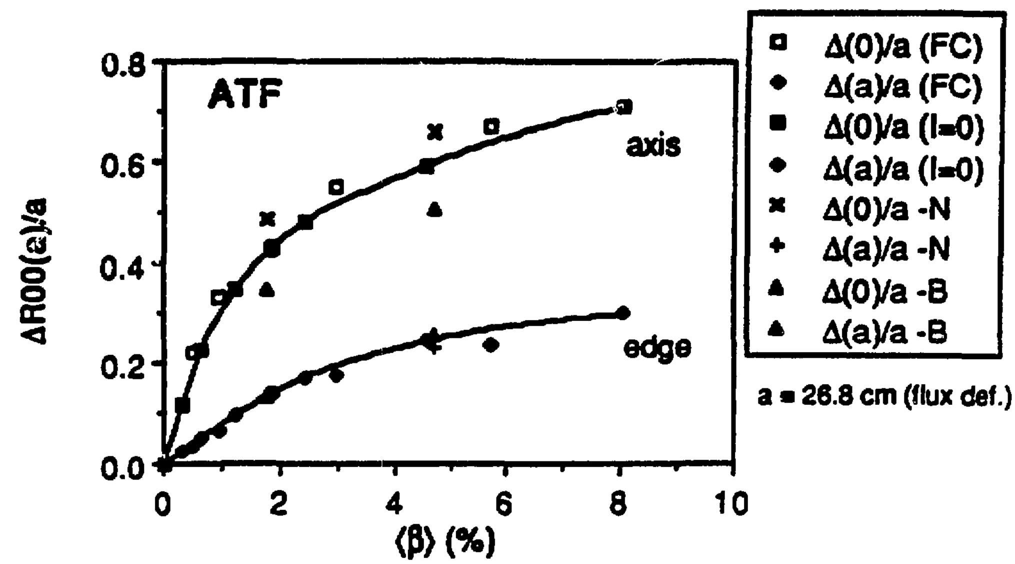

Finite-Beta Shift (2)

- Helical axis shift ($\Delta R_{0,12}$) varies ~linearly with axisymmetric component of shift (ΔR_{00})

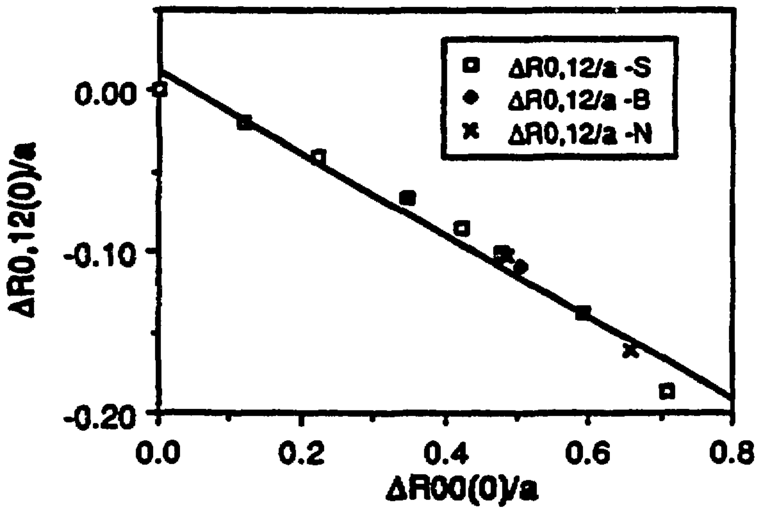

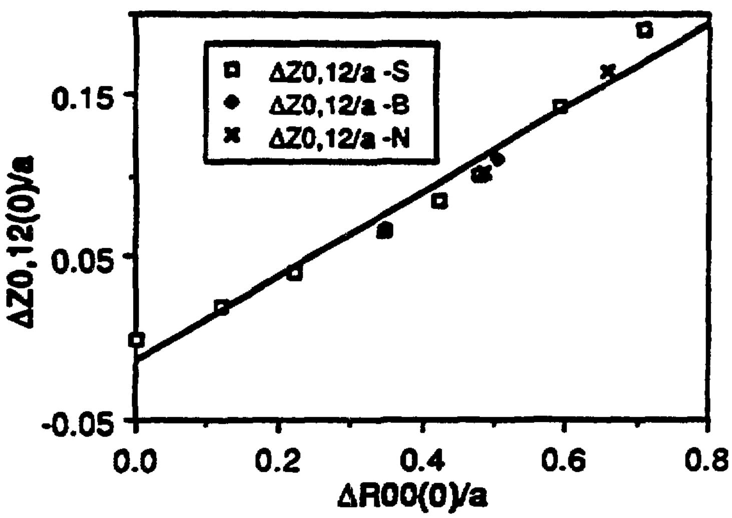

→*Simple relation for finite-beta axis shift:*

$$\Delta R_{axis} = f(\beta_0)(1 - \delta \cos 12\phi)$$

$$\Delta Z_{axis} = f(\beta_0)\,\delta \sin 12\phi$$

Radial Profiles of Fourier Harmonics

- Comparison of $\Delta(R_{00}(\rho)-R_{00}(a))$ for I = 0 equilibria with "broad" and "narrow" profiles at $\langle\beta\rangle$= 1.8% and 4.7% →profile shape retained as β increased.

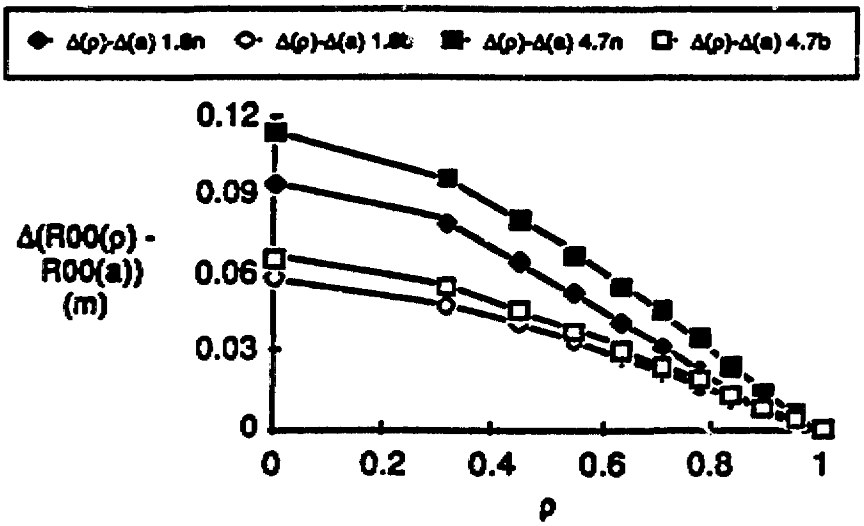

- Similar effects for higher harmonics ($\Delta R_{1,12}$ (ρ)shown). Magnitude of profile effects → small.

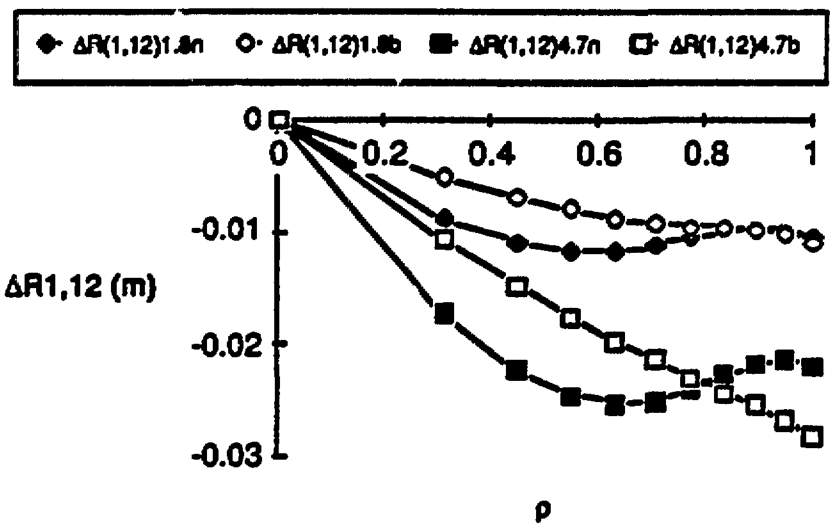

Conclusions

- Fourier representation remains compact as configuration changes; components vary smoothly and slowly → efficient for experiments and analysis.

- Finite-β shifts not sensitive to details of equilibrium:
  - Axis shift ↔ β_0
  - Edge shift ↔ $\langle\beta\rangle$
  - Useful for immediate experimental analysis

- Radial profiles of Fourier harmonics sensitive to pressure profile, etc., but retain shape as β is raised for fixed $p(\rho)$. For higher-order harmonics, absolute magnitudes of differences due to profile effects are small. → Possibilities for mock-up of equilibrium without full 3-D calculation.

- Next tasks:
  - Effects of configuration changes to hold ι ~ fixed as β increases.
  - Effects of plasma current (ohmic, beam-driven, bootstrap).

Equilibrium Diagnostics

- $\beta_0 \leftrightarrow \Delta R_{axis}$
  - Look for peak or inflection point of profile
  - Possiblities: FIR interferometer, soft X-ray array, fit to Thomson scattering profiles

- $\langle\beta\rangle$
  - Diamagnetic coil (compensate with Rogowski signal from helical winding current).
  - Segmented Rogowski coil—change in B_θ due to plasma pressure; model using equilibrium code.

ATF Multichannel FIR Interferometer System

15 channels, radial resolution = 3 cm

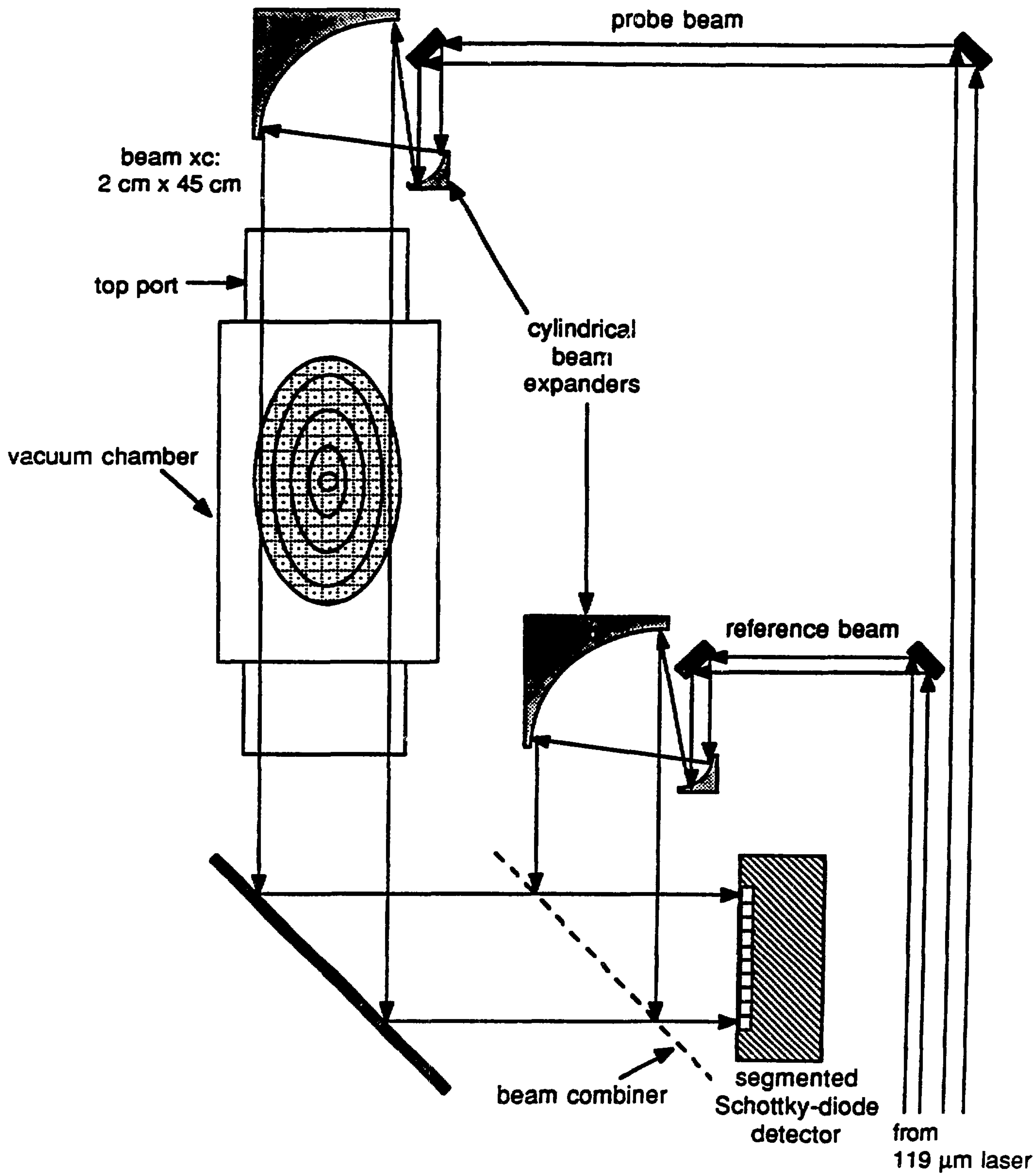

Concept for X-ray configuration array

- Soft X-ray signal $\propto n_e^2 T_e^{7/2} \Rightarrow$ peaked emission profile
- Example: T_e, $n_e \sim (1-\rho^2)$

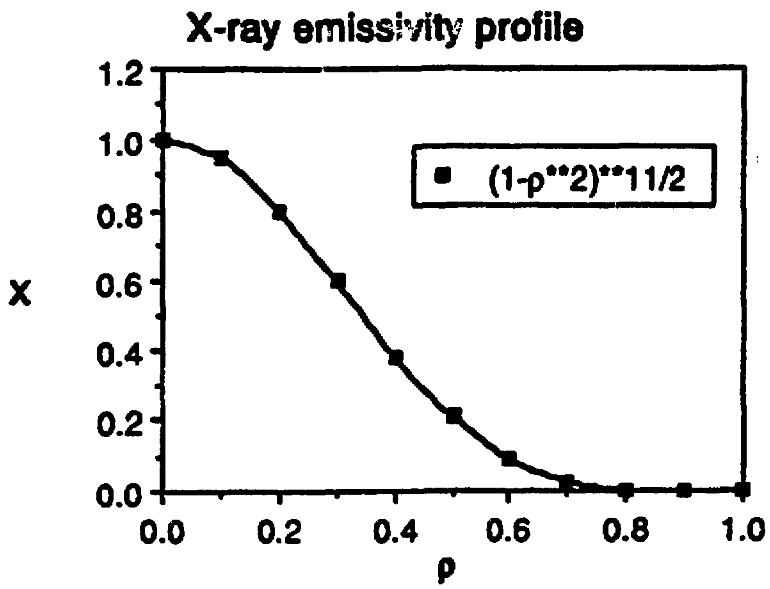

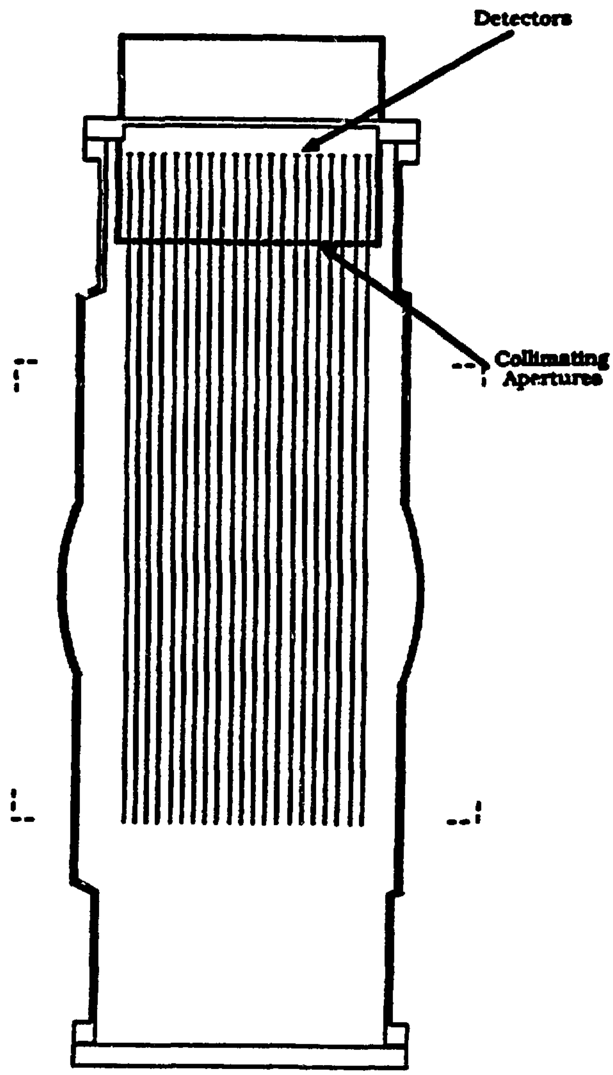

Proposed 15° Segments

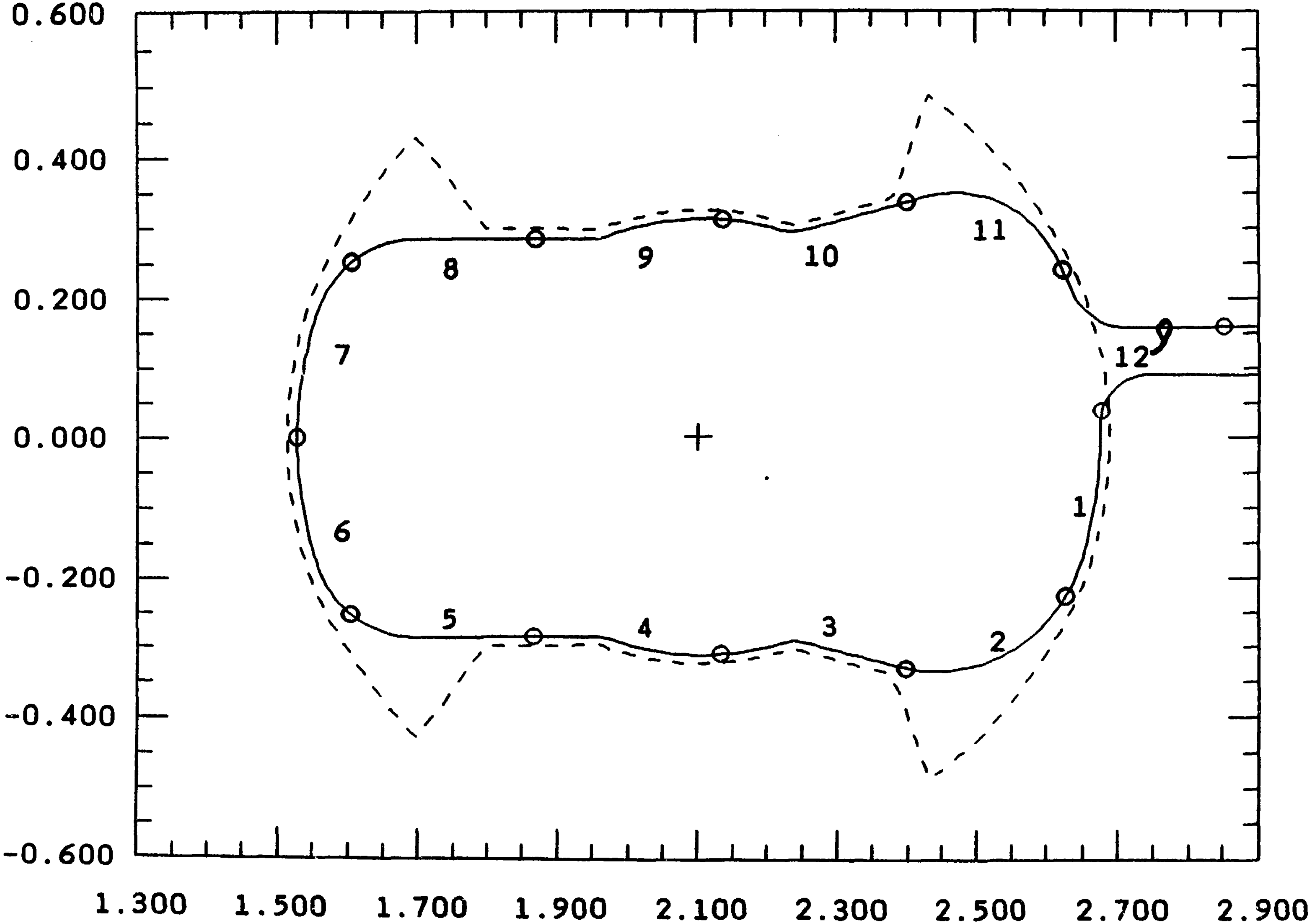

Tangential field calculated from field harmonics (Y_{mn})
fit to VMEC run, $\langle\beta\rangle = 2.4\%$, $B_o = \pm 1T$, Std. Vac. Config.
Fit file: ATFL24.OUT

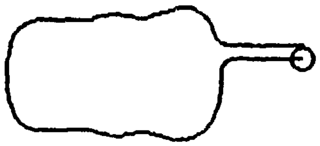

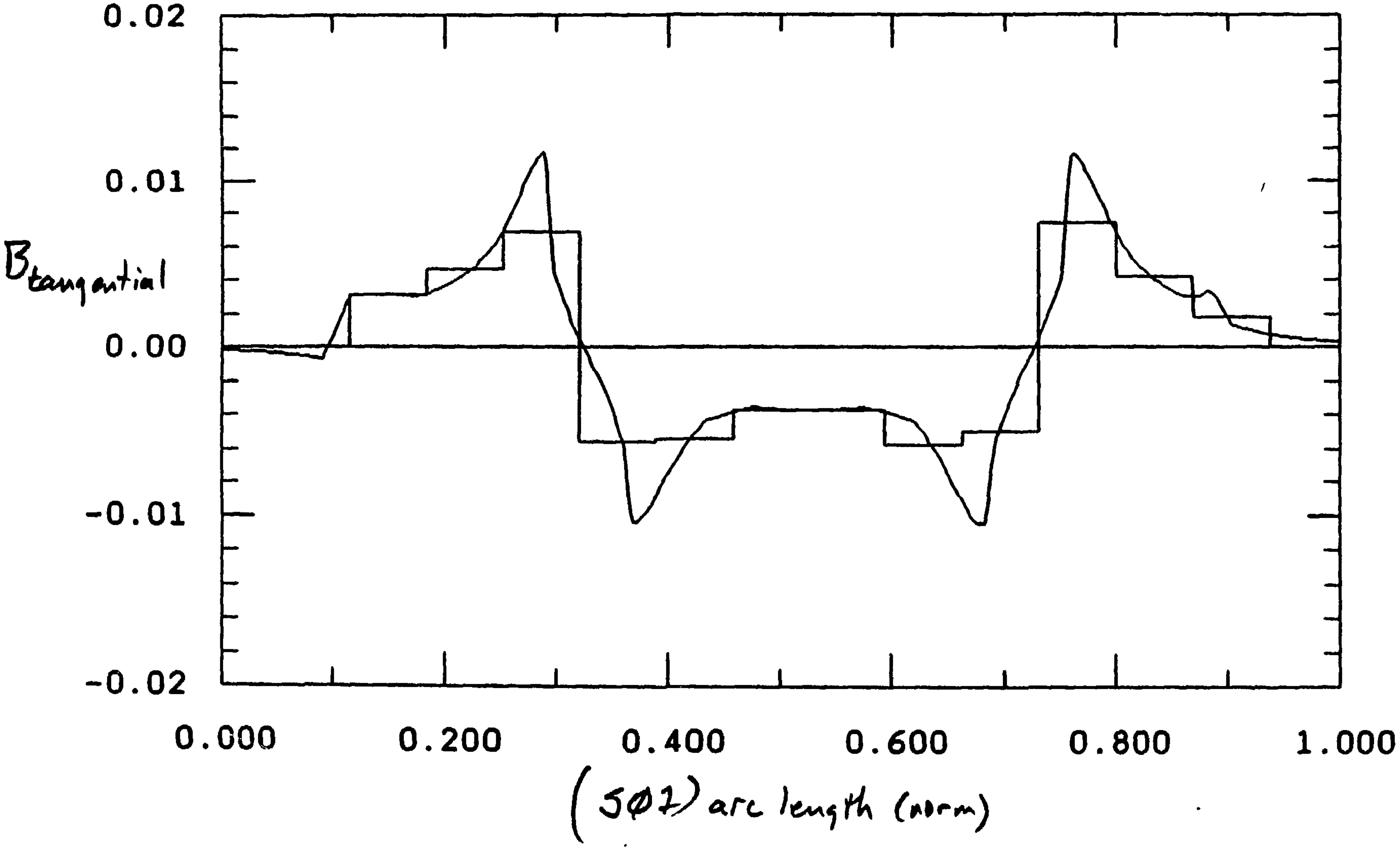

MAGNETIC FIELD ALIGNMENT

AND

MAGNETIC SURFACE MAPPING

ON

A.T.F.

SIMON ANDERSON
DICK COLCHIN
CLIFF EBERLE
DON HILLIS
AL ENGLAND
DOUG LEE
* A.T.F. GROUP
* AUBURN TORSATRON GROUP

OUTLINE

1) AREAS

COIL ALIGNMENT

SURFACE EXAMINATION

2) ALIGNMENT

ACCURACY

URAGAN III EXPERIMENT

A.T.F. TECHNIQUE

PROBLEMS

STATUS

3) SURFACE MAPPING

MOTIVATION

IMPLEMENTATION ON A.T.F.

TECHNIQUES AVAILABLE

A.T.F. ERRORS

STATUS

MAGNETIC FIELD ALIGNMENT MEASUREMENTS ON ATF

PROBLEM

- COIL MISALIGNMENTS AS SMALL AS 1% OF THE MAJOR RADIUS CAN CAUSE BREAKUP OF THE OUTER FLUX SURFACES ON TORSATRONS, THEREBY REDUCING THE CONFINED PLASMA VOLUME.

SOLUTION

- MAGNETIC FIELD MEASUREMENTS WILL BE USED ON ATF TO PINPOINT THE CENTRAL (DIPOLE) AXIS OF EACH COIL SET. (THERE ARE THREE VERTICAL FIELD AND ONE HELICAL COIL SETS ON ATF.)

  - THE ACCURACY OF THESE MEASUREMENTS MUST BE ~±1 mm.

  - ALL MAGNETIC FIELD MEASUREMENTS ARE TO BE MADE WITH THE COILS OPERATING STEADY STATE, AT REDUCED POWER.

ALIGNMENT CRITERIA

PREVIOUS WORK OF MASDEN
LYNCH
HARRIS
CANTRELL

NOW: D. COLCHIN
D. LEE.
A. ENGLAND
S. ANDERSON
& A.T.F. BODIES

TO STOP SURFACE BREAK-UP OR ISLATION

① V.F. AXES MUST BE CENTERED $\lesssim$ 1-2 cm

② V.F. TILTS MUST BE $\lesssim$ 1-2 cm EITHER ALONE OR AS PAIR

③ OUT-OF-ROUND $\lesssim$ 1 cm (ELLIPSE)

④ OUT-OF-PLANE $\lesssim$ 1-5 cm (WAVE)

⑤ CURRENT FEEDS ? [NOT TOO CRITICAL IF SMALL DIPOLE!]

CUMULATIVE ERRORS MAY OR MAY-NOT AFFECT OVERALL SURFACE QUALITY, DEPENDING ON PHASE OF RELATIVE ERRORS.

THE ALIGNMENT APPARATUS IS DESIGNED PRIMARILY FOR AXIS-SHIFT MEASUREMENTS.

IF OTHER PROBLEMS ARE FOUND, SOME SORT OF FITTING TO A REPRESENTATIVE MODEL, FROM A LARGE NUMBER OF MEASUREMENTS, WILL NEED TO BE PERFORMED

⇒ NEED TO CORRELATE TO ELECTRON-BEAM SURFACE MAPPING MEASUREMENTS

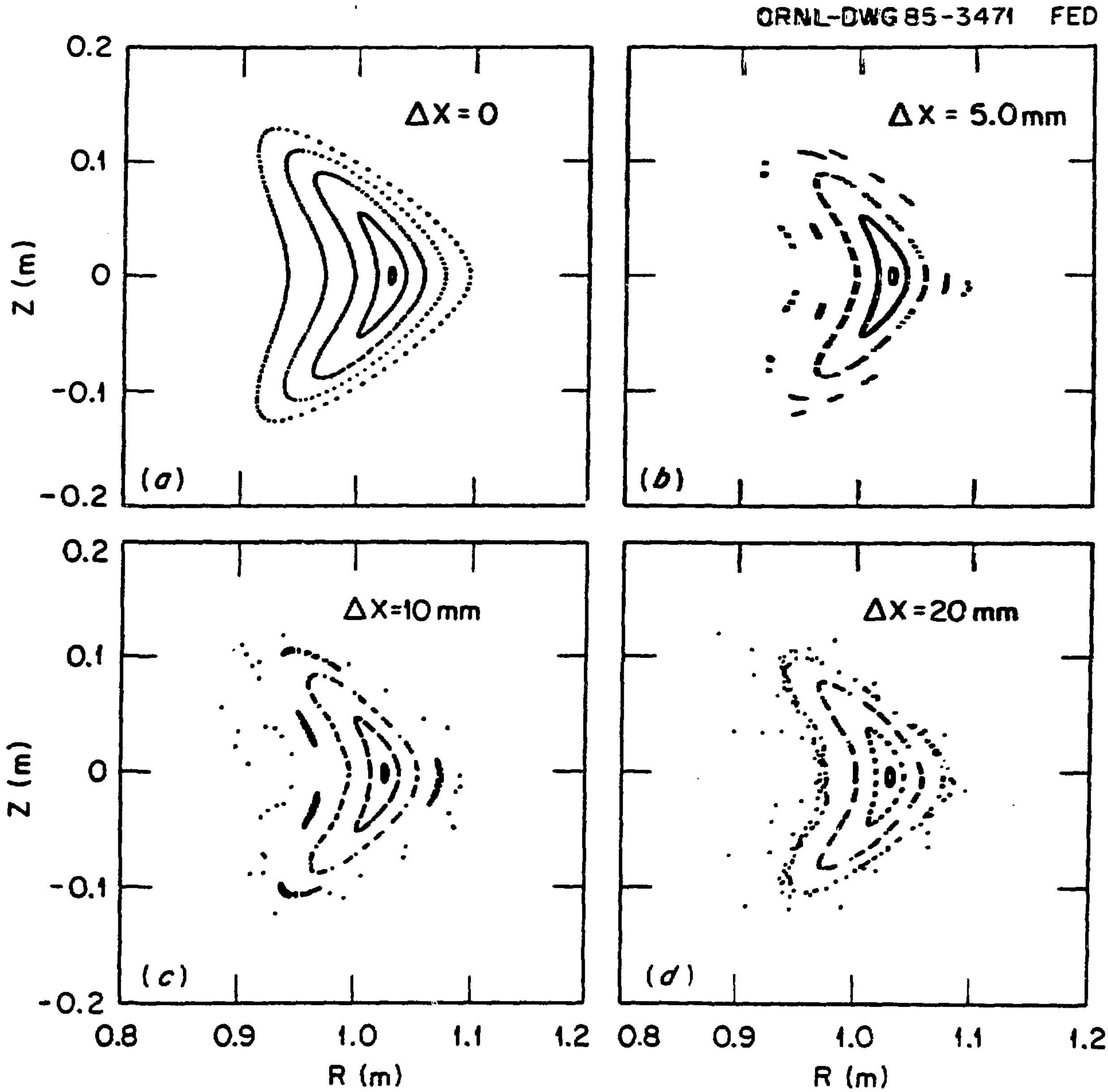
ORNL-DWG 85-3471 FED
ΔX = 0
ΔX = 5.0 mm
ΔX = 10 mm
ΔX = 20 mm
(a)
(b)
(c)
(d)
Z (m)
R (m)
0.2
0.1
0
-0.1
-0.2
0.8
0.9
1.0
1.1
1.2

ATF transform profile

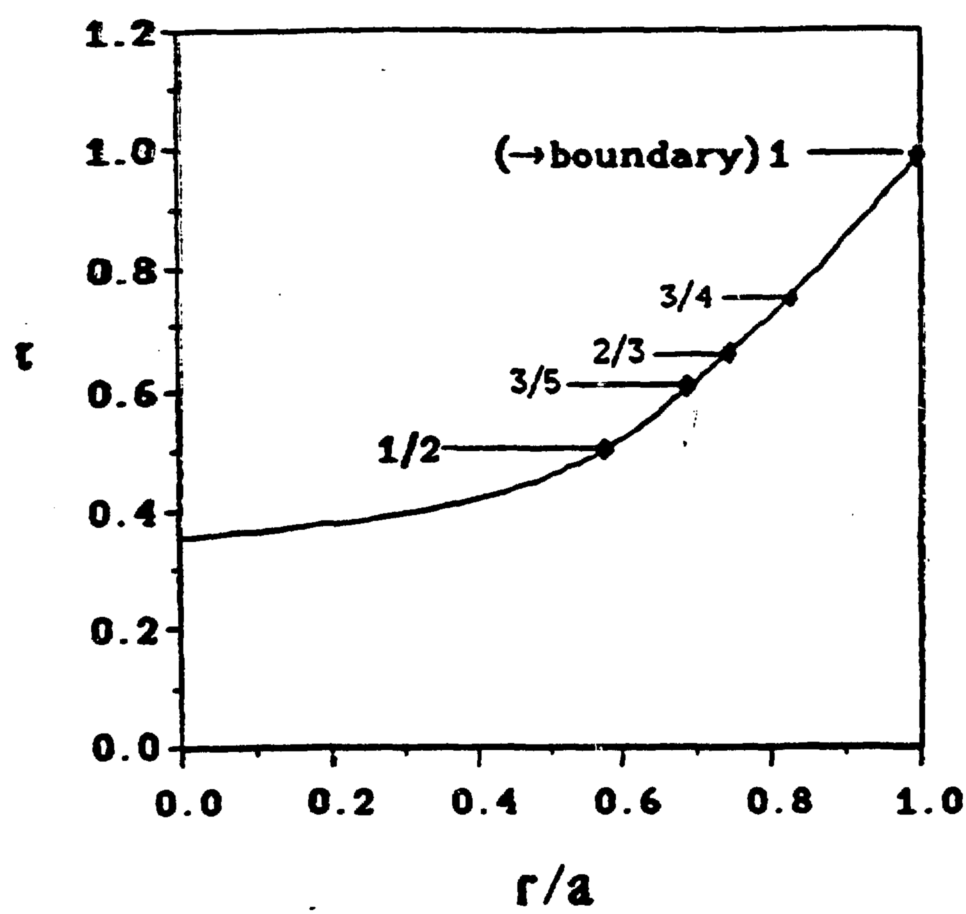

Key resonances: $\iota = 1/2$

$\iota = 1$

Defense Against Field Errors

- Overall system design
  - Choice (or avoidance) of resonances
  - Engineering design concept
- Construction and alignment
  - Tolerances
- Perturbations
  - Buswork
  - Magnetic materials
- Measurements
  - Magnetic fields
  - Flux surfaces (ultimately)
- Error correction
  - Concepts for correction coils

External perturbation fields

- Magnetic materials
  - Significant stray field

    → $|B| \gtrsim 1$ kG for $R \lesssim 3$ m in plane of device
  - Iron used in beamlines, diagnostic shielding, etc.
  - Model as equivalent dipoles using local fields
  - Field line studies show that perturbations drop rapidly if iron moved out from outer VF coils
- Buswork and current feeds
  - Model using line segments in field line code
  - Minimize dipole-like fields by minimizing loop area and using cancellation, higher-order multipoles wherever possible

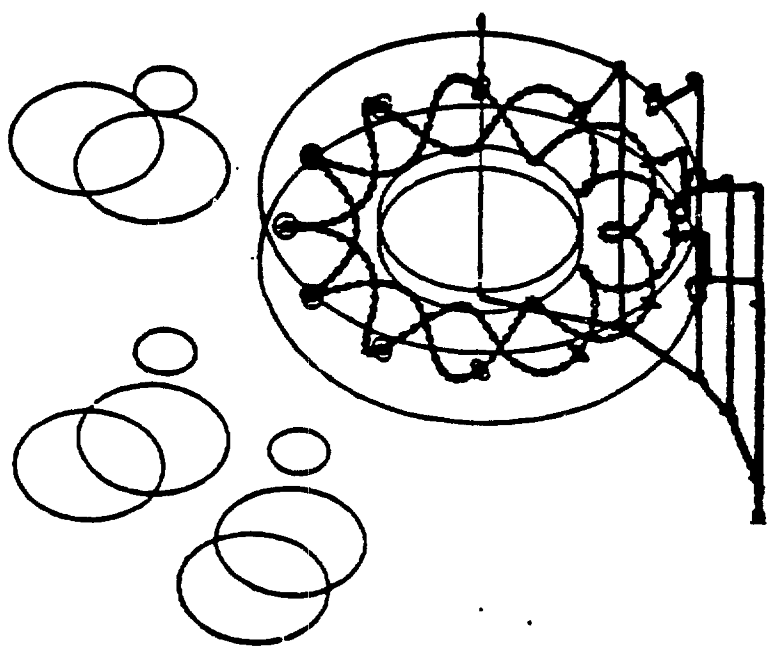

Islands produced by magnetized iron

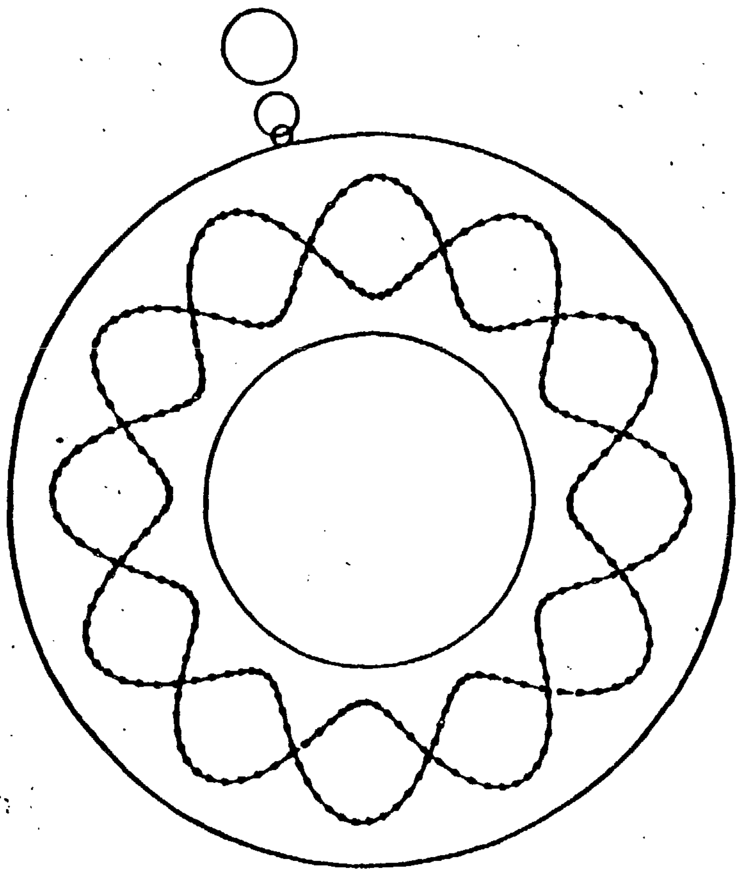

Asymmetric

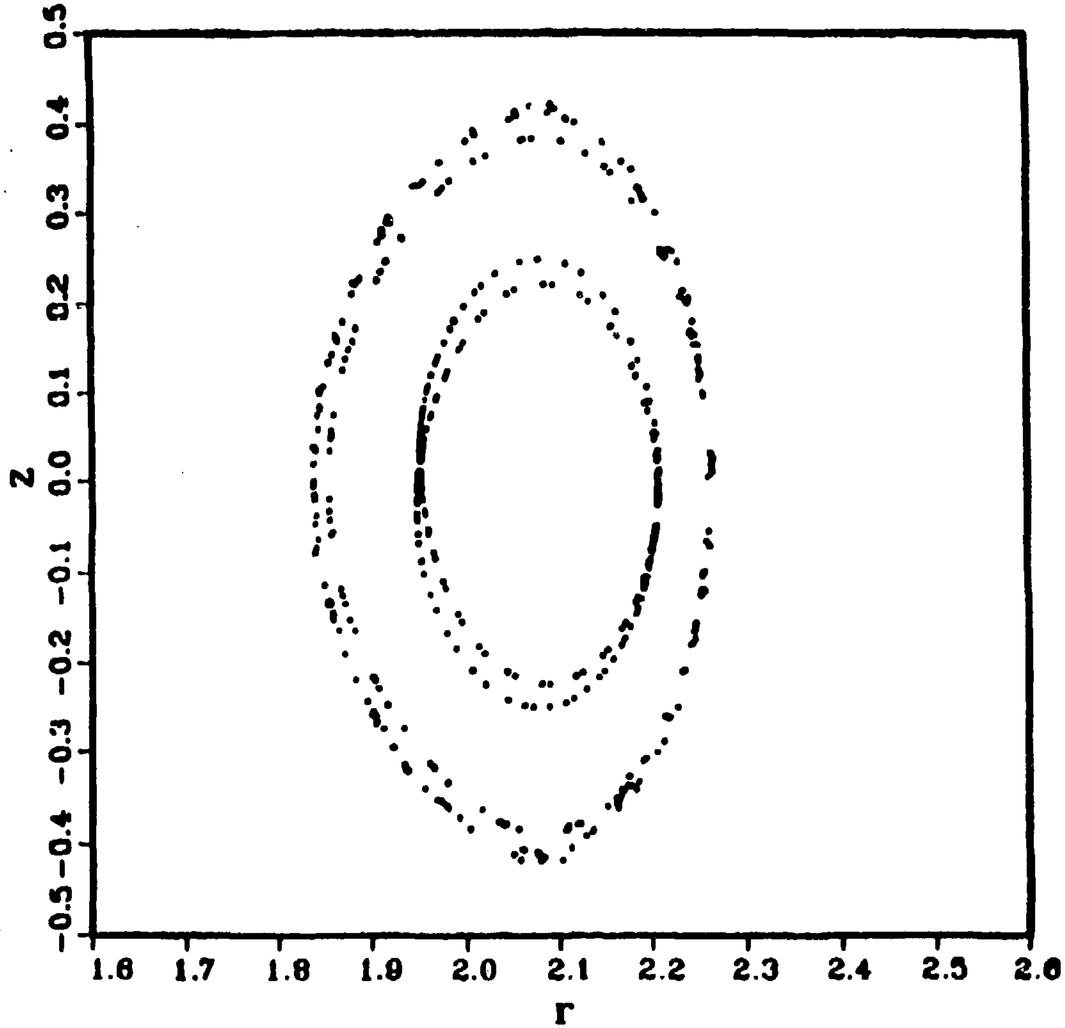

Effect of resonant field error

$$\frac{\Delta B}{B} = \delta \cos(2\theta - \phi)$$

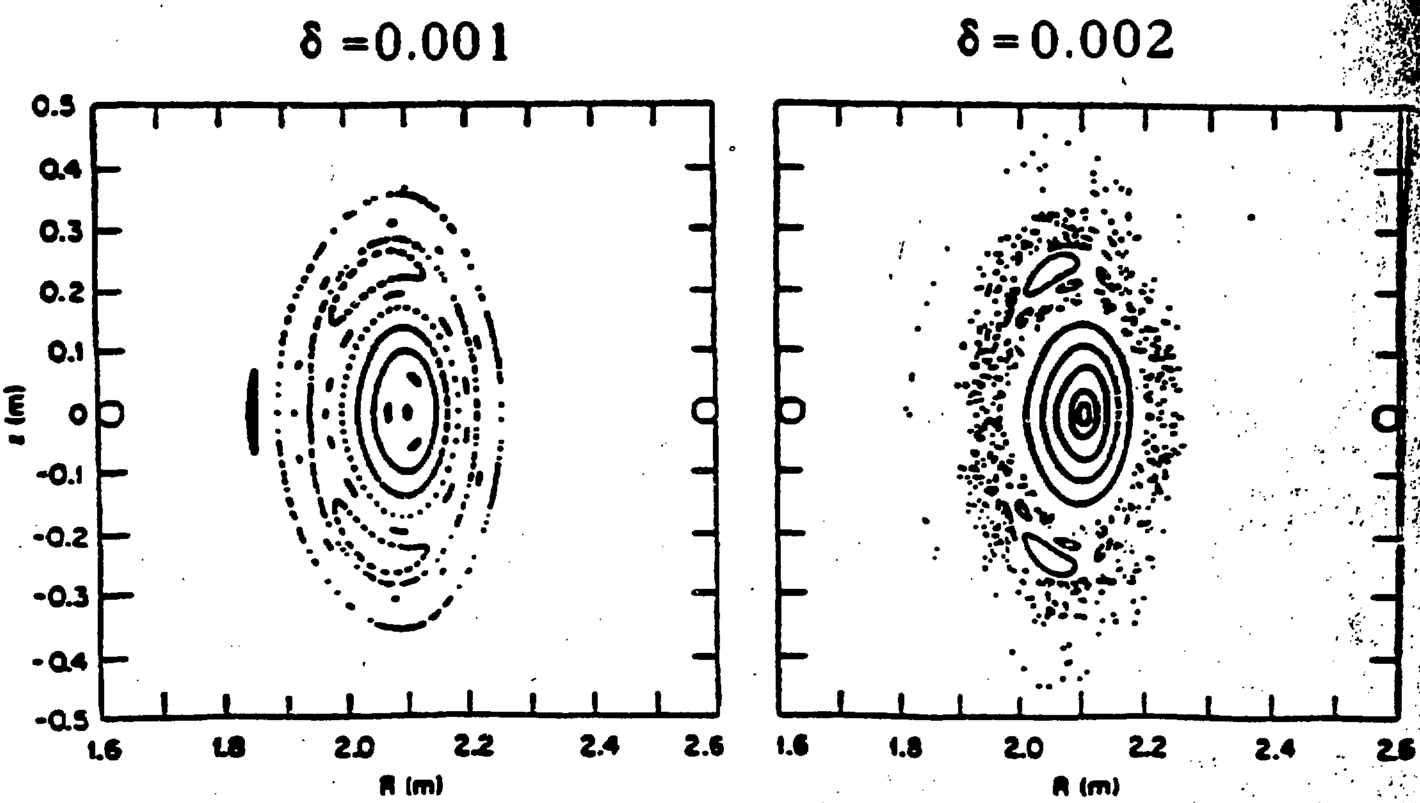

MAGNETIC FIELD ALIGNMENT MEASUREMENTS ON ATF

- THE CENTRAL REGION OF ATF HAS BEEN KEPT CLEAR SO THAT MAGNETIC FIELD MEASUREMENTS MAY BE MADE AROUND THE MACHINE AXIS.
- THESE TECHNIQUES WERE PIONEERED ON THE URAGAN-3 TORSATRON AT KHARKOV*.

*REV. SCI. INSTRUM. 57(7) JULY 1986, 1233

MAGNETIC FIELD ALIGNMENT PROBE IN ATF

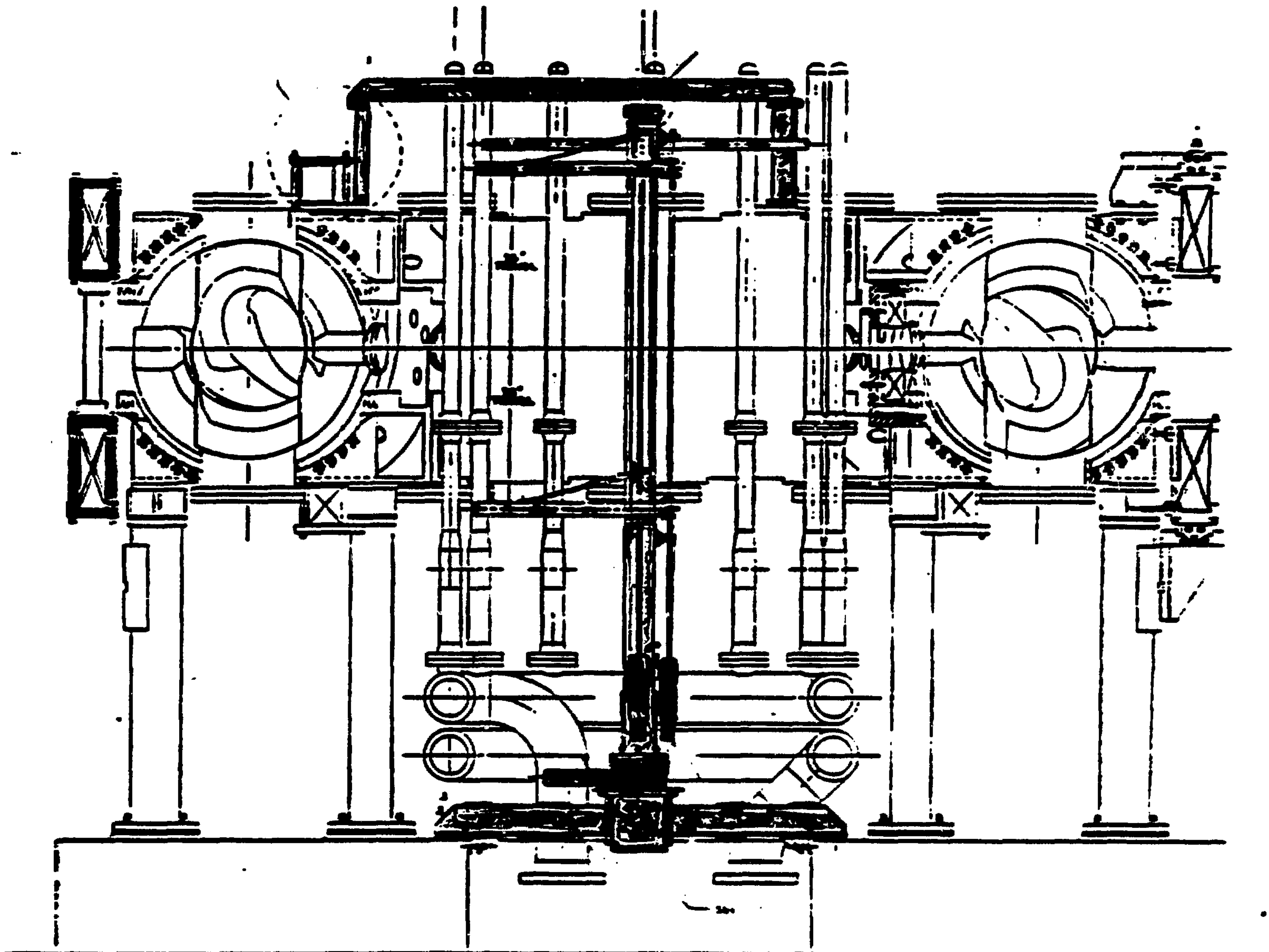

OUTER VERTICAL FIELD COILS - B_r

PLOT IN THE X-Y PLANE, Z-0, B_r(TESLA),COIL CURRENTS OPPOSING

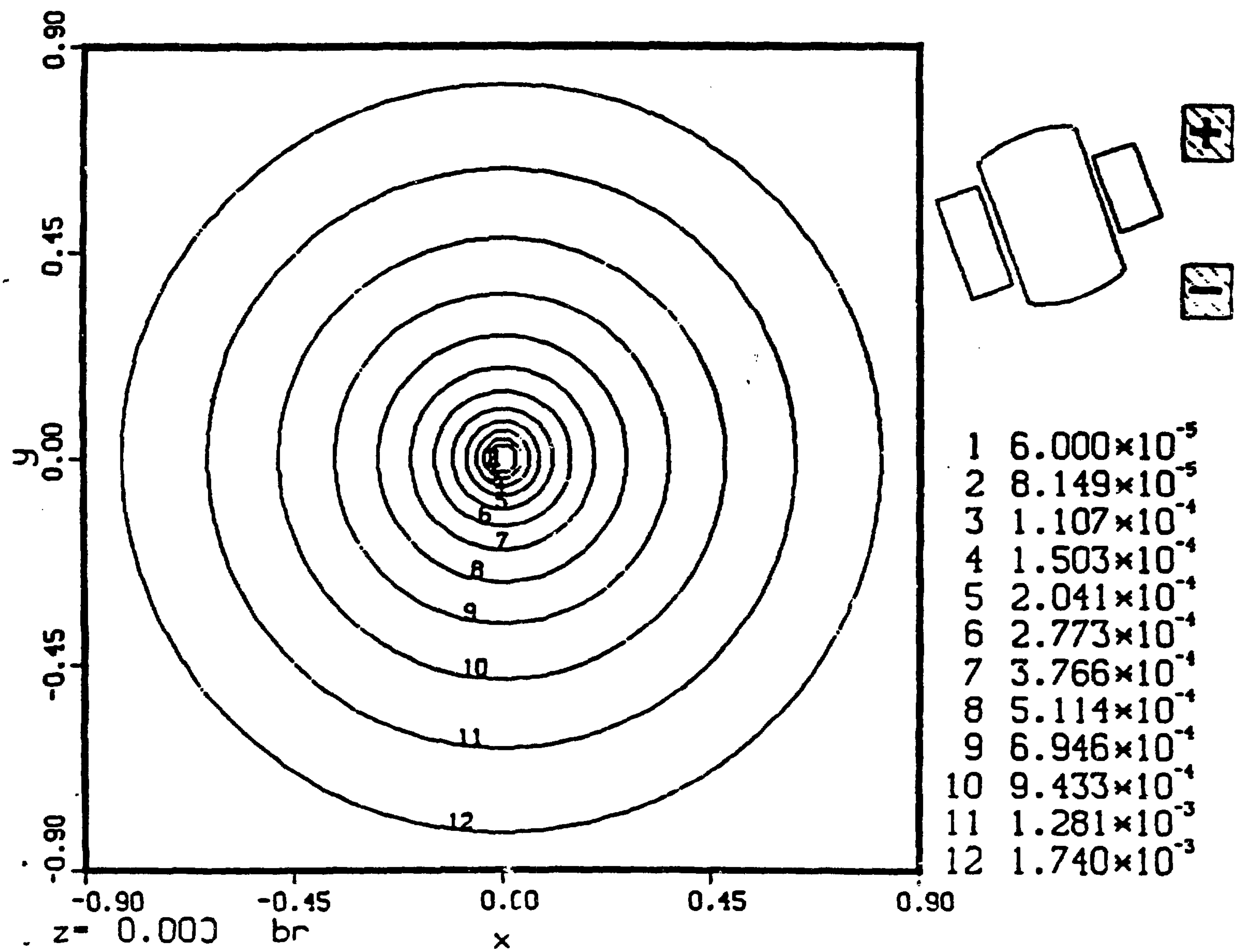

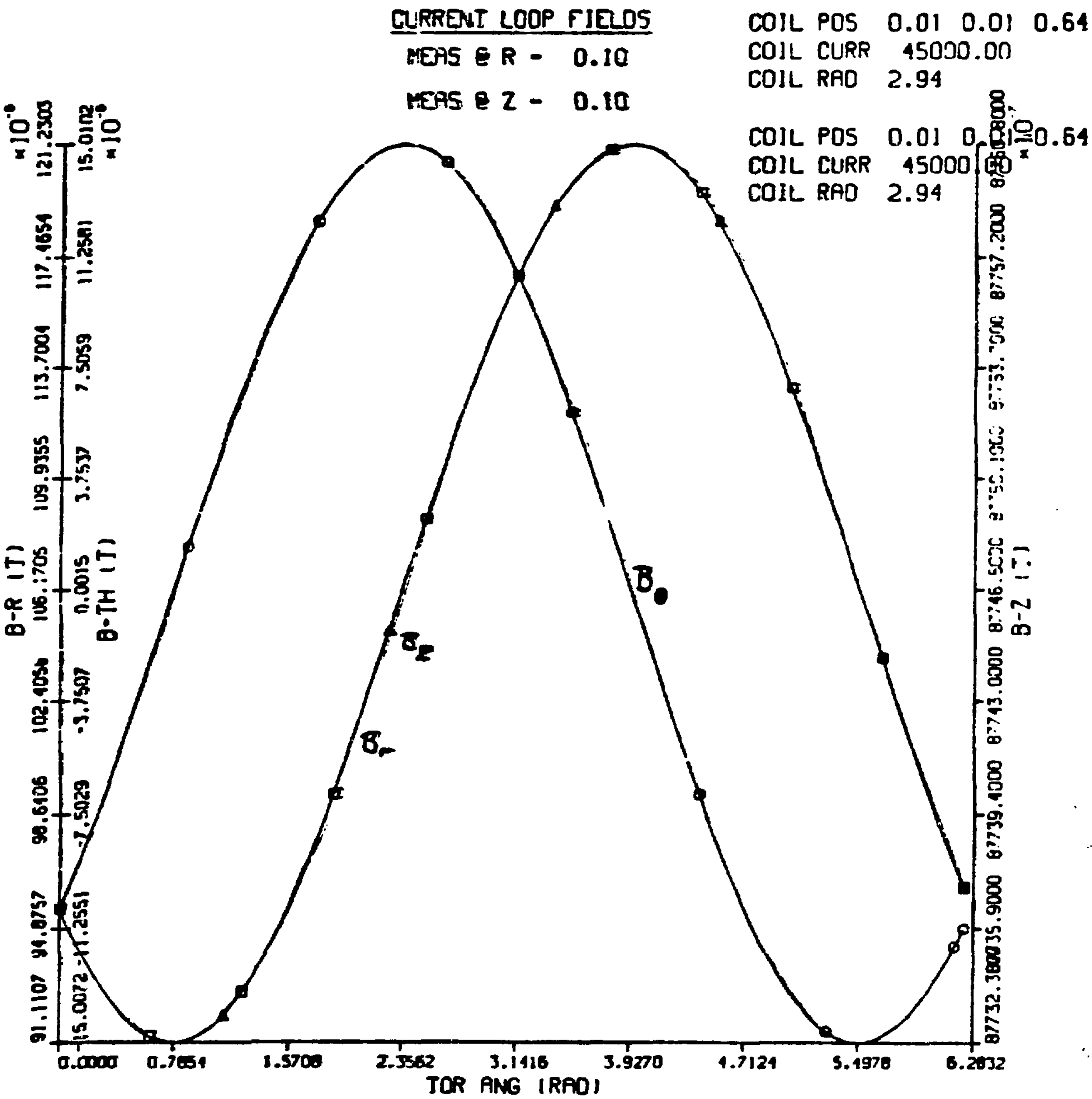

CURRENT LOOP FIELDS
MEAS @ R - 0.10
MEAS @ Z - 0.10
COIL POS 0.01 0.01 0.64
COIL CURR 45000.00
COIL RAD 2.94
COIL POS 0.01 0.01 0.64
COIL CURR 45000.00
COIL RAD 2.94
B-R (T)
B-TH (T)
B-Z (T)
TOR ANG (RAD)
0.0000
0.7854
1.5708
2.3562
3.1416
3.9270
4.7124
5.4978
6.2832
91.1107
94.8757
98.6406
102.4056
106.1705
109.9355
113.7004
117.4654
121.2303
15.0072
11.2551
7.5029
3.7507
0.0015
3.7537
7.5059
11.2581
15.0102
87732.3800
87735.9000
87739.4000
87743.0000
87746.5000
87757.2000
87760.8000

HELICAL FIELD COILS - B_r

PLOT IN THE X-Y PLANE, Z=0, B_r(TESLA), COIL CURRENTS OPPOSING

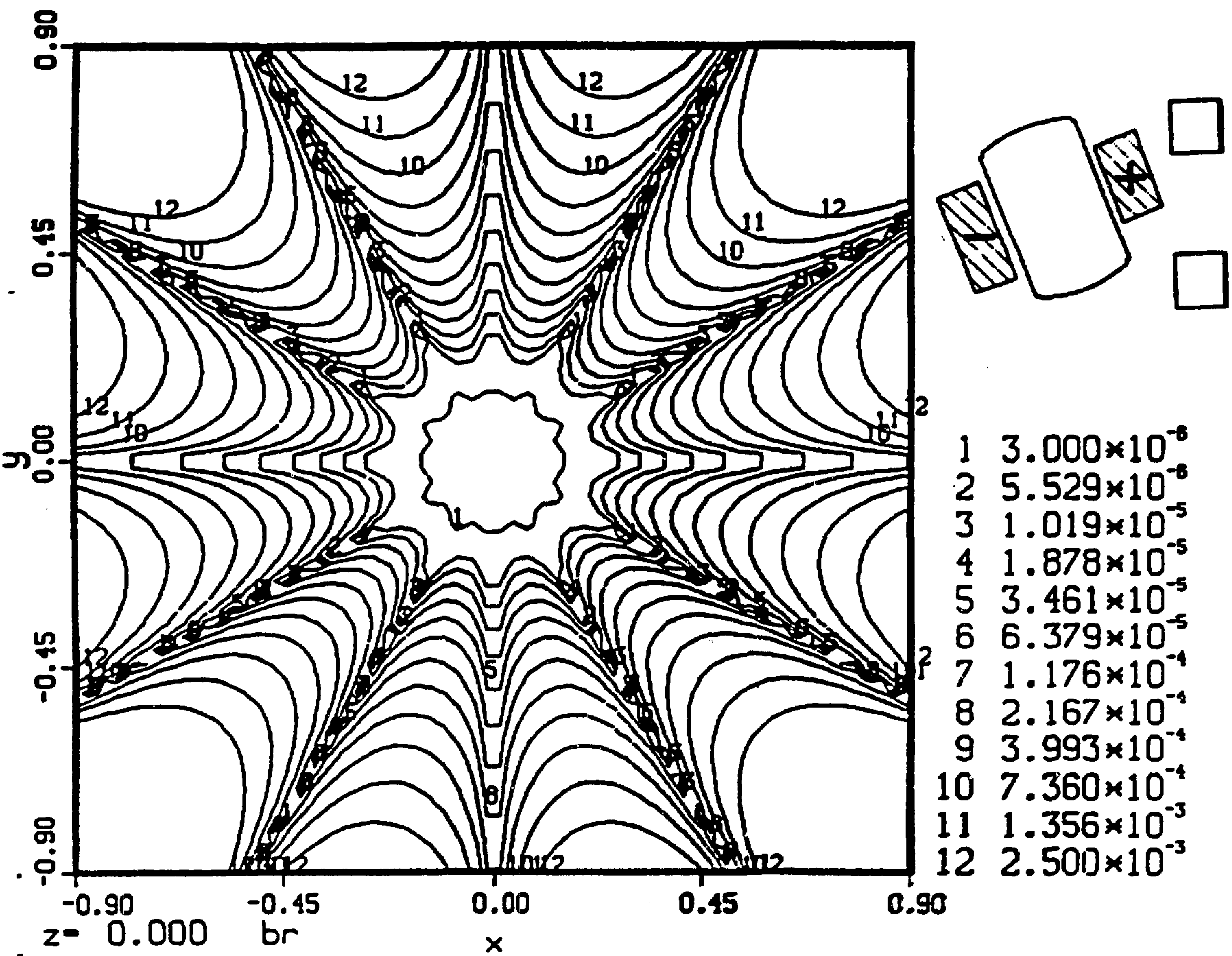

STATUS

- FIXTURE MANUFACTURE IS COMPLETE
- COMPUTER CONTROL PROGRAM IS COMPLETE
- COMPUTER ANALYSIS PROGRAMS ARE COMPLETE

TO BE DONE

- TEST FIXTURE
- REWORK BUSS FEEDS TO COIL SETS TO GET APPROPRIATE CURRENT SENSES
- INSTALL AND ALIGN FIXTURE IN THE CENTER OF A.T.F.
- PERFORM EXPERIMENT

ELECTRON BEAM MEASUREMENTS ON ATF

- PROVISIONS HAVE BEEN MADE FOR MAPPING FLUX SURFACES IN ATF BY THE FOLLOWING TECHNIQUES:
  - ELECTRON BEAM PICKUP PROBES (TRADITIONAL METHOD).
  - DIODE TECHNIQUE.
  - TRIODE TECHNIQUE.
  - FLUORESCENT SCREEN/WIRE METHOD.
- ALL MEASUREMENTS WILL BE MADE STEADY STATE, AT REDUCED FIELDS.

Model problem for error field correction studies

Unperturbed

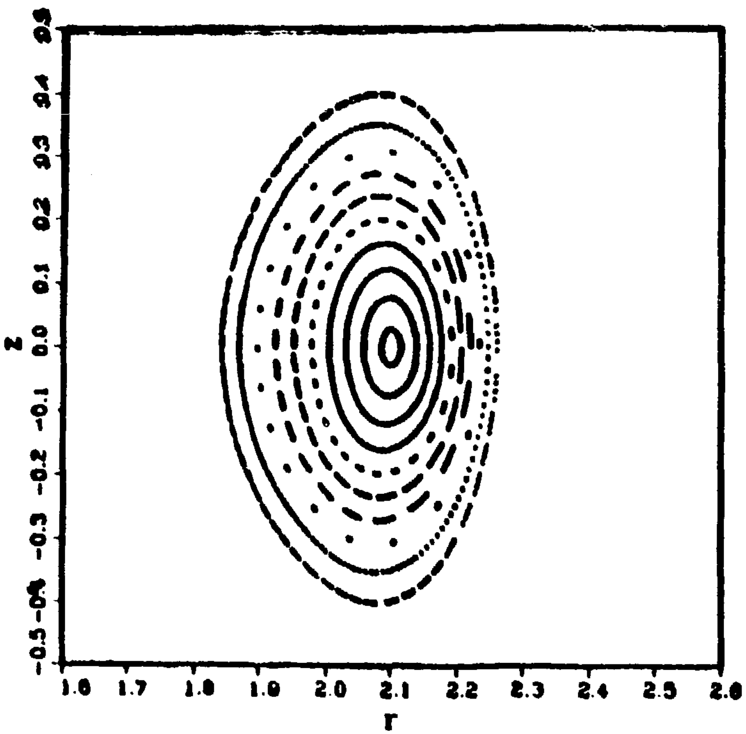

With horizontal error field

$$\frac{B_{hor}}{B_0} = 5 \times 10^{-4}$$

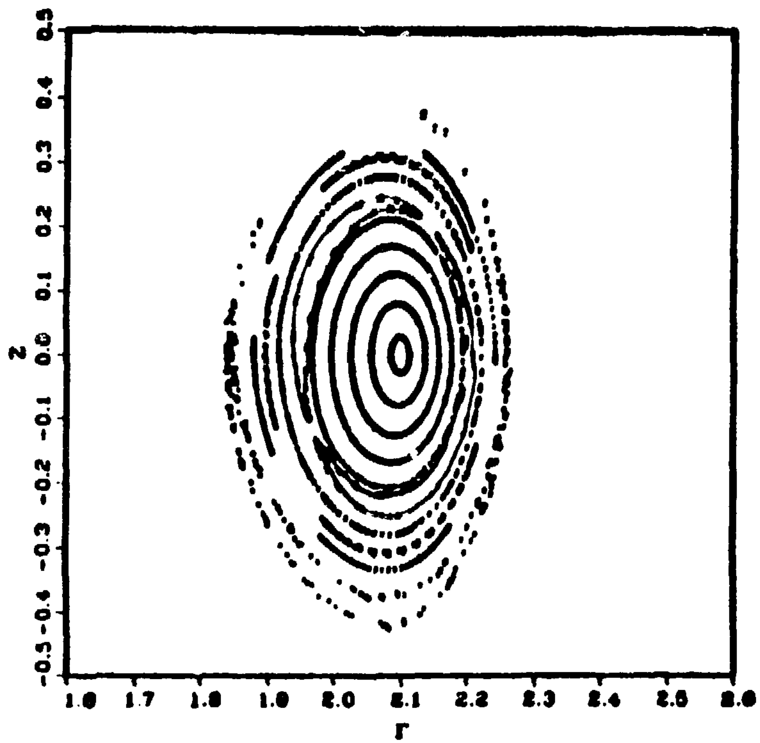

PICKUP PROBE TECHNIQUE

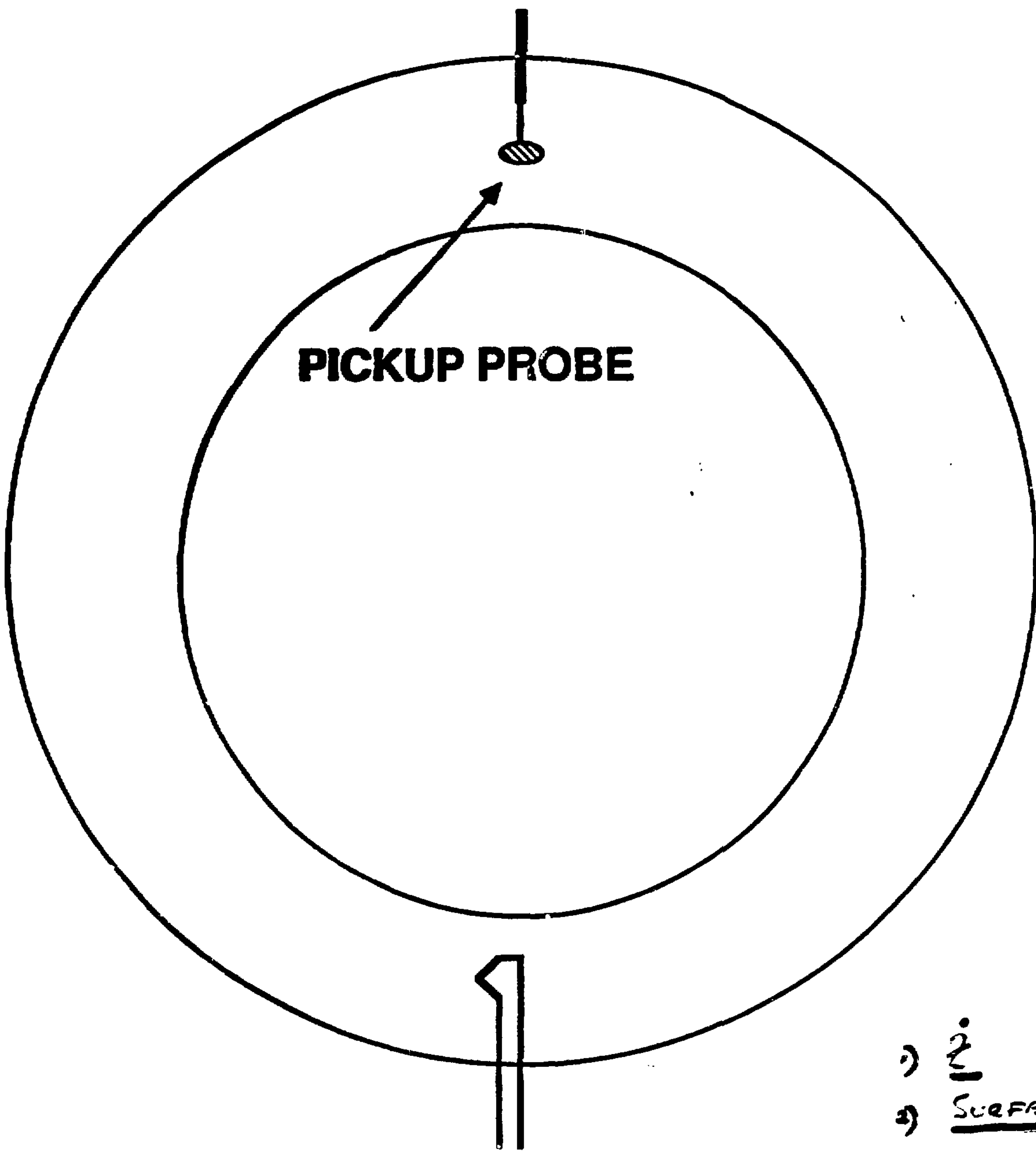

1) $\dot{z}$
2) SURFACES
3) r_0

DIODE TECHNIQUE

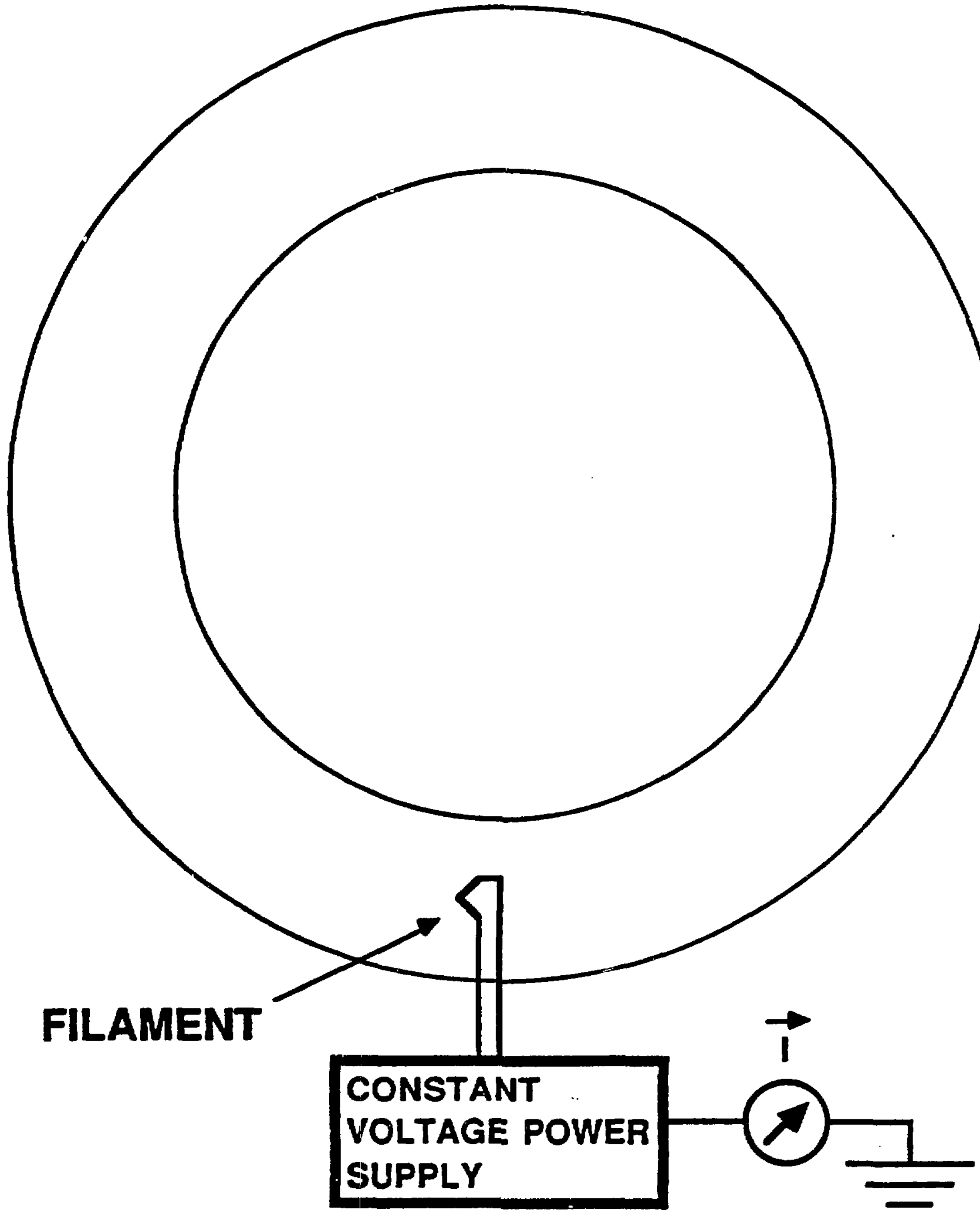

TRIODE TECHNIQUE

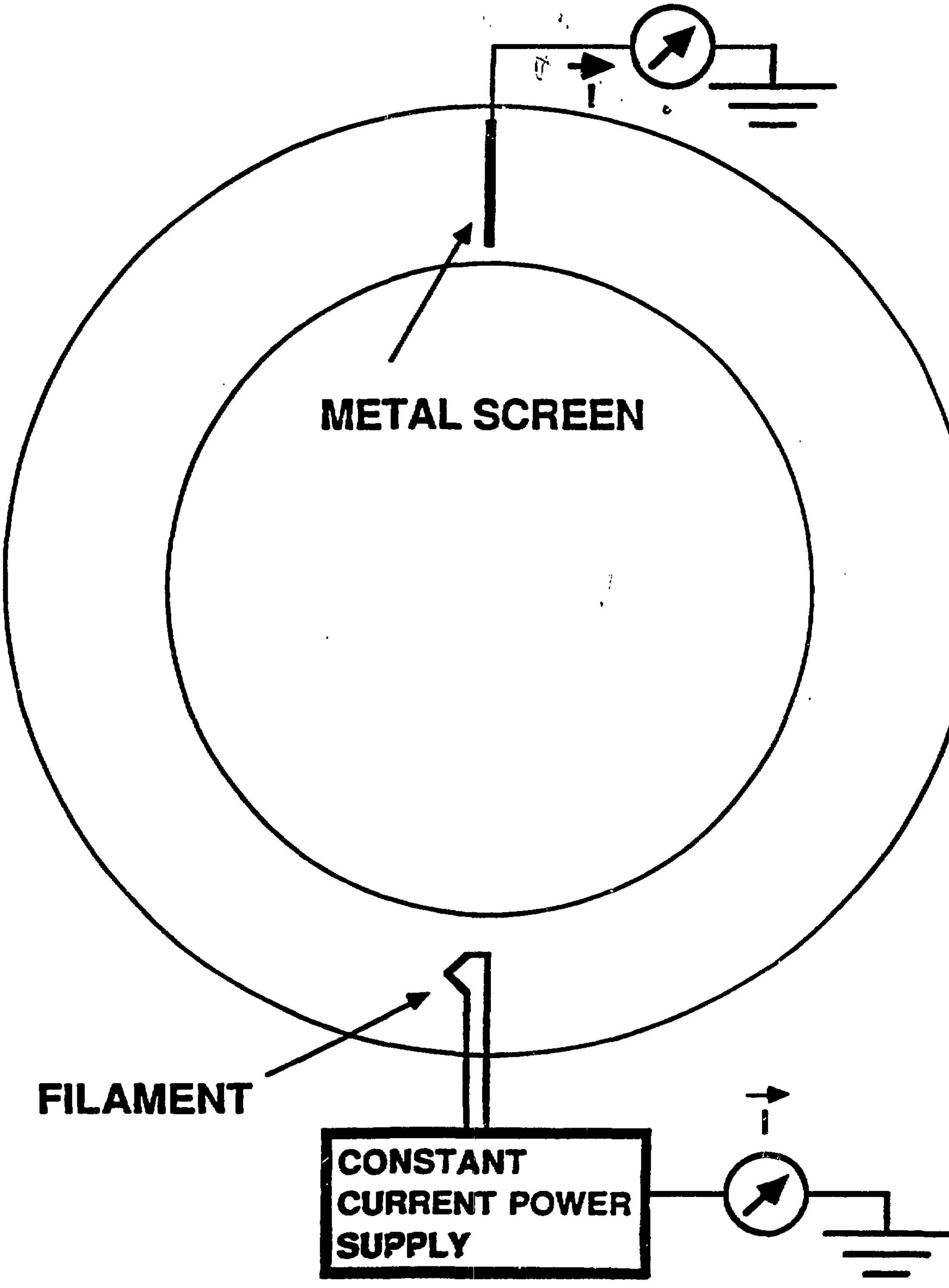

FLUORESCENT SCREEN TECHNIQUE

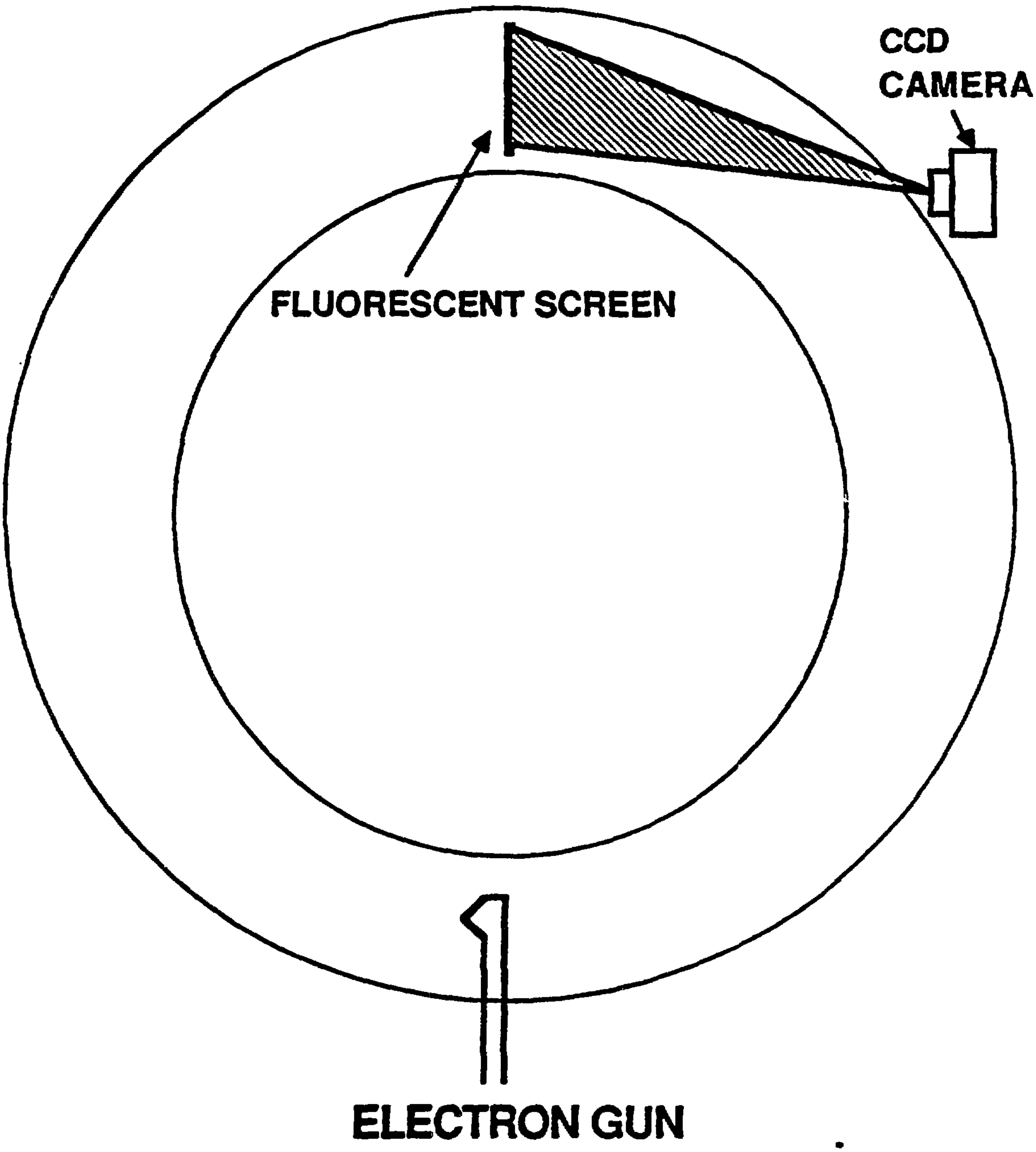

COMPARISON BETWEEN EMISSIVE DIODE AND FLUORESCENT GRID

TECHNIQUE IN MAGNETIC FLUX MAPPING ON AUBURN TORSATRON

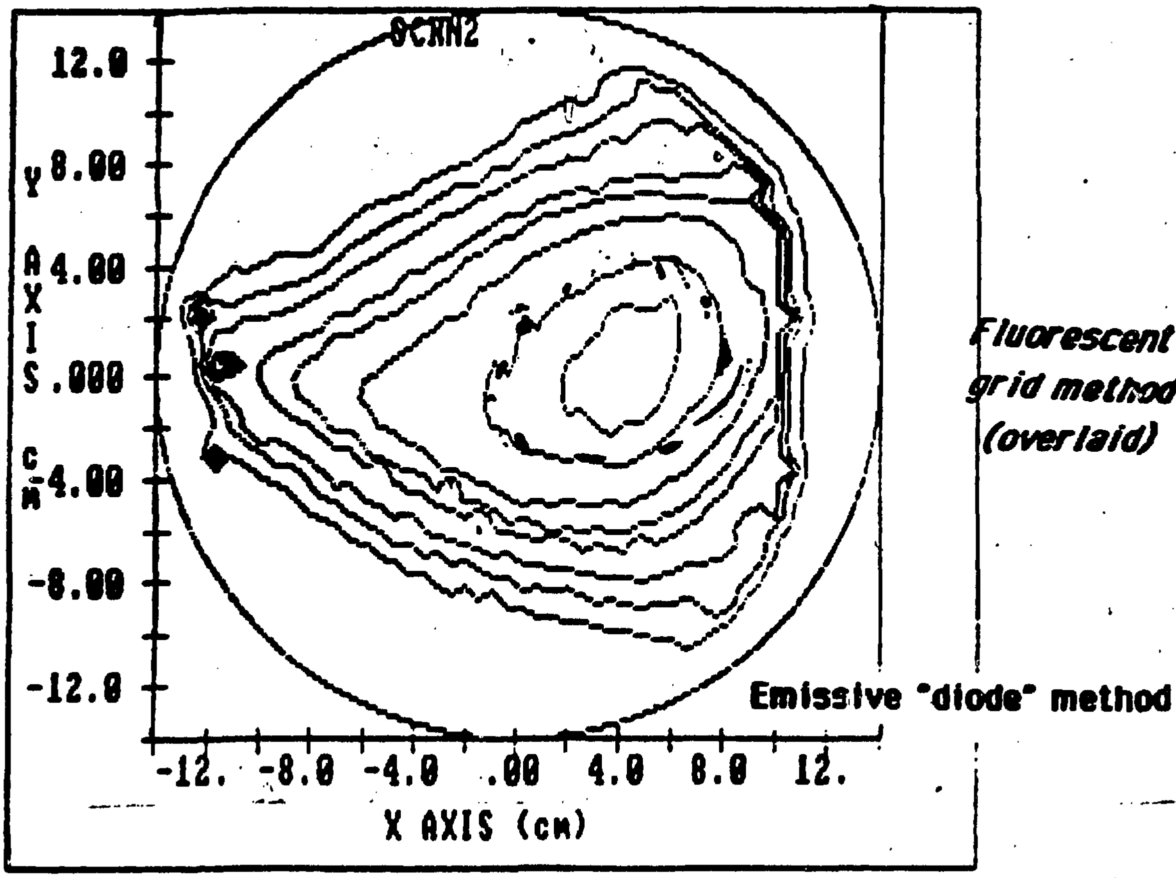

Fluorescent grid method

(courtesy of R. F. Gandy)

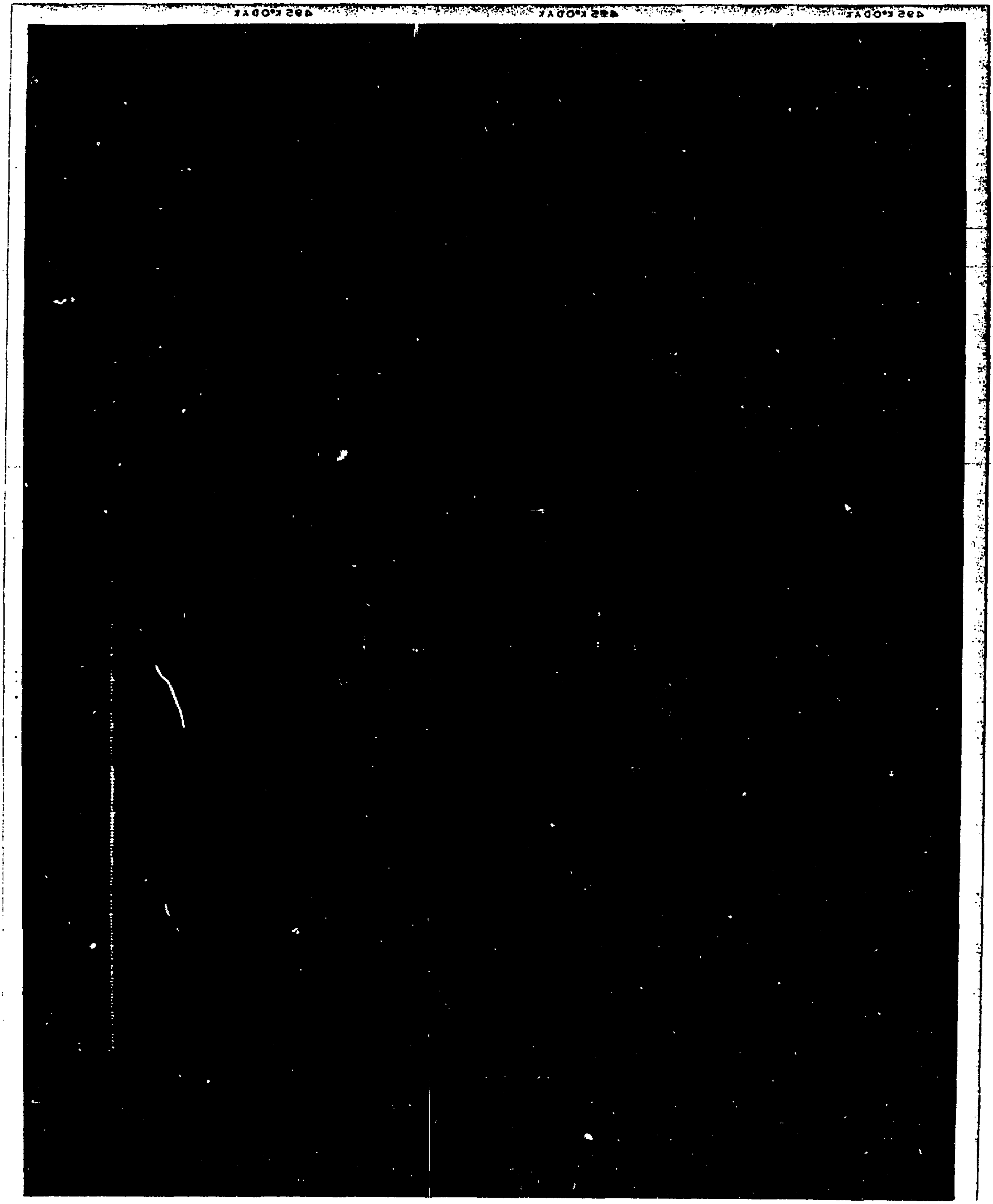

Auburn Torsatron

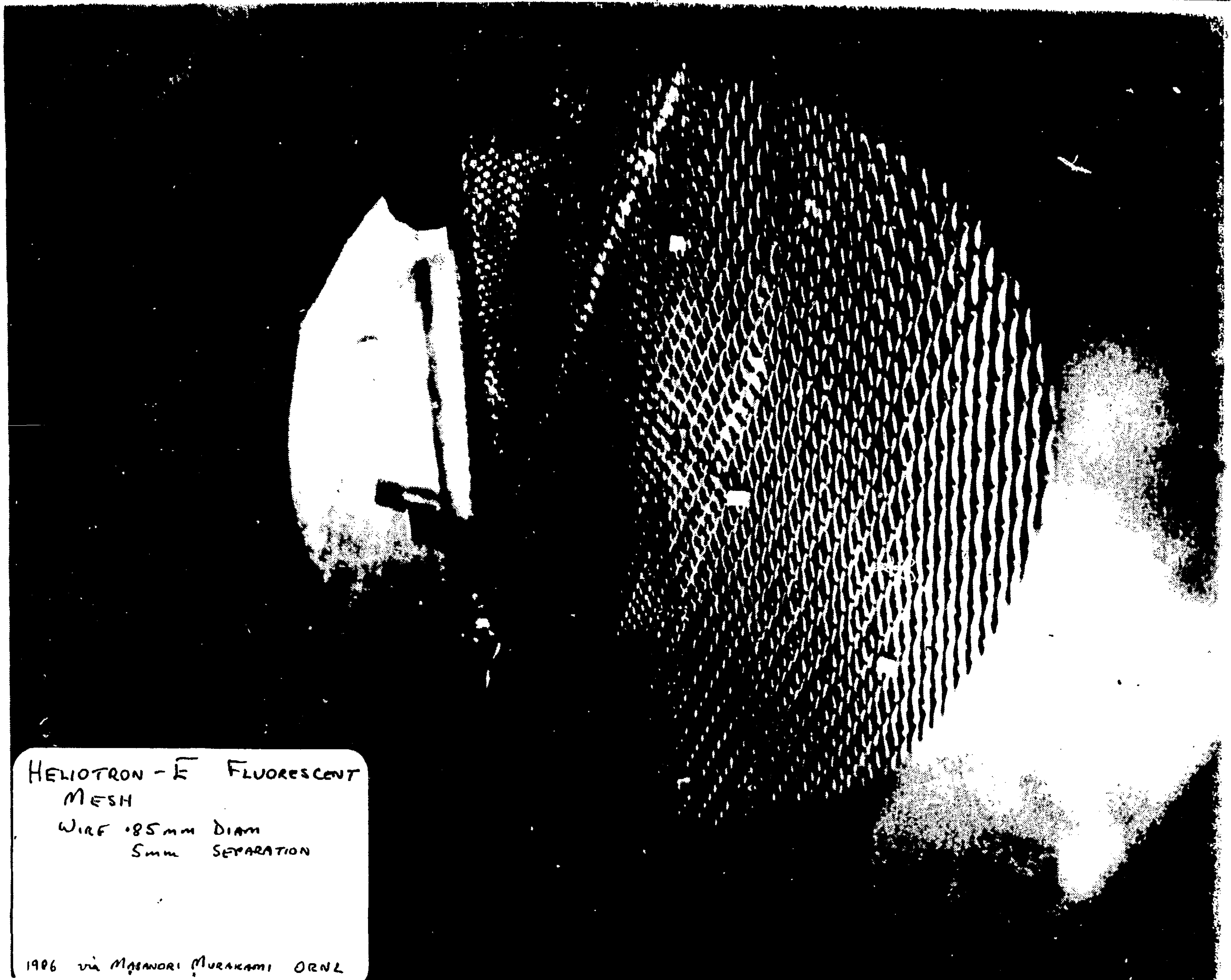
HELIOTRON - E FLUORESCENT
MESH
WIRE ·85mm DIAM
5mm SEPARATION
1986 via MASANORI MURAKAMI ORNL

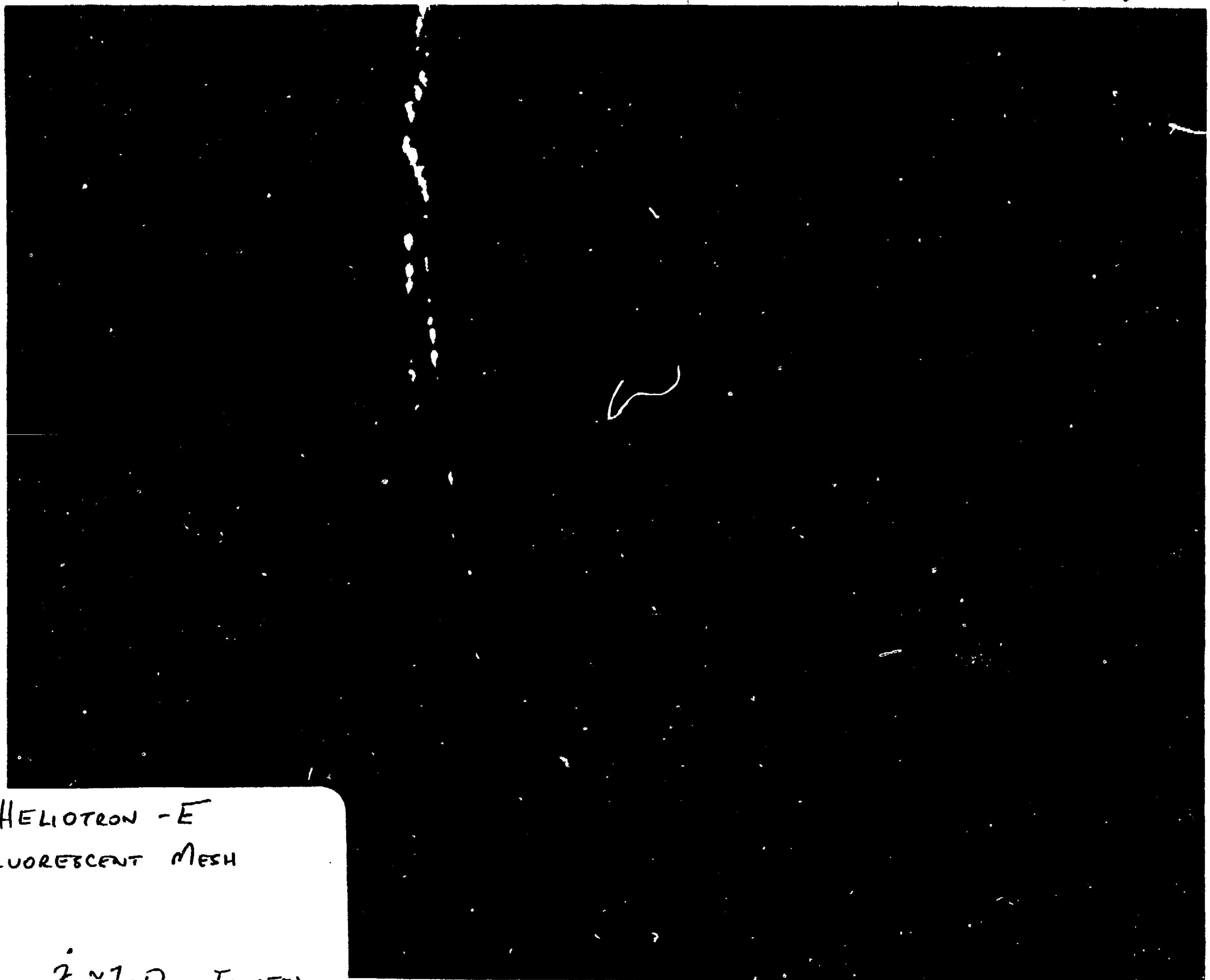

HELIOTRON -E
FLUORESCENT MESH

$\dot{\iota} \sim 1.0$ ISLATED

1986

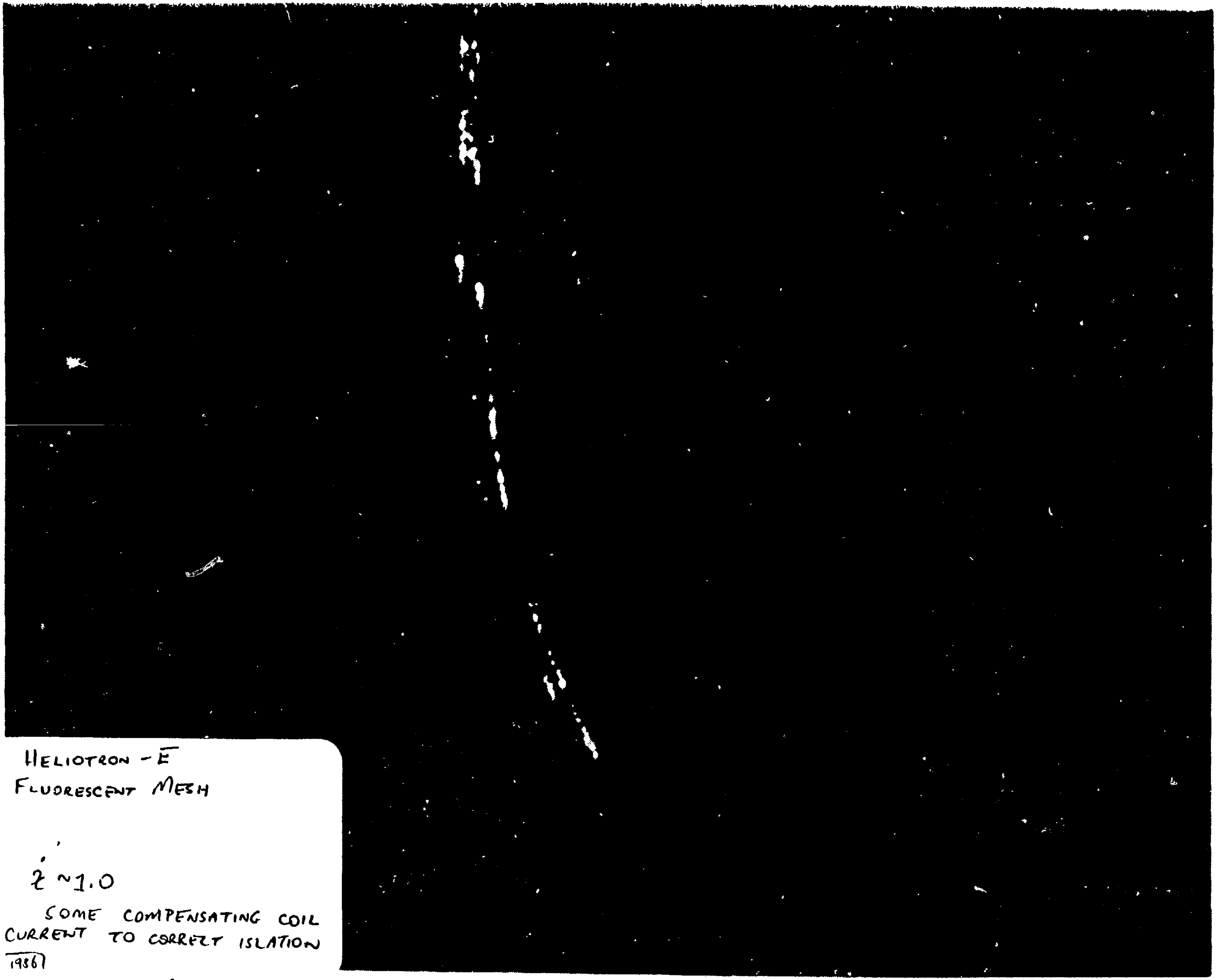

HELIOTRON - E
FLUORESCENT MESH

$\dot{\iota} \sim 1.0$

SOME COMPENSATING COIL CURRENT TO CORRECT ISLATION

1986

X-Y PROBE DRIVE

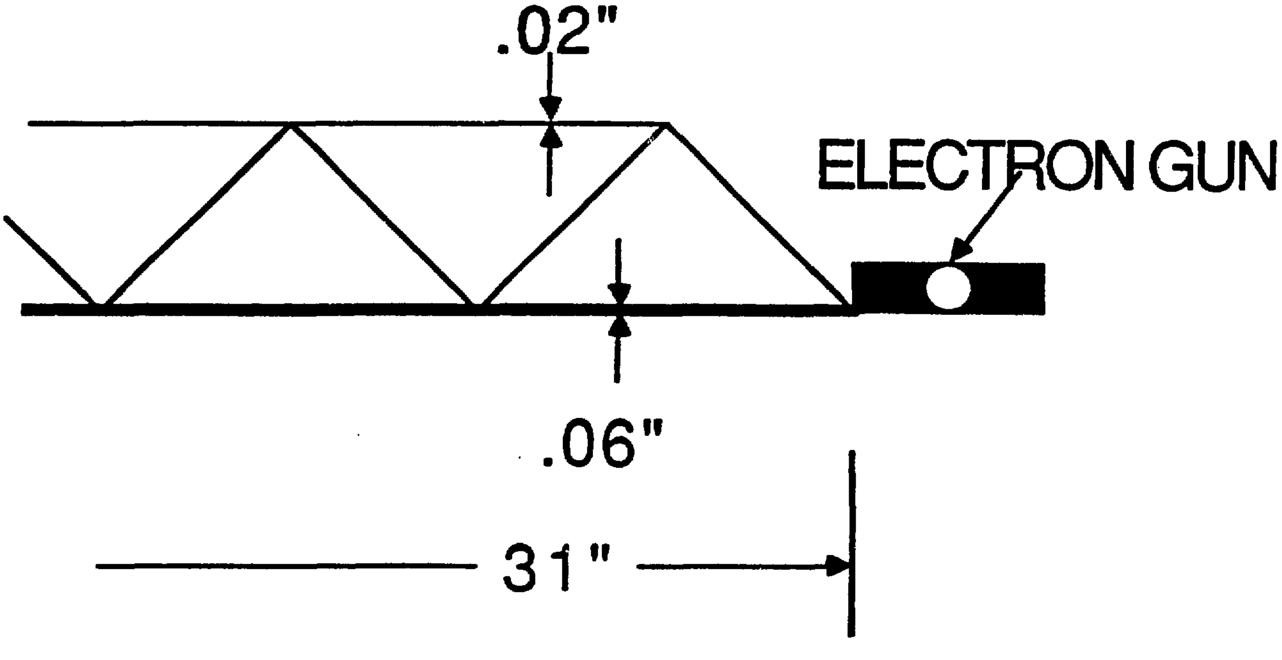

ELECTRON BEAM MEASUREMENTS ON ATF

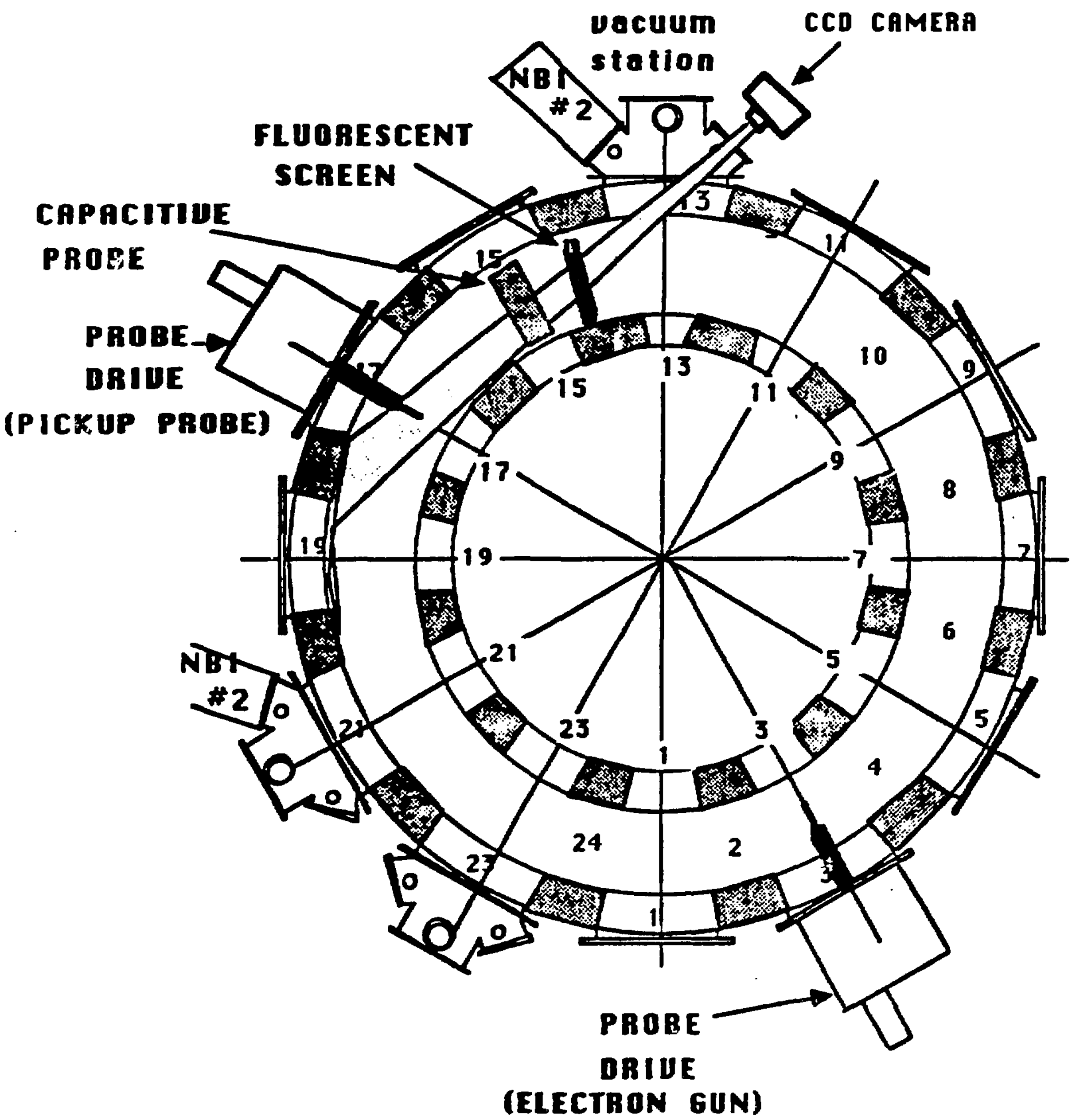

SURFACE MAPPING STATUS

- DRIVES FOR GUN AND PROBE HAVE BEEN FABRICATED AND TESTED
- BEAM SOURCE HAS BEEN TESTED
- MESH HOLDER HAS BEEN FABRICATED
- CCD CAMERA HAS BEEN TESTED AT AUBURN
- CAPACITATIVE PROBE HAS BEEN FABRICATED.
- COMPUTER PROGRAM FOR CONTROL IS COMPLETE

YET TO BE DONE

- VACUUM CLEAN AND DELIVER DRIVES
- INSTALL HARDWARE
- IMPLEMENT POWER SUPPLIES
- PERFORM EXPERIMENT

SUMMARY

- THE MAGNETIC FIELD ALIGNMENT PROCEEDURE WILL INSURE THAT THE AXES OF THE VARIOUS COIL SETS ARE ALIGNED.
- OTHER FIELD ERRORS WILL BE DISCOVERED BY MAPPING FLUX SURFACES WITH AN ELECTRON BEAM. HOWEVER, THIS TECHNIQUE DOES NOT REVEAL THE SOURCES OF FIELD ERRORS.
- MEASUREMENTS WILL BE CONDUCTED SHORTLY AFTER THE ATF TORSATRON IS COMMISSIONED.

Divertor Experiments in IMS†

D.T. Anderson
F.S.B. Anderson
R.P. Doerner
J.L. Shohet
C.A. Storlie
J.N. Talmadge
P.K. Trost

Torsatron / Stellarator Laboratory
University of Wisconsin - Madison

† Funded by USDOE + ORNL

- DIVERTOR STRUCTURE IN IMS
- EFFECTS OF EXTERNAL VERICAL MAGNETIC FIELDS
- SHIELD BIASING
- CONNECTION LENGTHS AND DIVERTED FLUX ORIGINS
- DIVERTED FLOWS
- SUMMARY AND FUTURE PLANS

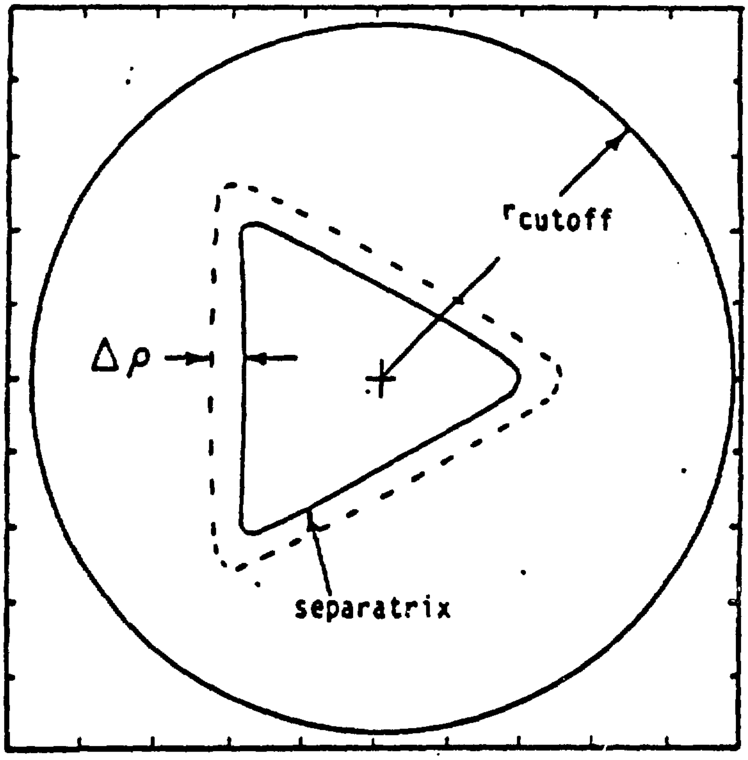

SCHEMATIC OF THE BOUNDARY LAYER USED FOR MODULAR DIVERTOR CALCULATIONS. THE CUTOFF RADIUS IS THE RADIAL EXTENT TO WHICH THE FIELD LINES WERE FOLLOWED. THE CUTOFF RADIUS WAS VARIED FROM 6.0 CM. TO 9.9 CM.

$\Delta\rho$ = 0.5 CM.

↑ FROM [illegible]

IMS MODULAR DIVERTORS

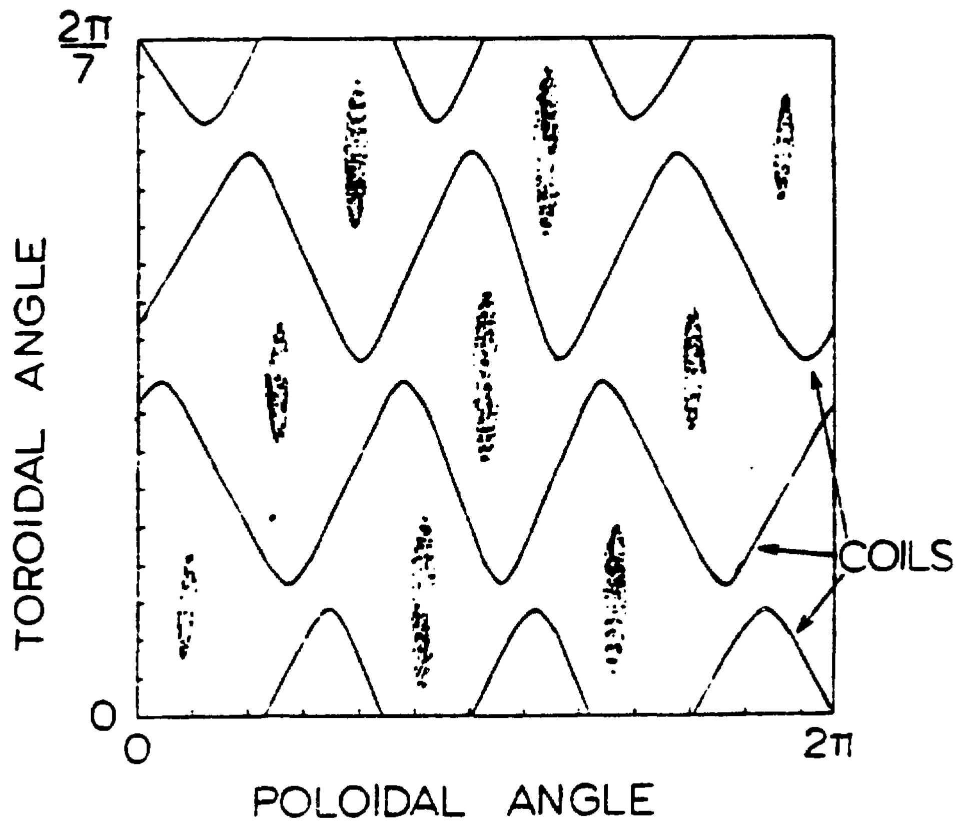

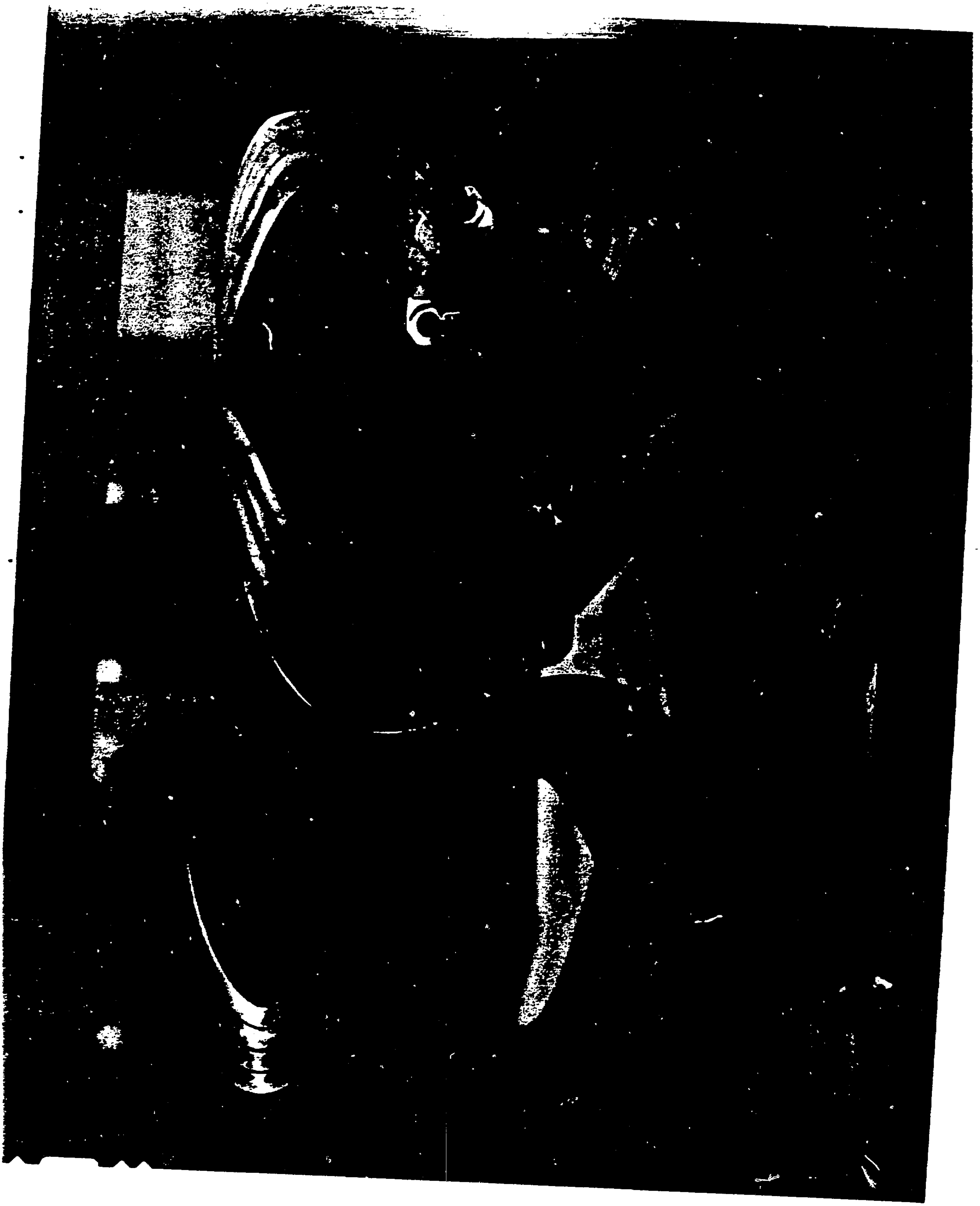

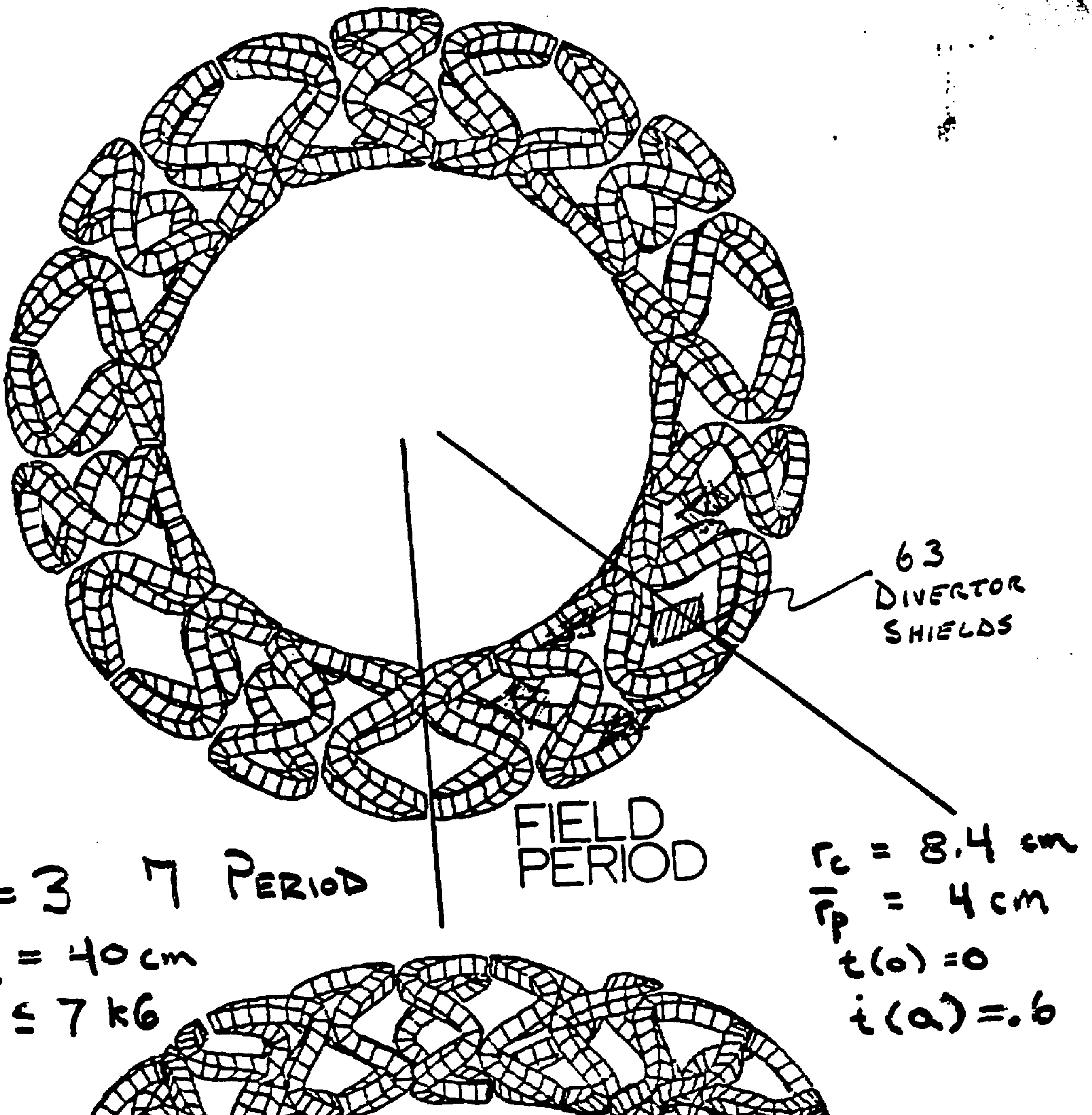
63 DIVERTOR SHIELDS
FIELD PERIOD
l = 3 7 PERIOD
R = 40 cm
B0 ≤ 7 kG
rc = 8.4 cm
rp = 4 cm
ι(0) = 0
ι(a) = .6

IMS COIL SET

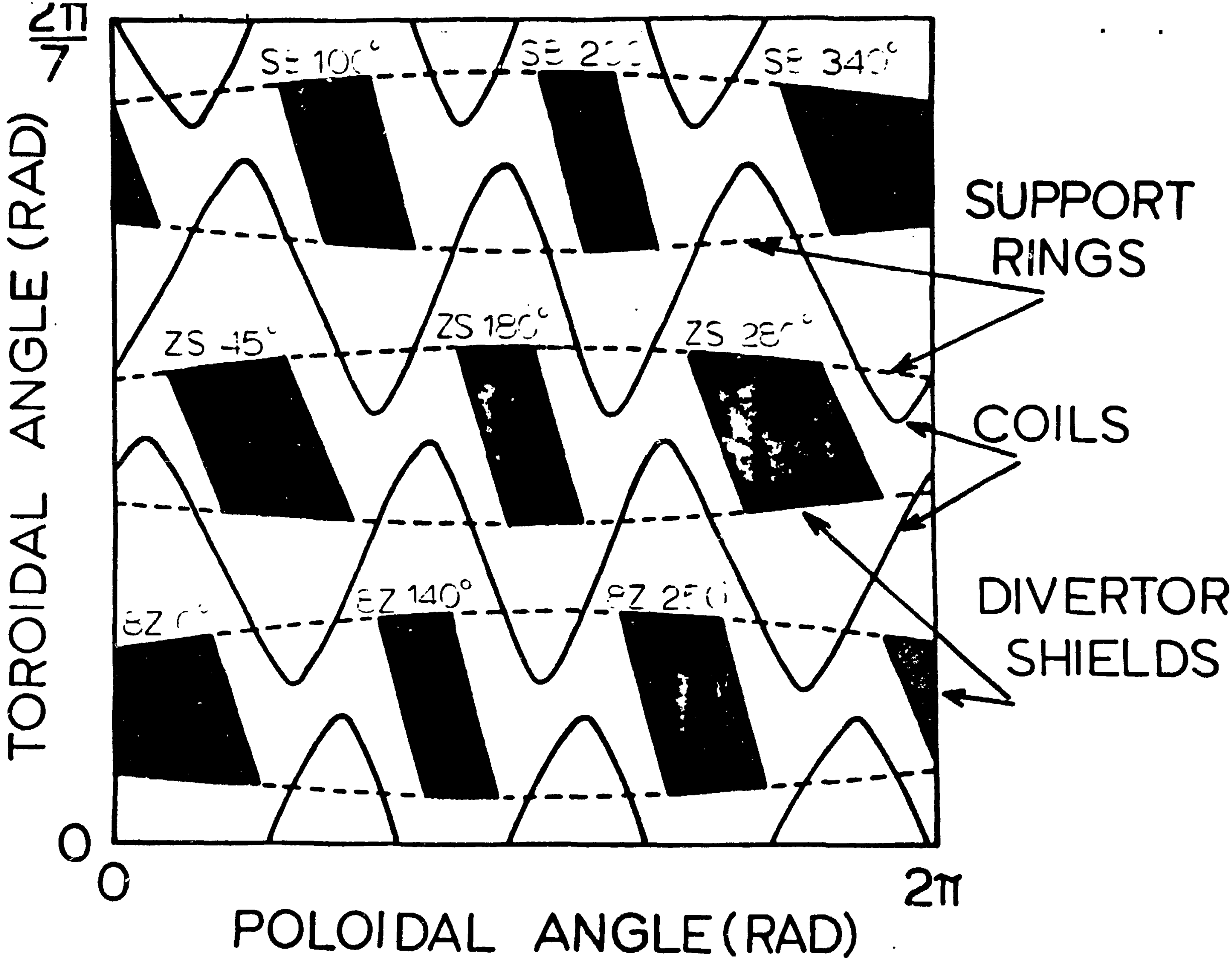
SE 340°
ZS 45°
ZS 180°
EZ 140°
SUPPORT RINGS
COILS
DIVERTOR SHIELDS
TOROIDAL ANGLE (RAD)
$\frac{2\pi}{7}$
0
0
2π
POLOIDAL ANGLE (RAD)

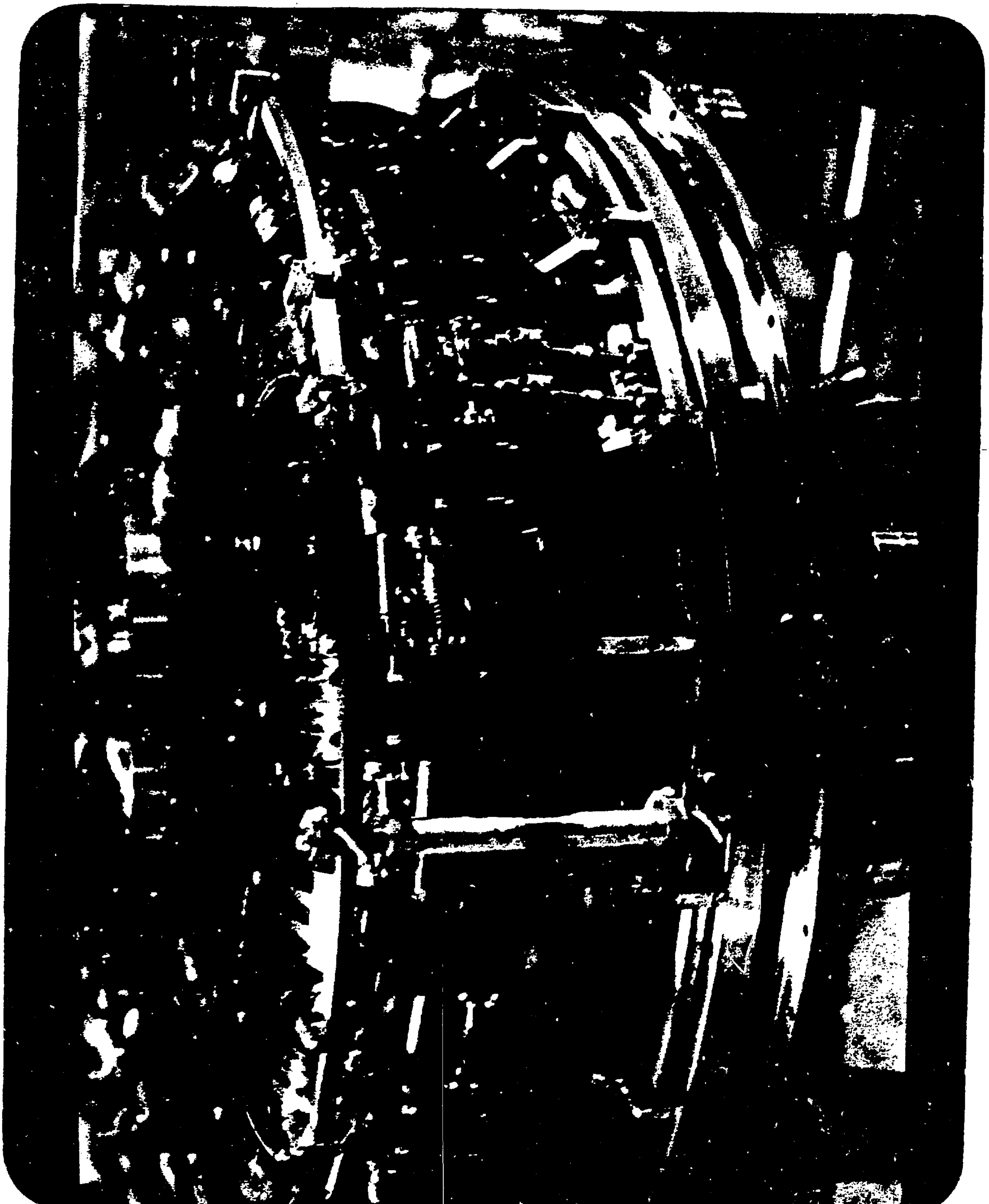

200 IONS LAUNCHED 6 MM FROM SEPARATRIX
50% PARALLEL AND 50% PERPENDICULAR ENERGY AT LAUNCH
10 EV INITIAL TOTAL ENERGY

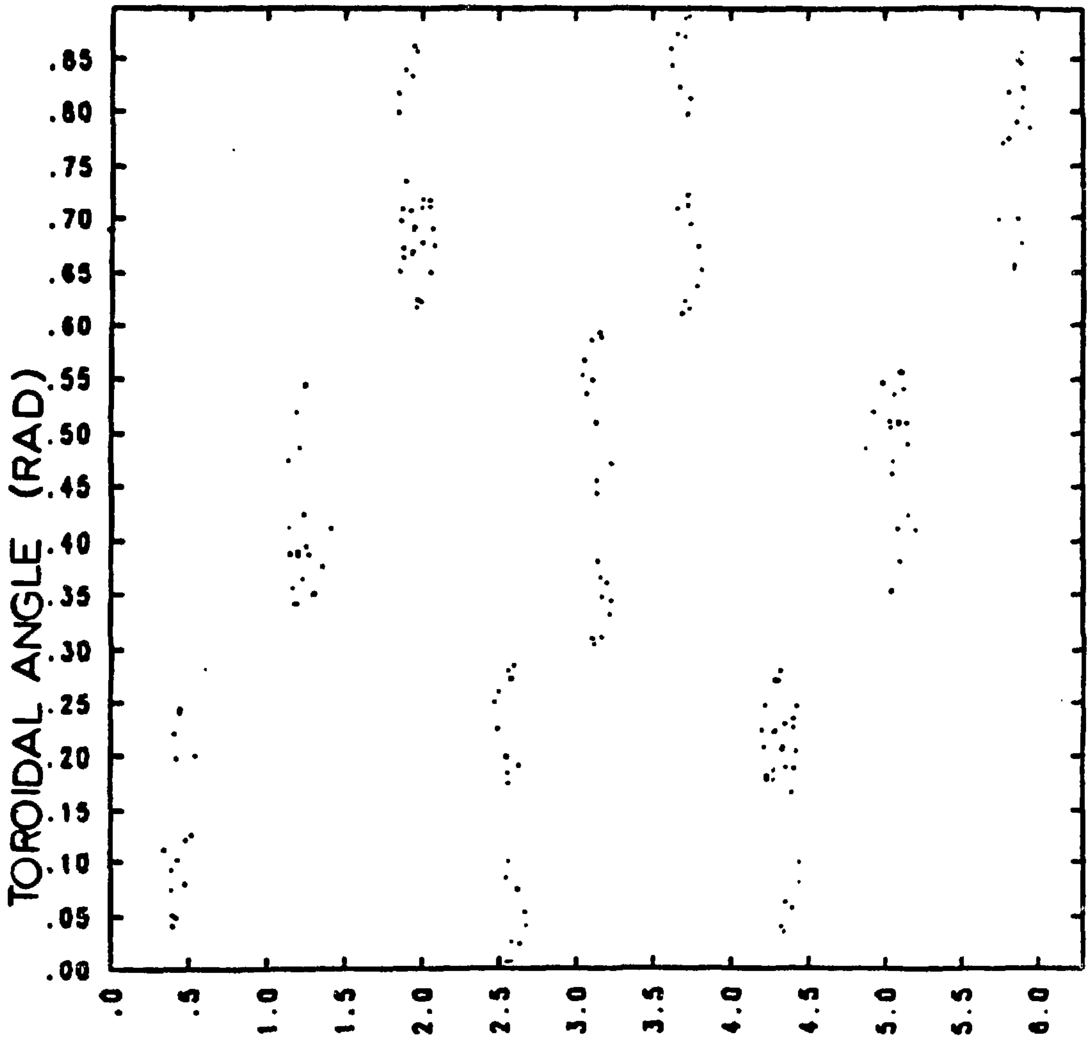

FIGURE 3

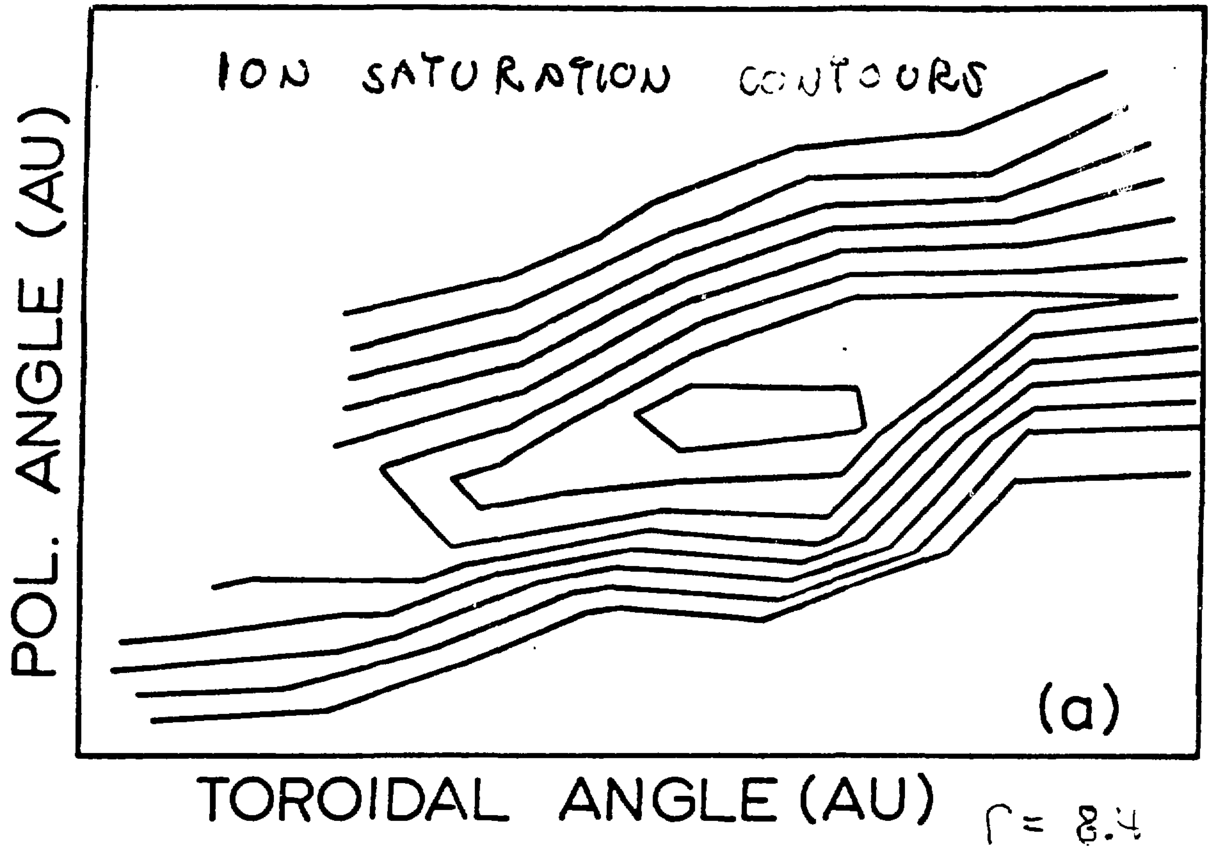
ION SATURATION CONTOURS
POL. ANGLE (AU)
(a)
TOROIDAL ANGLE (AU)
Γ = 8.4

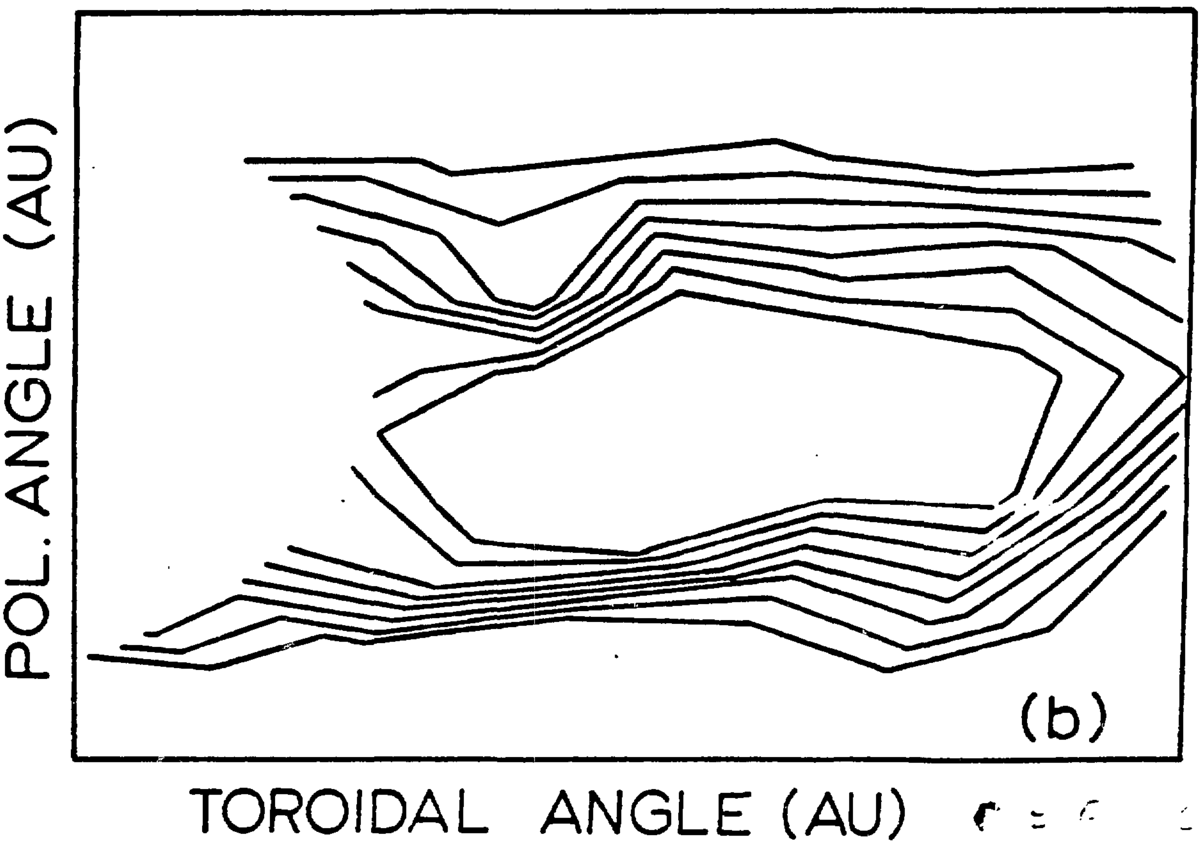
POL. ANGLE (AU)
(b)
TOROIDAL ANGLE (AU)

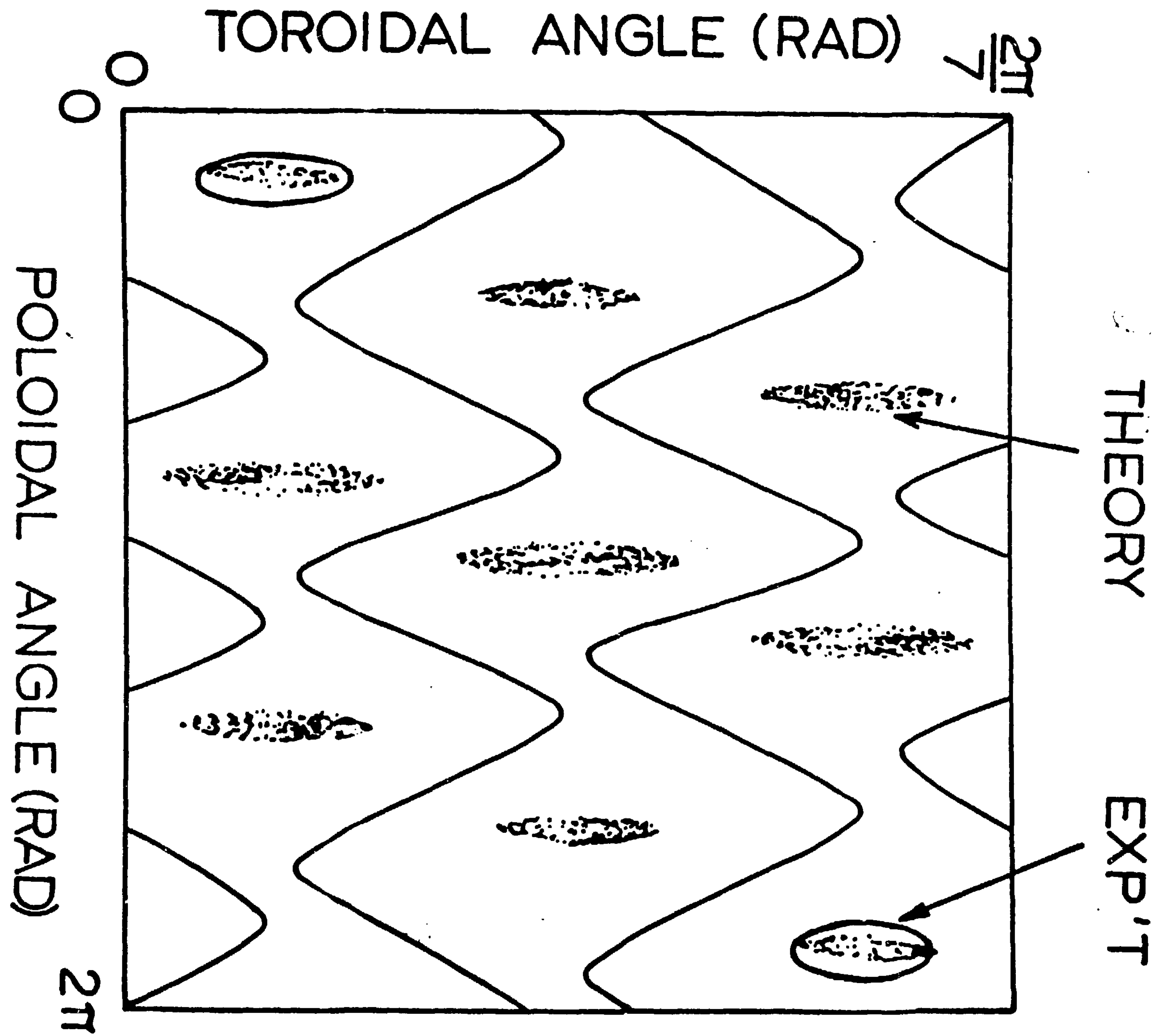

TOROIDAL ANGLE (RAD)
0
0
2π/7
POLOIDAL ANGLE (RAD)
2π
THEORY
EXP'T

Symmetries give global-type PATTERNS TO DIVERTED FLUXES

⇒ complex + EXPENSIVE

THERE IS A NEED TO USE A small SET OF LOCALIZED PARTICLE collection DEVICES IN the EDGE / DIVERTED plasma REGION

{ Magnetic Alteration
Electric Fields (Edge)

lju

APPLICATION OF AN EXTERNAL VERTICAL FIELD CAN EFFECT THE DIVERTED FIELD PATTERN.

- SHIFTING SURFACES INWARD CONCENTRATES FLUX TO INBOARD DIVERTORS

- SHIFTING SURFACES OUTWARD CONCENTRATES FLUX TO OUTBOARD DIVERTORS

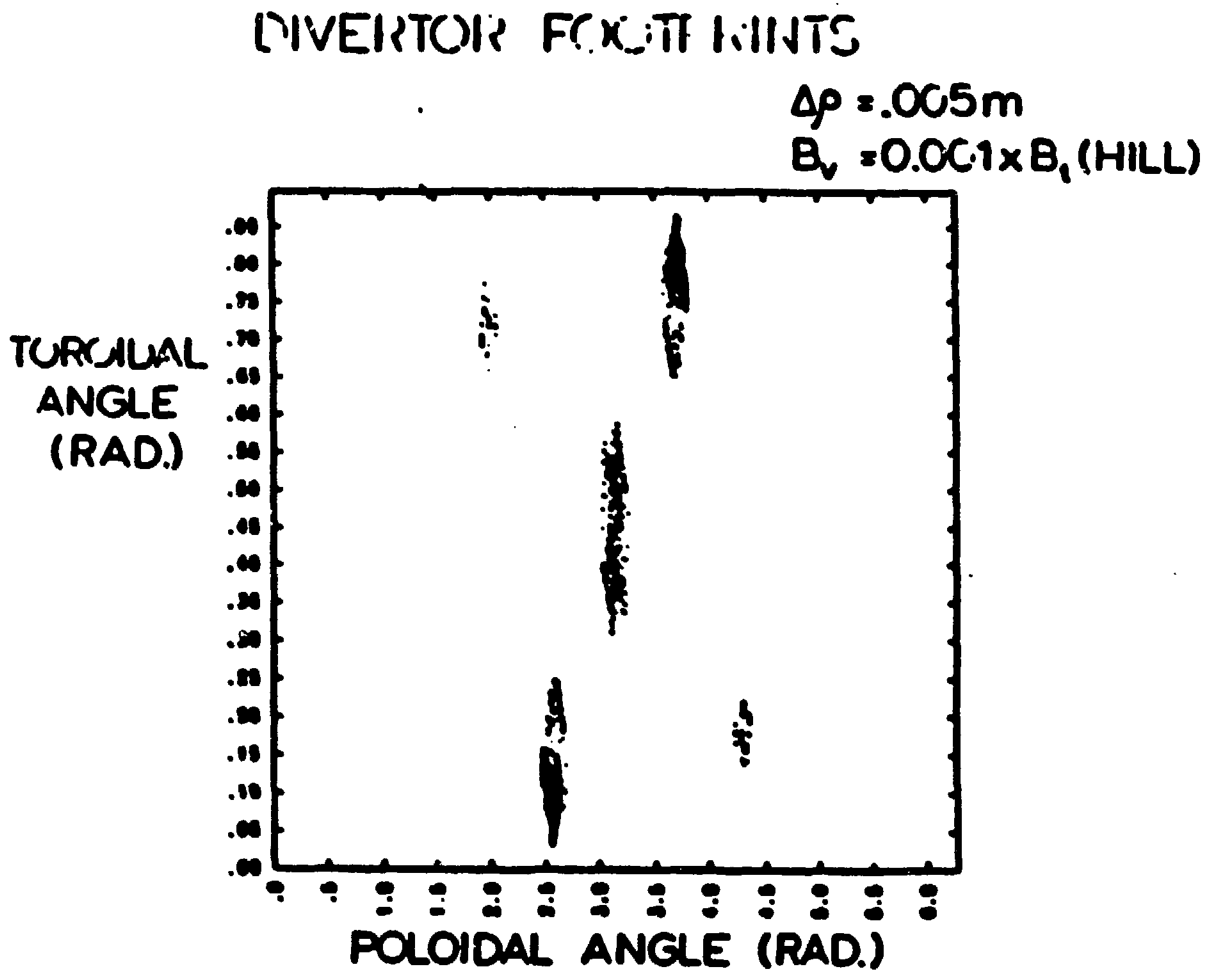
DIVERTOR FOOTPRINTS
$\Delta\rho$ =.005m
B_v =0.001 x B_t (HILL)
TOROIDAL ANGLE (RAD.)
POLOIDAL ANGLE (RAD.)

FIGURE 6a

DIVERTOR FOOTPRINTS

$\Delta\rho$ =.005m

B_v =0.001xB_t (WELL)

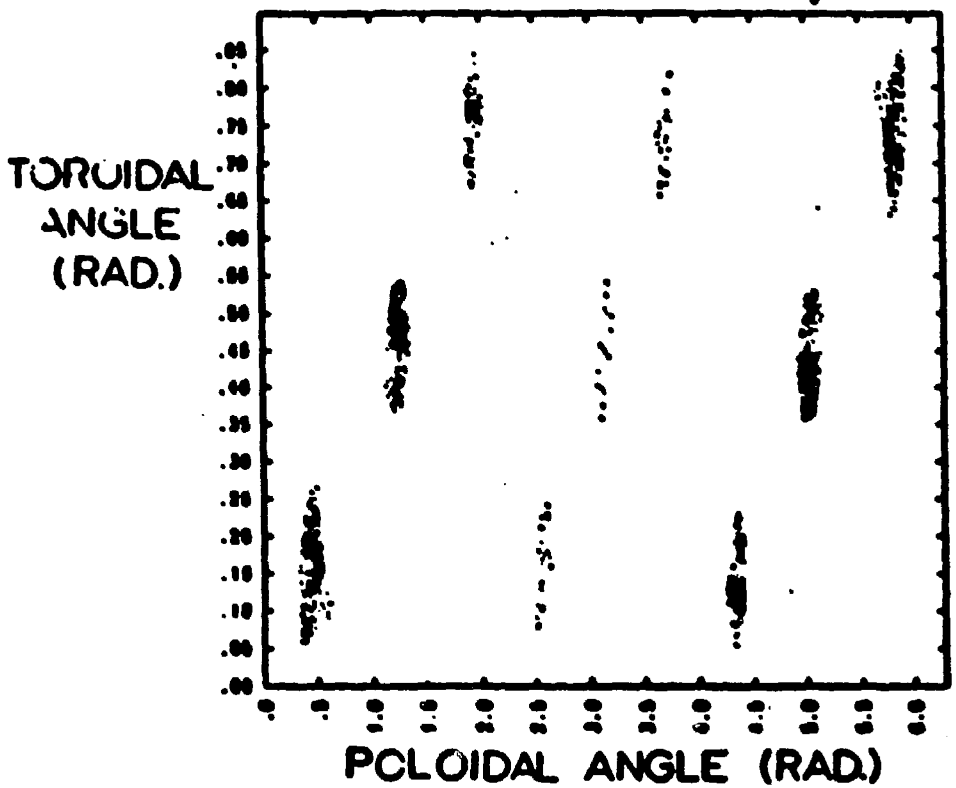

FIGURE 6b

I.M.S.

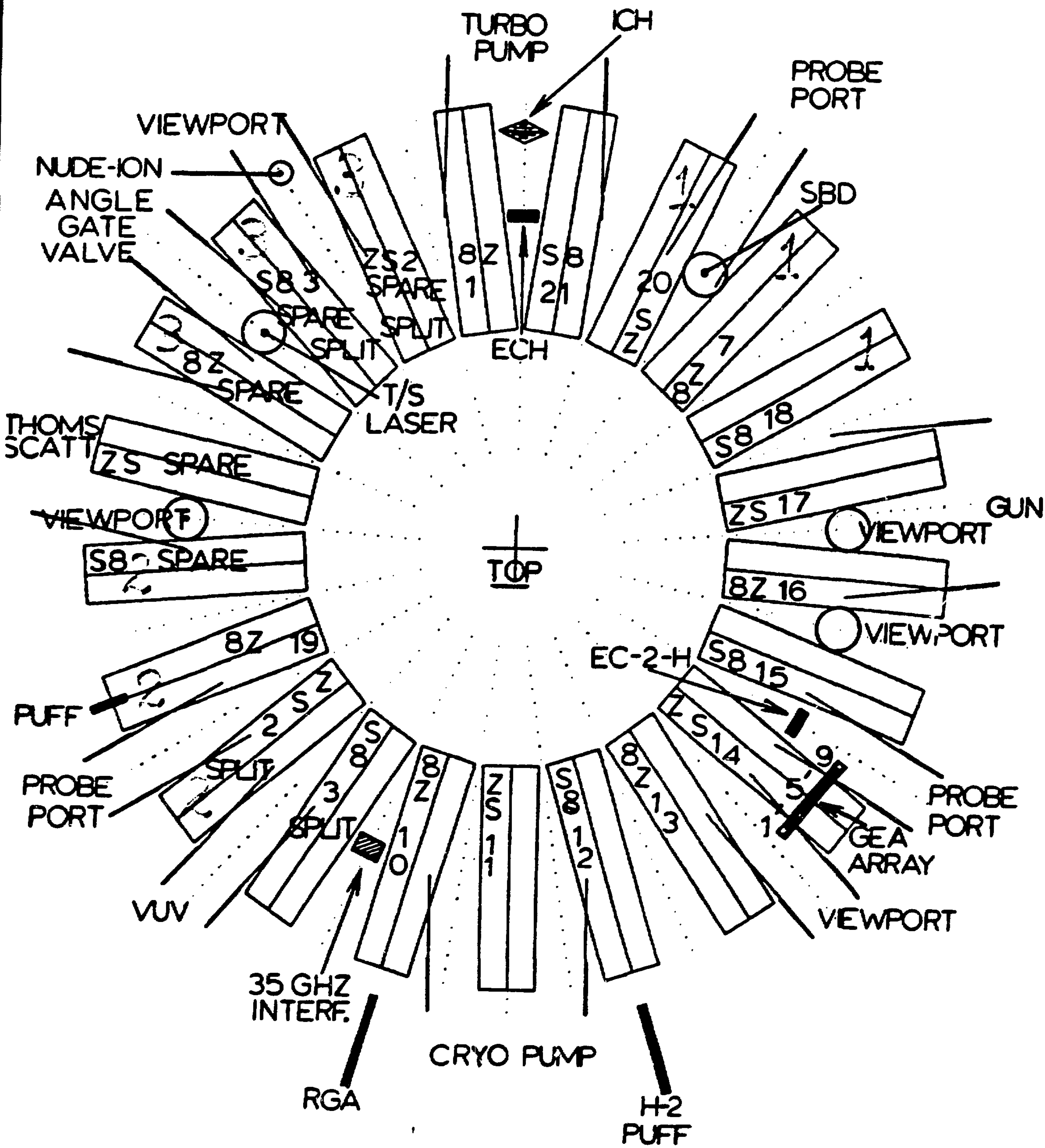
TURBO PUMP
ICH
PROBE PORT
VIEWPORT
NUDE-ION
ANGLE GATE VALVE
SBD
ZS2 SPARE SPLIT
8Z 1
S8 21
S8 3 SPARE SPLIT
20 SZ
8Z 7
8Z SPARE
ECH
T/S LASER
S8 18
THOMS SCATT
ZS SPARE
ZS 17
GUN
VIEWPORT
VIEWPORT
TOP
8Z 16
VIEWPORT
8Z 19
EC-2-H
S8 15
PUFF
2 SZ SPLIT
PROBE PORT
ZS14
PROBE PORT
3 S8 SPLIT
8Z 10
ZS 11
S8 12
8Z 13
GEA ARRAY
VUV
VIEWPORT
35 GHZ INTERF.
CRYO PUMP
RGA
H-2 PUFF

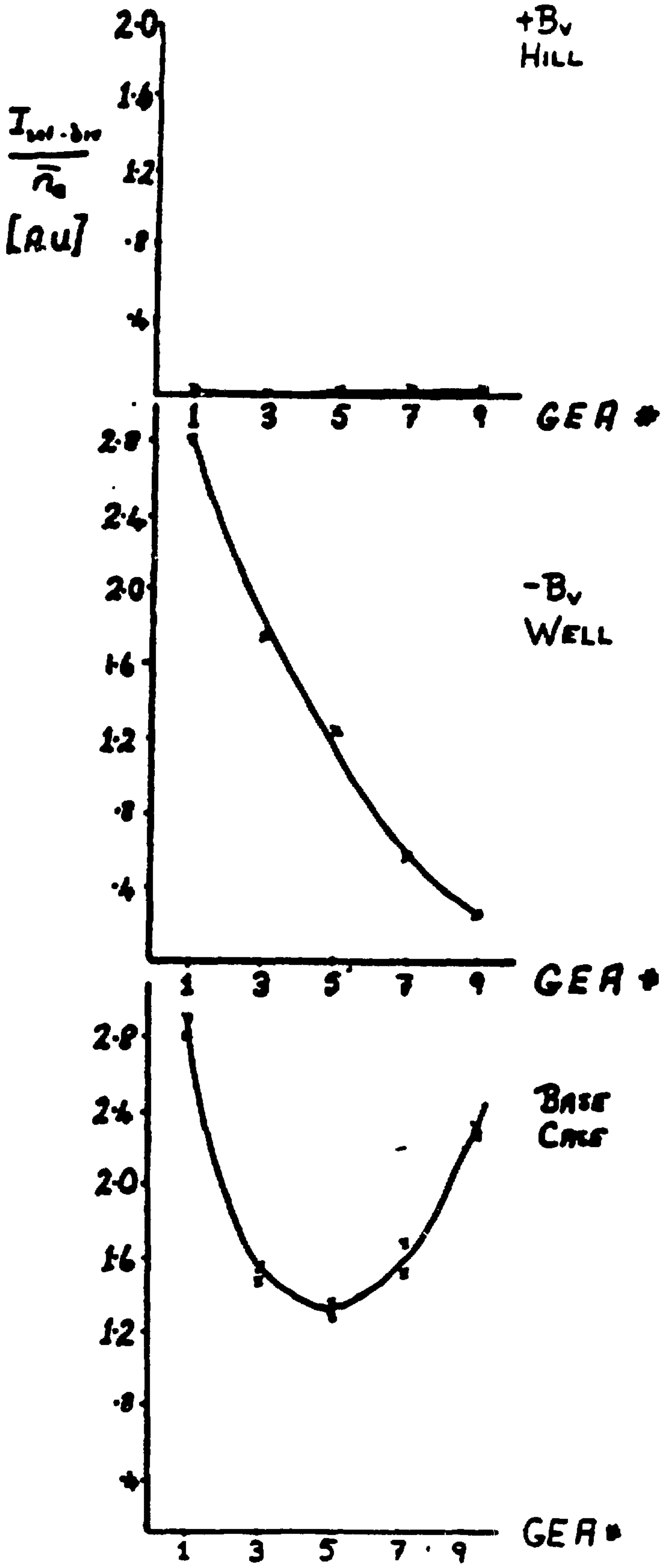
+Bv
HILL
[AU]
2.0
1.6
1.2
.8
.4
GEA #
1
3
5
7
9
-Bv
WELL
2.8
2.4
2.0
1.6
1.2
.8
.4
GEA #
BASE CASE
2.8
2.4
2.0
1.6
1.2
.8
.4
GEA #

A SET OF SCREENS (200 MESH) HAS BEEN INSTALLED OVER 21 OF THE IMS DIVERTOR SHIELDS TO MONITOR PARTICLE CURRENTS.

<DIVERTOR PARTICLE CURRENT>/<LINE DENSITY>

	BASE	OUTWARD	INWARD
INBOARD DIVERTOR	.76	.1	1.6
OUTBOARD DIVERTOR	.79	2.1	.6

CURRENT SHOT # -- D00205 DATE === .H-RG-86
START PLOT --- 1 END PLOT --- 8000

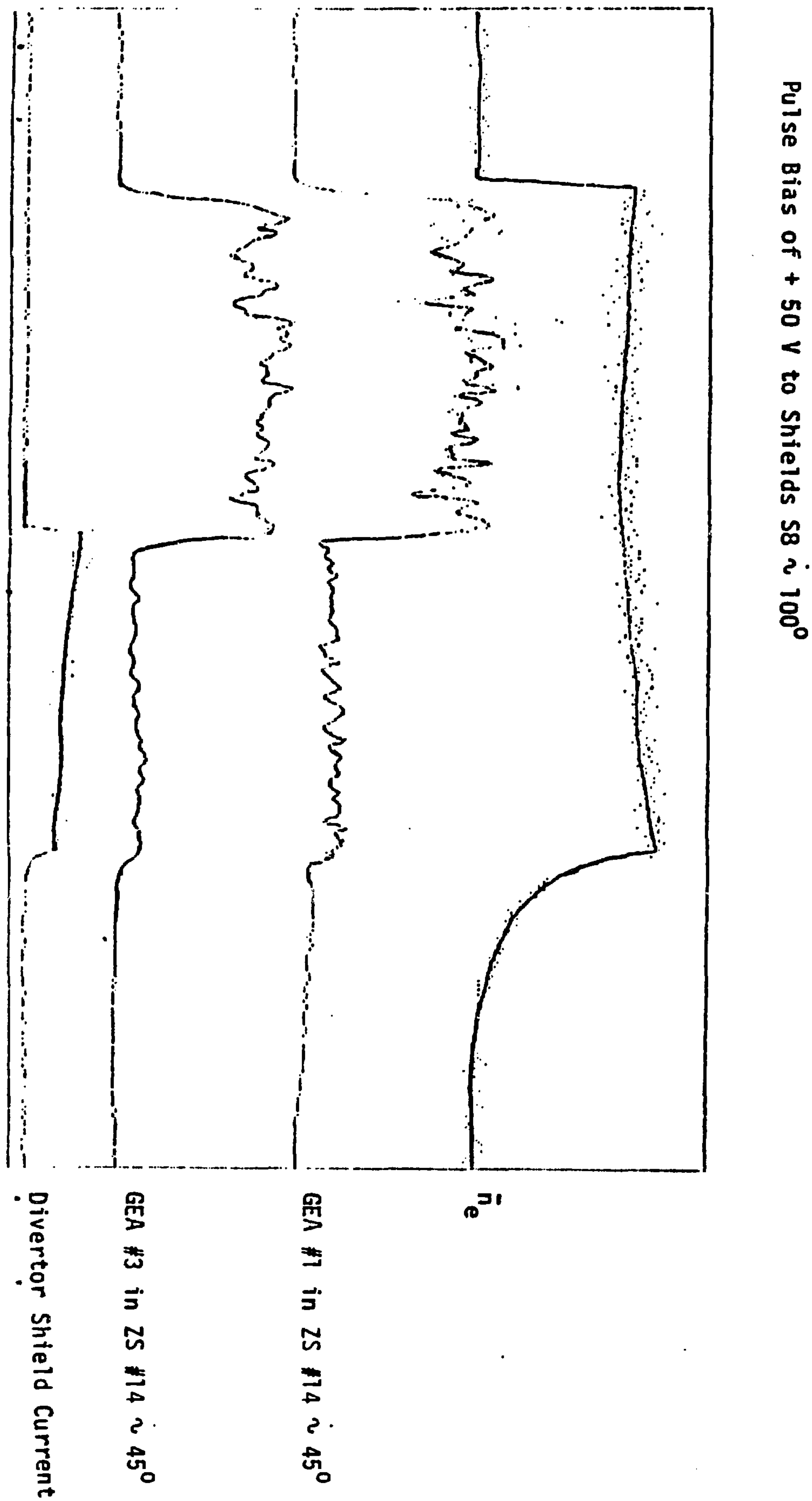

Shields	Which ?	Bias 82/S-8	Change in Divertor Flux (%) Gen 1&3	Gen 5&7
8-2 θ=0° & S-8 θ=200°	ALL	+50/+50	-50	0
	ALL	+50/-50	-55	-50
	ALL	-50/+50	-90	-50
	ALL	-50/-50	-25	+40
	ALL	-100/+100	-90	-55
	8219 S818	+50/+50	-80	-70
	8219 S818	+50/0	-45	-55
	8-219 S818	0/+50	-60	-10
	82 ALL S818	+50/0	-20	-25
	82 S8 ALL	0/+50	-85	-40

TABLE II(cont.)

DIVERTOR FLUX : DIVERTOR-PLATE BIAS

Shield(s) Biased	Bias Volt	% Change in Flux 1 Field Period Away: Gea's 1+3	Gea's 5+7	% Change 2 Field Periods Away: Gea's 1+3	Gea's 5+7	% Change 3 Field Periods Away: Gea's 1+3	Gea's 5+7
S-8 100°	+50	-60	-10	-10	0	0	+20
Z-S 45°	+50	-35	0	0	0	0	0
S-8 340°	+50	+30	+30	+20	+25	0	-15
S-8 200°	+50	+15	+10	+15	+15	0	0
Z-S 180°	+50	+10	+15	+15	+20	—	—
Z-S 280°	+50	-30	-35	-10	-10	-10	0
8-Z 0°	+50	-15	-10	-45	-55	+20	+20
8Z 140°	+50	0	0	+20	+15	—	—
8Z 250°	+50	-15	-25	0	0	0	0
All Shields in 1 F.P.	+50	-65	-30	0	0	+10	0
All in 1 F.P.	-50	+25	0	+25	+25	-20	-25

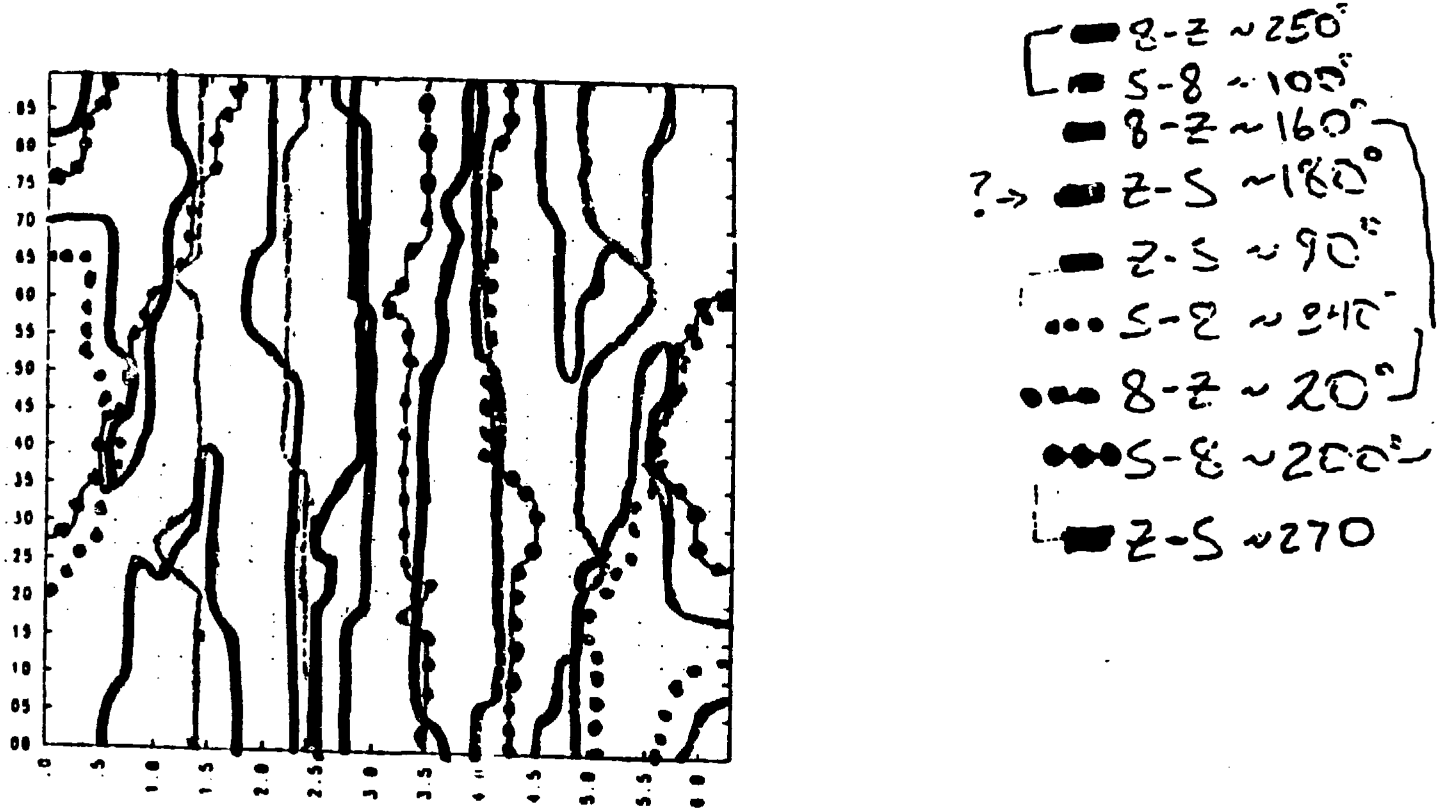

THIS PICTURE REPRESENTS THE LOCATION OF THE ORIGINS OF THE FIELD LINES WHICH DEVELOP TO FORM THE VARIOUS DIVERTOR FOOTPRINTS IN IMS.

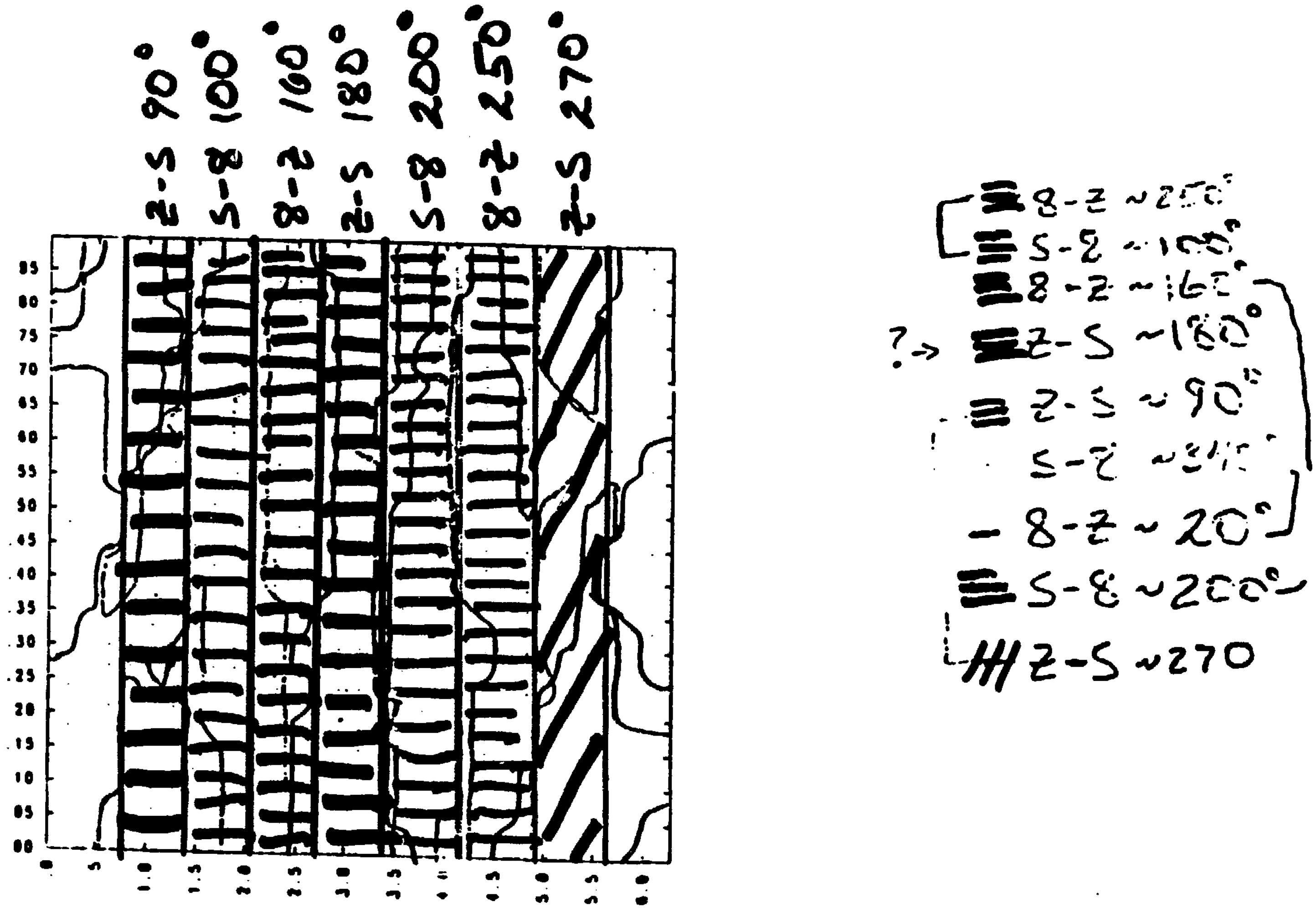

THIS PICTURE REPRESENTS THE LOCATION OF THE ORIGINS OF THE FIELD LINES WHICH DEVELOPE TO FORM THE VARIOUS DIVERTOR FOOTPRINTS IN IMS.

- Numerically generated 'origins' have been examined experimentally.
  - A probe placed in the S.O.L. is used to excite an ion acoustic wave.
  - Each divertor shield within a field period was monitored
  - The signal was detected on at most two shield for each launch position
- The signal appeared on all shields if launched well inside the separatrix

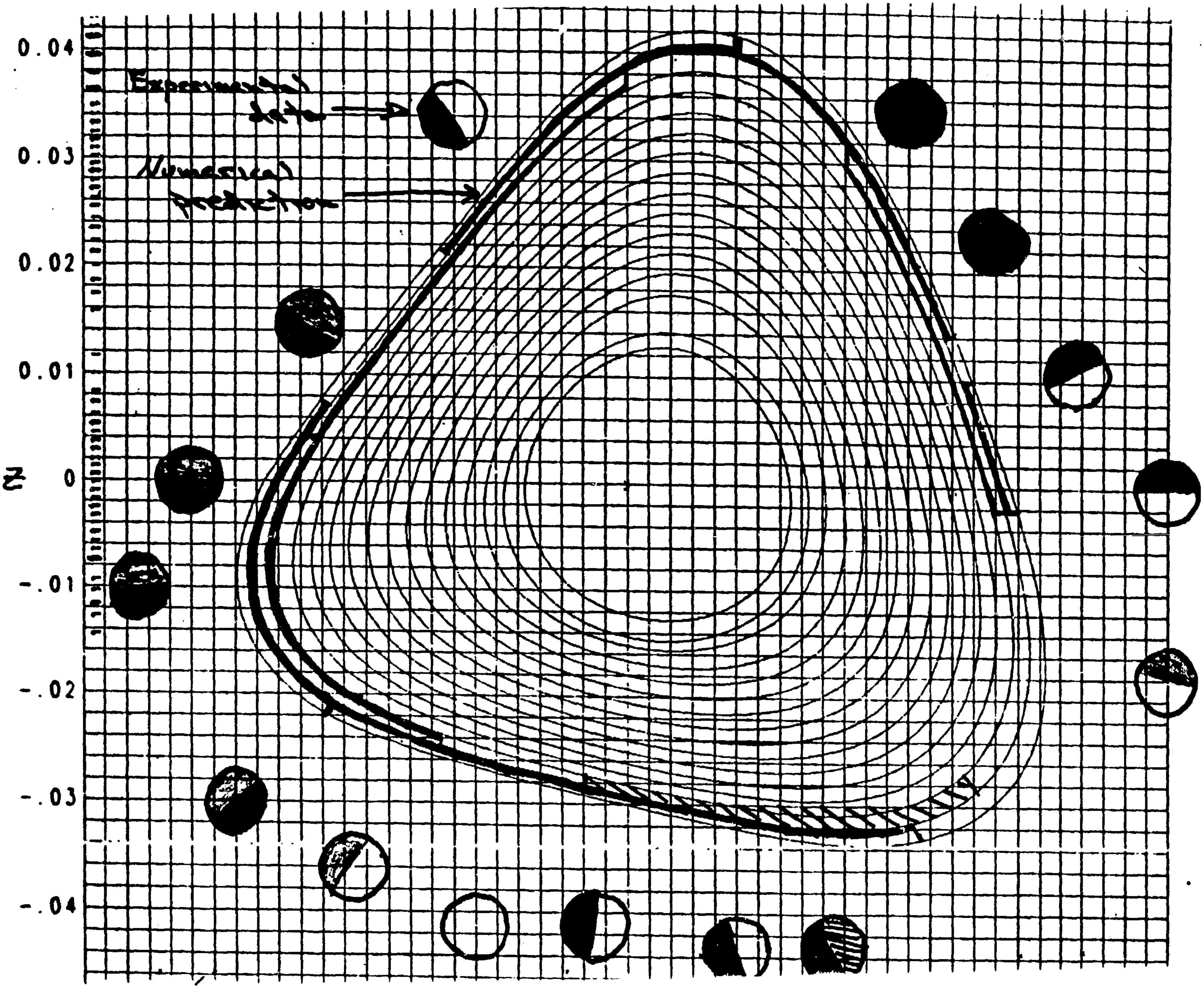
0.04
0.03
0.02
0.01
0
-.01
-.02
-.03
-.04
z̃
Experimental data
Numerical prediction

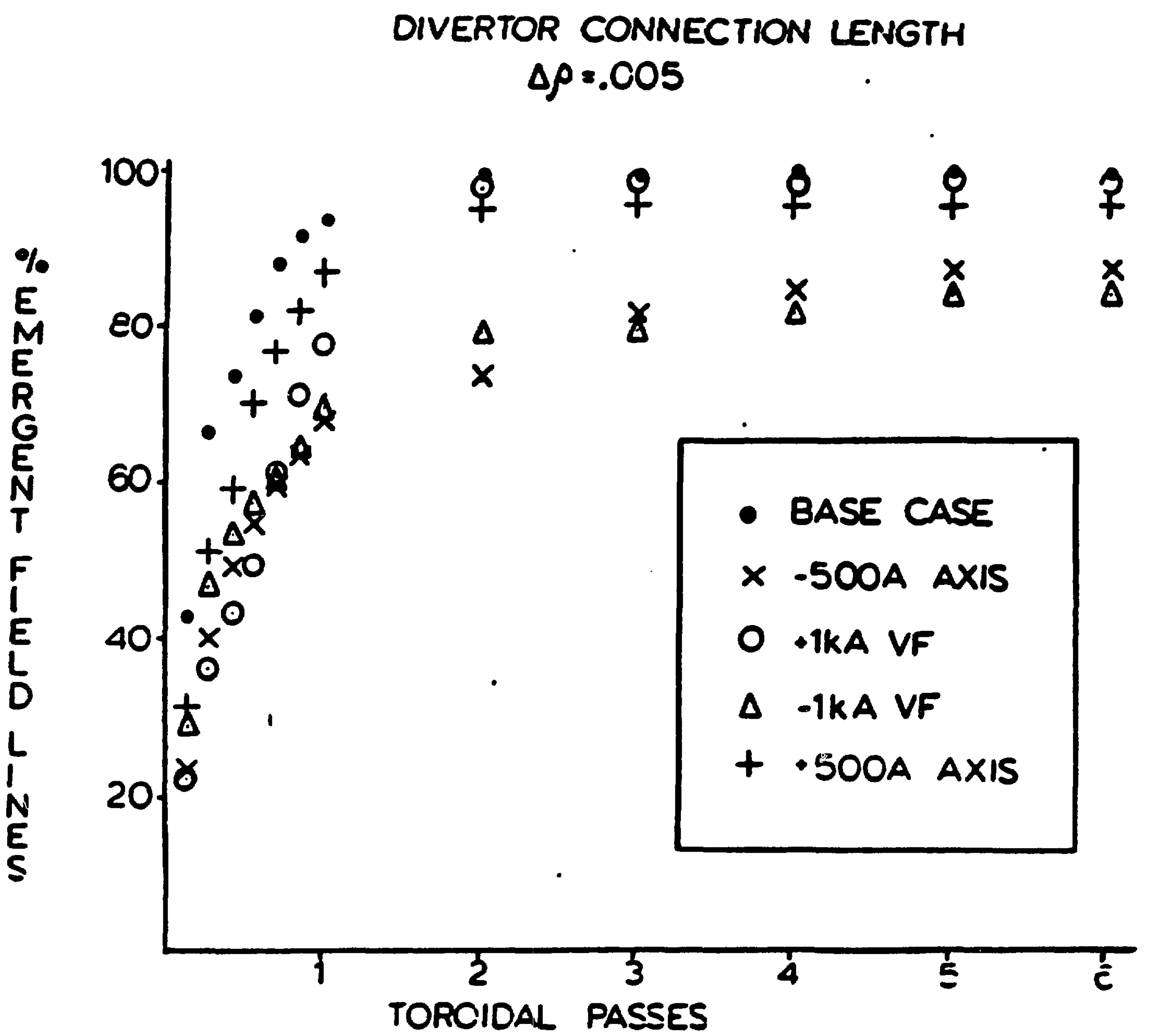
DIVERTOR CONNECTION LENGTH
Δρ=.005
% EMERGENT FIELD LINES
100
80
60
40
20
1
2
3
4
5
6
TOROIDAL PASSES
BASE CASE
-500A AXIS
+1kA VF
-1kA VF
+500A AXIS

FIGURE 8

- ION-ACOUSTIC WAVES ARE NOW BEING USED TO MEASURED DIVERTED FLOW VELOCITIES
  - WAVE IS LAUNCHED FROM NEAR SEPARATRIX AND PHASE MONITORED AT SHIELD
  - WAVE IS LAUNCHED AT SHIELD AND PHASE MEASURED AT SEPARATRIX

- USING EQUATION OF ION ACOUSTIC WAVE PROPAGATION IN PRESENCE OF FLOW DEVELOPED BY WONG, MOTLEY & D'ANGELO

$$V_f \sim 1.5 \times 10^6 \text{ cm/s}$$

- DIRECT MEASUREMENT OF FLOW FROM PARTICLE CURRENTS AND DIVERTOR DENSITIES GIVES

$$V_f \sim 1.2 \times 10^6 \text{ cm/s}$$

- Simple analysis (Divertor Expts in DIVA).
[Nuc. Fus 1978]

$$\tau_p = \frac{L \bar{n}_e a}{2 V_f \bar{n}_{es} d}$$

$L \equiv$ connection length - code
$a \equiv$ plasma radius
$V_f \equiv$ flow velocity
$n_e =$ central density
$n_{es} =$ edge density
} measured
$d =$ SOL thickness
$= (D_\perp L / V_f)^{1/2}$ $D_\perp$ from x-port studies

$\Rightarrow$ $\tau_p \sim 2$ ms

$\bar{n}_e$ decay (interferometer) $\sim$ 1 ms

Summary

- Predicted divertor patterns have been experimentally verified
- Divertor patterns can be focussed to the inboard/outboard divertors through a vertical magnetic field
- Potentials applied to remote divertor shields can effect edge-plasma flows into other divertors
- Ion acoustic wave propagation has been used to show separatrix origins of diverted flux bundles
- Diverted flow velocities have been measured to be ~ 1/2 the ion sound speed.
- Particle confinement times calculated from simple models, using experimentally measured parameters, show good agreement with direct experimental measurements,

FUTURE PLANS

- HOW DO DIVERTED FLUXES redistribute IN SHIELD BIASING EXPERIMENTS
- EXPERIMENTALLY MEASURE CONNECTION lengths AS A FUNCTION OF DISTANCE OUTSIDE SEPARATRIX USING ION ACOUSTIC technique.
- MEASURE PARTITIONING for toroidally DISTANT divertors
- MEASURE POTENTIALS IN DIVERTOR THROATS AND BACK TO ORIGIN AREAS NEAR SEPARATRIX – Compare with models UNDER Development by Emmert
- EXAMINE ELECTRIC FIELDS IN S.O.L. WITH shield BIASING to provide DATA TO UNDERSTAND mechanism for AFFECTING DIVERTED PARTICLE flows.

PLASMA EDGE PHYSICS AND PARTICLE CONTROL

IN ATF

P.K. Mioduszewski
D.L. Hillis
C.C. Klepper
J.E. Simpkins
T. Uckan

Presented By D.L. Hillis

Oak Ridge National Laboratory

U.S.-Japan Workshop, Oak Ridge , November 9 - 13, 1987

TASKS

1. IMPURITY CONTROL

- Sources
- Release Mechanisms
- Transport
- Control

2. PARTICLE HANDLING

- Particle Confinement
- Recycling
- Particle Exhaust

3. PLASMA-EDGE CHARACTERIZATION

- Plasma Parameters
- Edge Diagnostics
- Configuration Studies

PARTICLE EXHAUST

Assumption:

Modest fueling in steady state: ~ 10 Torr l/s

(NBI, Pellets, Gas)

Total plasma efflux: $\frac{n_e V_{PL}}{\tau_p}$

$n_e = 5 \cdot 10^{19}\ cm^{-3}$

$\tau_p = 0.03\ s$

$$\frac{n_e V_{PL}}{\tau_p} = 5.8 \cdot 10^{21}\ s^{-1}$$

source

In steady state:

$$\varepsilon \left(\frac{n_e V_{PL}}{\tau_p} \right) = \Phi_{fueling} = 7 \cdot 10^{20}\ s^{-1}$$

$$\varepsilon = 12\%$$

Exhaust Efficiency

$(\tau_p = 0.01 s \longrightarrow \varepsilon = 4\%)$

Even with short connection length, 2-4 particle collectors might be sufficient.

EXPERIMENT ON DIVERTOR CONFIGURATION AND CONNECTION LENGTH IN ATF

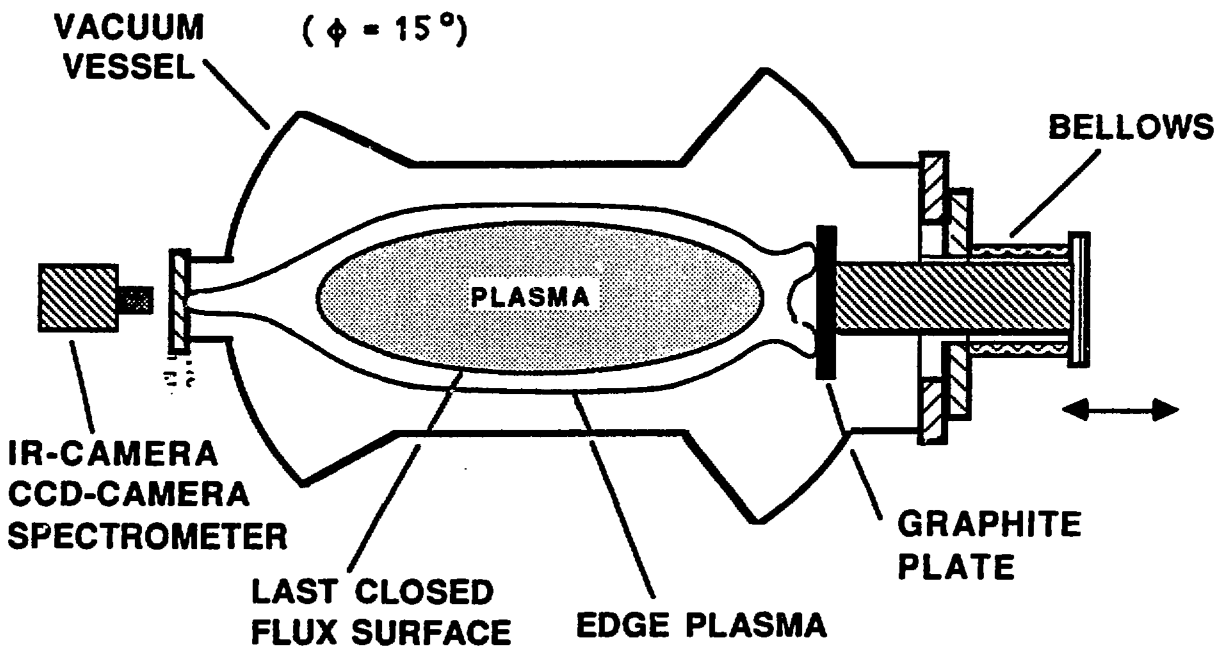

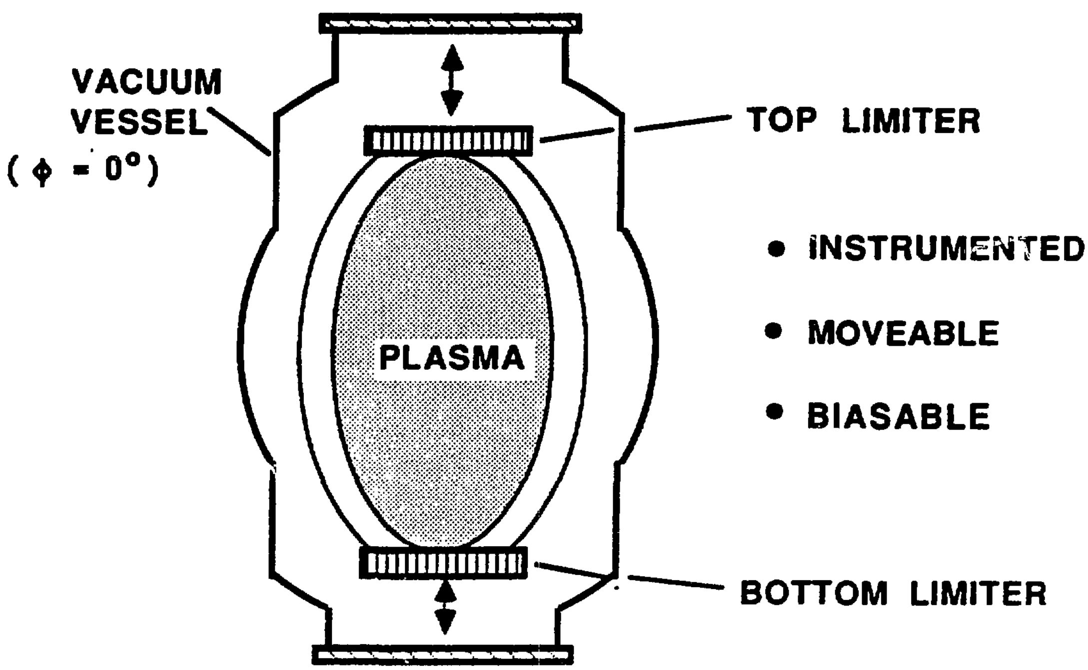

PKM
1987

EDGE DIAGNOSTICS

- CCD - Camera
  + H_α -Filter,
  + Imp. Filter
- IR - Camera
- H_α - Arrays
- Moveable Langmuir Probe
- Reciprocating Langmuir Probe
- Limiter Spectrometer
- Instrumented Limiter
- Surface Analysis Station
- Fast pressure Gauges (neutral density)

ATF INSTRUMENTED LIMITER SYSTEM

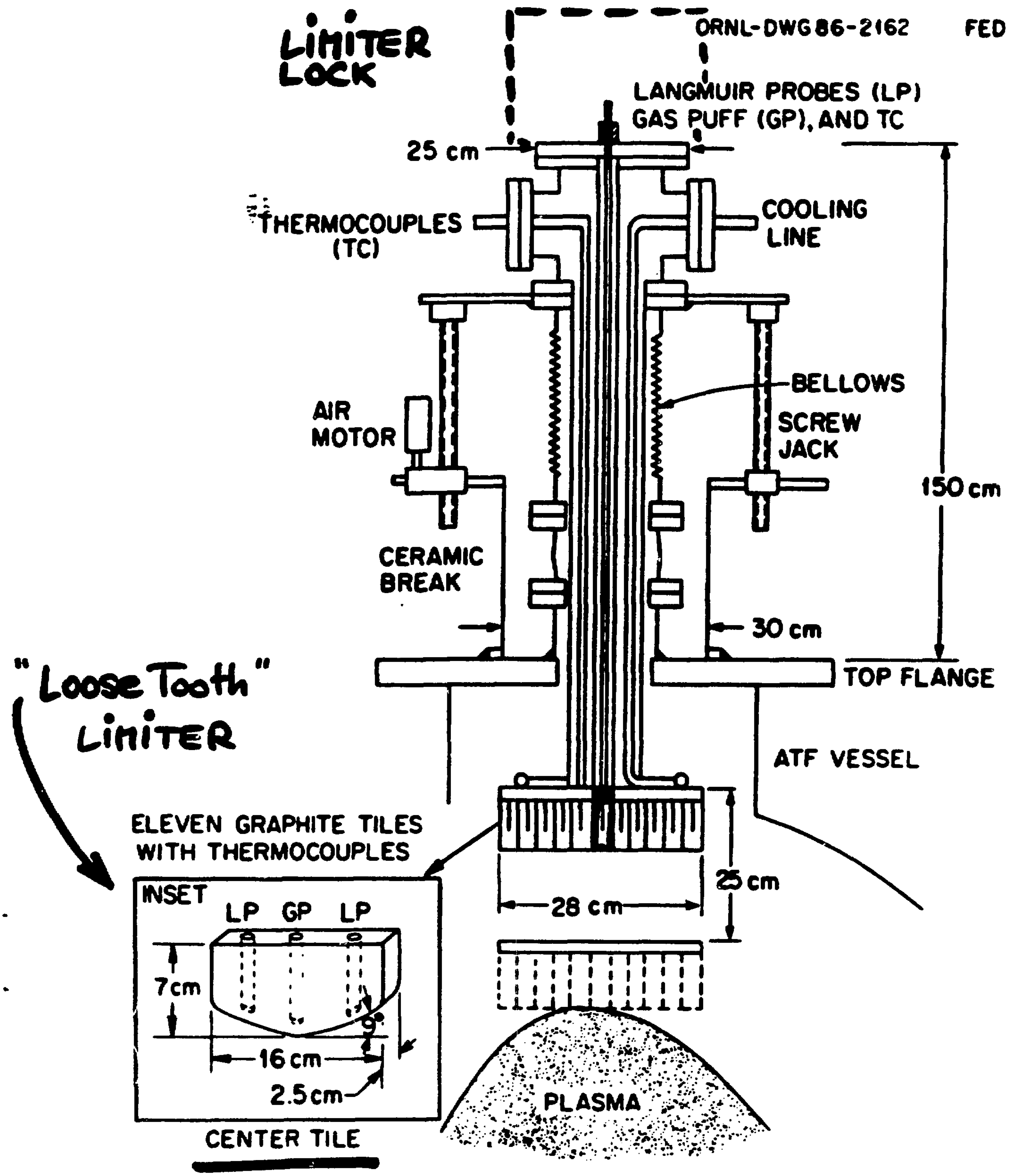

ENERGY DEPOSITION PROFILE ON LIMITER.

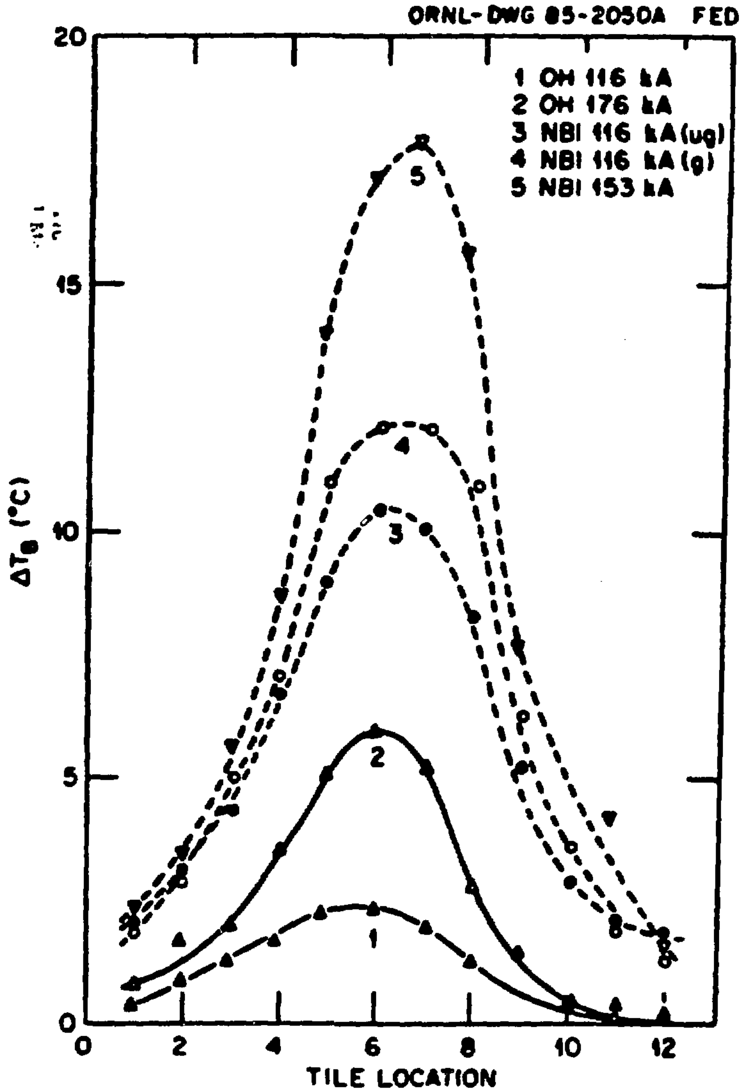

INSTRUMENTED LIMITER DATA FROM ISX-B
(BERYLLIUM LIMITER)

VERTICAL H_α–ARRAY (NF) CAN MONITOR PLASMA BOUNDRY

ORNL-DWG 86-2160 FED

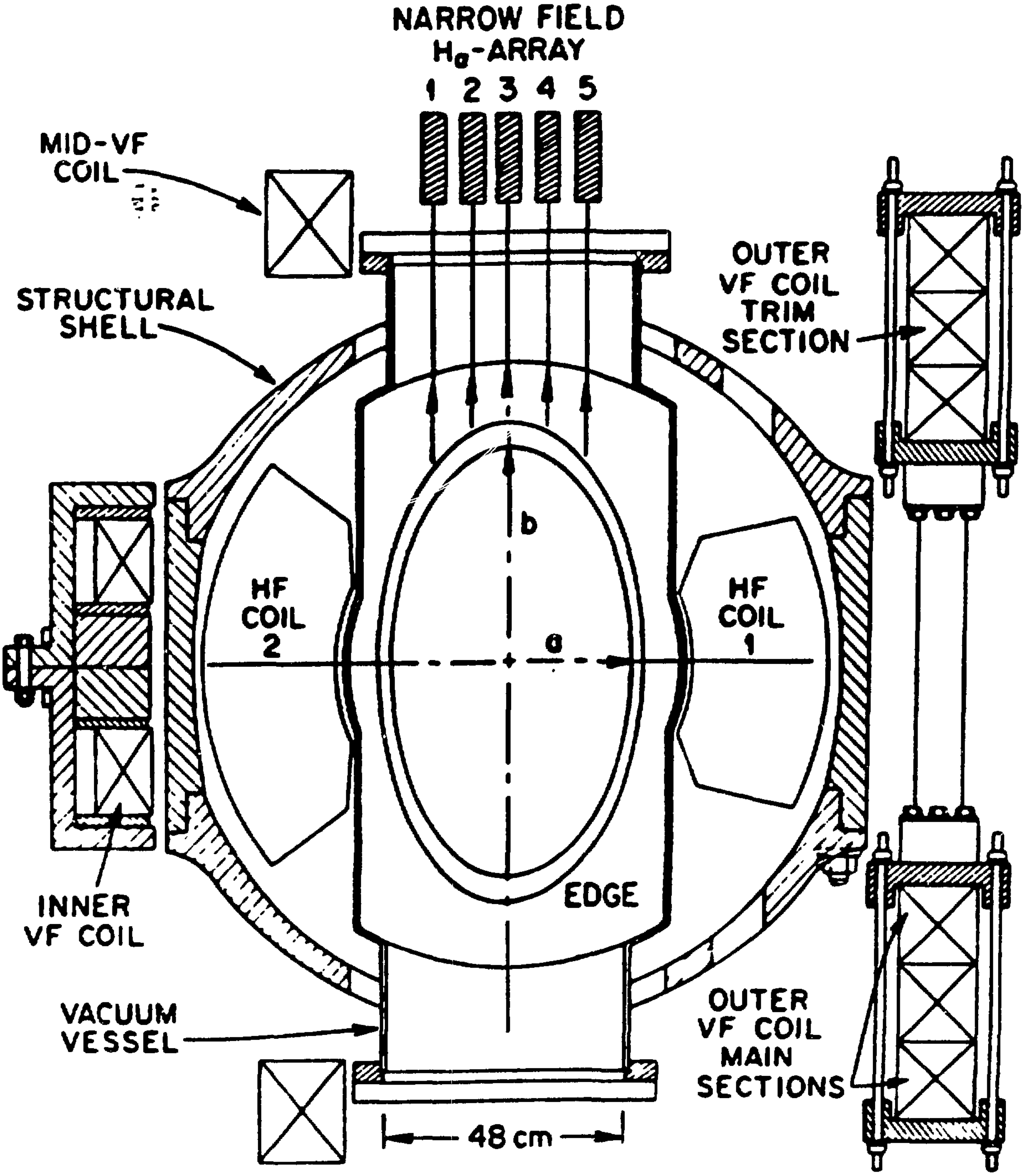

$R_0 = 210$ cm

$a_{vessel} = 66$ cm

$a = 24$ cm, $b = 36$ cm, $\bar{a} = 30$ cm

LIMITER LOCK FOR PMI STUDIES

- FOR MATERIALS STUDIES, THE INSTRUMENTED LIMITER WAS DESIGNED SO THAT THE CENTRAL TILE CAN BE REMOVED THROUGH A VACUUM LOCK WHILE THE MACHINE IS UNDER VACUUM.
- THE TILE IS INSTRUMENTED TO MEASURE HEAT AND PARTICLE FLUX. THIS ALLOWS FOR AN ACCURATE DETERMINATION OF THE EXPOSURE CONDITIONS.
- THE REMOVABLE TILE WILL BE USED FOR
  - EROSION/REDEPOSITION MEASUREMENTS (WITH C-13 MARKER OR DIFFERENT MATERIALS)
  - MATERIALS TESTS:

    GRAPHITES

    COATINGS

    PyC, ETC.
  - CONDITIONING STUDIES
  - MATERIALS TRANSPORT BETWEEN LIMITER AND WALL (AND VICE VERSA) (WITH SURFACE ANALYSIS STATION)
- THE ATF LIMITER LOCK OFFERS A UNIQUE OPPORTUNITY FOR MATERIALS STUDIES IN A REALISTIC ENVIRONMENT

IR Camera View of ATF Instrumented Limiter

Sector #14

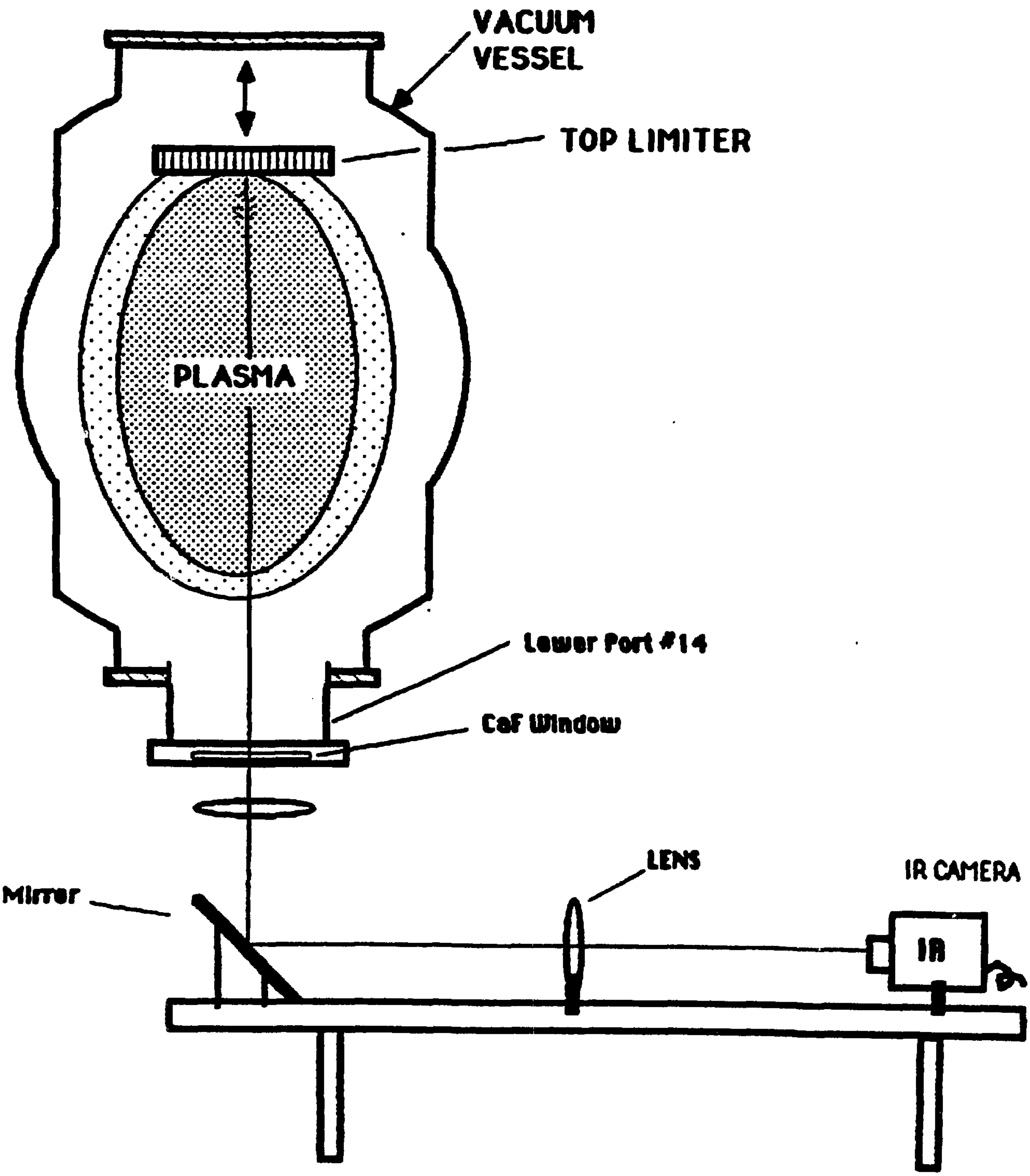

DLH 3/19/87

DIVERTOR CONFIGURATION EXPERIMENT ON ATF

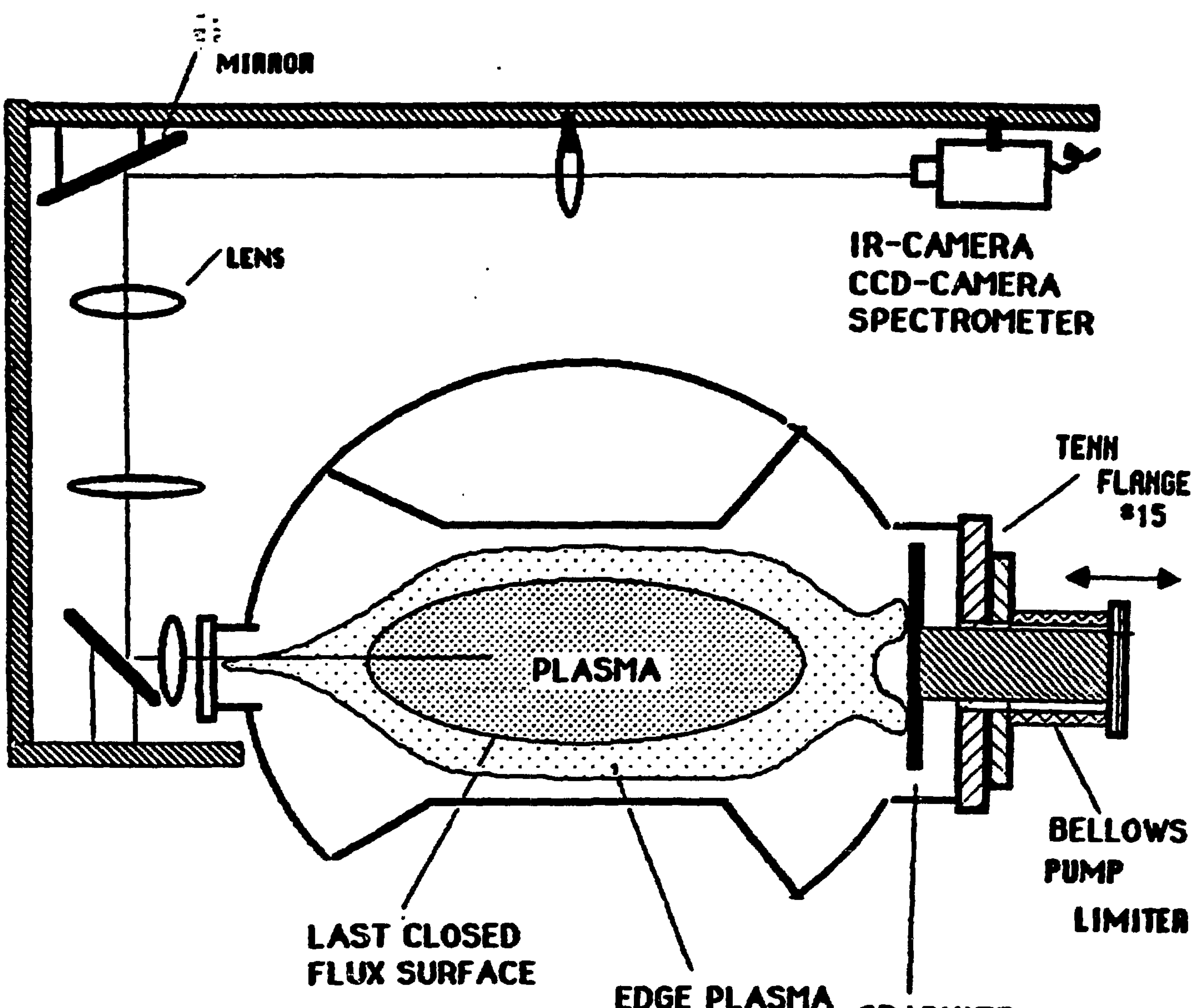

DLH 4/9/87

TENN PORT #15

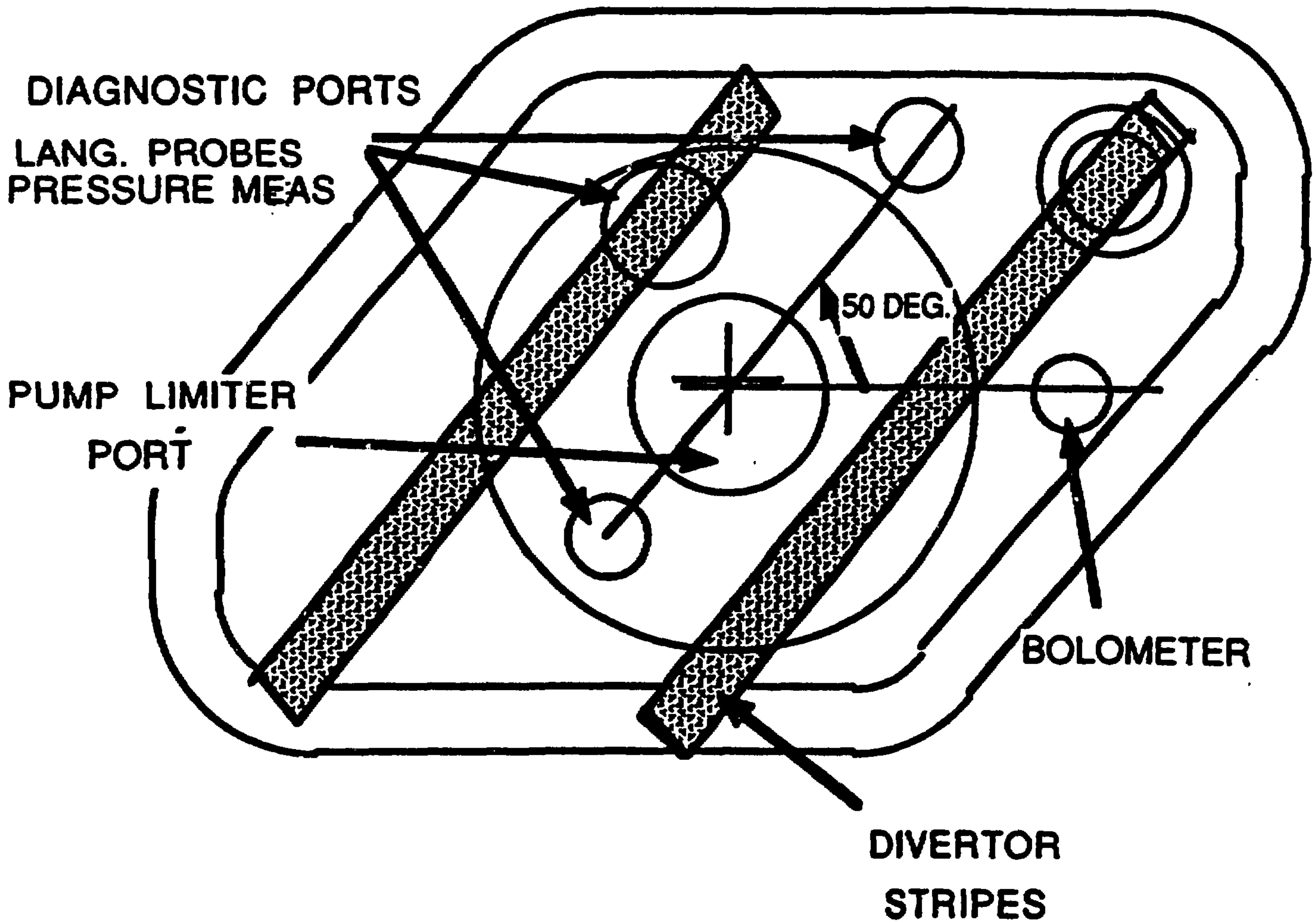

EDGE DIAGNOSTICS AND PUMP LIMITER

DLH 4/9/87

Graphite Plate

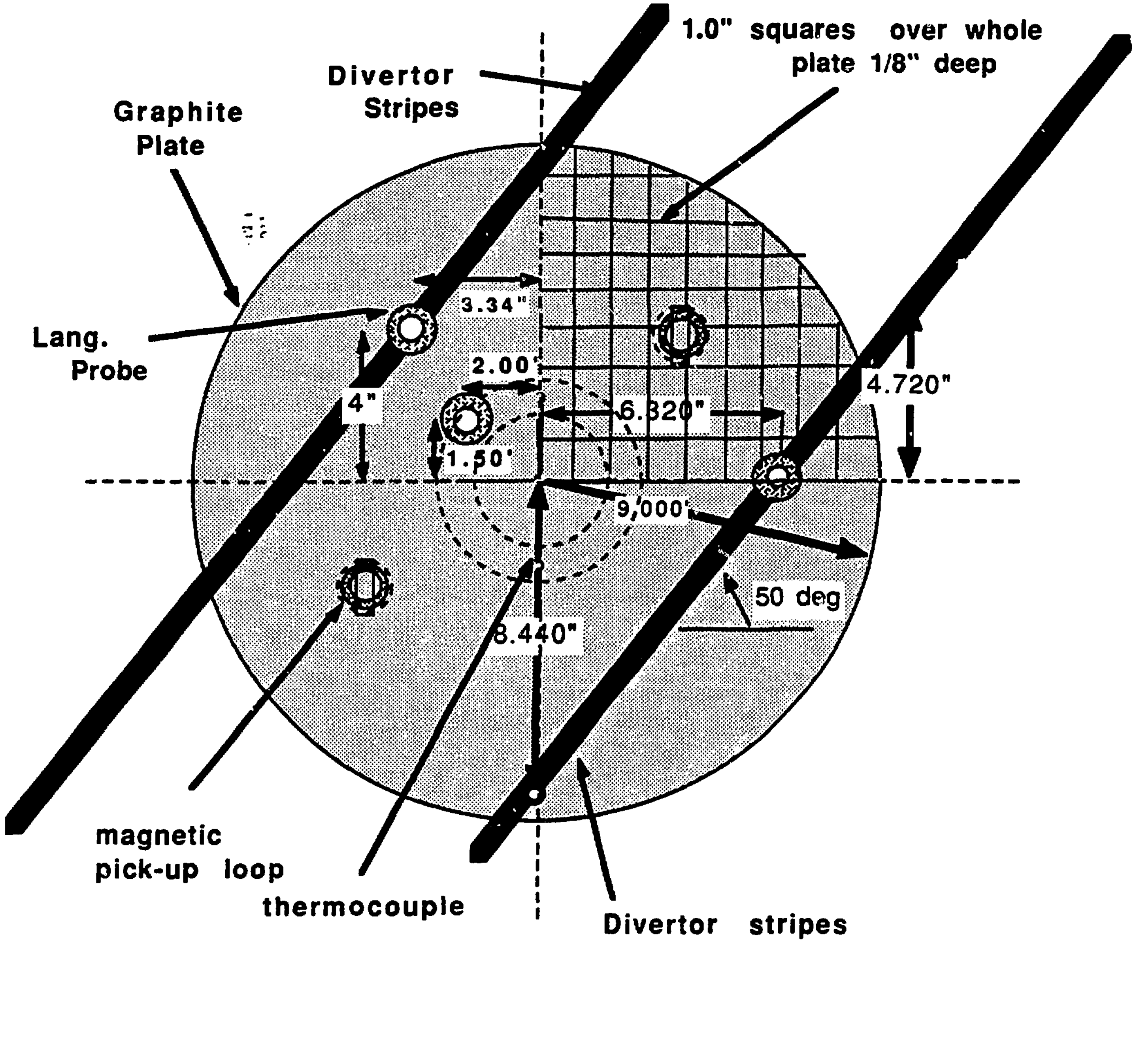

DLH 4/27/87

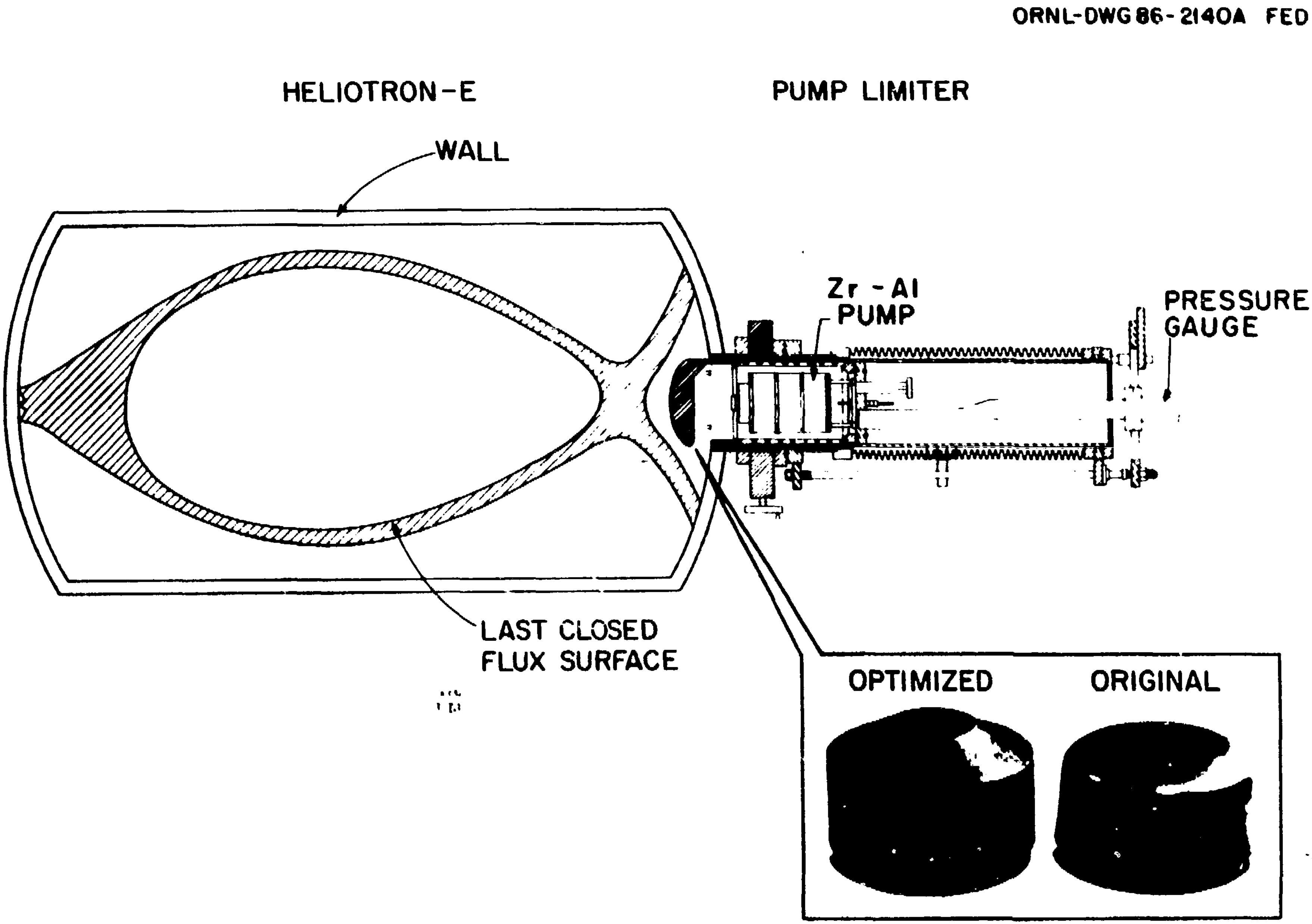
ORNL-DWG 86-2140A FED
HELIOTRON-E
PUMP LIMITER
WALL
Zr-Al
PUMP
PRESSURE
GAUGE
LAST CLOSED
FLUX SURFACE
OPTIMIZED
ORIGINAL

ATF PLASMA EDGE PROGRAM

PLASMA BOUNDARY	VACUUM/WALL
EDGE DIAGNOSTICS:	VACUUM
INSTRUMENTED LIMITER DIVERTOR PLATE IR/CCD-CAMERAS H-ALPHA ARRAY LANGMUIR PROBES	PUMPING BAKING LEAK CHECK RGA GAS PUFFING
PARTICLE CONTROL/HEAT REMOVAL:	WALL CONDITIONING
PARTICLE SCOOP DIVERTOR MODULE COOLING PANEL	DISCHARGE CLEANING GETTERING CARBONISATION OUTGASSING/IN-VESSEL COMPONENTS
PLASMA INTERACTION/RF-COMPONENTS	SURFACE ANALYSIS
STUDY RF-SHEATH PARTICLE ENERGY DISTR. SURFACE ANALYSIS	AUGER SPECTROMETER
HILLIS UCKAN KLEPPER GALLOWAY	LANGLEY SIMKINS RAYBURN CLAUSING

SUMMARY

- THE PLASMA EDGE CONFIGURATION IN STELLARATORS IS MORE COMPLICATED THAN IN TOKAMAKS. ITS STUDY WILL BE THE FIRST TASK OF THE PARTICLE AND IMPURITY CONTROL PROGRAM.

- PARTICLE CONFINEMENT TIMES HAVE BEEN OBSERVED TO BE VERY LONG IN STELLARATORS (100 ms in W-VII A). AS A CONSEQUENCE, IMPURITY CONTROL IS A KEY ISSUE IN THE PERFORMANCE OF STELLARATORS.

- THE CRITICAL PARAMETER OF THE EDGE PLASMA CONFIGURATION IS THE CONNECTION LENGTH , SINCE IT DETERMINES THE NUMBER OF NECESSARY DIVERTOR MODULES.

- ONCE A SUFFICIENT DATA BASE ON THE PLASMA EDGE CONFIGURATION HAS BEEN ESTABLISHED, A PROTO-TYPE DIVERTOR MODULE WILL BE DESIGNED AND BUILD.

- EXPERIMENTAL STUDIES ON DIVERTOR CONFIGURATION AND PARTICLE CONTROL ARE COMPLEMENTED BY EXTENSIVE MODELING OF PLASMA TRANSPORT, NEUTRALS TRANSPORT (DEGAS) AND SHEATH EFFECTS AT THE PLASMA-WALL INTERFACE.

ORNL PMI

Suppression of X-rays Generated by Runaway Electrons in ATF

D.A.Rasmussen, A.C.England, C.C.Eberle, W.R.Devan,
J.H.Harris, T.C.Jernigan, R.R.Kindsfather, R.N.Morris,
M.Murakami, G.H.Neilson, J.A.Rome, M.J.Saltmarsh, R.B.Wysor
ORNL

and

O.Motojima, H.Okada, K.Uo
Kyoto University

US-JAPAN STELLARATOR/HELIOTRON WORKSHOP
NOVEMBER 9-13, 1987

Introduction

Torsatrons are susceptible to hard x-rays generated by runaway electrons.

- The x-rays are generated when the runaway electrons impact solid material such as the vacuum vessel, limiter, or antenna structures.

- The runaways result from the combined effect of loop voltages (up to 20 V in ATF) induced during the ramp-up and ramp-down of the helical field, and good electron confinement on closed magnetic surfaces.

Summary of Heliotron-E Information

- Hard X-rays are worst during the ramp-down phase
- Hard X-rays can be suppresed with relatively mild, time varying outward shift of flux surfaces by axisymmetric VF and mild gas injection (typically 0.01 mrem/shot at R=15 m)
- An inward shift is "very dangerous" and enhances hard X-rays
- Localized error fields are not effective
- Heavy gas puff helps to suppress X-rays in conjunction with VF programming but probably ineffective by itself
- Base vacuum pressure important: mid 10^{-7} torr produces the minimum hard X-rays.
- Disabling the VF programming and gas puff results in doses as high as 21 mrem/shot at R=17 m.

X-rays are succesfully controlled on Heliotron-E because:

- Few free electrons are available during the ramp-up

- Free electrons from the experimental portion of the discharge are available for acceleration only during the ramp-down

- Outward orbit shift plus the programmed outward configuration shift, directs energetic electrons to the outer wall or limiter during ramp-down

Runaways in Proto-Cleo

- Small torsatron: $R = 40$ cm, $a_p \sim 5$ cm
  $B(max) = 2.5$ kG
  $\iota(0) \sim 0$, $\iota(a_p) = 0.6$

- Typical waveforms:

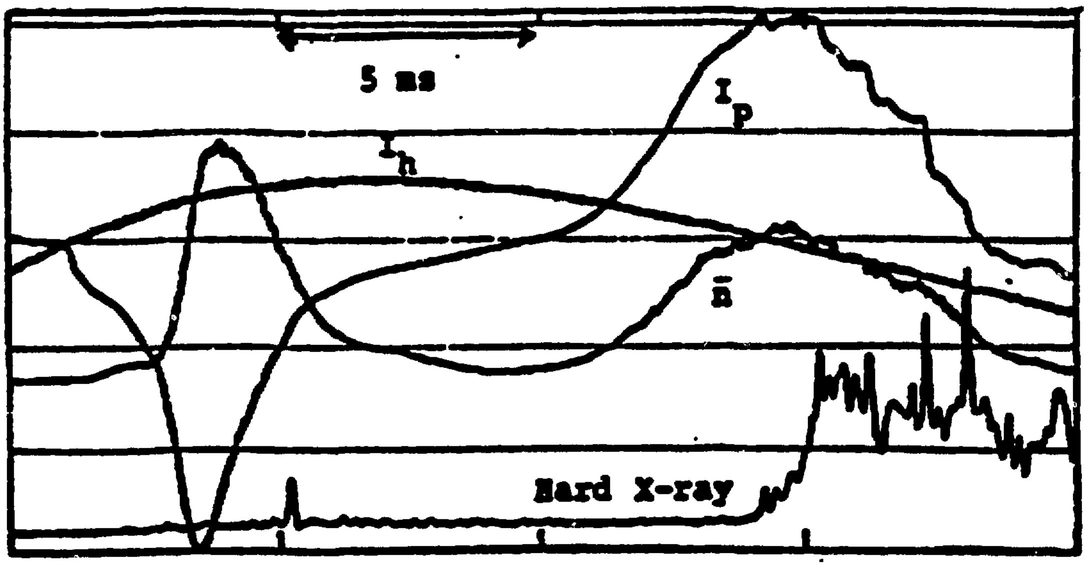

$\bar{n} \rightarrow 2 \times 10^{11} \text{cm}^{-3}/\text{div.}$
$I_p \rightarrow 50$ A/div.

- Energy of "walkaways" ~ 100 KeV. Ramp-up plasma sensitive: could be eliminated with control of gas puff, pre-ionization.

[J. H. Harris, et al., Nucl. Fusion, 24, 159 (1984)]

An assessment of this problem for ATF indicates that:

- Hard x-rays pose a potential hazard to personnel and internal ATF components

- Suppression techniques developed on the Heliotron-E device may not be sufficient for ATF (configuration cannot be strongly shifted to the outside)

- It is desirable to inhibit runaway formation entirely (ATF has no radiation shielding)

- It is necessary to have a backup system.

- Extensive monitoring is required for initial operation and following major changes to the device

There are several aspects to the problem:

Prevention/Suppression

- Mechanical Intercept Probe
- Fast Gas Puff
- Spoiling of Magnetic Surfaces

Detection

- Personnel monitoring
- Occupied areas monitoring
- Surveys
- Real time feedback

Shielding

- Local
- Global

Access Controls

- Personnel restrictions
- Interlocks

The chosen approach to suppress X-rays is three pronged:

1) The first approach is to fabricate one or more removable probes that intersect all magnetic flux surfaces. The probe is inserted across the flux surfaces as a standard procedure during the ramp-up and ramp-down of the helical field. The probe intercepts electrons before they can complete, on average, 100 transits around the torus. This limits their final energy to less than ~ 2 kev, hence preventing dangerous x-ray emission.

2) The second approach is to use vertical field programing in conjuction with gas puffing during the field ramps. While vertical field programming was found to be effective on Heliotron-E, it is not obvious that it will be successful on ATF; nevertheless, this technique will be investigated as well.

3) Finally as a backup system, for example in the case of an abnormal termination of the magnetic fields (ie. power failure) a fast acting valve will open to release a stored reservoir of high pressure Argon into the ATF vacuum vessel. This will result in a rapid increase in the vessel pressure to ~ 10^{-2} torr, thereby suppressing runaway production. During unanticipated operating conditions (fault conditions) the gas puff is the only system capable of responding in the time period required (ie. less than 10-15 ms) to prevent the acceleration of runaways to energies (greater than 100 kev) where they produce dangerous x-ray emission.

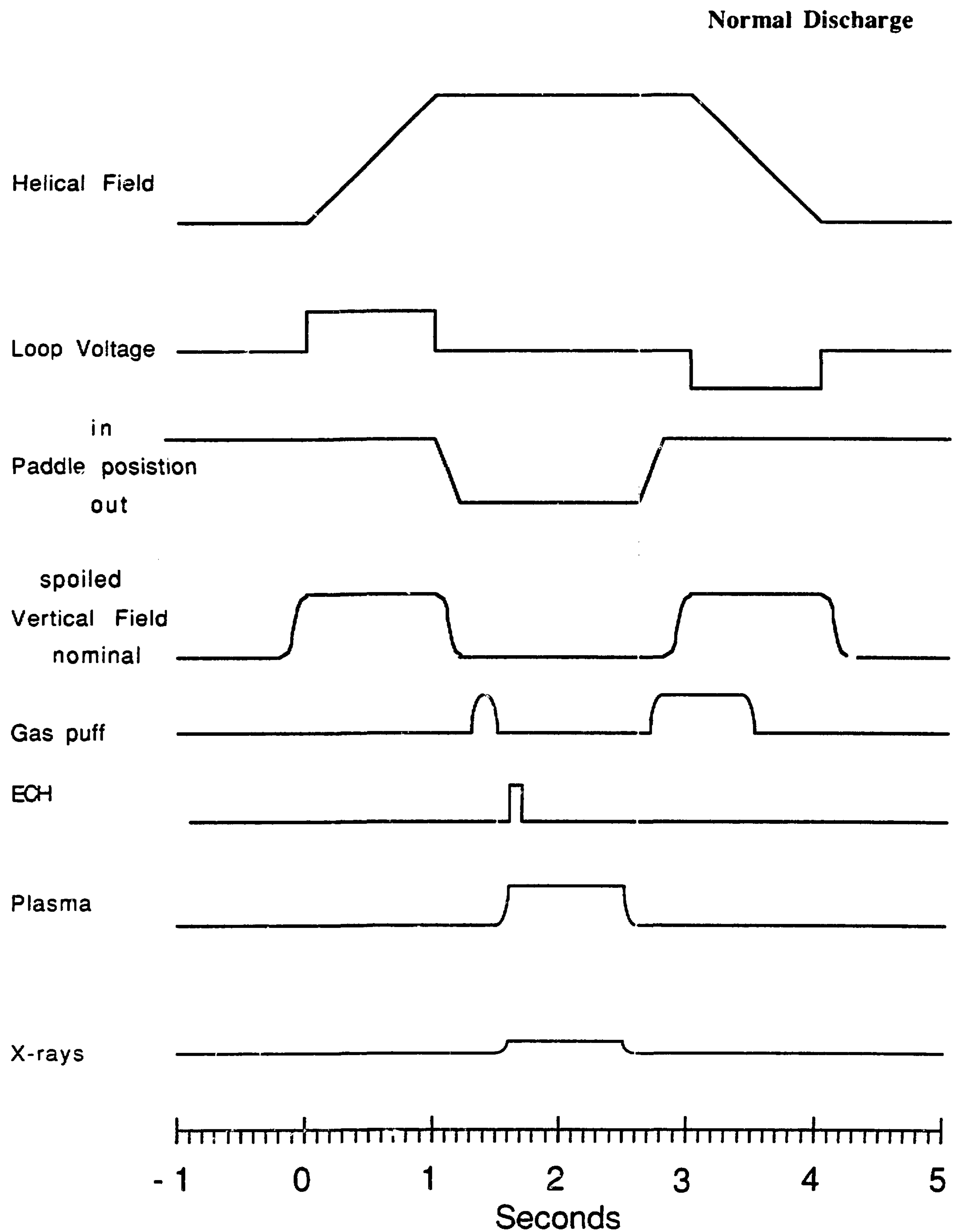
Normal Discharge
Helical Field
Loop Voltage
in
Paddle posistion
out
spoiled
Vertical Field
nominal
Gas puff
ECH
Plasma
X-rays
-1
0
1
2
3
4
5
Seconds

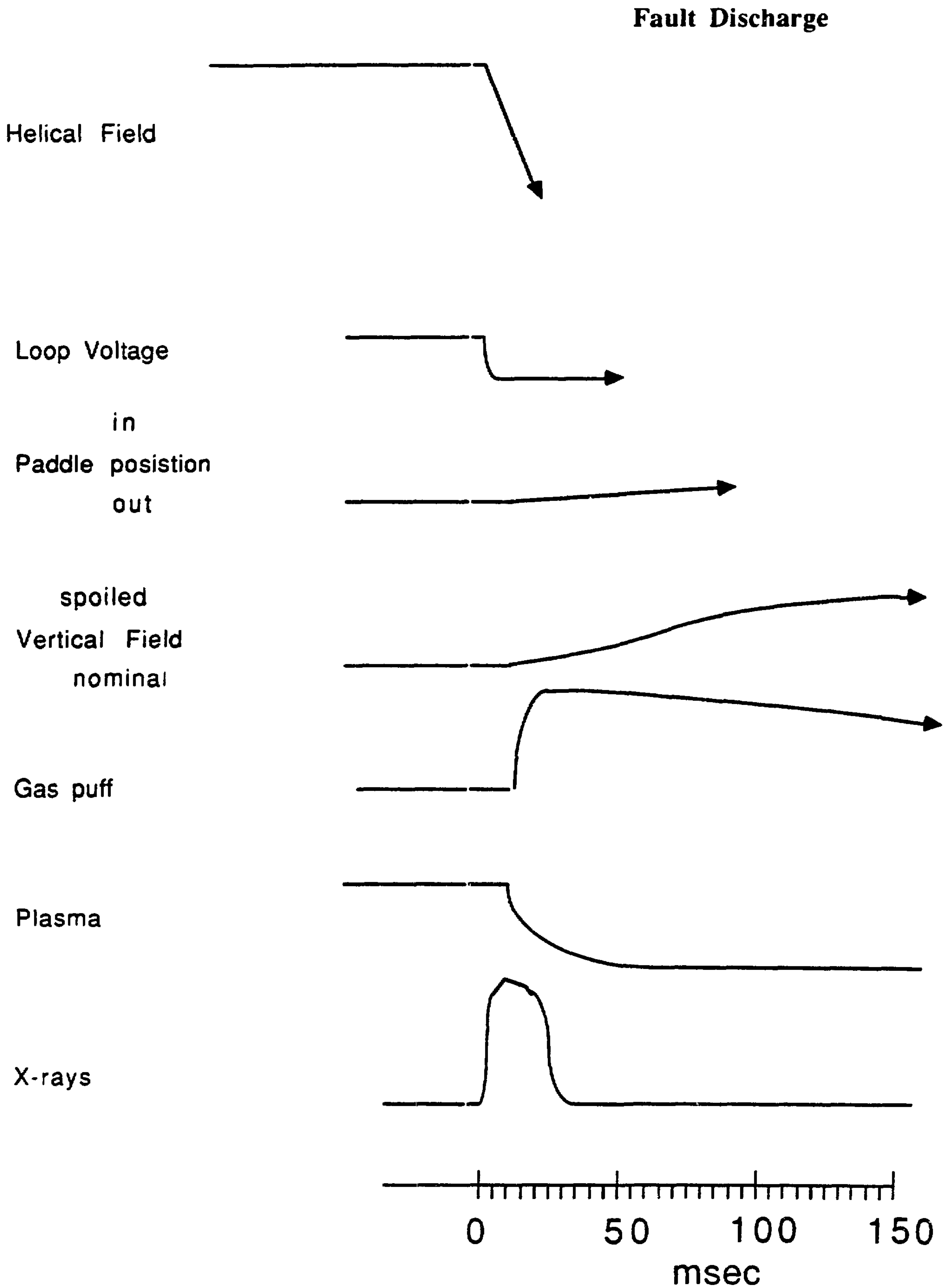
Fault Discharge
Helical Field
Loop Voltage
in
Paddle posistion
out
spoiled
Vertical Field
nominal
Gas puff
Plasma
X-rays
0
50
100
150
msec

X-Ray Suppression System Logic

- **Rotary probe**

  Operation of the rotary probe is never inhibited during the course of normal operations. The default position is with the probe in. Failure of the probe to withdraw during the shot sequence will result in the generation of an end of event (EOE) pulse

Rotating Intercept Probe

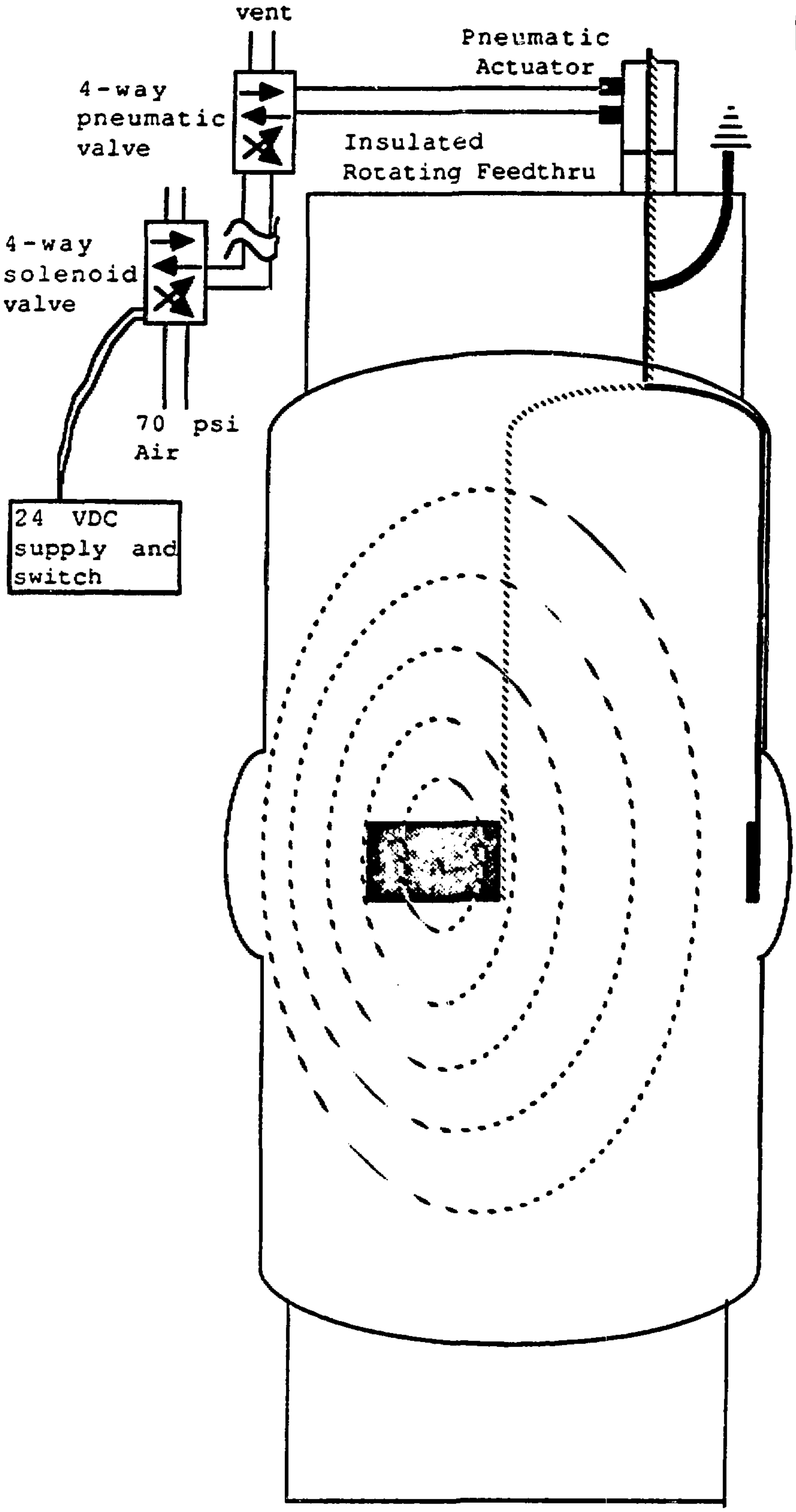

- **Vertical Field Programming**
  The inner VF and trim VF coils and moderate gas puffing will be programmed for maximum inhibition of runaway confinement, however this may not be as effective as on Heliotron-E because;

  - The arrangement of power supplies and coils makes large outward shifts difficult (eg., the trim VF supply polarity cannot be reversed)

  - For realistic values of the coil currents, it is impossible to eliminate <u>all</u> of the closed flux surfaces

  - Use of the mid-VF coils to move the plasma up or down also will not eliminate <u>all</u> of the closed flux surfaces

- **Fast Gas Puff**

  The fast gas puff will fire if:

  - **The loop voltage exceeds a predefined threshold, <u>and</u>**
  - **the vessel is under vacuum, <u>and</u>**
  - **the rotary probe is not in position, <u>or</u> X-radiation above a predefined threshold is present**

  The gas valves require power (24 VDC) in order to seal. Loss of power will fire the gas puff.

Fast Gas Puff X-Ray Suppression System

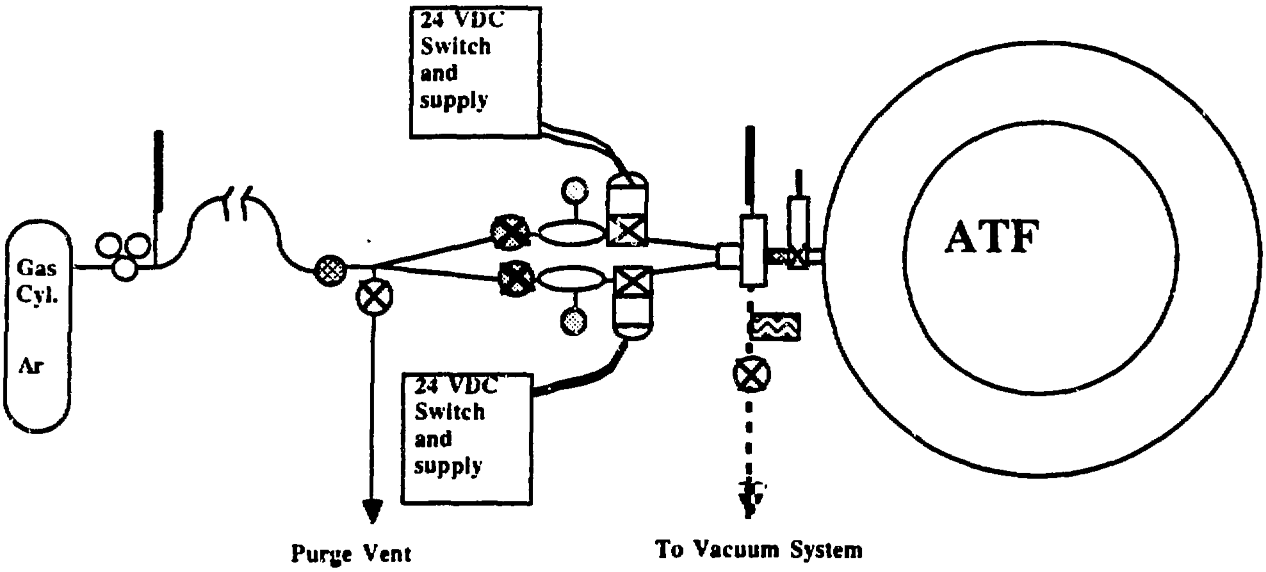

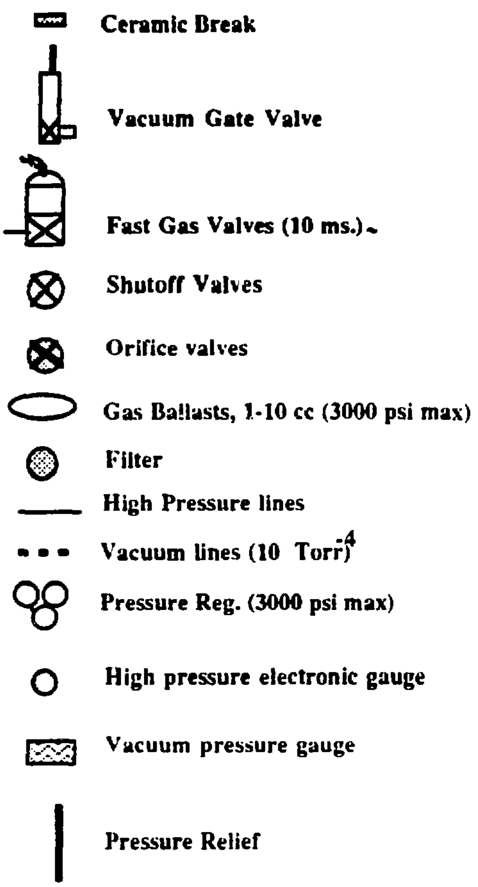

D.A.Rasmussen
10/6/87

ATF Operations X-Ray Suppression Interlocks/Controls

- **Automatic Interlocks**

  The PLC will allow ATF to operate if, prior to the start of the shot sequence:

  - There is sufficient pressure in the fast gas puff ballasts, <u>and</u>
  - The fast gas puff gate valve is open, <u>and</u>
  - No X-rays were seen on the last shot, <u>and</u>
  - The rotary probe is inserted and remains intact

- **Administrative Controls**

  ATF can begin operations each day after a successful test of:

  - **Fast gas valve fired into a closed system (gate valve closed), <u>and</u>**

  - **One cycle of the the rotary probe.**

Alternate Intercept Probe Concepts

- *B* Field driven half loop
  (Rometron) *J* X *B*

- Linear Intercept Probes
  1) Bellows sealed,
  pneumatically driven
  2) Linear induction motor
  driven

Electromagnetic Intercept Probe

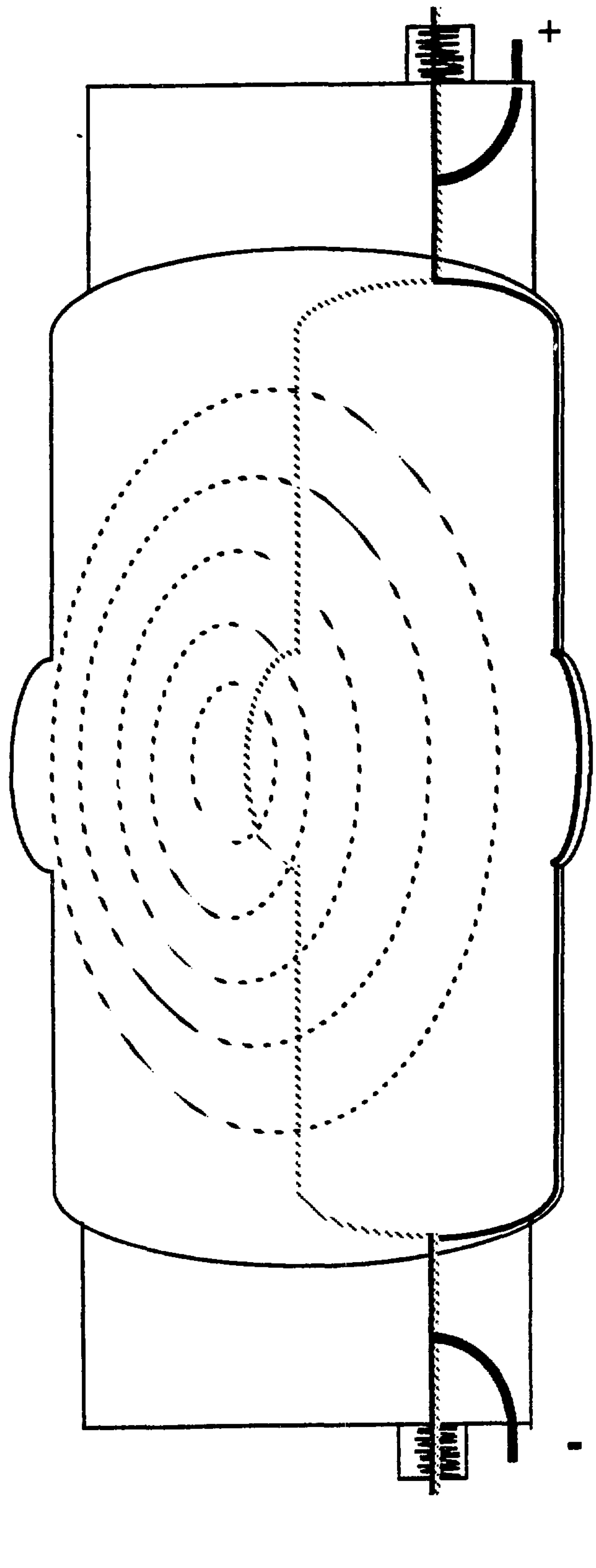

Summary

- X-ray emission from runaway electrons on ATF is a serious issue
- Runaway suppression techniques used on Heliotron-E are not adequate for ATF
- Three approaches have been developed to suppress runaway production
- Monitoring devices have been installed in occupied areas
- Personnel access and exposure will be limited
- Additional shielding will be added as required
- Systems will be ready for installation and testing on ATF prior to commissioning or first plasma operation.

Plasma Rotation and Potential Measurement

O. Motojima

Plasma Physics Laboratory
Kyoto University
Uji, Japan

Friday Morning
Motojima

POLOIDAL ROTATION MEASUREMENT

MOTIVATION

(1) ACCUMULATING DATA BASE IN THE WIDE RANGE OF COLLISIONALITY $\nu_{**}=2\pi\nu/\varepsilon_h^{3/2}\cdot 2\pi R_o/mV_{th}$ WHICH CONTAINS THE $1/\nu$ REGIME AND THE PLATEAU REGIME PLASMAS HEATED BY ECRH, NBI AND ICRF.

(2) ANALYSIS BASED ON THE NEOCLASSICAL THEORY ESTIMATING THE RADIAL ELECTRIC FIELD FROM POLOIDAL ROTATION.

Top View of Heliotron E

$R = 2.2m$
$\bar{a}_p = 0.2m$
$B_h(0) = 2.0T$

- high shear,
- large rotational transform
- built-in divertor

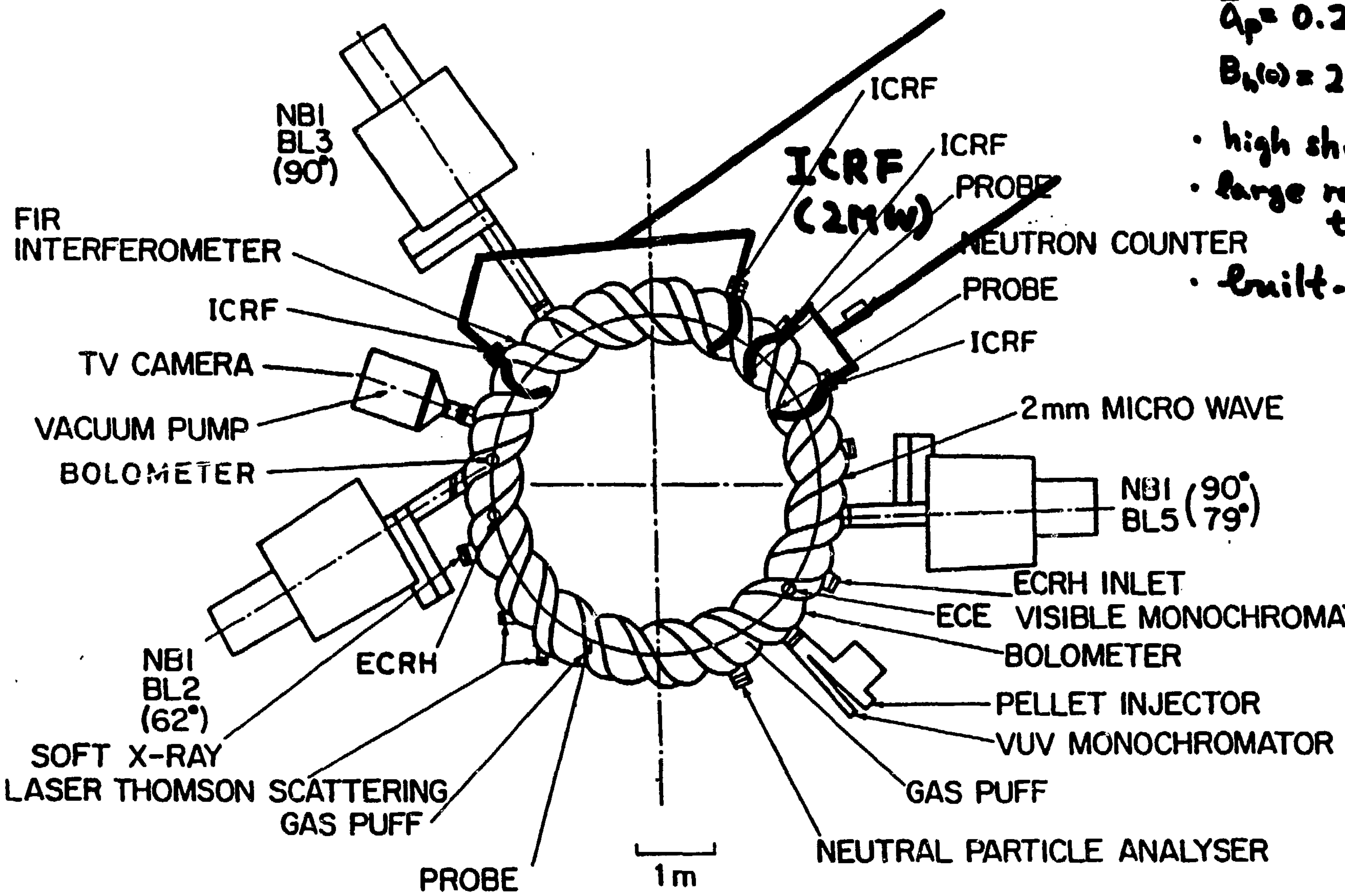

Experimental Set up

(a) Vertical

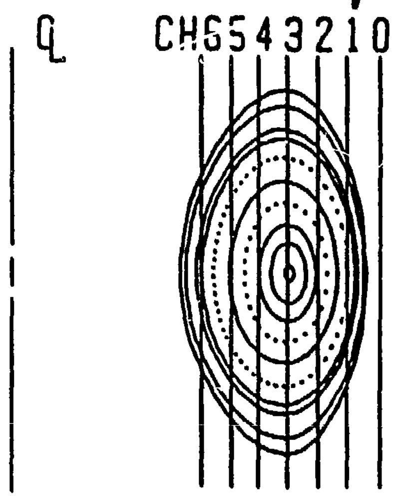

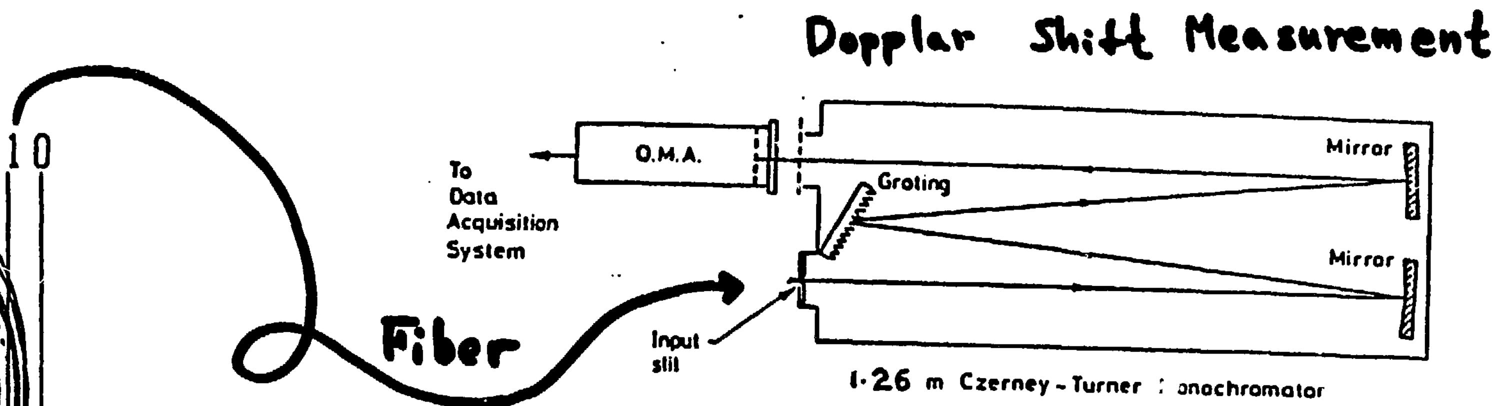

(b) Horizontal

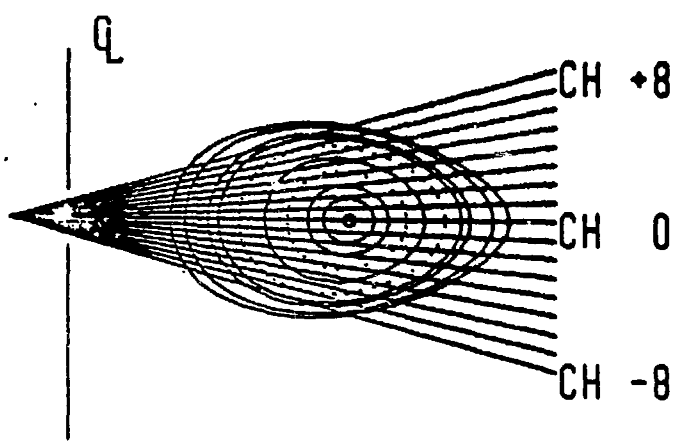

- **Detector :**

  512 ch (Tracor Northern Model 6133)

  Integration time ~ 10÷20 ms

- **Line**

  CV : 2271 Å × 4 th order

Doppler Shift of CV Line

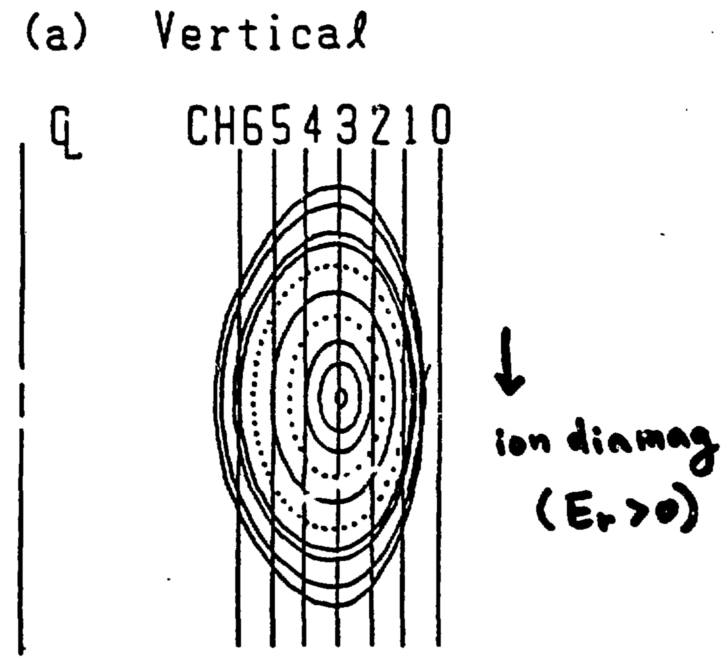

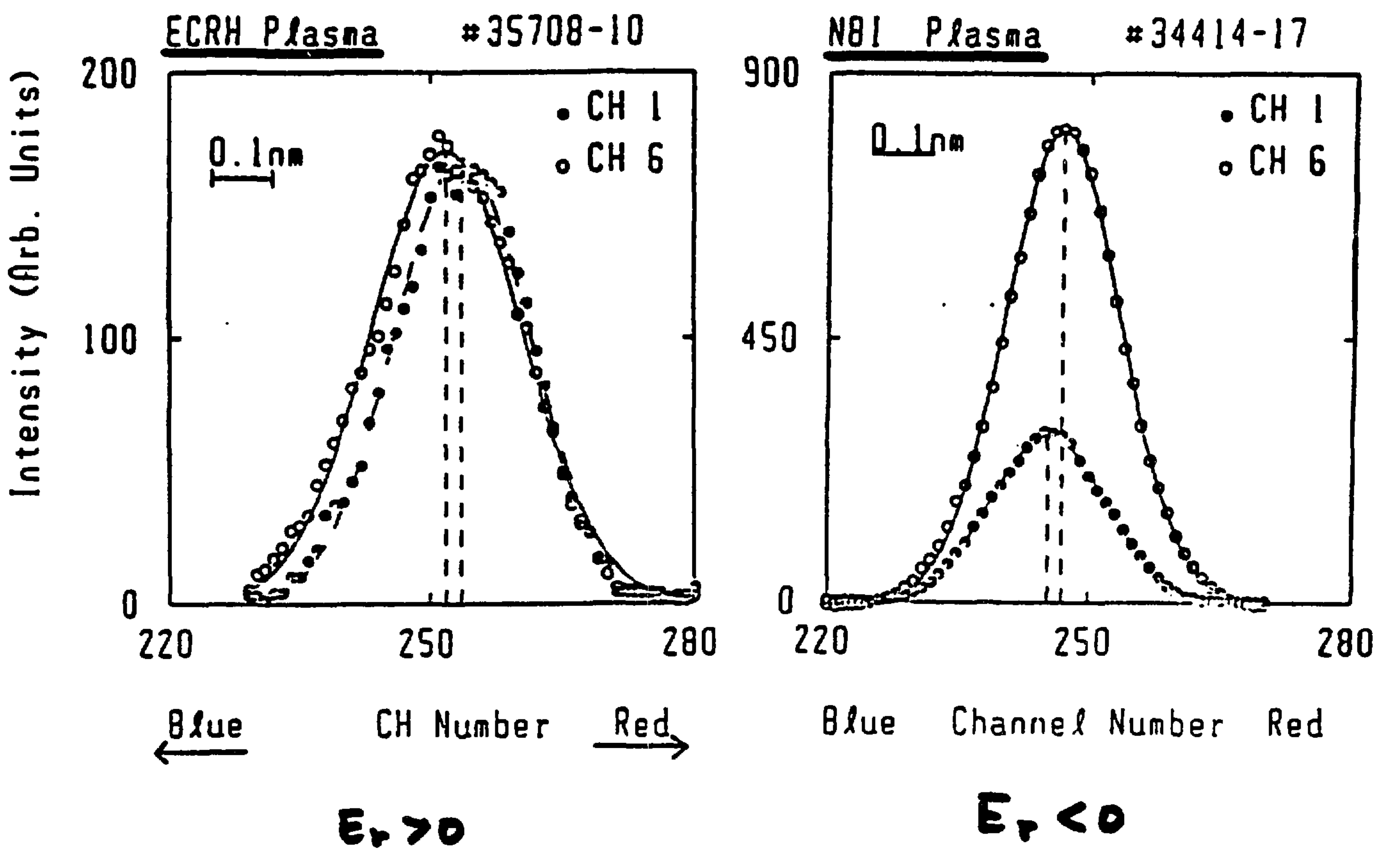

CV density profile calculation

$$\Gamma_z = -D\frac{\partial n_z}{\partial r} + V n_z$$

$$\frac{\partial n_z}{\partial t} = -\frac{1}{r}\frac{\partial}{\partial r}(r\Gamma_z) + \text{Source Term}$$

$D \sim \begin{cases} 3000 \text{ cm}^2/\text{s} & (\text{ECH}) \\ 1000 \text{ cm}^2/\text{s} & (\text{NBI}) \end{cases}$

$V \sim \begin{cases} 0 \text{ cm/s} & (\text{ECH}) \\ 300 \text{ cm/s} & (\text{NBI}) \end{cases}$

Observable $0.7 \sim 0.9\,\bar{a}_p$

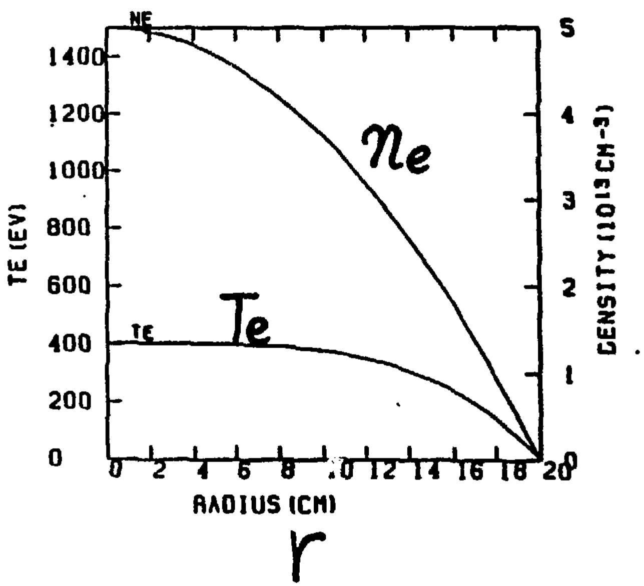

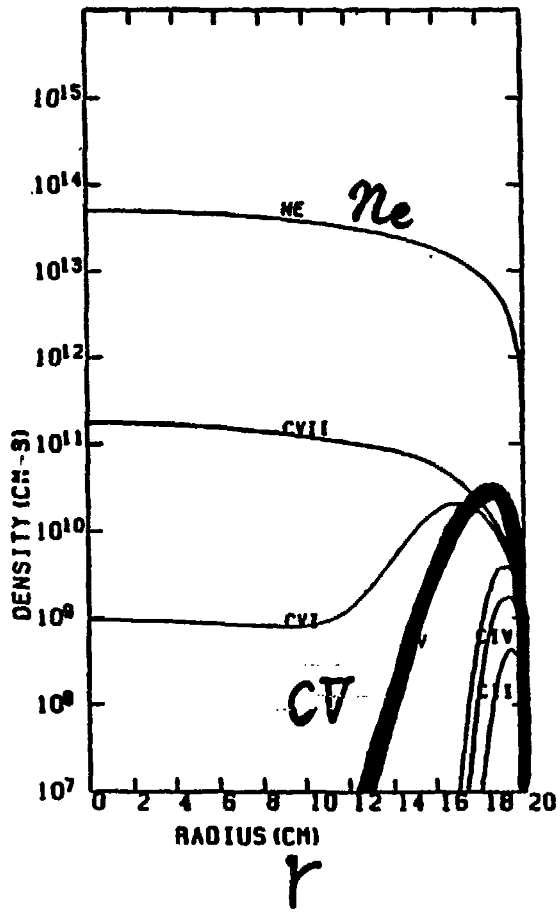

Experiment

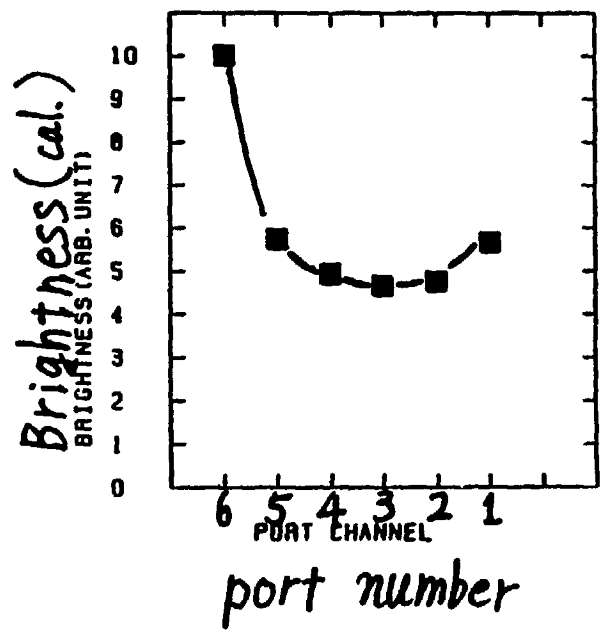

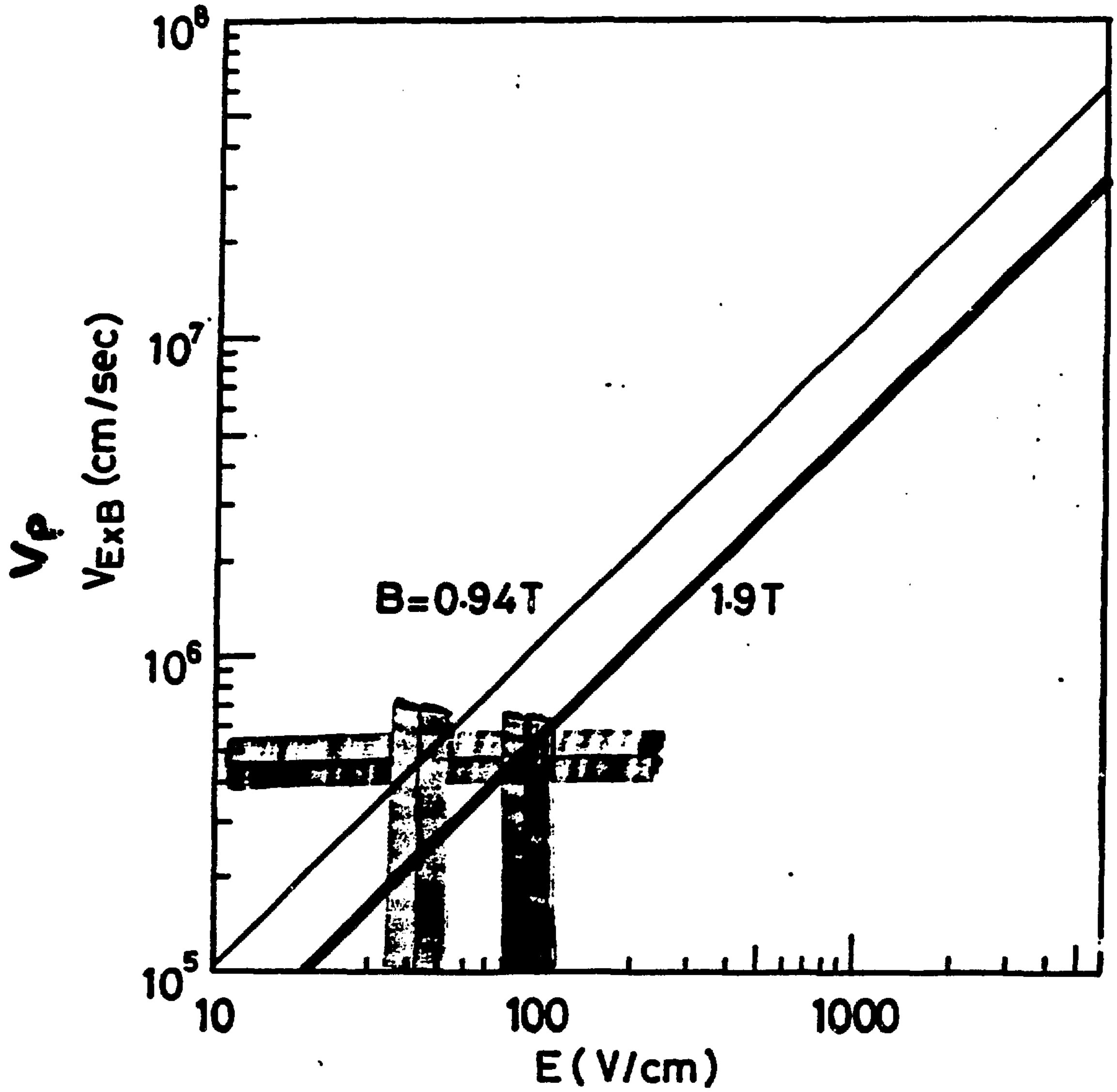

10^8
10^7
10^6
10^5
V_P
$V_{E\times B}$ (cm/sec)
B=0.94T
1.9T
10
100
1000
E (V/cm)

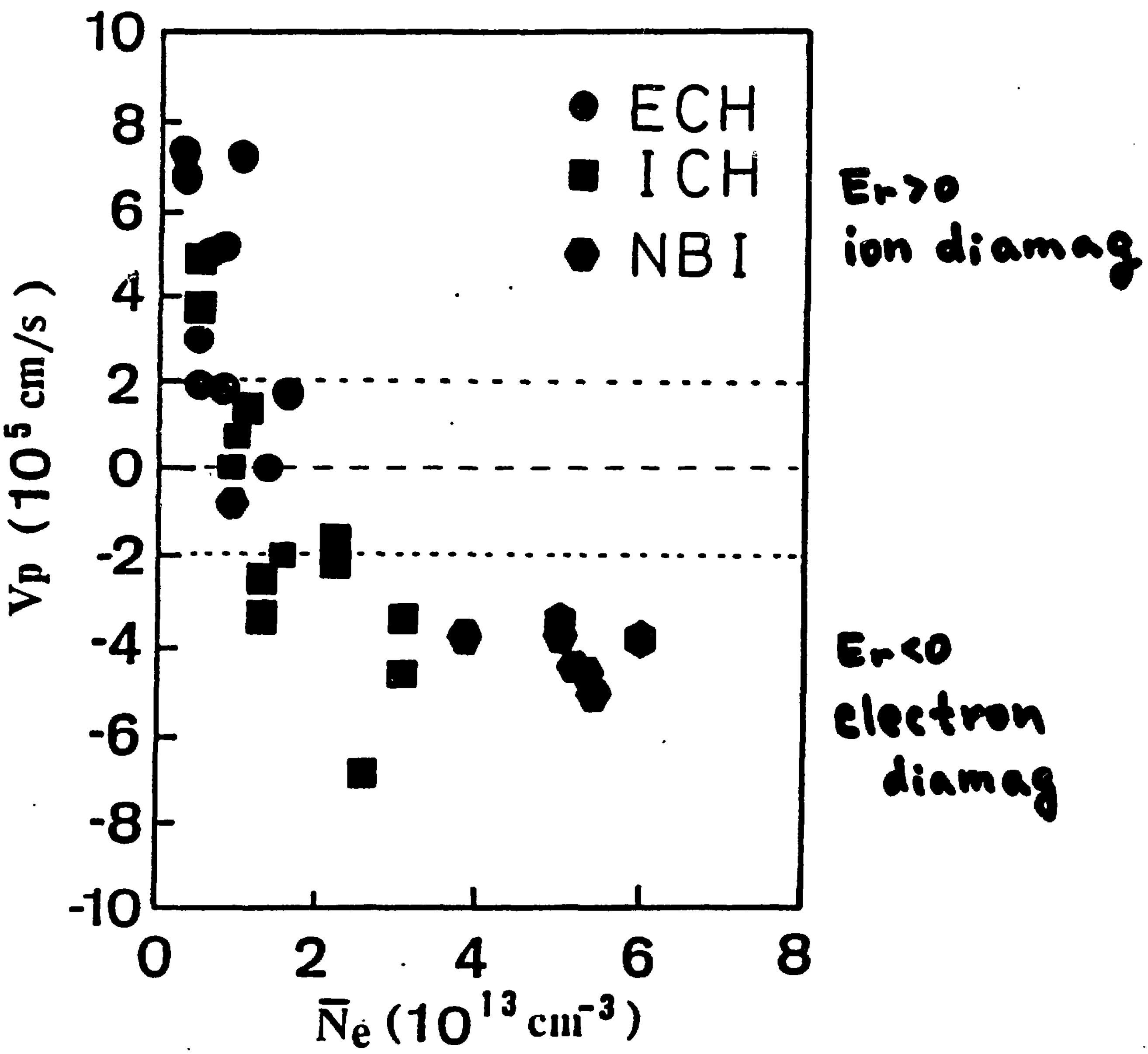

ECH
ICH
NBI
Er>0
ion diamag
Er<0
electron
diamag
Vp (10^5 cm/s)
N̄e (10^13 cm^-3)
10
8
6
4
2
0
-2
-4
-6
-8
-10
0
2
4
6
8

NUMERICAL CALCULATION

NEOCLASSICAL FORMULATION WAS APPLIED FOR RIPPLE TRANSPORT.

$$\Gamma_a^{na} = -\epsilon_t^2 \sqrt{\epsilon_h} v_{d_a}^2 n_a \int_0^\infty dx\, x^{5/2} e^{-x} \tilde{\nu}_a(x) \frac{A_a(x)}{\omega_a^2(x)}$$

SHAING, PHYSICS FLUIDS 27 ((1984) 1567

FOR PLATEAU REGIME

$$\Phi' = -\frac{p_i'}{ne} - \frac{1}{2}\frac{T_i'}{e}.$$

$\Gamma_e = \Gamma_i$ (Ambipolarity Condition)

SHAING, HIRSHMAN AND CALLEN, PHYSICS FLUIDS 29 (1986) 521

ION DIAMAGNETIC DRIFT WAS NEGLECTED

$T_e(r)$, $T_i(r)$, $n_e(r)$ PROFILES-- APPROXIMATED WITH POLYNOMIAL ACCORDING TO THE MEASURED PROFILE

(a) ECRH $T_e(r)/T_{eo}=1-r^2$
$T_i(r)/T_{io}=1-r^4$
$n_e(r)/n_{eo}=1-r^6$

(b) NBI $T_e(r)/T_{eo}=1-r^4$
$T_i(r)/T_{io}=1-r^4$
$n_e(r)/n_{eo}=1-r^2$

(c) ICRF $T_e(r)/T_{eo}=1-r^2$
$T_i(r)/T_{io}=1-r^4$
$n_e(r)/n_{eo}=1-r^6$

$r = 0.8 \cdot \bar{a}_p$

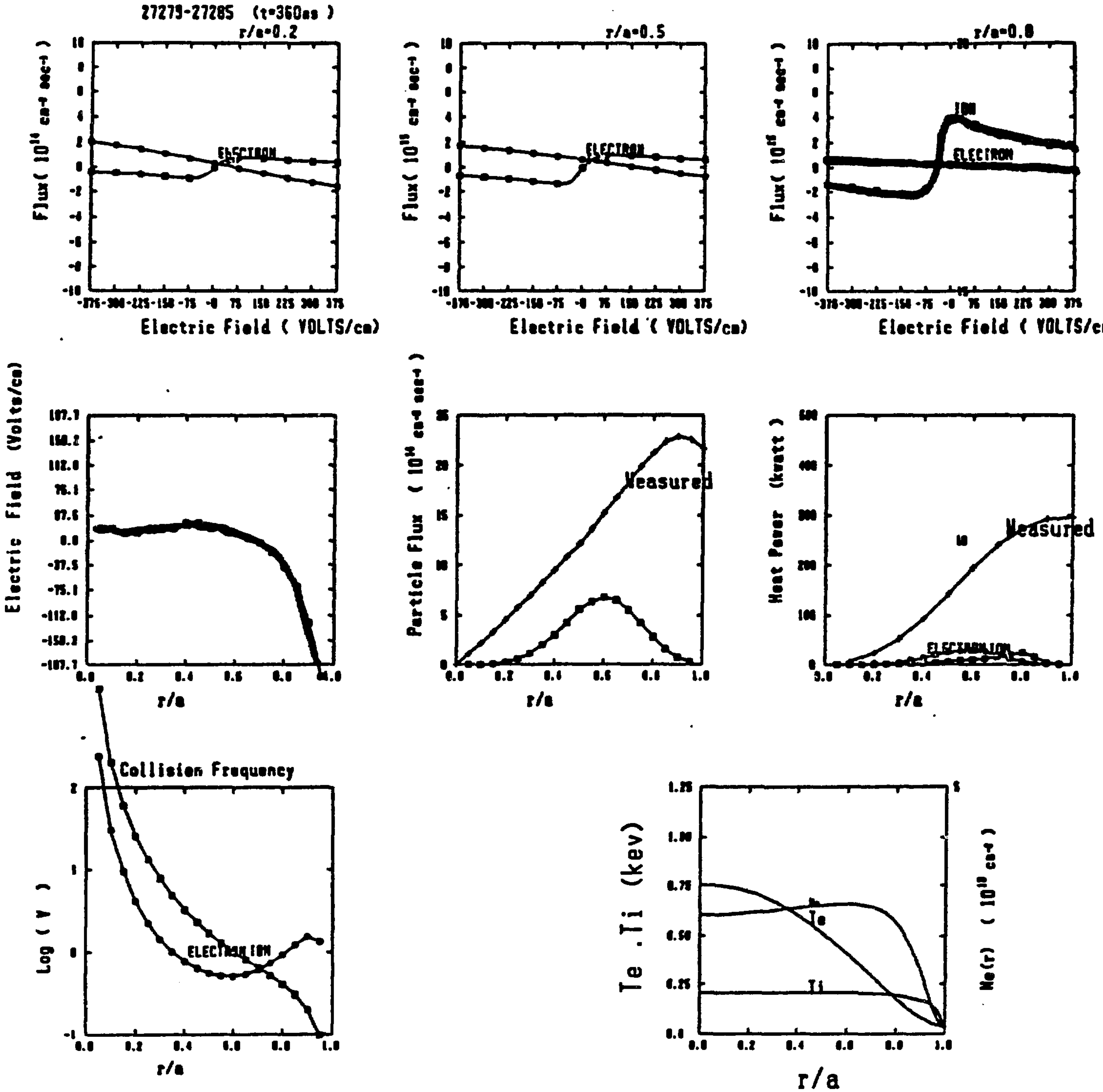
27279-27285 (t=360ms)
r/a=0.2
r/a=0.5
r/a=0.8
ELECTRON
ION
Electric Field (VOLTS/cm)
Electric Field (Volts/cm)
Particle Flux
Measured
Heat Power (kwatt)
Collision Frequency
Log (ν)
ELECTRON ION
r/a
Te
Ti
Te .Ti (kev)
Ne(r)

ECR Plasma

ECRH Plasma

Experiment

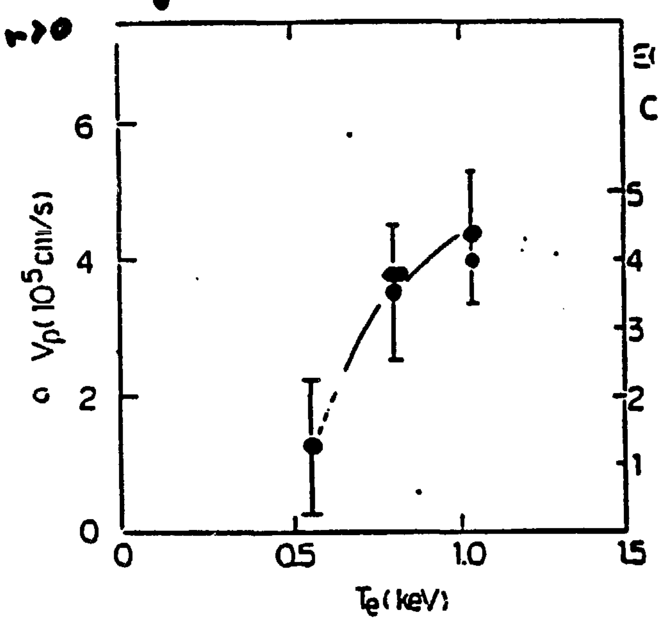

Calculation

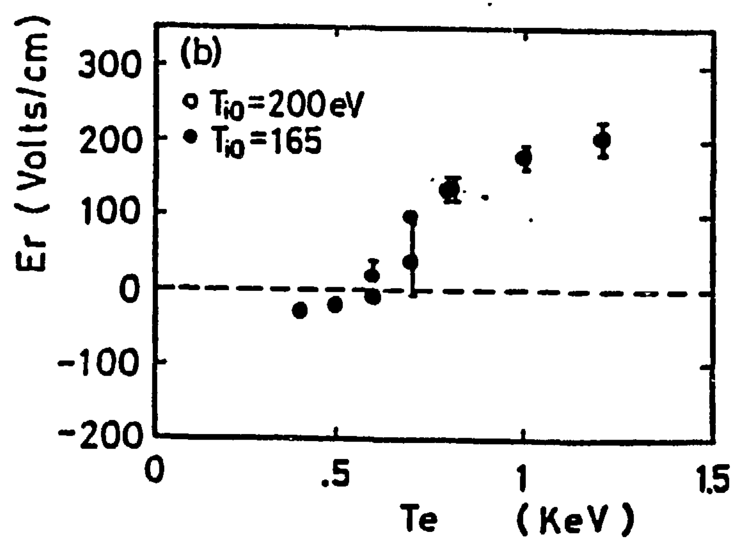

$\bar{n}_e = 0.8 \times 10^{13}\ cm^{-3}$

NBI Plasma

Experiment

$250 \le T_e \le 570$ eV
$150 \le T_i \le 340$ eV

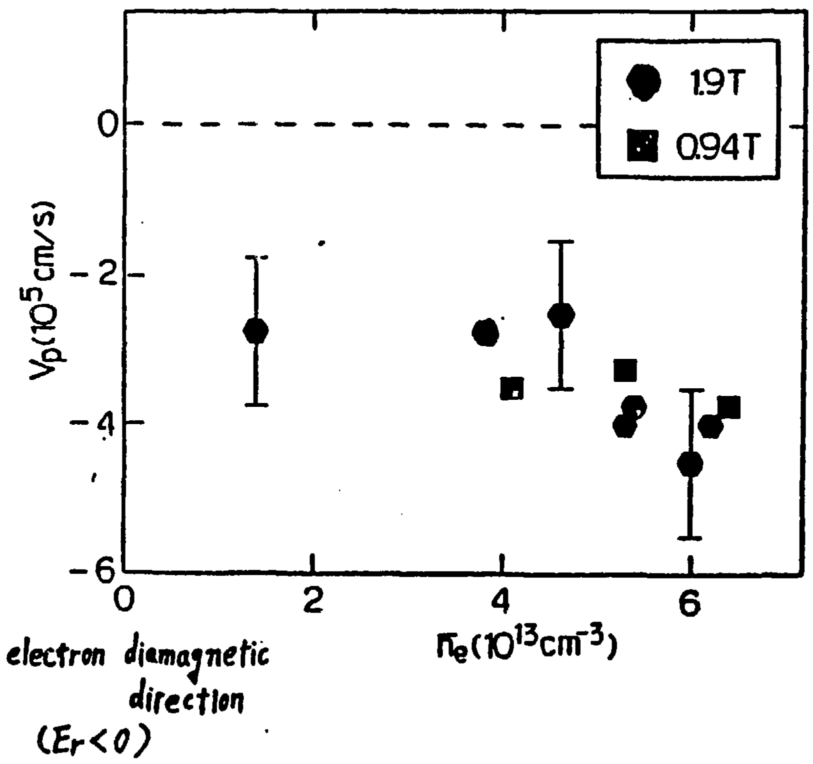

Calculation

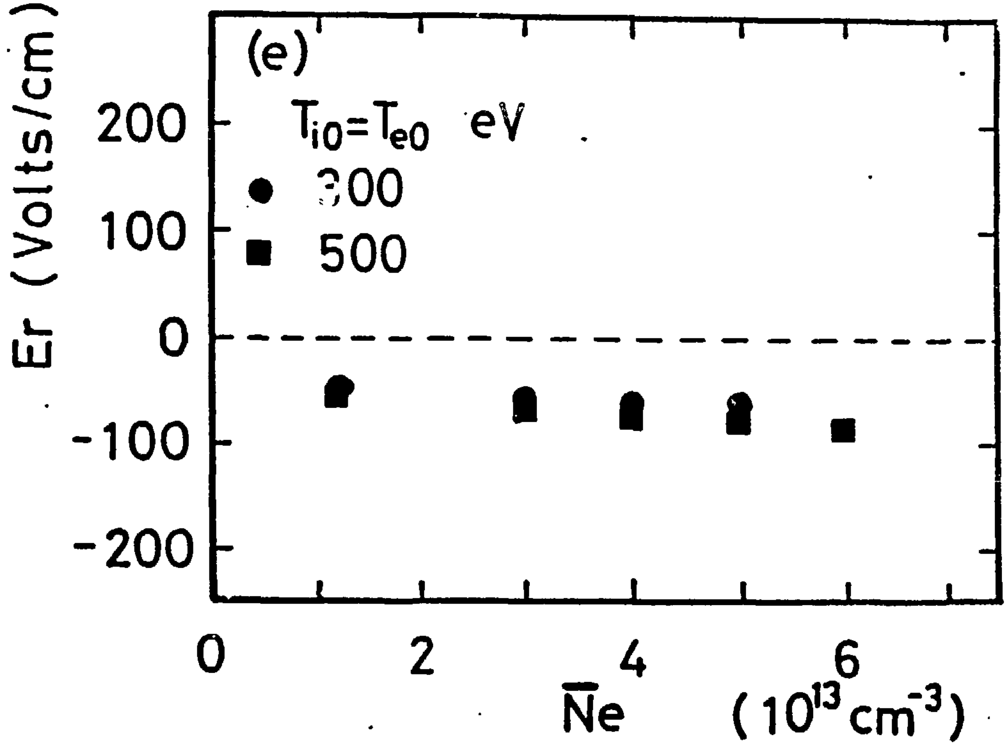

ICRF Plasma

Experiment

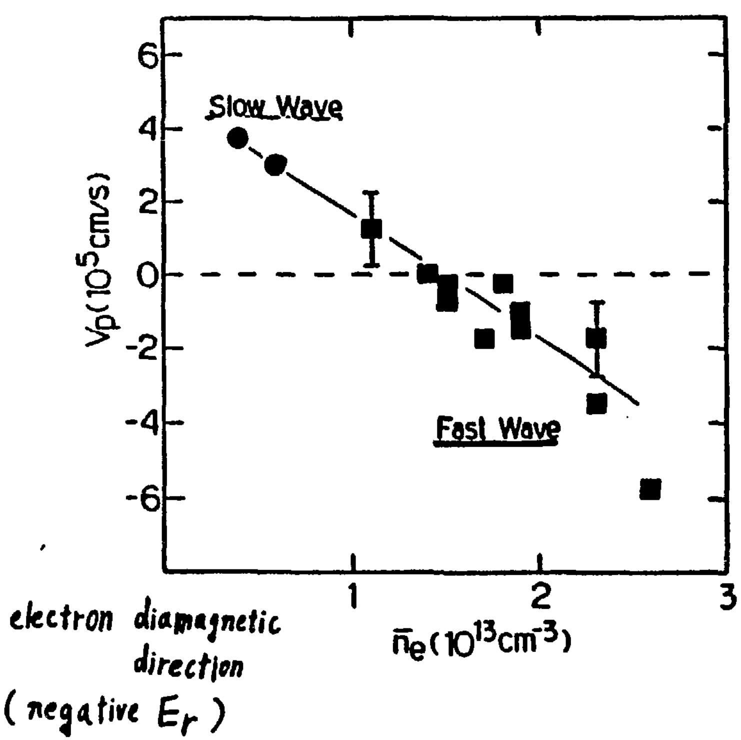

Calculation

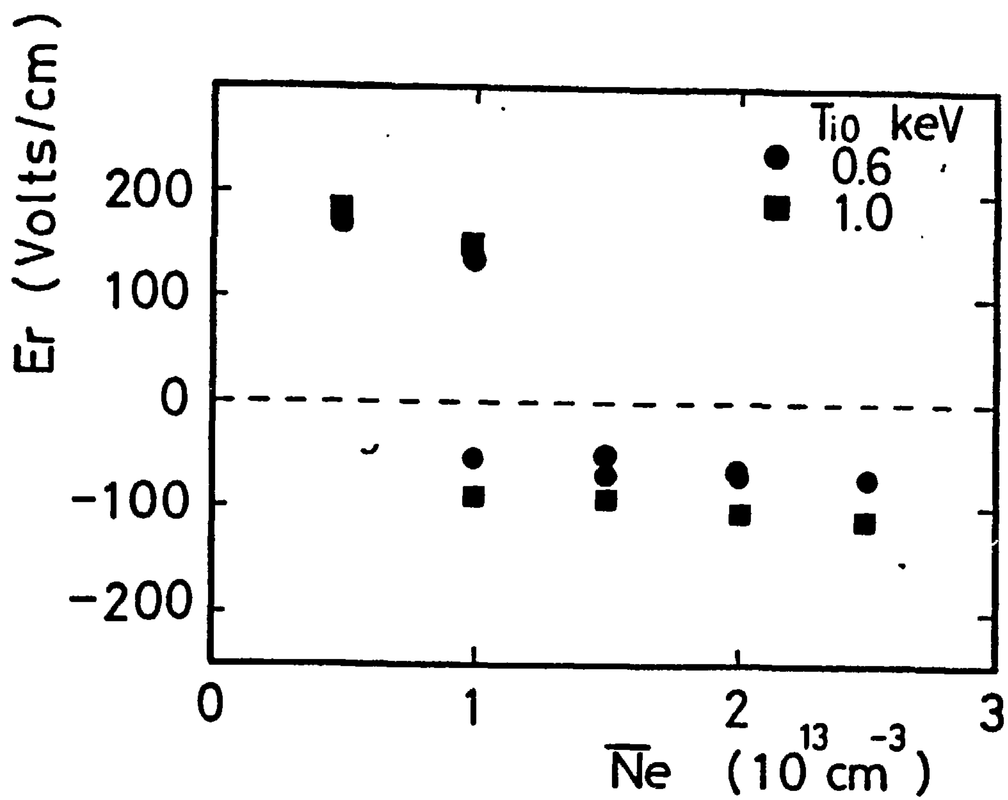

V_p v.s. Heating Power

NBI- plasma

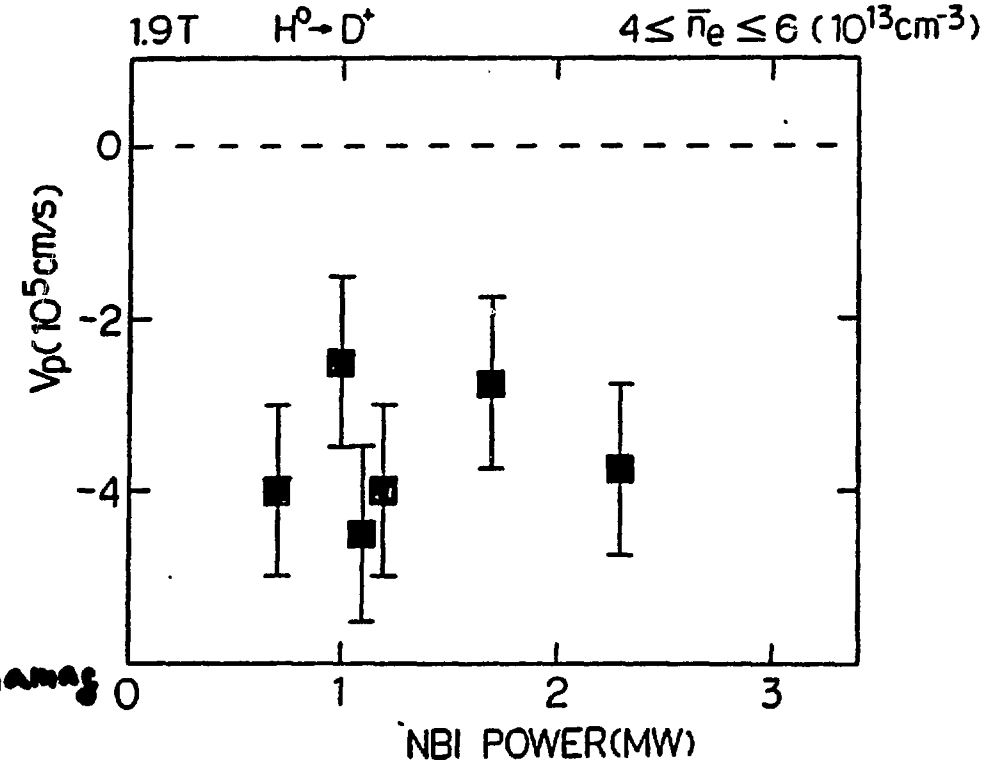

electron diamag

$E_r < 0$

ICRF. plasma

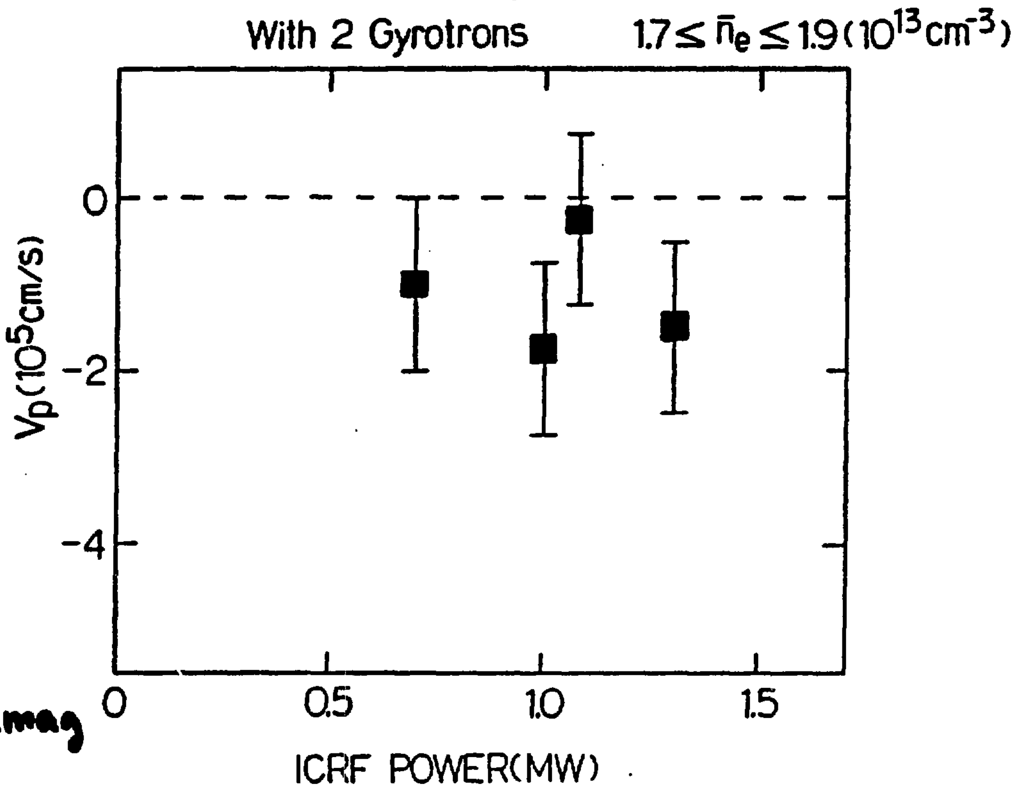

electron diamag

$E_r < 0$

W-VII A
(FRG)

ECRH

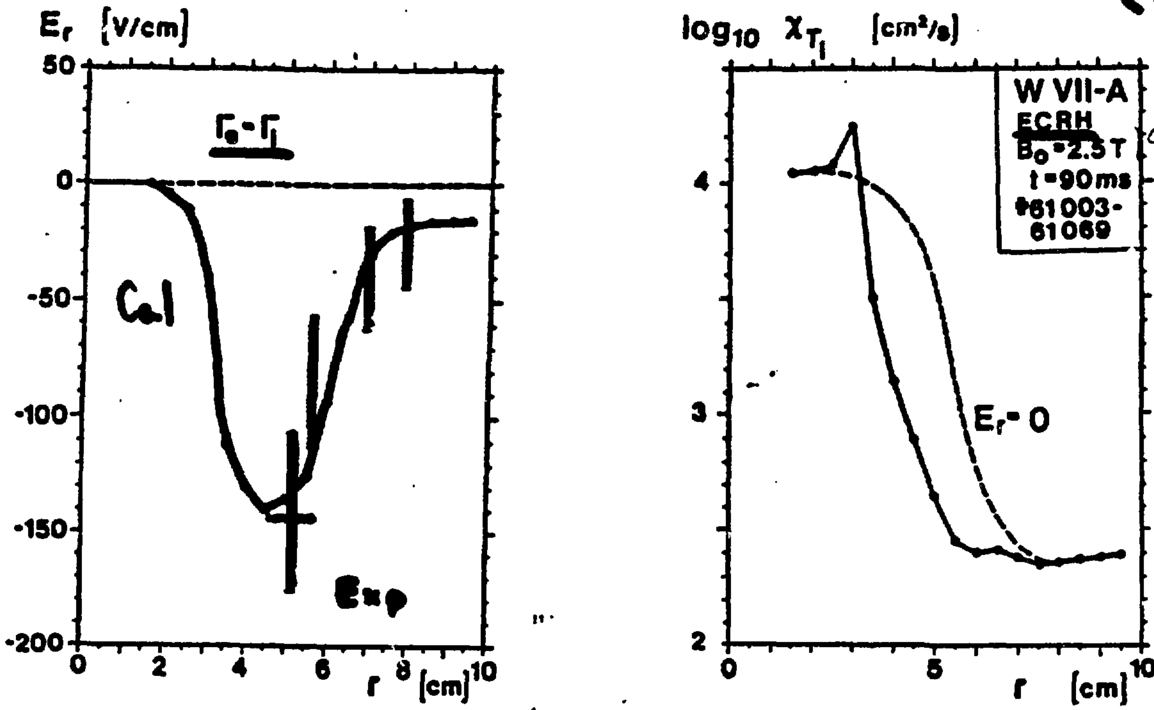

Fig. 10a: Electric field corresponding to measured poloidal rotation by means of Doppler shift at O5, C lines. Comparison to theoretical predictions: $\Gamma_e = \Gamma_i$ (left).
Local ion heat diffusivities and modifications by the calculated electric fields (right).

NBI

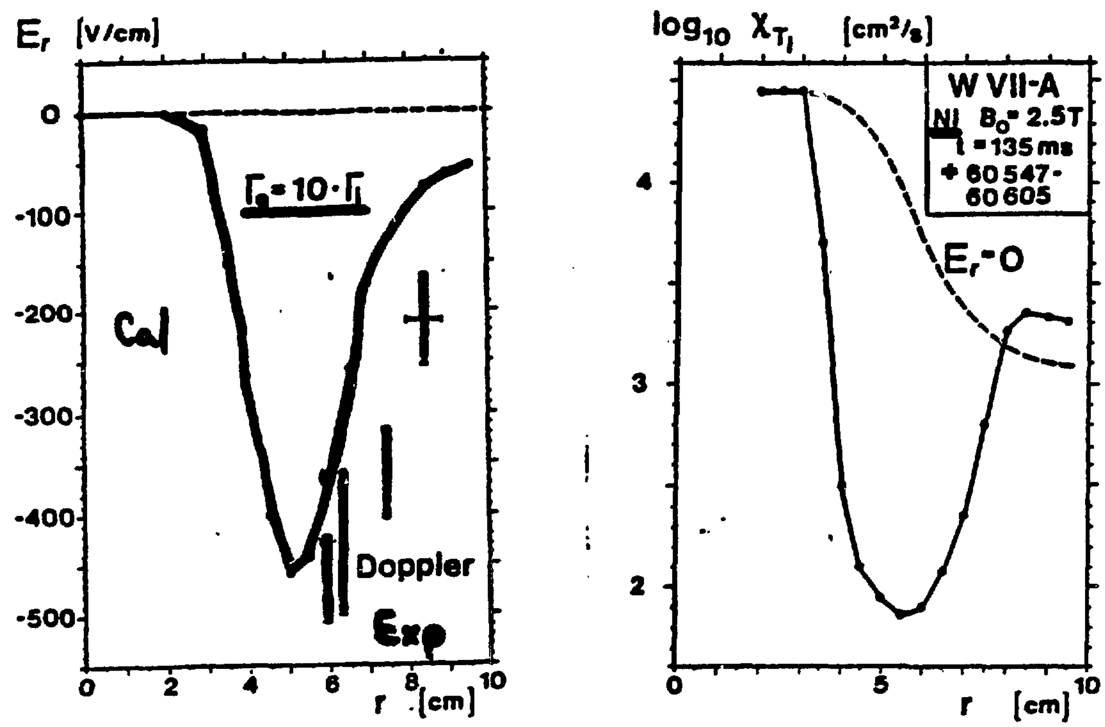

Fig. 11a: Electric fields as derived during NI. To take into account the orbit loss of injected particles, the ion flux has to be enlarged for the fit (left). Local ion heat diffusivities and modifications by the calculated electric fields (right).

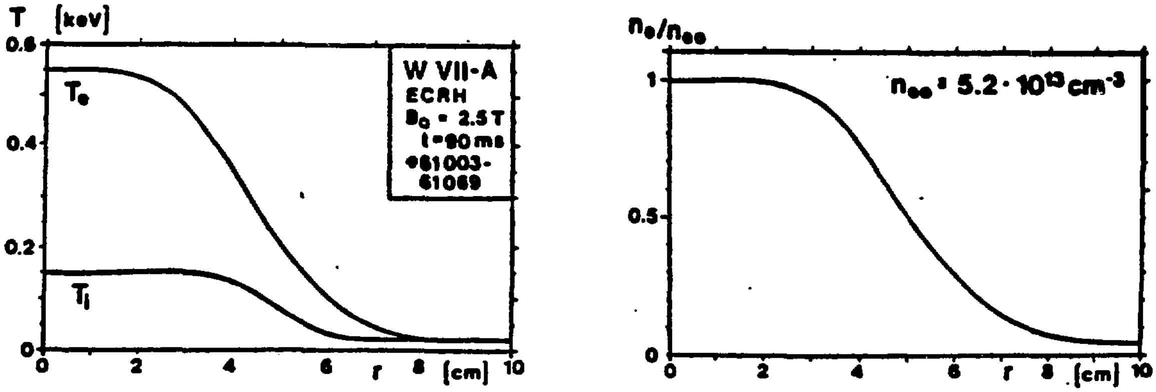

Fig. 10b: Measured temperature and density profiles during ECF heating used for the calculations.

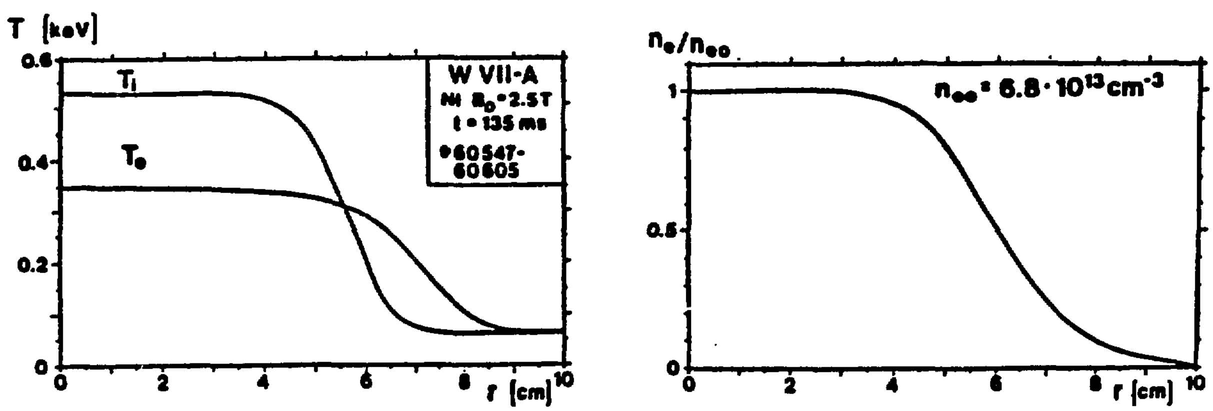

Fig. 11b: Measured temperature and density profiles during ECF heating used for the calculations.

SUMMARIZING

(1) THE ELECTRIC FIELD WAS ESTIMATED FROM V_p AND SURVEYED IN A WIDE RANGE OF COLLISIONALITY OF $0.01 \leq \nu^{e}_{**},\ \nu^{I}_{**} \leq 1$ AT r/a=0.7-0.9.

(2) OBSERVED DEPENDENCE OF E_r ON PLASMA PARAMETERS OF DIFFERENT PLASMAS (ECR, NBI, ICRF) WAS WELL EXPLAINED BY THE AMBIPOLAR ELECTRIC FIELD BASED ON THE NEOCLASSICAL TRANSPORT PROCESS.

(3) THE POWER DEPENDENCE OF V_p WAS NOT OBSERVED (ICRF, AND NBI).

(4) DIRECT (ORBIT) LOSS EFFECT OF THE HIGH ENERGY PARTICLE DID NOT APPEAR EXPLICITLY IN THE NUMERICAL ANALYSIS.

(5) THE ANOMALY TRANSPORT IS DOMINANT IN THIS OBSERVED REGION. (W-VIIA)

Status of the Heavy Ion Beam Probe for ATF

A. Carnevali

S. Aceto

K. Connor

J. Lewis

Rensselaer Polytechnic Institute

J. Glowienka

D. Shipley

Oak Ridge National Laboratory

OUTLINE

- Motivation
- Basic Principles of HIBP
- HIBP for ATF
- Expected Measurement Capabilities
- Calibration Issues
- Schedule.

MOTIVATION

NEOCLASSICAL THEORY PREDICTS THAT RADIAL ELECTRIC FIELDS OF EITHER POLARITY REDUCE HELICAL RIPPLE LOSS, THEREBY IMPROVE CONFINEMENT

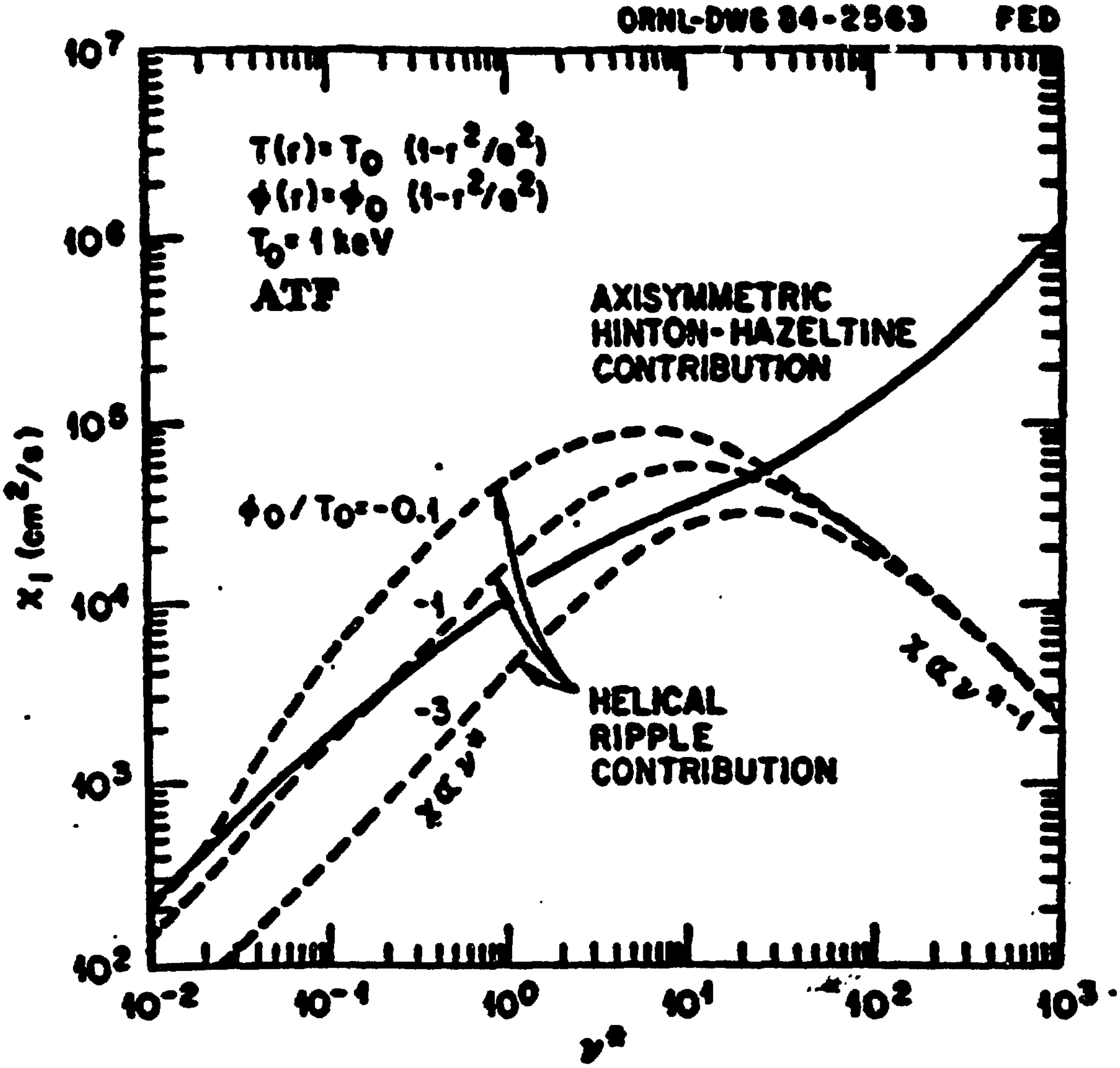

- Electric potential measured with HIBP (*with RPI*)

- Control of potential with:
  - Momentum inputs from opposing tangential beams (as in ISX-B)
  - Overlapping ECH and NBI (?) (as in H-E and W7A)

am 87-055

MOTIVATION

THE BETA SELF-STABILIZATION IS PREDICTED TO REDUCE TURBULENT FLUCTUATIONS

--- and improve confinement

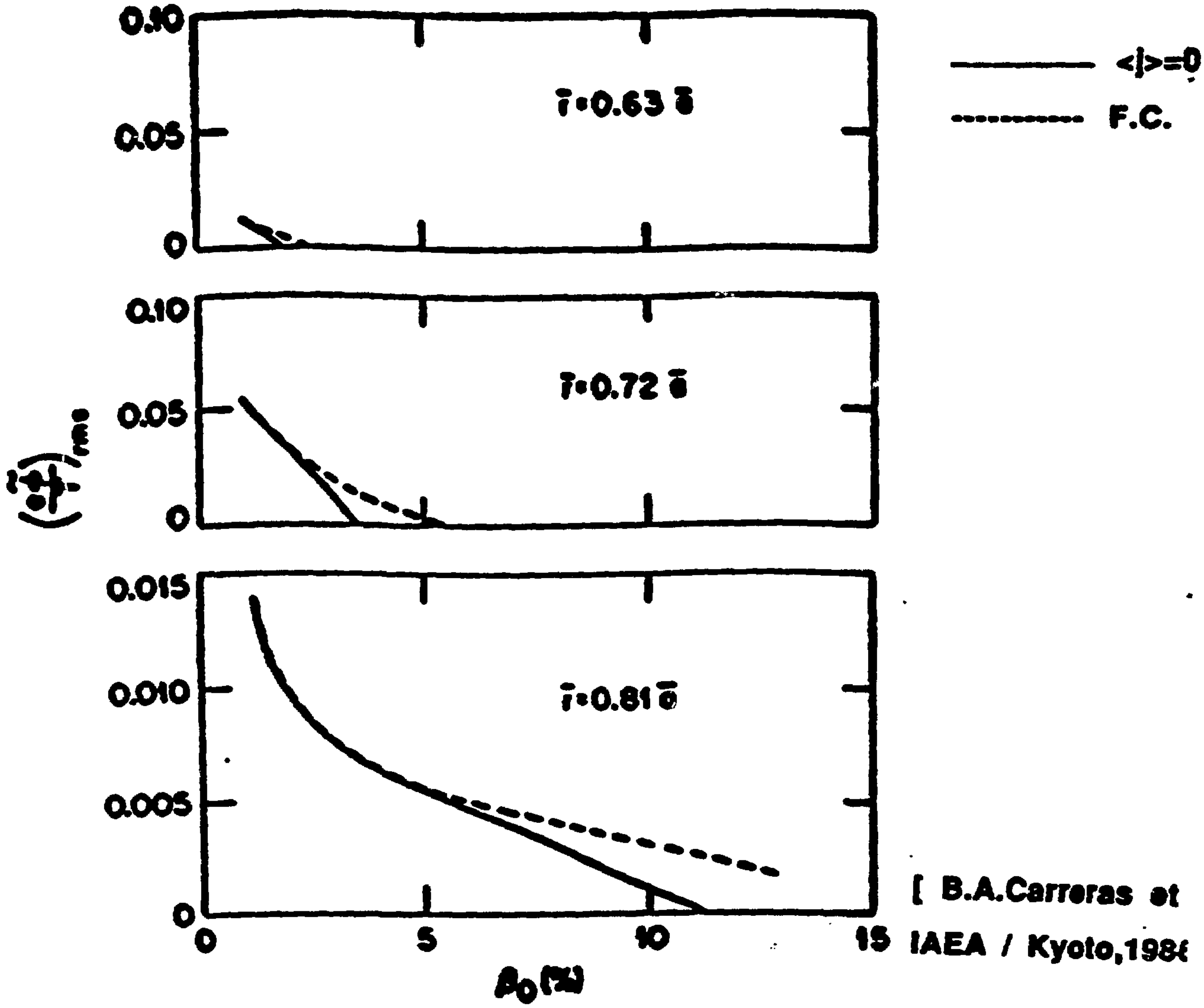

[B.A.Carreras et al. IAEA / Kyoto,1986

- The nonlinear model for resistive ∇p - driven instabilities (higher m,n) predicts flucuation levels.

- Variations of the turbulent fluctuations can be observed by:
  - Microwave reflectometry (with CIEMAT, Madrid)
  - Heavy ion beam probe (with RPI)
  - FIR Scattering
  - Edge Langmuir Probes

87-159

PHYSICAL PRINCIPLE OF THE DIAGNOSTIC TECHNIQUE

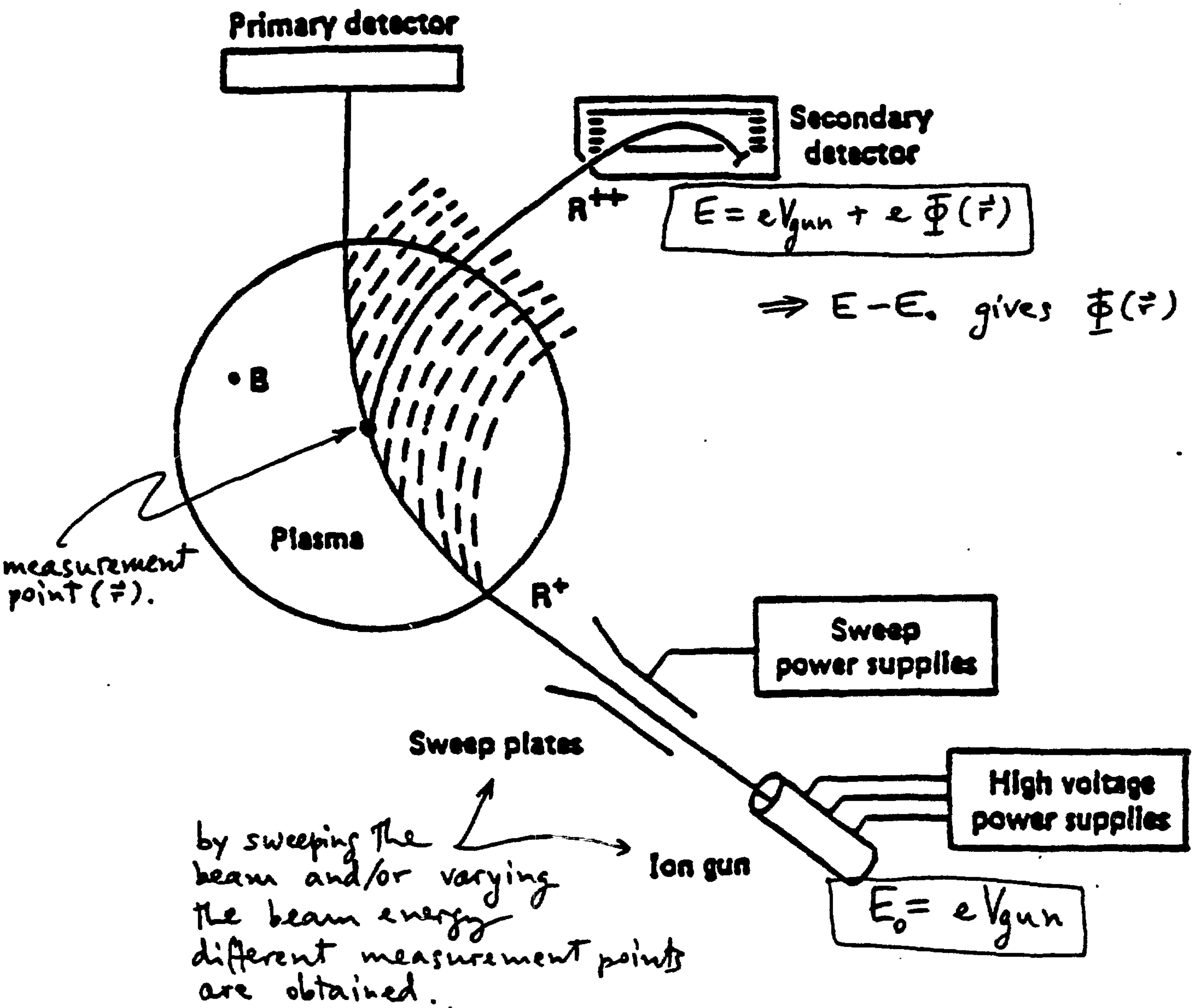

Heavy Ion Beam Probe for the ISX-B

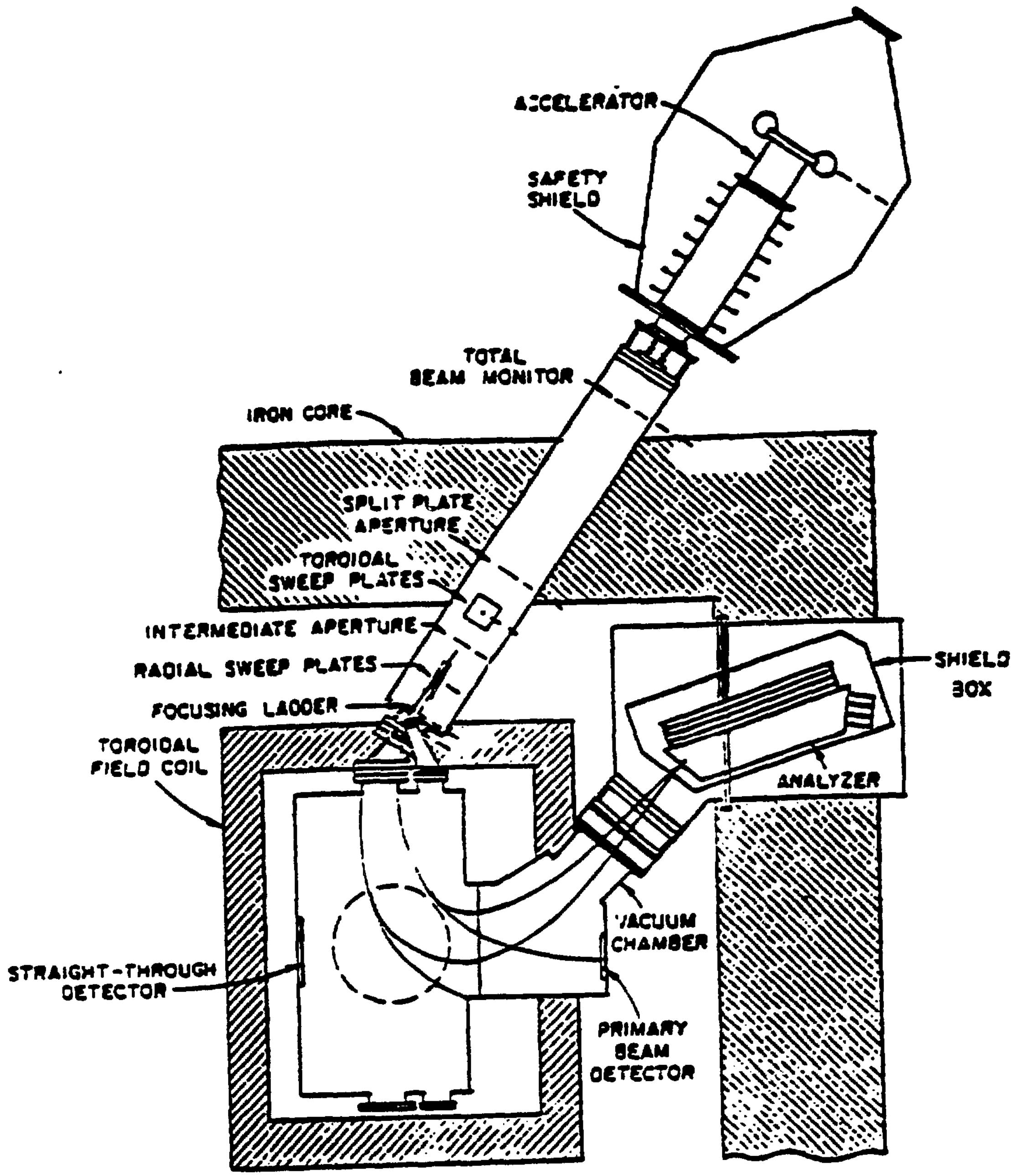

Figure 8. Components of a diagnostic system

HIBP FOR STELLARATORS

The major factors that influence HIBP systems for stellarators:

1. Separation of input and output ports (15° in ATF)

2. Large magnetic field outside coil system
   (~ 500 gauss at beamline and detector for B_0 = 1 Tesla in ATF)

3. Vacuum magnetic field not significantly altered during a plasma discharge.

Major Consequences:

1. Fully 3-dimensional trajectory simulations are required.

2. System can be calibrated without a plasma.

ATF PLAN VIEW

showing the location of the HIBP

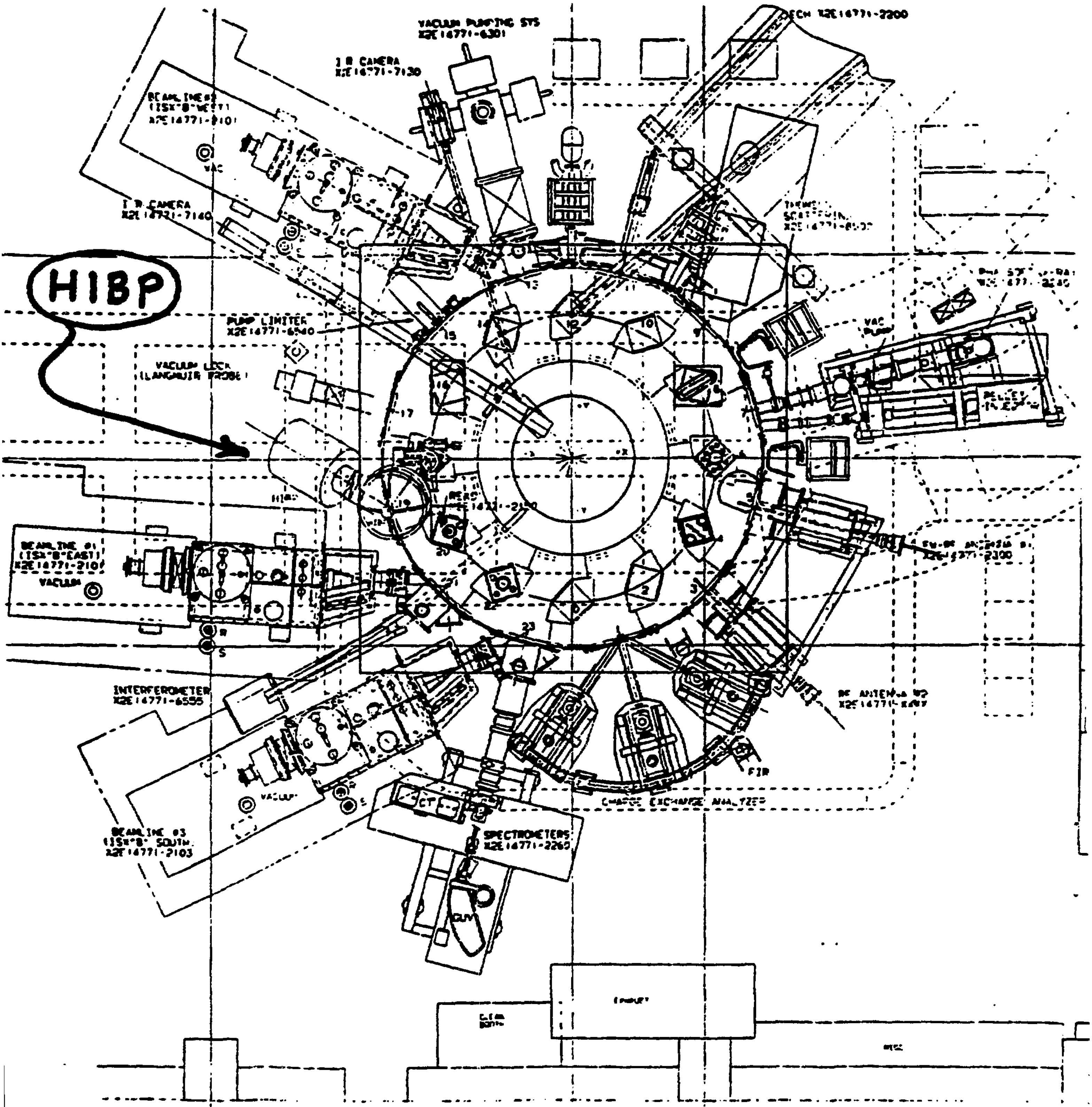

Heavy Ion Beam Probe for the ATF

LAYOUT

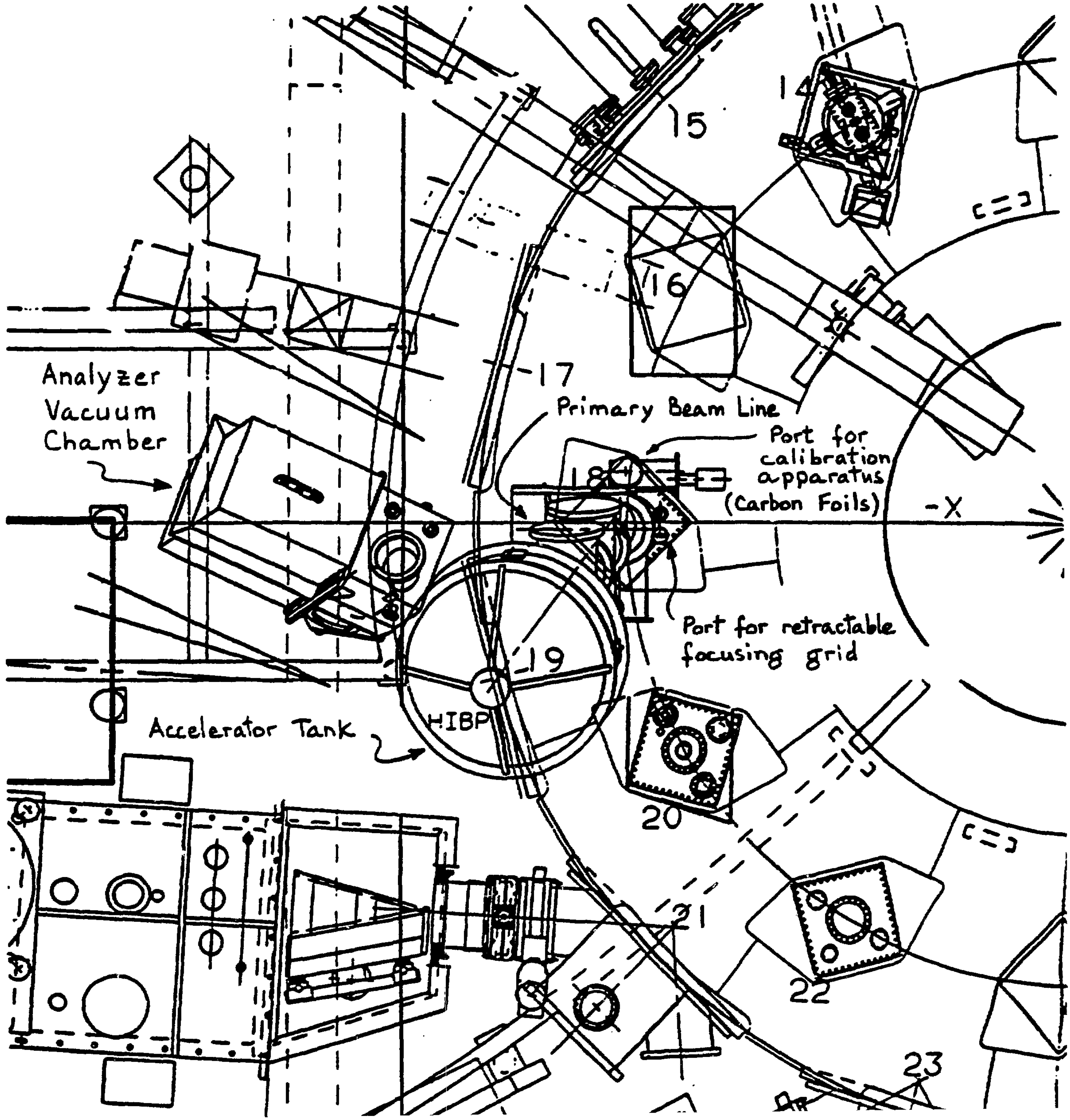

PRIMARY BEAM LINE

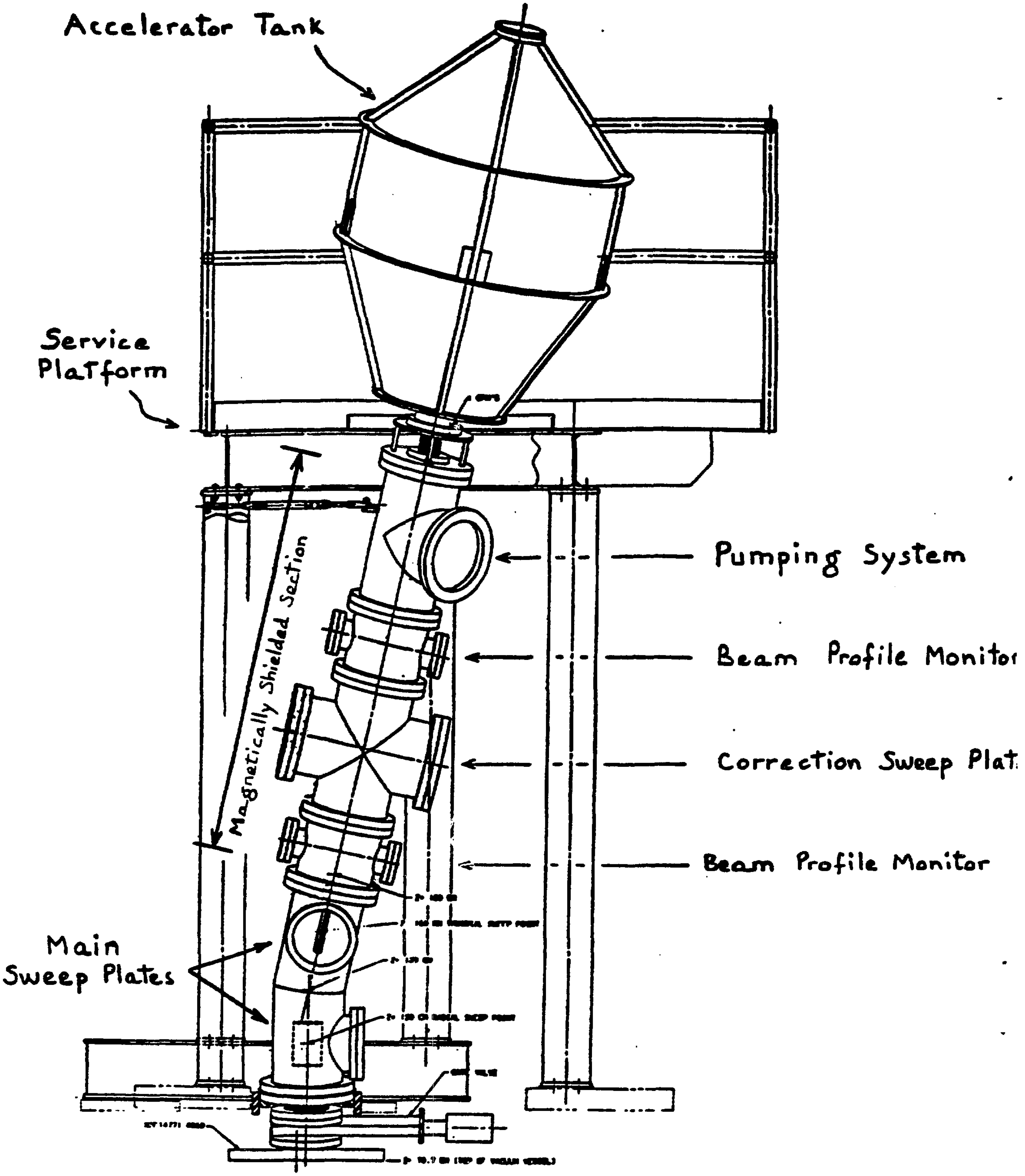

ATF-HIBP Input Port

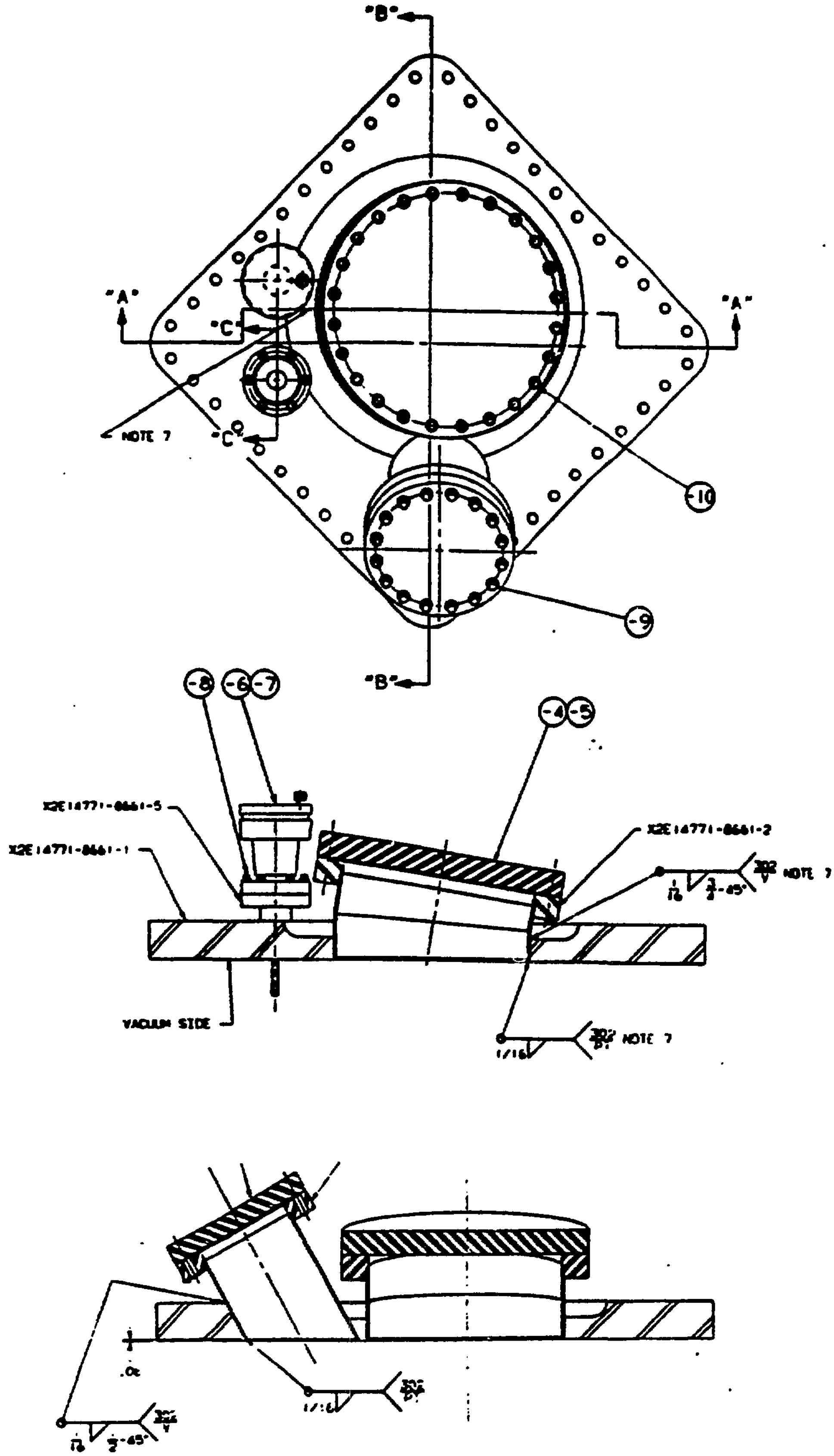

OUTPUT PORT

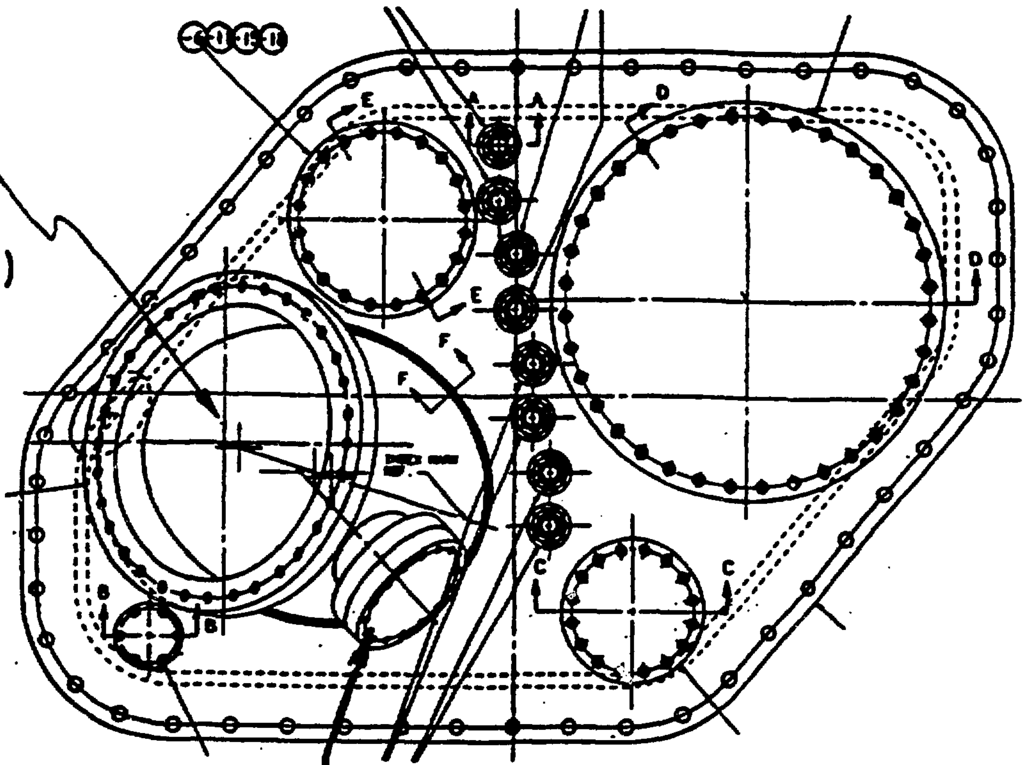
output port for secondary beam ions (to analyzer)
A
A
D
D
E
E
F
F
B
B
C
C
Port for primary beam detector (at E = 85 keV,

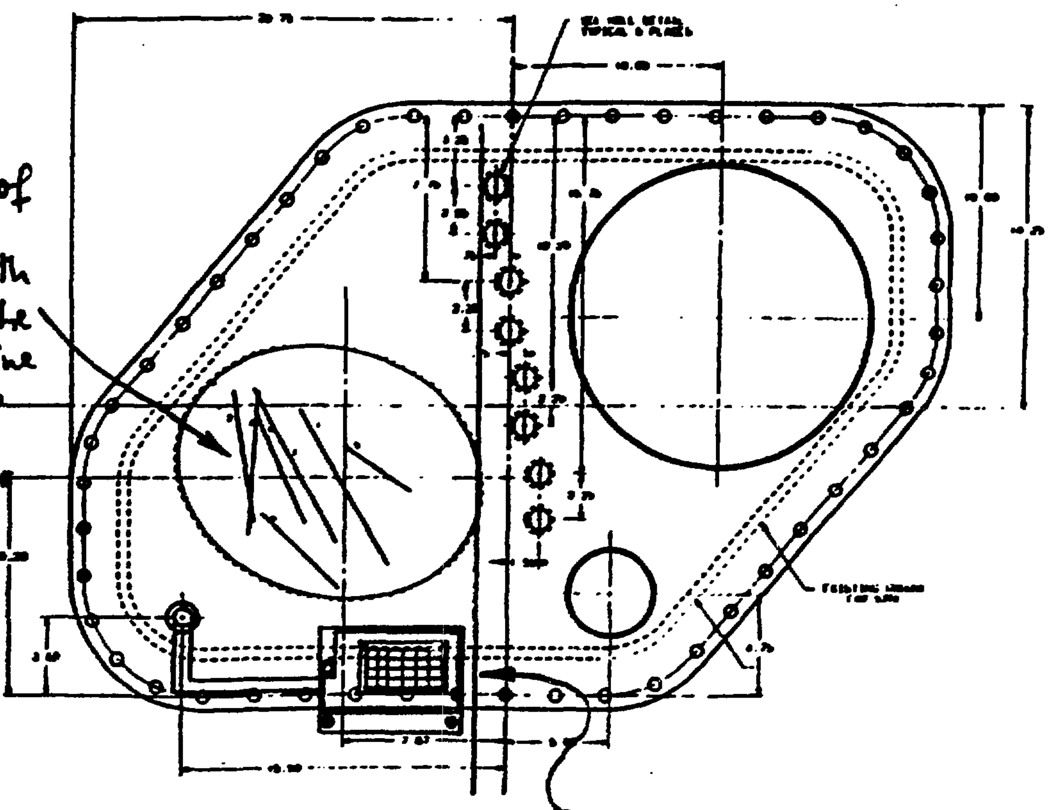
intersections of secondary ion trajectories with the plane of the port. Each line corresponds to a scan line at a particular energy for the standard TF configuration
Primary beam detector (at E = 16
inside vacuum chamber.

Basic Radial Scan. Measurement Points.

B_0 = 1 Tesla   160 KeV $Cs^+ \rightarrow Cs^{++}$

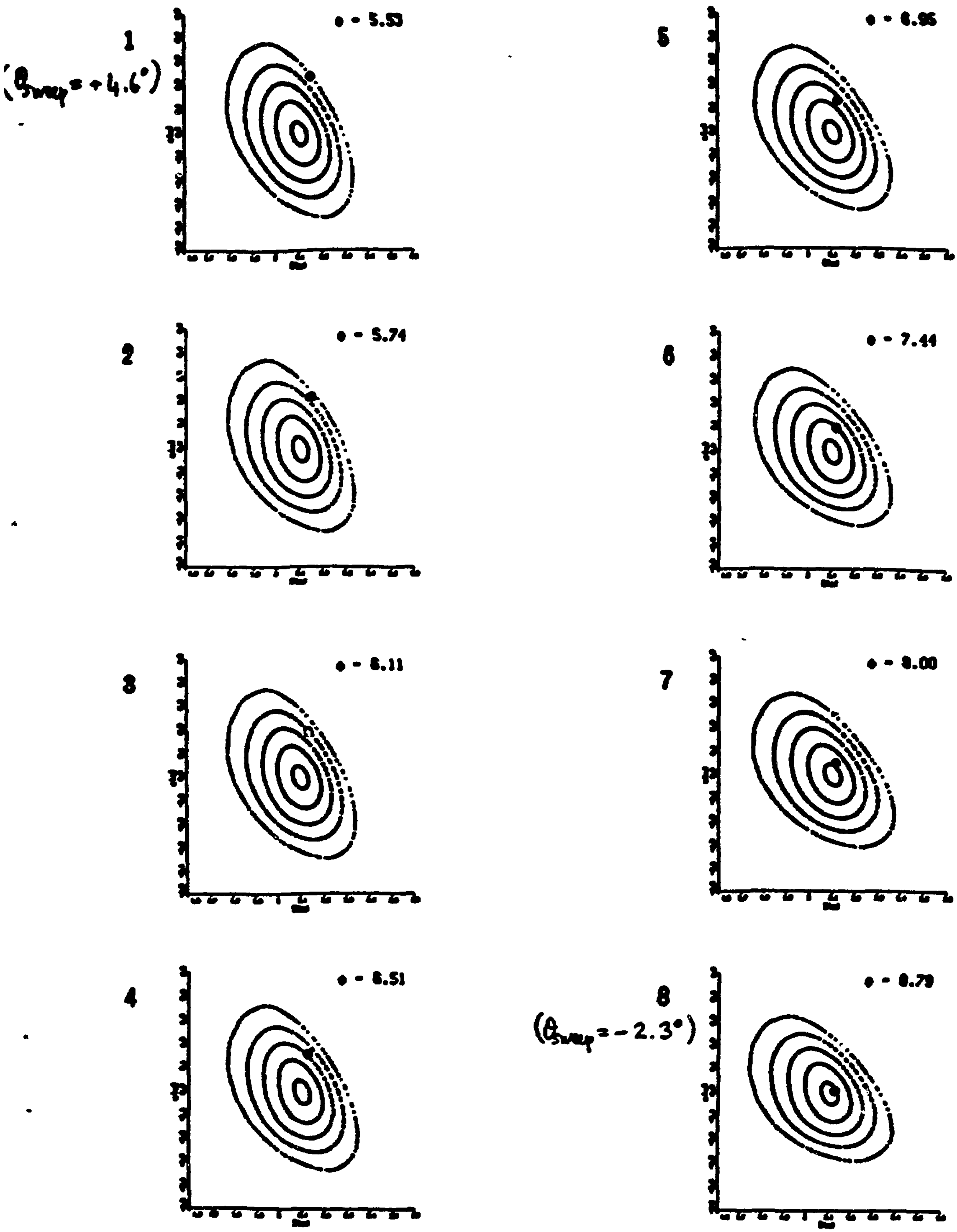

D. K. Lee, Computer Services, ORNL

BASIC RADIAL SCAN

a two-dimensional representation

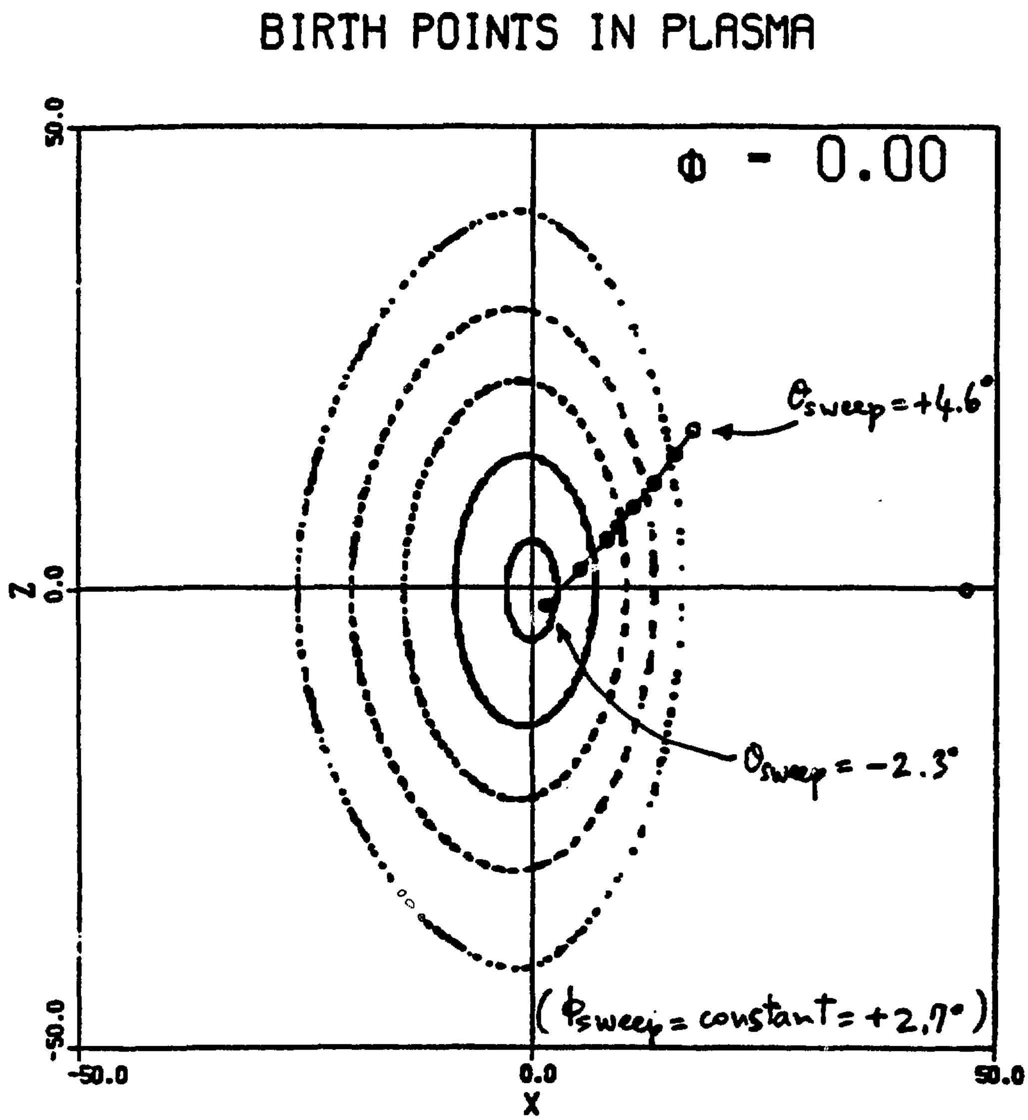

$\theta_s = 4.6°$ probes the plasma periphery ($q = 1$) at a toroidal location $\phi = 5.5°$

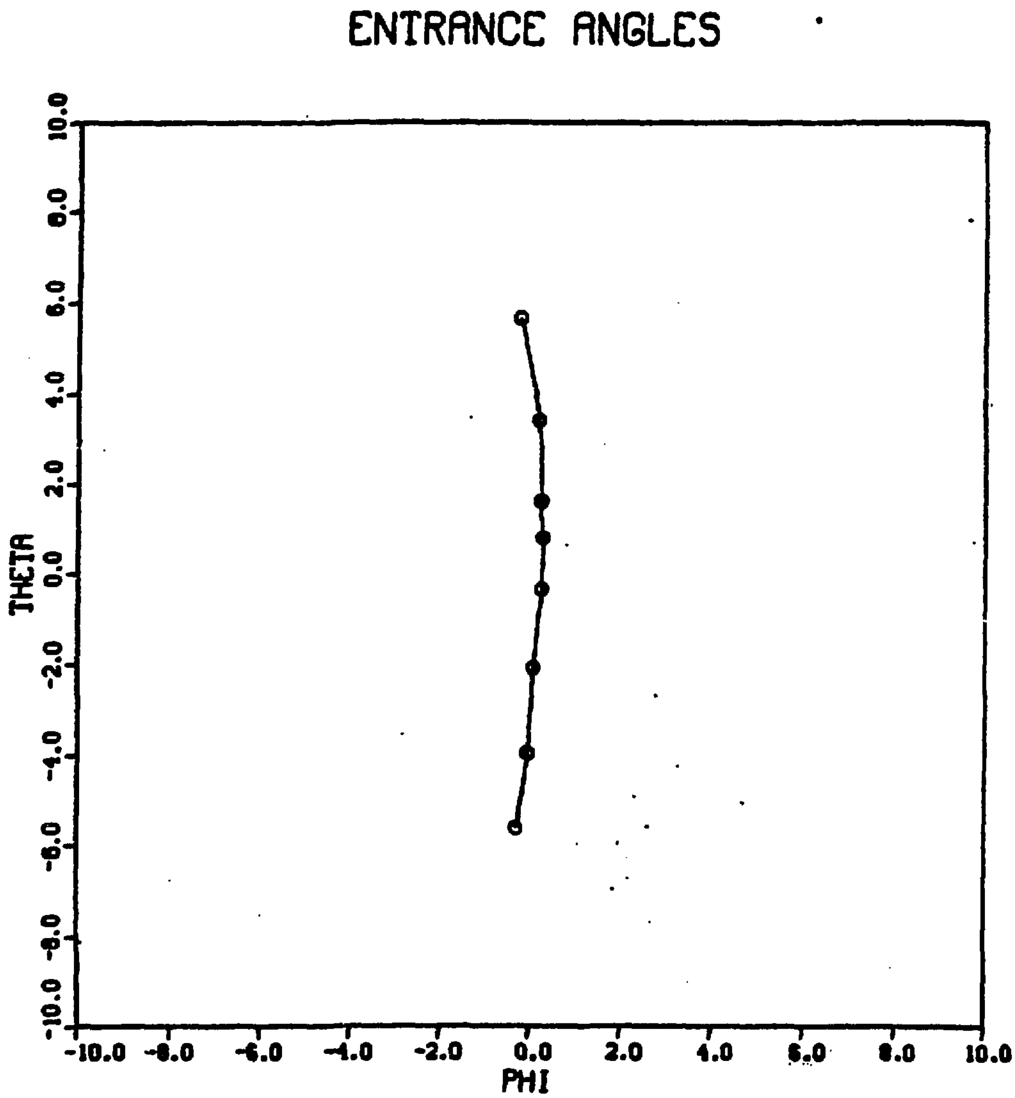

Basic Radial Scan

Ranges in entrance angles:

$\Delta\theta \simeq \pm 5.6^\circ$

$\Delta\phi \simeq \pm 0.3^\circ$

These ranges are acceptable for a standard parallel-plate energy analyzer.

PRIMARY AND SECONDARY ORBITS HAVE CLEAR PATHS INSIDE THE ATF VESSEL

160 KeV, $Cs^{+} \rightarrow Cs^{++}$, $\phi_{sweep} = 2.7°$, $\theta_{sweep} = -4.8°$

(a primary beam detector is located inside the vessel at $\phi = 14°$)

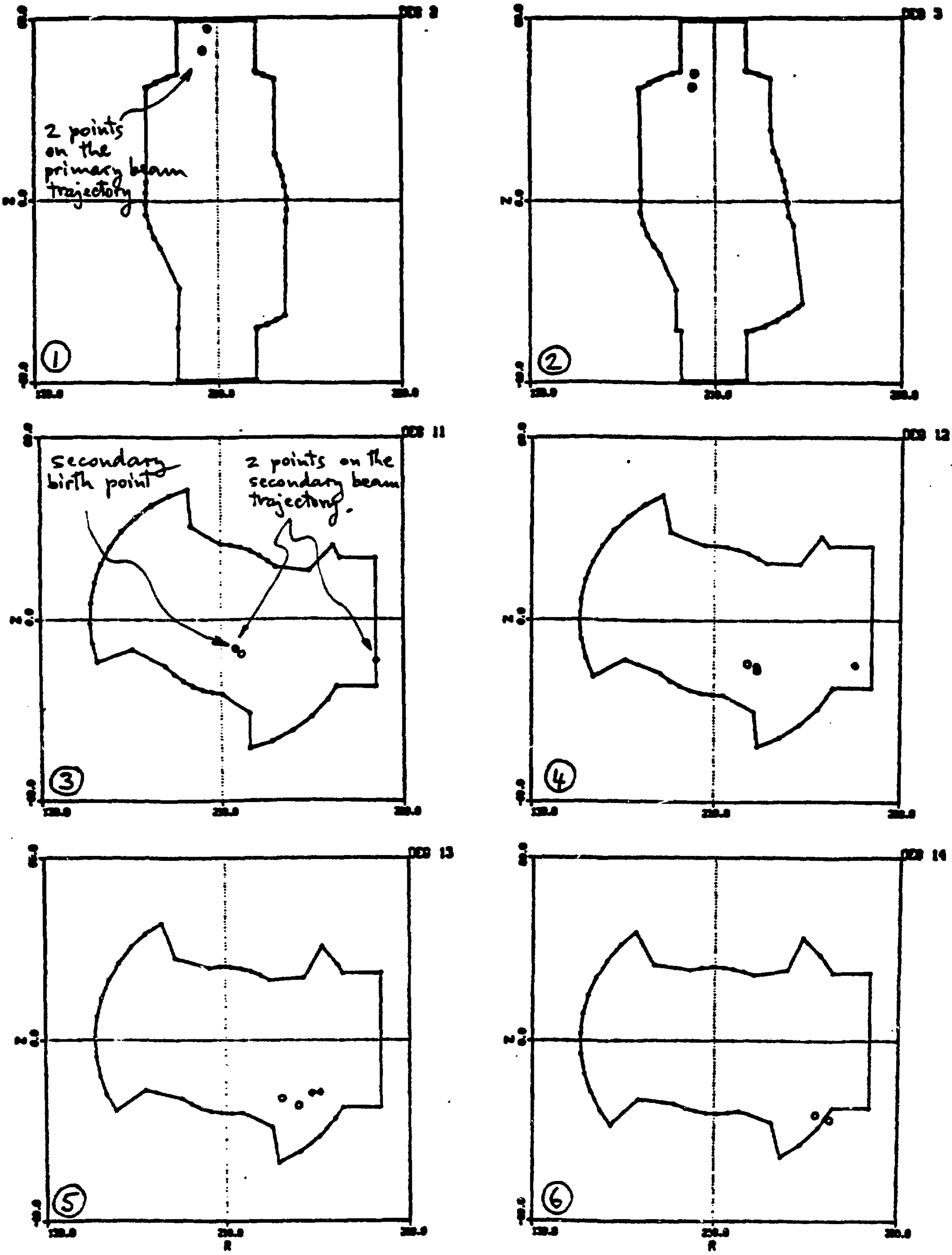

INTERSECTIONS WITH EXIT PORTS

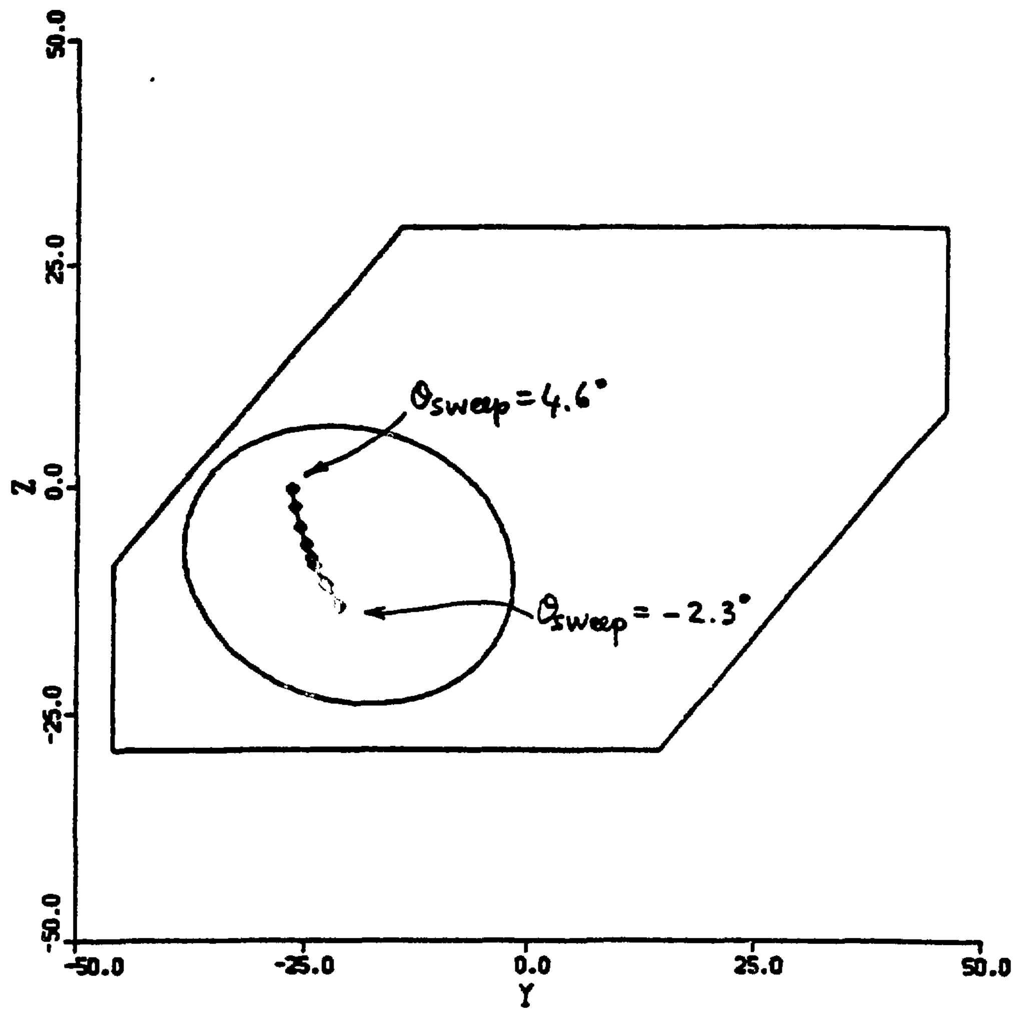

All the secondaries of the basic radial scan have a clear path through the output port

Estimated Effects of E_r on Radial Scan

$\Phi = \Phi_0 \left[1 - \left(\frac{r}{a}\right)^2\right]$ $a = 25$ cm (circular cross section)

$\Phi_0 = -2$ KV

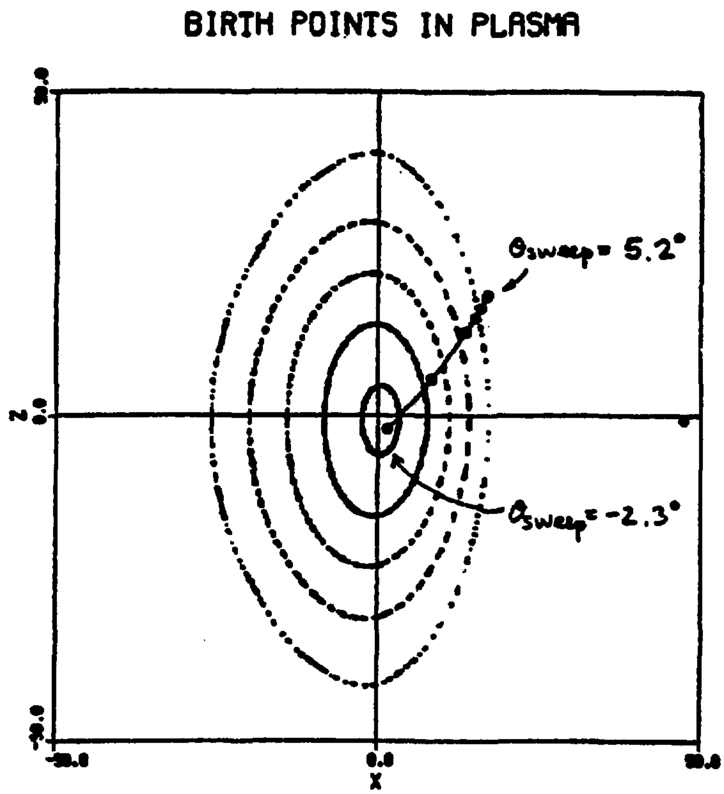

$\Phi_0 = +5$ KV

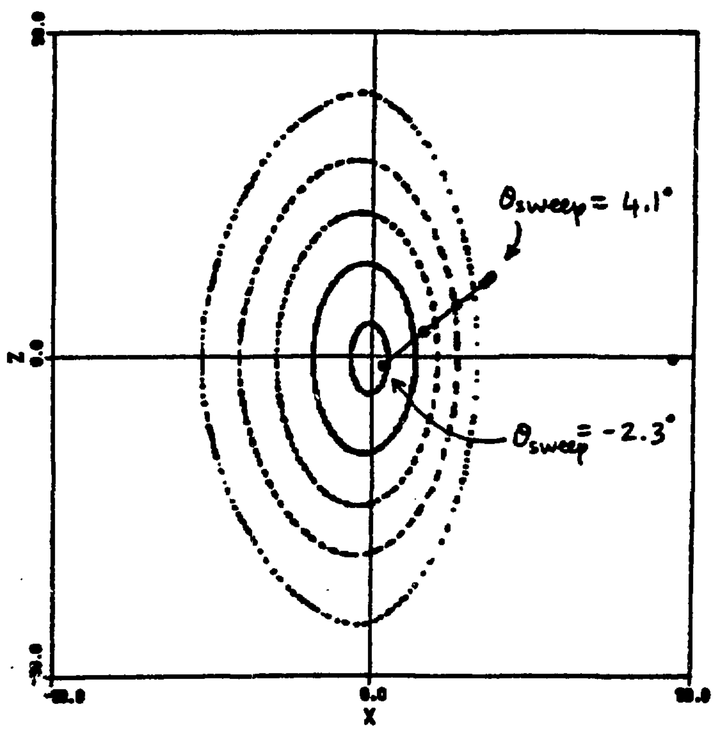

Estimated Effects of E_r and β on Radial Scan (160 KeV)

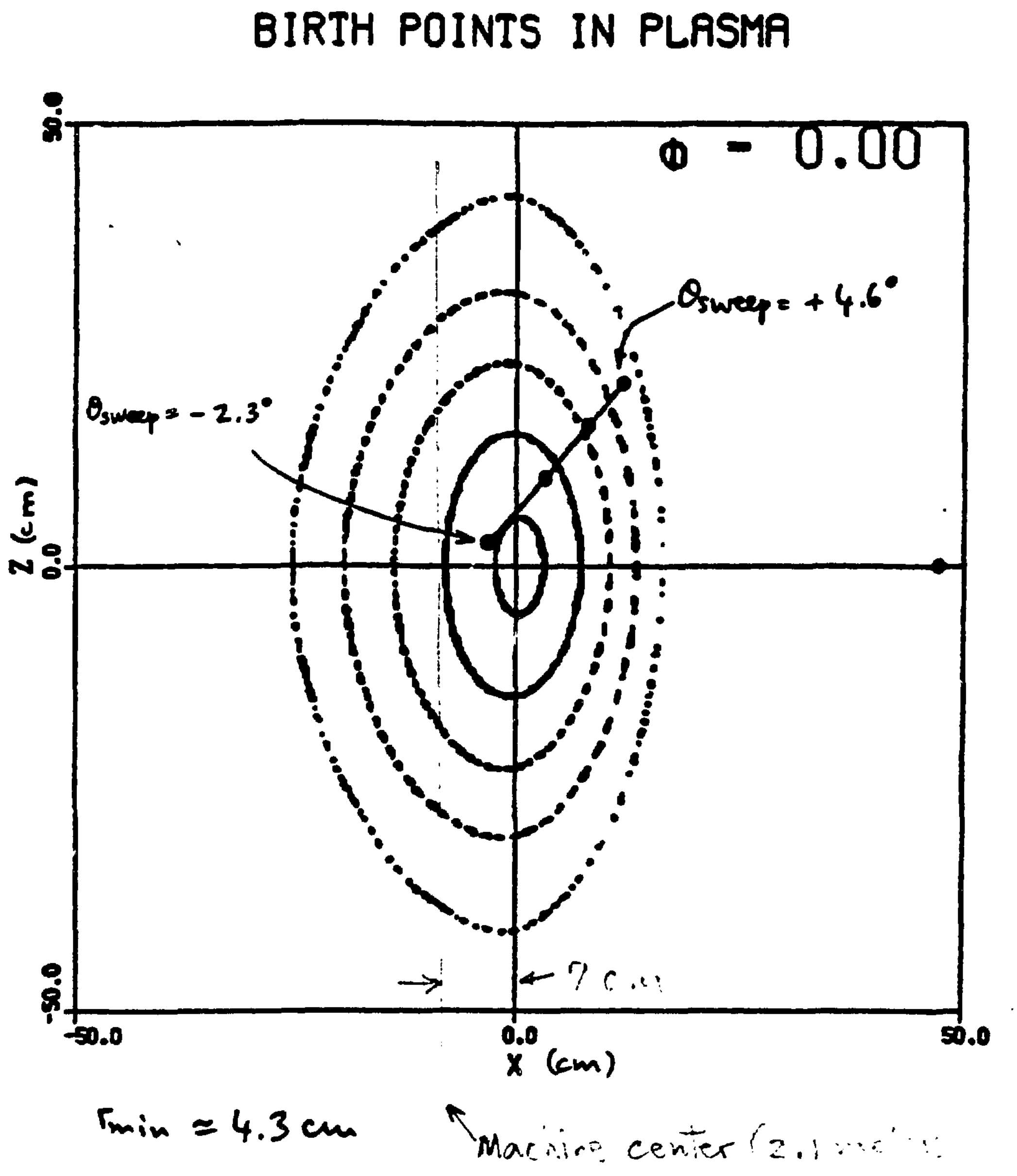

$r_{min} \simeq 4.3$ cm

Φ and β parabolic in r

a = 30 cm. $\Phi_0 = -2$ KV. $\beta_0 = 7$ %

Note: the plasma center can be probed by reducing the beam energy (to ≃ 145 KeV)

Constant Energy Scan Lines

(Standard ATF configuration – No Er and β effects included

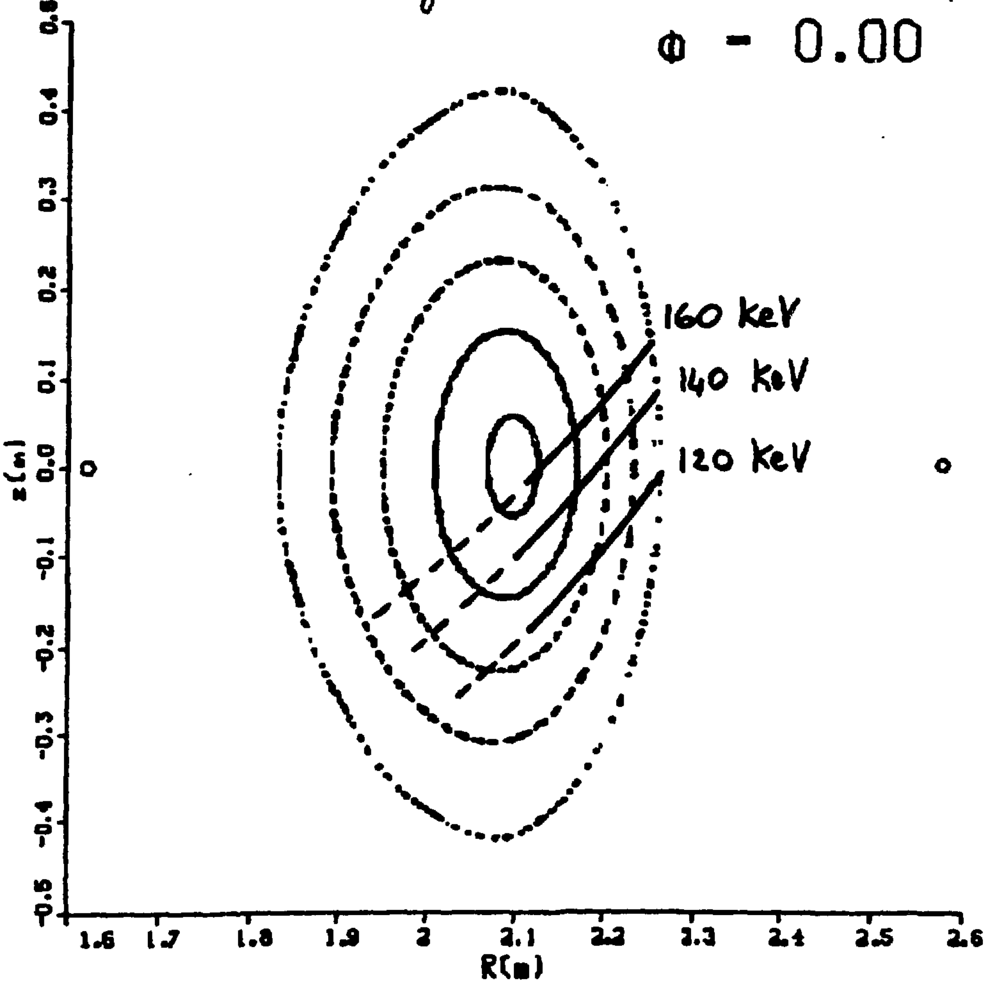

Analyzer motions from location for basic scan

beam energy	slit horiz. width	displacement	rotation	$\Delta\Theta$	$\Delta\phi$
160 KeV	1 cm	-	-	± 5.5°	± 0.3°
140	1.6	7.5 cm	2.8°	± 6°	± 0.4°
120	1.4	13	5.4°	± 5°	± 0.1°
160 * (diam. scan)	4	1.3	2.6°	± 9°	± 2.9°

↑ ↑ spreads in entrance angles

* the spread in entrance angles is too large. the scan may be completed in two shots.

SIMULTANEOUS MULTIPLE-POINT MEASUREMENTS OF PLASMA FLUCTUATIONS

fluctuations in $\tilde{\Phi}$ and $\tilde{n}_e$ are typically measured at the same time. The bandwidth is ≤ 500 kHz

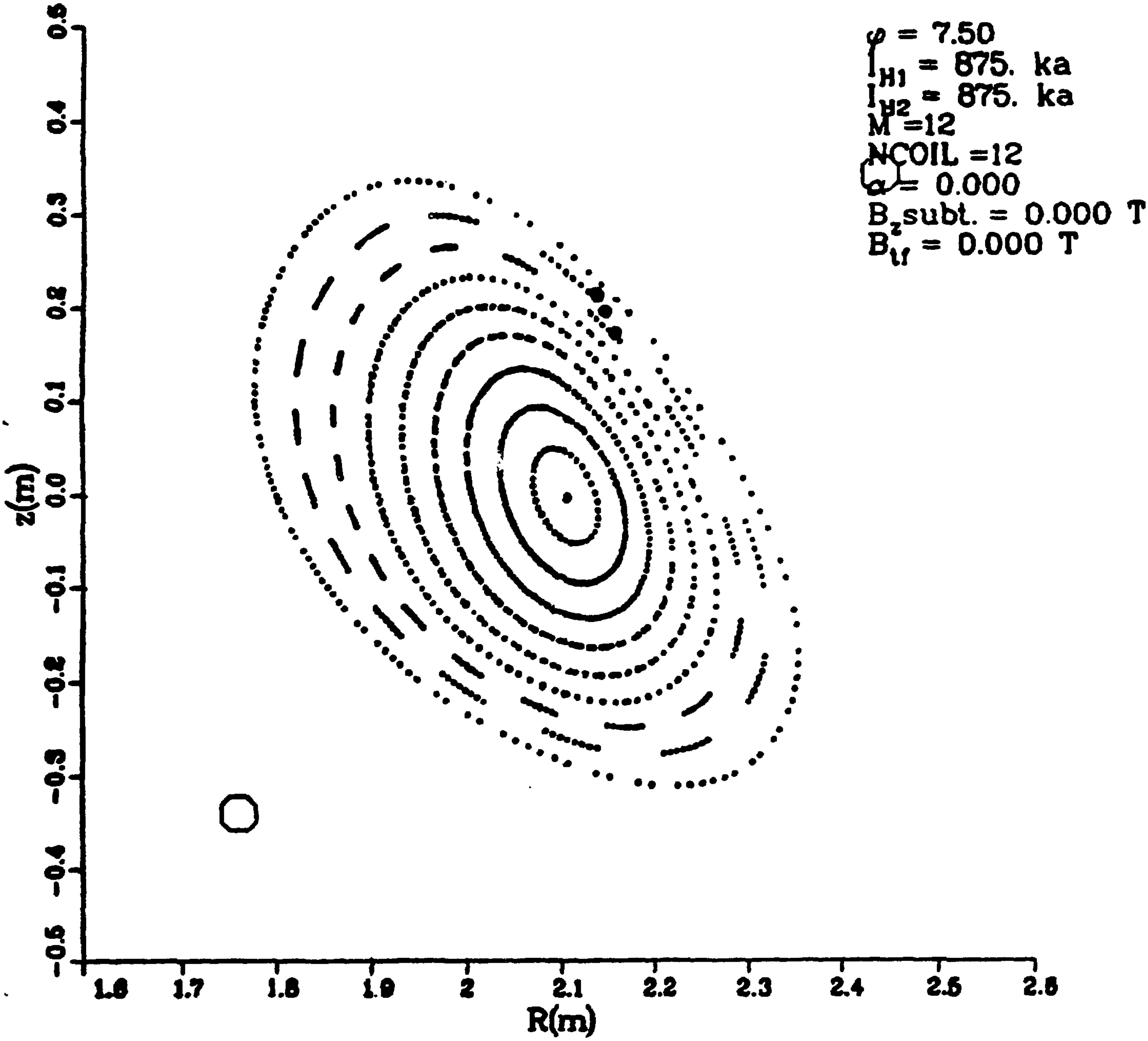

Analyzer with 3 slits, 2 cm apart.

three locations probed near the plasma periphery (E=160 keV, $\theta_s=3^0$).

adjacent locations are 2.7 cm apart, 0.3^0 toroidally

TYPICAL DENSITY POTENTIAL CORRELATION (r=24 cm)

HIBP on TEXT TOKAMAK

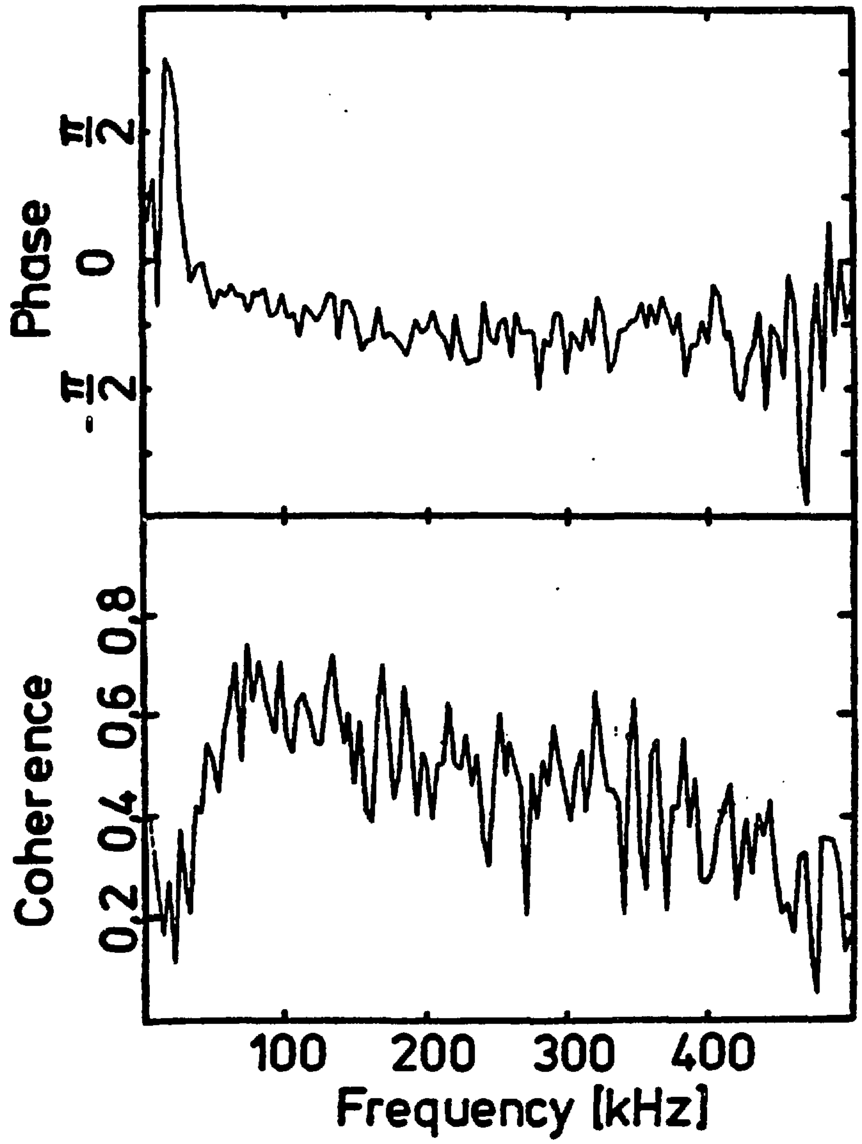

(P.M. Schoch, J.C. Forster, R.L. Hickok)

TRANSPORT

HIBP on TEXT TOKAMAK

$$\Gamma_r(\omega) = \frac{2}{B} k_\theta(\omega) \mid S_{n\phi}(\omega) \mid \sin(\alpha_{n\phi}(\omega))$$

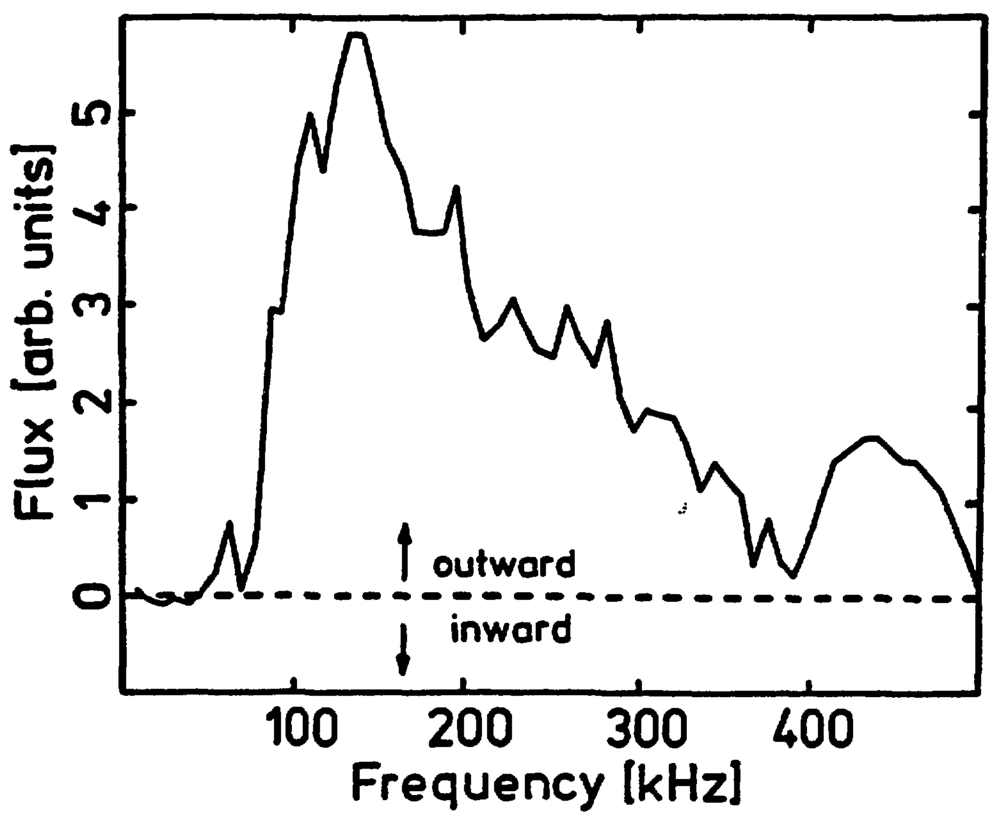

Experimentally Measured Particle Flux

on the TEXT tokamak

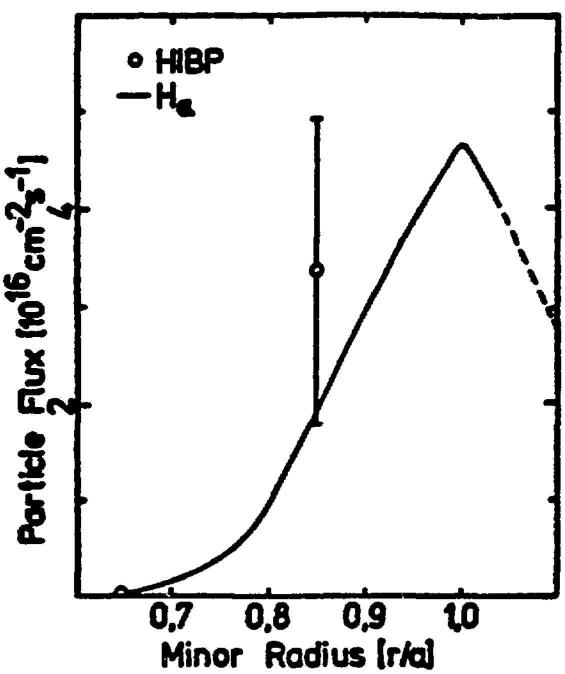

(HIBP data: P.M. Schoch, J.C. Forster, R.L. Hickok)

CARBON FOIL CALIBRATION CONFIGURATION

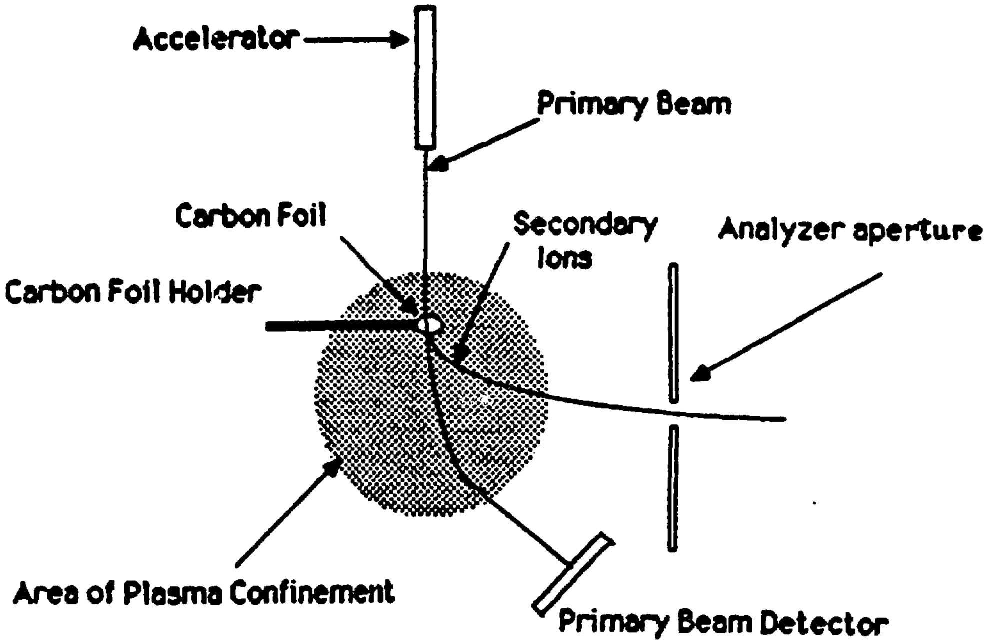

- The carbon foil is a 100 angstrom thick layer of carbon capable of stripping electrons from a sufficiently energetic primary ion beam.

- This layer of carbon is placed on a metal disc approximately 1.5 cm in diameter with a 0.5 cm hole in the center. The foil is supported over the hole by a nickel screen.

During preliminary tests on a high voltage test stand, secondary ion production from a carbon foil was observed using a 128 keV Na^+ beam. $\frac{I_s^{++}}{I_p^{+}}$ was $\sim 80 \frac{nA}{\mu A}$ and $\Delta E \simeq -5.2$ %.

Operation of an HIBP in large $\vec{B}$ fields

- A large section of the primary beam line will be magnetically shielded.
- Computer simulations predict that the stray ATF field in the analyzer will produce only systematic errors.
- An in-situ calibration of the system will be performed using Carbon foils.
- The HIBP on the TARA experiment operates in a comparatively similar stray field. Simulation predictions and in-situ calibration are in good agreement. (G. Hallock, APS '87).

SCHEDULE

- March 88 : begin installation of primary beam line.

- July 88 : begin installation of secondary beam line (analyzer)

- February 89 : initial measurements.